

# **Nickel-Catalyzed Cross-Electrophile Coupling: Methodology**

## **Development and Mechanistic Insights**

By

Zhi-Ming Su

A dissertation submitted in partial fulfillment of

the requirements for the degree of

Doctor of Philosophy

(Chemistry)

at the

UNIVERSITY OF WISCONSIN-MADISON

2024

Date of Final Oral Examination: 7/2/2024

The dissertation is approved by the following members of the Final Oral Committee:

Shannon S. Stahl, Professor, Chemistry

Daniel J. Weix, Professor, Chemistry

Marcel Schreier, Assistant Professor, Engineering

Zachary K. Wickens, Assistant Professor, Chemistry

# Nickel-Catalyzed Cross-Electrophile Coupling: Methodology

## Development and Mechanistic Insights

Zhi-Ming Su

Under the supervision of Professor Shannon S. Stahl

At the University of Wisconsin-Madison

### Abstract

Transition metal-catalyzed coupling reactions are the predominant methods for carbon-carbon bond formation in synthetic chemistry. Nickel-catalyzed cross-electrophile coupling (XEC) reactions have emerged as a promising alternative to conventional cross-coupling strategies that employ organometallic nucleophiles as coupling partners. Ni-catalyzed XEC reactions feature the direct coupling of two electrophiles enabled by Ni-catalysis that requires a stoichiometric source of electrons from chemical reductants or electroreduction. This strategy offers several benefits, such as the utilization of stable and widely available carbon electrophiles, operational simplicity, and great functional group tolerance. Consequently, notable advancements in Ni-catalyzed XEC reactions have been achieved over the past decades. This thesis describes the efforts towards the development, mechanistic understanding, and application of Ni-catalyzed XEC methods.

Chapter 1 provides a high-level overview of Ni-catalyzed XEC reactions, including their first disclosures, development, and current state of the art. Reaction mechanisms and strategies for achieving cross-selectivity in Ni-catalyzed XEC reactions are also discussed.

Chapter 2 discloses an electrochemical method that converts lignin-derived aromatic compounds into a collective of substituted biphenyl-4,4'-dicarboxylic acid (BPDA) derivatives via Ni- and Ni/Pd-catalyzed XEC. The synergy between chemical and electrochemical conditions is highlighted, showing that high-throughput experimentation with chemical reductants enables rapid

catalyst discovery while electrochemistry improves reaction yields and/or facilitates implementation on larger scale. The resultant BPDA derivatives exhibit improved poly(vinyl chloride) (PVC) plasticizer performance and reduced toxicity relative to a commercial plasticizer.

Chapter 3 describes the application of open-circuit potential measurements to determine the redox potentials of metal reductants in organic solutions. Different organic solvents and reaction additives are shown to significantly impact the thermodynamic potentials of metal reductants. Fundamental insights can be gained through the study of the relationship between reductant redox potentials and critical redox processes in XEC reactions. Finally, Ni-catalyzed XEC of *N*-alkyl-2,4,6-triphenylpyridinium reagents (Katritzky salts) with aryl halides is used to demonstrate how some of the limitations related to using metal reductants can be overcome by highly tunable electrochemical reduction.

Chapter 4 details the development of a general strategy for the XEC of heteroaryl chlorides with aryl bromides via Ni-catalysis. Two sets of reaction conditions (A and B) have been identified to enable the coupling of a variety of heteroaryl chlorides and aryl bromides containing an array of functional groups and steric environments. Condition A is particularly effective for the coupling of 2-chloropyridines with aryl bromides. Mechanistic investigations into condition A suggest a Ni-catalyzed *in situ* aryl-zinc formation, followed by a Ni-catalyzed cross-coupling between aryl-zinc and 2-chloropyridines. Condition B is usually preferred for the XEC of diazaheteroaryl chlorides with aryl bromides. In this case, preliminary studies reveal the synergistic effects of NaI and FeBr<sub>2</sub> to match the relative reactivity of the two coupling partners and achieve high cross-selectivity.

Collectively, the studies presented herein are envisioned to enable the utilization of a broader scope of electrophiles in Ni-catalyzed XEC reactions and facilitate a better mechanistic understanding.

## Acknowledgements

I have been pursuing the journey in Chemistry since almost nine years ago, when I started as a freshman at Nanjing University. The courses provided by the undergraduate program have equipped me with the basic knowledge of chemistry, and the final-year project with Prof. Cheng-Hui Li had been an invaluable experience for me. For the first time, I had the chance to engage in a research project from conceiving the idea and conducting experiments, to data analysis and manuscript writing. I am also grateful for the research experience in the lab of Dr. Shiliang Shi at Shanghai Institute of Organic Chemistry. I was able to work there full-time for the summer, during which I improved my experimental skills and started to develop the research mindset for organic methodology and catalysis. I was fortunate to work with Dr. Wubin Zhang and Dr. Xintuo Yang, both of whom were great mentors and colleagues. I am not nostalgic for those nights of leaving lab near midnight, but I certainly treasured those bike rides back to dorm with my friend through the quiet streets.

My story with UW-Madison began prior to the graduate program. I first landed on Madison in a cold and snowy day during the winter of 2018 and started as a visiting student to live and study here for a whole semester. I had the opportunity to enroll in some of the highest quality classes and conduct research part time in the lab of Prof. John Berry. John welcomed me into his lab even though I could only work very limited hours and might not contribute much, for which I am really thankful. In the afterhours, I had time to hang out with my friends, enjoy the ice cream from Daily Scoop, and go out travelling during the spring break. These experiences, to some extent, have helped me prepare myself for the upcoming years of life in Madison.

My research experience in the Stahl Group, and more broadly in the Department of Chemistry at UW-Madison, has been fulfilling and inspiring. My personal growth and scientific development

would not be possible without the support from an incredible collection of mentors, friends, co-workers, and staff. I would like to first thank my advisor, Prof. Shannon Stahl, for his mentoring throughout my graduate studies. Working with Shannon, I was able to develop some of the most important traits for a researcher, such as attention to detail, open-mindedness, effective communication, and scientific rigor. I have also honed my abilities in experiment design, scientific writing and presentation, and project management, owing to the training received in the past few years. I would like to thank the rest of my committee members as well, namely, Prof. Dan Weix, Prof. Marcel Schreier, and Prof. Zach Wickens, for their guidance and feedback along my way of pursuing the degree. They are all role models that I can emulate.

There are many more individuals in the Stahl lab that I am grateful for having the opportunity to work with. Prof. Fei Wang was an exceptional mentor, introducing me to everything about graduate-level research and showing me what a motivated, talented, and hard-working young chemist looks like. Dr. Jack Twilton contributed a lot to my first project on high-throughput experimentation and data interpretation, and I am always amazed by his synthetic expertise. Dr. Md Asmaul Hoque was another senior member in the group that I could turn to for advice, whether it is setting up an electrochemical reaction or enhancing the visual appeal of a ChemDraw figure. I also had many helpful discussions with Jieru Zhu about troubleshooting experimental issues and deciphering CV results, often pointing me in a direction that I had not thought about before. While my interactions with other group members were not frequent, I truly appreciate the friendly and positive environment in the Stahl lab, made possible by contributions from everyone.

I was fortunate to have many great project collaborators over the years. I need to start by acknowledging Prof. Dan Weix and his group members for their indispensable help in nearly all my research projects. Dan consistently provided constructive feedback whenever we had the

chance to discuss science. Dr. Kai Kang, Dr. Nate Loud, Dr. Marrena Franke, and Ben Chi are all gracious individuals who always responded promptly when I sought research suggestions or needed to borrow chemicals from their lab. I am also grateful for the opportunity of working with Kaitlyn Michael from the Jin Group, Dr. Caroline Hoyt from the Beckham Group and Dr. Mihai Popescu from the Paton Group, all of whom were essential contributors to our projects and introduced me to expertise in other disciplines of chemistry, such as materials science and computational chemistry.

It was a privilege for me to work in a department with support from an incredible group of staff and access to a variety of instruments and facilities. I would like to thank Dr. Martha Vestling in the Mass Spectrometer Center, Dr. Heike Hoffstetter in the NMR facility, Tracy Drier in the glass shop, Steve Myers in the machine shop, and many others for their outstanding assistance in my research. I have also enjoyed those regular seminars held in the department, which have enriched my understanding of different research areas of chemistry and broadened my exposure to different viewpoints.

I am not a sociable or emotionally expressive person, meaning that it could be difficult for me to be friends with others, and vice versa; however, I am lucky to be able to forge close friendships with a couple of individuals here at Madison. Jieru Zhu and Dr. Qijun Zhang helped me get through some difficult times along the way, and always welcomed me to have hotpots and play board games over their apartment. Dr. Si-Jie Chen and I only overlapped for approximately two years in the group, but we have remained actively connected after his graduation. He has influenced me in cultivating my own research taste, as well as introduced me to several nice little restaurants around campus. Hiking, dinner parties, meteor shower watching, and adventures of chasing the Northern lights were some of the most unforgettable experiences that I shared with my friends.

There are also important individuals that I met long before I came to Madison. I couldn't be more grateful for Yixin Zhang and everything she has done. Despite us being in different cities and even on different continents for most of the time, her support and companionship have meant the world to me. I owe much of my personal growth to her influence, and I am committed to always striving to be a healthy, self-reflective, and genuine person.

Lastly, but certainly, not least, I would like to thank my family for being there for me since I was a little kid. My mother has always cared for me and made sure that I feel warm and comfortable every time I come back home. My father ensured that my academic needs were fulfilled and taught me to the best of his abilities. I was only able to visit them twice in the past several years due to all the restrictions and challenges associated with travelling during the pandemics, but those video calls still enabled us to connect and pass along the messages of care and support.

I dedicate this thesis to my family.

## Table of Contents

Abstract .....	i
Acknowledgements .....	iii
Table of Contents .....	vii
List of Figures .....	xi
List of Tables .....	xxi
Abbreviations and Acronyms.....	xxiv
<b>Chapter 1. An Overview of Nickel-Catalyzed Cross-Electrophile Coupling .....</b>	<b>1</b>
1.1. Introduction.....	2
1.2. Early Development of Nickel-Mediated Reductive Coupling.....	3
1.3. Mechanisms of Ni-Catalyzed XEC Reactions .....	6
1.4. Scope of Ni-Catalyzed XEC Reactions .....	8
1.5. General Strategies for Achieving Cross-Selectivity in Ni-Catalyzed XEC Reactions .	17
1.6. Concluding Remarks.....	29
1.7. References .....	30
<b>Chapter 2. Ni- and Ni/Pd-Catalyzed Reductive Coupling of Lignin-Derived Aromatics to Access Biobased Plasticizers .....</b>	<b>37</b>
2.1. Abstract .....	38
2.2. Introduction.....	39
2.3. Results and Discussion.....	42
2.4. Conclusion .....	50
2.5. Acknowledgements .....	51
2.6. Author Contributions .....	51

2.7. Conflicts of Interest.....	52
2.8. References.....	52
<b>Chapter 3. Zinc and Manganese Redox Potentials in Organic Solvents and Their Influence on Nickel-Catalyzed Cross-Electrophile Coupling .....</b>	<b>55</b>
3.1. Abstract.....	56
3.2. Introduction.....	57
3.3. Results and Discussion.....	60
3.4. Conclusion .....	69
3.5. Acknowledgements.....	70
3.6. Author Contributions .....	70
3.7. References.....	70
<b>Chapter 4. Selective Ni-Catalyzed Cross-Electrophile Coupling of Heteroaryl Chlorides with Aryl Bromides at 1:1 Substrate Ratio .....</b>	<b>74</b>
4.1. Abstract.....	75
4.2. Introduction.....	76
4.3. Results and Discussion.....	78
4.4. Conclusion .....	88
4.5. Acknowledgments.....	89
4.6. Author Contributions .....	89
4.7. References.....	89
<b>Appendix A. Supporting Information for Chapter 2 .....</b>	<b>92</b>
2A.I. General Experimental Considerations .....	92
2A.II. General Procedure for Aryl Sulfonate Esters Syntheses (GP 1) .....	94

2A.III. General Procedures for Bulk Electrolysis .....	94
2A.IV. General Procedures for Flow Electrolysis .....	97
2A.V. Optimization of Reaction Conditions.....	100
2A.VI. Cyclic Voltammetry Studies .....	113
2A.VII. Plasticizers .....	114
2A.VIII. Compound Characterization Data .....	122
2A.IX. References.....	134
2A.X. NMR Spectra of Compounds .....	135
<b>Appendix B. Supporting Information for Chapter 3.....</b>	<b>156</b>
3B.I. General Experimental Considerations .....	156
3B.II. General Procedure for Open-Circuit Potential (OCP) Measurements.....	159
3B.III. General Procedures for Reductive Coupling of Benzyl Chloride with Iodobenzene .....	164
3B.IV. Synthesis of Substrates.....	168
3B.V. Optimization of Electrochemical Reductive Coupling of Katritzky Salts with Aryl Halides .....	169
3B.VI. General Procedures for Reductive Coupling of Katritzky Salts with Aryl Halides	173
3B.VII. Cyclic Voltammetry Studies.....	177
3B.VIII. Compound Characterization Data .....	180
3B.IX. References .....	189
3B.X. NMR Spectra of Compounds .....	190
<b>Appendix C. Supporting Information for Chapter 4 .....</b>	<b>205</b>
4C.I. General Experimental Considerations .....	205

4C.II. Reaction Optimization .....	206
4C.III. General Procedures for Scope Investigation .....	217
4C.IV. Mechanistic Studies .....	219
4C.V. Compound Characterization Data .....	228
4C.VI. References .....	258
4C.VII. NMR Spectra of Compounds.....	260

**Appendix D. Pairing of Aqueous and Nonaqueous Electrosynthetic Reactions Enabled by a Redox Reservoir Electrode..... 315**

D.I. Abstract.....	316
D.II. Introduction .....	317
D.III. Results and Discussion.....	321
D.IV. Conclusion .....	335
D.V. Acknowledgements .....	336
D.VI. Author Contributions .....	336
D.VII. Supporting Information .....	337
D.VIII. References .....	364

## List of Figures

<b>Figure 1.1.</b> Common features of palladium- and nickel-catalysis. ....	2
<b>Figure 1.2.</b> Early examples of Ni-mediated reductive coupling reactions. (A) Semmelhack reductive biaryl synthesis mediated by stoichiometric nickel(0). (B) Kumada Ni-catalyzed aryl halide homocoupling. (C) Product distribution in Ni-catalyzed electroreductive cross-coupling of two aryl halides. ....	4
<b>Figure 1.3.</b> Early examples of Ni-catalyzed XEC reactions. (A) Electrochemical Ni-catalyzed XEC of aryl halides with activated alkyl electrophiles. (B) Electrochemical Ni-catalyzed XEC of heteroaryl halides with aryl halides. ....	5
<b>Figure 1.4.</b> Mechanistic models for Ni-catalyzed XEC reactions. (A) Sequential oxidative addition mechanism. (B) Radical chain mechanism. ....	7
<b>Figure 1.5.</b> Ni-Catalyzed C( <i>sp</i> <sup>2</sup> )-C( <i>sp</i> <sup>3</sup> ) XEC reactions using metal reductants. (A) Seminal report from Weix and co-workers on XEC of aryl halides with alkyl halides. (B) Representative examples. (C) Ligands used in reactions illustrated in (A) and (B). ....	9
<b>Figure 1.6.</b> Common carbon electrophiles in Ni-catalyzed XEC reactions. ....	10
<b>Figure 1.7.</b> Ni-Catalyzed XEC reactions using non-halide electrophiles. ....	12
<b>Figure 1.8.</b> Ni-Catalyzed enantioselective XEC reactions. ....	14
<b>Figure 1.9.</b> Ni-Catalyzed C( <i>sp</i> <sup>2</sup> )-C( <i>sp</i> <sup>2</sup> ) and C( <i>sp</i> <sup>3</sup> )-C( <i>sp</i> <sup>3</sup> ) XEC reactions. ....	16
<b>Figure 1.10.</b> Aryl electrophile oxidative addition to nickel(0): rates and influencing factors. ....	17
<b>Figure 1.11.</b> Ni-Catalyzed XEC of heteroaryl chlorides and aryl halides by Lautens and co-workers. ....	18
<b>Figure 1.12.</b> Tuning reactivity of NHP esters by backbone modification. ....	19
<b>Figure 1.13.</b> Tuning reactivity of alkyl mesylates by mesylate-iodide exchange. ....	20
<b>Figure 1.14.</b> Bipyridine/terpyridine dual-ligand system for Ni-catalyzed C( <i>sp</i> <sup>2</sup> )-C( <i>sp</i> <sup>3</sup> ) XEC reaction. ....	21
<b>Figure 1.15.</b> Sevov dual-ligand system for electroreductive Ni-catalyzed C( <i>sp</i> <sup>2</sup> )-C( <i>sp</i> <sup>3</sup> ) coupling. ....	22
<b>Figure 1.16.</b> Baran and Engle dual-ligand system for electroreductive Ni-catalyzed C( <i>sp</i> <sup>3</sup> )-C( <i>sp</i> <sup>3</sup> ) coupling. ....	23
<b>Figure 1.17.</b> Mechanism (A) and application (B) of cobalt co-catalysis in Ni-catalyzed XEC reactions. ....	24

<b>Figure 1.18.</b> Weix Ni/Pd-catalyzed C( <i>sp</i> <sup>2</sup> )–C( <i>sp</i> <sup>2</sup> ) reductive coupling. ....	26
<b>Figure 1.19.</b> Sevov synergistic catalyst/mediator pairings for electroreductive C( <i>sp</i> <sup>2</sup> )–C( <i>sp</i> <sup>3</sup> ) coupling. ....	27
<b>Figure 1.20.</b> AgNP-functionalized cathode enables XEC of NHP esters with alkenyl iodides...	28
<b>Figure 2.1.</b> Summary of this work. ....	38
<b>Figure 2.2.</b> Lignin is an abundant biomass-derived source of aromatics that represent potential precursors to commercially important biaryl-4,4' -dicarboxylates.....	40
<b>Figure 2.3.</b> Precedents relevant to reductive coupling of lignin-derived aryl sulfonates.....	42
<b>Figure 2.4.</b> Ni-catalyzed reductive homocoupling of <b>S–OTf</b> : translating conditions optimized with Zn reductant (A) to electrochemical conditions (B). See Appendix A for full experimental details. <sup>a</sup> Yields are determined by <sup>1</sup> H NMR analysis of the crude reaction mixture using mesitylene as an internal standard, yields shown in parentheses are isolated. <sup>b</sup> 60 °C. <sup>c</sup> DMSO solvent.....	45
<b>Figure 2.5.</b> Ni/Pd-catalyzed reductive cross-coupling of lignin-derived aryl sulfonates. <b>A.</b> HTE optimization of G/S cross-coupling. Left chart: <b>S–OTf</b> : <b>G–OTs</b> = 1:1; right chart: DMSO solvent, <b>S–OTf</b> : <b>G–OTs</b> = 1:1.25. The Hetero:Homo coupling ratio is defined as <b>G–S</b> yield/( <b>G–G</b> yield + <b>S–S</b> yield). <b>B.</b> Optimization of electrochemical Ni/Pd-catalyzed cross-coupling. See Appendix A for full experimental details. <sup>a</sup> Yields determined by UPLC-MS analysis using 1,3,5-trimethoxybenzene as an internal standard, yields shown in parentheses are isolated. <sup>b</sup> RVC cathode. <sup>c</sup> L1 = 4,4' -dPhbp, L2 = dppb (3.6 mol%), DMA instead of DMSO, 60 °C.....	47
<b>Figure 2.6.</b> Thermal analysis of lignin-derived biaryl plasticizers. From left to right: unplasticized PVC, 10 wt% plasticized PVC with DEHP, and 10 wt% plasticized PVC with lignin-derived biaryl plasticizers. ....	50
<b>Figure 3.1.</b> Summary of this work. ....	56
<b>Figure 3.2.</b> Metal reductants in Ni-catalyzed XEC. (A) General depiction of Ni-catalyzed C( <i>sp</i> <sup>2</sup> )–C( <i>sp</i> <sup>3</sup> ) cross-electrophile coupling (XEC) reactions. (B) Selected examples of Ni-catalyzed XEC reactions showing the impact of metal reductants on product yields. (C) Pourbaix diagrams for Zn and Mn in aqueous solution and an illustration of common applications of open-circuit potential/voltage, a technique that could be used to determine the redox potentials of Zn and Mn in organic solvents. (D) Schematic diagram illustrating open-circuit potential measurement of thermodynamic potentials of metal reductants. Dme = 1,2-dimethoxyethane, bpy = 2,2' -bipyridine, dmbpy = 5,5' -dimethyl-2,2' -bipyridine, DMO = dimethyl oxalate, phen = 1,10-phenanthroline, dppf = 1,1' -bis(diphenylphosphino)ferrocene, SHE = standard hydrogen electrode, Fc/Fc <sup>+</sup> = ferrocene/ferrocenium.....	58

- Figure 3.3.** Formal thermodynamic potentials of Zn and Mn. (A) Experimental set-up for open-circuit potential measurements. (B) Solvent effects on the formal thermodynamic potentials of Zn and Mn and the redox potential of  $[\text{Ni}(\text{bpy})_3]\text{Cl}_2$  (<sup>a</sup> see Figure 3B.8). (C) Comparison of the results of chemical and electrochemical Ni/Bubpy-catalyzed coupling of benzyl chloride and phenyl iodide. (D) Additive effects on the formal thermodynamic potentials of Zn and Mn..... 61
- Figure 3.4.** Correlation of Zn and Mn redox potentials with Ni-based redox processes in Ni-catalyzed XEC. (A) Reductive cross-coupling of styrenyl acetate with an alkyl bromide using a Ni/dmbpy catalyst (dmbpy = 5,5'-dimethyl-2,2'-bipyridine). (B) The net cross-coupling of benzyl alcohol with aryl triflate using dimethyl oxalate to activate the alcohol using a Ni/mixed-ligand catalyst system (ligands: phen = 1,10-phenanthroline, dppf = 1,1'-bis(diphenylphosphino)ferrocene). (C) CV analysis of Ni/dmbpy in the absence and presence of the substrate. (D) CV analysis of Ni/dppf/phen in the absence and presence of the substrate. .... 65
- Figure 3.5.** Cross-electrophile coupling reactions of alkyl Katritzky salts with aryl bromides. Reactions were conducted thermochemically with Zn or Mn as the reductant, or electrochemically at varied applied potential. See Appendix B for full experimental details. Yields determined by <sup>1</sup>H NMR spectroscopy; isolated yields are shown in parentheses. <sup>a</sup> LiBr (2 equiv) instead of KPF<sub>6</sub>. <sup>b</sup> Aryl chloride was used instead of aryl bromide. .... 67
- Figure 4.1.** Summary of this work. .... 75
- Figure 4.2.** Heteroaryl-aryl core structures are commonly encountered in bioactive molecules (A). Existing coupling methods typically use Pd-based catalyst, but Ni-catalyzed methods would offer compelling alternatives, if they could overcome selectivity challenges (B). This study targets the development of Ni-catalyzed cross-electrophile coupling methods that are compatible with equimolar substrate ratios (C). .... 77
- Figure 4.3.** Reaction optimization. See Section 4C.II of Appendix C for experimental details. Yields are determined by <sup>1</sup>H NMR spectroscopy of the crude reaction mixture using 1,3,5-trimethoxybenzene as an internal standard. Cross-selectivity ratio reflects <sup>1</sup>H NMR yields of cross-coupled product:(heteroaryl dimer + aryl dimer). (A) Illustration of (adapted) literature conditions and informer library substrates. (B) Optimization of XEC of **1a** with **2b**. (C) Optimization of XEC of **1c** with **2a**. (D) Use informer library to test the generality of the adapted literature condition, condition A, and condition B. <sup>a</sup> Used 10 mol% Ni catalyst and added 30 mol% FeBr<sub>2</sub> when **1** contains more than one nitrogen atom in the ring. <sup>b</sup> 7 mol% Ni catalyst..... 80
- Figure 4.4.** Synthetic scope of heteroaryl chlorides coupling with aryl bromides with conditions A and B. Cross-selectivity ratio reflects <sup>1</sup>H NMR yields of cross-coupled product:(heteroaryl dimer + aryl dimer). See Section 4C.III of Appendix C for experimental details. <sup>a</sup> Used 10 mol% Ni catalyst and added 30 mol% FeBr<sub>2</sub> when **1** contains two or more nitrogen atoms in the ring. <sup>b</sup> **L3** instead of **L6**, 10 mol% Ni catalyst. <sup>c</sup> Added 2 equiv LiCl. .... 83

- Figure 4.5.** Mechanistic studies on reaction condition A. Iodine quenching experiments (A), time-course plot (B), stepwise reactions (C), and proposed mechanism (D) for XEC of **1a** with **2b** under condition A. See Section 4C.IV of Appendix C for experimental details. Yields are determined by  $^1\text{H}$  NMR spectroscopy of the crude reaction mixture using 1,3,5-trimethoxybenzene as an internal standard. .... 86
- Figure 4.6.** Time-course experiments for XEC of **1c** with **2a** or **2a-I** under condition B. See Section 4C.IV of Appendix C for experimental details. Yields are determined by  $^1\text{H}$  NMR spectroscopy of the crude reaction mixture using 1,3,5-trimethoxybenzene as an internal standard..... 88
- Figure 2A.1.** Graphic illustration of the divided cell before (left) and after (right) assembly..... 95
- Figure 2A.2.** Graphic illustration of the undivided cell before (left) and after (right) assembly. 97
- Figure 2A.3.** Graphic illustration of the components of the undivided flow cell reactor. Figure adapted with permission from Ref. , Copyright 2021, *Org. Process Res. Dev.* ..... 98
- Figure 2A.4.** Graphic illustration of the undivided flow cell for 12 mmol (left) and 48 mmol (right) scale-up. .... 100
- Figure 2A.5.** Electrochemical Ni/Pd-catalyzed G/S cross-coupling. Yields were determined by  $^1\text{H}$  NMR spectroscopy using 1,3,5-trimethoxybenzene as the internal standard..... 108
- Figure 2A.6.** CVs of  $\text{NiCl}_2(\text{dme})$  (denoted as Ni, 10 mM) in DMF with different loadings of bpy ligand (denoted as L), with NaBr (0.4 M) as supporting electrolyte, under  $\text{N}_2$  protection, scan rate = 100 mV/s. Each experiment was scanned twice. .... 113
- Figure 2A.7.** CVs of  $\text{NiBr}_2(\text{bpy})_3$  (5 mM) in DMF with different loadings of substrate **G-OMs** (denoted as sub), with LiBr (0.4 M) as supporting electrolyte, under  $\text{N}_2$  protection, scan rate = 20 mV/s.  $\text{NiBr}_2(\text{bpy})_3$  was synthesized according to literature reports for the ease of CV studies..... 113
- Figure 2A.8.** CVs of  $\text{NiCl}_2(\text{dme})$  (4 mM) and DPEPhos (4.8 mM) in DMSO with or without substrate **S-OTf** (8 mM), with LiBr (0.6 M) as supporting electrolyte, under  $\text{N}_2$  protection, scan rate = 20 mV/s. .... 114
- Figure 2A.9.** Thermogravimetric analysis of DEH-BPDA derivatives (**H-H<sup>PL</sup>** through **S-S<sup>PL</sup>**) at a heating rate of 10 °C/min under nitrogen. .... 115
- Figure 2A.10.** Thermogravimetric analysis of PVC with 10 wt% DEH-BPDA derivatives (**H-H<sup>PL</sup>** through **S-S<sup>PL</sup>**) compared with DEHP at a heating rate of 10 °C/min in nitrogen.. 116
- Figure 2A.11.** Differential scanning calorimetry of PVC with 10 wt% DEH-BPDA derivatives (**H-H<sup>PL</sup>** through **S-S<sup>PL</sup>**) compared with DEHP at a heating rate of 10 °C/min in nitrogen. .... 117
- Figure 2A.12.** Predicted metabolic and environmental transformations of plasticizers. .... 118

- Figure 2A.13.** Predicted metabolites from 2-ethylhexanol and diacids. Main metabolic pathways predicted by the EPA Chemical Transformation System. Colors are used to highlight metabolites common to multiple diacids. .... 119
- Figure 3B.1.** Picture of the undivided cell for OCP and CV experiments before (left) and after (right) assembly (working electrode varies based on each experiment, shown is with Zn plate). .... 160
- Figure 3B.2.** A typical trace obtained in OCP measurements (after conversion using the Nernst equation). Conditions: Zn working electrode, 10 mM ZnBr<sub>2</sub>, 0.2 M <sup>n</sup>Bu<sub>4</sub>NPF<sub>6</sub>, DMF. .... 160
- Figure 3B.3.** Chloride concentration effect on Zn reduction potential in DMF. <sup>a</sup> 0.2 M <sup>n</sup>Bu<sub>4</sub>NPF<sub>6</sub> as electrolyte. .... 164
- Figure 3B.4.** Picture of the undivided cell before (left) and after (right) assembly. .... 165
- Figure 3B.5.** Optimization for electrochemical XEC reactions of alkyl Katritzky salt **1** with aryl bromides. Yields were determined by <sup>1</sup>H NMR spectroscopy using 1,3,5-trimethoxybenzene as the internal standard. .... 172
- Figure 3B.6.** Optimization for electrochemical XEC reactions of alkyl Katritzky salt **2** with aryl bromides. Yields were determined by <sup>1</sup>H NMR spectroscopy using 1,3,5-trimethoxybenzene as the internal standard. <sup>a</sup> Current dropped to < 20 μA after 24 h of electrolysis, and the reaction was manually stopped; 2 F/mol of charge was passed. .... 172
- Figure 3B.7.** CVs of metal salts (10 mM) in DMF (5 mL) or MeCN (5 mL), with <sup>n</sup>Bu<sub>4</sub>NPF<sub>6</sub> (0.2 M) as supporting electrolyte, under N<sub>2</sub> atmosphere, at room temperature, scan rate = 20 mV/s, initially scanning towards a more negative potential. .... 177
- Figure 3B.8.** CVs of [Ni(bpy)<sub>3</sub>]Cl<sub>2</sub> (4 mM) in various organic solvents, with <sup>n</sup>Bu<sub>4</sub>NPF<sub>6</sub> (0.1 M) as supporting electrolyte, under N<sub>2</sub> atmosphere, at room temperature, scan rate = 100 mV/s, initially scanning towards a more negative potential. .... 178
- Figure 3B.9.** CVs of Ni/dmbpy catalyst in the presence or absence of substrates for cross-coupling of alkenyl acetate with alkyl bromide. Black trace: Ni catalyst [5 mM NiBr<sub>2</sub>(dme) + 7.5 mM 5,5'-dimethyl-2,2'-bipyridine]. Blue trace: Ni catalyst + 10 equiv 1-phenylvinyl acetate. Green trace: Ni catalyst + 35 equiv ethyl 4-bromobutanoate. Red trace: Ni catalyst + 10 equiv 1-phenylvinyl acetate + 35 equiv ethyl 4-bromobutanoate. All CVs were recorded in DMA (5 mL), with KPF<sub>6</sub> (0.1 M) as supporting electrolyte, under N<sub>2</sub> atmosphere, at 40 °C, scan rate = 20 mV/s, initially scanning towards a more negative potential. .... 179
- Figure 3B.10.** CVs of Ni/dppf/phen catalyst system in the presence or absence of substrates for cross-coupling of benzyl oxalate with aryl triflate. Black trace: Ni catalyst [2.5 mM NiCl<sub>2</sub>(dppf) + 2.5 mM dppf + 0.5 mM 1,10-phenanthroline]. Blue trace: Ni catalyst + 20 equiv benzyl methyl oxalate. Green trace: Ni catalyst + 30 equiv methyl 4-

((trifluoromethyl)sulfonyl)oxy)benzoate. Red trace: Ni catalyst + 20 equiv benzyl methyl oxalate + 30 equiv methyl 4-((trifluoromethyl)sulfonyl)oxy)benzoate. All CVs were recorded in DMF (5 mL), with KPF<sub>6</sub> (0.1 M) as supporting electrolyte, under N<sub>2</sub> atmosphere, at 80 °C, scan rate = 20 mV/s, initially scanning towards a more negative potential. .... 179

**Figure 4C.1.** Ligands used for optimization of conditions A and B. .... 209

**Figure 4C.2.** Time-course studies using only **2b** (A) or only **1a** (B) under condition A. Yields are determined by <sup>1</sup>H NMR spectroscopy of the crude reaction mixture using 1,3,5-trimethoxybenzene as an internal standard. .... 221

**Figure 4C.3.** Reactions of organozinc reagents with substrates or Ni catalyst. Yields are determined by <sup>1</sup>H NMR spectroscopy of the crude reaction mixture using 1,3,5-trimethoxybenzene as an internal standard. Yields of homo-coupled dimers are reported with respect to the stoichiometry of the reaction, i.e., the maximal theoretical yield is 50%. (A) Reactions of **1a** with **2b-Zn** (top) and **1a-Zn** with **2b** (bottom) catalyzed by NiBr<sub>2</sub>(dme)/**L6**. (B) Stoichiometric reactions of **2b-Zn** (top) or **1a-Zn** (bottom) with NiBr<sub>2</sub>(dme)/**L6**. (C) Decoupled aryl-zinc formation/cross-coupling reaction catalyzed by NiBr<sub>2</sub>(dme)/**L6**. .... 224

**Figure 4C.4.** XEC reactions in the presence or absence of 30 mol% FeBr<sub>2</sub>. Yields are determined by <sup>1</sup>H NMR spectroscopy of the crude reaction mixture using 1,3,5-trimethoxybenzene as an internal standard. Yields of homo-coupled dimers are reported with respect to the stoichiometry of the reaction, i.e., the maximal theoretical yield is 50%. <sup>a</sup> Used 10 mol% Ni catalyst in entries 3 and 4. .... 227

**Figure D.1.** Summary of this work. .... 316

**Figure D.2.** Schematic illustration of RR-enabled ModES for paired oxidation of 4-*t*-butyltoluene in methanol and reduction of oxygen to H<sub>2</sub>O<sub>2</sub> in water in comparison to conventional electrolysis processes. (a) Schematic of the BASF paired electrolysis that takes place in methanol where two organic products are synthesized simultaneously at both the cathode and anode. (b) In conventional electrochemical H<sub>2</sub>O<sub>2</sub> production (HPR), the nonproductive OER takes place on the anode to charge balance the cathodic reaction. This process requires a membrane to prevent H<sub>2</sub>O<sub>2</sub> decomposition on the anode. (c) In the ModES process, the anodic and cathodic processes take place in two undivided cells and an RR electrode serves as the counter electrode for the process of interest, storing ions and charge and ensuring ion balance. This allows the two reactions to take place in different solvents, with different scales and rates and without a complicated separation process. .... 318

**Figure D.3.** Electrochemical characterizations of the NiHCF RR material in both aqueous and methanol solutions. (a) Galvanostatic charge–discharge tests in a methanol solution containing 0.1 M TBAClO<sub>4</sub>, 20 mM NiNO<sub>3</sub>, and 0.01 M H<sub>2</sub>SO<sub>4</sub> with a NiHCF working electrode (WE) and counter electrode (CE). The inset shows a representative SEM image of NiHCF crystals. (b) CVs of NiHCF in 0.1 M TBAClO<sub>4</sub> and 0.01 M H<sub>2</sub>SO<sub>4</sub>

in methanol at a scan rate from 0.1 to 5 mV/s. (c) Galvanostatic discharge curve of NiHCF in methanol with 0.1 M TBAClO<sub>4</sub>, 20 mM NiNO<sub>3</sub>, and 0.01 M H<sub>2</sub>SO<sub>4</sub>. (d) Galvanostatic charge–discharge tests in aqueous 0.5 M H<sub>2</sub>SO<sub>4</sub> with a NiHCF WE and CE. (e) CVs of NiHCF conducted in 0.5 M H<sub>2</sub>SO<sub>4</sub> at a scan rate of 0.5, 1, and 5 mV/s. (f) Galvanostatic charge curve of NiHCF in 1.7 M Na<sub>2</sub>SO<sub>4</sub> and 1 mM NaOH (pH = 11) after discharge in MeOH. .... 322

**Figure D.4.** Electrochemical behaviors and product distributions of the separate electrochemical half-reactions. (a) CV data relevant to methylarene oxidation. Conditions: 0.1 M TBAPF<sub>6</sub> in acetonitrile, glassy carbon working electrode, Pt wire counter electrode, reference electrode Ag/AgNO<sub>3</sub> (10 mM AgNO<sub>3</sub> in acetonitrile) corrected vs Fc/Fc<sup>+</sup>. Oxidation of methanol prevents overoxidation of the acetal and aldehyde to the carboxylic acid. (b) Table for optimizing the product yield and distributions of methylarene oxidation with graphite rod working and counter electrodes. Entries 1–6 show optimization of the half-reaction. Entries 7 and 8 reflect conditions used to improve the anticipated performance of the RR. Entries 9 and 10 show the sensitivity of the reaction to excess proton concentration. (c) Linear sweep voltammetry (LSV) curve for the cathodic production of H<sub>2</sub>O<sub>2</sub> using an Fe-CNT working electrode with an area of 2 cm<sup>2</sup> at a scan rate of 10 mV/s in O<sub>2</sub>-saturated 1.7 M Na<sub>2</sub>SO<sub>4</sub> (adjusted to pH = 11) with a Pt counter electrode. .... 325

**Figure D.5.** Proton-balancing ability of the NiHCF RR. (a) Schematic of the Grotthuss mechanism, size of ions, and NiHCF cage illustrating the role of hydrogen bonding and the need to minimize ion competition. (b) pH shifts showing the proton intercalation and deintercalation ability of the RR. A pH = 11 solution was used in both the undivided and divided cells. The RR was reduced in 1 M H<sub>2</sub>SO<sub>4</sub> in methanol and then oxidized, releasing protons in the respective cells. H<sub>2</sub>O<sub>2</sub> production was performed at the working electrode to ensure proton release. (c) Electrochemical quartz crystal microbalance measured mass change of proton (de)intercalation of NiHCF in a 1:20 water-to-methanol solution of 1 mM H<sub>2</sub>SO<sub>4</sub>, 20 mM NiNO<sub>3</sub>, and 0.1 M TBAClO<sub>4</sub> in comparison with sodium (de)intercalation in 0.1 M Na<sub>2</sub>SO<sub>4</sub> in methanol. Slope trends are opposite of each other due to their differing (de)intercalation mechanisms. (d) The corresponding CVs during the measurements of the mass changes in panel (c). .... 328

**Figure D.6.** Modular electrosynthesis of 4-*t*-butylbenzaldehyde in methanol and H<sub>2</sub>O<sub>2</sub> in aqueous solution enabled by the proton-selective NiHCF RR. (a) Full schematic of the ModES process for pairing the methylarene oxidation reaction and H<sub>2</sub>O<sub>2</sub> production. (b) Reaction schematic of methylarene oxidation to 4-*t*-butylbenzaldehyde and the acetal product resulting from 23 cycles of ModES with the resulting product yields. (c) Potential of the NiHCF RR electrode during methylarene oxidation at the working electrode over 23 ModES cycles. (d) Reaction equation and pH after H<sub>2</sub>O<sub>2</sub> production for each cycle. The electrolyte had a starting pH of 11 and shifted minimally during the production of 200 ppm H<sub>2</sub>O<sub>2</sub> showing pH stability over the course of the ModES cycling. (e) FE and concentration of H<sub>2</sub>O<sub>2</sub> produced in the aqueous cell for each ModES cycle. A new 30 mL solution was used for each cycle. .... 332

- Figure D.7.** Modular electrosynthesis of 1-naphthylamine in acetonitrile and  $\text{H}_2\text{O}_2$  in aqueous solution enabled by the NiHCF RR. (a) Full schematic of the ModES process for pairing the oxidative C–H amination of naphthalene and  $\text{H}_2\text{O}_2$  production. (b) Potential evolution of the NiHCF RR counter electrode and carbon felt working electrode during naphthalene amination with  $\text{NaClO}_4$  (blue and red traces, respectively) and acetic acid (purple and green traces, respectively) added in the electrolyte. The inset shows the reaction schematic for naphthalene amination and the resulting product yields..... 334
- Figure D.S1.** Cyclic voltammograms (CVs) and galvanostatic charge/discharge (GCD) curves of the NiHCF electrode at a rate of 1C in 1 M  $\text{NaClO}_4$  in acetonitrile, methanol, and dimethylformamide..... 349
- Figure D.S2.** Structural characterization of the NiHCF product. SEM image (left) and PXRD pattern (right) of the as-synthesized NiHCF powder. The doublets indicate that the as synthesized NiHCF is rhombohedral. The JCPDS standard pattern is of the cubic polymorph..... 349
- Figure D.S3.** TGA analysis of a NiHCF sample. The analysis was done with a ramp rate of 5  $^\circ\text{C}/\text{min}$  under an  $\text{N}_2$  atmosphere..... 350
- Figure D.S4.** Illustration of the ion intercalation into NiHCF (left). NiHCF is synthesized in the fully reduced form with sodium present in the interstitial cages. Before use, NiHCF is oxidized to release the sodium ions. Then, protons are reversibly intercalated into NiHCF. The PXRD pattern supports that the NiHCF remains cubic when reduced with proton (right)..... 350
- Figure D.S5.** XRD pattern of the carbon cloth used as the current collector in Figure D.S4.... 350
- Figure D.S6.** Activation process of the NiHCF RR electrode. CV for 10 cycles for the redox to stabilize before use. .... 351
- Figure D.S7.** Cycling performance of the NiHCF RR in 1.7 M  $\text{Na}_2\text{SO}_4$  with pH = 11 (left) and 1.7 M  $\text{Na}_2\text{SO}_4$  with pH = 6 (right) at a rate of 1C. At higher pH, a clear color change was observed over the cycling showing the instability of the RR. At neutral pH, no obvious color change was observed over the cycling showing superior stability. However, when only discharging the RR in pH 11, no obvious color change of the solution was observed. .... 351
- Figure D.S8.** Rate capabilities of NiHCF RR in 0.1 M  $\text{TBAClO}_4$ , 20 mM  $\text{NiNO}_3$ , and 0.01 M  $\text{H}_2\text{SO}_4$  in MeOH. .... 351
- Figure D.S9.** Photographs of the electrolyte solution after 50 GCD cycles with NiHCF working and counter electrodes without (left) and with (right) 20 mM  $\text{NiNO}_3$  added. Clear dissolution of electrode material was observed without the addition of  $\text{NiNO}_3$ . .... 352

- Figure D.S10.** Photographs of the methylarene oxidation reaction solution without (left) and with (right) 20 mM NiNO<sub>3</sub> and the RR as the counter electrode. A dark blue precipitate was present if NiNO<sub>3</sub> was not added to stabilize the NiHCF crystal structure..... 352
- Figure D.S11.** Cell potential vs. time for the methylarene oxidation reaction with a graphite rod CE. .... 352
- Figure D.S12.** TEM images of carbon nanotube and Fe-decorated carbon nanotube catalysts for hydrogen peroxide production. .... 353
- Figure D.S13.** LSV in 1.7 M Na<sub>2</sub>SO<sub>4</sub> solution (pH = 6) for hydrogen peroxide production (red) and FE for CA runs at various applied potentials (blue) with carbon felt as the working electrode..... 353
- Figure D.S14.** LSV in 1.7 M Na<sub>2</sub>SO<sub>4</sub> solution (pH = 6) solution for hydrogen peroxide production with Fe-CNT as the working electrode..... 354
- Figure D.S15.** LSV in 1.7 M Na<sub>2</sub>SO<sub>4</sub> solution (adjusted to pH = 11) for hydrogen peroxide production (red) and FE for CA runs at various applied potentials (black) with carbon felt as the working electrode (the inset shows a representative SEM image of the carbon felt used). The FE was high for low charge passed but when enough charge was passed to produce 200 ppm H<sub>2</sub>O<sub>2</sub> the FE was consistently below 30%. Higher current densities were needed for high FE. .... 354
- Figure D.S16.** Chronoamperometry curves for hydrogen peroxide production in 1.7 M Na<sub>2</sub>SO<sub>4</sub> solution (adjusted to pH = 11) at various potentials vs. RHE with a RR CE. .... 355
- Figure D.S17.** Absorption spectra of the standard solutions of CeSO<sub>4</sub> in 0.5 M H<sub>2</sub>SO<sub>4</sub> (left) and the resulting calibration curve from the absorbance measured at 319 nm (right). .. 355
- Figure D.S18.** EQCM measurements in 0.1 M Mg(NO<sub>3</sub>)<sub>2</sub> and 1 mM HNO<sub>3</sub> in water. Mg(NO<sub>3</sub>)<sub>2</sub> was selected as the supporting electrolyte because Mg<sup>2+</sup> ions do not intercalate into NiHCF.<sup>14</sup> Each cycle begins with reduction followed by oxidation. The slopes are also opposite of what is expected, with mass loss occurring during reduction instead of mass gain due to the opposite movement of water molecules. During reduction (proton intercalation), the mass increase after a mass decrease may be attributed to the insertion of H<sub>3</sub>O<sup>+</sup>. During oxidation (proton deintercalation), the mass decrease seen after mass increase may be attributed to the de(insertion) of H<sub>3</sub>O<sup>+</sup>..... 356
- Figure D.S19.** EQCM measurements in 0.1 M TBAClO<sub>4</sub> and 1 mM H<sup>+</sup> in 1:20 water:methanol. Each cycle begins with oxidation followed by reduction. A bare Cr/Au coated quartz crystal was used as the working electrode and no pattern of frequency and mass change was observed as a potential was applied..... 356
- Figure D.S20.** Photograph of a NiHCF RR electrode. The active material area is 2×2 cm<sup>2</sup>. .... 357
- Figure D.S21.** NMR of the final products of the methylarene oxidation reaction after 23 ModES cycles. The aromatic region is used to quantify the yield of the reaction. The aromatic

peaks of the aldehyde are downfield to the aromatic peaks of the acetal. No peaks corresponding to the starting material were observed. .... 357

**Figure D.S22.** PXRD pattern of the NiHCF RR electrode in the fully oxidized state on SS mesh after the ModES cycling (left). PXRD pattern of bare SS mesh (right). .... 358

**Figure D.S23.** NMR of the 1-naphthylamine product after working up the electrochemically generated pyridinium. For the electrochemical step, a platinum counter electrode was used in a divided cell configuration. The doublet of doublets at 6.78 ppm was used to quantify the yield of the reaction. .... 358

**Figure D.S24.** NMR of the 1-naphthylamine product after working up the electrochemically generated pyridinium. For the electrochemical step, a platinum counter electrode was used in an undivided cell configuration. .... 359

**Figure D.S25.** NMR of the 1-naphthylamine product after working up the electrochemically generated pyridinium. For the electrochemical step, an RR counter electrode was used and 20 mg of NaClO<sub>4</sub> was added to the reaction vessel. .... 359

**Figure D.S26.** NMR of the 1-naphthylamine product after working up the electrochemically generated pyridinium. For the electrochemical step, an RR counter electrode was used and 60  $\mu$ L of acetic acid was added to the reaction vessel. .... 360

**Figure D.S27.** Cyclic voltammograms to determine the reduction potential of protons (HER onset potential) and the pyridinium produced from naphthalene amination on platinum in acetonitrile. The red trace is a CV taken before the naphthalene amination electro-synthesis is run with a platinum working electrode in the cathodic compartment of the divided cell used for electrolysis in the presence of triflic acid to determine the HER onset potential. The blue trace is a CV taken after the naphthalene amination is run in the anodic compartment (working electrode compartment) without acid to measure the reduction potential of the produced pyridinium. The purple trace is a CV taken after the naphthalene amination is run in the anodic compartment with 100  $\mu$ L of triflic acid added for comparison. 0.3 M KPF<sub>6</sub> was used as the supporting electrolyte for all traces instead of TBABF<sub>4</sub> and Argon gas was bubbled before scanning CV at a scan rate of 25 mV/s. .... 361

**Figure D.S28.** Cyclic voltammograms to determine the reduction potential of protons (HER onset potential) and the pyridinium produced from naphthalene amination on platinum in acetonitrile. The red trace is a CV taken before the naphthalene amination electro-synthesis is run with a platinum working electrode in an undivided cell in the presence of acetic acid to determine the HER onset potential. The blue trace is a CV taken after the naphthalene amination is run in the anodic compartment (working electrode compartment) of the divided cell used for electrolysis without acid to measure the reduction potential of the produced pyridinium. The purple trace is a CV taken after the naphthalene amination is run in the anodic compartment of the divided cell with 100  $\mu$ L of acetic acid added for comparison. 0.3 M KPF<sub>6</sub> was used as the

supporting electrolyte instead of TBABF<sub>4</sub> for all traces and Argon gas was bubbled before scanning CV at a scan rate of 25 mV/s..... 362

**Figure D.S29.** Potential evolution of the NiHCF RR counter electrode and carbon felt working electrode during naphthalene amination with NaClO<sub>4</sub> (blue and red traces, respectively) and acetic acid (purple and green traces, respectively) added to the reaction vessel, with potential evolution of a platinum counter electrode in an undivided configuration with acetic acid added shown in grey (working electrode potential in orange). ..... 362

**Figure D.S30.** Photos showing the electrodes used during electrochemical experiments. (a) Pt wire electrode. (b) 3 mm wide graphite rod used as the working electrode during methylarene oxidation. (c) Leak-free reference electrode used in nonaqueous solvent during ModES. (d) Fe-CNT catalyst on carbon paper used as catalyst for H<sub>2</sub>O<sub>2</sub> production. (e) 1 cm<sup>2</sup> carbon felt square at the end of a graphite rod used as the working electrode during naphthalene amination. (f) Four 4 cm<sup>2</sup> NiHCF RRs clipped for use as the counter electrode during ModES. .... 363

**Figure D.S31.** Photos showing the cell setups used during electrosynthesis. (a) Custom built undivided cell used for the optimization of methylarene oxidation reaction. (b) Undivided configuration setup used for H<sub>2</sub>O<sub>2</sub> production. The cell is a plastic beaker purchased from VWR International, Inc and the Teflon cap is custom made. (c) Undivided configuration setup for naphthalene oxidation. A 4-dram vial with the top cut off is used as the reaction vessel. A 4-dram vial lid with holes for the electrodes is used as the cap. This type of reaction vessel is used for all undivided configurations with the exception of H<sub>2</sub>O<sub>2</sub> production as shown in b. (d) Undivided configuration setup used for control experiments with a platinum counter electrode reported in Table D.S2. (e) Divided configuration setup for naphthalene C–H amination. A divided cell with a glass frit is used with Teflon caps. (f) Undivided configuration setup used during ModES for methylarene oxidation. .... 363

## List of Tables

**Table 2.1. Optimization of electrochemical Ni-catalyzed reductive homocoupling.<sup>a</sup>** ..... 44

**Table 2A.1. Optimization of thermochemical Ni-catalyzed reductive homocoupling of G–OMs.<sup>a</sup>**..... 101

**Table 2A.2. Conditions screening focused on nitrogen-based ligands for S/S homocoupling.<sup>a</sup>**  
..... 101

**Table 2A.3. Conditions screening focused on nitrogen-based ligands for S/S homocoupling.<sup>a</sup>**  
..... 102

**Table 2A.4. Conditions screening focused on phosphine-based ligands for S/S homocoupling.<sup>a</sup>**..... 102

<b>Table 2A.5. Conditions screening focused on ligand loading and additives for S/S homocoupling.<sup>a</sup></b> .....	103
<b>Table 2A.6. Conditions screening focused on temperature and solvents for S/S homocoupling.<sup>a</sup></b> .....	103
<b>Table 2A.7. Conditions screening focused on additive loadings for S/S homocoupling.<sup>a</sup></b> ...	104
<b>Table 2A.8. Conditions screening focused on molecular sieves and solvents for S/S homocoupling.<sup>a</sup></b> .....	104
<b>Table 2A.9. Optimization of electrochemical Ni catalyzed reductive S/S homocoupling.<sup>a</sup></b>	106
<b>Table 2A.10. Ni-only catalyzed reductive cross-coupling of LDMs.<sup>a</sup></b> .....	107
<b>Table 2A.11. Ligand, additive, and solvent screening for G/S cross-coupling.<sup>a</sup></b> .....	111
<b>Table 2A.12. Ligand screening for G/S cross-coupling.<sup>a</sup></b> .....	111
<b>Table 2A.13. Ligand and solvent screening for G/S cross-coupling.</b> .....	112
<b>Table 2A.14. Catalyst loading screening for G/S cross-coupling.<sup>a</sup></b> .....	112
<b>Table 2A.15. Thermogravimetric analysis of DEH-BPDA derivatives (H–H<sup>PL</sup> through S–S<sup>PL</sup>).</b> .....	115
<b>Table 2A.16. Thermal properties of PVC plasticized with 10 wt% DEH-BPDA derivatives (H–H<sup>PL</sup> through S–S<sup>PL</sup>) and DEHP.</b> .....	117
<b>Table 2A.17. Summary of EPA T.E.S.T. predictions.</b> .....	120
<b>Table 2A.18. Hazard classifications for EPA T.E.S.T. predictions</b> .....	121
<b>Table 3B.1. Formal thermodynamic potentials of Zn, Mn, Mg, Fe, and Al.</b> .....	160
<b>Table 3B.2. Formal thermodynamic potentials of Zn and Mn in mixed solvents.</b> .....	163
<b>Table 3B.3. The impact of dissolved oxygen to measured OCP.</b> .....	163
<b>Table 3B.4. Optimization of (electro)chemical reductive coupling of benzyl chloride with iodobenzene.<sup>a</sup></b> .....	167
<b>Table 3B.5. An example of optimization of electrochemical reductive coupling of Katritzky salts with aryl halides.<sup>a</sup></b> .....	170
<b>Table 3B.6. Zn salt effects in the cross-coupling of Katritzky salts with aryl halides.<sup>a</sup></b> .....	173
<b>Table 4C.1. Results of XEC reactions under adapted literature condition using informer library substrates.<sup>a</sup></b> .....	207

<b>Table 4C.2. Ligand evaluation for condition A.<sup>a</sup></b> .....	210
<b>Table 4C.3. Further optimization and control reactions for condition A.<sup>a</sup></b> .....	211
<b>Table 4C.4. Results of XEC reactions under condition A using informer library substrates.<sup>a</sup></b> .....	212
<b>Table 4C.5. Ligand evaluation for condition B.<sup>a</sup></b> .....	214
<b>Table 4C.6. Screening of reductants, additives, and solvents for condition B.<sup>a</sup></b> .....	215
<b>Table 4C.7. Further optimization and control reactions for condition B.<sup>a</sup></b> .....	216
<b>Table 4C.8. Results of XEC reactions under condition B using informer library substrates.<sup>a</sup></b> .....	217
<b>Table D.S1. Weight percentages of metal elements and water content in a NiHCF sample from ICP-OES and TGA. The exact formula is Na<sub>2.29</sub>Ni[Fe(CN)<sub>6</sub>]<sub>1.04</sub>·2.2 H<sub>2</sub>O.</b> .....	349
<b>Table D.S2. Summary of naphthalene amination experiments supporting the redox reservoir's ability to allow for effective reaction in an undivided cell configuration.</b> .....	360

## Abbreviations and Acronyms

acac	acetylacetonate
Ag	silver
AgNO <sub>3</sub>	silver chloride
AgNP	silver nanoparticle
Ar	aryl
Al	aluminum
Alk	alkyl
Au	gold
B	boron
BINAP	2,2'-bis(diphenylphosphino)-1,1'-binaphthyl
BiOX	bi-oxazoline
Bn	benzyl
B <sub>2</sub> neo <sub>2</sub>	bis(neopentyl glycolato)diboron
BOX	bisoxazoline
BPDA	biphenyl-4,4'-dicarboxylic acid
B <sub>2</sub> pin <sub>2</sub>	bis(pinacolato)diboron
bpp	2,6-bispyrazolylpyridine
bpy	2,2'-bipyridine
<sup>t</sup> Bubpy	4,4'-di- <i>tert</i> -butyl-2,2'-bipyridine
<sup>t</sup> Butpy	4,4',4''-tri- <i>tert</i> -butyl-2,2':6',2''-terpyridine
<sup>n</sup> Bu <sub>4</sub> NBF <sub>4</sub>	tetrabutylammonium tetrafluoroborate
<sup>n</sup> Bu <sub>4</sub> NBr	tetrabutylammonium bromide
<sup>n</sup> Bu <sub>4</sub> NCl	tetrabutylammonium chloride
<sup>n</sup> Bu <sub>4</sub> NI	tetrabutylammonium iodide
<sup>n</sup> Bu <sub>4</sub> NPF <sub>6</sub>	tetrabutylammonium hexafluorophosphate
CO <sub>2</sub>	carbon dioxide
COD	1,5-cyclooctadiene
C( <i>sp</i> <sup>2</sup> )	carbon with <i>sp</i> <sup>2</sup> hybridized orbitals
C( <i>sp</i> <sup>3</sup> )	carbon with <i>sp</i> <sup>3</sup> hybridized orbitals
CV	cyclic voltammetry

CyJohnPhos	2-(dicyclohexylphosphino)biphenyl
dDCC	doubly decarboxylative coupling
DEHP	di(2-ethylhexyl) phthalate
DFT	density functional theory
DIPEA	<i>N,N</i> -diisopropylethylamine, or Hünig's base
DMA	dimethylacetamide
DMAP	4-dimethylaminopyridine
dmbpy	5,5'-dimethyl-2,2'-bipyridine
dme	1,2-dimethoxyethane
DMF	dimethylformamide
DMI	1,3-dimethyl-2-imidazolidinone
DMO	dimethyl oxalate
DMPU	<i>N,N'</i> -dimethylpropyleneurea
DMSO	dimethyl sulfoxide
DPEPhos	bis[(2-diphenylphosphino)phenyl] ether
4,4'-dPhbpy	4,4'-diphenyl-2,2'-bipyridine
dppb	1,4-bis(diphenylphosphino)butane
dppf	1,1'-bis(diphenylphosphino)ferrocene
dppp	1,3-bis(diphenylphosphino)propane
DSC	differential scanning calorimetry
$E^{\circ'}$	formal thermodynamic potential
$E^{\circ'}_{Zn}$	formal thermodynamic potential of zinc
$E^{\circ'}_{Mn}$	formal thermodynamic potential of manganese
$e^-$	electron
Et	ethyl
equiv	equivalence
Fc/Fc <sup>+</sup>	ferrocene/ferrocenium
Fe	iron
FeBr <sub>2</sub>	iron(II) bromide
FeBr <sub>3</sub>	iron(III) bromide
<b>G</b>	vanillic acid

Ge	germanium
$^1\text{H}$	proton
<b>H</b>	4-hydroxybenzoic acid
Het	heteroaryl
HTE	high-throughput experimentation
KF	potassium fluoride
KI	potassium iodide
KPF <sub>6</sub>	potassium hexafluorophosphate
L	ligand
L*	chiral ligand
LDM	lignin-derived monomer
LiBr	lithium bromide
LiCl	lithium chloride
LiI	lithium iodide
LiPF <sub>6</sub>	lithium hexafluorophosphate
Me	methyl
MeCN	acetonitrile
Mg	magnesium
MgBr <sub>2</sub>	magnesium bromide
MgCl <sub>2</sub>	magnesium chloride
Mn	manganese
MnBr <sub>2</sub>	manganese(II) bromide
N <sub>2</sub>	nitrogen gas
NaBF <sub>4</sub>	sodium tetrafluoroborate
NaBr	sodium bromide
NaI	sodium iodide
NHP ester	<i>N</i> -hydroxyphthalimide ester
Ni	nickel
[Ni(bpy) <sub>3</sub> ]Cl <sub>2</sub>	tris(2,2'-bipyridine)dichloronickel(II)
Ni(COD) <sub>2</sub>	bis(1,5-cyclooctadiene)nickel(0)
NiBr <sub>2</sub>	nickel(II) bromide

NiBr <sub>2</sub> (dme)	nickel(II) bromide ethylene glycol dimethyl ether complex
NiBr <sub>2</sub> ·3H <sub>2</sub> O	nickel(II) bromide trihydrate
NiCl <sub>2</sub>	nickel(II) chloride
NiCl <sub>2</sub> (dme)	nickel(II) chloride ethylene glycol dimethyl ether complex
NiCl <sub>2</sub> ·6H <sub>2</sub> O	nickel(II) chloride hexahydrate
NHC	<i>N</i> -heterocyclic carbene
NiI <sub>2</sub>	nickel(II) iodide
NMP	<i>N</i> -methyl-2-pyrrolidone
NMR	nuclear magnetic resonance
Nphth	phthalimide
OCP	open-circuit potential
Pc	phthalocyanine
Pd	palladium
Ph	phenyl
pH	a logarithmic scale used to specify the acidity or basicity of aqueous solutions
phen	1,10-phenanthroline
PPh <sub>3</sub>	triphenylphosphine
<sup>i</sup> Pr	isopropyl
<sup>i</sup> PrQ	<sup>i</sup> Pr-Quinazolinap
PVC	poly(vinyl chloride)
Py	pyridine
PyBOX	pyridine-2,6-bisoxazoline
RVC	reticulated vitreous carbon
<b>S</b>	syringic acid
SCE	saturated calomel electrode
SHE	standard hydrogen electrode
Si	silicon
SM	starting material
SO <sub>2</sub>	sulfur dioxide
SPhos	2-dicyclohexylphosphino-2',6'-dimethoxybiphenyl
SS	stainless-steel

TDAE	tetrakis(dimethylamino)ethylene
TFA	trifluoroacetic acid
Tf <sub>2</sub> O	trifluoromethanesulfonic anhydride
T <sub>g</sub>	glass transition temperature (of polymer material)
TGA	thermogravimetric analysis
THF	tetrahydrofuran
Ti(OBu) <sub>4</sub>	titanium butoxide
TME	tetrakis(morpholino)ethylene
TMHD	2,2,6,6-tetramethyl-3,5-heptanedione
TMSCl	trimethylsilyl chloride
tosylate	4-toluenesulfonate
triflate	trifluoromethanesulfonate
UPLC-MS	ultra-performance liquid chromatography-mass spectrometry
$V_{app}$	applied potential
XantPhos	4,5-bis(diphenylphosphino)-9,9-dimethylxanthene
XEC	cross-electrophile coupling
Zn	zinc
ZnCl <sub>2</sub>	zinc chloride
ZnBr <sub>2</sub>	zinc bromide
ZnI <sub>2</sub>	zinc iodide
1°	primary
2°	secondary
3°	tertiary

## **Chapter 1.**

### **An Overview of Nickel-Catalyzed Cross-Electrophile Coupling**

## 1.1. Introduction

Transition metal-catalyzed cross-coupling has proven to be one of the most powerful, reliable, and commonly used transformations in the organic chemist's toolkit. Conventional cross-coupling features the coupling of nucleophiles with electrophiles enabled by a transition metal catalyst, with palladium catalysts standing as the premier. These technologies allow the efficient and modular construction of carbon-carbon and carbon-heteroatom bonds and have found numerous applications in the synthesis of pharmaceuticals, agrochemicals, polymers, among others.<sup>1-8</sup> More recently, nickel-catalyzed cross-electrophile coupling (XEC) has emerged as a promising alternative to conventional cross-coupling. This strategy avoids the use of precious-metal catalysts and circumvents the need for organometallic reagents that have limited stability and commercial availability. Instead, two electrophiles are coupled via nickel-catalysis under reductive conditions. Electrophiles are generally bench-stable and readily available or accessible from commercial sources. Additionally, nickel catalysts can engage in either one- or two-electron elementary steps with a substrate or a second nickel species, opening a plethora of opportunities for catalyst design and methodology development (Figure 1.1).<sup>9-12</sup>

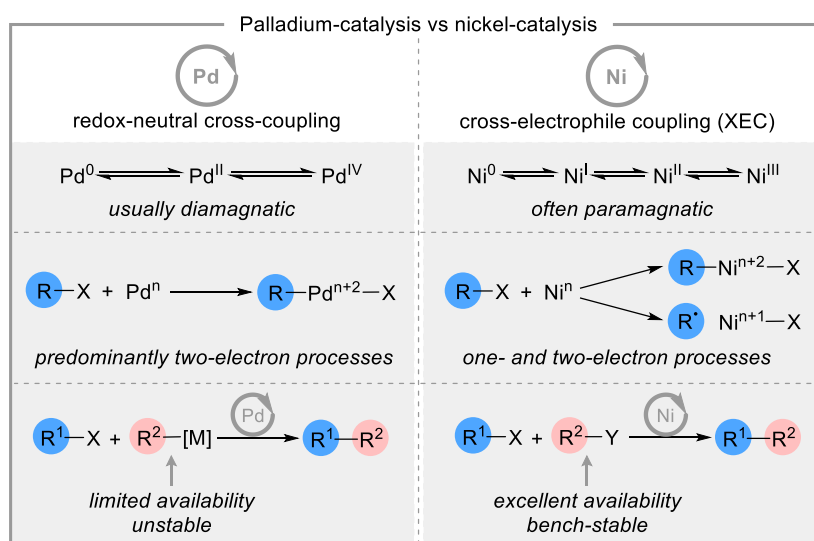


**Figure 1.1.** Common features of palladium- and nickel-catalysis.

## 1.2. Early Development of Nickel-Mediated Reductive Coupling

In 1970–1980s, Semmelhack and co-workers disclosed the homocoupling of aryl halides mediated by stoichiometric bis(1,5-cyclooctadiene)nickel(0) ( $\text{Ni}(\text{COD})_2$ ) at moderate temperatures in DMF solvent (Figure 1.2A). The reaction conditions were compatible with functional groups that would not survive in reaction with aryl-magnesium or aryl-lithium reagents (e.g., ketone, aldehyde, ester, and nitrile). Acidic functional groups (hydroxyl, carboxylic acid) failed to couple under these conditions.<sup>13</sup> This method was later extended to the homocoupling of alkenyl halides and successfully applied to the synthesis of cyclic biaryls. It is worth noting that the cyclization of bis(iodoaryl)alkanes was found to be promoted by a different form of nickel(0), tetrakis(triphenylphosphine)nickel(0) ( $\text{Ni}(\text{PPh}_3)_4$ ).<sup>14,15</sup>

Following these precedents, Kumada and co-workers in the late 1970s achieved a Ni-catalyzed aryl bromide homocoupling using stoichiometric zinc as an external reductant (Figure 1.2B). In this case, nickel(0) was *in situ* generated by stirring  $\text{Ni}(\text{PPh}_3)_2\text{Cl}_2$ ,  $\text{PPh}_3$ , and Zn in DMF for 30 min, after which aryl halides were added. Significant rate acceleration was observed upon the inclusion of a catalytic amount of potassium iodide (KI) as an additive, enabling the reaction to proceed at room temperature to give 85% yield after 24 h; the same reaction without KI only afforded 24% yield after 24 h. Electron-rich and -deficient *para*-substituted aryl bromides (methyl, methoxy, ketone, ester) were shown to be tolerated within this reaction.<sup>16</sup>

In 1986, Périchon and co-workers reported the use of  $\text{NiBr}_2(\text{bpy})$  ( $\text{bpy} = 2,2'$ -bipyridine) as the catalyst for electrochemical homocoupling of organic halides. The reaction was conducted in an undivided cell by applying a constant potential ( $-1.3$  V vs. SCE), using a gold cathode and a sacrificial magnesium anode. Cross-coupling of two aryl halides using  $\text{NiBr}_2(\text{bpy})$  catalyst was also evaluated. Homo-coupled products were exclusively obtained when one aryl halide was much

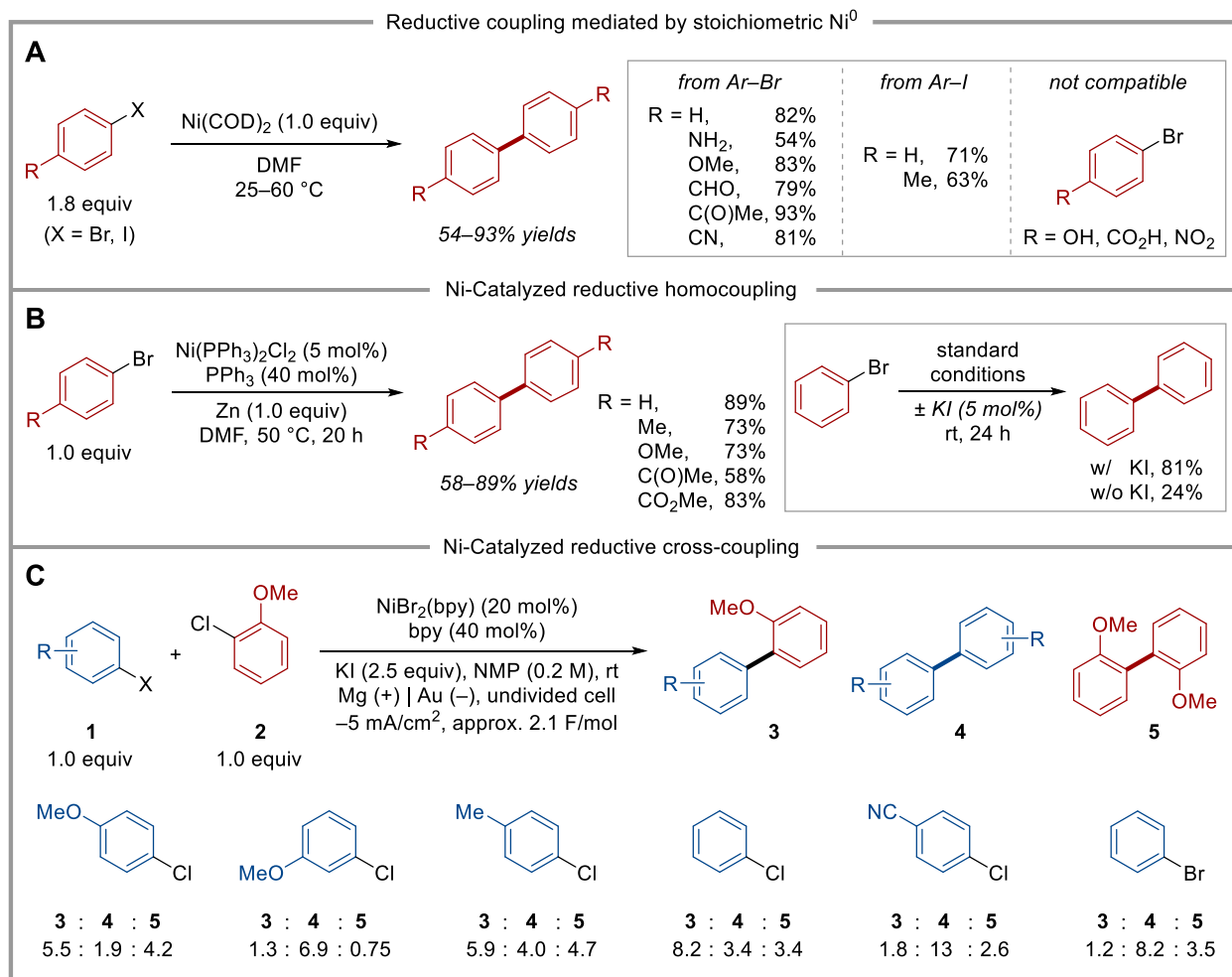


**Figure 1.2.** Early examples of Ni-mediated reductive coupling reactions. (A) Semmelhack reductive biaryl synthesis mediated by stoichiometric nickel(0). (B) Kumada Ni-catalyzed aryl halide homocoupling. (C) Product distribution in Ni-catalyzed electroreductive cross-coupling of two aryl halides.

more reactive than the other (e.g., iodobenzene and 4-bromotoluene). On the other hand, the coupling of aryl halides with similar reactivity (e.g., bromobenzene and 4-bromotoluene) afforded a statistical mixture of cross- and homo-coupled products.<sup>17</sup> Further investigations showed that the distribution of products could be perturbed by varying steric and electronic properties of one aryl halide coupling partner when the other coupling partner was an *ortho*-substituted aryl chloride; however, in most cases, less-than-statistical yields of the cross-coupled products were obtained (Figure 1.2C).<sup>18</sup> These preliminary studies revealed the difficulty of achieving selective XEC between two aryl halides using a single nickel catalyst.

In the early 1990s, Durandetti and co-workers demonstrated that  $\text{NiBr}_2(\text{bpy})$  was an effective catalyst for the coupling of aryl halides with activated alkyl electrophiles. Aryl halides were smoothly coupled with  $\alpha$ -chloro ketones and esters and could be extended to coupling with other activated alkyl electrophiles, such as allylic acetates,  $\alpha$ -chloro nitriles, and benzyl chlorides.<sup>19,20</sup> The reaction was promoted by electrolysis at a constant current using a sacrificial anode. Alkyl electrophiles were used in excess and slowly added into the reaction mixture throughout electrolysis, due to their high reactivities towards nickel(0) (Figure 1.3A).

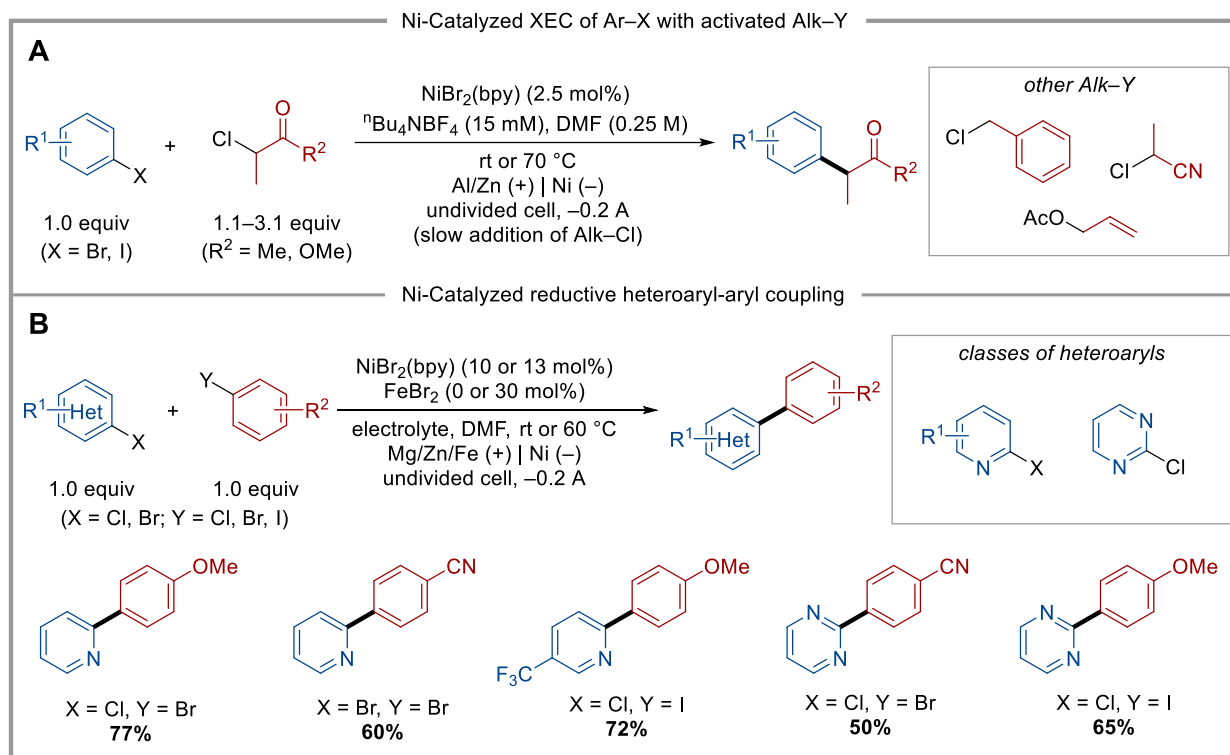


**Figure 1.3.** Early examples of Ni-catalyzed XEC reactions. (A) Electrochemical Ni-catalyzed XEC of aryl halides with activated alkyl electrophiles. (B) Electrochemical Ni-catalyzed XEC of heteroaryl halides with aryl halides.

Built upon these studies, electroreductive coupling of aryl halides with 2-halopyridines was achieved by Gosmini and co-workers, employing  $\text{NiBr}_2(\text{bpy})$  as the catalyst, using a magnesium or zinc anode.<sup>21</sup> Further studies found that using a sacrificial iron anode could enable XEC of aryl halides with more challenging heterocycles such as 2-chloropyrimidine.<sup>22</sup> Functionalized 2-

halopyridines were also successfully coupled with aryl halides using the sacrificial iron anode process.<sup>23</sup> Using an iron anode allowed *in situ* generation of FeBr<sub>2</sub> that was proposed to limit heterocycle ligation to the Ni catalyst. In these reports, the two electrophiles were carefully paired, based on their reactivities, to achieve selective cross-coupling. For example, pyridyl bromides were used for coupling with electron-deficient aryl bromides, while pyridyl chlorides were chosen for coupling with electron-rich aryl bromides (Figure 1.3B).

Overall, these studies laid the groundwork for the future development of Ni-catalyzed XEC reactions. Tremendous advancements have been achieved since then, both synthetically and mechanistically. The following content will first introduce the typical mechanisms proposed for Ni-catalyzed XEC reactions, followed by a summary of the scope of substrates that can be utilized in these reactions. General strategies for achieving selectivity in Ni-catalyzed XEC reactions will also be discussed.

### 1.3. Mechanisms of Ni-Catalyzed XEC Reactions

A sequential oxidative addition mechanism is usually proposed for Ni-catalyzed XEC of two aryl electrophiles. The reaction initiates from the oxidative addition of the reduced nickel catalyst (**A**) to the more reactive electrophile, affording an aryl-nickel(II) intermediate (**B**). Upon reduction by an external reductant, the resultant nickel(I) complex **C** performs a second oxidative addition into the other electrophile to generate a diaryl-nickel(III) complex (**D**). Subsequent reductive elimination from **D** forms the desired product and a nickel(I) (**E**), which is then reduced to regenerate the active nickel(0) catalyst (Figure 1.4A). In this mechanism, Ni catalysts activate both electrophiles via two-electron oxidative addition pathways. Therefore, it is crucial that the two low-valent nickel species (**A** and **C**) each selectively react with one of the coupling partners, so that cross-coupling can be achieved. This catalytic behavior can be attributed to reactivity

differences between the two electrophiles and the alignment of steric and electronic properties in low-valent nickel intermediates.<sup>12</sup>

The activation of  $C(sp^3)$  electrophiles by nickel catalysts in XEC is generally proposed to involve single-electron transfer pathways and organic radical intermediates. In a typical Ni-catalyzed  $C(sp^2)$ – $C(sp^3)$  XEC reaction, the aryl electrophile is proposed to first react with nickel(0) via oxidative addition to form an aryl-nickel(II). This intermediate intercepts the alkyl radical to form a high-valent nickel(III) complex, which undergoes reductive elimination to generate the product and a nickel(I). Activation of the alkyl electrophile by this nickel(I) intermediate then allows the alkyl radical to enter the catalytic cycle and, in turn, generates nickel(II), which re-enters the cycle via reduction to nickel(0) (Figure 1.4B). In this mechanism, Ni catalysts undergo both two-electron and one-electron activation pathways with the electrophiles, allowing sequential activation of different electrophiles via distinct mechanisms and imparting selectivity.<sup>12</sup>

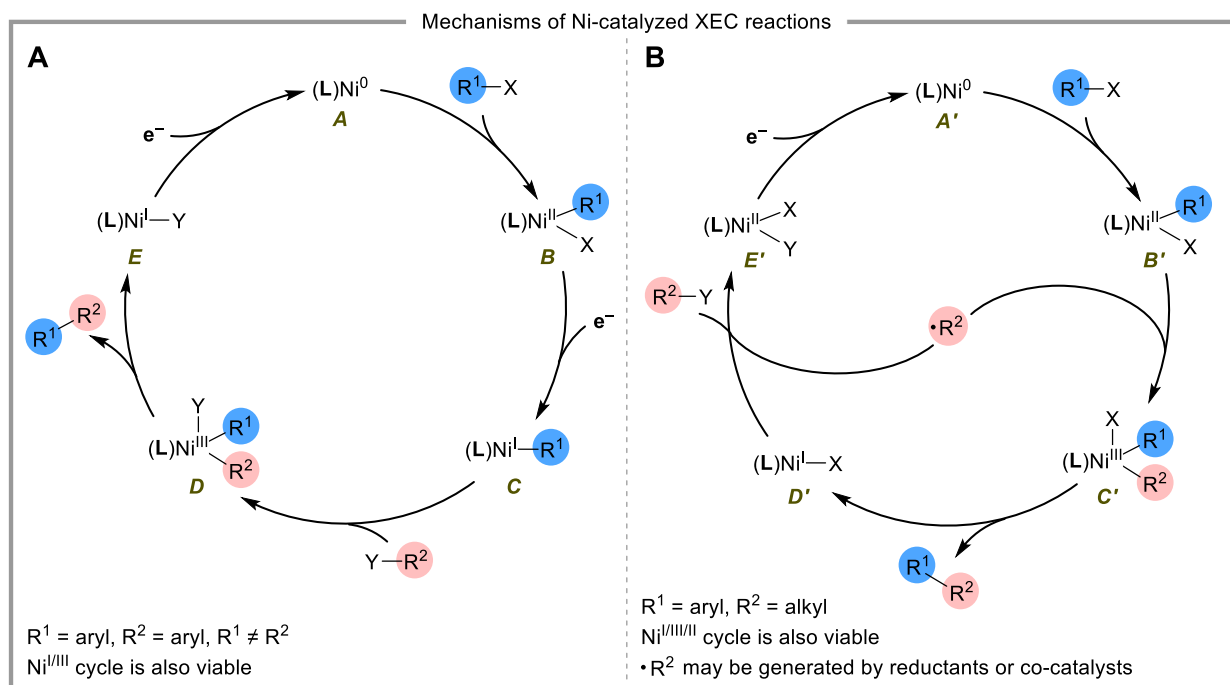


**Figure 1.4.** Mechanistic models for Ni-catalyzed XEC reactions. (A) Sequential oxidative addition mechanism. (B) Radical chain mechanism.

Variations on these general mechanisms have been proposed as the field continues to grow. For instance, mounting evidence suggests that aryl electrophiles are activated by nickel(I) instead of nickel(0) when nickel is complexed with nitrogen-based ligands.<sup>24–26</sup> Additionally, radicals can be generated from a separate co-catalytic cycle or from single-electron reduction of C(*sp*<sup>3</sup>) electrophiles by chemical reductants or electroreduction.<sup>12</sup> These variations greatly expand the ways to modulate reactivity and selectivity in XEC reactions, but inevitably introduce subtle differences into the reaction mechanisms that are not always distinguishable without extensive studies. The use of different ligands, solvents, additives and whether or not a co-catalyst is involved in the reaction may result in changes in the mechanism. Nonetheless, the mechanistic models described above build the framework for understanding the origin of cross-selectivity in Ni-catalyzed XEC reactions and provide guidance for reaction design and optimization.

#### 1.4. Scope of Ni-Catalyzed XEC Reactions

Cross-electrophile coupling as a general concept materialized with the seminal report in 2010 from Weix and co-workers, disclosing a dual-ligand nickel-catalyzed reductive coupling between aryl halides and unactivated alkyl halides at 1:1 substrate ratio (Figure 1.5A).<sup>27</sup> Tremendous efforts have been made since then to expand the scope of substrates that can be utilized in XEC reactions, which can be broadly categorized into three classes: (a) C(*sp*<sup>2</sup>) and C(*sp*<sup>3</sup>) halides, (b) carbon electrophiles that are readily converted from corresponding nucleophiles, and (c) small molecules (e.g., CO<sub>2</sub><sup>28–30</sup>, SO<sub>2</sub><sup>31</sup>) and heteroatom electrophiles (e.g., Si<sup>32,33</sup>, Ge<sup>34</sup>, B<sup>35</sup>). The following content will highlight the recent progress on Ni-catalyzed XEC reactions involving the first two classes of substrates.

The majority of Ni-catalyzed XEC reactions have been focused on the construction of C(*sp*<sup>2</sup>)–C(*sp*<sup>3</sup>) bonds as the inherent differences of C(*sp*<sup>2</sup>) and C(*sp*<sup>3</sup>) electrophiles can lead to robust cross-

selectivity. In many cases, the coupling between aryl halides and alkyl halides can be achieved in high yields and selectivity.<sup>12</sup> For instance, aryl iodides, bromides and activated aryl chlorides can be smoothly coupled with primary and secondary alkyl bromides, usually promoted by a nickel

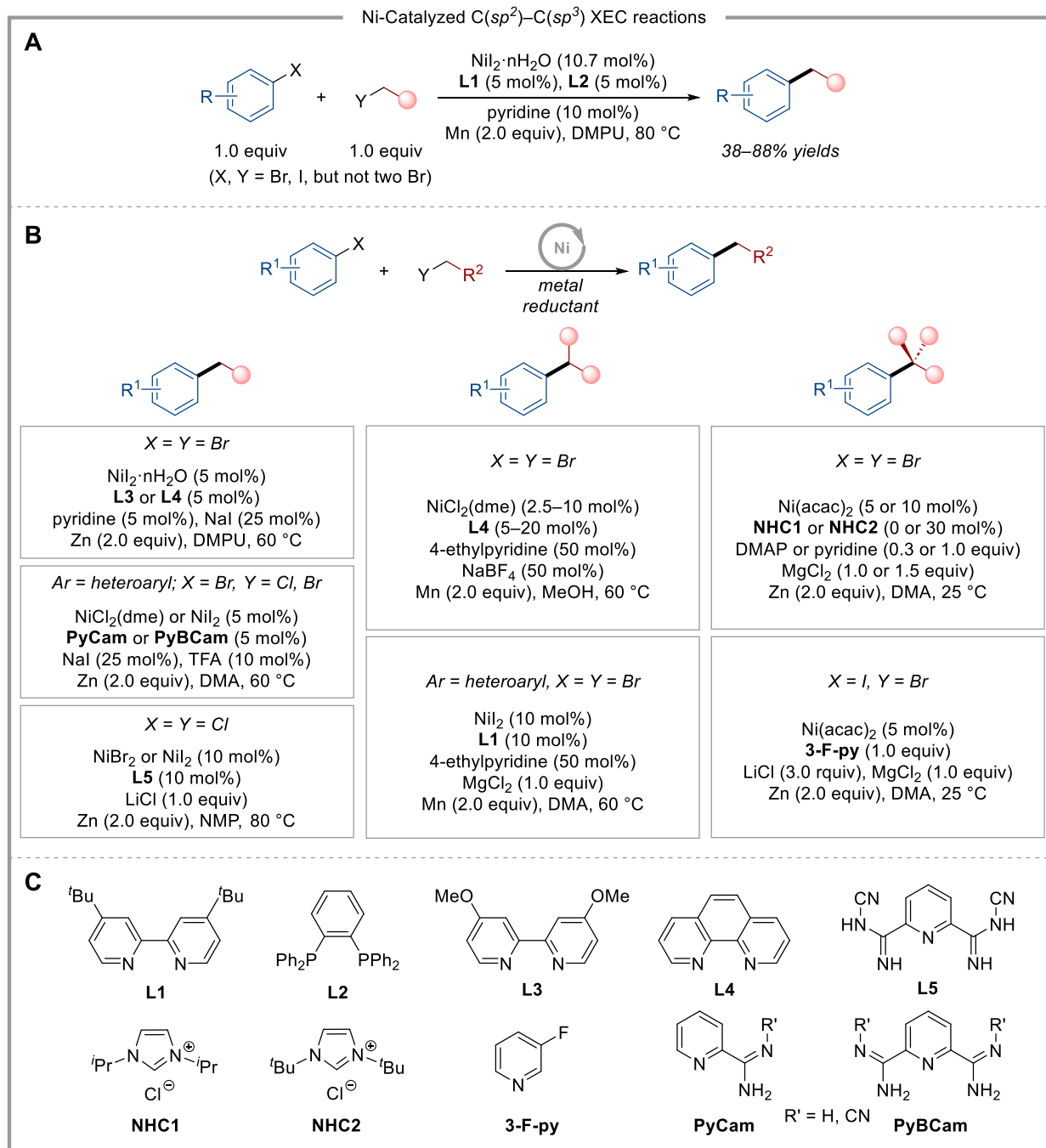


**Figure 1.5.** Ni-Catalyzed C(sp<sup>2</sup>)-C(sp<sup>3</sup>) XEC reactions using metal reductants. (A) Seminal report from Weix and co-workers on XEC of aryl halides with alkyl halides. (B) Representative examples. (C) Ligands used in reactions illustrated in (A) and (B).

catalyst complexed with bidentate nitrogen ligands in the presence of halide salts.<sup>36–38</sup> Highly reactive methyl iodides are shown to be compatible coupling partners with aryl halides.<sup>39</sup> XEC of unactivated aryl chlorides with alkyl chlorides has been achieved by including halide additives and employing a uniquely selective pyridyl carboxamidine ligand.<sup>40</sup> Ligands of this type are also shown to enable coupling of challenging heteroaryl halides with alkyl halides.<sup>41,42</sup> The coupling of aryl bromides with highly reactive tertiary alkyl bromides can be difficult but has been achieved using Ni(acac)<sub>2</sub> (acac = acetylacetonate) catalyst in the presence of NHC (*N*-heterocyclic carbene) additives, pyridine-type ligands, and chloride salts.<sup>43,44</sup> These reactions were conducted using a heterogeneous chemical reductant, typically zinc or manganese (Figure 1.5B). More recently, electrochemical Ni-catalyzed XEC methods have been developed for construction of C(*sp*<sup>2</sup>)–C(*sp*<sup>3</sup>) bonds, wherein sacrificial anodes or homogeneous chemical reductants are used to provide the reducing equivalents (see Section 1.5 for more discussion).

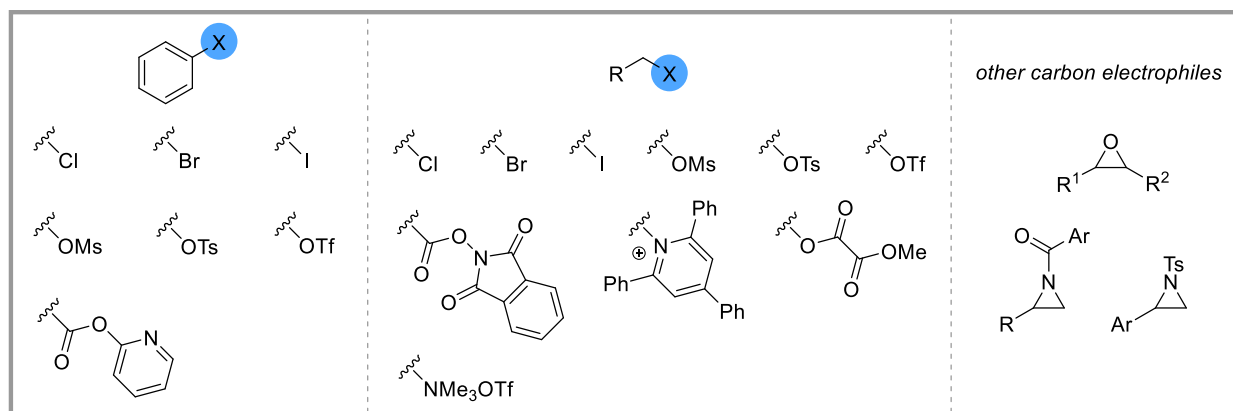


**Figure 1.6.** Common carbon electrophiles in Ni-catalyzed XEC reactions.

Besides organohalides, carbon electrophiles can be obtained through a convenient functional group conversion from the corresponding nucleophiles (Figure 1.6). Alkyl alcohols and phenols can be converted to sulfonate esters (often known as pseudohalides) and other oxygen electrophiles (e.g., alkyl oxalates)<sup>45–47</sup>. Alkyl amines can become accessible substrates by conversion into pyridinium salts (often known as Katritzky salts)<sup>48–51</sup> or occasionally ammonium salts<sup>52</sup>. Organic

carboxylic acids have been primarily activated as *N*-hydroxyphthalimide esters (NHP esters)<sup>53,54</sup>, with isolated examples showing other possibilities such as 2-pyridyl esters<sup>55</sup>. Epoxides and aziridines can be readily used as radical precursors upon reductive ring opening.<sup>56,57</sup>

The utilization of these electrophiles not only allows Ni-catalyzed XEC to cover a broader chemical space, but also provides opportunities for achieving cross-selectivity via different activation mechanisms (Figure 1.7). For example, methyl tosylates as a less reactive methyl source than methyl iodides can be compatible coupling partners in the XEC with alkyl and aryl bromides.<sup>58,59</sup> Gong and co-workers have achieved XEC of alkyl oxalates with aryl halides, wherein Zn/MgCl<sub>2</sub> triggers a Barton-type C–O bond radical scission of the oxalates that is further promoted by Ni catalysts.<sup>47</sup> Watson and co-workers, in collaboration with Merck, have showed that XEC of amino acid pyridinium salts with aryl bromides could enable efficient synthesis of noncanonical amino acids and diversification of peptides.<sup>60</sup> Katritzky salts are proposed to undergo single-electron reduction by an external reductant, rather than a reduced Ni catalyst, to generate alkyl radicals.<sup>50</sup> This feature allows Hazari and co-workers to modulate the rates of alkyl radical formation from Katritzky salts by using organic reductants with different reduction potentials and achieve XEC of highly reactive benzylic Katritzky salts with aryl iodides using a milder reductant, TME (tetrakis(morpholino)ethylene), compared to TDAE (tetrakis(dimethylamino)ethylene).<sup>61</sup> Baran, Kawamata, and co-workers have developed an electrochemical Ni-catalyzed C(*sp*<sup>3</sup>)–C(*sp*<sup>3</sup>) reductive coupling method that utilizes two NHP esters as coupling partners, termed as doubly decarboxylative coupling (dDCC). In this case, NHP esters are proposed to be reduced by the cathode or low-valent nickel species.<sup>62</sup> They later reported an improved reaction condition to allow modular construction of complex molecular architectures, showcased in the synthesis of a series of natural products.<sup>63</sup>

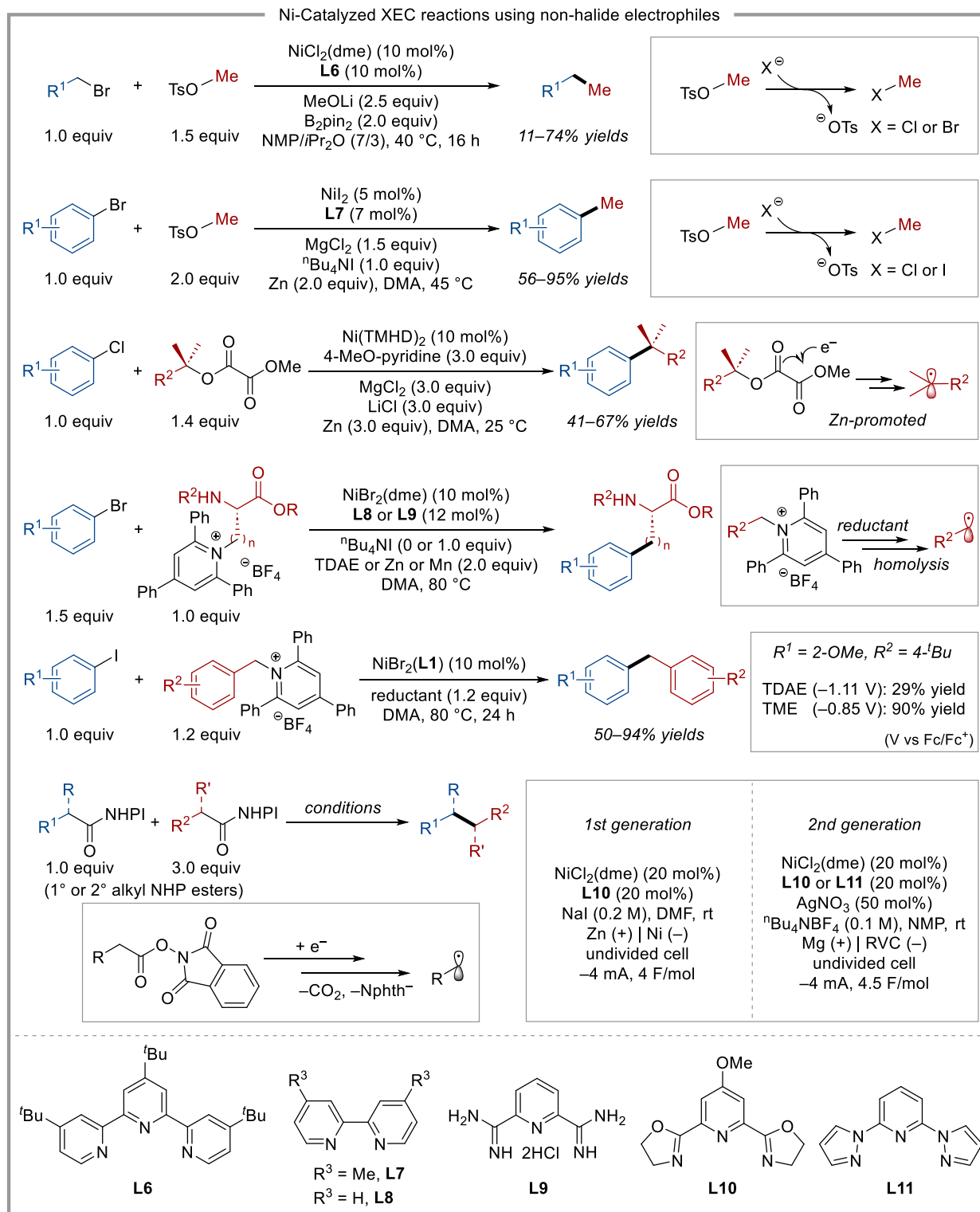


**Figure 1.7.** Ni-Catalyzed XEC reactions using non-halide electrophiles.

Formation of radicals from racemic  $C(sp^3)$  electrophiles provides opportunities for stereoconvergent XEC reactions (Figure 1.8).<sup>64</sup> This concept has been demonstrated by Reisman

and co-workers in several Ni-catalyzed asymmetric  $C(sp^2)$ – $C(sp^3)$  reductive coupling reactions, including acylation, vinylation, and arylation of benzylic chlorides, vinylation of benzylic NHP esters, and arylation of  $\alpha$ -chloronitriles and  $\alpha$ -chloroesters.<sup>65</sup> Weix and co-workers have shown that regioselective ring opening of epoxides can be achieved to generate radicals for coupling with aryl halides in the presence of a Ni catalyst and a co-catalyst, wherein iodide co-catalysis results in opening at the less hindered position via an iodohydrin intermediate and titanocene co-catalysis results in opening at the more hindered position, presumably via  $Ti^{III}$ -mediated radical generation.<sup>56</sup> Employing a chiral titanocene co-catalyst can then render this transformation enantioselective.<sup>66</sup> Aziridines can be reductively activated in a similar manner. Doyle and co-workers have reported the Ni-catalyzed XEC of styrenyl aziridines with aryl iodides in the presence of NaI additives, which is amenable to asymmetric catalysis using a chiral bi-oxazoline (BiOX) ligand. In this case, aziridine rings open at the less hindered position to give linear cross-coupled products.<sup>57</sup> It is worth mentioning that the same group then adopted a Ni/Ti co-catalysis strategy to enable a branch-selective, although non-enantioselective, XEC between 2-alkyl aziridines and (hetero)aryl iodides.<sup>67</sup> Asymmetric Ni-catalyzed  $C(sp^3)$ – $C(sp^3)$  XEC reactions can be achieved, albeit within a limited scope. Baran and co-workers have disclosed an enantioselective version of dDCC reaction employing a chiral pyridine-2,6-bisoxazoline (PyBOX) ligand on nickel, in the presence of  $MgBr_2$  and  $FeBr_3$  additives. This method is restricted to the coupling of NHP esters from malonate half amides and primary carboxylic acids.<sup>68</sup> Shu and co-workers have demonstrated the enantioconvergent XEC of unactivated alkyl halides with  $\beta$ -bromoamides, promoted by a chiral nickel bisoxazoline (BOX) catalyst in the presence of a large excess of  $ZnI_2$  additives. Mechanistic studies suggest that  $ZnI_2$  can activate  $\beta$ -bromoamides through coordination to the amide group, which also weakly binds to Ni center during catalysis.<sup>69</sup>

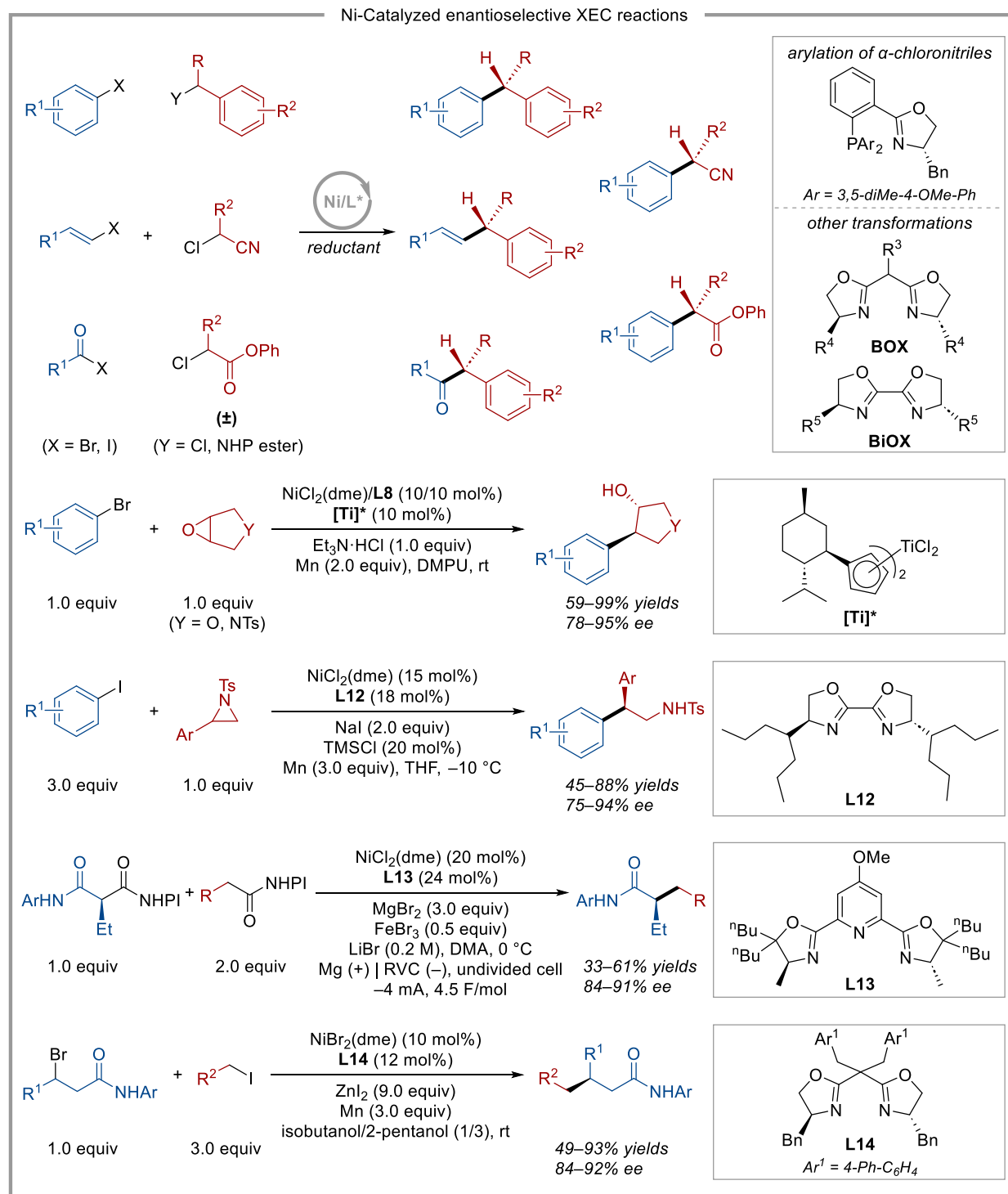


**Figure 1.8.** Ni-Catalyzed enantioselective XEC reactions.

Ni-Catalyzed XEC reactions between two carbon electrophiles with the same hybridization are more challenging due to difficulties in differentiating the two electrophiles and suppressing the

competing homocoupling pathways. Weix and co-workers have uncovered a Ni/Pd co-catalytic system for  $C(sp^2)$ – $C(sp^2)$  reductive coupling of aryl bromides with aryl triflates, wherein the Ni and Pd catalysts each favors activation of one of the coupling partners (see Section 1.5 for more discussion).<sup>70</sup> This strategy has been extended to the XEC of aryl chlorides and aryl tosylates with aryl triflates to access biaryls and biheteroaryls,<sup>71–74</sup> as well as XEC of vinyl bromides and vinyl triflates to access 1,3-dienes.<sup>75</sup> Stahl, Beckham, and co-workers have later applied this Ni/Pd co-catalysis method to the electrochemical XEC of lignin-derived aromatic monomers.<sup>76</sup> Gong and co-workers have pioneered the development of Ni-catalyzed  $C(sp^3)$ – $C(sp^3)$  reductive coupling methods, featuring  $B_2pin_2$  (bis(pinacolato)diboron) reductant as the critical element to enable coupling of secondary and hindered primary halides with primary bromides by leveraging the subtle steric and reactivity differences of the two coupling partners.<sup>77</sup> This strategy was also adopted by Wang and co-workers to enable XEC of primary alkyl halides or tosylates with  $\alpha$ -fluoro alkyl bromides using a  $B_2(neo)_2$  (bis(neopentyl glycolato)diboron) reductant.<sup>78,79</sup> Allylation of secondary alkyl halides with allyl carbonates by Ni-catalysis has been reported by Gong and co-workers using a zinc reductant, which was later expanded to include tertiary alkyl halides.<sup>80,81</sup> Cernak and co-workers have disclosed the XEC of alkyl NHP esters with alkyl Katritzky salts, wherein sequential substrate addition, a binary solvent system, and an electron-deficient bipyridine ligand on nickel all contributed to the final successful coupling.<sup>82</sup> Shu and co-workers have reported a ligand-controlled regiodivergent XEC of  $\delta$ -bromoamides and alkyl bromides by employing a BOX, bipyridine, or PyBOX ligand on nickel to access  $\beta$ -,  $\gamma$ -, or  $\delta$ -alkylated amide products, respectively.<sup>83</sup> More recently, several electrochemical methods have been developed for Ni-catalyzed  $C(sp^3)$ – $C(sp^3)$  reductive coupling, but mostly utilized a large excess of one of the coupling partners (3.0 equiv) to obtain good yields.<sup>62,63,68,84,85</sup> One example, reported by Cantillo

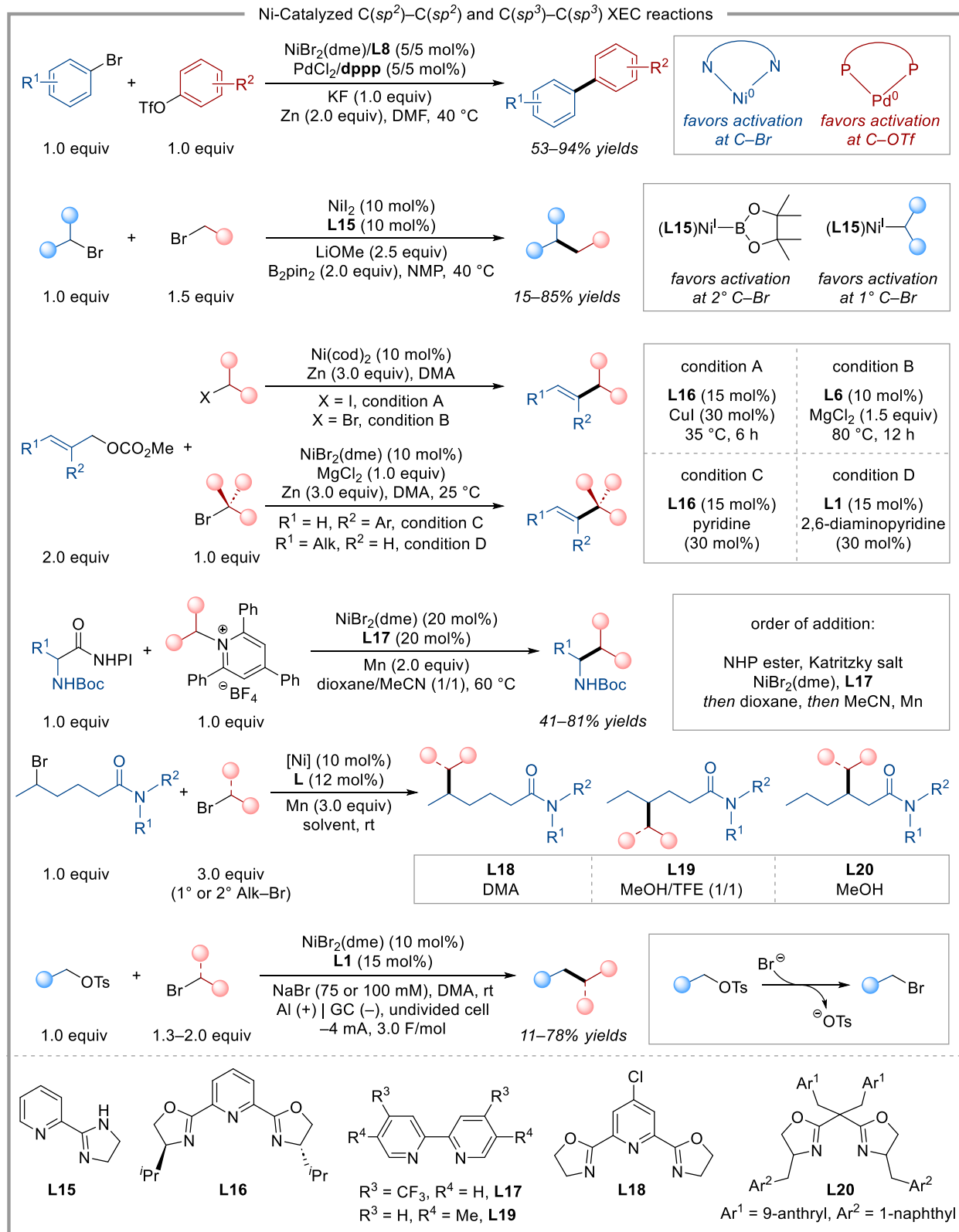


**Figure 1.9.** Ni-Catalyzed C(sp<sup>2</sup>)-C(sp<sup>2</sup>) and C(sp<sup>3</sup>)-C(sp<sup>3</sup>) XEC reactions.

and co-workers, has demonstrated a selective coupling of alkyl tosylates and alkyl bromides via Ni-catalysis with NaBr electrolyte, wherein 1.3–2.0 equiv of alkyl bromides were used and NaBr supported a tosylate–bromide exchange process (Figure 1.9).<sup>84</sup>

### 1.5. General Strategies for Achieving Cross-Selectivity in Ni-Catalyzed XEC Reactions

The proliferation of nickel-catalyzed cross-electrophile coupling reactions is not only attributed to the continuing efforts to expand the scope of viable electrophiles but also dependent on the discovery of new approaches to achieve cross-selectivity by leveraging the differences between electrophilic coupling partners. These approaches can be divided into three categories: (a) substrate-based differentiation, (b) catalyst-based differentiation and (c) others.

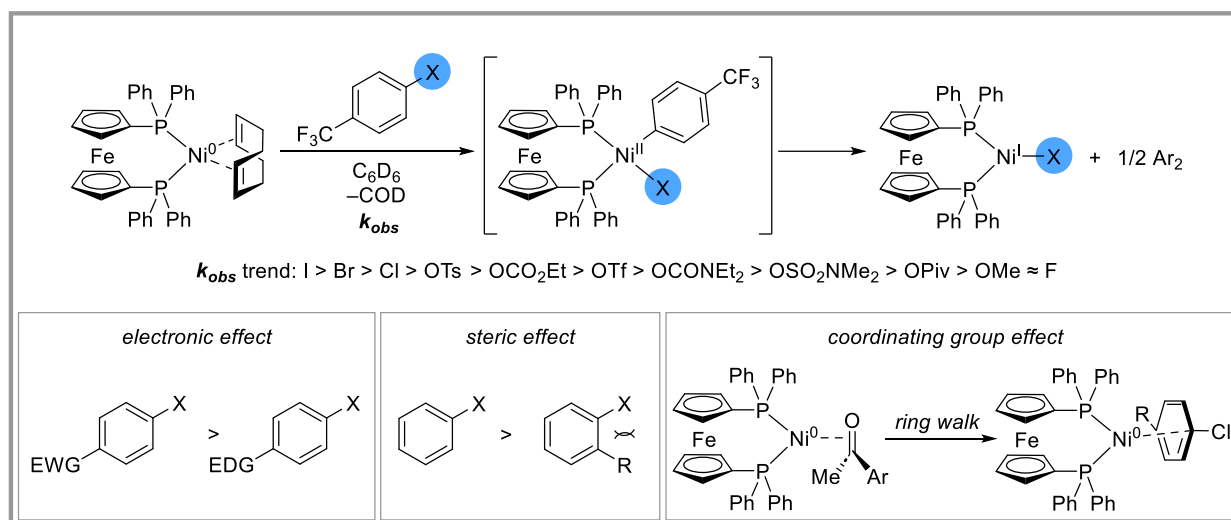


**Figure 1.10.** Aryl electrophile oxidative addition to nickel(0): rates and influencing factors.

Substrate-based differentiation may be one of the most common approaches to achieve cross-selectivity in Ni-catalyzed XEC reactions. Specifically, the rate of electrophile (R–X) activation can be tuned by manipulating the identity of the electrophilic handle (X) and the inherent steric and electronic properties of the substrate (R). Nelson, Sproules, and co-workers have conducted a systematic study on the influence of electrophilic handles on oxidative addition rates of aryl electrophiles to a Ni<sup>0</sup>(COD)(dppf) (dppf = 1,1'-bis(diphenylphosphino)ferrocene) complex in

benzene-d<sub>6</sub> solvent. The results show that rates of oxidative addition of aryl halides to Ni<sup>0</sup> follow the trend of Ar–I >> Ar–Br > Ar–Cl >> Ar–F, consistent with the bond strengths of the C–X bonds. Oxidative addition of sulfonate esters to Ni<sup>0</sup>(COD)(dppf) were all slower than aryl chlorides, following the trend of Ar–Cl > Ar–OTs > Ar–OTf.<sup>86</sup> Substituents on the substrates can also impact the rates of oxidative addition. Generally, electron-deficient aryl electrophiles undergo faster oxidative addition than the corresponding electron-rich substrates, and a more hindered aryl electrophile undergoes slower oxidative addition.<sup>26,86,87</sup> Additionally, aldehyde and ketone substituents on aryl chlorides were shown to promote the oxidative addition rates by coordinating with the low-valent nickel catalyst (Figure 1.10).<sup>88</sup> These features allow for fine tuning of the substrate pairs in Ni-catalyzed C(sp<sup>2</sup>)–C(sp<sup>2</sup>) reductive coupling reactions, as discussed in Section 1.2. More recently, Lautens and co-workers have achieved the XEC of heteroaryl chlorides with aryl chlorides at 1:1.5 substrate ratio (Figure 1.11). The reaction is proposed to follow a sequential oxidative addition mechanism, wherein heteroaryl chlorides preferentially react with nickel(0) due to their electron-deficiency, and oxidative addition of aryl chlorides to heteroaryl-nickel(I) is favored, possibly because of the steric matching. Aryl bromides were used instead of chlorides for electron-rich substrates to promote oxidative addition rates and improve yields.<sup>89</sup>

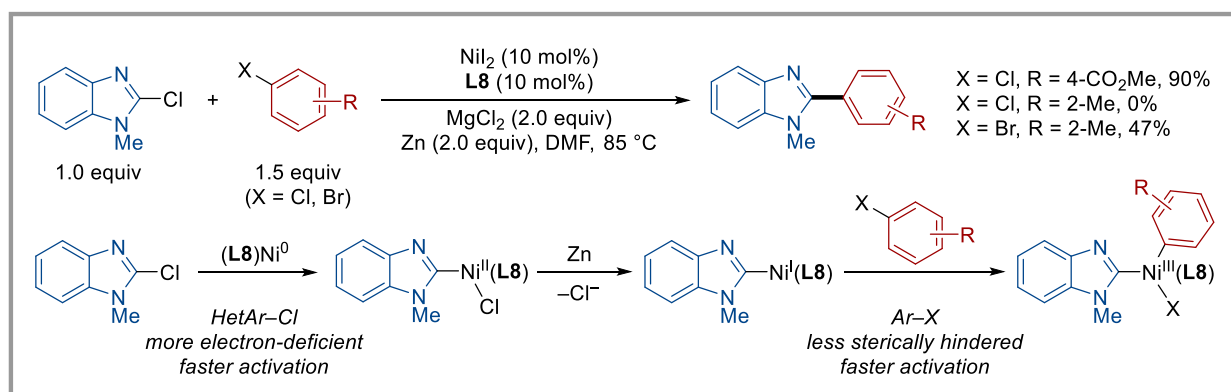


**Figure 1.11.** Ni-Catalyzed XEC of heteroaryl chlorides and aryl halides by Lautens and co-workers.

The activation rates of alkyl electrophiles generally follow the trend of Alk-I > Alk-Br > Alk-Cl and 3° Alk-X > 2° Alk-X > 1° Alk-X in reactions with nickel(I) complexed with nitrogen-based ligands.<sup>90,91</sup> Additionally, various oxygen electrophiles (e.g., sulfonate esters, oxalates) and nitrogen electrophiles (NHP esters, Katritzky salts) provide abundant opportunities for tuning substrate reactivities. For example, Weix and co-workers have reported the XEC of strained ring NHP esters with aryl iodides or bromides, wherein the backbones of NHP esters were strategically modified to tune their reactivities (Figure 1.12). More electron-rich NHP esters were harder to reduce and provided improved yields in XEC reactions with less reactive aryl bromides.<sup>92</sup> Similarly, altering the ancillary aromatic substituents on Katritzky salts could provide an alternative handle to control the rate of radical generation.<sup>61</sup>

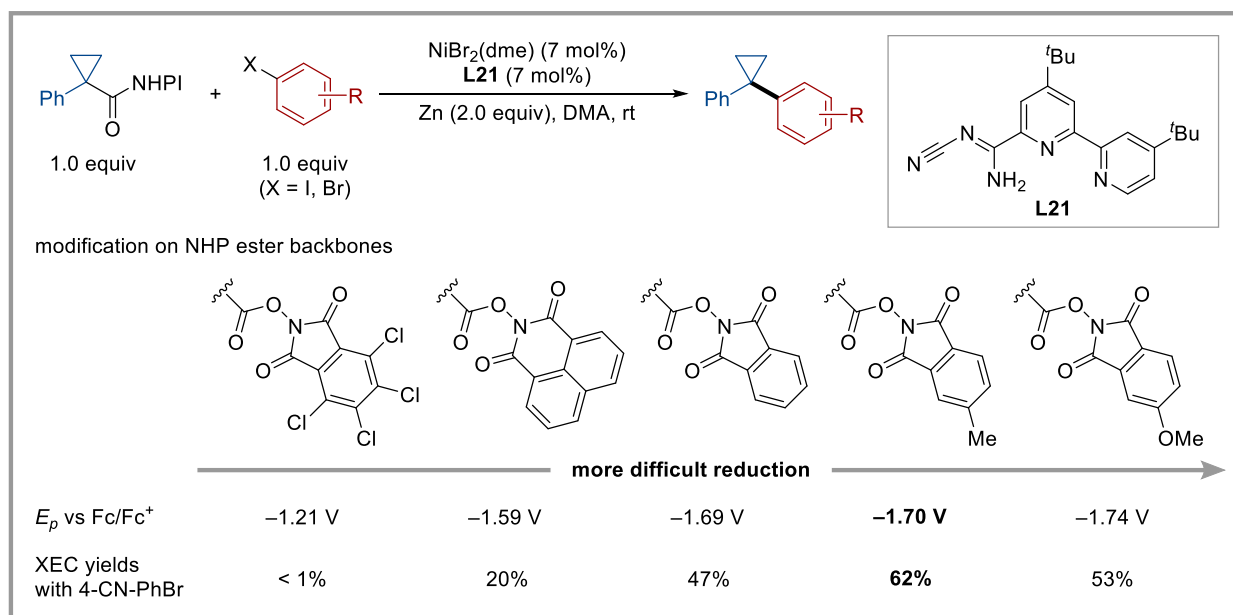


**Figure 1.12.** Tuning reactivity of NHP esters by backbone modification.

Modulating the reactivity of alkyl electrophiles can also be achieved through a sulfonate ester-halide exchange process between alkyl sulfonate esters and halide salts under reaction conditions. This strategy allows *in situ* generation of alkyl halides in low concentrations to provide a slow and steady supply of alkyl radicals into the catalytic cycle, thus enabling the rate matching of radical

generation with the activation of the other coupling partner and effectively limiting the rapid dimerization pathway.<sup>58,84,93,94</sup> For example, Shu and co-workers have conducted a series of control reactions to support the proposal of a mesylate–iodide exchange process in the coupling of alkyl mesylates with alkenyl triflates (Figure 1.13). Trace quantities of alkyl iodides were observed during the XEC reaction employing  $\text{NiI}_2$  as the pre-catalyst and replacing  $\text{NiI}_2$  with  $\text{NiCl}_2$  or  $\text{NiBr}_2$  led to significantly decreased yields. A direct mesylate–iodide exchange reaction was also proved viable in the reaction of alkyl mesylate with stoichiometric  $\text{NaI}$  without nickel catalyst, which afforded the corresponding alkyl iodide in quantitative yield.<sup>93</sup> Similarly, halide–halide exchange could convert less reactive alkyl chlorides into more reactive alkyl bromides and iodides, as demonstrated by Weix and co-workers in the XEC of aryl chlorides with primary alkyl chlorides.<sup>40</sup>

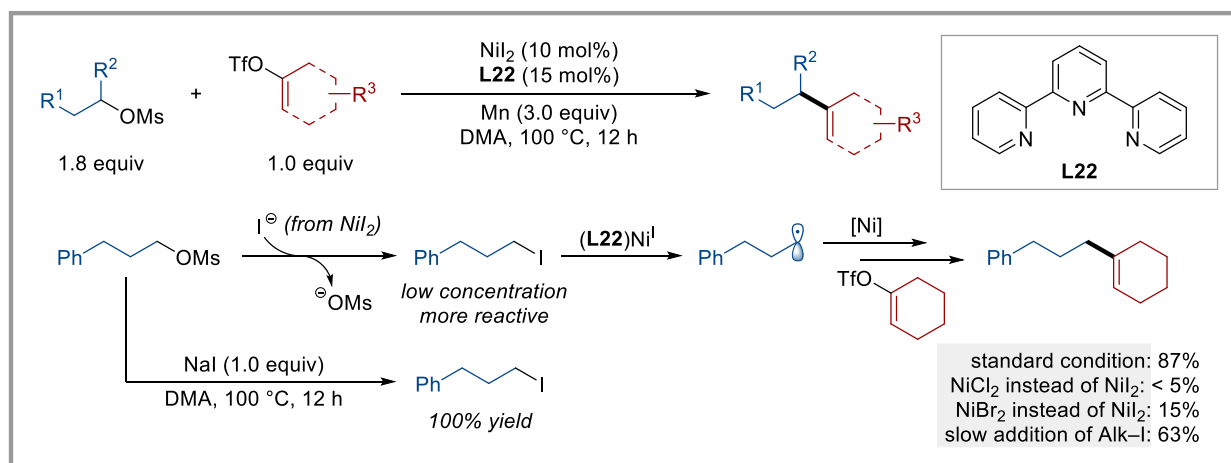


**Figure 1.13.** Tuning reactivity of alkyl mesylates by mesylate–iodide exchange.

Catalyst-based differentiation of the two electrophilic coupling partners represents another powerful strategy for achieving cross-selectivity in Ni-catalyzed XEC reactions. This strategy typically features the use of a nickel catalyst and a co-catalyst that each preferentially reacts with one of the electrophiles. The co-catalyst can be another nickel catalyst bearing a different ligand or a different transition metal catalyst. As briefly mentioned in Section 1.4, Weix and co-workers have disclosed a dual-ligand Ni-catalyzed XEC reaction between aryl iodides and alkyl iodides,

wherein a bipyridine ligand and a bisphosphine ligand were used together to provide best cross-selectivity. The origin of the synergistic effect was not clear, but control reactions suggested that the bipyridine ligand played a more important role in this reaction while the bisphosphine ligand only slightly increased the yield.<sup>27</sup> They later demonstrated the utility of another dual-ligand system in electroreductive Ni-catalyzed  $C(sp^2)$ – $C(sp^3)$  coupling in collaboration with a Pfizer process team (Figure 1.14). The reaction utilizes a combination of two ligands, 4,4'-di-*tert*-butyl-2,2'-bipyridine (**L1**) and 4,4',4''-tri-*tert*-butyl-2,2':6',2''-terpyridine (**L6**). Using the nickel bipyridine catalyst alone predominantly leads to proto-dehalogenation and homocoupling of aryl bromides, whereas the nickel terpyridine catalyst predominantly forms the alkyl dimer and cross-coupled product. Selective coupling can be achieved, however, by using **L1** and **L6** together with varied **L1:L6** ratios so that aryl bromides and alkyl bromides can be activated at comparable rates. As the aryl bromide becomes more electron-rich, the optimal ratio shifts to have more of the nickel bipyridine catalyst.<sup>95,96</sup> The optimal **L1:L6** ratio can also be dependent on other reaction parameters, such as solvents, supporting electrolytes, and current densities.<sup>95,97</sup>

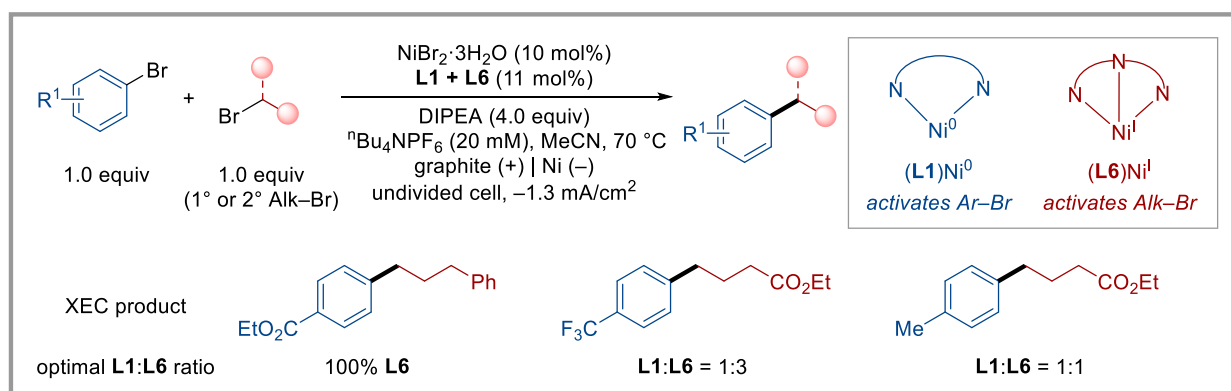


**Figure 1.14.** Bipyridine/terpyridine dual-ligand system for Ni-catalyzed  $C(sp^2)$ – $C(sp^3)$  XEC reaction.

In the previous dual-ligand systems, the combined quantities of the two ligands are approximately equivalent to that of the nickel source. Alternatively, an excess of ligands compared

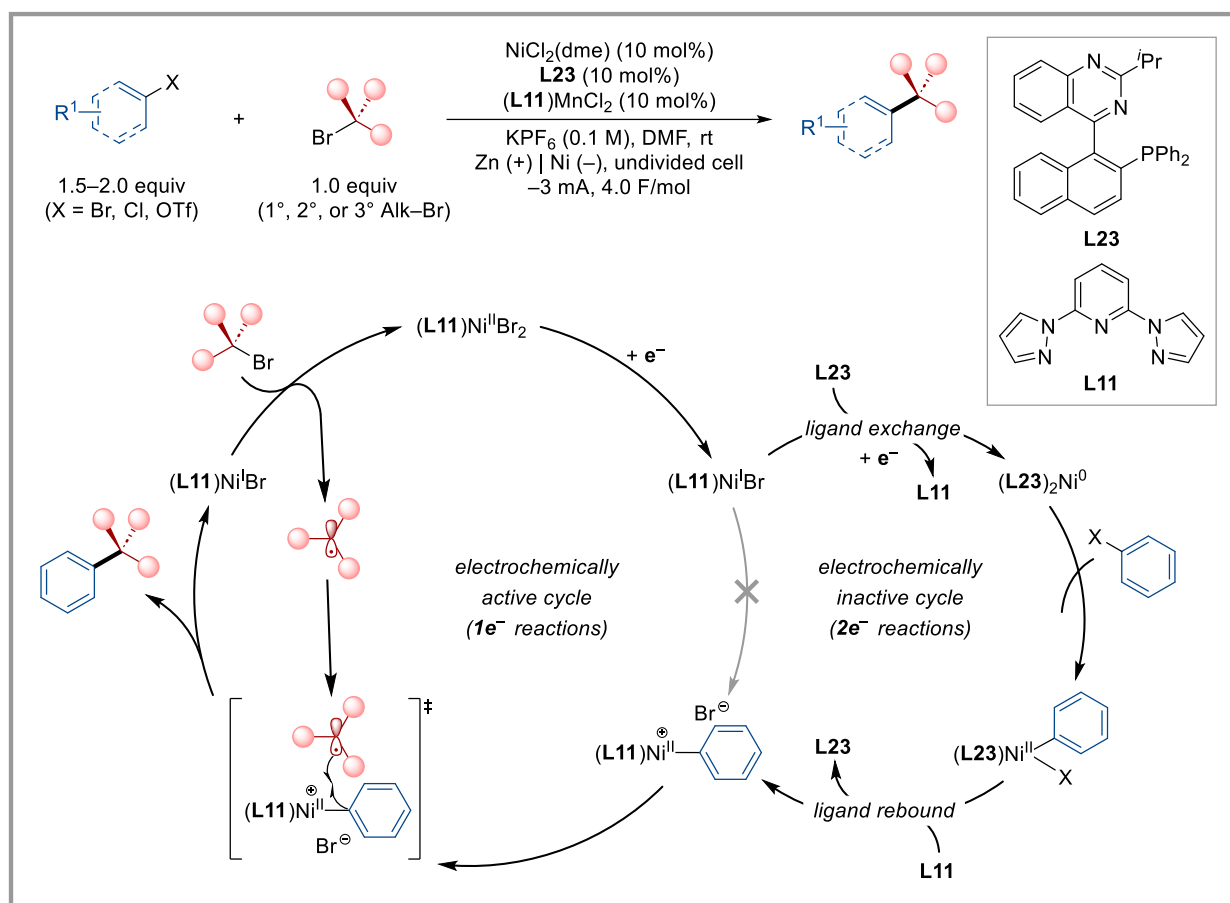


**Figure 1.15.** Sevov dual-ligand system for electroreductive Ni-catalyzed C(*sp*<sup>2</sup>)-C(*sp*<sup>3</sup>) coupling.

to nickel can be employed, triggering a dynamic ligand exchange process that can offer avenues to access nickel species with different reactivities. Sevov and co-workers have demonstrated this concept in electroreductive Ni-catalyzed C(*sp*<sup>2</sup>)-C(*sp*<sup>3</sup>) coupling, utilizing an electrochemically inactive Ni<sup>0</sup>(*i*PrQ)<sub>2</sub> complex (*i*PrQ = *i*Pr-Quinazolinap, **L23**) that selectively reacts with aryl electrophiles through 2e<sup>-</sup> processes and an electrochemically active nickel/bpp complex (bpp = 2,6-bispyrazolylpyridine, **L11**) that selectively reacts with alkyl bromides through 1e<sup>-</sup> processes (Figure 1.15). The reaction is initiated by 1e<sup>-</sup> electroreduction of Ni<sup>II</sup>(bpp)Br<sub>2</sub> followed by rapid ligand exchange with *i*PrQ with concomitant reduction to generate Ni<sup>0</sup>(*i*PrQ)<sub>2</sub>. This Ni<sup>0</sup> complex selectively reacts with aryl electrophiles via oxidative addition and forms a [(bpp)Ni<sup>II</sup>(aryl)]Br intermediate by ligand rebound in the presence of free or weakly-ligated bpp ligands. Subsequent

reaction of this  $\text{Ni}^{\text{II}}(\text{aryl})$  with the alkyl radical forms the product and a low-valent  $\text{Ni}^{\text{I}}(\text{bpp})\text{Br}$  complex, which is responsible for radical generation from alkyl bromides. Consequently, this strategy allows the XEC of aryl (pseudo)halides ( $\text{X} = \text{Cl}, \text{Br}, \text{OTf}$ ) and vinyl triflates with tertiary alkyl bromides, which can be challenging under previously reported coupling conditions.<sup>98</sup>

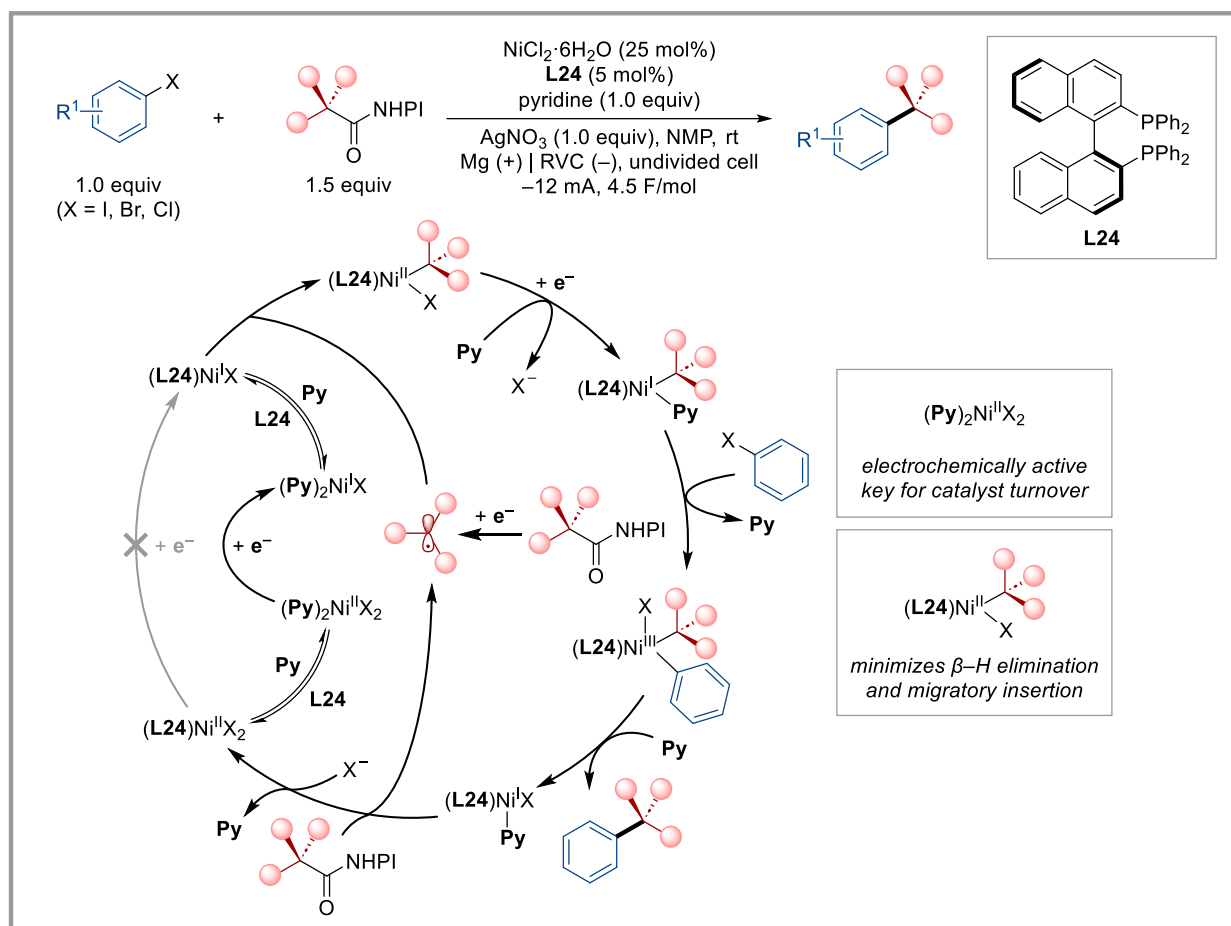


**Figure 1.16.** Baran and Engle dual-ligand system for electroreductive Ni-catalyzed  $\text{C}(\text{sp}^3)\text{-C}(\text{sp}^3)$  coupling.

Baran, Engle, and co-workers have also reported an electrochemical method that exploits a dynamic ligand exchange process to construct arylated quaternary carbon centers through Ni-catalyzed XEC of tertiary NHP esters with (hetero)aryl halides (Figure 1.16). The optimal catalytic system features the combination of  $\text{NiCl}_2 \cdot 6\text{H}_2\text{O}$  salt, BINAP ligand (**L24**), and pyridine (Py) ligand in a 1:5:20 ratio. The proposed mechanism excludes the involvement of a nickel(0) species; instead, it suggests that  $\text{Ni}^{\text{II}}(\text{Py})_2\text{X}_2$  ( $\text{X} = \text{halide}$ ) is electroreduced to  $\text{Ni}^{\text{I}}(\text{Py})_2\text{X}$ , followed by ligand

exchange with BINAP and radical capture to form a  $[(\text{BINAP})\text{Ni}^{\text{II}}(\text{alkyl})]\text{X}$  complex. This complex is then reduced to  $\text{Ni}^{\text{I}}(\text{alkyl})$ , which reacts with aryl halides via oxidative addition followed by reductive elimination to afford the product. The key to successful coupling can be attributed to the active pyridine-stabilized nickel(I) species that are sustained during the reaction and the BINAP ligand that minimizes the  $\beta$ -migration pathway.<sup>99</sup>

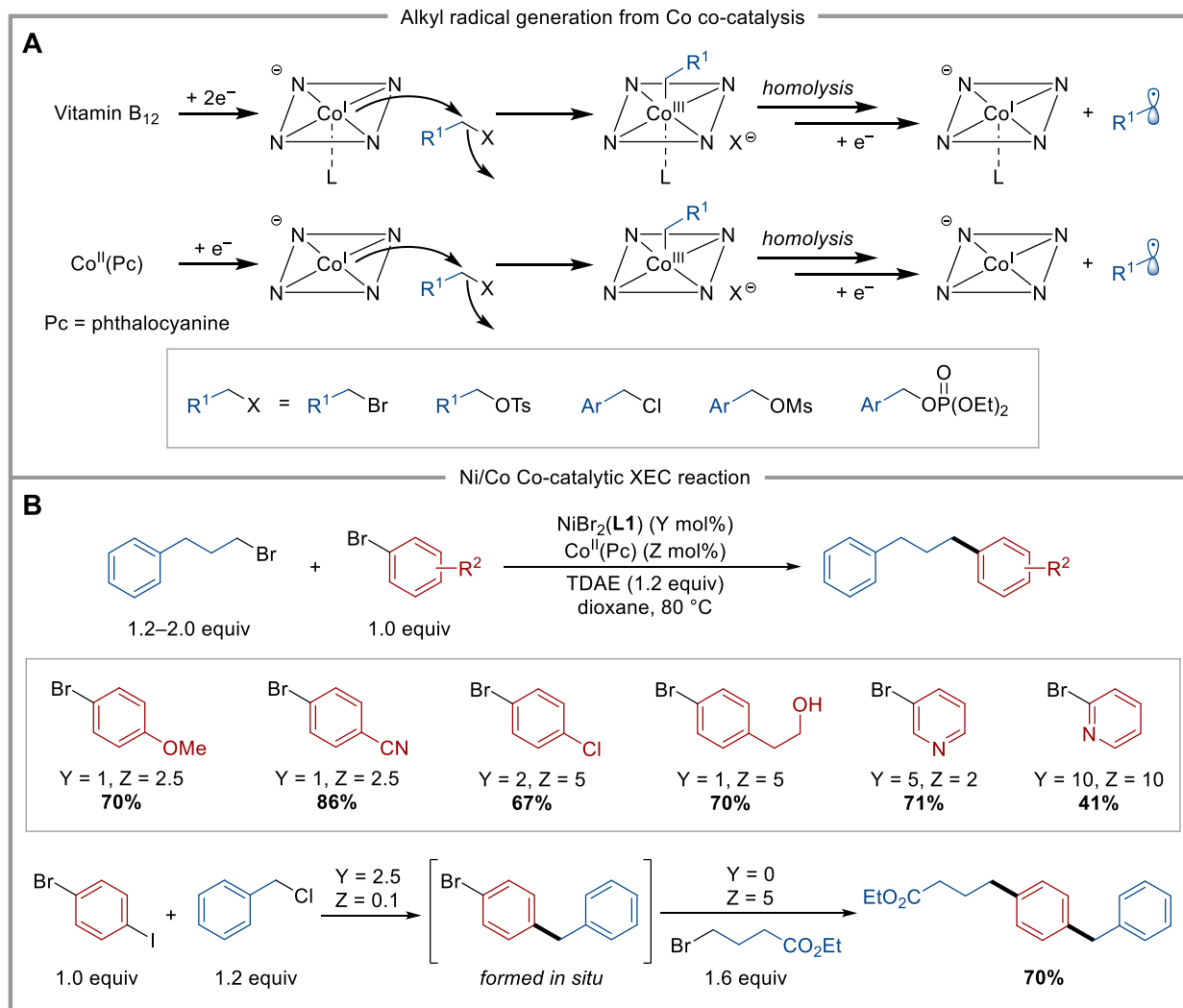


**Figure 1.17.** Mechanism (A) and application (B) of cobalt co-catalysis in Ni-catalyzed XEC reactions.

Inclusion of a non-nickel-based transition metal catalyst can provide a mechanistically distinct pathway for activating electrophiles in XEC reactions. Cobalt co-catalysis is an attractive approach to activate alkyl electrophiles because it generates radicals after two-electron nucleophilic

substitution rather than single-electron transfer. This not only allows for fine tuning of alkyl radical generation by changing the ligands on cobalt or the cobalt catalyst loading, but also enables activation of oxygen electrophiles that are unreactive towards single-electron transfer due to the strength of the C–O bonds, such as alkyl sulfonate and phosphate esters (Figure 1.17A).<sup>100–103</sup> In a comprehensive study by Hazari, Zultanski, and co-workers, a broad scope of alkyl and aryl electrophiles are tolerated within the Ni/Co co-catalytic system by modulating the nickel-to-cobalt ratios based on the reactivities of coupling partners. They further demonstrate the utility of this system in selective one-pot three-component XEC reactions of bromo(iodo)arenes with two distinct alkyl halides (Figure 1.17B).<sup>103</sup> Additionally, titanocene has been used as an effective transition metal co-catalyst to activate epoxides and *N*-acyl aziridines through a Ti<sup>III</sup>-mediated radical ring-opening process.<sup>56,66,67</sup>

Weix and co-workers have disclosed a Ni/Pd co-catalysis strategy for C(*sp*<sup>2</sup>)–C(*sp*<sup>2</sup>) reductive coupling (Figure 1.18). The XEC reaction of aryl bromides with aryl triflates utilizes a Ni<sup>0</sup>(bpy) complex that reacts faster with aryl bromides than aryl triflates and a Pd<sup>0</sup>(dppp) (dppp = 1,3-bis(diphenylphosphino)propane) complex that preferentially reacts with aryl triflates. The resultant [(bpy)Ni<sup>II</sup>(Ar<sup>1</sup>)]Br complex is transient due to its reactivity towards transmetallation, whereas [(dppp)Pd<sup>II</sup>(Ar<sup>2</sup>)]OTf is persistent since it is stable to self-reactivity. Transmetallation then occurs between Ni<sup>II</sup>(Ar<sup>1</sup>) and Pd<sup>II</sup>(Ar<sup>2</sup>), leading to the key Pd<sup>II</sup>(Ar<sup>1</sup>)(Ar<sup>2</sup>) intermediate, which undergoes reductive elimination to give the cross-coupled product. Inclusion of a salt additive, potassium fluoride (KF), is beneficial for this reaction, presumably by improving the selectivity of the palladium catalyst for aryl triflates over aryl bromides.<sup>70</sup> Variations on ligands and additives can extend this method to the coupling of other C(*sp*<sup>2</sup>) electrophiles. For example, in the XEC of aryl chlorides with aryl triflates, lithium chloride (LiCl) was found to accelerate the reduction of

nickel(II) to nickel(0) and counteract autoinhibition of reduction at zinc(0) by zinc(II) salts.<sup>71</sup> In the XEC of heteroaryl halides with heteroaryl triflates, a terpyridine ligand was used instead of bipyridine in reactions involving electron-deficient heteroaryl halides.<sup>74</sup> Additionally, a zinc(II)-mediated shuttling can be operative in the XEC of vinyl bromides with vinyl triflates and the XEC of aryl tosylates with aryl triflates, wherein zinc(II) salts facilitate the transfer of vinyl or aryl groups from nickel(II) to palladium(II).<sup>72,75</sup>

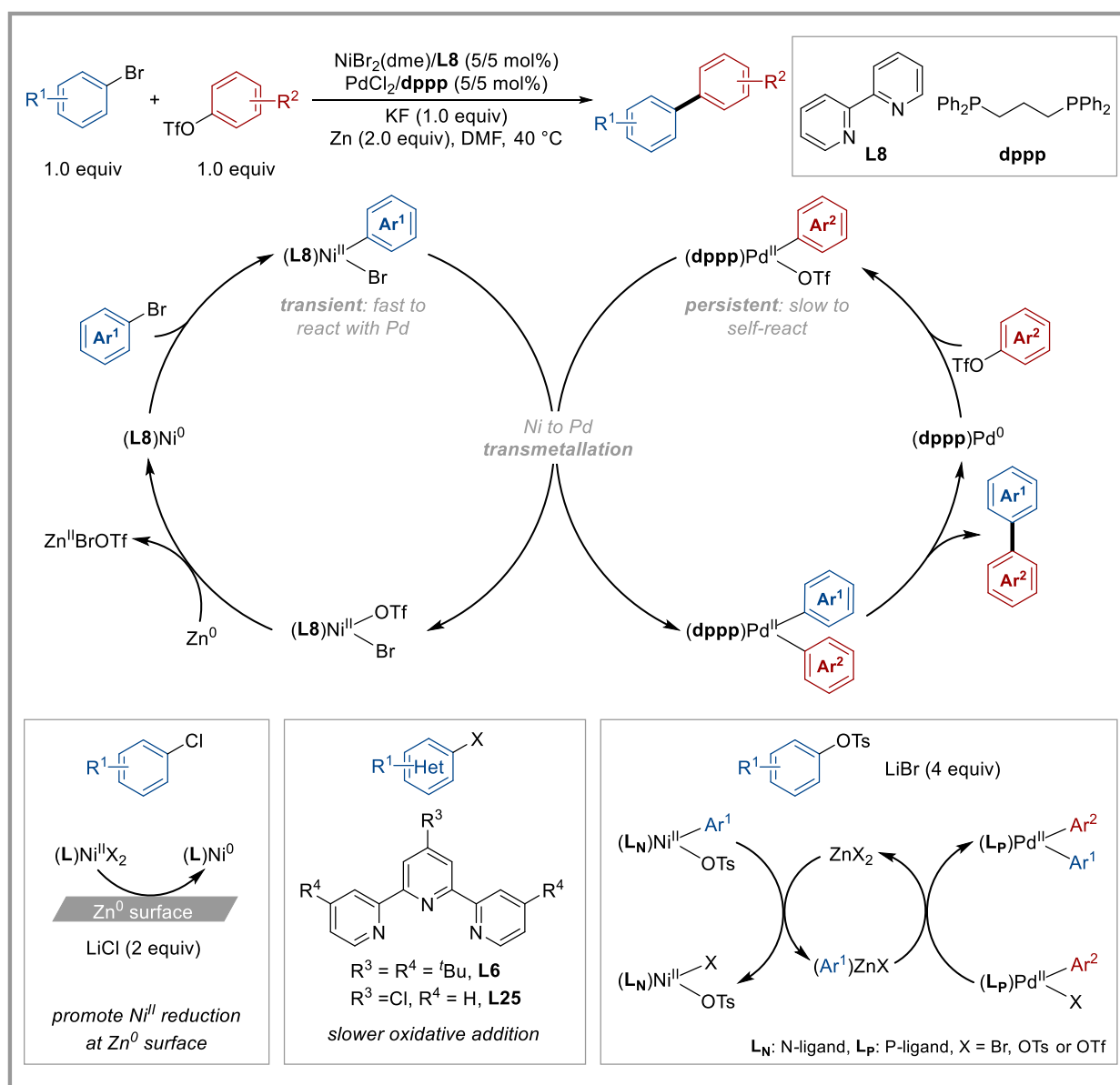


**Figure 1.18.** Weix Ni/Pd-catalyzed C(sp<sup>2</sup>)-C(sp<sup>2</sup>) reductive coupling.

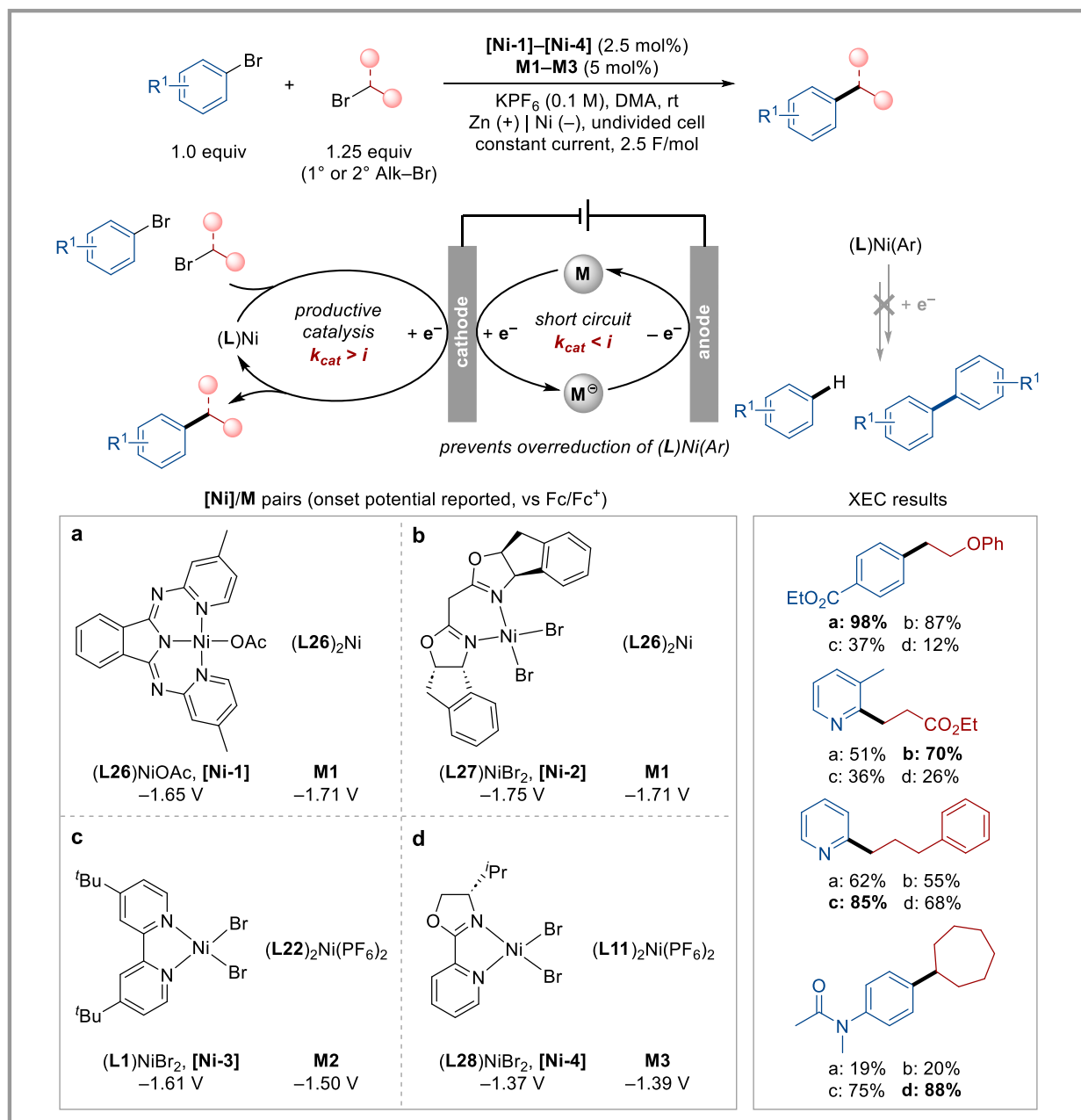


**Figure 1.19.** Sevov synergistic catalyst/mediator pairings for electroreductive C(*sp*<sup>2</sup>)-C(*sp*<sup>3</sup>) coupling.

Finally, a few more studies will be discussed to demonstrate other feasible strategies for achieving cross-selectivity in Ni-catalyzed XEC reactions. For example, Sevov and co-workers have designed a series of coordinatively-saturated nickel complexes as redox-active mediators to facilitate a selective electrochemical Ni-catalyzed XEC of aryl bromides with alkyl bromides. These mediators serve as overcharge protectors to shuttle electrons from the cathode to the anode

when the rate of reduction exceeds the rate of coupling, thus preventing deleterious catalyst overreduction or degradation pathways.<sup>104</sup> The appropriate pairing of mediator with nickel catalyst is critical for effective coupling: the system likely works best in cases where the onset potentials of catalyst and mediator are approximately equal. Preliminary studies have identified four catalyst/mediator pairs that span a wide voltaic window, each featuring a different type of ligands on the nickel catalyst. These catalytic systems were applied to the XEC of a range of (hetero)aryl electrophiles with primary and secondary alkyl bromides and showed complementary reactivities (Figure 1.19).<sup>105</sup>

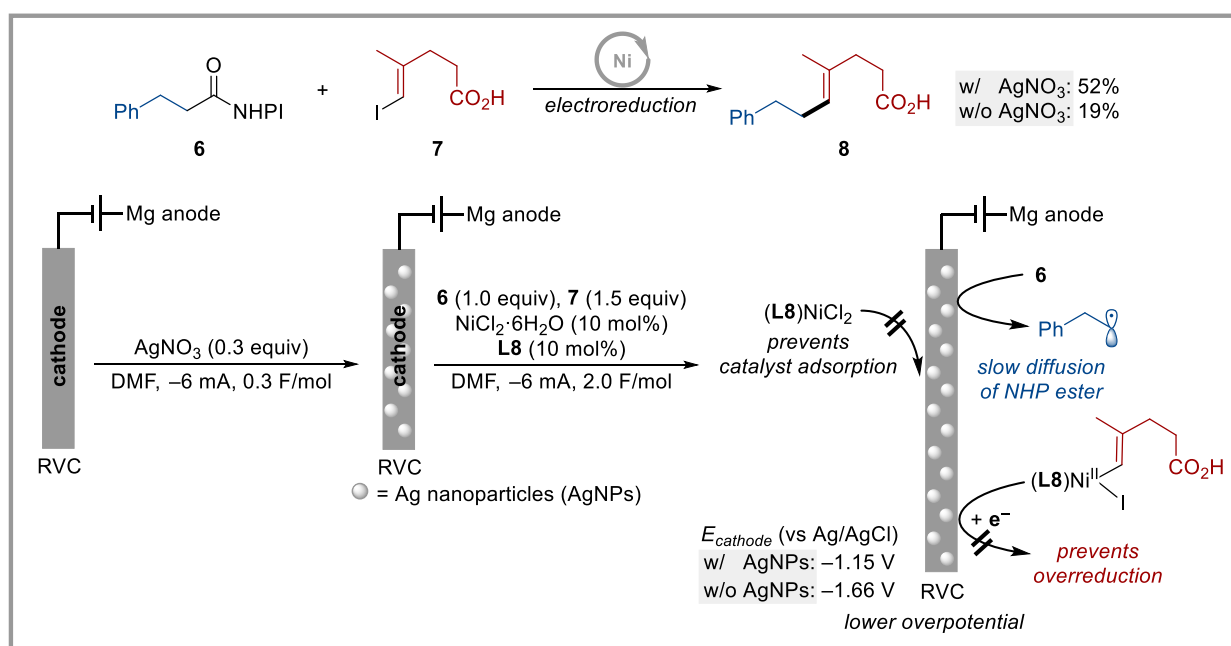


**Figure 1.20.** AgNP-functionalized cathode enables XEC of NHP esters with alkenyl iodides.

Baran and co-workers have shown how functionalized cathodes can be used to improve yields and selectivity in electrochemical Ni-catalyzed XEC of NHP esters with alkenyl iodides (Figure 1.20). Silver nanoparticles (AgNPs) were electrodeposited onto the surface of RVC cathode (RVC = reticulated vitreous carbon) prior to the XEC reaction. This AgNP layer on the cathode has several beneficial effects: (a) it prevents adsorption of reduced nickel catalysts to electrode surface that causes passivation, (b) it supports a mild operating potential at the cathode to prevent catalyst

overreduction and decomposition, and (c) it slows mass transport and reduction of NHP esters at the electrode surface.<sup>106</sup> This strategy has later been applied to other Ni-catalyzed electroreductive XEC reactions involving NHP esters.<sup>63,99,107,108</sup>

## 1.6. Concluding Remarks

Nickel-catalyzed cross-electrophile coupling has proved to be a versatile, reliable, and operationally efficient strategy for constructing carbon-carbon bonds. Previous efforts have focused on the expansion of accessible chemical space and improvement of cross-selectivity in Ni-catalyzed XEC reactions. Moving forward, this field can greatly benefit from advances in one or more of the following directions: (a) exploration of new ligands, catalysts, and co-catalysts that invoke improved or new reactivities, (b) fundamental investigations into the elementary steps involved in Ni-catalysis (e.g., oxidative addition, transmetalation, electron transfer, ancillary ligand exchange), and (c) new technologies that facilitate these synthetic and analytical studies. Specifically, the combined use of high-throughput experimentation (HTE), which efficiently generates extensive datasets, with computational tools capable of utilizing these data to construct predictive models, holds great potential for discovering new ligands and catalysts.<sup>109–113</sup> This process can be simplified by performing *in silico* HTE screening followed by experimental testing, which greatly improves the efficiency.<sup>114,115</sup> Synthesis of key nickel intermediates or accessing transient, highly reactive nickel species using new techniques can provide opportunities for investigating their reactivities and speciation under conditions that are relevant to Ni-catalyzed XEC reactions.<sup>25,26,87,91,116–120</sup> Furthermore, the merger of electrochemistry and Ni-catalysis, although in its infancy, has already demonstrated its unique value in developing Ni-catalyzed XEC reactions. The myriad reaction parameters that can be tuned in electrochemical systems, such as electrode materials, electrolytes, reaction vessel configurations, modes of electrolysis, provide

additional entries into the modulation of catalyst reactivities and accommodation of a broader scope of substrates.<sup>121–123</sup> It is anticipated that advances in these directions will propel the future development of Ni-catalyzed XEC reactions.

## 1.7. References

1. Corbet, J.-P.; Mignani, G. Selected Patented Cross-Coupling Reaction Technologies. *Chem. Rev.* **2006**, *106*, 2651–2710.
2. Chen, X.; Engle, K. M.; Wang, D.-H.; Yu, J.-Q. Palladium(II)-Catalyzed C–H Activation/C–C Cross-Coupling Reactions: Versatility and Practicality. *Angew. Chem. Int. Ed.* **2009**, *48*, 5094–5115.
3. Jana, R.; Pathak, T. P.; Sigman, M. S. Advances in Transition Metal (Pd,Ni,Fe)-Catalyzed Cross-Coupling Reactions Using Alkyl-Organometallics as Reaction Partners. *Chem. Rev.* **2011**, *111*, 1417–1492.
4. Xu, S.; Kim, E. H.; Wei, A.; Negishi, E. Pd- and Ni-Catalyzed Cross-Coupling Reactions in the Synthesis of Organic Electronic Materials. *Sci. Technol. Adv. Mater.* **2014**, *15*, 044201.
5. Ruiz-Castillo, P.; Buchwald, S. L. Applications of Palladium-Catalyzed C–N Cross-Coupling Reactions. *Chem. Rev.* **2016**, *116*, 12564–12649.
6. Brown, D. G.; Boström, J. Analysis of Past and Present Synthetic Methodologies on Medicinal Chemistry: Where Have All the New Reactions Gone? *J. Med. Chem.* **2016**, *59*, 4443–4458.
7. Devendar, P.; Qu, R.-Y.; Kang, W.-M.; He, B.; Yang, G.-F. Palladium-Catalyzed Cross-Coupling Reactions: A Powerful Tool for the Synthesis of Agrochemicals. *J. Agric. Food Chem.* **2018**, *66*, 8914–8934.
8. Buskes, M. J.; Blanco, M.-J. Impact of Cross-Coupling Reactions in Drug Discovery and Development. *Molecules* **2020**, *25*, 3493.
9. Wang, X.; Dai, Y.; Gong, H. Nickel-Catalyzed Reductive Couplings. *Top. Curr. Chem.* **2016**, *374*, 43.
10. Richmond, E.; Moran, J. Recent Advances in Nickel Catalysis Enabled by Stoichiometric Metallic Reducing Agents. *Synthesis* **2018**, *50*, 499–513.
11. Diccianni, J. B.; Diao, T. Mechanisms of Nickel-Catalyzed Cross-Coupling Reactions. *Trends Chem.* **2019**, *1*, 830–844.
12. Goldfogel, M. J.; Huang, L.; Weix, D. J. Cross-Electrophile Coupling. In *Nickel Catalysis in Organic Synthesis*; John Wiley & Sons, Ltd, 2020; pp 183–222.
13. Semmelhack, M. F.; Helquist, P. M.; Jones, L. D. Synthesis with Zerovalent Nickel. Coupling of Aryl Halides with Bis(1,5-Cyclooctadiene)Nickel(0). *J. Am. Chem. Soc.* **1971**, *93*, 5908–5910.
14. Semmelhack, M. F.; Ryono, L. S. Nickel-Promoted Synthesis of Cyclic Biphenyls. Total Synthesis of Alnusone Dimethyl Ether. *J. Am. Chem. Soc.* **1975**, *97*, 3873–3875.
15. Semmelhack, M. F.; Helquist, P.; Jones, L. D.; Keller, L.; Mendelson, L.; Ryono, L. S.; Gorzynski Smith, J.; Stauffer, R. D. Reaction of Aryl and Vinyl Halides with Zerovalent Nickel - Preparative Aspects and the Synthesis of Alnusone. *J. Am. Chem. Soc.* **1981**, *103*, 6460–6471.
16. Zembayashi, M.; Tamao, K.; Yoshida, J.; Kumada, M. Nickel-Phosphine Complex-Catalyzed Homo Coupling of Aryl Halides in the Presence of Zinc Powder. *Tetrahedron Lett.* **1977**, *18*, 4089–4091.
17. Rollin, Y.; Troupel, M.; Tuck, D. G.; Périchon, J. The Coupling of Organic Groups by the Electrochemical Reduction of Organic Halides: Catalysis by 2,2'-Bipyridinenickel Complexes. *J. Organomet. Chem.* **1986**, *303*, 131–137.
18. Meyer, G.; Rollin, Y.; Périchon, J. A Zerovalent Nickel-2,2'-Bipyridine Complex: An Efficient Catalyst for Electrochemical Homocoupling of *Ortho*-Substituted Halides and Their Heterocoupling with *Meta*- and *Para*-Substituted Halides. *J. Organomet. Chem.* **1987**, *333*, 263–267.
19. Durandetti, M.; Sibille, S.; Nédélec, J.-Y.; Périchon, J. A Novel Method of Arylation of  $\alpha$ -Chloroketones. *Synth. Commun.* **1994**, *24*, 145–151.

20. Durandetti, M.; Nédélec, J.-Y.; Périchon, J. Nickel-Catalyzed Direct Electrochemical Cross-Coupling between Aryl Halides and Activated Alkyl Halides. *J. Org. Chem.* **1996**, *61*, 1748–1755.
21. Gosmini, C.; Lasry, S.; Nédélec, J.-Y.; Périchon, J. Electrochemical Cross-Coupling between 2-Halopyridines and Aryl or Heteroaryl Halides Catalysed by Nickel-2,2'-Bipyridine Complexes. *Tetrahedron* **1998**, *54*, 1289–1298.
22. Gosmini, C.; Nédélec, J. Y.; Périchon, J. Electrochemical Cross-Coupling between Functionalized Aryl Halides and 2-Chloropyrimidine or 2-Chloropyrazine Catalyzed by Nickel 2,2'-Bipyridine Complex. *Tetrahedron Lett.* **2000**, *41*, 201–203.
23. Gosmini, C.; Nédélec, J. Y.; Périchon, J. Electrosynthesis of Functionalized 2-Arylpyridines from Functionalized Aryl and Pyridine Halides Catalyzed by Nickel Bromide 2,2'-Bipyridine Complex. *Tetrahedron Lett.* **2000**, *41*, 5039–5042.
24. Diccianni, J.; Lin, Q.; Diao, T. Mechanisms of Nickel-Catalyzed Coupling Reactions and Applications in Alkene Functionalization. *Acc. Chem. Res.* **2020**, *53*, 906–919.
25. Barman, K.; Edwards, M. A.; Hickey, D. P.; Sandford, C.; Qiu, Y.; Gao, R.; Minter, S. D.; White, H. S. Electrochemical Reduction of  $[\text{Ni}(\text{Meppy})_3]^{2+}$ : Elucidation of the Redox Mechanism by Cyclic Voltammetry and Steady-State Voltammetry in Low Ionic Strength Solutions. *ChemElectroChem* **2020**, *7*, 1473–1479.
26. Till, N. A.; Oh, S.; MacMillan, D. W. C.; Bird, M. J. The Application of Pulse Radiolysis to the Study of Ni(I) Intermediates in Ni-Catalyzed Cross-Coupling Reactions. *J. Am. Chem. Soc.* **2021**, *143*, 9332–9337.
27. Everson, D. A.; Shrestha, R.; Weix, D. J. Nickel-Catalyzed Reductive Cross-Coupling of Aryl Halides with Alkyl Halides. *J. Am. Chem. Soc.* **2010**, *132*, 920–921.
28. Fujihara, T.; Nogi, K.; Xu, T.; Terao, J.; Tsuji, Y. Nickel-Catalyzed Carboxylation of Aryl and Vinyl Chlorides Employing Carbon Dioxide. *J. Am. Chem. Soc.* **2012**, *134*, 9106–9109.
29. Tortajada, A.; Juliá-Hernández, F.; Börjesson, M.; Moragas, T.; Martín, R. Transition-Metal-Catalyzed Carboxylation Reactions with Carbon Dioxide. *Angew. Chem. Int. Ed.* **2018**, *57*, 15948–15982.
30. Sun, G.-Q.; Zhang, W.; Liao, L.-L.; Li, L.; Nie, Z.-H.; Wu, J.-G.; Zhang, Z.; Yu, D.-G. Nickel-Catalyzed Electrochemical Carboxylation of Unactivated Aryl and Alkyl Halides with  $\text{CO}_2$ . *Nat. Commun.* **2021**, *12*, 7086.
31. Lou, T. S.-B.; Kawamata, Y.; Ewing, T.; Correa-Otero, G. A.; Collins, M. R.; Baran, P. S. Scalable, Chemoselective Nickel Electrocatalytic Sulfinylation of Aryl Halides with  $\text{SO}_2$ . *Angew. Chem. Int. Ed.* **2022**, *61*, e202208080.
32. Duan, J.; Wang, K.; Xu, G.-L.; Kang, S.; Qi, L.; Liu, X.-Y.; Shu, X.-Z. Cross-Electrophile  $\text{C}(\text{sp}^2)$ -Si Coupling of Vinyl Chlorosilanes. *Angew. Chem. Int. Ed.* **2020**, *59*, 23083–23088.
33. Zhao, Z.-Z.; Pang, X.; Wei, X.-X.; Liu, X.-Y.; Shu, X.-Z. Nickel-Catalyzed Reductive  $\text{C}(\text{sp}^2)$ -Si Coupling of Chlorohydrosilanes via Si-Cl Cleavage. *Angew. Chem. Int. Ed.* **2022**, *61*, e202200215.
34. Su, P.-F.; Wang, K.; Peng, X.; Pang, X.; Guo, P.; Shu, X.-Z. Nickel-Catalyzed Reductive C-Ge Coupling of Aryl/Alkenyl Electrophiles with Chlorogermanes. *Angew. Chem. Int. Ed.* **2021**, *60*, 26571–26576.
35. Meng, C.-F.; Zhang, B.-B.; Liu, Q.; Chen, K.-Q.; Wang, Z.-X.; Chen, X.-Y. Achieving Nickel-Catalyzed Reductive  $\text{C}(\text{sp}^2)$ -B Coupling of Bromoboranes via Reversing the Activation Sequence. *J. Am. Chem. Soc.* **2024**, *146*, 7210–7215.
36. Everson, D. A.; Jones, B. A.; Weix, D. J. Replacing Conventional Carbon Nucleophiles with Electrophiles: Nickel-Catalyzed Reductive Alkylation of Aryl Bromides and Chlorides. *J. Am. Chem. Soc.* **2012**, *134*, 6146–6159.
37. Molander, G. A.; Traister, K. M.; O'Neill, B. T. Reductive Cross-Coupling of Nonaromatic, Heterocyclic Bromides with Aryl and Heteroaryl Bromides. *J. Org. Chem.* **2014**, *79*, 5771–5780.
38. Weix, D. J. Methods and Mechanisms for Cross-Electrophile Coupling of  $\text{Csp}^2$  Halides with Alkyl Electrophiles. *Acc. Chem. Res.* **2015**, *48*, 1767–1775.

39. Hu, L.; Liu, X.; Liao, X. Nickel-Catalyzed Methylation of Aryl Halides with Deuterated Methyl Iodide. *Angew. Chem. Int. Ed.* **2016**, *55*, 9743–9747.
40. Kim, S.; Goldfogel, M. J.; Gilbert, M. M.; Weix, D. J. Nickel-Catalyzed Cross-Electrophile Coupling of Aryl Chlorides with Primary Alkyl Chlorides. *J. Am. Chem. Soc.* **2020**, *142*, 9902–9907.
41. Hansen, E. C.; Pedro, D. J.; Wotal, A. C.; Gower, N. J.; Nelson, J. D.; Caron, S.; Weix, D. J. New Ligands for Nickel Catalysis from Diverse Pharmaceutical Heterocycle Libraries. *Nat. Chem.* **2016**, *8*, 1126–1130.
42. Hansen, E. C.; Li, C.; Yang, S.; Pedro, D.; Weix, D. J. Coupling of Challenging Heteroaryl Halides with Alkyl Halides via Nickel-Catalyzed Cross-Electrophile Coupling. *J. Org. Chem.* **2017**, *82*, 7085–7092.
43. Wang, X.; Wang, S.; Xue, W.; Gong, H. Nickel-Catalyzed Reductive Coupling of Aryl Bromides with Tertiary Alkyl Halides. *J. Am. Chem. Soc.* **2015**, *137*, 11562–11565.
44. Wang, X.; Ma, G.; Peng, Y.; Pitsch, C. E.; Moll, B. J.; Ly, T. D.; Wang, X.; Gong, H. Ni-Catalyzed Reductive Coupling of Electron-Rich Aryl Iodides with Tertiary Alkyl Halides. *J. Am. Chem. Soc.* **2018**, *140*, 14490–14497.
45. Yan, X.-B.; Li, C.-L.; Jin, W.-J.; Guo, P.; Shu, X.-Z. Reductive Coupling of Benzyl Oxalates with Highly Functionalized Alkyl Bromides by Nickel Catalysis. *Chem. Sci.* **2018**, *9*, 4529–4534.
46. Gao, M.; Sun, D.; Gong, H. Ni-Catalyzed Reductive C–O Bond Arylation of Oxalates Derived from  $\alpha$ -Hydroxy Esters with Aryl Halides. *Org. Lett.* **2019**, *21*, 1645–1648.
47. Ye, Y.; Chen, H.; Sessler, J. L.; Gong, H. Zn-Mediated Fragmentation of Tertiary Alkyl Oxalates Enabling Formation of Alkylated and Arylated Quaternary Carbon Centers. *J. Am. Chem. Soc.* **2019**, *141*, 820–824.
48. Ni, S.; Li, C.-X.; Mao, Y.; Han, J.; Wang, Y.; Yan, H.; Pan, Y. Ni-Catalyzed Deaminative Cross-Electrophile Coupling of Katritzky Salts with Halides via C–N Bond Activation. *Sci. Adv.* **2019**, *5*, eaaw9516.
49. Yue, H.; Zhu, C.; Shen, L.; Geng, Q.; Hock, K. J.; Yuan, T.; Cavallo, L.; Rueping, M. Nickel-Catalyzed C–N Bond Activation: Activated Primary Amines as Alkylating Reagents in Reductive Cross-Coupling. *Chem. Sci.* **2019**, *10*, 4430–4435.
50. Martin-Montero, R.; Yatham, V. R.; Yin, H.; Davies, J.; Martin, R. Ni-Catalyzed Reductive Deaminative Arylation at  $sp^3$  Carbon Centers. *Org. Lett.* **2019**, *21*, 2947–2951.
51. Liao, J.; Basch, C. H.; Hoerrner, M. E.; Talley, M. R.; Boscoe, B. P.; Tucker, J. W.; Garnsey, M. R.; Watson, M. P. Deaminative Reductive Cross-Electrophile Couplings of Alkylpyridinium Salts and Aryl Bromides. *Org. Lett.* **2019**, *21*, 2941–2946.
52. He, R.-D.; Li, C.-L.; Pan, Q.-Q.; Guo, P.; Liu, X.-Y.; Shu, X.-Z. Reductive Coupling between C–N and C–O Electrophiles. *J. Am. Chem. Soc.* **2019**, *141*, 12481–12486.
53. Huihui, K. M. M.; Caputo, J. A.; Melchor, Z.; Olivares, A. M.; Spiewak, A. M.; Johnson, K. A.; DiBenedetto, T. A.; Kim, S.; Ackerman, L. K. G.; Weix, D. J. Decarboxylative Cross-Electrophile Coupling of N-Hydroxyphthalimide Esters with Aryl Iodides. *J. Am. Chem. Soc.* **2016**, *138*, 5016–5019.
54. Niu, P.; Li, J.; Zhang, Y.; Huo, C. One-Electron Reduction of Redox-Active Esters to Generate Carbon-Centered Radicals. *Eur. J. Org. Chem.* **2020**, *2020*, 5801–5814.
55. Wang, J.; Ehehalt, L. E.; Huang, Z.; Beleh, O. M.; Guzei, I. A.; Weix, D. J. Formation of C( $sp^2$ )–C( $sp^3$ ) Bonds Instead of Amide C–N Bonds from Carboxylic Acid and Amine Substrate Pools by Decarbonylative Cross-Electrophile Coupling. *J. Am. Chem. Soc.* **2023**, *145*, 9951–9958.
56. Zhao, Y.; Weix, D. J. Nickel-Catalyzed Regiodivergent Opening of Epoxides with Aryl Halides: Co-Catalysis Controls Regioselectivity. *J. Am. Chem. Soc.* **2014**, *136*, 48–51.
57. Woods, B. P.; Orlandi, M.; Huang, C.-Y.; Sigman, M. S.; Doyle, A. G. Nickel-Catalyzed Enantioselective Reductive Cross-Coupling of Styrenyl Aziridines. *J. Am. Chem. Soc.* **2017**, *139*, 5688–5691.
58. Liang, Z.; Xue, W.; Lin, K.; Gong, H. Nickel-Catalyzed Reductive Methylation of Alkyl Halides and Acid Chlorides with Methyl *p*-Tosylate. *Org. Lett.* **2014**, *16*, 5620–5623.

59. Wang, J.; Zhao, J.; Gong, H. Nickel-Catalyzed Methylation of Aryl Halides/Tosylates with Methyl Tosylate. *Chem. Commun.* **2017**, *53*, 10180–10183.
60. Twitty, J. C.; Hong, Y.; Garcia, B.; Tsang, S.; Liao, J.; Schultz, D. M.; Hanisak, J.; Zultanski, S. L.; Dion, A.; Kalyani, D.; Watson, M. P. Diversifying Amino Acids and Peptides via Deaminative Reductive Cross-Couplings Leveraging High-Throughput Experimentation. *J. Am. Chem. Soc.* **2023**, *145*, 5684–5695.
61. Charboneau, D. J.; Huang, H.; Barth, E. L.; Germe, C. C.; Hazari, N.; Mercado, B. Q.; Uehling, M. R.; Zultanski, S. L. Tunable and Practical Homogeneous Organic Reductants for Cross-Electrophile Coupling. *J. Am. Chem. Soc.* **2021**, *143*, 21024–21036.
62. Zhang, B.; Gao, Y.; Hioki, Y.; Oderinde, M. S.; Qiao, J. X.; Rodriguez, K. X.; Zhang, H.-J.; Kawamata, Y.; Baran, P. S. Ni-Electrocatalytic Csp<sup>3</sup>–Csp<sup>3</sup> Doubly Decarboxylative Coupling. *Nature* **2022**, *606*, 313–318.
63. Zhang, B.; He, J.; Gao, Y.; Levy, L.; Oderinde, M. S.; Palkowitz, M. D.; Dhar, T. G. M.; Mandler, M. D.; Collins, M. R.; Schmitt, D. C.; Bolduc, P. N.; Chen, T.; Clementson, S.; Petersen, N. N.; Laudadio, G.; Bi, C.; Kawamata, Y.; Baran, P. S. Complex Molecule Synthesis by Electrocatalytic Decarboxylative Cross-Coupling. *Nature* **2023**, *623*, 745–751.
64. Jin, Y.; Wang, C. Nickel-Catalyzed Asymmetric Cross-Electrophile Coupling Reactions. *Synlett* **2020**, *31*, 1843–1850.
65. Chen, L.-M.; Reisman, S. E. Enantioselective C(sp<sup>2</sup>)–C(sp<sup>3</sup>) Bond Construction by Ni Catalysis. *Acc. Chem. Res.* **2024**, *57*, 751–762.
66. Zhao, Y.; Weix, D. J. Enantioselective Cross-Coupling of Meso-Epoxides with Aryl Halides. *J. Am. Chem. Soc.* **2015**, *137*, 3237–3240.
67. Williams, W. L.; Gutiérrez-Valencia, N. E.; Doyle, A. G. Branched-Selective Cross-Electrophile Coupling of 2-Alkyl Aziridines and (Hetero)Aryl Iodides Using Ti/Ni Catalysis. *J. Am. Chem. Soc.* **2023**, *145*, 24175–24183.
68. Gao, Y.; Zhang, B.; He, J.; Baran, P. S. Ni-Electrocatalytic Enantioselective Doubly Decarboxylative C(sp<sup>3</sup>)–C(sp<sup>3</sup>) Cross Coupling. *J. Am. Chem. Soc.* **2023**, *145*, 11518–11523.
69. Zhao, W.-T.; Shu, W. Enantioselective Csp<sup>3</sup>–Csp<sup>3</sup> Formation by Nickel-Catalyzed Enantioconvergent Cross-Electrophile Alkyl-Alkyl Coupling of Unactivated Alkyl Halides. *Sci. Adv.* **2023**, *9*, eadg9898.
70. Ackerman, L. K. G.; Lovell, M. M.; Weix, D. J. Multimetallic Catalysed Cross-Coupling of Aryl Bromides with Aryl Triflates. *Nature* **2015**, *524*, 454–457.
71. Huang, L.; Ackerman, L. K. G.; Kang, K.; Parsons, A. M.; Weix, D. J. LiCl-Accelerated Multimetallic Cross-Coupling of Aryl Chlorides with Aryl Triflates. *J. Am. Chem. Soc.* **2019**, *141*, 10978–10983.
72. Kang, K.; Huang, L.; Weix, D. J. Sulfonate Versus Sulfonate: Nickel and Palladium Multimetallic Cross-Electrophile Coupling of Aryl Triflates with Aryl Tosylates. *J. Am. Chem. Soc.* **2020**, *142*, 10634–10640.
73. Xiong, B.; Li, Y.; Wei, Y.; Kramer, S.; Lian, Z. Dual Nickel-/Palladium-Catalyzed Reductive Cross-Coupling Reactions between Two Phenol Derivatives. *Org. Lett.* **2020**, *22*, 6334–6338.
74. Kang, K.; Loud, N. L.; DiBenedetto, T. A.; Weix, D. J. A General, Multimetallic Cross-Ullmann Biheteroaryl Synthesis from Heteroaryl Halides and Heteroaryl Triflates. *J. Am. Chem. Soc.* **2021**, *143*, 21484–21491.
75. Olivares, A. M.; Weix, D. J. Multimetallic Ni- and Pd-Catalyzed Cross-Electrophile Coupling to Form Highly Substituted 1,3-Dienes. *J. Am. Chem. Soc.* **2018**, *140*, 2446–2449.
76. Su, Z.-M.; Twilton, J.; Hoyt, C. B.; Wang, F.; Stanley, L.; Mayes, H. B.; Kang, K.; Weix, D. J.; Beckham, G. T.; Stahl, S. S. Ni- and Ni/Pd-Catalyzed Reductive Coupling of Lignin-Derived Aromatics to Access Biobased Plasticizers. *ACS Cent. Sci.* **2023**, *9*, 159–165.
77. Xu, H.; Zhao, C.; Qian, Q.; Deng, W.; Gong, H. Nickel-Catalyzed Cross-Coupling of Unactivated Alkyl Halides Using Bis(Pinacolato)Diboron as Reductant. *Chem. Sci.* **2013**, *4*, 4022–4029.
78. Sheng, J.; Ni, H.-Q.; Ni, S.-X.; He, Y.; Cui, R.; Liao, G.-X.; Bian, K.-J.; Wu, B.-B.; Wang, X.-S. Diversity-Oriented Synthesis of Aliphatic Fluorides via Reductive C(sp<sup>3</sup>)–C(sp<sup>3</sup>) Cross-Coupling Fluoroalkylation. *Angew. Chem. Int. Ed.* **2021**, *60*, 15020–15027.

79. Cui, R.; Sheng, J.; Wu, B.-B.; Hu, D.-D.; Zheng, H.-Q.; Wang, X.-S. Nickel-Catalyzed Reductive Monofluoroalkylation of Alkyl Tosylate with Bromofluoromethane to Primary Alkyl Fluoride. *Chem. Commun.* **2021**, *57*, 9084–9087.
80. Dai, Y.; Wu, F.; Zang, Z.; You, H.; Gong, H. Ni-Catalyzed Reductive Allylation of Unactivated Alkyl Halides with Allylic Carbonates. *Chem. – Eur. J.* **2012**, *18*, 808–812.
81. Chen, H.; Jia, X.; Yu, Y.; Qian, Q.; Gong, H. Nickel-Catalyzed Reductive Allylation of Tertiary Alkyl Halides with Allylic Carbonates. *Angew. Chem. Int. Ed.* **2017**, *56*, 13103–13106.
82. Zhang, Z.; Cernak, T. The Formal Cross-Coupling of Amines and Carboxylic Acids to Form  $sp^3$ – $sp^3$  Carbon–Carbon Bonds. *Angew. Chem. Int. Ed.* **2021**, *60*, 27293–27298.
83. Zhao, W.-T.; Meng, H.; Lin, J.-N.; Shu, W. Ligand-Controlled Nickel-Catalyzed Regiodivergent Cross-Electrophile Alkyl-Alkyl Couplings of Alkyl Halides. *Angew. Chem. Int. Ed.* **2023**, *62*, e202215779.
84. Ibrahim, M. Y. S.; Cumming, G. R.; Gonzalez de Vega, R.; Garcia-Losada, P.; de Frutos, O.; Kappe, C. O.; Cantillo, D. Electrochemical Nickel-Catalyzed  $C(sp^3)$ – $C(sp^3)$  Cross-Coupling of Alkyl Halides with Alkyl Tosylates. *J. Am. Chem. Soc.* **2023**, *145*, 17023–17028.
85. Li, P.; Zhu, Z.; Guo, C.; Kou, G.; Wang, S.; Xie, P.; Ma, D.; Feng, T.; Wang, Y.; Qiu, Y. Nickel-Electrocatalysed  $C(sp^3)$ – $C(sp^3)$  Cross-Coupling of Unactivated Alkyl Halides. *Nat. Catal.* **2024**, *7*, 412–421.
86. Bajo, S.; Laidlaw, G.; Kennedy, A. R.; Sproules, S.; Nelson, D. J. Oxidative Addition of Aryl Electrophiles to a Prototypical Nickel(0) Complex: Mechanism and Structure/Reactivity Relationships. *Organometallics* **2017**, *36*, 1662–1672.
87. Ting, S. I.; Williams, W. L.; Doyle, A. G. Oxidative Addition of Aryl Halides to a Ni(I)-Bipyridine Complex. *J. Am. Chem. Soc.* **2022**, *144*, 5575–5582.
88. Cooper, A. K.; Leonard, D. K.; Bajo, S.; Burton, P. M.; Nelson, D. J. Aldehydes and Ketones Influence Reactivity and Selectivity in Nickel-Catalysed Suzuki–Miyaura Reactions. *Chem. Sci.* **2020**, *11*, 1905–1911.
89. Mirabi, B.; Marchese, A. D.; Lautens, M. Nickel-Catalyzed Reductive Cross-Coupling of Heteroaryl Chlorides and Aryl Chlorides. *ACS Catal.* **2021**, *11*, 12785–12793.
90. Gosden, C.; Healy, K. P.; Pletcher, D. Reaction of Electrogenerated Square-Planar Nickel(I) Complexes with Alkyl Halides. *J. Chem. Soc. Dalton Trans.* **1978**, *8*, 972–976.
91. Lin, Q.; Fu, Y.; Liu, P.; Diao, T. Monovalent Nickel-Mediated Radical Formation: A Concerted Halogen-Atom Dissociation Pathway Determined by Electroanalytical Studies. *J. Am. Chem. Soc.* **2021**, *143*, 14196–14206.
92. Salgueiro, D. C.; Chi, B. K.; Guzei, I. A.; García-Reynaga, P.; Weix, D. J. Control of Redox-Active Ester Reactivity Enables a General Cross-Electrophile Approach to Access Arylated Strained Rings\*\*. *Angew. Chem. Int. Ed.* **2022**, *61*, e202205673.
93. Duan, J.; Du, Y.-F.; Pang, X.; Shu, X.-Z. Ni-Catalyzed Cross-Electrophile Coupling between Vinyl/Aryl and Alkyl Sulfonates: Synthesis of Cycloalkenes and Modification of Peptides. *Chem. Sci.* **2019**, *10*, 8706–8712.
95. Sanford, A. B.; Thane, T. A.; McGinnis, T. M.; Chen, P.-P.; Hong, X.; Jarvo, E. R. Nickel-Catalyzed Alkyl–Alkyl Cross-Electrophile Coupling Reaction of 1,3-Dimesylates for the Synthesis of Alkylcyclopropanes. *J. Am. Chem. Soc.* **2020**, *142*, 5017–5023.
95. Perkins, R. J.; Hughes, A. J.; Weix, D. J.; Hansen, E. C. Metal-Reductant-Free Electrochemical Nickel-Catalyzed Couplings of Aryl and Alkyl Bromides in Acetonitrile. *Org. Process Res. Dev.* **2019**, *23*, 1746–1751.
96. Franke, M. C.; Longley, V. R.; Rafiee, M.; Stahl, S. S.; Hansen, E. C.; Weix, D. J. Zinc-Free, Scalable Reductive Cross-Electrophile Coupling Driven by Electrochemistry in an Undivided Cell. *ACS Catal.* **2022**, *12*, 12617–12626.
97. Twilton, J.; Johnson, M. R.; Sidana, V.; Franke, M. C.; Bottecchia, C.; Lehnher, D.; Lévesque, F.; Knapp, S. M. M.; Wang, L.; Gerken, J. B.; Hong, C. M.; Vickery, T. P.; Weisel, M. D.; Strotman, N.

- A.; Weix, D. J.; Root, T. W.; Stahl, S. S. Quinone-Mediated Hydrogen Anode for Non-Aqueous Reductive Electrosynthesis. *Nature* **2023**, *623*, 71–76.
98. Hamby, T. B.; LaLama, M. J.; Sevov, C. S. Controlling Ni Redox States by Dynamic Ligand Exchange for Electroreductive Csp<sup>3</sup>–Csp<sup>2</sup> Coupling. *Science* **2022**, *376*, 410–416.
99. Laudadio, G.; Neigenfind, P.; Péter, Á.; Rubel, C. Z.; Emmanuel, M. A.; Oderinde, M. S.; Ewing, T. E.-H.; Palkowitz, M. D.; Sloane, J. L.; Gillman, K. W.; Ridge, D.; Mandler, M. D.; Bolduc, P. N.; Nicastrì, M. C.; Zhang, B.; Clementson, S.; Petersen, N. N.; Martín-Gago, P.; Mykhailiuk, P.; Engle, K. M.; Baran, P. S. Nickel-Electrocatalytic Decarboxylative Arylation to Access Quaternary Centers\*\*. *Angew. Chem. Int. Ed.* **2024**, *63*, e202314617.
100. Ackerman, L. K. G.; Anka-Lufford, L. L.; Naodovic, M.; Weix, D. J. Cobalt Co-Catalysis for Cross-Electrophile Coupling: Diarylmethanes from Benzyl Mesylates and Aryl Halides. *Chem. Sci.* **2015**, *6*, 1115–1119
101. Komeyama, K.; Ohata, R.; Kiguchi, S.; Osaka, I. Highly Nucleophilic Vitamin B12-Assisted Nickel-Catalysed Reductive Coupling of Aryl Halides and Non-Activated Alkyl Tosylates. *Chem. Commun.* **2017**, *53*, 6401–6404.
102. Komeyama, K.; Michiyuki, T.; Osaka, I. Nickel/Cobalt-Catalyzed C(sp<sup>3</sup>)–C(sp<sup>3</sup>) Cross-Coupling of Alkyl Halides with Alkyl Tosylates. *ACS Catal.* **2019**, *9*, 9285–9291.
103. Charboneau, D. J.; Barth, E. L.; Hazari, N.; Uehling, M. R.; Zultanski, S. L. A Widely Applicable Dual Catalytic System for Cross-Electrophile Coupling Enabled by Mechanistic Studies. *ACS Catal.* **2020**, *10*, 12642–12656.
104. Truesdell, B. L.; Hamby, T. B.; Sevov, C. S. General C(sp<sup>2</sup>)–C(sp<sup>3</sup>) Cross-Electrophile Coupling Reactions Enabled by Overcharge Protection of Homogeneous Electrocatalysts. *J. Am. Chem. Soc.* **2020**, *142*, 5884–5893.
105. Zackasee, J. L. S.; Al Zubaydi, S.; Truesdell, B. L.; Sevov, C. S. Synergistic Catalyst–Mediator Pairings for Electroreductive Cross-Electrophile Coupling Reactions. *ACS Catal.* **2022**, *12*, 1161–1166.
106. Harwood, S. J.; Palkowitz, M. D.; Gannett, C. N.; Perez, P.; Yao, Z.; Sun, L.; Abruña, H. D.; Anderson, S. L.; Baran, P. S. Modular Terpene Synthesis Enabled by Mild Electrochemical Couplings. *Science* **2022**, *375*, 745–752.
107. Palkowitz, M. D.; Laudadio, G.; Kolb, S.; Choi, J.; Oderinde, M. S.; Ewing, T. E.-H.; Bolduc, P. N.; Chen, T.; Zhang, H.; Cheng, P. T. W.; Zhang, B.; Mandler, M. D.; Blaszczak, V. D.; Richter, J. M.; Collins, M. R.; Schioldager, R. L.; Bravo, M.; Dhar, T. G. M.; Vokits, B.; Zhu, Y.; Echeverria, P.-G.; Poss, M. A.; Shaw, S. A.; Clementson, S.; Petersen, N. N.; Mykhailiuk, P. K.; Baran, P. S. Overcoming Limitations in Decarboxylative Arylation via Ag–Ni Electrocatalysis. *J. Am. Chem. Soc.* **2022**, *144*, 17709–17720.
108. Laudadio, G.; Neigenfind, P.; Chebolu, R.; Blaszczak, V. D.; Maddirala, S. J.; Palkowitz, M. D.; Bolduc, P. N.; Nicastrì, M. C.; Puthukanoori, R. K.; Paraselli, B. R.; Baran, P. S. Synthesis of Unnatural Amino Acids via Ni/Ag Electrocatalytic Cross-Coupling. *Org. Lett.* **2024**, *26*, 2276–2281.
109. Ahneman, D. T.; Estrada, J. G.; Lin, S.; Dreher, S. D.; Doyle, A. G. Predicting Reaction Performance in C–N Cross-Coupling Using Machine Learning. *Science* **2018**, *360*, 186–190.
110. Zahrt, A. F.; Henle, J. J.; Rose, B. T.; Wang, Y.; Darrow, W. T.; Denmark, S. E. Prediction of Higher-Selectivity Catalysts by Computer-Driven Workflow and Machine Learning. *Science* **2019**, *363*, eaau5631.
111. Smith, S. R.; Borowski, J. E.; Peters, E.; Gensch, T.; Johnson, H. C.; Sigman, M. S.; Doyle, A. G. Univariate Classification of Phosphine Ligation State and Reactivity in Cross-Coupling Catalysis. *Science* **2021**, *374*, 301–308.
112. Prieto Kullmer, C. N.; Kautzky, J. A.; Krska, S. W.; Nowak, T.; Dreher, S. D.; MacMillan, D. W. C. Accelerating Reaction Generality and Mechanistic Insight through Additive Mapping. *Science* **2022**, *376*, 532–539.

113. Akana, M. E.; Tcyrulnikov, S.; Akana-Schneider, B. D.; Reyes, G. P.; Monfette, S.; Sigman, M. S.; Hansen, E. C.; Weix, D. J. Computational Methods Enable the Prediction of Improved Catalysts for Nickel-Catalyzed Cross-Electrophile Coupling. *J. Am. Chem. Soc.* **2024**, *146*, 3043–3051.
114. Rosales, A. R.; Wahlers, J.; Limé, E.; Meadows, R. E.; Leslie, K. W.; Savin, R.; Bell, F.; Hansen, E.; Helquist, P.; Munday, R. H.; Wiest, O.; Norrby, P.-O. Rapid Virtual Screening of Enantioselective Catalysts Using CatVS. *Nat. Catal.* **2019**, *2*, 41–45.
115. Burai Patrascu, M.; Pottel, J.; Pinus, S.; Bezanson, M.; Norrby, P.-O.; Moitessier, N. From Desktop to Benchtop with Automated Computational Workflows for Computer-Aided Design in Asymmetric Catalysis. *Nat. Catal.* **2020**, *3*, 574–584.
116. Newman-Stonebraker, S. H.; Raab, T. J.; Roshandel, H.; Doyle, A. G. Synthesis of Nickel(I)–Bromide Complexes via Oxidation and Ligand Displacement: Evaluation of Ligand Effects on Speciation and Reactivity. *J. Am. Chem. Soc.* **2023**, *145*, 19368–19377.
117. Tang, T.; Hazra, A.; Min, D. S.; Williams, W. L.; Jones, E.; Doyle, A. G.; Sigman, M. S. Interrogating the Mechanistic Features of Ni(I)-Mediated Aryl Iodide Oxidative Addition Using Electroanalytical and Statistical Modeling Techniques. *J. Am. Chem. Soc.* **2023**, *145*, 8689–8699.
118. Lin, Q.; Spielvogel, E. H.; Diao, T. Carbon-Centered Radical Capture at Nickel(II) Complexes: Spectroscopic Evidence, Rates, and Selectivity. *Chem* **2023**, *9*, 1295–1308.
119. Dawson, G. A.; Lin, Q.; Neary, M. C.; Diao, T. Ligand Redox Activity of Organonickel Radical Complexes Governed by the Geometry. *J. Am. Chem. Soc.* **2023**, *145*, 20551–20561.
120. Tcyrulnikov, S.; Hubbell, A. K.; Pedro, D.; Reyes, G. P.; Monfette, S.; Weix, D. J.; Hansen, E. C. Computationally Guided Ligand Discovery from Compound Libraries and Discovery of a New Class of Ligands for Ni-Catalyzed Cross-Electrophile Coupling of Challenging Quinoline Halides. *J. Am. Chem. Soc.* **2024**, *146*, 6947–6954.
121. Ma, C.; Fang, P.; Liu, D.; Jiao, K.-J.; Gao, P.-S.; Qiu, H.; Mei, T.-S. Transition Metal-Catalyzed Organic Reactions in Undivided Electrochemical Cells. *Chem. Sci.* **2021**, *12*, 12866–12873.
122. Liu, Y.; Li, P.; Wang, Y.; Qiu, Y. Electroreductive Cross-Electrophile Coupling (eXEC) Reactions. *Angew. Chem. Int. Ed.* **2023**, *62*, e202306679.
123. Franke, M. C.; Weix, D. J. Recent Advances in Electrochemical, Ni-Catalyzed C–C Bond Formation. *Isr. J. Chem.* **2024**, *64*, e202300089.

## Chapter 2.

# Ni- and Ni/Pd-Catalyzed Reductive Coupling of Lignin-Derived Aromatics to Access Biobased Plasticizers

The content presented in this Chapter is reproduced with permission from a published manuscript:

**Zhi-Ming Su**, Jack Twilton, Caroline B. Hoyt, Fei Wang, Lisa Stanley, Heather B. Mayes, Kai Kang, Daniel J. Weix, Gregg T. Beckham, and Shannon S. Stahl. Ni- and Ni/Pd-Catalyzed Reductive Coupling of Lignin-Derived Aromatics to Access Biobased Plasticizers. *ACS Cent. Sci.* **2023**, 9, 159–165. Copyright 2023 American Chemical Society.

## 2.1. Abstract

Lignin-derived aromatic chemicals offer a compelling alternative to petrochemical feedstocks, and new applications are the focus of extensive interest. 4-hydroxybenzoic acid (**H**), vanillic acid (**G**) and syringic acid (**S**) are readily obtained via oxidative depolymerization of hardwood lignin substrates. Here, we explore the use of these compounds to access biaryl dicarboxylate esters that represent bio-based, less toxic alternatives to phthalate plasticizers. Chemical and electrochemical methods are developed for catalytic reductive coupling of sulfonate derivatives of **H**, **G**, and **S** to access all possible homo- and cross-coupling products. A conventional  $\text{NiCl}_2/\text{bipyridine}$  catalyst is able to access the **H–H** and **G–G** products, but new catalysts are identified to afford the more challenging coupling products, including a  $\text{NiCl}_2/\text{bisphosphine}$  catalyst for **S–S** and a  $\text{NiCl}_2/\text{phenanthroline}/\text{PdCl}_2/\text{phosphine}$  cocatalyst system for **H–G**, **H–S**, and **G–S**. High-throughput experimentation methods with a chemical reductant ( $\text{Zn}$  powder) are shown to provide an efficient screening platform for identification of new catalysts, while electrochemical methods can access improved yields and/or facilitate implementation on larger scale. Plasticizer tests are performed with poly(vinyl chloride), using esters of the 4,4'-biaryl dicarboxylate products. The **H–G** and **G–G** derivatives, in particular, exhibit performance advantages relative to an established petroleum-based phthalate ester plasticizer.

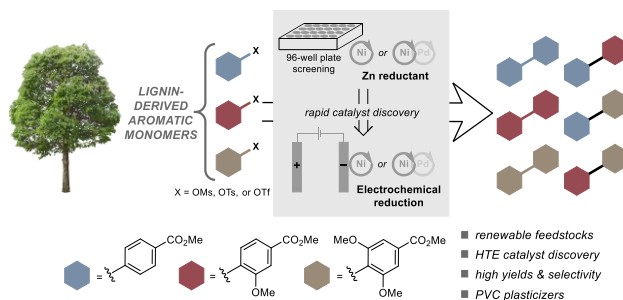


**Figure 2.1.** Summary of this work.

## 2.2. Introduction

Lignin represents the largest source of biomass-derived aromatic chemicals and is an ideal supplement or alternative to petroleum-based feedstocks.<sup>1-9</sup> Significant progress has been made in lignin depolymerization into aromatic monomers,<sup>4-9</sup> but methods for conversion of lignin-derived monomers (LDMs) into value-added chemicals are still in the nascent stages of development.<sup>1-3,10</sup> In connection with efforts focused on oxidative lignin depolymerization,<sup>11-13</sup> we recognized that some of the most common products, 4-hydroxybenzoic acid (**H**), vanillic acid (**G**) and syringic acid (**S**), could serve as precursors to biaryl dicarboxylates (Figure 2.2).<sup>14</sup> The parent analog, biphenyl-4,4'-dicarboxylic acid (BPDA), has been the focus of commercial interest as a monomer for polyesters and as the core structure for non-phthalate plasticizers for poly(vinyl chloride) (PVC).<sup>15-18</sup> Existing methods for the synthesis of BPDA use petroleum-based precursors in multi-step routes (e.g., involving oxidative coupling, alkylation, and/or dehydrogenation steps, paired with autoxidation of alkyl groups into carboxylic acids), and they often afford a mixture of regioisomers.<sup>16,19-21</sup> Reductive coupling of phenol derivatives represents a different route to BPDA derivatives that accesses a single product regioisomer. The biomass-derived **H** compound provides a means to access the same BPDA analog currently sourced from petroleum, while the **G** and **S** compounds that have methoxy substituents will afford BPDA derivatives that could have favorable properties (e.g., as a PVC plasticizer).

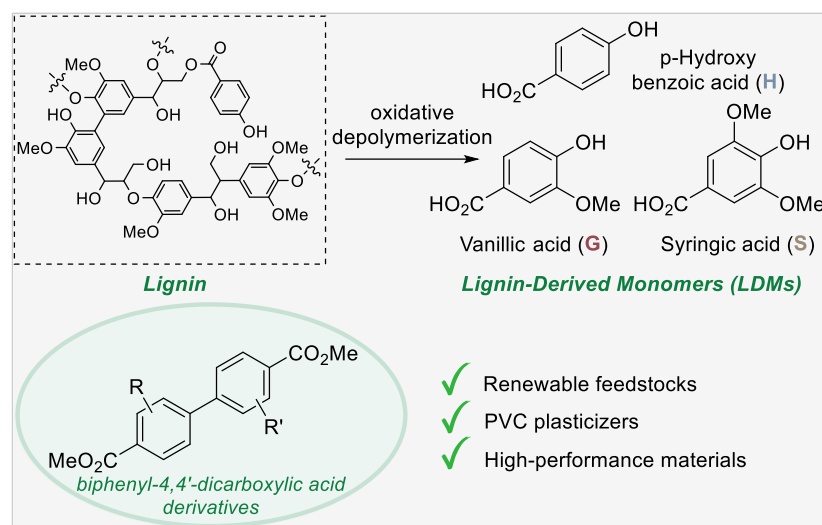
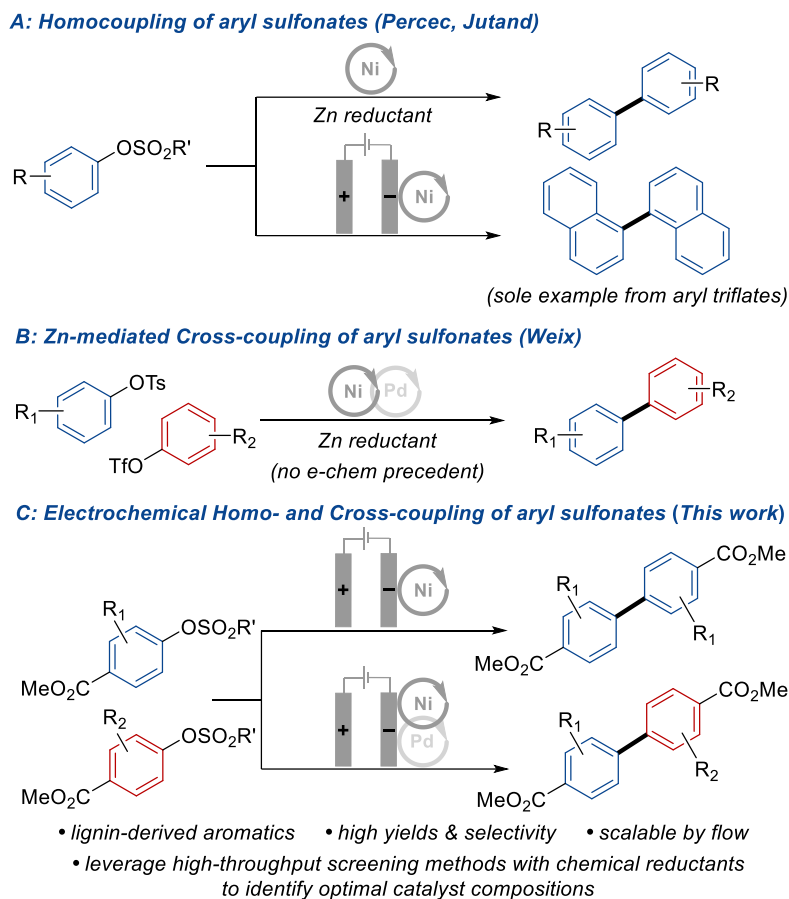


**Figure 2.2.** Lignin is an abundant biomass-derived source of aromatics that represent potential precursors to commercially important biaryl-4,4'-dicarboxylates.

We postulated that the **H**, **G**, and **S** products of lignin depolymerization could be readily converted to aryl sulfonates amenable to reductive cross-coupling. Ni-catalyzed coupling of aryl electrophiles to access biaryls was first reported in the 1970s, and the field advanced significantly in subsequent decades.<sup>22–31</sup> These reactions typically feature stoichiometric metal reductants, such as Zn powder, but important electrochemical precedents also exist. Several examples provide an important foundation for the present work. In 1995, Percec *et al.* demonstrated that a Ni/PPh<sub>3</sub> catalyst system with Zn reductant promotes homocoupling of aryl sulfonates to biaryls (Figure 2.3A).<sup>32</sup> Shortly thereafter, Jutand and co-workers achieved homocoupling of aryl triflates with phosphine-ligated Pd *or* Ni catalysts. This study included a single example of electrochemical Ni-catalyzed homocoupling, using 1-naphthyl triflate as the substrate (Figure 2.3A).<sup>29,30,33</sup> In recent years, Weix and co-workers have developed methods for selective cross-coupling of aryl electrophiles with a co-catalyst system containing both Ni and Pd in the presence of Zn as the reductant.<sup>34–36</sup> The groups of Weix<sup>37</sup> and Kramer/Lian<sup>38</sup> independently reported reductive cross-coupling of two different aryl sulfonates by pairing Pd/bisphosphine and Ni/diimine co-catalysts [diimine = substituted 2,2'-bipyridine (bpy) or 1,10-phenanthroline (phen) derivatives] with Zn

(Figure 2.3B). To date, no electrochemical methods to our knowledge have been reported for reductive cross-coupling of phenol derivatives (Figure 2.3C).<sup>39-42</sup>

Chemical and electrochemical conditions have complementary advantages for reductive coupling reactions. Chemical conditions are more straightforward to implement on small scale, owing to their use of standard laboratory equipment, and they are more amenable to high-throughput experimentation (HTE) techniques for catalyst discovery and reaction optimization. Electrochemical methods offer advantages for large scale applications by avoiding the challenges of handling dense metal-powder reagents and creating opportunities to improve sustainability. Although advances have been made in the development of electrochemical reactors for parallel reaction screening,<sup>43,44</sup> chemical HTE methodology retains substantially improved efficiency and is compatible with smaller quantities of reagents. In this context, we postulated that HTE screening methods using chemical reductants could enable rapid identification of promising catalyst systems and conditions for subsequent development of electrochemical methods. The results outlined below validate this hypothesis and achieve successful chemical and electrochemical conditions for all possible homo- and cross-coupling permutations between **H**-, **G**-, and **S**-derived reaction partners. Additional important outcomes of this study include (a) identification of mono- and bidentate phosphine ligands that lack precedent in Ni-catalyzed reductive coupling reactions, (b) successful adaptation of catalysts from chemical to electrochemical conditions, with matching or superior performance, (c) the first demonstration of Ni/Pd co-catalyzed reductive biaryl cross-coupling under electrochemical conditions, and (d) data showing that biaryl dicarboxylic esters prepared from LDMs exhibit improved PVC plasticizer performance and reduced toxicity relative to a commercial phthalate-based plasticizer.<sup>45</sup>

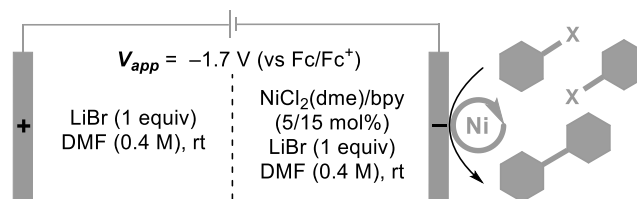


**Figure 2.3.** Precedents relevant to reductive coupling of lignin-derived aryl sulfonates.

## 2.3. Results and Discussion

**Ni-Catalyzed Homocoupling of LDMs.** The methyl esters of **H**, **G**, and **S** are readily converted into electrophiles by reaction of the phenols with sulfonyl chlorides,  $\text{RSO}_2\text{Cl}$  [ $\text{R}$  = methyl (Ms) or tosyl (Ts)], or triflic anhydride ( $\text{Tf}_2\text{O}$ ). Initial studies evaluated the electrochemical homocoupling of methyl 3-methoxy-4-((methylsulfonyl)oxy)benzoate (**G-OMs**). The two possible byproducts are denoted as the Ar-H and ArO-H species, derived from reductive cleavage of the C-O or the S-O bond of the **G-OMs** substrate. A combination of  $\text{NiCl}_2(\text{dme})/\text{bpy}$  has been used previously for reductive homocoupling of Ar-X species<sup>29,30</sup> and this catalyst system was tested initially in an undivided cell with LiBr as the electrolyte and stainless steel as the anode. However, these conditions only afforded the **G-G** product in 29% yield, with a significant amount of byproduct

and unreacted starting material (Table 2.1, entry 1). Use of increased bpy ligand loading (bpy:Ni = 3:1) stabilizes the catalyst<sup>46</sup> and leads to a higher yield of the desired product (72%), together with the Ar–H byproduct (27%; Table 2.1, entry 2). Other sacrificial anodes were tested in an effort to optimize the yield of biaryl product (Table 2.1, entries 3–5). Significant reductive C–O cleavage was also observed when Al or Zn was used as the anode (Table 2.1, entries 3 and 4). This C–O cleavage is rationalized by previous observations that aryl-Ni species can transfer an aryl group to Zn<sup>2+</sup>, generating aryl-zinc species that are susceptible to protonolysis and Ar–H byproduct formation.<sup>37,47</sup> Electrolysis in an undivided cell using a Mg anode proved ineffective (Table 2.1, entry 5). In this case, reductive S–O bond cleavage was favored, likely reflecting single-electron reduction of the sulfonyl group at the Mg surface.<sup>33</sup> These considerations prompted us to test a sacrificial anode with a divided cell configuration that would avoid the contact of substrate with the anode surface and minimize the presence of Lewis acidic metal ions in the cathodic chamber. This hypothesis was validated by observation of a 92% **G–G** product yield when using a Mg anode in a divided cell (Table 2.1, entry 7). This outcome is noteworthy because it is significantly better than that achieved when performing the same reaction under previously reported chemical conditions<sup>32</sup> or optimized variations thereof with Zn powder as the reductant (48% and 59% **G–G** yields, respectively; Table 2A.1). Use of analogous conditions with **H–OMs** as the substrate leads to near-quantitative yield of the biaryl **H–H** product (Table 2.1, entry 8). This outcome was achieved, even when lowering the Ni catalyst loading to 1 mol%. Use of a stainless-steel anode in an undivided cell retained good yield (Table 2.1, entry 9). The latter conditions are readily implemented in a recirculating flow electrolysis cell with a parallel-plate reactor. This approach was used to conduct a larger scale reaction (11 g, 48 mmol **H–OMs**), accessing the **H–H** product in 80% yield with 2 mol% Ni catalyst (see Section 2A.IV of Appendix A for details).

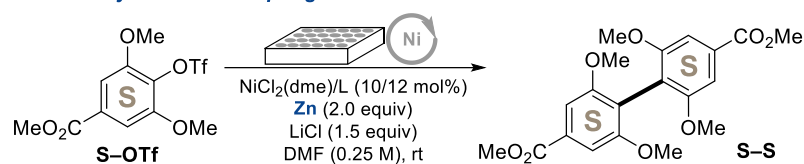
**Table 2.1. Optimization of electrochemical Ni-catalyzed reductive homocoupling.<sup>a</sup>**

Entry	Ar-X	Cell type	Anode	Ar-H (%)	ArO-H (%)	Yield (%)
1 <sup>b</sup>		undivided	stainless-steel	42	0	29
2		undivided	stainless-steel	27	0	72
3		undivided	Al	20	0	20
4		undivided	Zn	95	2	3
5		undivided	Mg	7	37	4
6		divided	stainless-steel	7	4	80
<b>7</b>		<b>divided</b>	<b>Mg</b>	8	0	<b>92 (90)</b>
<b>8<sup>c</sup></b>		<b>divided</b>	<b>Mg</b>	0	0	<b>99 (97)</b>
9 <sup>c</sup>		undivided	stainless-steel	10	0	89
10		divided	Mg	2	1	3

<sup>a</sup> See Appendix A for full experimental details. Yields are determined by <sup>1</sup>H NMR analysis of the crude reaction mixture using mesitylene as an internal standard, yields shown in parentheses are isolated. <sup>b</sup> 5 mol% bpy. The rest of the mass corresponds to recovered starting material. <sup>c</sup> 1 mol% Ni catalyst.

The catalyst and conditions identified for homocoupling of **H-OMs** and **G-OMs** proved ineffective with the more sterically demanding syringic acid derivative **S-OMs**. Only trace quantities of **S-S** product were obtained (Table 2.1, entry 10). To facilitate evaluation of modified conditions, we used a 24-well screening platform with Zn powder as a chemical reductant. The triflate derivative **S-OTf** was found to be more reactive than the mesylate (Table 2A.2), and this substrate was tested with dozens of nitrogen- and phosphine-based ligands. Selected results are summarized in Figure 2.4A, with full screening data provided in Section 2A.V of Appendix A (Tables 2A.2–2A.8). DPEPhos was the only ligand that showed modest success; even the closely

**A: Ni-Catalyzed Homocoupling of S-OTf with Zn Reductant<sup>a</sup>**



Entry	Ligand	Conversion (%)	ArH (%)	ArOH (%)	Yield (%)
1	bpy	75	26	32	8
2	phen	74	29	34	6
3	4,4'-dPhbpy	82	30	35	10
4	<sup>t</sup> Butpy	100	38	40	0
5	DPEPhos	82	54	11	16
6	XantPhos	62	33	18	0
7 <sup>b</sup>	DPEPhos	98	37	8	38
8 <sup>b,c</sup>	DPEPhos	100	32	5	55

**B: Electrochemical Ni-Catalyzed Homocoupling of S-OTf**

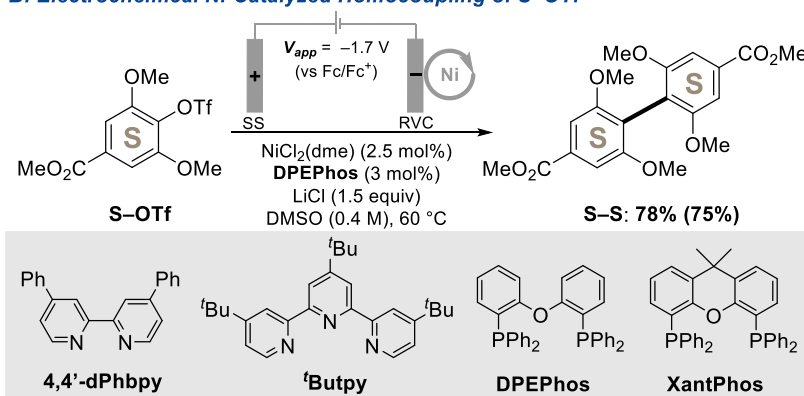


**Figure 2.4.** Ni-catalyzed reductive homocoupling of **S-OTf**: translating conditions optimized with Zn reductant (A) to electrochemical conditions (B). See Appendix A for full experimental details. <sup>a</sup> Yields are determined by <sup>1</sup>H NMR analysis of the crude reaction mixture using mesitylene as an internal standard, yields shown in parentheses are isolated. <sup>b</sup> 60 °C. <sup>c</sup> DMSO solvent.

related, conformationally more rigid XantPhos ligand was completely ineffective (Figure 2.4A, entries 5 and 6). Increasing the temperature to 60 °C led to an increase in conversion and product yield (Figure 2.4A, entry 7), and changing the solvent to DMSO led to a 55% yield of **S-S** (Figure 2.4A, entry 8). The outcome improved even further when the conditions were adapted to an undivided electrochemical cell with a stainless-steel anode: the desired dimer **S-S** was generated in 78% yield (Figure 2.4B; see Table 2A.9 for full screening data). This improved electrochemical outcome was achieved, even though the NiCl<sub>2</sub>/DPEPhos catalyst loading was lowered to 2.5 mol%.

**Optimization of Ni/Pd-Catalyzed Cross-Coupling.** The Ni-only catalyst systems noted above were evaluated in the cross-coupling of **H**, **G**, and **S** sulfonates; however, these reactions led to poor selectivity and yields of the desired products (Table 2A.10). These complications prompted us to evaluate the recently disclosed dual Ni/Pd co-catalyst systems.<sup>35–38</sup> For example, the method of Weix and co-workers, which employs Ni/Pd chloride salts in combination with 4,4'-diphenylbpy (4,4'-dPhbpy) and 1,4-bis(diphenylphosphino)butane (dppb) and Zn as a chemical reductant, supports cross-coupling of aryl triflates and tosylates.<sup>37</sup> Efforts to translate this catalyst system to electrochemical cross-coupling of **G** and **S** sulfonates were unsuccessful, regardless of the sulfonate activating groups: biaryl products formed in  $\leq 15\%$  yield and favored the homocoupling products (Figure 2A.5). Consequently, we again elected to use the high throughput experimentation platform with Zn as the chemical reductant to evaluate modified conditions. Initial studies focused on cross-coupling of **G** and **S** sulfonates, evaluating different combinations of ligands, solvents, additives, sulfonate activating groups, and Ni/Pd ratios, and the results were visualized in Figure 3A (see Tables 2A.11–2A.14 for full screening). The size of the circles in these charts corresponds to the yield, while the color reflects the hetero:homo coupling ratio (darker blue reflects higher selectivity). Among the most noteworthy outcome from these experiments is the beneficial effect of bulky biaryl dialkyl monophosphine ligands ("Buchwald ligands"<sup>48</sup>). The utility of these ligands could reflect their ability to promote the difficult reductive elimination steps.<sup>48</sup> CyJohnPhos was the most effective ligand under screening conditions with Zn powder as the reductant (Figure 2.5A). Subsequent studies revealed that CyJohnPhos decomposes under electrochemical reaction conditions. In contrast, SPhos is stable and supports good reactivity. Further chemical screening evaluated different Ni:Pd ratios in a co-catalyst system

derived from  $\text{NiCl}_2(\text{dme})/\text{phen}$  and  $\text{PdCl}_2(\text{MeCN})_2/\text{SPhos}$  (Figure 2.5A). These studies showed that the highest yields were obtained with 10 mol% Ni and a Pd loading ranging from 0.5–5 mol%.

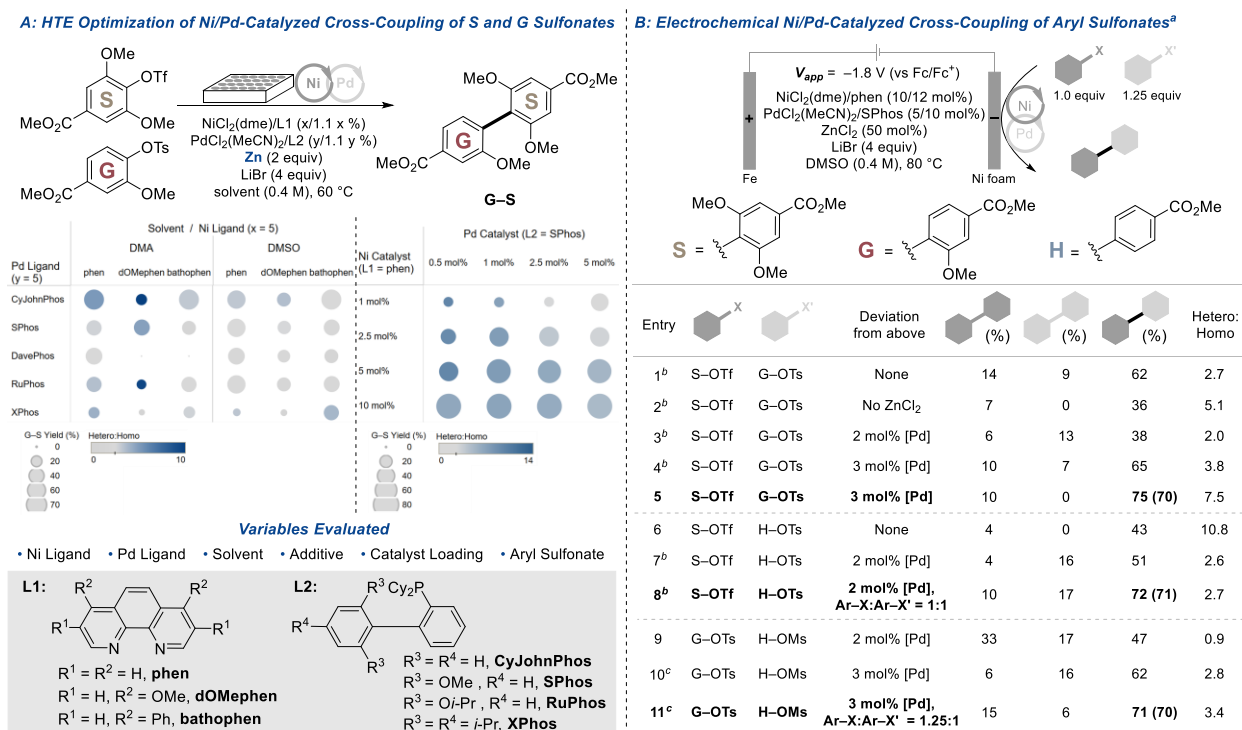


**Figure 2.5.** Ni/Pd-catalyzed reductive cross-coupling of lignin-derived aryl sulfonates. **A.** HTE optimization of G/S cross-coupling. Left chart:  $\text{S-OTf}:\text{G-OTs} = 1:1$ ; right chart: DMSO solvent,  $\text{S-OTf}:\text{G-OTs} = 1:1.25$ . The Hetero:Homo coupling ratio is defined as  $\text{G-S yield}/(\text{G-G yield} + \text{S-S yield})$ . **B.** Optimization of electrochemical Ni/Pd-catalyzed cross-coupling. See Appendix A for full experimental details. <sup>a</sup> Yields determined by UPLC-MS analysis using 1,3,5-trimethoxybenzene as an internal standard, yields shown in parentheses are isolated. <sup>b</sup> RVC cathode. <sup>c</sup> L1 = 4,4'-dPhbpy, L2 = dppb (3.6 mol%), DMA instead of DMSO, 60 °C.

We then initiated electrochemical studies to access cross-coupled products **G-S**, **H-S**, and **H-G**, starting with a co-catalyst composed of 10 mol%  $\text{NiCl}_2(\text{dme})/\text{phen}$  and 5 mol%  $\text{PdCl}_2(\text{MeCN})_2/\text{SPhos}$  (Figure 2.5B). Promising performance was identified with a reticulated vitreous carbon (RVC) cathode, sacrificial iron anode, and a constant applied potential of  $-1.8 \text{ V}$  vs.  $\text{Fc}/\text{Fc}^+$ . Inclusion of 0.5 equiv  $\text{ZnCl}_2$  significantly improved the reaction outcome (Figure 2.5B, entries 1 and 2), consistent with previous evidence that  $\text{Zn}^{2+}$  salts mediate transmetalation between Ni and Pd centers.<sup>37,49,50</sup> Increasing the phosphine ligand loading from 1.1 to 2.0 equiv with respect

to Pd stabilized the Pd catalyst. These initial conditions afforded the desired product **G–S** in 62% yield with 23% homo-coupled byproducts, similar to the yields obtained in the chemical screening studies with Zn as a chemical reductant. It is not surprising that the reaction selectivity varies somewhat between chemical and electrochemical conditions. One important factor is that the cathode potential will not directly match the reduction potential of Zn, and variations in substrate consumption (i.e., via byproduct formation) will lead to differences in the selectivity between chemical and electrochemical conditions. Also, because the selectivity is dictated by pairing of the Ni and Pd catalytic cycles, different rates of catalyst turnover at the Zn surface (chemical) vs. cathode surface (electrochemical) will affect the hetero:homo coupling selectivity. Adjusting the Ni:Pd ratio from 2:1 to 3.3:1 and using a Ni foam cathode instead of RVC increased the **G–S** product yield to 75% (Figure 2.5B, entries 3–5). Slight modification of these conditions accessed the **H–S** cross-coupling product in 72% yield (Figure 2.5B, entry 8). Analogous conditions were less effective for cross-coupling of the less sterically demanding **H** and **G** sulfonates (Figure 2.5B, entry 9), but adaptation of the chemical catalyst system reported by Weix and co-workers proved effective for the cross-coupling of **H–OMs/G–OTs**, accessing **H–G** in 71% yield (Figure 2.5B, entry 11). This reaction represents the first selective cross-coupling (under chemical or electrochemical conditions) of aryl mesylate/aryl tosylate partners, which are significantly more economical than aryl triflates.

**Plasticizer properties of lignin-derived biaryls.** The above results provide access to all possible homo- and cross-coupled BPDA derivatives of **H**, **G**, and **S**. These structures provide the basis for testing of these materials as plasticizers for PVC and comparison of their performance relative to the existing petroleum-derived incumbent, di(2-ethylhexyl) phthalate (DEHP). Each of the BPDA methyl esters was subjected to Ti(OBu)<sub>4</sub>-promoted transesterification with 2-

ethylhexanol to afford the corresponding DEH-BPDA derivatives, designated **H-H<sup>PL</sup>**, **H-G<sup>PL</sup>**, **H-S<sup>PL</sup>**, **G-G<sup>PL</sup>**, **G-S<sup>PL</sup>**, and **S-S<sup>PL</sup>**. The thermal properties of these structures were characterized by thermogravimetric analysis (TGA) and differential scanning calorimetry (DSC) (Figure 2A.9, Table 2A.15). DEHP and the DEH-BPDA derivatives were then individually integrated with PVC at 10 wt%, and the materials were analyzed by TGA and DSC to measure their glass transition temperature ( $T_g$ ) and the temperature at which the polymer degrades with 10% or 50% loss of its original weight ( $T_{d10}$ ,  $T_{d50}$ ) (Figures 2A.10 and 2A.11, Table 2A.16). The former metric reflects the ability of the plasticizer to soften PVC, while the latter metrics reflect the thermostability of the plasticized materials. Preferred plasticizers will achieve lower  $T_g$  and higher  $T_{d10}/T_{d50}$  values. The results, summarized in Figure 2.6, show that the different plasticizers lower the  $T_g$  of PVC from 83.0 °C to 52.1–61.0 °C. The greatest effect is observed with DEHP, **G-G<sup>PL</sup>** and **G-S<sup>PL</sup>**, which lead to  $T_g$  values of 52.1, 54.4 and 54.6 °C, respectively. Meanwhile, **H-G<sup>PL</sup>** and **G-G<sup>PL</sup>** show a notable enhancement in thermostability, with these plasticized materials exhibiting even higher  $T_{d10}$  (278 and 281 °C) than PVC itself (272 °C). The same series of compounds were then evaluated using tools developed by the US Environmental Protection Agency to predict their potential toxicity<sup>51</sup> and their metabolic and environmental transformation<sup>52</sup> (see Section 2A.VII of Appendix A for details). The results assign these materials to the lowest hazard category with respect to acute toxicity to mammals (> 5,000 mg/kg), and the lignin-derived BPDAs arising from hydrolysis of the esters are predicted to be metabolized more easily than phthalic acid. Further experimental studies will be needed to validate this assessment, but these results and the promising performance characteristics in Figure 2.6 reinforce the potential performance-advantaged properties of bio-based plasticizers derived from these BPDAs.

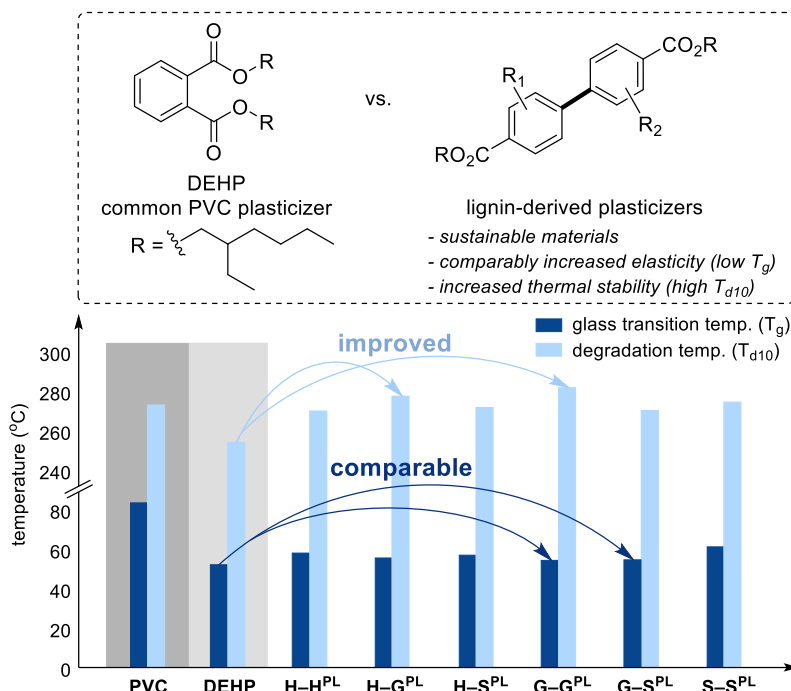


**Figure 2.6.** Thermal analysis of lignin-derived biaryl plasticizers. From left to right: unplasticized PVC, 10 wt% plasticized PVC with DEHP, and 10 wt% plasticized PVC with lignin-derived biaryl plasticizers.

## 2.4. Conclusion

The results above demonstrate the utility of Ni- and Ni/Pd-catalyzed cross-electrophile coupling to convert lignin-derived aromatic compounds into a collective of substituted biphenyl dicarboxylic acids. All possible combinations of **H**, **G**, and **S** monomers have been prepared, with symmetrical dimers accessed using a Ni-only catalyst system and the unsymmetrical dimers accessed using Ni/Pd cocatalyst systems. The results highlight the synergy between chemical and electrochemical reduction methods. HTE screening methods with a chemical reductant offer advantages for identification of effective catalyst compositions. For example, chemical HTE methods identified Ni/DPEPhos catalyst and Ni/phen/Pd/SPhos cocatalyst systems, which lacked precedent for homo- and cross-biaryl coupling, respectively. In each case, the chemical reaction conditions were successfully translated to electrochemical conditions, often resulting in improved performance. The beneficial effect of bulky phosphine ligands with the **S**-derived monomers has

important implications for other cross-electrophile coupling reactions with sterically congested aryl electrophiles, beyond those studied here. Finally, the new BPDA derivatives bearing methoxy substituents, which are intrinsic to lignin-based aromatics, exhibit appealing plasticizer properties that merit further investigation and development.

## **2.5. Acknowledgements**

We thank Dr. Md Asmaul Hoque (UW) for assistance with electrochemical flow cell set-up and Joseph Edgecomb (UW) for experimental assistance in early stages of the project. Financial support to S.S.S. for this work was provided by the Great Lakes Bioenergy Research Center (DOE Office of Science BER DE-SC0018409; generation of lignin-derived monomers) and the NIH (R35GM134929; chemical and electrochemical method development). Funding for D.J.W. was provided by the NIH (R01GM097243). This work was authored in part by the National Renewable Energy Laboratory, operated by the Alliance for Sustainable Energy, LLC, for the U.S. Department of Energy (DOE) under Contract No. DE-AC36-08GO28308. Funding was provided by the U.S. DOE Office of Energy Efficiency and Renewable Energy Bioenergy Technologies Office. Spectroscopic instrumentation was supported by a generous gift from Paul J. and Margaret M. Bender, the NIH (S10 OD020022), and the NSF (CHE-1048642).

## **2.6. Author Contributions**

S.S.S., G.T.B., and Z.-M.S. conceived the project. Z.-M.S. led the efforts on reaction condition optimization, bulk and flow electrolysis, product isolation and characterization, and CV studies. J.T. performed the HTE screening experiments. F.W. conducted optimization of the homocoupling reactions and contributed in part to CV studies. C.B.H., L.S., and H.B.M. prepared the plasticizers and plasticized PVC, then conducted relevant characterizations. K.K. and D.J.W. served as consultants for this work. S.S.S., Z.-M.S., and C.B.H. wrote the manuscript.

## 2.7. Conflicts of Interest

Patent applications have been filed on the electrochemical process and the plasticizers described herein.

## 2.8. References

1. Upton, B. M.; Kasko, A. M. Strategies for the Conversion of Lignin to High-Value Polymeric Materials: Review and Perspective. *Chem. Rev.* **2016**, *116*, 2275–2306.
2. Fache, M.; Darroman, E.; Besse, V.; Auvergne, R.; Caillol, S.; Boutevin, B. Vanillin, a Promising Biobased Building-Block for Monomer Synthesis. *Green Chem.* **2014**, *16*, 1987–1998.
3. Gandini, A.; Belgacem, M. N.; Guo, Z.-X.; Montanari, S. Lignins as Macromonomers for Polyesters and Polyurethanes. In *Chemical Modification, Properties and Usage of Lignin*; Hu, T. Q., Ed.; Kluwer Academic/Plenum: New York, 2002; pp 57–80.
4. Li, C.; Zhao, X.; Wang, A.; Huber, G. W.; Zhang, T. Catalytic Transformation of Lignin for the Production of Chemicals and Fuels. *Chem. Rev.* **2015**, *115*, 11559–11624.
5. Rinaldi, R.; Jastrzebski, R.; Clough, M. T.; Ralph, J.; Kennema, M.; Bruijninx, P. C. A.; Weckhuysen, B. M. Paving the Way for Lignin Valorisation: Recent Advances in Bioengineering, Biorefining and Catalysis. *Angew. Chem. Int. Ed.* **2016**, *55*, 8164–8215.
6. Schutyser, W.; Renders, T.; Van den Bosch, S.; Koelewijn, S.-F.; Beckham, G. T.; Sels, B. F. Chemicals from Lignin: An Interplay of Lignocellulose Fractionation, Depolymerisation, and Upgrading. *Chem. Soc. Rev.* **2018**, *47*, 852–908.
7. Sun, Z.; Fridrich, B.; de Santi, A.; Elangovan, S.; Barta, K. Bright Side of Lignin Depolymerization: Toward New Platform Chemicals. *Chem. Rev.* **2018**, *118*, 614–678.
8. Cui, Y.; Goes, S. L.; Stahl, S. S. Chapter Four - Sequential Oxidation-Depolymerization Strategies for Lignin Conversion to Low Molecular Weight Aromatic Chemicals. In *Advances in Inorganic Chemistry*; Ford, P. C., van Eldik, R., Eds.; Catalysis in Biomass Conversion; Academic Press, 2021; Vol. 77, pp 99–136.
9. Liu, B.; Abu-Omar, M. M. Chapter Five - Lignin Extraction and Valorization Using Heterogeneous Transition Metal Catalysts. In *Advances in Inorganic Chemistry*; Ford, P. C., van Eldik, R., Eds.; Catalysis in Biomass Conversion; Academic Press, 2021; Vol. 77, pp 137–174.
10. Liguori, F.; Moreno-Marrodan, C.; Barbaro, P. Biomass-derived chemical substitutes for bisphenol A: Recent Advancements in Catalytic Synthesis. *Chem. Soc. Rev.* **2020**, *49*, 6329–6363.
11. Rahimi, A.; Ulbrich, A.; Coon, J. J.; Stahl, S. S. Formic-Acid-Induced Depolymerization of Oxidized Lignin to Aromatics. *Nature* **2014**, *515*, 249–252.
12. Luo, H.; Weeda, E. P.; Alherech, M.; Anson, C. W.; Karlen, S. D.; Cui, Y.; Foster, C. E.; Stahl, S. S. Oxidative Catalytic Fractionation of Lignocellulosic Biomass under Non-alkaline Conditions. *J. Am. Chem. Soc.* **2021**, *143*, 15462–15470.
13. Alherech, M.; Omolabake, S.; Holland, C. M.; Klinger, G. E.; Hegg, E. L.; Stahl, S. S. From Lignin to Valuable Aromatic Chemicals: Lignin Depolymerization and Monomer Separation via Centrifugal Partition Chromatography. *ACS Cent. Sci.* **2021**, *7*, 1831–1837.
14. The abbreviations **H**, **G**, **S** are commonly used in the lignin literature for the three canonical monolignols, *p*-coumaryl alcohol, coniferyl alcohol, and sinapyl alcohol. For simplicity, we use the same nomenclature here for the three lignin-derived monomers obtained from oxidative depolymerization of lignin.
15. Jose, J. P.; Joesph, K. Advances in Polymer Composites: Macro- and Microcomposites - State of the Art, New Challenges, and Opportunities. In *Polymer Composites: Vol. I*; Thomas, S.; Joseph, K.;

- Malhotra, S. K.; Goda, K.; Sadasivan, S. M., Eds.; Wiley-VCH Verlag GmbH & Co.: New York, 2012; pp 1–16.
16. Matsuda, T.; Nakamura, T.; Sasakawa, A.; Hayashi, S.; Konai, Y. Preparation Process of Biphenyl-4,4'-Dicarboxylic Acid. US4970338A, November 13, 1990.
  17. Edling, H. E.; Liu, H.; Sun, H.; Mondschein, R. J.; Schiraldi, D. A.; Long, T. E.; Turner, S. R. Copolyesters Based on Bibenzoic acids. *Polymer* **2018**, *135*, 120–130.
  18. Asrar, J. Synthesis and Properties of 4,4'-Biphenyldicarboxylic Acid and 2,6-Naphthalenedicarboxylic Acid. *J. Polym. Sci., Part A: Polym. Chem.* **1999**, *37*, 3139–3146.
  19. Dakka, J. M.; Decaul, L. C.; Costello, C. A.; Mozeleski, E. J.; Osterrieth, P. J.; Smirnova, D. S.; Zushma, S.; Godwin, A. D.; Faler, C. A.; Deflorio, V.; Naert, D. Alkyl Aromatic Hydroalkylation for the Production of Plasticizers. WO2014117076A9, April 23, 2015.
  20. Dakka, J. M.; DeCaul, L. C. Methyl-Substituted Biphenyl Compounds, Their Production and Their Use in the Manufacture of Plasticizers. US9663417B2, May 30, 2017.
  21. Mazoyer, E.; Lotz, M. D.; Bokis, C. P.; Guzman, J. Preparation and Purification of Biphenyldicarboxylic Acids. US20200361847A1, November 19, 2020.
  22. Zembayashi, M.; Tamao, K.; Yoshida, J.; Kumada, M. Nickel-Phosphine Complex-Catalyzed Homocoupling of Aryl Halides in the Presence of Zinc Powder. *Tetrahedron Lett.* **1977**, 4089–4091.
  23. Iyoda, M.; Sato, K.; Oda, M. Nickel-catalyzed Coupling of Bromides of 1,6-Methano[10]annulene and Azulene. A facile Synthesis of Biannulene and Bi-, Ter-, Quater-, and Polyazulenes. *Tetrahedron Lett.* **1985**, *26*, 3829–3832.
  24. Qian, Q.; Zang, Z. H.; Wang, S. L.; Chen, Y.; Lin, K. H.; Gong, H. G. Nickel-Catalyzed Reductive Cross-Coupling of Aryl Halides. *Synlett* **2013**, *24*, 619–624.
  25. Liao, L. Y.; Kong, X. R.; Duan, X. F. Reductive Couplings of 2-Halopyridines without External Ligand: Phosphine-Free Nickel-Catalyzed Synthesis of Symmetrical and Unsymmetrical 2,2'-Bipyridines. *J. Org. Chem.* **2014**, *79*, 777–782.
  26. Yamashita, J.; Inoue, Y.; Kondo, T.; Hashimoto, H. Ullmann-Type Coupling Reaction of Aryl Trifluoromethanesulfonates Catalyzed by in Situ-Generated Low Valent Nickel Complexes. *Chem. Lett.* **1986**, *15*, 407–408.
  27. Jutand, A.; Mosleh, A. Palladium and Nickel Catalyzed Synthesis of Biaryls from Aryl Triflates in the Presence of Zinc Powder. *Synlett* **1993**, *1993*, 568–570.
  28. Rosen, B. M.; Quasdorf, K. W.; Wilson, D. A.; Zhang, N.; Resmerita, A.; Garg, N. K.; Percec, V. Nickel-Catalyzed Cross-Couplings Involving Carbon–Oxygen Bonds. *Chem. Rev.* **2011**, *111*, 1346–1416.
  29. Maddaluno, J.; Durandetti, M. Dimerization of Aryl Sulfonates by in Situ Generated Nickel(0). *Synlett* **2015**, *26*, 2385–2388.
  30. Rahil, R.; Sengmany, S.; Gall, E. L.; Léonel, E. Nickel-Catalyzed Electrochemical Reductive Homocouplings of Aryl and Heteroaryl Halides: A Useful Route to Symmetrical Biaryls. *Synthesis* **2018**, *50*, 146–154.
  31. Qiu, H.; Shuai, B.; Wang, Y.-Z.; Liu, D.; Chen, Y.-G.; Gao, P.-S.; Ma, H.-X.; Chen, S.; Mei, T.-S. Enantioselective Ni-Catalyzed Electrochemical Synthesis of Biaryl Atropisomers. *J. Am. Chem. Soc.* **2020**, *142*, 9872–9878.
  32. Percec, V.; Bae, J.-Y.; Zhao, M.; Hill, D. H. Aryl Mesylates in Metal-Catalyzed Homocoupling and Cross-Coupling Reactions. 1. Functional Symmetrical Biaryls from Phenols via Nickel-Catalyzed Homocoupling of Their Mesylates. *J. Org. Chem.* **1995**, *60*, 176.
  33. Jutand, A.; Mosleh, A. Nickel- and Palladium-Catalyzed Homocoupling of Aryl Triflates. Scope, Limitation, and Mechanistic Aspects. *J. Org. Chem.* **1997**, *62*, 261–274.
  34. Ackerman, L. K. G.; Lovell, M. M.; Weix, D. J. Multimetallic Catalysed Cross-Coupling of Aryl Bromides with Aryl Triflates. *Nature* **2015**, *524*, 454–457.

35. Huang, L.; Ackerman, L. K. G.; Kang, K.; Parsons, A.; Weix, D. J. LiCl-Accelerated Multimetallic Cross-Coupling of Aryl Chlorides with Aryl Triflates. *J. Am. Chem. Soc.* **2019**, *141*, 10978–10983.
36. Kang, K.; Loud, N. L.; DiBenedetto, T. A.; Weix, D. J. A General, Multimetallic Cross-Ullmann Biheteroaryl Synthesis from Heteroaryl Halides and Heteroaryl Triflates. *J. Am. Chem. Soc.* **2021**, *143*, 21484–21491.
37. Kang, K.; Huang, L.; Weix, D. J. Sulfonate Versus Sulfonate: Nickel and Palladium Multimetallic Cross-Electrophile Coupling of Aryl Triflates with Aryl Tosylates. *J. Am. Chem. Soc.* **2020**, *142*, 10634–10640.
38. Xiong, B.; Li, Y.; Wei, Y.; Kramer, S.; Lian, Z. Dual Nickel-/Palladium-Catalyzed Reductive Cross-Coupling Reactions between Two Phenol Derivatives. *Org. Lett.* **2020**, *22*, 6334–6338.
39. Ni-only catalyst systems have been used under electrochemical conditions to support reductive biaryl cross-coupling with certain privileged substrate classes, such as the coupling of 2-halopyridine with aryl halides. See, for example, refs. 40–42.
40. Gosmini, C.; Lasry, S.; Nédélec, J.-Y.; Périchon, J. Electrochemical Cross-Coupling between 2-Halopyridines and Aryl or Heteroaryl Halides Catalysed by Nickel-2,2'-Bipyridine Complexes. *Tetrahedron* **1998**, *54*, 1289–1298.
41. Gosmini, C.; Nédélec, J. Y.; Périchon, J. Electrochemical Cross-Coupling between Functionalized Aryl Halides and 2-Chloropyrimidine or 2-Chloropyrazine Catalyzed by Nickel 2,2'-Bipyridine Complex. *Tetrahedron Lett.* **2000**, *41*, 201–203.
42. Gosmini, C.; Nédélec, J. Y.; Périchon, J. Electrosynthesis of Functionalized 2-Arylpyridines from Functionalized Aryl and Pyridine Halides Catalyzed by Nickel Bromide 2,2'-Bipyridine Complex. *Tetrahedron Lett.* **2000**, *41*, 5039–5042.
43. Wills, A. G.; Charvet, S.; Battilocchio, C.; Scarborough, C. C.; Wheelhouse, K. M. P.; Poole, D. L.; Carson, N.; Vantourout, J. C. High-Throughput Electrochemistry: State of the Art, Challenges, and Perspective. *Org. Process Res. Dev.* **2021**, *25*, 2587–2600.
44. Rein, J.; Annand, J. R.; Wismer, M. K.; Fu, J.; Siu, J. C.; Klapars, A.; Strotman, N. A.; Kalyani, D.; Lehnher, D.; Lin, S. Unlocking the Potential of High-Throughput Experimentation for Electrochemistry with a Standardized Microscale Reactor. *ACS Cent. Sci.* **2021**, *7*, 1347–1355.
45. Cywar, R. M.; Rorrer, N. A.; Hoyt, C. B.; Beckham, G. T.; Chen, E. Y.-X. Bio-Based Polymers with Performance-Advantaged Properties. *Nat Rev Mater* **2022**, *7*, 83–103.
46. For similar observations, see: Kawamata, Y.; Vantourout, J. C.; Hickey, D. P.; Bai, P.; Chen, L.; Hou, Q.; Qiao, W.; Barman, K.; Edwards, M. A.; Garrido-Castro, A. F.; deGruyter, J. N.; Nakamura, H.; Knouse, K.; Qin, C.; Clay, K. J.; Bao, D.; Li, C.; Starr, J. T.; Garcia-Irizarry, C.; Sach, N.; White, H. S.; Neurock, M.; Minter, S. D.; Baran, P. S. Electrochemically Driven, Ni-Catalyzed Aryl Amination: Scope, Mechanism, and Applications. *J. Am. Chem. Soc.* **2019**, *141*, 6392–6402.
47. Klein, P.; Lechner, V. D.; Schimmel, T.; Hintermann, L. Generation of Organozinc Reagents by Nickel Diazadiene Complex Catalyzed Zinc Insertion into Aryl Sulfonates. *Chem. Eur. J.* **2020**, *26*, 176–180.
48. Martin, R.; Buchwald, S. L. Palladium-Catalyzed Suzuki-Miyaura Cross-Coupling Reactions Employing Dialkylbiaryl Phosphine Ligands. *Acc. Chem. Res.* **2008**, *41*, 1461–1473.
49. Olivares, A. M.; Weix, D. J. Multimetallic Ni- and Pd-Catalyzed Cross-Electrophile Coupling to Form Highly Substituted 1,3-Dienes. *J. Am. Chem. Soc.* **2018**, *140*, 2446–2449.
50. Xiong, B.; Chen, X.; Liu, J.; Zhang, X.; Xia, Y.; Lian, Z. Stereoselective Gem-Difluorovinylation of Gem-Difluorinated Cyclopropanes Enabled by Ni/Pd Cooperative Catalysis. *ACS Catal.* **2021**, *11*, 11960–11965.
51. Martin, T. M. *T. E. S. T. (Toxicity Estimation Software Tool) Version 5.1*, 5.1; United State Environmental Protection Agency: 2020.
52. EPA, U. S., Chemical Transformation Simulator (CTS), Version 1.0. *Chemical Transformation Simulator (CTS), Version 1.0* 2019.

### Chapter 3.

## Zinc and Manganese Redox Potentials in Organic Solvents and Their Influence on Nickel-Catalyzed Cross-Electrophile Coupling

The content presented in this Chapter is reproduced from a submitted manuscript: **Zhi-Ming Su**, Ruohan Deng, and Shannon S. Stahl. Zinc and Manganese Redox Potentials in Organic Solvents and Their Influence on Nickel-Catalyzed Cross-Electrophile Coupling.

### 3.1. Abstract

Zinc and manganese are widely used as reductants in synthetic methods, such as nickel-catalyzed cross-electrophile coupling (XEC) reactions, but their redox potentials are unknown in organic solvents. Here, we show how open-circuit potential measurements may be used to determine the thermodynamic potentials of Zn and Mn in different organic solvents and in the presence of common reaction additives. The impact of these Zn and Mn potentials is analyzed for a pair of Ni-catalyzed reactions, each showing a preference for one of the two reductants. Ni-catalyzed coupling of *N*-alkyl-2,4,6-triphenylpyridinium reagents (Katritzky salts) with aryl halides are then compared under chemical reaction conditions, using Zn or Mn reductants, and under electrochemical conditions performed at applied potentials corresponding to the Zn and Mn reduction potentials and at potentials optimized to achieve the maximum yield. The collective results illuminate the important role of reductant redox potential in Ni-catalyzed XEC reactions.

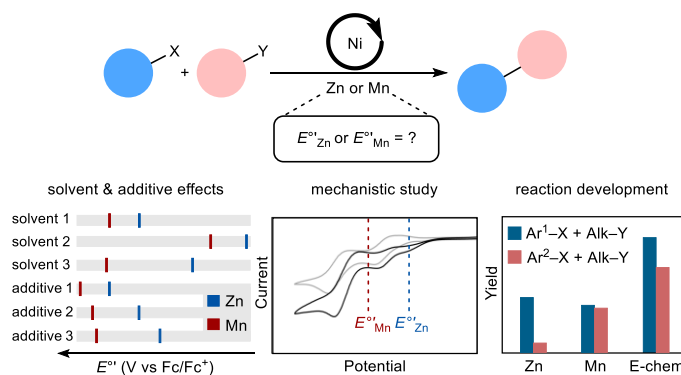


**Figure 3.1.** Summary of this work.

### 3.2. Introduction

Transition metal-catalyzed coupling reactions are the predominant methods for carbon-carbon bond formation in synthetic chemistry.<sup>1-3</sup> Ni-catalyzed cross-electrophile coupling (XEC) reactions have been the focus of growing development and application, motivated by their use of non-precious-metal catalysts and access to more diverse and lower-cost reagents relative to reactions that employ organometallic nucleophiles as coupling partners (Figure 3.2A).<sup>4-8</sup> Initial applications developed in the 1990s featured aryl halides and activated alkyl halides as coupling partners,<sup>9-12</sup> but the available methods have expanded significantly and now include an array of other synthetically useful substrates.<sup>8,13-16</sup>

Ni-catalyzed XEC reactions require a stoichiometric source of electrons to support the overall cross-coupling reaction, and electron transfer is featured in key steps in the catalytic mechanisms. For example, reduction of the Ni catalyst to low-valent intermediates is needed to initiate oxidative addition or halogen-atom transfer from the organic electrophiles. Various reductants have been used to promote these reactions,<sup>17-28</sup> but heterogeneous zinc or manganese metal powders are the most widely used.<sup>8</sup> The choice of Zn or Mn as the reductant can significantly impact the reaction outcome. This behavior is illustrated by two representative XEC reactions reported recently by Shu and co-workers (Figure 3.2B).<sup>29,30</sup> In the first example, cross-coupling of a vinyl acetate and an alkyl bromide proceeds effectively with Zn, but not with Mn, as the reductant (93% and 18% yields, respectively).<sup>29</sup> The second example, which features cross-coupling of aryl triflates and benzylic alcohols activated *in situ* to generate benzyl oxalates, shows the opposite trend, with higher yields obtained with Mn rather than Zn (82% and 15% yields, respectively).<sup>30</sup> Observations could be qualitatively rationalized by the reduction potentials of Zn and Mn, relative to the redox potentials needed to promote individual steps in catalytic mechanisms with different Ni catalyst

systems and/or substrates.<sup>31–33</sup> The thermodynamic potentials of Zn and Mn in organic solvents, however, are not known, and factors that influence their potentials under typical reaction conditions have not been explored.

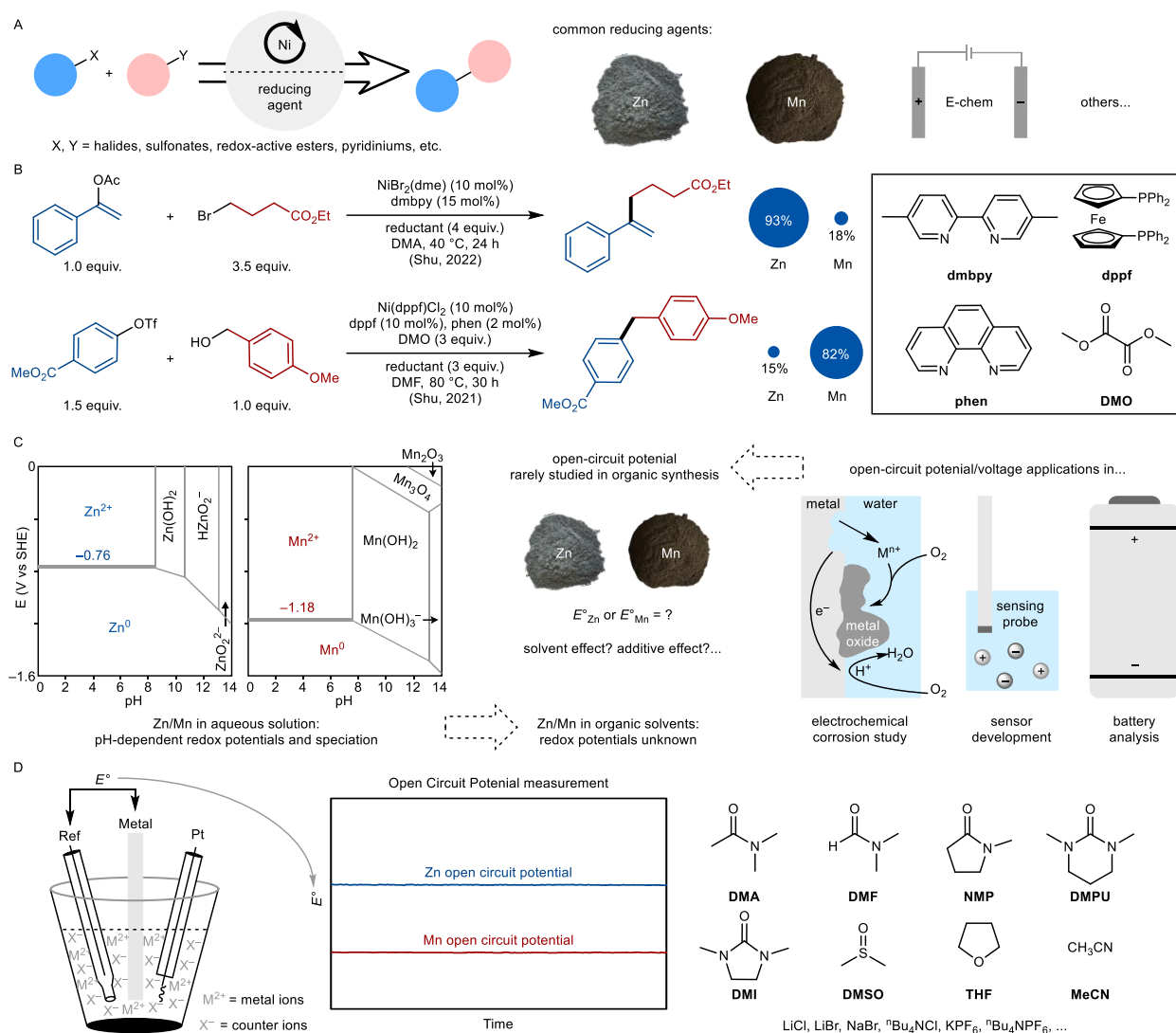


**Figure 3.2.** Metal reductants in Ni-catalyzed XEC. (A) General depiction of Ni-catalyzed  $C(sp^2)$ – $C(sp^3)$  cross-electrophile coupling (XEC) reactions. (B) Selected examples of Ni-catalyzed XEC reactions showing the impact of metal reductants on product yields. (C) Pourbaix diagrams for Zn and Mn in aqueous solution and an illustration of common applications of open-circuit potential/voltage, a technique that could be used to determine the redox potentials of Zn and Mn in organic solvents. (D) Schematic diagram illustrating open-circuit potential measurement of thermodynamic potentials of metal reductants. Dme = 1,2-dimethoxyethane, bpy = 2,2'-bipyridine, dmbpy = 5,5'-dimethyl-2,2'-bipyridine, DMO = dimethyl oxalate, phen = 1,10-phenanthroline, dppf = 1,1'-bis(diphenylphosphino)ferrocene, SHE = standard hydrogen electrode, Fc/Fc<sup>+</sup> = ferrocene/ferrocenium.

The thermodynamic potentials and speciation of Zn and Mn are well defined in aqueous solution from pH 0–14, as depicted in their Pourbaix diagrams (Figure 3.2C);<sup>34,35</sup> however, the potentials from these diagrams are not straightforwardly translated to organic solvents. The redox potentials for Zn and Mn,  $-0.76$  V and  $-1.18$  V, respectively, versus the standard hydrogen electrode (SHE), are commonly cited in the XEC literature. In many cases, these values are adjusted by simple mathematical conversion from SHE to a reference electrode or reference potential used in an organic solvent, such as the saturated calomel electrode, SCE, or ferrocene/ferrocenium, Fc/Fc<sup>+</sup>.<sup>36</sup> Values obtained by this approach are fraught with complications, however, as they fail to account for the influence of the solvent or reaction additives on the Zn<sup>2+/0</sup> and Mn<sup>2+/0</sup> potentials. A direct approach to evaluate redox potentials of Zn and Mn in organic solvents could have significant value.

Open-circuit potentials (OCPs) represent thermodynamic potentials that are unaffected by electrochemical kinetics.<sup>37</sup> OCP measurements are widely used in other scientific disciplines, for example, to study the metal corrosion,<sup>38,39</sup> develop potentiometric sensors,<sup>40</sup> and analyze batteries in electrochemical energy storage (Figure 3.2C).<sup>41</sup> Similar measurements in the context of synthetic organic chemistry are exceedingly rare, with historical examples limited to studies of alkali metals.<sup>42</sup> A systematic study of the thermodynamic potentials of Zn and Mn in organic solvent could contribute significantly to the fundamental understanding and development of Ni-catalyzed XEC reactions that employ these reductants .

Here, we report OCP measurements that directly analyze the thermodynamic potentials of Zn and Mn reductants in organic solvents (Figure 3.2D). The results reveal the impact of solvents and additives on the reduction potentials of heterogeneous metal reductants, and they enable direct comparison of these values with the potentials of substrates, catalysts, and other homogeneous

redox-active species in organic reactions. The implications of these measurements are illustrated through a pair of studies that correlate the Zn and Mn reduction potentials with the product yields associated with these reductants and redox potentials of the Ni complexes used in the catalytic reactions. Finally, we analyze the XEC reaction of *N*-alkyl-2,4,6-triphenylpyridinium reagents (Katritzky salts) with aryl halides using Zn and Mn as heterogeneous reductants. The results are directly compared to the performance of these reactions with constant-potential electrolysis reactions conducted at variable potentials, including electrochemical potentials that match the thermodynamic potentials of Zn and Mn under the reaction conditions. The results of this analysis show how control over the reduction potential of a chemical reagent or an electrode has significant impact on the outcome of Ni-catalyzed XEC reactions.

### 3.3. Results and Discussion

**Measurement of thermodynamic potentials of Zn and Mn.** OCPs are measured without passing current or applying an external voltage, and we initiated our study by measuring OCPs for zinc and manganese relative to a reference electrode (Ag/AgNO<sub>3</sub>) under a variety of conditions relevant to Ni-catalyzed XEC reactions (Figure 3.3A). A three-electrode set-up was used to enable determination of the Fc/Fc<sup>+</sup> redox potential (used for referencing the OCP) in the same solution.<sup>37,43</sup> Eight solvents commonly used in Ni-catalyzed XEC reactions were selected for OCP measurement to probe the influence of solvent on the Zn and Mn reduction potentials (Figure 3.3B): dimethylformamide (DMF), dimethylacetamide (DMA), *N*-methyl-2-pyrrolidone (NMP), *N,N'*-dimethylpropyleneurea (DMPU), 1,3-dimethyl-2-imidazolidinone (DMI), dimethyl sulfoxide (DMSO), acetonitrile (MeCN), and tetrahydrofuran (THF). Zn<sup>2+</sup> or Mn<sup>2+</sup> salts were included in the solution (10 mM) to ensure well-defined thermodynamic conditions for the redox process of interest (i.e.,  $M \rightleftharpoons M^{2+} + 2e^-$ ). The OCPs measured in the different solvents were converted to

formal thermodynamic potentials versus  $\text{Fc}/\text{Fc}^+$  ( $E^{\circ'}$ ) by correcting for the non-standard-state concentration of the  $\text{M}^{2+}$  ions (see Section 3B.II of Appendix B for details). The redox potential of  $[\text{Ni}(\text{bpy})_3]\text{Cl}_2$  was also measured in each of these solvents to provide a benchmark for Ni-based redox potentials (black data, Figure 3.3B).

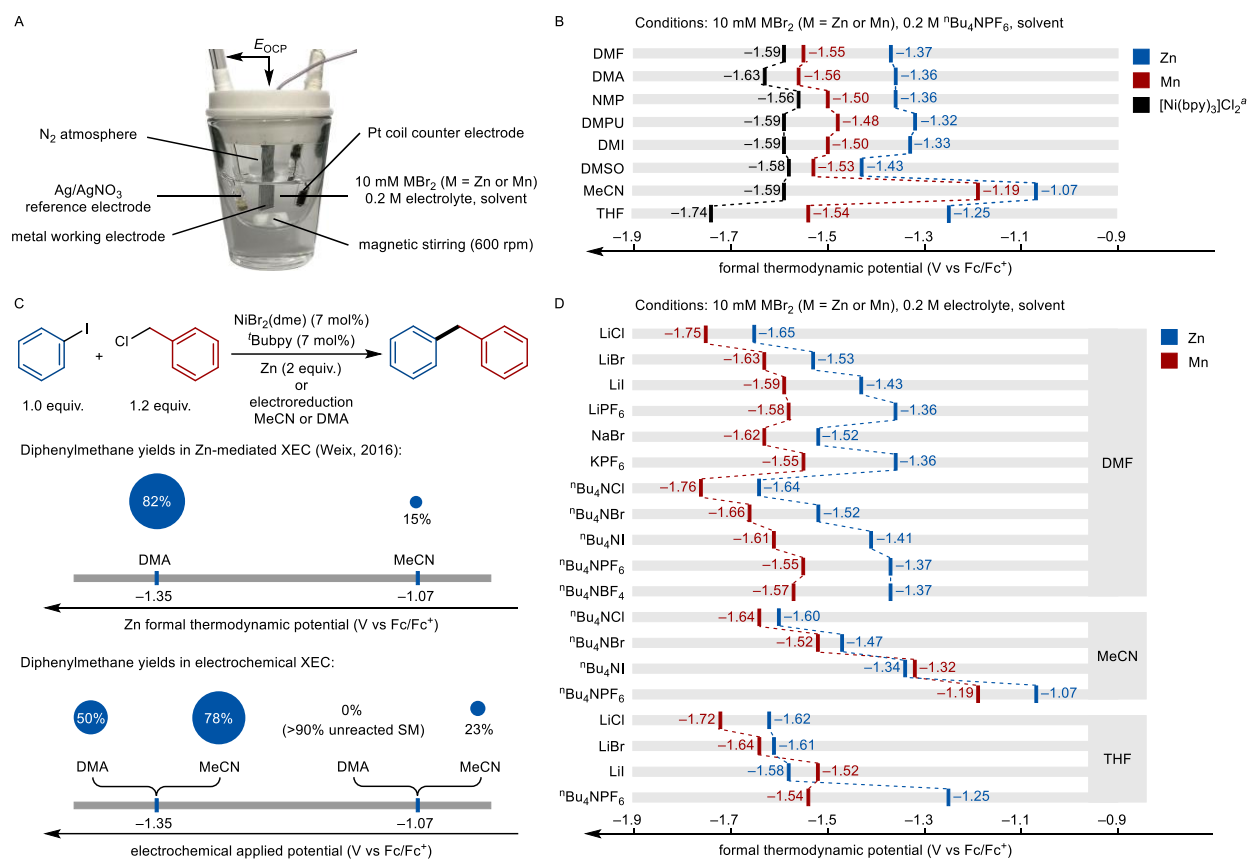


**Figure 3.3.** Formal thermodynamic potentials of Zn and Mn. (A) Experimental set-up for open-circuit potential measurements. (B) Solvent effects on the formal thermodynamic potentials of Zn and Mn and the redox potential of  $[\text{Ni}(\text{bpy})_3]\text{Cl}_2$  (<sup>a</sup> see Figure 3B.8). (C) Comparison of the results of chemical and electrochemical Ni/<sup>n</sup>Bubpy-catalyzed coupling of benzyl chloride and phenyl iodide. (D) Additive effects on the formal thermodynamic potentials of Zn and Mn.

The Zn and Mn reduction potentials show modest variation in a series of amide and urea solvents (DMF, DMA, NMP, DMPU, and DMI):  $\Delta E^{\circ'} \leq 50$  mV for Zn,  $\Delta E^{\circ'} \leq 80$  mV for Mn. The Mn potentials in DMSO and THF are similar to the corresponding potentials observed in amide solvents. The Zn potential is more negative in DMSO and more positive in THF, relative to the corresponding potentials in amide solvents. The Zn and Mn potentials change substantially in

MeCN, increasing by up to 260–370 mV relative to those measured in DMSO and amide solvents. The redox potentials of Zn and Mn are more positive than those of  $[\text{Ni}(\text{bpy})_3]\text{Cl}_2$ , although the difference is rather small for Mn in DMSO and amide solvents ( $\Delta E^{\circ'} \leq 90$  mV). A somewhat larger difference is evident for Zn in these solvents ( $\Delta E^{\circ'} \leq 270$  mV).

The unique behavior of MeCN has important implications for Ni-catalyzed XEC reactions. The high reduction potentials observed for Zn and Mn in MeCN likely explain why XEC reactions are rarely conducted with these reductants in MeCN.<sup>17,24</sup> For example, Weix and co-workers evaluated a series of solvents, including MeCN, for the cross-coupling of benzyl chloride with phenyl iodide. Efficient cross-coupling was observed in DMA with Zn as the reductant, affording 82% yield of diphenylmethane, while only 15% yield was observed in MeCN (Figure 3.3C).<sup>24</sup> This result could be rationalized by unfavorable thermodynamics for Zn reduction of the Ni catalyst in MeCN. Support for this hypothesis was obtained by conducting constant-potential electrolysis experiments in DMA and MeCN, applying potentials associated with the reduction potential of Zn in each solvent. At an applied potential of  $-1.07$  V, the Zn reduction potential in MeCN, negligible current was observed in DMA with  $> 90\%$  unreacted starting materials remained after 36 h, while a 23% yield of product was observed in MeCN. At the more reducing potential of  $-1.35$  V, the Zn reduction potential in DMA, sustained current and moderate-to-good product yields were observed in both solvents (50% in DMA, 78% in MeCN; see full screening data in Table 3B.4). These observations show how solvent effects on the reduction potential of metallic reductants can have a significant influence on the outcome of reductive coupling reactions.

DMF is one of the most common solvents used for XEC reactions, and additives, such as LiCl, LiBr, among others, are often included in the reaction mixture.<sup>8</sup> OCP measurements for Zn and Mn in the presence of various additives (200 mM) in DMF show that the Zn and Mn reduction

potentials can change by nearly 300 mV (Figure 3.3D), depending on the additive identity. Halide ions, especially chloride salts, shift the Zn and Mn reduction potentials to more negative values relative to those recorded in the presence of weakly coordinating anions. The influence of halide ions was further probed in MeCN and THF, and a similar phenomenon was observed. One exception is a shift in the Mn potential to a slightly more positive value in the presence of LiI relative to that measured in the presence of  ${}^n\text{Bu}_4\text{NPF}_6$ . As the quantity of these additives is commonly screened in the development of XEC reactions,<sup>44,45</sup> OCP measurements were performed with different concentrations of chloride salts. The results show that Zn becomes more reducing at higher chloride concentration ( $\Delta E^{\circ'} = 360$  mV from  $[\text{Cl}^-] = 0\text{--}1.2$  M; see Figure 3B.3). These observations show that halide ions could have a significant influence on XEC reactions by changing the potential of the metal reductant. For example, the significantly lower reduction potentials of Zn and Mn in the presence of chloride salts in MeCN and THF could provide new opportunities to develop XEC reactions in these non-amide solvents. In another aspect, LiCl has been reported to accelerate Ni-catalyzed XEC reactions, and this behavior was attributed to the kinetic influence of chloride and/or lithium ions on  $\text{Ni}^{\text{II}}$  reduction by Zn metal.<sup>46</sup> The results in Figure 3.3D, however, show that Zn is a stronger reductant in the presence of LiCl, highlighting an important, but previously unrecognized, thermodynamic contribution to this reaction. It is worth noting that the methodology outlined herein can be readily extended to the study of other conditions, such as those using mixed solvents (e.g., DMF/THF) or other additives (e.g., trimethylsilyl chloride) (see Tables 3B.1 and 3B.2 for full data).

**Analyzing the preference for Zn or Mn reductants in Ni-catalyzed XEC reactions.** The preferred reductant in Ni-catalyzed XEC reactions can vary between Zn and Mn. The reduction potentials measured for these metals together with redox potentials of the Ni catalysts used in the

reactions provide a foundation for understanding the origin of the preferred reductant. We elected to explore this approach using two reactions reported by Shu and co-workers depicted in Figure 3.1B. The cross-coupling of alkenyl acetates and alkyl bromides proceeds effectively with Zn, but not with Mn, as the reductant (Figure 3.4A).<sup>29</sup> This reaction was proposed to be initiated by reduction of Ni<sup>II</sup> to Ni<sup>I</sup>, followed by coordination and oxidative addition of the alkenyl acetate to form an alkenyl-Ni<sup>III</sup> species. One-electron reduction of this species to give an alkenyl-Ni<sup>II</sup> species and reaction with an alkyl radical was then proposed to generate the desired product. The cross-coupling of benzyl alcohols with aryl triflates uses dimethyl oxalate (DMO) to convert the alcohol to an oxalic ester electrophile, and this reaction proceeds effectively with Mn, but not with Zn, as the reductant (Figure 3.4B).<sup>30</sup> The reaction was proposed to be initiated by reduction of Ni<sup>II</sup> to Ni<sup>0</sup>, in this case, followed by reaction of Ni<sup>0</sup> with the benzyl oxalate to afford a benzyl-Ni<sup>II</sup> species. One-electron reduction of this species to give a benzyl-Ni<sup>I</sup> and oxidative addition of aryl triflate was then proposed to afford the desired product.

Analysis of these reactions was initiated by recording CVs of the Ni catalysts in their corresponding reaction solvents (DMA, DMF). CVs were obtained in the presence and absence of alkenyl acetate or benzyl oxalate, the substrates proposed to initiate reaction with their respective catalysts (Figures 3.4C and 3.4D; see Figures 3B.9 and 3B.10 for CVs involving both coupling partners). For the first reaction, the CV of the Ni catalyst alone reveals two quasi-reversible redox couples, reflecting sequential one-electron reduction of Ni<sup>II</sup>. In the presence of 10 equiv alkenyl acetate, a new reduction peak is evident at -1.29 V, more positive than the original Ni<sup>II/I</sup> feature. An increased current is observed for the peak at -1.46 V and, even more significantly, at -1.73 V (Figure 3.4C). The reduction potentials of Zn and Mn, determined from OCP measurements under the same conditions, are -1.31 V (Zn) and -1.55 V (Mn). These data suggest that the preference

for Zn as the reductant for this reaction reflects the ability of Zn to reduce  $\text{Ni}^{\text{II}}$  to  $\text{Ni}^{\text{I}}$  without significant generation of  $\text{Ni}^0$ . The reduction potential of Mn is sufficiently close to  $\text{Ni}^{\text{I}/0}$  potential to generate  $\text{Ni}^0$ , which was shown to promote alkyl-alkyl and vinyl-vinyl homocoupling in addition to the formation of other side products.<sup>29</sup>

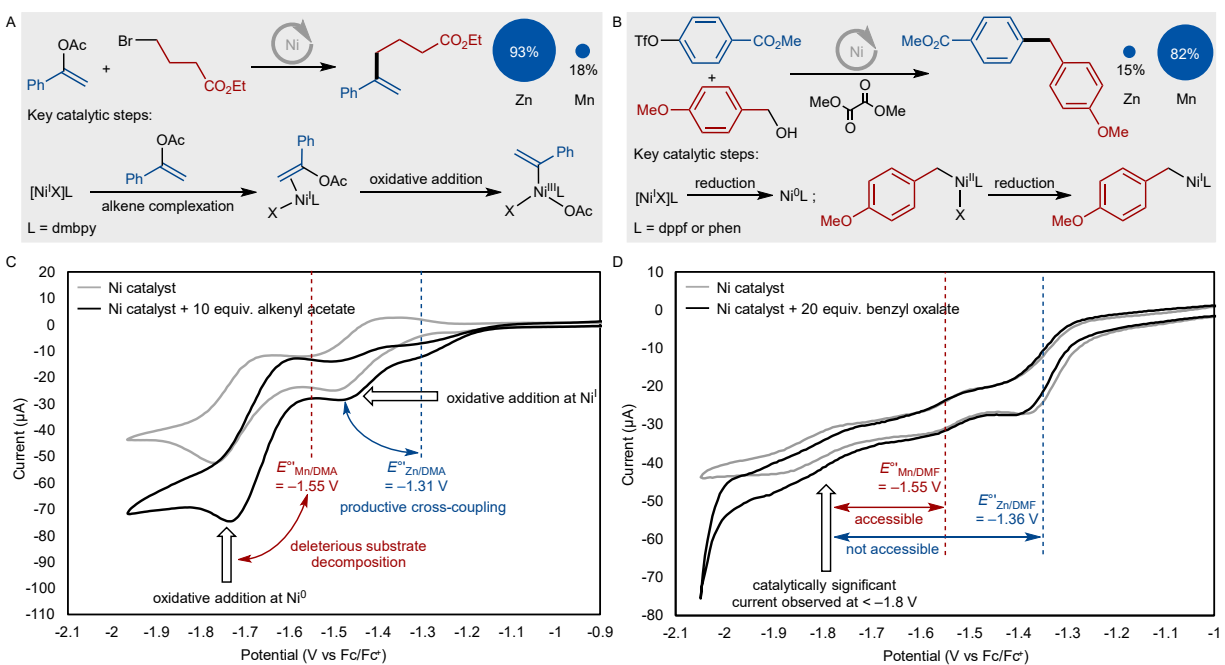


**Figure 3.4.** Correlation of Zn and Mn redox potentials with Ni-based redox processes in Ni-catalyzed XEC. (A) Reductive cross-coupling of styrenyl acetate with an alkyl bromide using a Ni/dmbpy catalyst (dmbpy = 5,5'-dimethyl-2,2'-bipyridine). (B) The net cross-coupling of benzyl alcohol with aryl triflate using dimethyl oxalate to activate the alcohol using a Ni/mixed-ligand catalyst system (ligands: phen = 1,10-phenanthroline, dppf = 1,1'-bis(diphenylphosphino)ferrocene). (C) CV analysis of Ni/dmbpy in the absence and presence of the substrate. (D) CV analysis of Ni/dppf/phen in the absence and presence of the substrate.

A similar approach was adopted to analyze the cross-coupling of benzyl alcohol and aryl triflate (Figure 3.4D), using a benzyl oxalate directly as the coupling partner to facilitate the CV analysis. This reaction features two different ancillary ligands, dppf or phen (dppf = 1,1'-bis(diphenylphosphino)ferrocene; phen = 1,10-phenanthroline), and the CV trace of the Ni catalyst shows multiple reduction peaks. The first peak at  $-1.37$  V is attributed to one-electron reduction of  $\text{Ni}^{\text{II}}$  to  $\text{Ni}^{\text{I}}$ , while assignments of the peaks at lower potentials,  $-1.56$  V and  $-1.86$  V, are complicated by the mixture of ligands present. Addition of benzyl oxalate (20 equiv) to the solution

leads to a small increase in current at potentials lower than approximately  $-1.60$  V, relative to the Ni-only CV. The reduction potentials of Zn ( $-1.36$  V) and Mn ( $-1.55$  V), determined by OCP measurements under these conditions, suggest that the preference for Mn as the reductant for this reaction arises from the need to access the lower-potential Ni species in this reaction, unlike the first reaction, which leads to deleterious reactivity at lower potentials. These results, for the first time, show how redox potentials of metal reductants in organic solvents correlate with catalyst redox potentials in XEC reactions.

**Comparison of Ni-catalyzed XEC reactions using chemical (Zn, Mn) and electrochemical reduction.** Metallic Zn and Mn are effective reductants for many reductive cross-coupling reactions, but their individual redox potentials are not necessarily optimal for every reaction, while electrochemical potentials can be tuned continuously over a wide range.<sup>47</sup> The OCP measurements outlined herein enable the first direct comparison of chemical and electrochemical Ni-catalyzed XEC reactions at reduction potentials of Zn and Mn under the reaction conditions, and these results may be compared with electrochemical reactions conducted at other applied potentials. Reactions with *N*-alkyl-2,4,6-triphenylpyridinium reagents (Katritzky salts)<sup>32,48–51</sup> represent a compelling target for exploration of these issues because they exhibit variable performance in Ni-catalyzed XEC reactions when using homogenous organic reductants with different reduction potentials.<sup>26</sup>

Two Katritzky salts, one with a 1° alkyl and one with a 2° alkyl substituent (**1** and **2**, respectively), were investigated in XEC reactions with six different (hetero)aryl bromides (Figure 3.5). Previously reported thermochemical conditions using Mn as the reductant<sup>49</sup> were used as the starting point for development of electrochemical conditions for the coupling of **1** and **2** with ethyl 4-bromobenzoate (Conditions **A** and **B**, Figure 3.5; see Table 3B.5 for evaluation of different cell configurations, electrode materials, and electrolytes). Good results were observed under constant

potential conditions in an undivided cell with a Ni foam cathode and sacrificial Fe anode. Each pair of substrates was then compared under four reaction conditions: two thermochemical conditions using metallic Zn and Mn powder as the reductant, and two electrochemical conditions conducted at applied potentials corresponding to  $E^{\circ}_{\text{Zn}}$  ( $-1.31$  V) and  $E^{\circ}_{\text{Mn}}$  ( $-1.55$  V) determined from OCP measurements with Zn and Mn under the reaction conditions. A fifth condition was then used for each substrate pair, based on optimization of the applied potential (see Figures 3B.5 and 3B.6 for optimization details).

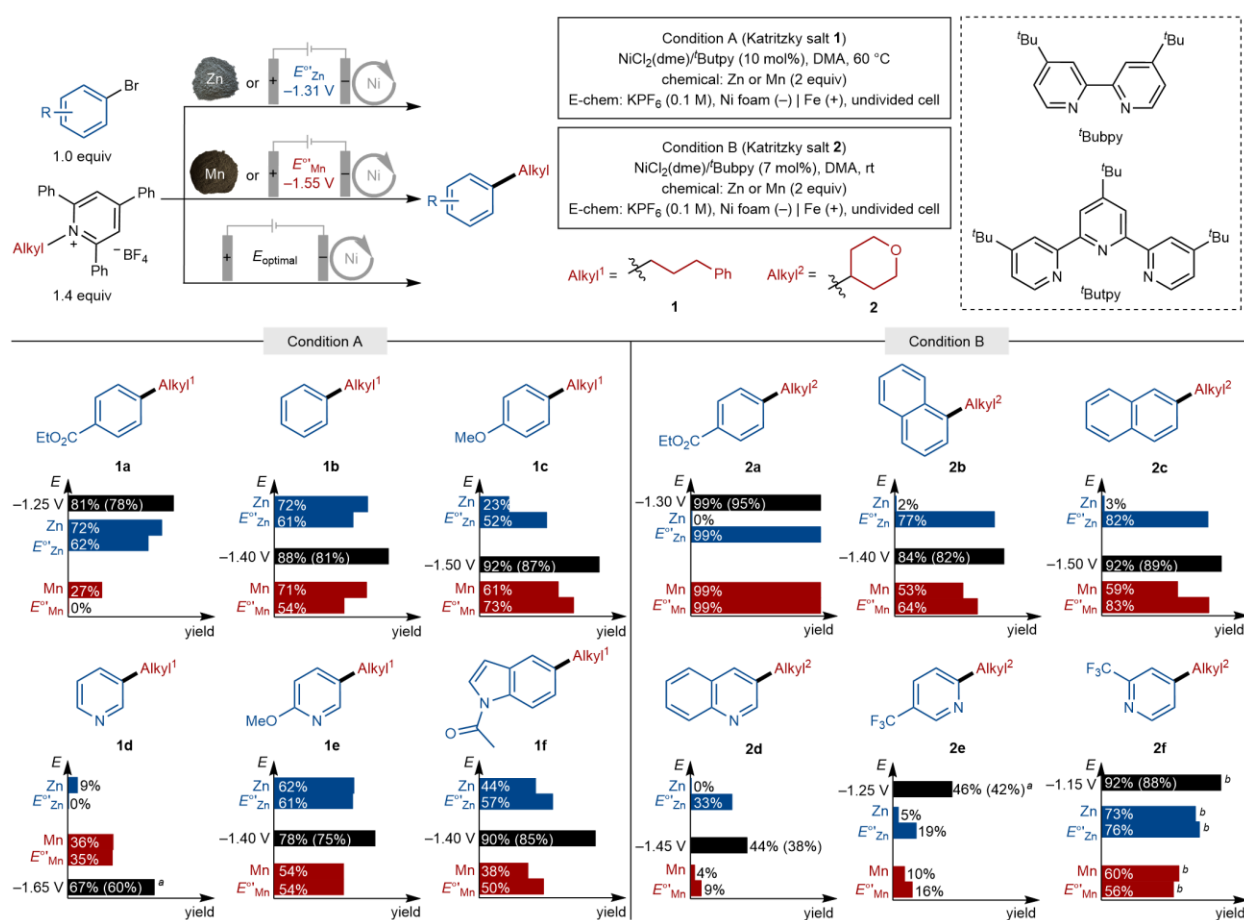


**Figure 3.5.** Cross-electrophile coupling reactions of alkyl Katritzky salts with aryl bromides. Reactions were conducted thermochemically with Zn or Mn as the reductant, or electrochemically at varied applied potential. See Appendix B for full experimental details. Yields determined by  $^1\text{H}$  NMR spectroscopy; isolated yields are shown in parentheses. <sup>a</sup> LiBr (2 equiv) instead of  $\text{KPF}_6$ . <sup>b</sup> Aryl chloride was used instead of aryl bromide.

The data in Figure 3.5 show how thermochemical and electrochemical reduction methods perform at the same potential ( $E^{\circ}_{\text{Zn}}$  and  $E^{\circ}_{\text{Mn}}$ ). For example, coupling product **1a** was obtained in 72% yield with Zn and a 62% yield under electrochemical conditions at the Zn potential (−1.31 V). Significantly lower yields were observed with Mn (27%) and under electrochemical conditions at the Mn potential (0%; −1.55 V). Quantitative differences between electrochemical and thermochemical conditions can arise from various factors, for example, differences in the mass transport behavior of dissolved species interacting with suspended metal particles versus a solid-state electrode, and differences in the redox-active surface area of the metal powders and electrodes, that could alter the outcome. Additionally, the composition of reaction mixtures will evolve as the reaction progresses through the release of metal salts that alter redox equilibria. Thus, the electrochemical reduction at  $E^{\circ}_{\text{Zn}}$  and  $E^{\circ}_{\text{Mn}}$  represents only a first-order approximation of the potential supplied by the stoichiometric metal reductant. Nonetheless, the results in Figure 3.5 show good qualitative agreement between thermochemical and electrochemical results obtained at the Zn potential of substrates **1a–f** and **2f**, and at the Mn potential for all substrates. Notable differences were observed for many of the XEC reactions of **2** at the Zn potential: negligible quantities of **2a–e** were observed under thermochemical conditions, while the corresponding electrochemical conditions (at  $E^{\circ}_{\text{Zn}}$ ) led to moderate-to-good product yields. Further analysis of this behavior showed that soluble  $\text{Zn}^{\text{II}}$  salts, generated in the reactions that used metallic Zn, convert the aryl bromide into the proto-dehalogenation byproduct, likely via the formation of protolytically sensitive aryl-zinc species (see Table 3B.6).<sup>45,52</sup>

The reactions of each substrate pair were then evaluated at different applied potentials, and the results showed that higher yields could be obtained at potentials other than  $E^{\circ}_{\text{Zn}}$  or  $E^{\circ}_{\text{Mn}}$  in all cases. For example, **1a** was generated in 81% yield at −1.25 V, a redox potential higher than  $E^{\circ}_{\text{Zn}}$

and  $E^{\circ}_{\text{Mn}}$ . A survey of the results shows that the optimal potential changes for each reaction, and even the position of the optimal potentials relative to the Zn and Mn potentials changes. For the six reactions performed with the 1° Katritzky salt **1**, only **1a** performs best at a potential higher than  $E^{\circ}_{\text{Zn}}$ . Four products (**1b**, **1c**, **1e**, **1f**) exhibit an optimal yield at a potential between Zn and Mn, and one (**1d**) maximizes at a potential more negative than  $E^{\circ}_{\text{Mn}}$  (Figure 3.5). With the 2° Katritzky salt **2**, three of the products afford the highest yields at a potential higher than  $E^{\circ}_{\text{Zn}}$  (**2a**, **2e**, **2f**), while three are optimal at potentials between Zn and Mn (**2b**, **2c**, **2d**).

The results in Figure 3.5 have important implications for Ni-catalyzed XEC reactions. Large-scale applications of these reactions with chemical reductants are already complicated by challenges in using metal-powder reagents (non-uniform particle properties/reactivity, difficulty in suspending dense powders in reactors<sup>53</sup>) or air-sensitive organic reductants<sup>28</sup>. The data in Figure 3.5 show that the quantized/non-tunable redox potentials of chemical reagents will limit opportunities to optimize the reaction performance. Each of these challenges may be addressed by using electrochemistry to supply the electrons needed in the reaction.

### 3.4. Conclusion

The results outlined above document thermodynamic potentials of Zn and Mn reductants in organic solutions for the first time, revealing the influence of different solvents and additives on the reduction potentials. These data are ideally paired with cyclic voltammetry studies to gain fundamental insights into the relationship between the redox potential of the reductant and critical redox processes in the reaction. The approach used here is readily adapted to other reduction and reductive coupling reactions, including those using different metal reductants, solvents, and reaction conditions. Access to the Zn and Mn reduction potentials also provided the first opportunity to directly compare the influence of chemical versus electrochemical reduction

methods on the reaction outcome. Good qualitative agreement is observed from reactions conducted at the same potential (e.g., at  $E^{\circ}_{\text{Zn}}$  or  $E^{\circ}_{\text{Mn}}$ ), but the optimization studies show that the best performance is often observed at reduction potentials different from the specific potentials accessible from the chemical reductants. These results highlight the importance of tuning the reductant redox potential when optimizing Ni-catalyzed XEC, and presumably other reductive coupling, reactions. The tunability of electrochemistry will offer significant advantages in the future development of these reactions.

### 3.5. Acknowledgements

Financial support for this work was provided by the NSF (CHE-2154698; thermodynamic potential measurements) and NIH (R35 GM134929; synthetic methodology studies). Spectroscopic instrumentation was supported by a generous gift from Paul J. and Margaret M. Bender, the NIH (S10 OD020022), and the NSF (CHE-1048642).

### 3.6. Author Contributions

S.S.S. and Z.-M.S. conceived the project and designed the experiments. Z.-M.S. conducted all the experiments. R.D. contributed in part to electrochemical analysis and product purification. S.S.S. and Z.-M.S. wrote the manuscript.

### 3.7. References

1. Corbet, J.-P. & Mignani, G. Selected Patented Cross-Coupling Reaction Technologies. *Chem. Rev.* **106**, 2651–2710 (2006).
2. Boström, J., Brown, D. G., Young, R. J. & Keserü, G. M. Expanding the medicinal chemistry synthetic toolbox. *Nat Rev Drug Discov* **17**, 709–727 (2018).
3. Buskes, M. J. & Blanco, M.-J. Impact of Cross-Coupling Reactions in Drug Discovery and Development. *Molecules* **25**, 3493 (2020).
4. Moragas, T., Correa, A. & Martin, R. Metal-Catalyzed Reductive Coupling Reactions of Organic Halides with Carbonyl-Type Compounds. *Chem. Eur. J.* **20**, 8242–8258 (2014).
5. Weix, D. J. Methods and Mechanisms for Cross-Electrophile Coupling of Csp<sup>2</sup> Halides with Alkyl Electrophiles. *Acc. Chem. Res.* **48**, 1767–1775 (2015).

6. Wang, X., Dai, Y. & Gong, H. Nickel-Catalyzed Reductive Couplings. in *Ni- and Fe-Based Cross-Coupling Reactions* (ed. Correa, A.) 61–89 (Springer International Publishing, 2017).
7. Richmond, E. & Moran, J. Recent Advances in Nickel Catalysis Enabled by Stoichiometric Metallic Reducing Agents. *Synthesis* **50**, 499–513 (2018).
8. Goldfogel, M. J., Huang, L. & Weix, D. J. Cross-Electrophile Coupling. in *Nickel Catalysis in Organic Synthesis* 183–222 (John Wiley & Sons, Ltd, 2020).
9. Chaussard, J. *et al.* Use of Sacrificial Anodes in Electrochemical Functionalization of Organic Halides. *Synthesis* **1990**, 369–381 (1990).
10. Durandetti, M., Nédélec, J.-Y. & Périchon, J. Nickel-Catalyzed Direct Electrochemical Cross-Coupling between Aryl Halides and Activated Alkyl Halides. *J. Org. Chem.* **61**, 1748–1755 (1996).
11. Durandetti, M., Périchon, J. & Nédélec, J.-Y. Asymmetric Induction in the Electrochemical Cross-Coupling of Aryl Halides with  $\alpha$ -Chloropropionic Acid Derivatives Catalyzed by Nickel Complexes. *J. Org. Chem.* **62**, 7914–7915 (1997).
12. Durandetti, M., Gosmini, C. & Périchon, J. Ni-catalyzed activation of  $\alpha$ -chloroesters: a simple method for the synthesis of  $\alpha$ -arylesters and  $\beta$ -hydroxyesters. *Tetrahedron* **63**, 1146–1153 (2007).
13. Everson, D. A., Jones, B. A. & Weix, D. J. Replacing Conventional Carbon Nucleophiles with Electrophiles: Nickel-Catalyzed Reductive Alkylation of Aryl Bromides and Chlorides. *J. Am. Chem. Soc.* **134**, 6146–6159 (2012).
14. Rosen, B. M. *et al.* Nickel-Catalyzed Cross-Couplings Involving Carbon–Oxygen Bonds. *Chem. Rev.* **111**, 1346–1416 (2011).
15. He, F.-S., Ye, S. & Wu, J. Recent Advances in Pyridinium Salts as Radical Reservoirs in Organic Synthesis. *ACS Catal.* **9**, 8943–8960 (2019).
16. Karmakar, S., Silamkoti, A., Meanwell, N. A., Mathur, A. & Gupta, A. K. Utilization of C(*sp*<sup>3</sup>)-Carboxylic Acids and Their Redox-Active Esters in Decarboxylative Carbon–Carbon Bond Formation. *Adv. Syn. Catal.* **363**, 3693–3736 (2021).
17. Perkins, R. J., Hughes, A. J., Weix, D. J. & Hansen, E. C. Metal-Reductant-Free Electrochemical Nickel-Catalyzed Couplings of Aryl and Alkyl Bromides in Acetonitrile. *Org. Process Res. Dev.* **23**, 1746–1751 (2019).
18. Hamby, T. B., LaLama, M. J. & Sevov, C. S. Controlling Ni redox states by dynamic ligand exchange for electroreductive Csp<sup>3</sup>–Csp<sup>2</sup> coupling. *Science* **376**, 410–416 (2022).
19. Zhang, B. *et al.* Ni-electrocatalytic Csp<sup>3</sup>–Csp<sup>3</sup> doubly decarboxylative coupling. *Nature* **606**, 313–318 (2022).
20. Franke, M. C. *et al.* Zinc-free, Scalable Reductive Cross-Electrophile Coupling Driven by Electrochemistry in an Undivided Cell. *ACS Catal.* **12**, 12617–12626 (2022).
21. Su, Z.-M. *et al.* Ni- and Ni/Pd-Catalyzed Reductive Coupling of Lignin-Derived Aromatics to Access Biobased Plasticizers. *ACS Cent. Sci.* **9**, 159–165 (2023).
22. Twilton, J. *et al.* Quinone-mediated hydrogen anode for non-aqueous reductive electrosynthesis. *Nature* **623**, 71–76 (2023).
23. Zhang, G., Xie, Y., Wang, Z., Liu, Y. & Huang, H. Diboron as a reductant for nickel-catalyzed reductive coupling: rational design and mechanistic studies. *Chem. Commun.* **51**, 1850–1853 (2015).
24. Anka-Lufford, L. L., Huihui, K. M. M., Gower, N. J., Ackerman, L. K. G. & Weix, D. J. Nickel-Catalyzed Cross-Electrophile Coupling with Organic Reductants in Non-Amide Solvents. *Chem. Eur. J.* **22**, 11564–11567 (2016).
25. Lv, L., Qiu, Z., Li, J., Liu, M. & Li, C.-J. N<sub>2</sub>H<sub>4</sub> as traceless mediator for homo- and cross- aryl coupling. *Nat. Commun.* **9**, 4739 (2018).
26. Charboneau, D. J. *et al.* Tunable and Practical Homogeneous Organic Reductants for Cross-Electrophile Coupling. *J. Am. Chem. Soc.* **143**, 21024–21036 (2021).
27. Fu, H. *et al.* An asymmetric sp<sup>3</sup>–sp<sup>3</sup> cross-electrophile coupling using ‘ene’-reductases. *Nature* **610**, 302–307 (2022).

28. Charboneau, D. J., Hazari, N., Huang, H., Uehling, M. R. & Zultanski, S. L. Homogeneous Organic Electron Donors in Nickel-Catalyzed Reductive Transformations. *J. Org. Chem.* **87**, 7589–7609 (2022).
29. He, R.-D. *et al.* Reductive Alkylation of Alkenyl Acetates with Alkyl Bromides by Nickel Catalysis. *Angew. Chem. Int. Ed.* **61**, e202114556 (2022).
30. Guo, P. *et al.* Dynamic Kinetic Cross-Electrophile Arylation of Benzyl Alcohols by Nickel Catalysis. *J. Am. Chem. Soc.* **143**, 513–523 (2021).
31. Lin, Q. & Diao, T. Mechanism of Ni-Catalyzed Reductive 1,2-Dicarbonylfunctionalization of Alkenes. *J. Am. Chem. Soc.* **141**, 17937–17948 (2019).
32. Martin-Montero, R., Yatham, V. R., Yin, H., Davies, J. & Martin, R. Ni-catalyzed Reductive Deaminative Arylation at sp<sup>3</sup> Carbon Centers. *Org. Lett.* **21**, 2947–2951 (2019).
33. Day, C. S. *et al.* Elucidating electron-transfer events in polypyridine nickel complexes for reductive coupling reactions. *Nat. Catal.* **6**, 1–10 (2023).
34. Pourbaix, M. *Atlas of electrochemical equilibria in aqueous solutions. 2nd ed.* (National Association of Corrosion Engineers, 1974).
35. Yu, Y. *et al.* High-Voltage Rechargeable Aqueous Zinc-Based Batteries: Latest Progress and Future Perspectives. *Small Sci.* **1**, 2000066 (2021).
36. Pavlishchuk, V. V. & Addison, A. W. Conversion constants for redox potentials measured versus different reference electrodes in acetonitrile solutions at 25 °C. *Inorganica Chim. Acta* **298**, 97–102 (2000).
37. Kissinger, P. & Heineman, W. R. *Laboratory Techniques in Electroanalytical Chemistry, Revised and Expanded.* (CRC Press, 2018).
38. Khedr, M. G. A. & Lashien, A. M. S. Corrosion Behavior of Aluminum in the Presence of Accelerating Metal Cations and Inhibition. *J. Electrochem. Soc.* **136**, 968 (1989).
39. Brett, C. M. A., Gomes, I. A. R. & Martins, J. P. S. The electrochemical behaviour and corrosion of aluminium in chloride media. The effect of inhibitor anions. *Corros Sci.* **36**, 915–923 (1994).
40. Zdrachek, E. & Bakker, E. Potentiometric Sensing. *Anal. Chem.* **91**, 2–26 (2019).
41. Pillai, P., Sundaresan, S., Kumar, P., Pattipati, K. R. & Balasingam, B. Open-Circuit Voltage Models for Battery Management Systems: A Review. *Energies* **15**, 6803 (2022).
42. Connelly, N. G. & Geiger, W. E. Chemical Redox Agents for Organometallic Chemistry. *Chem. Rev.* **96**, 877–910 (1996).
43. Elgrishi, N. *et al.* A Practical Beginner's Guide to Cyclic Voltammetry. *J. Chem. Educ.* **95**, 197–206 (2018).
44. Mirabi, B., Marchese, A. D. & Lautens, M. Nickel-Catalyzed Reductive Cross-Coupling of Heteroaryl Chlorides and Aryl Chlorides. *ACS Catal.* **11**, 12785–12793 (2021).
45. Kang, K., Huang, L. & Weix, D. J. Sulfonate Versus Sulfonate: Nickel and Palladium Multimetallic Cross-Electrophile Coupling of Aryl Triflates with Aryl Tosylates. *J. Am. Chem. Soc.* **142**, 10634–10640 (2020).
46. Huang, L., Ackerman, L. K. G., Kang, K., Parsons, A. M. & Weix, D. J. LiCl-Accelerated Multimetallic Cross-Coupling of Aryl Chlorides with Aryl Triflates. *J. Am. Chem. Soc.* **141**, 10978–10983 (2019).
47. Rafiee, M., Mayer, M. N., Punchedewa, B. T. & Mumau, M. R. Constant Potential and Constant Current Electrolysis: An Introduction and Comparison of Different Techniques for Organic Electrosynthesis. *J. Org. Chem.* **86**, 15866–15874 (2021).
48. Ni, S. *et al.* Ni-catalyzed deaminative cross-electrophile coupling of Katritzky salts with halides via C–N bond activation. *Sci. Adv.* **5**, eaaw9516 (2019).
49. Yue, H. *et al.* Nickel-catalyzed C–N bond activation: activated primary amines as alkylating reagents in reductive cross-coupling. *Chem. Sci.* **10**, 4430–4435 (2019).
50. Liao, J. *et al.* Deaminative Reductive Cross-Electrophile Couplings of Alkylpyridinium Salts and Aryl Bromides. *Org. Lett.* **21**, 2941–2946 (2019).

51. Twitty, J. C. *et al.* Diversifying Amino Acids and Peptides via Deaminative Reductive Cross-Couplings Leveraging High-Throughput Experimentation. *J. Am. Chem. Soc.* **145**, 5684–5695 (2023).
52. Klein, P., Lechner, V. D., Schimmel, T. & Hintermann, L. Generation of Organozinc Reagents by Nickel Diazadiene Complex Catalyzed Zinc Insertion into Aryl Sulfonates. *Chem. Eur. J.* **26**, 176–180 (2020).
53. Nimmagadda, S. K.; Korapati, S.; Dasgupta, D.; Malik, N. A.; Vinodini, A.; Gangu, A. S.; Kalidindi, S.; Maity, P.; Bondigela, S. S.; Venu, A.; Gallagher, W. P.; Aytar, S.; González-Bobes, F.; Vaidyanathan, R. Development and Execution of an Ni(II)-Catalyzed Reductive Cross-Coupling of Substituted 2-Chloropyridine and Ethyl 3-Chloropropanoate. *Org. Process Res. Dev.* **24**, 1141–1148 (2020).

## Chapter 4.

### Selective Ni-Catalyzed Cross-Electrophile Coupling of Heteroaryl Chlorides with Aryl Bromides at 1:1 Substrate Ratio

The content presented in this Chapter is reproduced from a manuscript in preparation: **Zhi-Ming Su**, Darren L. Poole, Mohammad Rafiee, Robert S. Paton, Daniel J. Weix, and Shannon S. Stahl. Selective Ni-Catalyzed Cross-Electrophile Coupling of Heteroaryl Chlorides with Aryl Bromides at 1:1 Substrate Ratio.

#### 4.1. Abstract

Nickel-catalyzed cross-electrophile coupling (XEC) reactions of (hetero)aryl electrophiles represent appealing alternatives to palladium-catalyzed methods for biaryl synthesis, but they often generate significant quantities of homocoupling and/or proto-dehalogenation side products. In this study, an informer library of heteroaryl chloride and aryl bromide coupling partners is used to identify Ni-catalyzed XEC conditions that access high selectivity for the cross-product when using equimolar quantities of the two substrates. Two different catalyst systems are identified that show complementary scope and broad functional-group tolerance, and time-course data suggest the two methods follow different mechanisms. A NiBr<sub>2</sub>/terpyridine catalyst system with Zn as the reductant converts the aryl bromide into an aryl-zinc intermediate that undergoes in situ coupling with 2-chloropyridines, while a NiBr<sub>2</sub>/bipyridine catalyst system with tetrakis(dimethylamino)ethylene as the reductant uses FeBr<sub>2</sub> and NaI as additives to achieve selective cross-coupling.

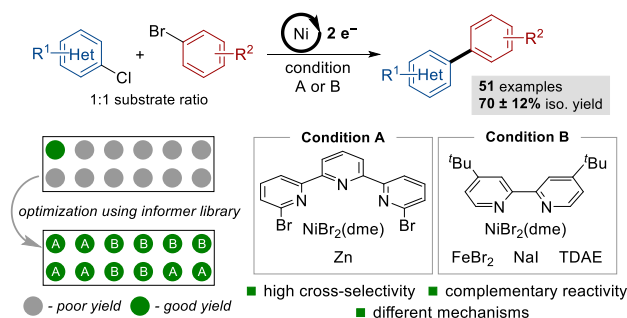


**Figure 4.1.** Summary of this work.

## 4.2. Introduction

Nitrogen-containing biaryls are prevalent in biologically active compounds, pharmaceuticals, and agrochemicals,<sup>1-3</sup> and these structures are commonly accessed by transition metal-catalyzed cross-coupling reactions.<sup>4-17</sup> Conventional biaryl cross-coupling features the coupling of (hetero)aryl organometallic reagents, Ar-[M] ([M] = zinc, magnesium, stannane, silicon, or boron species), with (hetero)aryl electrophiles, Ar-X (X = (pseudo)halides), enabled by palladium or other transition-metal catalysts. The complementary polarity and different activation mechanisms of the nucleophilic and electrophilic coupling partners can lead to highly selective cross-coupling of the two substrates, even when used in a 1:1 stoichiometry. Nonetheless, several factors have been motivating efforts to develop new methods to access biaryl structures. Aryl-organometallic coupling partners are much less readily available than aryl electrophiles, limiting access to structural diversity. This issue is especially relevant to medicinal chemistry and high-throughput screening efforts that target rapid access to diverse compounds, but it also impacts large-scale applications arising from the higher cost and operational complexities associated with organometallic reagents. The instability of heteroaryl organometallic reagents can limit their use in cross-coupling reactions. This issue is most prominently evident in the "2-pyridyl problem", a term commonly used to describe challenges associated with preparation and use of 2-pyridyl and related heteroaryl organometallic reagents.<sup>18,19</sup> Finally, while palladium catalyst systems are the most widely used for cross-coupling, the increasing and fluctuating cost of palladium underlies growing interest in the development of non-precious-metal catalyst systems (Figure 4.2A).

Nickel-catalyzed cross-electrophile coupling (XEC) represents an attractive alternative to palladium-catalyzed cross-coupling for forming C(*sp*<sup>2</sup>)-C(*sp*<sup>2</sup>) bonds, as it directly utilizes stable and widely available carbon electrophiles as coupling partners, and nickel is an earth abundant,

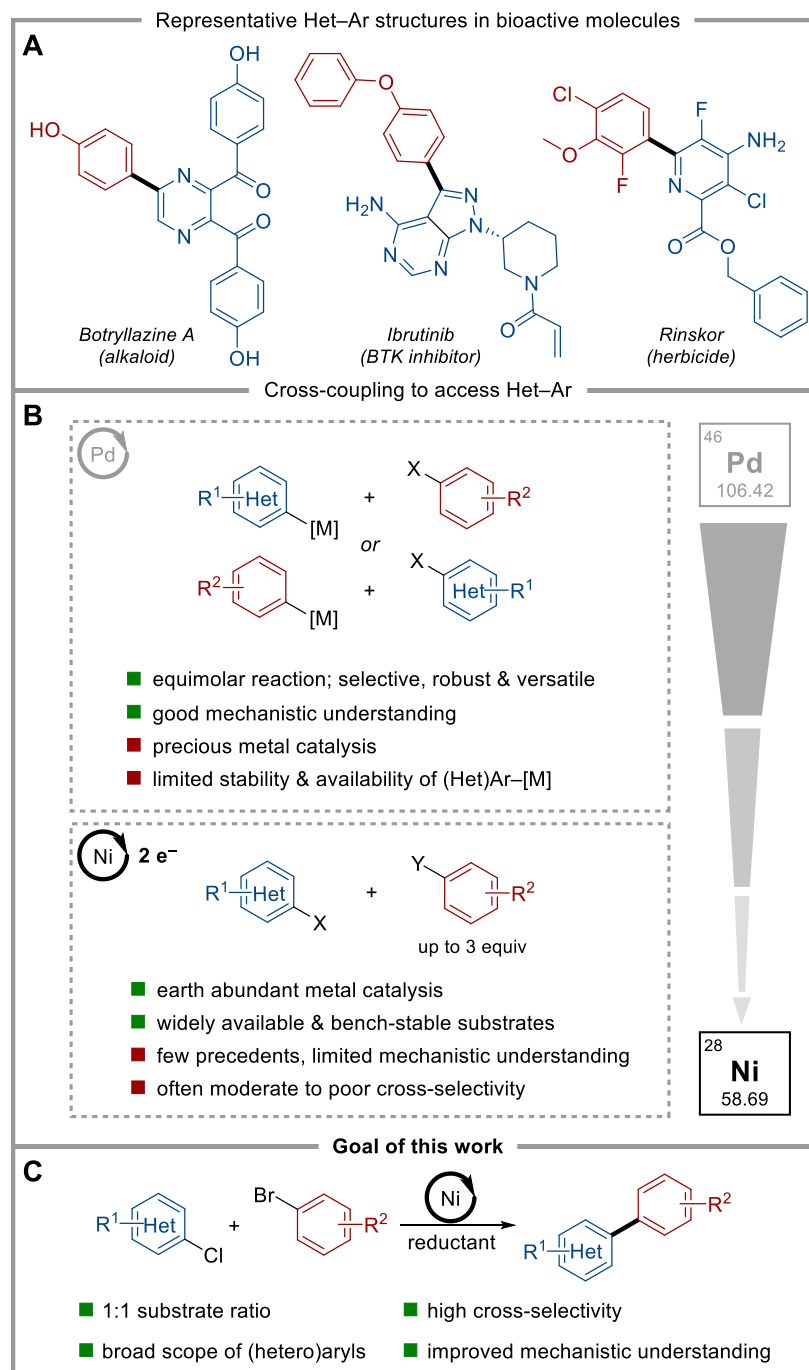


**Figure 4.2.** Heteroaryl-aryl core structures are commonly encountered in bioactive molecules (A). Existing coupling methods typically use Pd-based catalyst, but Ni-catalyzed methods would offer compelling alternatives, if they could overcome selectivity challenges (B). This study targets the development of Ni-catalyzed cross-electrophile coupling methods that are compatible with equimolar substrate ratios (C).

non-precious metal that is much less expensive than palladium.<sup>20-23</sup> A central challenge of this strategy is selectively accessing the cross-coupled product over the two homo-coupled products

due to the subtle differences between two coupling partners.<sup>24,25</sup> Only a small number of reports have explored Ni-catalyzed heteroaryl-aryl XEC reactions, and they typically exhibit limited substrate scope and a moderate-to-poor cross-selectivity (Figure 4.2B).<sup>26-33</sup> In these precedents, two approaches were generally adopted to improve the yield of the cross-coupled product. The first uses an excess of one of the coupling partners (up to 3 equiv) to improve the yield of cross-coupled products with respect to the limiting reagent. This approach, however, often generates significant quantities of homo-coupled dimers from the excess reagent, introducing undesirable waste and complicating product isolation. In the second approach, the (pseudo)halide substituents on the two electrophiles are adjusted on a case-by-case basis until the two coupling partners show comparable reactivity and improved cross-selectivity. For instance, aryl iodides are effective with more reactive heteroaryl chlorides, while aryl bromides or chlorides may be used to achieve selective coupling with less reactive heteroaryl chlorides. These approaches are often implemented simultaneously to maximize the yield of cross-coupled products. Ideally, one could identify effective catalyst systems that achieve general XEC reactivity with different coupling partners, and the present study was initiated to explore this possibility (Figure 4.2C). Specifically, we targeted high cross-selectivity using an equimolar ratio of the coupling partners. We prioritized reactions with 2-chloro-substituted aromatic heterocycles, including pyridines, pyrimidines, pyrazines, and pyridazines, which present unique challenges in conventional cross-coupling reactions with organometallic nucleophiles.

### 4.3. Results and Discussion

**Reaction optimization using an informer library.** Precedents for Ni-catalyzed heteroaryl-aryl XEC reactions show strong similarity among the catalyst systems employed. Early studies by Gosmini<sup>26-28</sup> and subsequent studies by Léonel<sup>29-32</sup> utilized electrochemical reduction, while more

recent reports by Lautens<sup>33</sup> and Surgenor<sup>34</sup> used Zn or Mn chemical reductants. Each of these reports used NiX<sub>2</sub>/bpy (X = Br or I, bpy = 2,2'-bipyridine) catalyst systems. Gosmini and Léonel noted a beneficial effect of FeBr<sub>2</sub> on reactions with heteroaryl electrophiles that contain two or more nitrogen atoms in the ring (e.g., pyrimidine, pyrazine, and pyridazine), wherein FeBr<sub>2</sub> was proposed to limit catalyst poisoning by the heterocycle through coordination to Ni.<sup>27</sup>

Building on these reports, we initiated reactivity studies with a reaction system comprising a (bpy)NiBr<sub>2</sub> catalyst (10 mol%), Zn as the reductant, and DMF as the solvent (Figure 4.3A). A panel of six different heteroaryl chlorides (Het-Cl, **1a–1f**) and two aryl bromides (Ar-Br, **2a** and **2b**) were used as an "informer library"<sup>35</sup> to evaluate XEC reactivity with equimolar quantities of the Het-Cl and Ar-Br substrates. With the diazaheteroaryl substrates **1c–1f**, 30 mol% FeBr<sub>2</sub> was included in the reaction (see Table 4C.1 and Section 4C.II of Appendix C for full screening data). The majority of the reactions led to poor or modest yields of the desired XEC (Figure 4.3D-i), with more than half affording < 20% yields. The reactions typically proceed to high conversion, but they favor formation of homo-coupled dimers and/or proto-dehalogenation byproducts (Table 4C.1). This outcome highlights the predominant challenge facing such reactions, particularly when using a 1:1 ratio of the electrophilic coupling partners.

Results from XEC reactions using the adapted literature condition highlight the need for new catalyst systems. We initiated the reaction optimization by evaluating a series of nitrogen-based ligands for the coupling of 2-chloropyridine (**1a**) with ethyl 4-bromobenzoate (**2b**) (Figure 4.3B). Reactions catalyzed by Ni complexed with bidentate nitrogen ligands showed that a hindered ligand, 6,6'-dimethyl-2,2'-bipyridine (**L4**), slightly increased the yield of the cross-coupled product **3ab**, compared to other bipyridine or phenanthroline ligands evaluated (**L1** to **L4**; see full ligand screening in Table 4C.2). Tridentate ligands were also evaluated, and Ni complexed with a

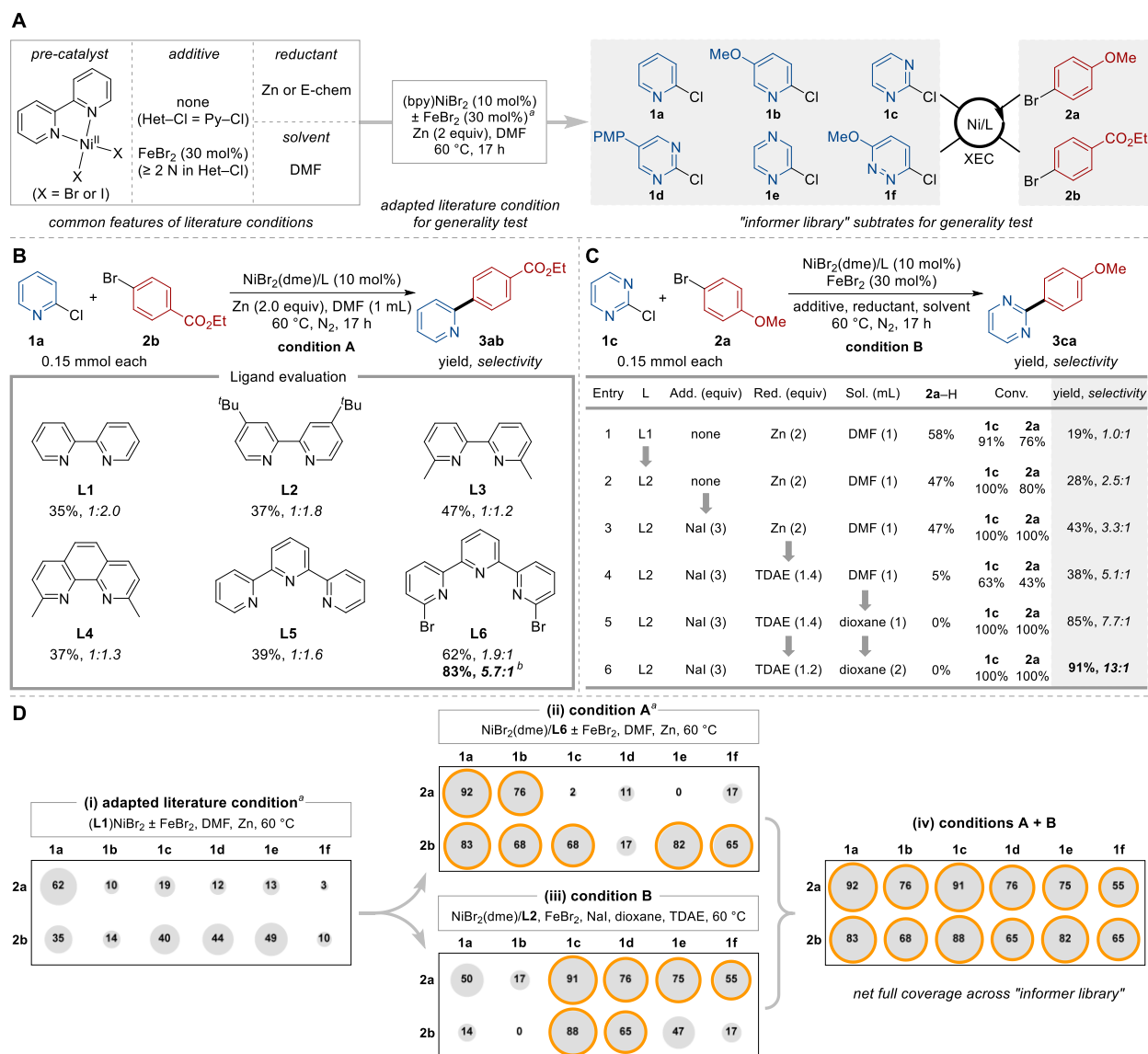


**Figure 4.3.** Reaction optimization. See Section 4C.II of Appendix C for experimental details. Yields are determined by  $^1\text{H}$  NMR spectroscopy of the crude reaction mixture using 1,3,5-trimethoxybenzene as an internal standard. Cross-selectivity ratio reflects  $^1\text{H}$  NMR yields of cross-coupled product:(heteroaryl dimer + aryl dimer). (A) Illustration of (adapted) literature conditions and informer library substrates. (B) Optimization of XEC of **1a** with **2b**. (C) Optimization of XEC of **1c** with **2a**. (D) Use informer library to test the generality of the adapted literature condition, condition A, and condition B. <sup>a</sup> Used 10 mol% Ni catalyst and added 30 mol%  $\text{FeBr}_2$  when **1** contains more than one nitrogen atom in the ring. <sup>b</sup> 7 mol% Ni catalyst.

hindered, electron-poor **L6** afforded **3ab** in 62% yield. Reducing the loading of the Ni/**L6** catalyst to 7 mol% further improved the result (83%). NMR analysis of the crude mixture indicates that the C–Br bond on **L6** remains intact during the reaction. Use of the Ni/**L6** catalyst system results

in more than a ten-fold increase in the cross-selectivity relative to the original Ni/**L1** catalyst (from 1:2.0 to 5.7:1). This catalyst system, designated "condition A", was then evaluated with the other substrates in the informer library (using 30 mol% FeBr<sub>2</sub> with **1c–1f**). Significantly improved outcomes were observed for many of the substrate pairs, with good-to-excellent results obtained from XEC of 2-chloropyridines **1a** and **1b** with **2a** and **2b**, and from the reactions of pyrimidine **1c**, pyrazine **1e**, and pyridazine **1f** with **2b** (Figure 4.3D-ii). The reduced yields in the remaining reactions correlated with formation of significant quantities of proto-dehalogenation byproducts (Table 4C.4).

To achieve effective coupling of the substrates that reacted poorly under condition A, we explored new modified reaction conditions for the XEC of 2-chloropyrimidine (**1c**) and 4-bromoanisole (**2a**) (Figure 4.3C; see Tables 4C.5–4C.7 for additional screening data). Switching the ligand from **L1** to **L2** slightly increased the yield from 19% to 28% (entries 1 and 2). Addition of 3 equiv of NaI enhanced the aryl bromide conversion and led to a higher yield of **3ca** (43%, entry 3), but a significant quantity of the proto-dehalogenation byproduct of **2a** (**2a–H**) was observed. This side reaction was attributed to the use of Zn as the reductant, as soluble Zn<sup>II</sup> salts generated during the reaction could form protolytically sensitive aryl-zinc species *in situ*.<sup>36,37</sup> Formation of the proto-debromination byproduct **2a–H** was suppressed upon replacing Zn with tetrakis(dimethylamino) ethylene (TDAE), a mild organic reductant,<sup>38</sup> and changing from DMF to dioxane as the solvent led to an 85% yield of **3ca**, with full conversion of both coupling partners (entries 4 and 5). Reducing the TDAE loading and reaction concentration led to the optimal yield (91%, entry 6), and these conditions were designated "condition B". No product was observed when replacing TDAE with Zn or replacing **L2** with **L6** under optimized condition B, implicating key differences between conditions A and B, as elaborated below. The condition B catalytic method

was then evaluated with the other substrates in the informer library (Table 4C.8). The yields obtained from the reaction of **2a** with **1c–1f** and **2b** with **1c–1d** showed significant enhancement under condition B (Figure 4.3D-iii). Collectively, the informer library data show that conditions A and B exhibit complementary reactivity, enabling successful outcomes with all 12 XEC reactions (Figure 4.3D-iv).

**Reaction scope.** With the optimal conditions in hand, we examined the coupling of a variety of heteroaryl chlorides and aryl bromides containing an array of functional groups and steric environments (Figure 4.4). Coupling reactions of 2-chloropyridine (**1a**) with aryl bromides bearing different substituents, ranging from electron-rich ( $-\text{NMe}_2$ ) to electron-deficient ( $-\text{CF}_3$ ), were all effective under condition A, affording the cross-coupled products in high yields (**3aa–3af**). The tolerance of the boronic ester allows room for further diversification (**3ag**). Sterically hindered aryl bromide **2h** was smoothly coupled with **1a**, using 10 mol% Ni complexed with **L3** instead of **L6**. Electron-donating and -withdrawing groups at different positions of the pyridine ring were compatible with the reaction conditions (**3ga, 3gb, 3hb, 3ib, 3bb, 3ba, 3ja**).

The reaction also shows broad scope with diazaheteroaryl chlorides. Unsubstituted 2-chloropyrimidine (**1c**) and 2-chloropyrazine (**1e**) can be coupled with an array of electronically diverse aryl bromides (**2a, 2b, 2d, 2e, 2i**). Exclusive activation of the C–Cl bond at C2 position of **1m** showed great site-selectivity of this method. Variations of substituents on the 2-chloropyrimidine or 2-chloropyrazine ring were tolerated (**3ka, 3lb, 3mb, 3da, 3db, 3pa, 3pb, 3qa, 3qb**). 4-Chloropyrimidine and 3-chloropyridazine derivatives can be coupled with electron-rich, -neutral, and -deficient aryl bromides under condition A or B (**3na, 3nb, 3re, 3fa, 3fb, 3se**).

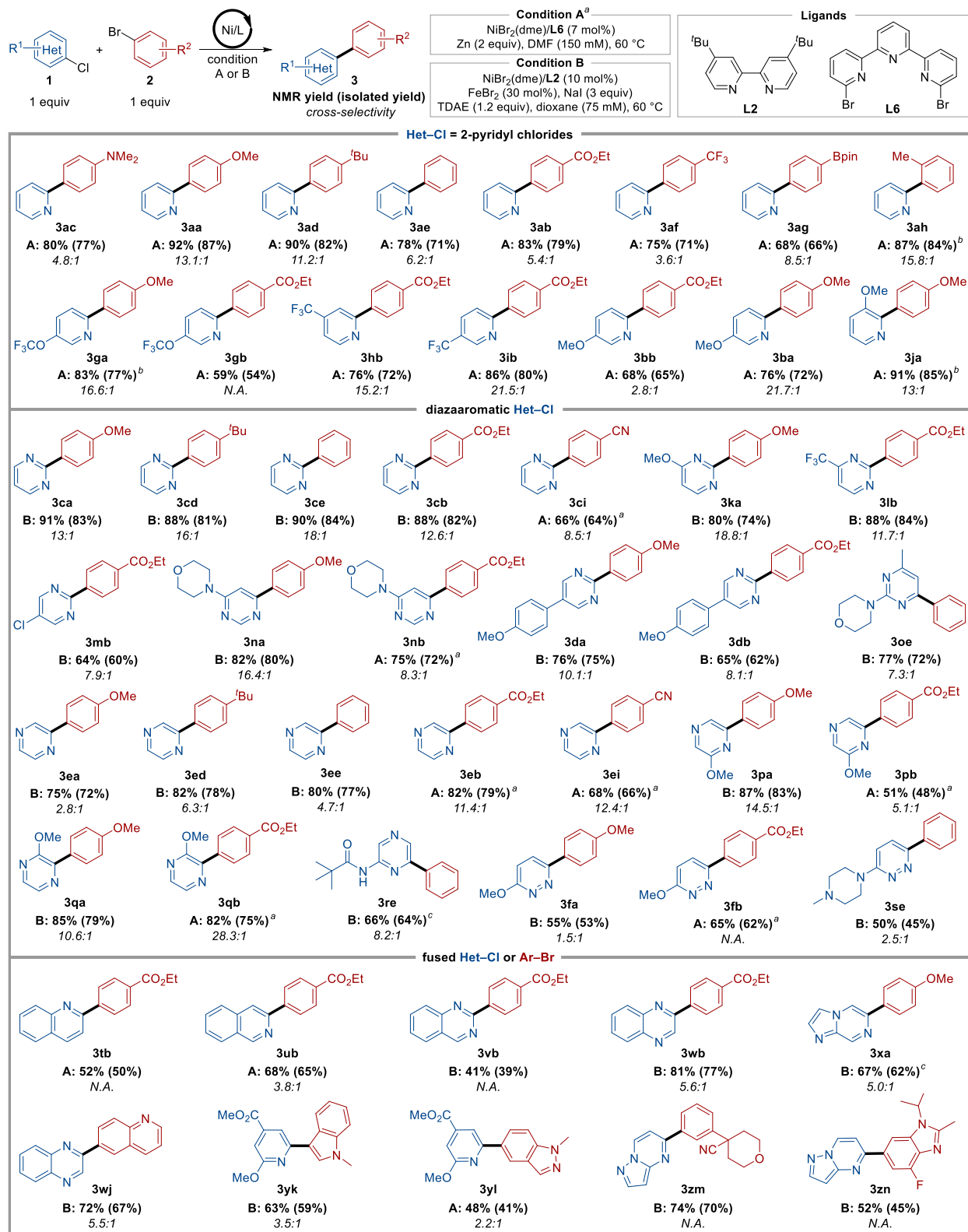


**Figure 4.4.** Synthetic scope of heteroaryl chlorides coupling with aryl bromides with conditions A and B. Cross-selectivity ratio reflects <sup>1</sup>H NMR yields of cross-coupled product:(heteroaryl dimer + aryl dimer). See Section 4C.III of Appendix C for experimental details. <sup>a</sup>Used 10 mol% Ni catalyst and added 30 mol%

FeBr<sub>2</sub> when **1** contains two or more nitrogen atoms in the ring. <sup>b</sup> **L3** instead of **L6**, 10 mol% Ni catalyst. <sup>c</sup> Added 2 equiv LiCl.

The coupling of **1n** with **2a** was effective under condition A, while its coupling with **2b** was effective under condition B. Several more examples showcased this complementary reactivity accessible with conditions A and B (cf. **3pa** and **3pb**, **3qa** and **3qb**, **3fa** and **3fb**).

The reaction conditions can be extended to the XEC of heteroaryl chlorides with aryl bromides in which one or both substrates features a fused bicyclic structure. Multi-substituted 2-chloropyridines can be coupled with fused aryl bromides (**3yk**, **3yl**). The reactions of electron-deficient and -rich aryl bromides with fused bicyclic heteroaryl chlorides afforded the cross-coupled products in moderate to high yields (**3tb**, **3ub**, **3vb**, **3wb**, **3xa**, **3wj**). Heteroaryl chlorides with multiple nitrogen atoms in the ring can increase the likelihood of catalyst poisoning, but three such structures were shown to undergo effective coupling (**3xa**, **3zm**, **3zn**).

Overall, an average isolated yield of  $70 \pm 12\%$  was achieved across 51 products containing 12 heteroaryl core structures, highlighting the efficacy and generality of conditions A and B for heteroaryl-aryl XEC.

**Time-course analysis and mechanistic features of reaction condition A.** The reductive coupling of 2-chloropyridine (**1a**) and ethyl 4-bromobenzoate (**2b**) was used to probe the reaction time course of XEC under condition A (Figure 4.5A). Organometallic intermediates were probed by quenching reaction aliquots with iodine, an established protocol that converts aryl-zinc and aryl-nickel species into aryl iodides.<sup>37,39</sup> Specifically, 2-pyridyl-NiX or -ZnX species are converted into 2-iodopyridine (**1a-I**), and Ar-NiX or -ZnX (Ar = *p*-CO<sub>2</sub>Et-C<sub>6</sub>H<sub>4</sub>) species are converted into ethyl 4-iodobenzoate (**2b-I**). These aryl iodides (**1a-I** and **2b-I**) and other catalytic reaction products (**3ab**, **1aa**, **2bb**) were analyzed and quantified by <sup>1</sup>H NMR spectroscopy at each time point.

The time-course data in Figure 4.5B reveal rapid formation of **2b-I** during the first 40 min of the reaction, along with fast depletion of the aryl bromide (**2b**). Small quantities of the aryl dimer (**2bb**) are also detected during this period. In contrast, substrate **1a** is slowly consumed and **1a-I** is not observed at early stages of the reaction. The cross-coupled product (**3ab**) begins forming slowly at 20 min and then accelerates after 40 min, as **2b-I** reaches a maximum concentration. Formation of **3ab** ceases upon depletion of **2b-I** and **1a**, reaching a final yield of 81%. The two homo-coupled dimers (**1aa**, **2bb**) form in < 10% yields.

The nickel catalyst is present only in 7 mol% with respect to the substrate, so the build-up of **2b-I** to 72% is attributed to formation of a **2b**-derived organozinc species *in situ*. To probe this hypothesis, **2b** was subjected to the same reaction conditions in the absence of **1a** and quenched with iodine, resulting in a 75% yield of **2b-I**. The aryl-zinc species appears to be relatively stable, as the quantity of **2b-I** decreased by only 10% when the product mixture was allowed to sit for 2 h (Figure 4C.2A). A similar test of **1a** in the absence of **2b** led to no evidence for pyridyl-zinc species (via formation of **1a-I**). This mixture instead generated significant quantities of the homo-coupled dimer **1aa** (69% yield, Figure 4C.2B). No direct reaction of Zn with **2b** (or **1a**) was observed in the absence of the Ni catalyst (Table 4C.3).

A further test was conducted by stirring substrate **2b** under condition A for 40 min in the absence of **1a**. Analysis of an aliquot of this solution using the iodine quench revealed the formation of **2b-I** in 75% yield (Figure 4.5C, step 1). Then, one equivalent of **1a** was added to the reaction mixture, and the solution was stirred for an additional 3 h. The 73% yield of the cross-coupled product **3ab** obtained from this stepwise sequence (Figure 4.5C, step 2) indicates that the second Negishi-like coupling step is very efficient.

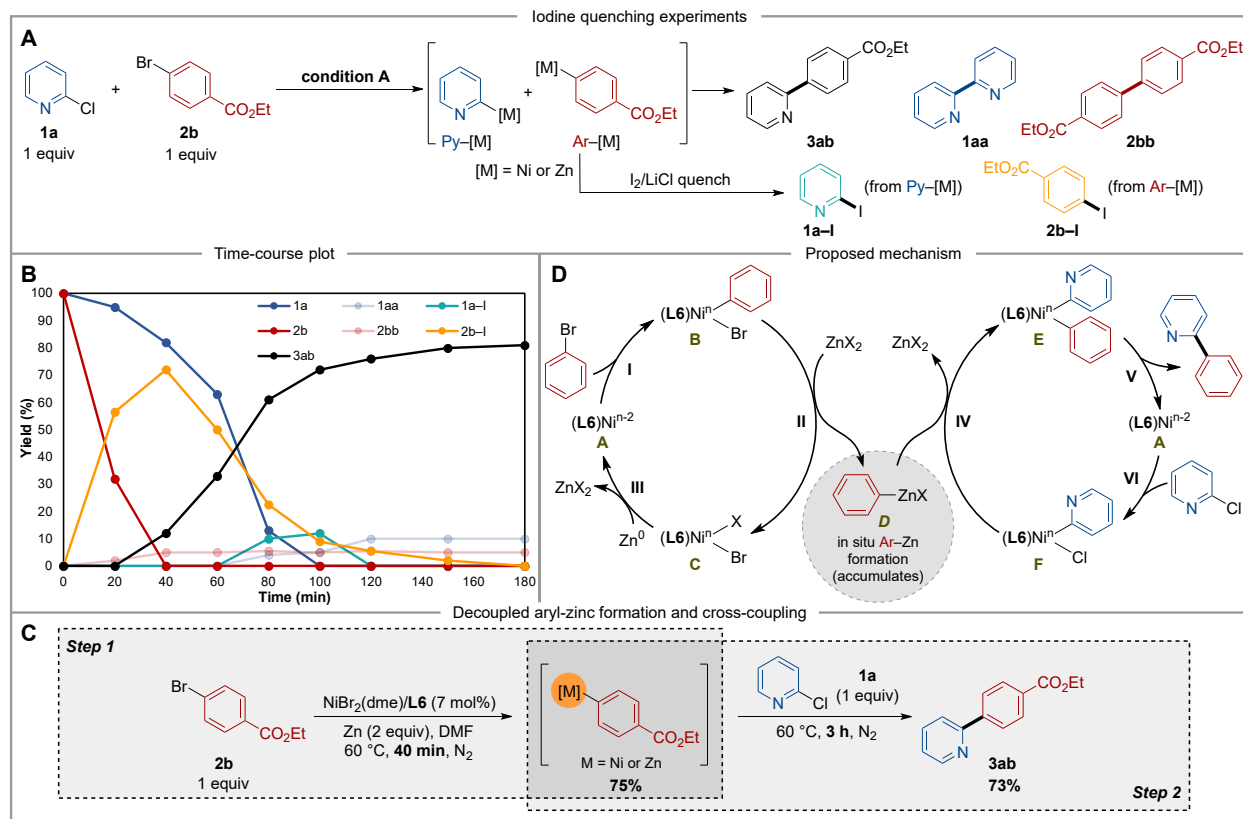


**Figure 4.5.** Mechanistic studies on reaction condition A. Iodine quenching experiments (A), time-course plot (B), stepwise reactions (C), and proposed mechanism (D) for XEC of **1a** with **2b** under condition A. See Section 4C.IV of Appendix C for experimental details. Yields are determined by  $^1\text{H}$  NMR spectroscopy of the crude reaction mixture using 1,3,5-trimethoxybenzene as an internal standard.

The formation of an aryl-zinc intermediate from **2b** is consistent with previous observations that aryl-zinc species can be formed from aryl halides under reductive conditions with a different Ni/terpyridine catalyst.<sup>40</sup> This precedent and the data summarized above support a mechanism for nickel-catalyzed heteroaryl-aryl coupling under condition A that is outlined in Figure 4.5D. A reduced nickel catalyst **A** undergoes oxidative addition of aryl bromide to form an aryl-nickel intermediate **B**, followed by transmetalation to  $\text{ZnX}_2$  salts derived from the reductant to form aryl-zinc species **D** and nickel salt **C**. The aryl-zinc species accumulate in the reaction mixture before they undergo transmetalation to a pyridyl-nickel species **F**, arising from oxidative addition of 2-chloropyridine to **A**. The resultant nickel complex **E** reductively eliminates to form the cross-coupled product and regenerates the low-valent nickel catalyst **A**. This decoupled sequence enables

differentiation between the two coupling partners, which leads to high XEC yields and cross-selectivity.

**Time-course analysis and mechanistic features of reaction condition B.** We next sought to gain insights into the XEC mechanism associated with condition B, using **1c** and **2a** as coupling partners. The use of TDAE as the reductant, rather than Zn, excludes the possibility of aryl-zinc formation under these conditions. The contributions of NaI and FeBr<sub>2</sub> to the reaction were probed through time-course experiments of the reaction in the absence and presence of these additives. The data show that both substrates exhibit minimal reactivity when either of the two additives is excluded from the reaction mixture (Figures 4.6-i and 4.6-ii). In the presence of both NaI and FeBr<sub>2</sub>, the consumption of two coupling partners proceeds at a similar rate, leading to steady formation of the cross-coupled product (**3ca**) with minimal formation of two homo-coupled byproducts **1cc** and **2aa** (Figures 4.6-iii). In all three experiments, **1c** appears to react slightly more quickly than that of **2a**, and more **1cc** is observed than **2aa**.

The time-course data show that both FeBr<sub>2</sub> and NaI are needed to support effective reactivity. A similar beneficial effect of FeBr<sub>2</sub> was observed by Gosmini and co-workers when studying analogous reactions under electrochemical conditions.<sup>27</sup> They proposed that heterocycle coordination to FeBr<sub>2</sub> prevents poisoning of the Ni catalyst. Related effects could be evident here, but FeBr<sub>2</sub> alone cannot support the reaction. We postulate that NaI could activate the aryl bromide substrate through Ni-catalyzed halide exchange, as has been observed by others.<sup>41,42</sup> Although the iodide analog of **2a** (i.e., **2a-I**) is not observed during the reaction, it could form transiently and undergo rapid reaction. To probe this hypothesis, we conducted two additional time-course experiments using 4-iodoanisole (**2a-I**) instead of **2a** and NaI (Figures 4.6-iv and 4.6-v). Aryl iodide **2a-I** is consumed faster than heteroaryl chloride **1c** in the absence and presence of FeBr<sub>2</sub>,

contrasting the relative rates displayed in the XEC of aryl bromide **2a** with **1c**.<sup>43</sup> Slow reactivity is observed with both substrates in the absence of FeBr<sub>2</sub>, possibly reflecting inhibition of the reaction by the heteroaryl substrate (Figures 4.6-iv). Efficient conversion of **2a-I** is observed in the presence of FeBr<sub>2</sub>, affording a 62% yield of the cross-coupled product **3ca** and 16% yield of the homo-coupled dimer **2aa** (accounting for 32% of **2a-I**) (Figures 4.6-v). These results indicate that **2a-I** is too reactive to achieve high cross-selectivity. On the other hand, *in situ* formation a transient aryl iodide in the presence of NaI could support the requisite balance in reactivity between the two coupling partners.

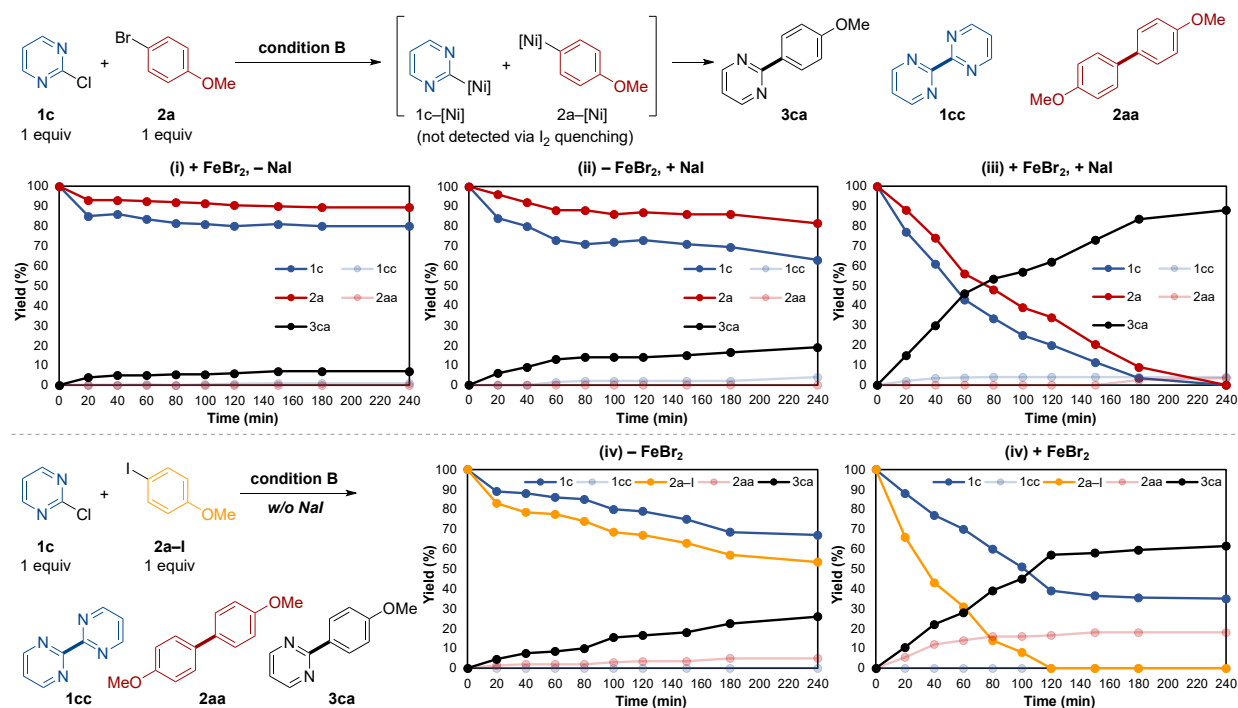


**Figure 4.6.** Time-course experiments for XEC of **1c** with **2a** or **2a-I** under condition B. See Section 4C.IV of Appendix C for experimental details. Yields are determined by <sup>1</sup>H NMR spectroscopy of the crude reaction mixture using 1,3,5-trimethoxybenzene as an internal standard.

#### 4.4. Conclusion

The results outlined above introduce two highly effective Ni-only catalyst systems to support XEC that accesses heteroaryl-aryl structures. Both reaction conditions (A and B) enable XEC with a 1:1 ratio of heteroaryl chloride and aryl bromide substrates, and they exhibit high cross-

selectivity, good functional group tolerance, and compatibility with multiple different aromatic heterocycles. The reactions show complementary reactivity, and mechanistic studies provide evidence for different XEC pathways for the reactions under conditions A and B. XEC condition A uses a sterically hindered terpyridine ligand on the Ni catalyst, which promotes *in situ* formation of aryl-zinc species that undergo subsequent coupling with the heteroaryl electrophile. XEC condition B leverages synergistic contributions of FeBr<sub>2</sub> and NaI additives to match the relative reactivity of the two coupling partners and achieve high cross-selectivity. Together, these methods achieve general XEC reactivity and provide access to an unprecedented scope of nitrogen-containing biaryls.

#### 4.5. Acknowledgments

We thank Dr. Mihai Popescu (CSU) and Jieru Zhu (UW-Madison) for helpful discussions. Financial support for this work was provided by the NSF (CHE-2154698). Some compounds in the substrate scope were supplied by GlaxoSmithKline plc. Spectroscopic instrumentation was supported by a generous gift from Paul J. and Margaret M. Bender, the NIH (S10 OD020022), and the NSF (CHE-1048642).

#### 4.6. Author Contributions

S.S.S. and Z.-M.S. conceived the project and designed the experiments. Z.-M.S. led the efforts on reaction condition optimization, scope exploration, product isolation and characterization, and mechanistic investigation. D.L.P. provided some compounds. M.R., R.S.P., and D.J.W. served as consultants for this work. S.S.S. and Z.-M.S. wrote the manuscript.

#### 4.7. References

1. Durán, R.; Zubía, E.; Ortega, M. J.; Naranjo, S.; Salvá, J. Novel Alkaloids from the Red Ascidian *Botryllus Leachi*. *Tetrahedron* **1999**, *55*, 13225–13232.
2. Biaryls. In *Privileged Structures in Drug Discovery*; John Wiley & Sons, Ltd, 2018; pp 83–154.
3. Meanwell, N. A. The Pyridazine Heterocycle in Molecular Recognition and Drug Discovery. *Med. Chem. Res.* **2023**, *32*, 1853–1921.

- Littke, A. F.; Fu, G. C. Palladium-Catalyzed Coupling Reactions of Aryl Chlorides. *Angew. Chem. Int. Ed.* **2002**, *41*, 4176–4211.
- Molander, G. A.; Biolatto, B. Palladium-Catalyzed Suzuki–Miyaura Cross-Coupling Reactions of Potassium Aryl- and Heteroaryltrifluoroborates. *J. Org. Chem.* **2003**, *68*, 4302–4314.
- Corbet, J.-P.; Mignani, G. Selected Patented Cross-Coupling Reaction Technologies. *Chem. Rev.* **2006**, *106*, 2651–2710.
- Torborg, C.; Beller, M. Recent Applications of Palladium-Catalyzed Coupling Reactions in the Pharmaceutical, Agrochemical, and Fine Chemical Industries. *Adv. Synth. Catal.* **2009**, *351*, 3027–3043.
- Xue, L.; Lin, Z. Theoretical Aspects of Palladium-Catalysed Carbon–Carbon Cross-Coupling Reactions. *Chem. Soc. Rev.* **2010**, *39*, 1692–1705.
- Nakao, Y.; Hiyama, T. Silicon-Based Cross-Coupling Reaction: An Environmentally Benign Version. *Chem. Soc. Rev.* **2011**, *40*, 4893.
- I. Knappke, C. E.; Wangelin, A. J. von. 35 Years of Palladium-Catalyzed Cross-Coupling with Grignard Reagents: How Far Have We Come? *Chem. Soc. Rev.* **2011**, *40*, 4948–4962.
- Lundgren, R. J.; Stradiotto, M. Addressing Challenges in Palladium-Catalyzed Cross-Coupling Reactions Through Ligand Design. *Chem. – Eur. J.* **2012**, *18*, 9758–9769.
- de Vries, J. G. Palladium-Catalysed Coupling Reactions. In *Organometallics as Catalysts in the Fine Chemical Industry*; Beller, M., Blaser, H.-U., Eds.; Springer: Berlin, Heidelberg, 2012; pp 1–34.
- Brown, D. G.; Boström, J. Analysis of Past and Present Synthetic Methodologies on Medicinal Chemistry: Where Have All the New Reactions Gone? *J. Med. Chem.* **2016**, *59*, 4443–4458.
- Devendar, P.; Qu, R.-Y.; Kang, W.-M.; He, B.; Yang, G.-F. Palladium-Catalyzed Cross-Coupling Reactions: A Powerful Tool for the Synthesis of Agrochemicals. *J. Agric. Food Chem.* **2018**, *66*, 8914–8934.
- Zhang, Y.-F.; Shi, Z.-J. Upgrading Cross-Coupling Reactions for Biaryl Syntheses. *Acc. Chem. Res.* **2019**, *52*, 161–169.
- Buskes, M. J.; Blanco, M.-J. Impact of Cross-Coupling Reactions in Drug Discovery and Development. *Molecules* **2020**, *25*, 3493.
- D'Alterio, M. C.; Casals-Cruañas, È.; Tzouras, N. V.; Talarico, G.; Nolan, S. P.; Poater, A. Mechanistic Aspects of the Palladium-Catalyzed Suzuki–Miyaura Cross-Coupling Reaction. *Chem. – Eur. J.* **2021**, *27*, 13481–13493.
- J. Lennox, A. J.; C. Lloyd-Jones, G. Selection of Boron Reagents for Suzuki–Miyaura Coupling. *Chem. Soc. Rev.* **2014**, *43*, 412–443.
- Cook, X. A. F.; de Gombert, A.; McKnight, J.; Pantaine, L. R. E.; Willis, M. C. The 2-Pyridyl Problem: Challenging Nucleophiles in Cross-Coupling Arylations. *Angew. Chem. Int. Ed.* **2021**, *60*, 11068–11091.
- Wang, X.; Dai, Y.; Gong, H. Nickel-Catalyzed Reductive Couplings. *Top. Curr. Chem.* **2016**, *374*, 43.
- Richmond, E.; Moran, J. Recent Advances in Nickel Catalysis Enabled by Stoichiometric Metallic Reducing Agents. *Synthesis* **2018**, *50*, 499–513.
- Goldfogel, M. J.; Huang, L.; Weix, D. J. Cross-Electrophile Coupling. In *Nickel Catalysis in Organic Synthesis*; John Wiley & Sons, Ltd, 2020; pp 183–222.
- Yi, L.; Ji, T.; Chen, K.-Q.; Chen, X.-Y.; Rueping, M. Nickel-Catalyzed Reductive Cross-Couplings: New Opportunities for Carbon–Carbon Bond Formations through Photochemistry and Electrochemistry. *CCS Chem.* **2021**, *4*, 9–30.
- Weix, D. J. Methods and Mechanisms for Cross-Electrophile Coupling of Csp<sup>2</sup> Halides with Alkyl Electrophiles. *Acc. Chem. Res.* **2015**, *48*, 1767–1775.
- Diccianni, J. B.; Diao, T. Mechanisms of Nickel-Catalyzed Cross-Coupling Reactions. *Trends Chem.* **2019**, *1*, 830–844.
- Gosmini, C.; Lasry, S.; Nédélec, J.-Y.; Périchon, J. Electrochemical Cross-Coupling between 2-Halopyridines and Aryl or Heteroaryl Halides Catalysed by Nickel-2,2'-Bipyridine Complexes. *Tetrahedron* **1998**, *54*, 1289–1298.

27. Gosmini, C.; Nédélec, J. Y.; Périchon, J. Electrochemical Cross-Coupling between Functionalized Aryl Halides and 2-Chloropyrimidine or 2-Chloropyrazine Catalyzed by Nickel 2,2'-Bipyridine Complex. *Tetrahedron Lett.* **2000**, *41*, 201–203.
28. Gosmini, C.; Nédélec, J. Y.; Périchon, J. Electrosynthesis of Functionalized 2-Arylpyridines from Functionalized Aryl and Pyridine Halides Catalyzed by Nickel Bromide 2,2'-Bipyridine Complex. *Tetrahedron Lett.* **2000**, *41*, 5039–5042.
29. Sengmany, S.; Léonel, E.; Polissaint, F.; Nédélec, J.-Y.; Pipelier, M.; Thobie-Gautier, C.; Dubreuil, D. Preparation of Functionalized Aryl- and Heteroarylpyridazines by Nickel-Catalyzed Electrochemical Cross-Coupling Reactions. *J. Org. Chem.* **2007**, *72*, 5631–5636.
30. Sengmany, S.; Le Gall, E.; Léonel, E. An Electrochemical Synthesis of Functionalized Arylpyrimidines from 4-Amino-6-Chloropyrimidines and Aryl Halides. *Molecules* **2011**, *16*, 5550–5560.
31. Sengmany, S.; Vitu-Thiebaud, A.; Le Gall, E.; Condon, S.; Léonel, E.; Thobie-Gautier, C.; Pipelier, M.; Lebreton, J.; Dubreuil, D. An Electrochemical Nickel-Catalyzed Arylation of 3-Amino-6-Chloropyridazines. *J. Org. Chem.* **2013**, *78*, 370–379.
32. Sengmany, S.; Vasseur, S.; Lajnef, A.; Le Gall, E.; Léonel, E. Beneficial Effects of Electrochemistry in Cross-Coupling Reactions: Electroreductive Synthesis of 4-Aryl- or 4-Heteroaryl-6-Pyrrolylpyrimidines. *Eur. J. Org. Chem.* **2016**, *2016*, 4865–4871.
33. Mirabi, B.; Marchese, A. D.; Lautens, M. Nickel-Catalyzed Reductive Cross-Coupling of Heteroaryl Chlorides and Aryl Chlorides. *ACS Catal.* **2021**, *11*, 12785–12793.
34. Surgenor, R. R.; Lee, H. Synthesis of (Hetero)Biaryls via Nickel Catalyzed Reductive Cross-Electrophile Coupling Between (Hetero)Aryl Iodides and Bromides. *Chem. – Eur. J.* **2024**, e202401552.
35. Kutchukian, P. S.; Dropinski, J. F.; Dykstra, K. D.; Li, B.; DiRocco, D. A.; Streckfuss, E. C.; Campeau, L.-C.; Cernak, T.; Vachal, P.; Davies, I. W.; Krska, S. W.; Dreher, S. D. Chemistry Informatics Enabled Approach to Evaluate and Advance Synthetic Methods. *Chem. Sci.* **2016**, *7*, 2604–2613.
36. Klein, P.; Lechner, V. D.; Schimmel, T.; Hintermann, L. Generation of Organozinc Reagents by Nickel Diazadiene Complex Catalyzed Zinc Insertion into Aryl Sulfonates. *Chem. – Eur. J.* **2020**, *26*, 176–180.
37. Kang, K.; Huang, L.; Weix, D. J. Sulfonate Versus Sulfonate: Nickel and Palladium Multimetallic Cross-Electrophile Coupling of Aryl Triflates with Aryl Tosylates. *J. Am. Chem. Soc.* **2020**, *142*, 10634–10640.
38. Charboneau, D. J.; Hazari, N.; Huang, H.; Uehling, M. R.; Zultanski, S. L. Homogeneous Organic Electron Donors in Nickel-Catalyzed Reductive Transformations. *J. Org. Chem.* **2022**, *87*, 7589–7609.
39. Krasovskiy, A.; Knochel, P. Convenient Titration Method for Organometallic Zinc, Magnesium, and Lanthanide- Reagents. *Synthesis* **2006**, *2006*, 890–891.
40. Gilbert, M. M.; Trenerry, M. J.; Longley, V. R.; Castro, A. J.; Berry, J. F.; Weix, D. J. Ligand–Metal Cooperation Enables Net Ring-Opening C–C Activation/Difunctionalization of Cyclopropyl Ketones. *ACS Catal.* **2023**, *13*, 11277–11290.
41. Chen, L. M.; Shin, C. K.; Delano, T.; Reisman, S. Ni-Catalyzed Asymmetric Reductive Arylation of  $\alpha$ -Substituted Imides. ChemRxiv December 21, 2023.
42. Chen, M.-Y.; Charvet, S.; Payard, P.-A.; Perrin, M.-E. L.; Vantourout, J. C. Electrochemically Driven Nickel-Catalyzed Halogenation of Unsaturated Halide and Triflate Derivatives. *Angew. Chem. Int. Ed.* **2024**, *63*, e202311165.
43. Bajo, S.; Laidlaw, G.; Kennedy, A. R.; Sproules, S.; Nelson, D. J. Oxidative Addition of Aryl Electrophiles to a Prototypical Nickel(0) Complex: Mechanism and Structure/Reactivity Relationships. *Organometallics* **2017**, *36*, 1662–1672.

## Appendix A. Supporting Information for Chapter 2

### 2A.I. General Experimental Considerations

#### *Solvents and reagents*

All solvents (anhydrous) and reagents were purchased from commercial sources and used as received without further purification. Starting materials were purchased from MilliporeSigma, Alfa Aesar, and Combi-Blocks. Zn powder (average 4–7 micron) was purchased from Alfa Aesar. Nickel salts, palladium salts, and ligands were purchased from MilliporeSigma or Alfa Aesar. Anhydrous solvents were purchased from MilliporeSigma and handled in a nitrogen-filled glove box.

#### *Electrodes*

All electrode materials were purchased from commercial sources and used as received. RVC foams (pore size 30 ppi) were purchased from Ultramet. Ni foams (1.6 mm thickness, 80–110 pores per inch, average hole diameter 0.25 mm, > 99.9 wt% purity) were purchased from MTI. Fe rods (5 mm diameter) were purchased from American-Scientific. Other metal electrodes (Zn, Mg, Al) were purchased from MilliporeSigma. Glassy carbon working electrodes (MF-2012) and non-aqueous reference electrodes (MF-1085) were purchased from BASi. Pt wires were purchased from MilliporeSigma and custom-made as Pt counter electrodes (~ 4 cm, 5–7 spiral coils).

#### *Characterization of products*

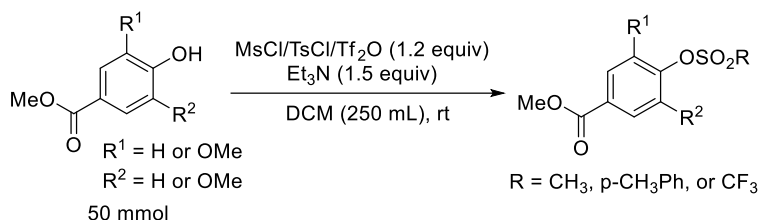
$^1\text{H}$  and  $^{13}\text{C}$  NMR spectra were recorded on Bruker 400 or 600 MHz spectrometers. Chemical shifts are given in parts per million (ppm) relative to residual solvent peaks in the  $^1\text{H}$  and  $^{13}\text{C}$  NMR spectra or are referenced as noted. The following abbreviations (and their combinations) are used to label the multiplicities: s (singlet), d (doublet), t (triplet), m (multiplet) and br (broad). High-resolution mass spectra were obtained using a Thermo Q Exactive<sup>TM</sup> Plus by the mass

spectrometry facility at the University of Wisconsin. UPLC-MS analysis was conducted on a Waters-Acquity. Chromatographic purification of products was accomplished by chromatography on silica gel 60 M (particle size 40–63  $\mu\text{m}$ , 230–400 mesh) from MACHEREY-NAGEL Inc. Thin-layer chromatography (TLC) was performed on Silicycle silica gel UV254 pre-coated plates (0.25 mm). Visualization of the developed chromatogram was performed by using UV lamps or  $\text{KMnO}_4$  stain.

### *Electrochemical experiments*

All cyclic voltammetric (CV) and chronoamperometric (CA) experiments were performed using Nuvant Array PGStats or a Pine WaveNow PGstat. The CV experiments were carried out in a three-electrode cell configuration with a glassy carbon (GC) working electrode (3 mm diameter), and a platinum wire counter electrode (~ 4 cm, 5–7 spiral coils). The working electrode potentials were measured versus Ag/AgNO<sub>3</sub> reference electrode (internal solution, 0.1 M Bu<sub>4</sub>NPF<sub>6</sub> and 0.01 M AgNO<sub>3</sub> in DMF). The redox potential of ferrocene/ferrocenium (Fc/Fc<sup>+</sup>) was measured (under same experimental conditions) and used to provide an internal reference. The potential values were then adjusted relative to Fc/Fc<sup>+</sup>, and electrochemical studies in organic solvents were recorded accordingly. The GC working electrode was polished with alumina powder (5  $\mu\text{m}$ ) before each experiment. All solutions used for CV analysis were prepared 30 min before the experiments and kept under nitrogen atmosphere using a thin Teflon tube to allow continuous nitrogen bubbling. Bulk electrolysis experiments were performed in custom-built undivided or divided cells, with RVC or Ni foam working electrodes, Mg, Fe or stainless-steel counter electrodes and Ag/AgNO<sub>3</sub> (internal solution, 0.1 M Bu<sub>4</sub>NPF<sub>6</sub> and 0.01 M AgNO<sub>3</sub> in DMF) for a reference electrode.

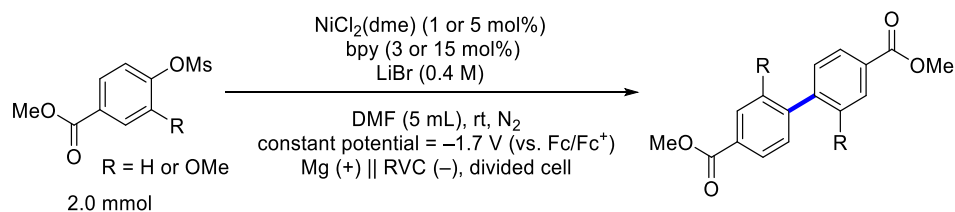
## 2A.II. General Procedure for Aryl Sulfonate Esters Syntheses (GP 1)



The following procedure was adapted from precedents reported in literatures.<sup>1,2</sup> To a 500 mL round-bottom flask was added the substrate (50 mmol, 1.0 equiv) and anhydrous DCM (200 mL). Et<sub>3</sub>N (10.4 mL, 75 mmol, 1.5 equiv) was then injected into the solution. Another 200 mL round-bottom flask was charged with the sulfonating reagent (60 mmol, 1.2 equiv) and anhydrous DCM (50 mL), mixed thoroughly, then this solution was added dropwise to the 500 mL flask. The reaction mixture was stirred at room temperature and stopped when full conversion was observed via TLC. The DCM solution was washed with 300 mL water and 300 mL brine sequentially. The aqueous layers were collected and extracted with 200 mL DCM. The organic layers were combined, dried over anhydrous Na<sub>2</sub>SO<sub>4</sub>, and concentrated *in vacuo*. The crude product was purified by column chromatography to furnish the desired product (eluent: hexane/ethyl acetate, 2/1).

## 2A.III. General Procedures for Bulk Electrolysis

### *Electrochemical reductive homocoupling in a divided cell (GP 2)*



To the cathodic chamber of the divided cell (Figure 2A.1) was added NiCl<sub>2</sub>(dme) (4.4 or 22 mg, 1 or 5 mol%), LiBr (174 mg, 2 mmol, 1.0 equiv), 2,2'-bipyridyl (9.4 or 47 mg, 3 or 15 mol%),

substrate (2 mmol, 1.0 equiv), and anhydrous DMF (5 mL). Then to the anodic chamber of the divided cell was added LiBr (174 mg, 1.0 equiv) and anhydrous DMF (5 mL). The cathodic chamber was then installed a RVC cathode and a Ag/AgNO<sub>3</sub> reference electrode, and the anodic chamber was installed a Mg anode. The two chambers were sealed with rubber septa, respectively, and to each chamber was introduced a thin Teflon tube to allow continuous nitrogen bubbling. The reaction mixture was stirred at 1000 rpm for 30 min to allow full dissolution of LiBr and exclusion of adventitious oxygen. After that, the reaction mixture was electrolyzed under a constant potential of -1.7 V (vs. Fc/Fc<sup>+</sup>) for 18 h at room temperature. The resultant solution was directly concentrated *in vacuo*. The crude product was purified by column chromatography to furnish the desired product (eluent: hexane/ethyl acetate, 3/1).

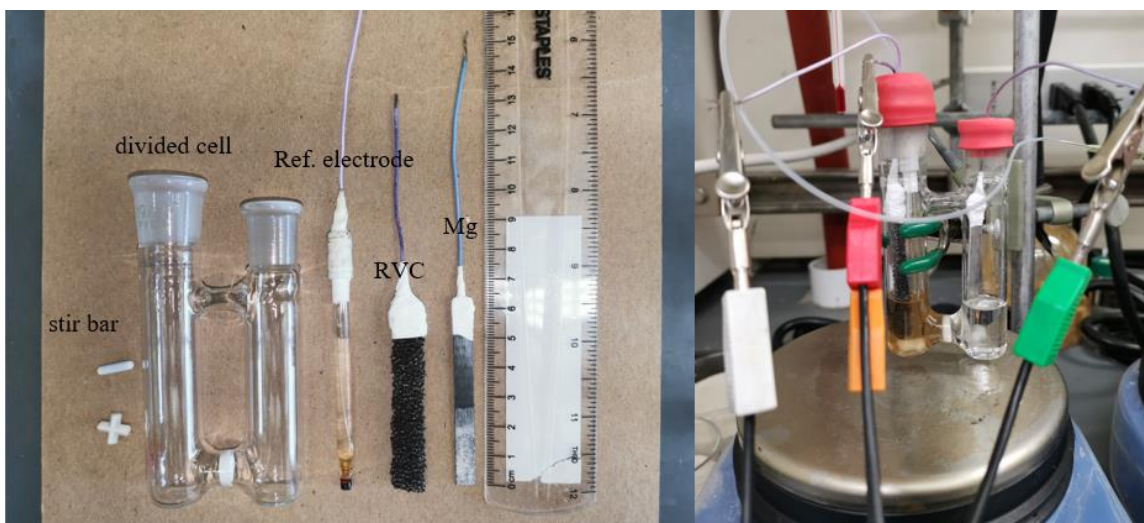
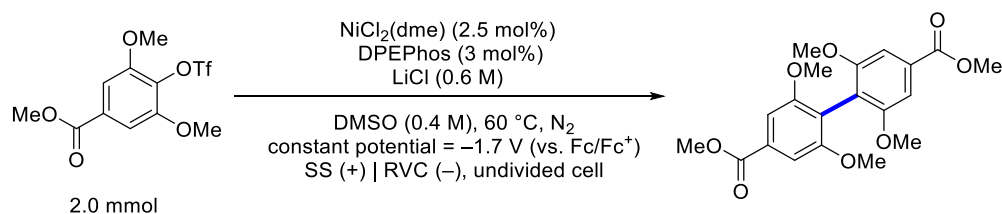


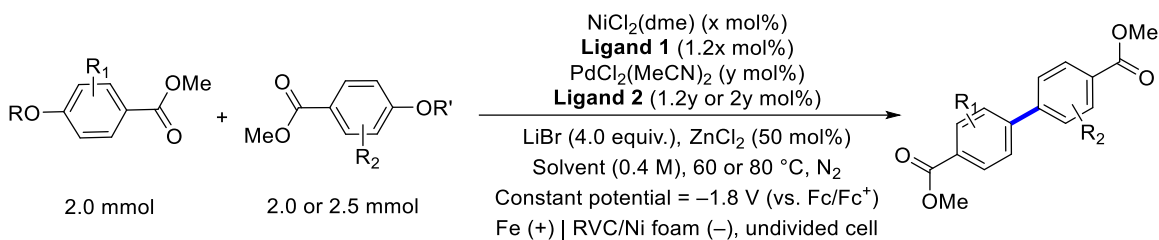
**Figure 2A.1.** Graphic illustration of the divided cell before (left) and after (right) assembly.

### *Electrochemical reductive homocoupling in an undivided cell (GP 3)*



To the undivided cell (Figure 2A.2) was added NiCl<sub>2</sub>(dme) (11 mg, 2.5 mol%), DPEPhos (32 mg, 3 mol%), LiCl (125 mg, 3 mmol, 1.5 equiv), and substrate (2 mmol, 1.0 equiv). The cell was then introduced in a nitrogen-filled glove box and installed a RVC cathode, a Ag/AgNO<sub>3</sub> reference electrode, and a stainless steel anode. Anhydrous DMSO (5 mL) was injected into the cell with a 5 mL syringe. The cell was sealed with a rubber septum and removed from the glove box. A thin Teflon tube was introduced immediately into the cell to allow continuous nitrogen bubbling. The reaction mixture was stirred at 1000 rpm for 30 min to allow full dissolution of LiCl and exclusion of adventitious oxygen. After that, the reaction mixture was electrolyzed under a constant potential of -1.7 V (vs. Fc/Fc<sup>+</sup>) for 24 h at 60 °C. The resultant solution was directly concentrated *in vacuo*. The crude product was purified by column chromatography to furnish the desired product (eluent: hexane/ethyl acetate, 3/1).

*Electrochemical reductive cross-coupling in an undivided cell (GP 4)*



Under nitrogen atmosphere, NiCl<sub>2</sub>(dme) (22 or 44 mg, 5 or 10 mol%), Ligand 1 (6 or 12 mol%), and anhydrous solvent (1 mL) was added to a 1.5-dram vial capped with a Teflon septum. Another 1.5-dram vial was charged with PdCl<sub>2</sub>(MeCN)<sub>2</sub> (10.4 ~ 26 mg, 2 ~ 5 mol%), Ligand 2 (4 ~ 10 mol%), and anhydrous solvent (1 mL) under nitrogen. The two vials were stirred for 30 min so that the ligands are well complexed with the metal.

To the undivided cell (Figure 2A.2) was added the two coupling partners (2 or 2.5 mmol, 1.0 or 1.25 equiv) and the cell was introduced in a nitrogen-filled glove box and installed a Ni foam or RVC cathode, a Ag/AgNO<sub>3</sub> reference electrode, and an iron rod anode. The cell was then

charged with LiBr (695 mg, 8 mmol, 4.0 equiv), ZnCl<sub>2</sub> (136 mg, 1 mmol, 0.5 equiv), the two catalyst solutions and anhydrous solvent (3 mL), sealed with rubber septum, and removed from the glove box. A thin Teflon tube was introduced immediately into the cell to allow continuous nitrogen bubbling. The reaction mixture was stirred at 1000 rpm for 30 min to allow full dissolution of LiBr and exclusion of adventitious oxygen. After that, the reaction mixture was electrolyzed under a constant potential of  $-1.8$  V (vs. Fc/Fc<sup>+</sup>) for 36 or 48 h at 60 or 80 °C. The resultant solution was directly concentrated *in vacuo*. The crude product was purified by column chromatography to furnish the desired product (eluent: hexane/ethyl acetate, 3/1).

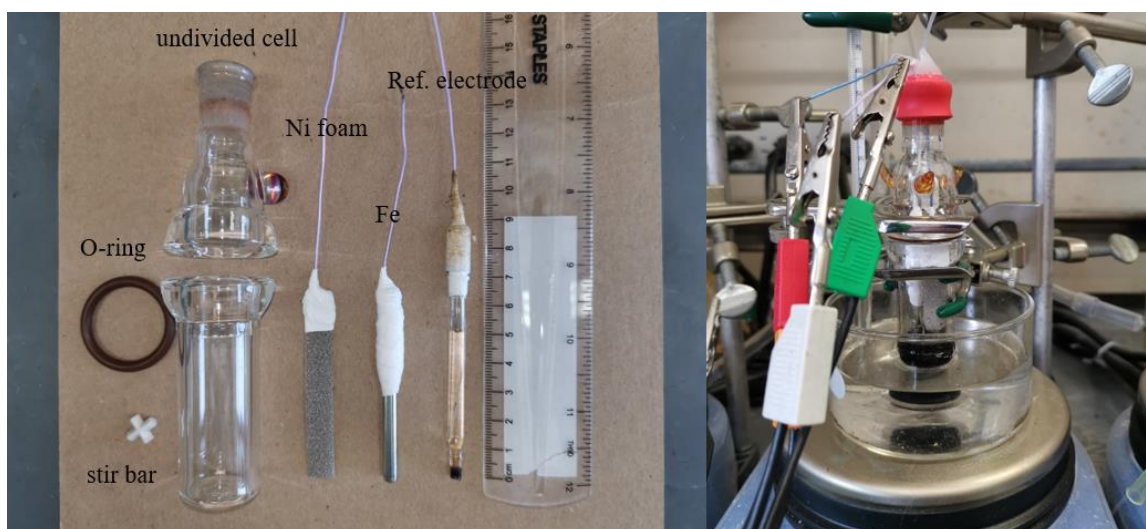


**Figure 2A.2.** Graphic illustration of the undivided cell before (left) and after (right) assembly.

#### 2A.IV. General Procedures for Flow Electrolysis

For the electrochemical flow reactions, a commercial Micro Flow Cell (purchased from ElectroCell) with an electrode area of 10 cm<sup>2</sup> was used, the active reactor volume is 5 mL, and a Pine WaveNow PGstat or Bipotentiostat BP-300 was used as power supply. The undivided flow cell consists of PTFE end frames, stainless steel plate (316L) as the anode, stainless steel plate and graphite plate overlay together as the cathodic electron collector. The flow cell also contains the flow frames and gaskets. RVC with approx. dimensions = 3.5 × 3.0 × 0.5 cm was used to increase

the surface area of cathode and as a turbulence material for diffusion. All electrolysis reactions were performed in DMF solutions. A magnetic stir bar was used in the reservoirs and the reaction mixture was stirred (600 rpm) during flow electrolysis reactions. The reaction mixture is pumped through the system via peristaltic pump with a flow rate of 40 mL/min. The components of the electrochemical cell are shown in Figure 2A.3.

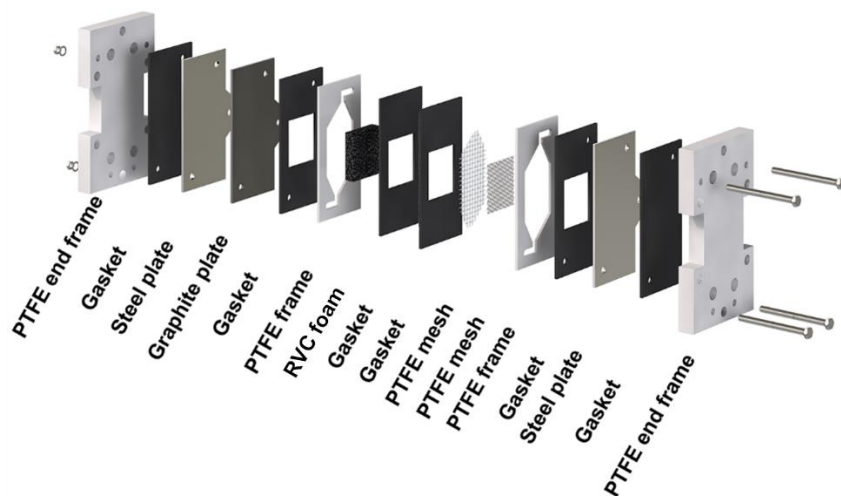
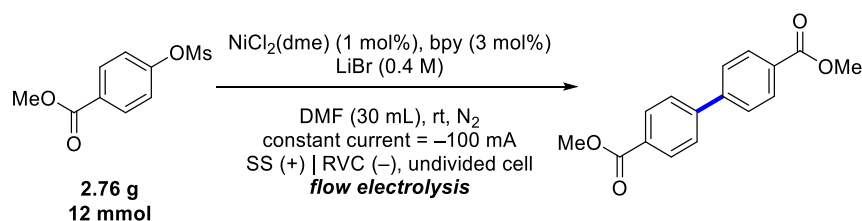
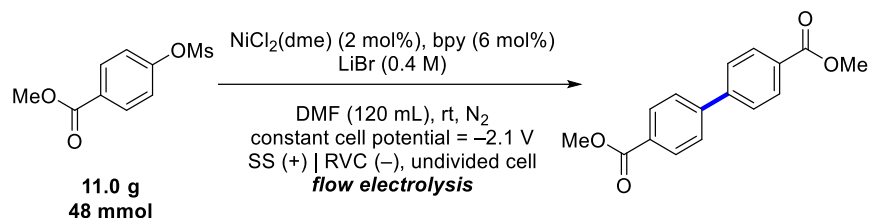


**Figure 2A.3.** Graphic illustration of the components of the undivided flow cell reactor. Figure adapted with permission from Ref. 3, Copyright 2021, *Org. Process Res. Dev.*



12 mmol scale: To a 100 mL round-bottom flask was injected a solution containing NiCl<sub>2</sub>(dme) (26.4 mg, 0.12 mmol, 1 mol%), LiBr (1044 mg, 12 mmol, 1.0 equiv), 2,2'-bipyridyl (56.4 mg, 0.36 mmol, 3 mol%), methyl 4-((methylsulfonyl)oxy)benzoate (2.76 g, 12 mmol, 1.0 equiv), and anhydrous DMF (30 mL). A thin Teflon tube was introduced immediately into the flask to allow continuous nitrogen bubbling. This solution was pushed via a peristaltic pump to pass through the undivided flow cell, with a flow rate of 40 mL min<sup>-1</sup> and electrolyzed at a constant current of –

100 mA at room temperature until full conversion of the substrate was determined by TLC. The resultant solution was directly concentrated *in vacuo* and analyzed by  $^1\text{H}$  NMR using mesitylene as an internal standard to give the NMR yield (87%).



48 mmol scale: To a 250 mL three-neck round-bottom flask was injected a solution containing  $\text{NiCl}_2(\text{dme})$  (106 mg, 0.48 mmol, 1 mol%),  $\text{LiBr}$  (4.17 g, 48 mmol, 1.0 equiv), 2,2'-bipyridyl (226 mg, 1.44 mmol, 3 mol%), methyl 4-((methylsulfonyl)oxy)benzoate (11.0 g, 48 mmol, 1.0 equiv), and anhydrous DMF (120 mL). A thin Teflon tube was introduced immediately into the flask to allow continuous nitrogen bubbling. This solution was pushed via a peristaltic pump to pass through the undivided flow cells, with a flow rate of  $40 \text{ mL min}^{-1}$  and electrolyzed at a constant cell potential of  $-2.1$  V at room temperature. Two flow cells were connected in parallel via copper wire to increase the electrode surface area in total. An additional amount of catalyst (1 mol%) (106 mg  $\text{NiCl}_2(\text{dme})$ , 226 mg 2,2'-bipyridyl dissolved in 5 mL DMF) was injected into the reaction mixture via a syringe after 24 h of electrolysis without stopping the reaction. Electrolysis was conducted until full conversion of the substrate was determined by TLC. The resultant solution was directly concentrated *in vacuo* and analyzed by  $^1\text{H}$  NMR using mesitylene as an internal standard to give the NMR yield (80%).



**Figure 2A.4.** Graphic illustration of the undivided flow cell for 12 mmol (left) and 48 mmol (right) scale-up.

## 2A.V. Optimization of Reaction Conditions

### *Optimization of Ni-catalyzed reductive homocoupling using Zn reductant*

To a 1-dram vial fitted with cross-shaped stir bar was added  $\text{NiCl}_2(\text{dme})$ , the appropriate ligand, additive, substrate (0.4 mmol, 1.0 equiv), and Zn dust (52 mg, 0.8 mmol, 2.0 equiv, unless otherwise noted). This vial was transferred into a nitrogen-filled glove box, then additive and solvent (1 mL, unless otherwise noted) were added. The vial was capped with a screw cap fitted with a PTFE-faced silicone septum, then removed from the glovebox and heated in a sand bath to the desired temperature with stirring (1000 rpm) for 15–27 h. The reaction mixture was then cooled to room temperature and diluted with DMF (3 mL). Mesitylene (1.0 equiv) was added to the crude material. Then a 100  $\mu\text{L}$  aliquot of the solution was filtered through a 2-cm silica gel plug in a Pasteur pipette into a vial. 500  $\mu\text{L}$   $\text{CDCl}_3$  was also added to the pipette and eluted into the same vial. The resultant sample was analyzed by  $^1\text{H}$  NMR spectroscopy and the yields were determined using mesitylene as the internal standard.

**Table 2A.1. Optimization of thermochemical Ni-catalyzed reductive homocoupling of G-OMs.<sup>a</sup>**

Entry	Additive	Concentration (M)	MB	Conversion	C-H bp	C-OH bp	Product
1 <sup>b</sup>	LiBr	0.4	93%	100%	90%	0%	3%
2 <sup>c</sup>	Et <sub>4</sub> Ni	1.0	94%	63%	3%	0%	45%
3	NaBr	0.25	95%	100%	86%	3%	6%
4	NaBr	0.5	93%	100%	79%	3%	11%
5	NaBr	0.5	92%	100%	76%	4%	12%
6	NaBr	0.25	98%	48%	27%	16%	3%
7 <sup>d</sup>	LiBr	0.25	94%	33%	7%	18%	2%
8	KBr	0.25	97%	100%	38%	0%	59%
9 <sup>e</sup>	LiBr	0.25	95%	100%	59%	20%	16%
10 <sup>f</sup>	LiBr	0.25	99%	92%	40%	15%	36%

<sup>a</sup> Yields were determined by <sup>1</sup>H NMR spectroscopy using mesitylene as the internal standard. <sup>b</sup> 5 mol% NiCl<sub>2</sub>(dme), 15 mol% bpy, 0.4 M LiBr, 0.4 M G-OMs. <sup>c</sup> Following the Percec condition<sup>4</sup>: 10 mol% Ni(PPh<sub>3</sub>)<sub>2</sub>Cl<sub>2</sub>, 1.5 equiv Et<sub>4</sub>Ni, 1.7 equiv Zn dust, THF, 1.0 M G-OMs, 67 °C. <sup>d</sup> < 5% yield was obtained with 8 more bpy derivatives (shown is with 2,2'-bipyridine). <sup>e</sup> With 1,10-Phen as ligand. <sup>f</sup> With 2,9-dimethyl-1,10-Phen as ligand.

**Table 2A.2. Conditions screening focused on nitrogen-based ligands for S/S homocoupling.<sup>a</sup>**

Ligand	Substrate	Conversion	MB	C-H bp	C-OH bp	Product
1	25%	75%	91%	26%	32%	8%
2	14%	86%	90%	50%	25%	1%
3	26%	74%	95%	29%	34%	6%
4	23%	77%	94%	31%	39%	1%
5	33%	67%	93%	27%	23%	10%
6	47%	53%	102%	25%	23%	7%
7	36%	64%	94%	27%	26%	5%
8	18%	82%	93%	30%	35%	10%
9	15%	85%	90%	35%	35%	5%
10	55%	45%	103%	22%	25%	1%
11	1%	99%	87%	79%	6%	1%
12	9%	91%	92%	64%	12%	7%

1

2

3

4

5

6

7

8

9

10

11

12

<sup>a</sup> Yields were determined by <sup>1</sup>H NMR spectroscopy using mesitylene as the internal standard.

**Table 2A.3. Conditions screening focused on nitrogen-based ligands for S/S homocoupling.<sup>a</sup>**

Ligand	Substrate	Conversion	MB	C-H bp	C-OH bp	Product
1	15%	85%	82%	29%	35%	3%
2	46%	54%	97%	24%	24%	3%
3	30%	70%	101%	44%	27%	0%
4	61%	39%	98%	14%	22%	1%
5	0%	100%	95%	88%	4%	3%
6	60%	40%	99%	18%	21%	0%
7	0%	100%	78%	38%	40%	0%
8	46%	54%	97%	19%	32%	0%
9	43%	57%	86%	16%	27%	0%
10	7%	93%	70%	36%	27%	0%
11	9%	91%	86%	45%	32%	0%
12	42%	58%	90%	32%	16%	0%

1

2

3

4

5

6

7

8

9

10

11

12

<sup>a</sup> Yields were determined by <sup>1</sup>H NMR spectroscopy using mesitylene as the internal standard.**Table 2A.4. Conditions screening focused on phosphine-based ligands for S/S homocoupling.<sup>a</sup>**

Ligand	Substrate	Conversion	MB	C-H bp	C-OH bp	Product
1	37%	63%	89%	22%	29%	1%
2	49%	51%	86%	17%	20%	0%
3	42%	58%	91%	20%	29%	0%
4	47%	53%	83%	15%	21%	0%
5	80%	20%	94%	6%	8%	0%
6	44%	56%	93%	20%	29%	0%
7	42%	58%	90%	19%	29%	0%
8	35%	65%	70%	13%	22%	0%
9	31%	69%	80%	21%	28%	0%
10	77%	23%	93%	5%	9%	2%
11	36%	64%	84%	21%	27%	0%
12	57%	43%	97%	14%	26%	0%
13	52%	48%	96%	16%	28%	0%
14	44%	56%	77%	12%	21%	0%
15	43%	57%	82%	17%	22%	0%
16	38%	62%	89%	33%	18%	0%
17	36%	64%	87%	33%	18%	0%
18	32%	68%	94%	48%	9%	5%
19	18%	82%	99%	54%	11%	16%
20	55%	45%	94%	13%	26%	0%

1

2

3

4

5

6

7

8

9

10

11, n = 1, Ph

12, n = 2, Ph

13, n = 2, 4-CF<sub>3</sub>-Ph

14, n = 3, Ph

15, n = 4, Ph

16

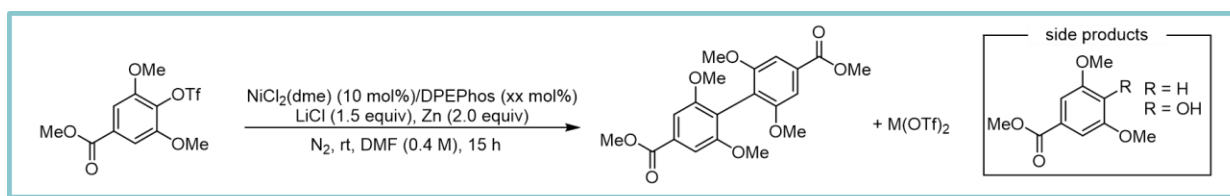
17

18

19 (DPEphos)

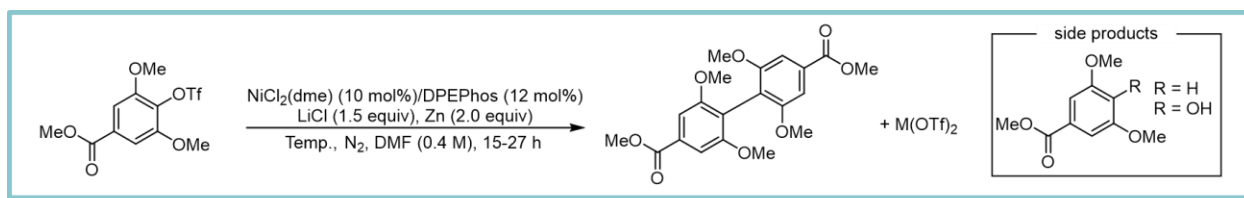
20

<sup>a</sup> Yields were determined by <sup>1</sup>H NMR spectroscopy using mesitylene as the internal standard.

**Table 2A.5. Conditions screening focused on ligand loading and additives for S/S homocoupling.<sup>a</sup>**


Entry	Ligand loading (xx mol%)	MB	Conversion	C–H bp	C–OH bp	Yield
1	8 mol%	82%	82%	44%	3%	17%
2	12 mol%	83%	82%	46%	4%	15%
3	15 mol%	92%	75%	46%	8%	13%
4	20 mol%	84%	59%	36%	12%	6%
5 <sup>b</sup>	12 mol%	93%	69%	55%	3%	4%
6 <sup>c</sup>	12 mol%	82%	77%	54%	2%	3%
7 <sup>d</sup>	12 mol%	93%	61%	38%	12%	4%
8 <sup>e</sup>	12 mol%	99%	74%	72%	0%	1%

<sup>a</sup> Yields were determined by <sup>1</sup>H NMR spectroscopy using mesitylene as the internal standard. <sup>b</sup> LiBr instead of LiCl. <sup>c</sup> <sup>n</sup>Bu<sub>4</sub>NBr instead of LiCl. <sup>d</sup> <sup>n</sup>Bu<sub>4</sub>NCl instead of LiCl. <sup>e</sup> <sup>n</sup>Bu<sub>4</sub>NI instead of LiCl.

**Table 2A.6. Conditions screening focused on temperature and solvents for S/S homocoupling.<sup>a</sup>**


Entry	Temperature	Solvent	MB	Conversion	C–H bp	C–OH bp	Yield
1	rt	DMF	83%	82%	46%	4%	15%
2	~ 40 °C	DMF	85%	>99%	58%	<3%	24%
3	~ 50 °C	DMF	90%	>99%	49%	5%	36%
4	~ 60 °C	DMF	85%	98%	37%	8%	<b>38%</b>
5	~ 70 °C	DMF	93%	91%	42%	10%	32%
6	~ 80 °C	DMF	73%	>99%	35%	26%	12%
7	rt	CH <sub>3</sub> CN	76%	>99%	72%	0%	4%
8	~ 60 °C	CH <sub>3</sub> CN	87%	>99%	73%	0%	10%
9	rt	THF	90%	58%	45%	3%	0%
10	~ 60 °C	THF	76%	98%	66%	1%	7%
11	rt	DMA	88%	75%	37%	7%	19%
12	~ 60 °C	DMA	82%	89%	32%	10%	29%

<sup>a</sup> Yields were determined by <sup>1</sup>H NMR spectroscopy using mesitylene as the internal standard.

**Table 2A.7. Conditions screening focused on additive loadings for S/S homocoupling.<sup>a</sup>**

Entry	m	MB	Conv.	C–H bp	C–OH bp	Yield
1	1.0	94%	99%	75%	1%	17%
2	1.5	93%	91%	42%	10%	32%
3	2.5	103%	93%	49%	22%	25%
4	4.0	81%	>99%	36%	36%	9%
5	6.0	79%	>99%	31%	40%	8%

<sup>a</sup> Yields were determined by <sup>1</sup>H NMR spectroscopy using mesitylene as the internal standard.

**Table 2A.8. Conditions screening focused on molecular sieves and solvents for S/S homocoupling.<sup>a</sup>**

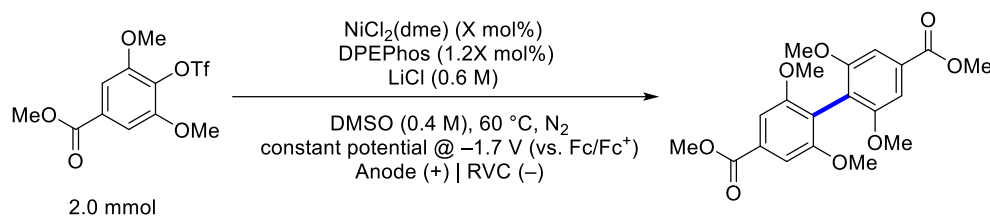
Entry	Ligand	Mol. sieves (100 mg)	Solvent	Conv.	C–H bp	C–OH bp	Yield
1	DPEPhos	No	DMF	77%	29%	23%	27%
2	DPEPhos	No	DMA	74%	29%	7%	33%
3	DPEPhos	Yes	DMF	85%	30%	15%	36%
4	DPEPhos	Yes	DMA	83%	37%	7%	37%
5	DPEPhos	Yes	DMSO	100%	32%	5%	55%
6	DPEPhos	Yes	NMP	58%	20%	15%	17%
7	DPEPhos	Yes	DMPU	100%	32%	61%	0%
8	DCEPhos	Yes	DMF	39%	15%	19%	0%
9	DCEPhos	Yes	DMA	34%	13%	17%	0%
10	DCEPhos	Yes	DMSO	35%	14%	30%	0%
11	DCEPhos	Yes	NMP	67%	1%	35%	0%
12	DCEPhos	Yes	DMPU	47%	41%	8%	2%

<sup>a</sup> Yields were determined by <sup>1</sup>H NMR spectroscopy using mesitylene as the internal standard.

### Optimization of electrochemical Ni-catalyzed reductive S/S homocoupling

To a divided/undivided cell (Figures 2A.1, 2A.2) was added NiCl<sub>2</sub>(dme), DPEPhos, LiCl (125 mg, 3 mmol, 1.5 equiv), and methyl 3,5-dimethoxy-4-(((trifluoromethyl)sulfonyl)oxy)benzoate (688 mg, 2 mmol, 1.0 equiv). The cell was then introduced in a nitrogen-filled glove box and installed a RVC cathode, a Ag/AgNO<sub>3</sub> reference electrode, and a sacrificial anode. Anhydrous

DMSO (5 mL) was injected into the cell with a 5 mL syringe. The cell was sealed with a rubber septum and removed from the glove box. A thin Teflon tube was introduced immediately into the cell to allow continuous nitrogen bubbling. The reaction mixture was stirred at 1000 rpm for 30 min to allow full dissolution of LiCl and exclusion of adventitious oxygen. After that, the reaction mixture was electrolyzed under a constant potential of  $-1.7$  V (vs. Fc/Fc<sup>+</sup>) for 24 h at 60 °C. The reaction mixture was then cooled to room temperature and diluted with DMF (25 mL). Mesitylene (278  $\mu$ L, 2 mmol, 1.0 equiv) was added to the crude material. Then a 150  $\mu$ L aliquot of the solution was filtered through a 2-cm silica gel plug in a Pasteur pipette into a vial. 500  $\mu$ L CDCl<sub>3</sub> was also added to the pipette and eluted into the same vial. The resultant sample was analyzed by <sup>1</sup>H NMR spectroscopy and the yields were determined using mesitylene as the internal standard. The results are summarized in Table 2A.9. We postulated that the metal salts from anode oxidation could serve as an overcharge protector in an undivided cell to prevent overreduction of redox-active species in the solution,<sup>5</sup> thus explaining the poor results in entries 6 and 7.

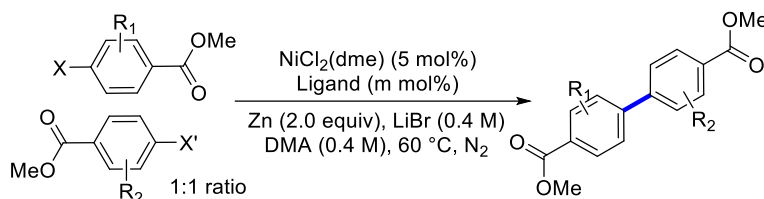
**Table 2A.9. Optimization of electrochemical Ni catalyzed reductive S/S homocoupling.<sup>a</sup>**

Entry	Cell type	Anode	X	Mass balance (%)	Ar-H (%)	ArO-H (%)	Yield (%)
1	undivided	stainless steel	10	95	18	2	73
2 <sup>b</sup>	undivided	stainless steel	5	103	16	2	75
3	undivided	stainless steel	5	99	22	0	72
4	undivided	Fe	5	95	20	0	65
5	undivided	stainless steel	2.5	100	12	0	<b>78</b>
6 <sup>c,d</sup>	undivided	stainless steel	\	97	34	0	0
7 <sup>d</sup>	divided	Fe	5	88	11	1	12
8 <sup>d</sup>	divided	Mg	5	100	0	0	0

<sup>a</sup> Yields were determined by <sup>1</sup>H NMR spectroscopy using mesitylene as the internal standard. <sup>b</sup> Added 500 mg 4 Å molecular sieves. <sup>c</sup> No Ni catalyst. <sup>d</sup> The rest of the mass corresponds to unreacted starting material.

#### *Ni-only catalyzed reductive cross-coupling*

To a 1-dram vial fitted with cross-shaped stir bar was added NiCl<sub>2</sub>(dme) (2.2 mg, 5 mol%), the appropriate ligand, two coupling partners (0.2 mmol, 1.0 equiv), and Zn dust (26 mg, 0.4 mmol, 2.0 equiv). This vial was transferred into a nitrogen-filled glove box, then LiBr (87 mg, 0.2 mmol, 1.0 equiv) and DMA (1 mL) were added. The vial was capped with a screw cap fitted with a PTFE-faced silicone septum, then removed from the glovebox and heated in a sand bath to 60 °C with stirring (1000 rpm) for 17 h. The reaction mixture was then cooled to room temperature and diluted with DMA (3 mL). Mesitylene (27.8 μL, 0.2 mmol, 1.0 equiv) was added to the crude material. Then a 100 μL aliquot of the solution was filtered through a 2-cm silica gel plug in a Pasteur pipette into a vial. 500 μL CDCl<sub>3</sub> was also added to the pipette and eluted into the same vial. The resultant sample was analyzed by <sup>1</sup>H NMR spectroscopy and the yields were determined using mesitylene as the internal standard. The results are summarized in Table 2A.10.

**Table 2A.10. Ni-only catalyzed reductive cross-coupling of LDMs.<sup>a</sup>**

Entry	Ligand	m	Ar-X	Ar-X'	Yield (%)	Hetero:Homo
1	bpy	15	H-OMs	G-OTs	7	2.0
2 <sup>b</sup>	bpy	30	H-OTs	S-OTf	48	1.1
3	bpy	15	G-OTs	S-OTf	0	N.A.
4	DPEPhos	6	H-OMs	G-OTs	14	1.3
5	DPEPhos	6	H-OTs	S-OTf	27	1.9
6	DPEPhos	6	G-OTs	S-OTf	0	N.A.

<sup>a</sup> Yields were determined by <sup>1</sup>H NMR spectroscopy using mesitylene as the internal standard. <sup>b</sup> 10 mol%  $\text{NiCl}_2(\text{dme})$ .

#### Optimization of electrochemical Ni/Pd-catalyzed reductive cross-coupling

Under nitrogen atmosphere,  $\text{NiCl}_2(\text{dme})$  (22 mg, 5 mol%), 4,4'-dPhbpy (37 mg, 6 mol%), and DMA (1 mL) was added to a 1.5-dram vial capped with a Teflon septum. Another 1.5-dram vial was charged with  $\text{PdCl}_2(\text{MeCN})_2$  (26 mg, 5 mol%), dppb (51 mg, 6 mol%), and DMA (1 mL) under nitrogen. The two vials were stirred for 30 min so that the ligands are well complexed with the metal.

To the undivided cell (Figure 2A.2) was added the two coupling partners (2 mmol, 1.0 equiv) and the cell was introduced in a nitrogen-filled glove box and installed a Ni foam cathode, a Ag/AgNO<sub>3</sub> reference electrode, and an iron rod anode. The cell was then charged with LiBr (695 mg, 8 mmol, 4.0 equiv), ZnCl<sub>2</sub> (136 mg, 1 mmol, 0.5 equiv), the two catalyst solutions and DMA (3 mL), sealed with rubber septum, and removed from the glove box. A thin Teflon tube was introduced immediately into the cell to allow continuous nitrogen bubbling. The reaction mixture

was stirred at 1000 rpm for 30 min to allow full dissolution of LiBr and exclusion of adventitious oxygen. After that, the reaction mixture was electrolyzed under a constant potential of  $-1.8$  V (vs.  $\text{Fc}/\text{Fc}^+$ ) for 36 h at  $60$  °C. The reaction mixture was then cooled to room temperature and diluted with DMA (30 mL). 1,3,5-trimethoxybenzene (168 mg, 1 mmol, 0.5 equiv) was added to the crude material. Then a 150  $\mu\text{L}$  aliquot of the solution was filtered through a 2-cm silica gel plug in a Pasteur pipette into a vial. 500  $\mu\text{L}$   $\text{CDCl}_3$  was also added to the pipette and eluted into the same vial. The resultant sample was analyzed by  $^1\text{H}$  NMR spectroscopy and the yields were determined using 1,3,5-trimethoxybenzene as the internal standard. The results are summarized in Figure 2A.5.

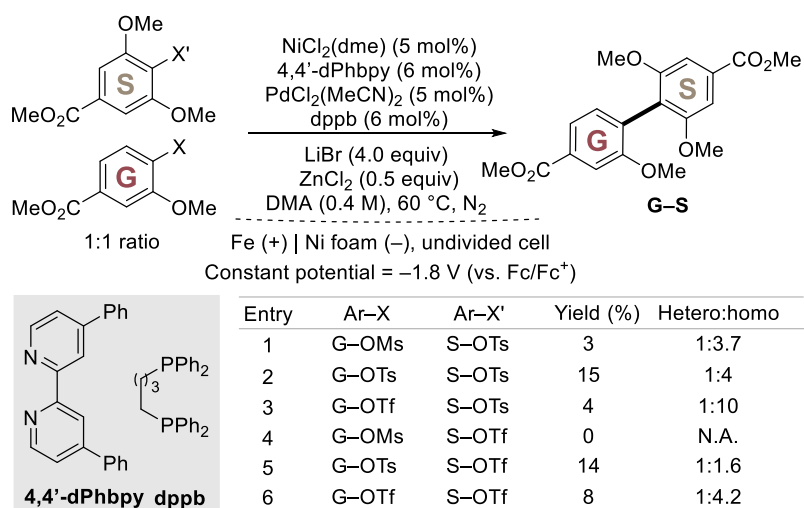
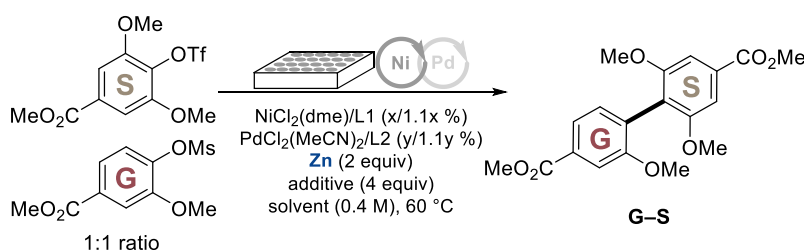


**Figure 2A.5.** Electrochemical Ni/Pd-catalyzed G/S cross-coupling. Yields were determined by  $^1\text{H}$  NMR spectroscopy using 1,3,5-trimethoxybenzene as the internal standard.

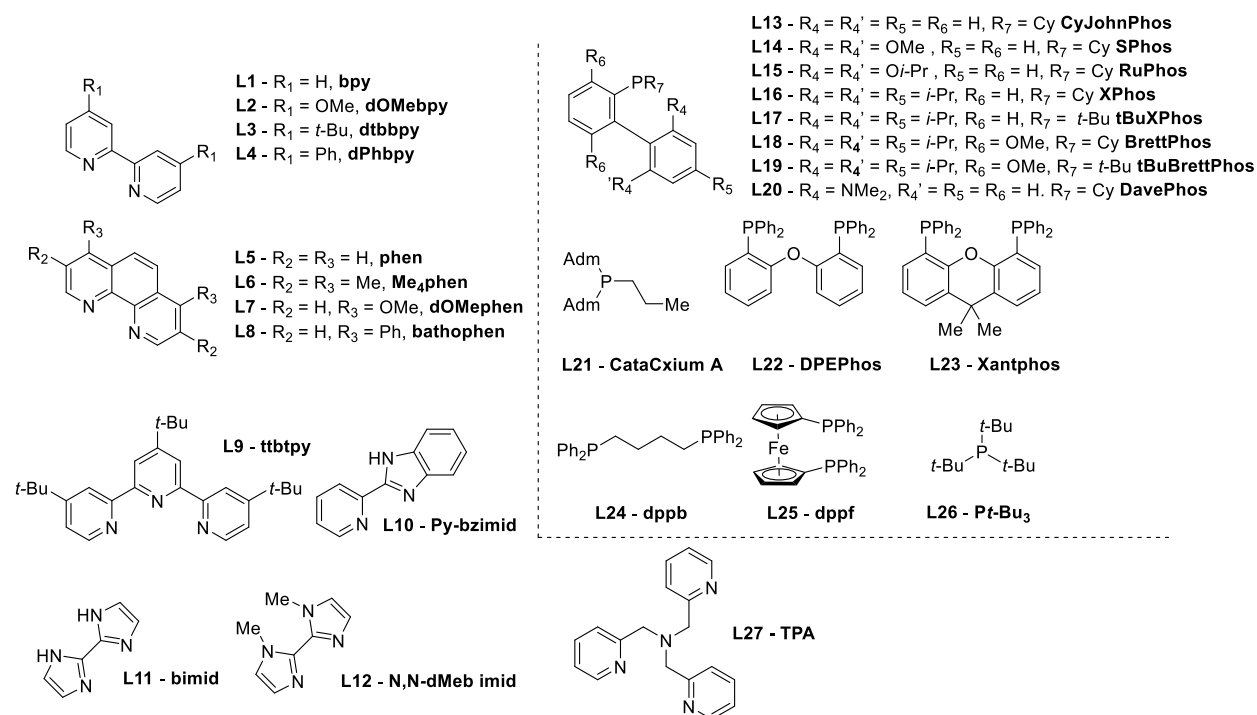
#### Optimization of Ni/Pd-catalyzed reductive cross-coupling (HTE Optimization)

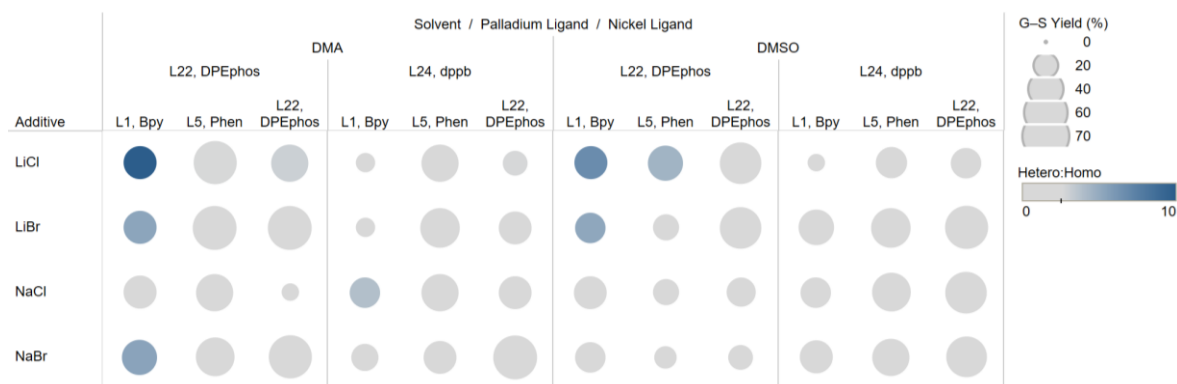


To a 2-dram vial fitted with cross-shaped stir bar was added  $\text{NiCl}_2(\text{dme})$  and appropriate nitrogen-based ligand. This vial was then transferred into a nitrogen-filled glove box and solvent was added. In a separate 2-dram vial fitted with a cross-shaped stir bar was added  $\text{PdCl}_2(\text{MeCN})_2$  and appropriate phosphine ligand. This vial was then transferred into a nitrogen-filled glove box and solvent was added. These stock solutions were stirred for 1 h. To a 96-well optimization block (Analytical Sales and Services) with 1-mL glass vial inserts (Analytical Sales and Services) fitted with stainless-steel stir bars (V&P scientific) in a nitrogen-filled glove box, was dispensed appropriate quantities of the stock solutions of the catalysts (concentrations of stock solutions were adjusted so that around 10  $\mu\text{L}$  of each stock solution was dispensed). The blocks were then aged for 15 min. To a 2-dram vial fitted with a cross-shaped stir bar was added both aryl sulfonate coupling partners (0.40 M, 1.0 equiv), LiBr (1.60 M, 4 equiv), Zn dust (0.80 M, 2.0 equiv), and solvent. This mixture was then stirred vigorously for 5 min. To the aged 96-well optimization block, 50  $\mu\text{L}$  of a suspension containing the two aryl sulfonates (20 mmol, 0.40 M), LiBr (80 mmol, 1.6 M), and Zn dust (40 mmol, 0.80 M) in solvent was dispensed to each vial from the rapidly stirred 2-dram vial containing substrate, LiBr, and Zn. The plate was then sealed with a screwdriver and placed in a zip lock bag inside the glove box. The plate was then removed from the glove box and agitated on a tumble stirrer (V&P Scientific) at 60  $^\circ\text{C}$  for 20 h. The block was then diluted with a solution of 1,3,5-trimethoxybenzene in 3:1 MeCN/DMSO (10 mmol, 0.067 M, 150 mL) and sampled (5  $\mu\text{L}$ ) into an HPLC collection block (Analytical Sales and Services) pre-filled with 3:1 MeCN/DMSO (200  $\mu\text{L}$ ). The HPLC collection block was then analyzed utilizing UPLC-MS (Waters-Acquity) analysis and yields were determined with respect to 1,3,5-trimethoxybenzene utilizing calibration curves. Data was then visualized on Tableau<sup>®</sup>. Changes were made to this procedure to minimize the number of operations for each variable that was

evaluated. It is worth noting that CyJohnPhos gave a higher selectivity in Zn-mediated chemical screening but was ineffective under electrochemical conditions, furnishing the desired product in only 14% yield. UPLC-MS analysis of the reaction mixture in this case revealed the presence of significant quantities of CyJohnPhos phosphine oxide suggesting the possibility of an electrochemical catalyst decomposition pathway not observed with Zn as the terminal reductant. Thus, SPhos was used in the co-catalyst system presented in Figure 2.5B.

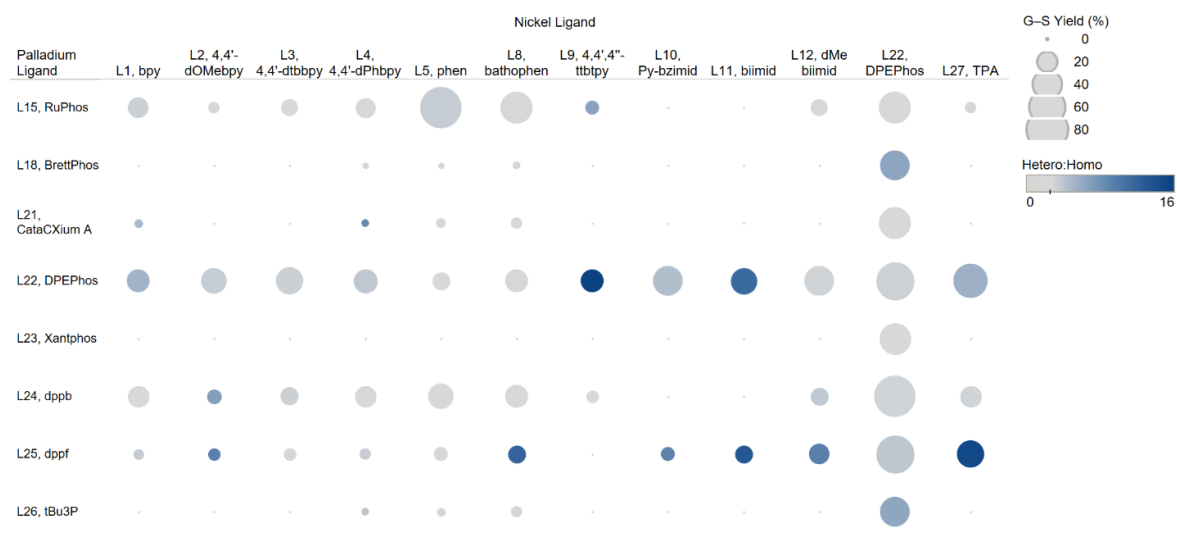
Separate stock solutions for each ligand were prepared before addition to the 96-well plate to ensure pre-complexation. Ligand structures are shown below:



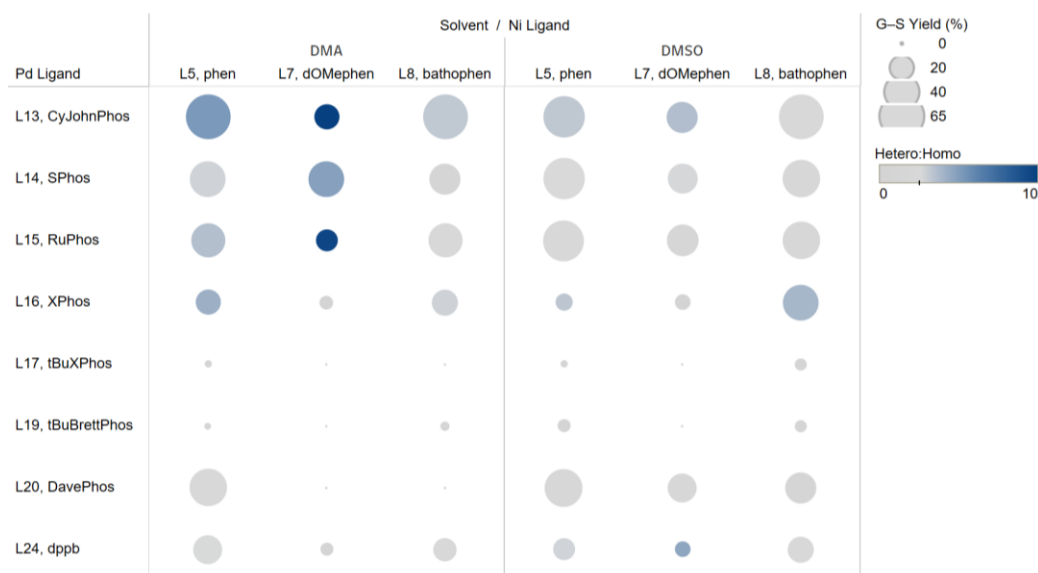
**Table 2A.11. Ligand, additive, and solvent screening for G/S cross-coupling.<sup>a</sup>**

<sup>a</sup> Yields were determined by UPLC using 1,3,5-trimethoxybenzene as the internal standard.

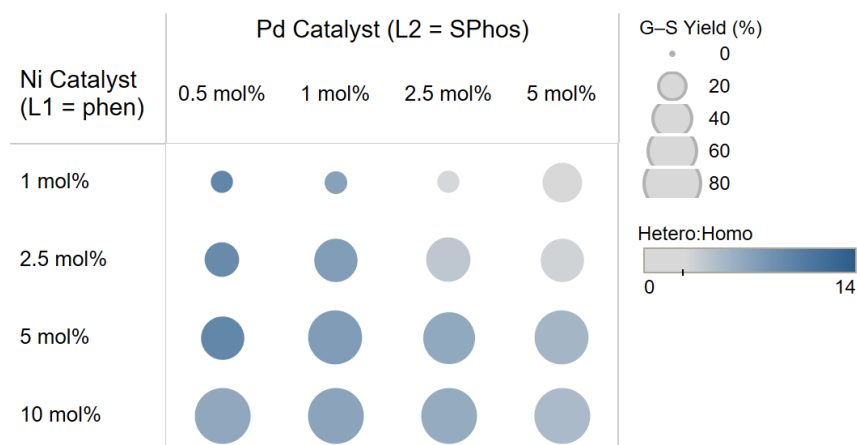
Here, the Hetero:Homo ratio is defined as [cross-coupled product yield/sum of the two homocoupled byproduct yields] and applies to Tables 2A.11 to 2A.14.

**Table 2A.12. Ligand screening for G/S cross-coupling.<sup>a</sup>**

<sup>a</sup> Yields were determined by UPLC using 1,3,5-trimethoxybenzene as the internal standard, DMSO solvent.

**Table 2A.13. Ligand and solvent screening for G/S cross-coupling.**

<sup>a</sup> Yields were determined by UPLC using 1,3,5-trimethoxybenzene as the internal standard.

**Table 2A.14. Catalyst loading screening for G/S cross-coupling.<sup>a</sup>**

<sup>a</sup> Yields were determined by UPLC using 1,3,5-trimethoxybenzene as the internal standard. This table is also presented in Figure 2.5A.

## 2A.VI. Cyclic Voltammetry Studies

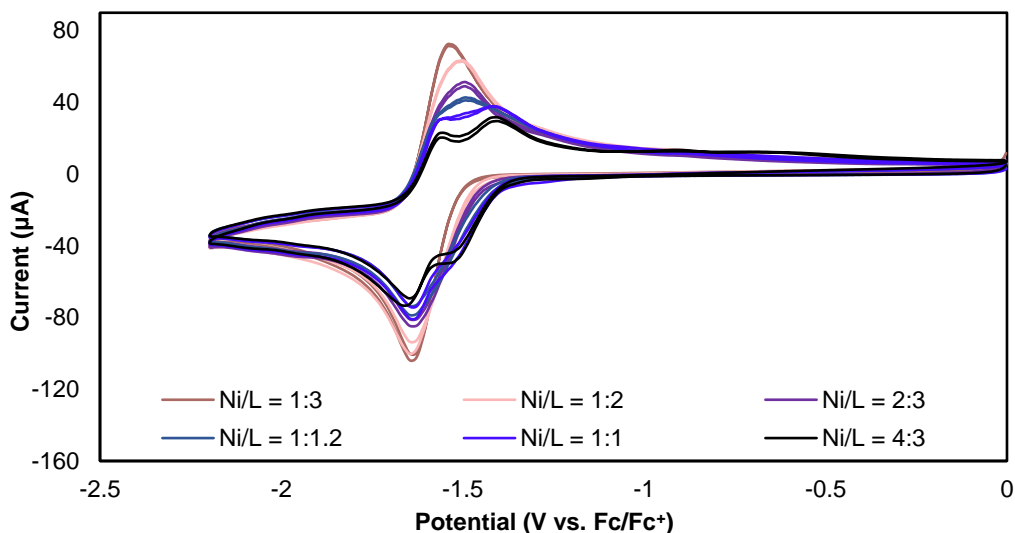


**Figure 2A.6.** CVs of  $\text{NiCl}_2(\text{dme})$  (denoted as Ni, 10 mM) in DMF with different loadings of bpy ligand (denoted as L), with NaBr (0.4 M) as supporting electrolyte, under  $\text{N}_2$  protection, scan rate = 100 mV/s. Each experiment was scanned twice.

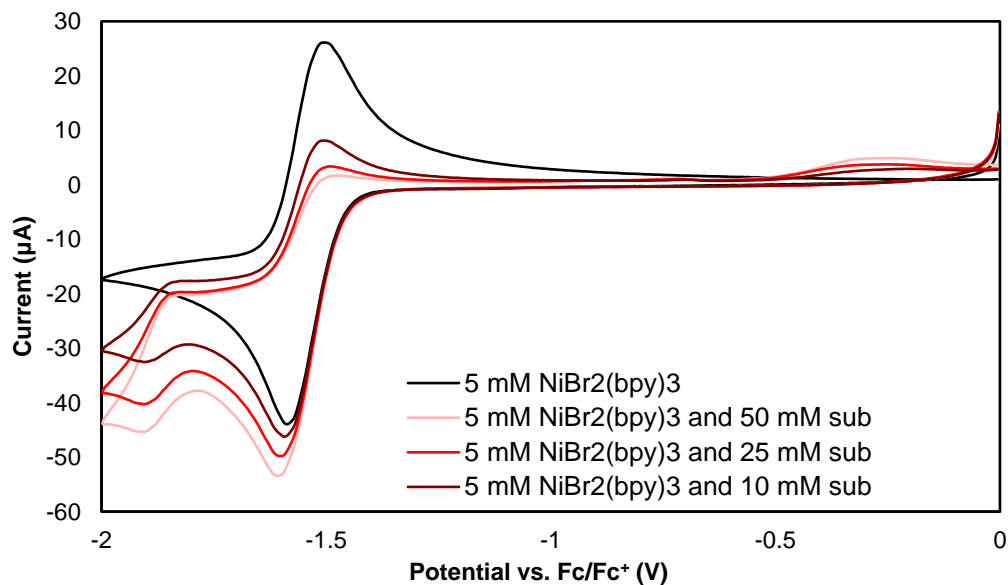


**Figure 2A.7.** CVs of  $\text{NiBr}_2(\text{bpy})_3$  (5 mM) in DMF with different loadings of substrate **G-OMs** (denoted as sub), with LiBr (0.4 M) as supporting electrolyte, under  $\text{N}_2$  protection, scan rate = 20 mV/s.  $\text{NiBr}_2(\text{bpy})_3$  was synthesized according to literature reports for the ease of CV studies.<sup>6</sup>

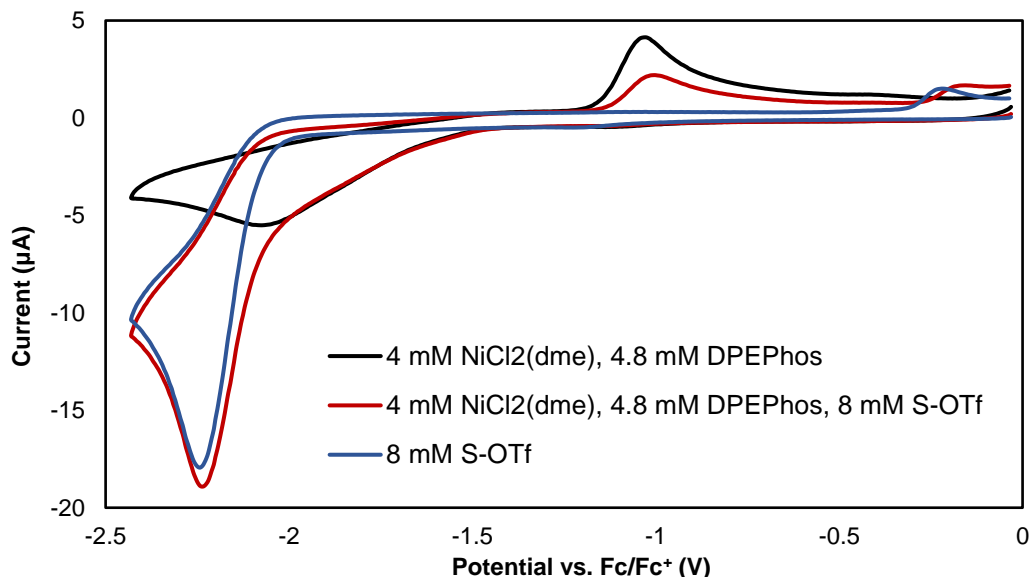


**Figure 2A.8.** CVs of NiCl<sub>2</sub>(dme) (4 mM) and DPEPhos (4.8 mM) in DMSO with or without substrate S-OTf (8 mM), with LiBr (0.6 M) as supporting electrolyte, under N<sub>2</sub> protection, scan rate = 20 mV/s.

## 2A.VII. Plasticizers

### *Synthesis and thermal properties of lignin-derived biphenyl plasticizers*

**Materials:** 2-ethylhexanol, titanium butoxide, ethyl acetate, hexanes were purchased from Sigma Aldrich and used as received. Poly(vinyl chloride) (PVC; unplasticized, 250 microns) was purchased from Goodfellow and used as received.

**Instruments:** The chemical structures of the lignin biphenyl plasticizers were confirmed by <sup>1</sup>H and <sup>13</sup>C NMR on a Bruker Advance III HD 400 MHz NMR spectrometer using CDCl<sub>3</sub>. The typical relaxation time (T<sub>1</sub>) used was 10 s and the average number of transient scans was 16. The <sup>13</sup>C NMR spectrum was also acquired in CDCl<sub>3</sub> with an average number of transient scans of 512. Thermal properties of plasticized PVC films and plasticizers were studied using a TA Instruments Q-500 thermal gravimetric analyzer (TGA) at a heating rate of 10 °C/min with a nitrogen flow of 60 mL/min up to 800 °C and a TA instruments Q-5000 digital scanning calorimeter (DSC) was utilized at with a heating rate of 10 °C/min and a nitrogen flow rate of 60 mL/min.

General procedure for synthesizing lignin-derived biphenyl plasticizers (GP 5): The following procedure was adapted from previous literature reports synthesizing plasticizers.<sup>7</sup> To a 100 mL round-bottom flask was added the lignin-derived BPDA methyl esters (**H–H** through **S–S**; 500 mg, 1.0 equiv), 2-ethyl hexanol (10 equiv) and titanium butoxide (1.5 wt%) were stirred and heated to 150 °C for 2 h. The crude reaction was monitored by TLC for full conversion of the starting material. The crude product was purified by column chromatography using a gradient of hexanes to 10/1 hexane/ethyl acetate to furnish purified plasticizer as a transparent to slightly yellow tinted, viscous oil.

Preparation of plasticized PVC films: The following procedure was adapted from previous literature reports synthesizing polyesters.<sup>8</sup> Unplasticized poly(vinyl chloride) (UPVC) (100 mg) was solubilized in 1 mL THF and 10 weight percent of each plasticizer was added and stirred for 30 min. The resulting solubilized polymer solution was cast in a mold and slowly evaporated for 48 h. The films were then placed in an ambient vacuum oven under reduced pressure for 24 h to remove residual THF and the thin films were obtained for analysis.

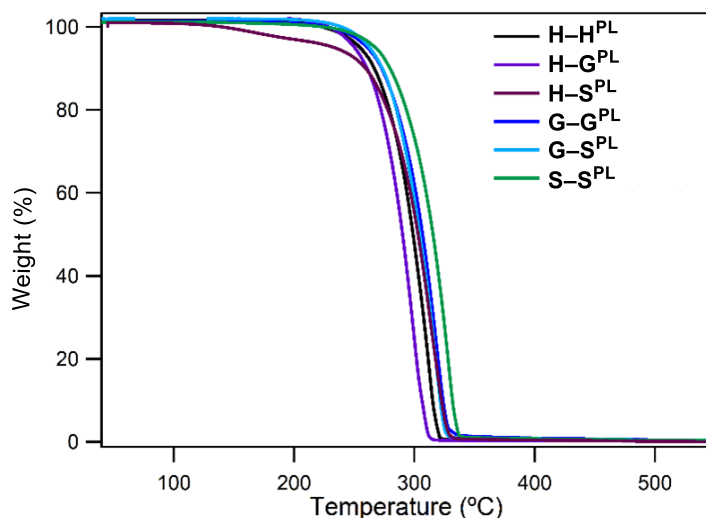


**Figure 2A.9.** Thermogravimetric analysis of DEH-BPDA derivatives (**H–H<sup>PL</sup>** through **S–S<sup>PL</sup>**) at a heating rate of 10 °C/min under nitrogen.

**Table 2A.15.** Thermogravimetric analysis of DEH-BPDA derivatives (**H–H<sup>PL</sup>** through **S–S<sup>PL</sup>**).

Plasticizer	$T_{d10}$ ( $^{\circ}\text{C}$ ) <sup>a</sup>	$T_{d50}$ ( $^{\circ}\text{C}$ ) <sup>b</sup>
H-H <sup>PL</sup>	267	299
H-G <sup>PL</sup>	260	290
H-S <sup>PL</sup>	259	303
G-G <sup>PL</sup>	272	307
G-S <sup>PL</sup>	273	305
S-S <sup>PL</sup>	280	316

<sup>a</sup>  $T_{d10}$  corresponds to the temperature at which 10% mass loss is observed.

<sup>b</sup>  $T_{d50}$  corresponds to the temperature at which 50% mass loss is observed.

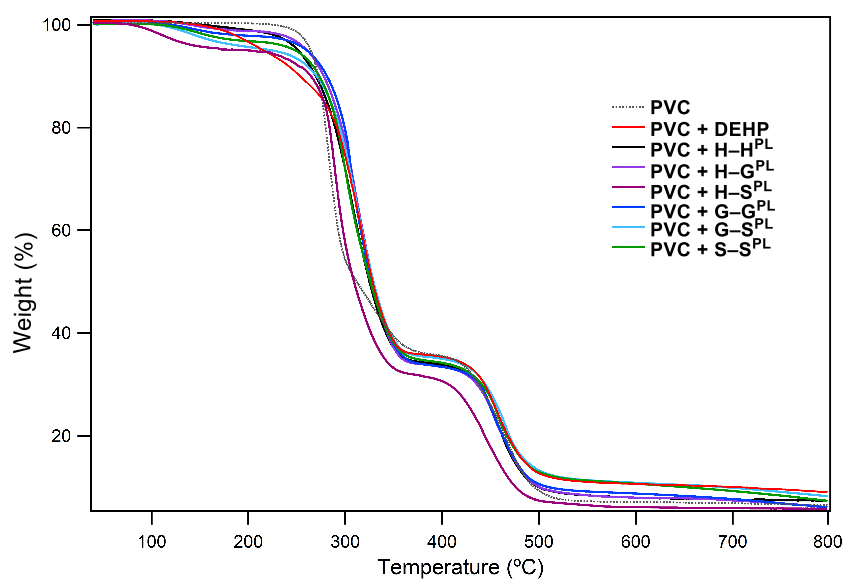


**Figure 2A.10.** Thermogravimetric analysis of PVC with 10 wt% DEH-BPDA derivatives (H-H<sup>PL</sup> through S-S<sup>PL</sup>) compared with DEHP at a heating rate of 10 °C/min in nitrogen.

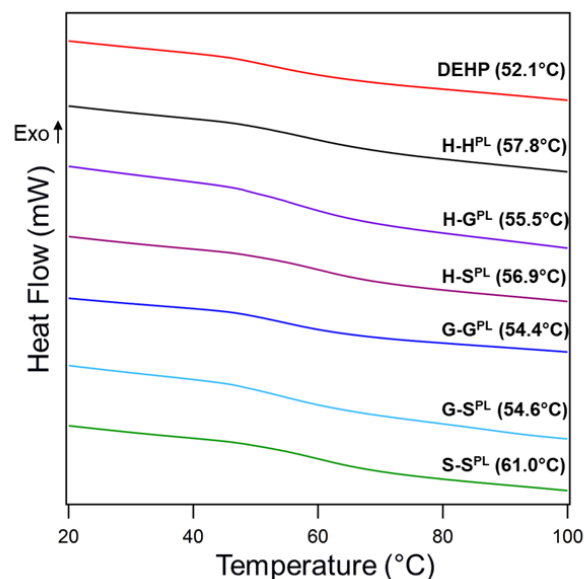


**Figure 2A.11.** Differential scanning calorimetry of PVC with 10 wt% DEH-BPDA derivatives (**H-H<sup>PL</sup>** through **S-S<sup>PL</sup>**) compared with DEHP at a heating rate of 10 °C/min in nitrogen.

**Table 2A.16. Thermal properties of PVC plasticized with 10 wt% DEH-BPDA derivatives (**H-H<sup>PL</sup>** through **S-S<sup>PL</sup>**) and DEHP.**

Polymer	T <sub>g</sub> (°C)	T <sub>d10</sub> (°C) <sup>a</sup>	T <sub>d50</sub> (°C) <sup>a</sup>	Char Yield (%)
PVC	83.0	272	311	6.5
PVC + DEHP	52.1	253	328	9.0
PVC + H-H <sup>PL</sup>	57.8	270	325	7.4
PVC + H-G <sup>PL</sup>	55.5	278	329	6.1
PVC + H-S <sup>PL</sup>	56.9	271	309	5.8
PVC + G-G <sup>PL</sup>	54.4	281	327	6.0
PVC + G-S <sup>PL</sup>	54.6	270	329	8.2
PVC + S-S <sup>PL</sup>	61.0	273	326	7.3

<sup>a</sup> T<sub>d10</sub> corresponds to the temperature at which 10% mass loss is observed. <sup>b</sup> T<sub>d50</sub> corresponds to the temperature at which 50% mass loss is observed.

#### *Toxicity predictions from EPA tools*

Toxicity predictions were obtained from the EPA Toxicity Estimation Software Tool (TEST)<sup>9</sup> and the human metabolism and environmental breakdown products were estimated with the EPA

Chemical Transformation Simulator (CTS).<sup>10</sup> We created in-house scripts in Python to allow high-throughput workflow and analysis.

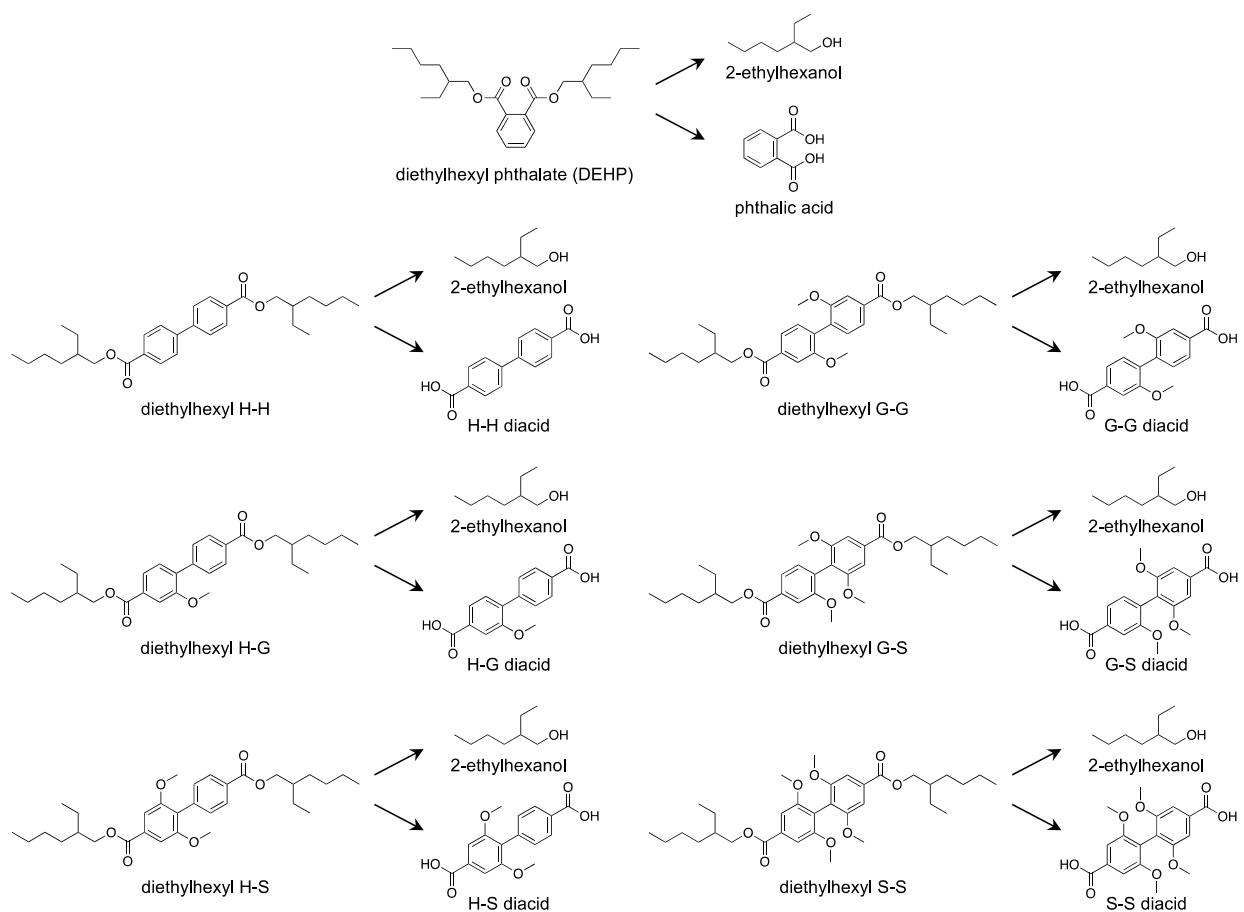


**Figure 2A.12.** Predicted metabolic and environmental transformations of plasticizers.

All plasticizers in this study were predicted by the EPA Chemical Transformation System to hydrolyse to their component diacids and alcohols, both in the environment via abiotic hydrolysis and in human via phase I metabolism. Toxicity predictions for these compounds in blue are provided in Table 2A.17. None of these compounds were predicted to further react in the environment via abiotic means, while 2-ethylhexanol and all diacids except for phthalic acid were predicted to be further metabolized in humans (Figure 2A.13).

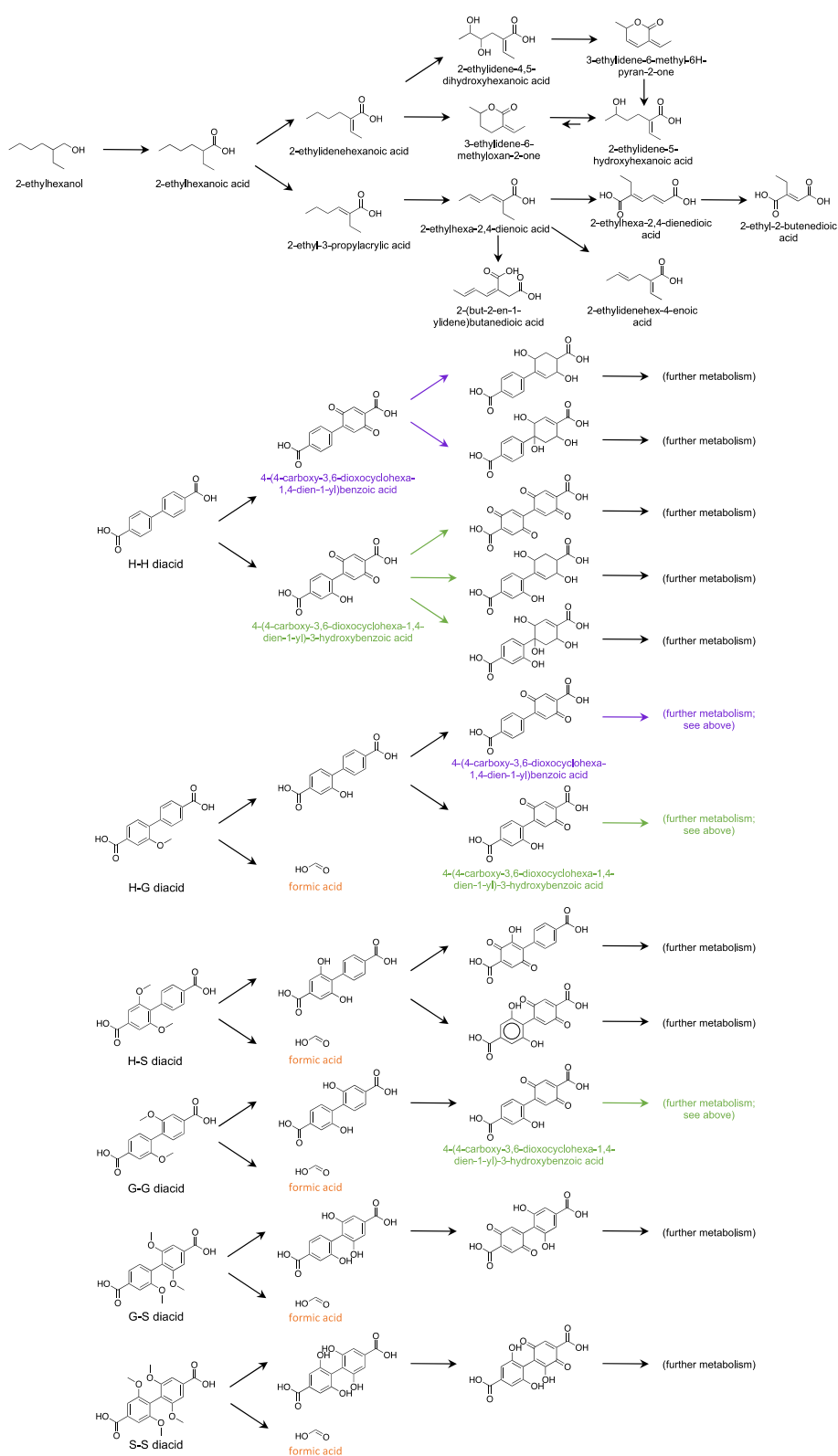


**Figure 2A.13.** Predicted metabolites from 2-ethylhexanol and diacids. Main metabolic pathways predicted by the EPA Chemical Transformation System. Colors are used to highlight metabolites common to multiple diacids.

**Table 2A.17. Summary of EPA T.E.S.T. predictions.**

	Tests for human health impacts			Tests for environmental impact			
	Develop. Toxicity	Ames Mutagen	Rat LD <sub>50</sub> mg/kg**	Bioconcent. Factor	Minnow LC <sub>50</sub> mg/L	<i>Daphnia</i> LC <sub>50</sub> mg/L	<i>T. pyriformis</i> IGC <sub>50</sub> mg/L
<b>Methylated Dimers</b>							
H-H			7,270	16	0.98	6.3	9.4
H-G			9,500	15	0.99	5.0	9.3
H-S			10,400	20	0.91	5.0	9.8
G-G			10,400	20	0.93	5.1	14
G-S			584	14	1.0	6.3	12
S-S			296	16	0.85	11	13
<b>Plasticizers</b>							
DEHP			31,000	18	0.24	1.6	0.09
DEH H-H			36,200	37	0.01	0.38	0.05
DEH H-G			38,600	36	0.01	0.34	0.05
DEH H-S			40,900	37	0.00	0.33	0.05
DEH G-G			44,800	37	0.00	0.32	0.05
DEH G-S			47,400	37	0.00	0.31	0.05
DEH S-S			36,200	38	0.00	0.32	0.06
<b>Oxoalcohol and Diacids</b>							
2-ethylhexanol			1,720	20	31	31	31
phthalic acid			5,130	0.5	30	30	30
H-H diacid			3,050	2.7	N/A	27	73
H-G diacid			3,430	2.1	N/A	17	82
H-S diacid			3,020	3.6	N/A	8.3	87
G-G diacid			3,240	2.8	N/A	5.6	87
G-S diacid			2,640	3.8	N/A	18	178
S-S diacid			3,010	3.6	N/A	6.8	N/A

Output from the Environmental Protection Agency (EPA) toxicity estimation software tool (T.E.S.T.) provided predicted results for experimental tests. The tests for developmental toxicity and Ames mutagenicity have either positive or negative outcomes, reported by the tool as true or false, and negative/false is the desired outcome corresponding to the lowest hazard category (Table 2A.18). Each cell is colored according to the corresponding color for the hazard category shown in Table 2A.18, with green corresponding to the lowest hazard and red to the highest. "N/A" (colored gray) indicates that the EPA tool did not provide a prediction, which occurs when there is insufficient training data for a confident prediction. *Brief definitions of the hazard test names:* the bioconcentration factor is defined as the ratio of the chemical concentration in fish to that in

water at steady state, and thus lower values correspond to lower hazard. Higher values correspond to lower hazard for the remaining categories: oral rat 50 percent lethal dose (LD<sub>50</sub>), fathead minnow 50 percent lethal concentration (LC<sub>50</sub>) after 96 hours of exposure, *D. magna* LC<sub>50</sub> after 48 hours, and 50 percent growth inhibition concentration (IGC<sub>50</sub>) after 48 hours for *T. pyriformis*. Colors correspond to the hazard levels shown in Table 2A.18. *Abbreviations:* the *methylated dimers H–H* through *S–S* correspond to the coupling products created from methylated 4-hydroxy benzoic acid (**H**), vanillic acid (**G**), and syringic acid (**S**) monomers. *Plasticizers:* each diethylhexyl (DEH) structure is shown as the parent molecules in Figure 2A.12. *Oxoalcohol and diacids:* these structures are the product molecules shown in Figure 2A.12.

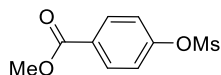
**Table 2A.18. Hazard classifications for EPA T.E.S.T. predictions**

Hazard Indicators	I (highest)	II	III	IV (lowest)
Developmental toxin	positive			negative
Ames Mutagenicity	positive			negative
Oral Rat LD <sub>50</sub> <sup>a</sup>	≤ 50 mg/kg	50 to 500 mg/kg	500 to 5,000	>5,000 mg/kg
Bioconcentration Factor <sup>b</sup>	≥ 5000	1000 to 5000		< 1000
96 hour fathead minnow LC <sub>50</sub> <sup>c</sup>				
48 hour <i>D. magna</i> LC <sub>50</sub> <sup>c</sup>	≤1 mg/L	1 to ≤10 mg/L	>10 to 100 mg/L	> 100 mg/L
48 hour <i>T. pyriformis</i> IGC <sub>50</sub> <sup>c</sup>				

<sup>a</sup> *Protection of Environment*; Code of Federal Regulations, Title 40, Chapter I, Subchapter E, Part 156, Subpart D, § 156.62. <sup>b</sup> United Nations, *Globally harmonized system of classification and labelling of chemical (GHS)*, sixth revised edition; ST/SG/AC.10/30/Rev.6; 2015. <sup>c</sup> United States Environmental Protection Agency, *Persistent Bioaccumulative Toxic (PBT) Chemicals; Lowering of Reporting Thresholds for Certain PBT Chemicals; Addition of Certain PBT Chemicals; Community Right-to-Know Toxic Chemical Reporting*; 40 CFR Part 372; 1999.

## 2A.VIII. Compound Characterization Data

methyl 4-((methylsulfonyl)oxy)benzoate (**H-OMs**)



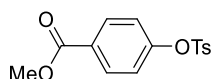
From methyl 4-hydroxybenzoate (7.6 g, 50 mmol) and methanesulfonyl chloride (9.9 mL, 60 mmol), the title compound was prepared following **GP 1** as a pale-yellow powder (11.1 g, 96% yield). The spectroscopic data matched those reported in the literature.<sup>11</sup>

**<sup>1</sup>H NMR** (400 MHz, CDCl<sub>3</sub>) δ 8.15 – 8.07 (m, 2H), 7.40 – 7.32 (m, 2H), 3.93 (s, 3H), 3.19 (s, 3H).

**<sup>13</sup>C NMR** (101 MHz, CDCl<sub>3</sub>) δ 165.9, 152.4, 131.7, 129.2, 121.9, 52.4, 37.8.

**HRMS (ESI<sup>+</sup>)** Calc: [M+H]<sup>+</sup> (C<sub>9</sub>H<sub>11</sub>O<sub>5</sub>S) 231.0322; measured: 231.0321 = 0.4 ppm difference.

methyl 4-(tosyloxy)benzoate (**H-OTs**)

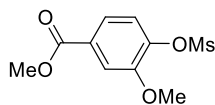


From methyl 4-hydroxybenzoate (7.6 g, 50 mmol) and *p*-toluenesulfonyl chloride (11.4 g, 60 mmol), the title compound was prepared following **GP 1** as a white powder (14 g, 93% yield). The spectroscopic data matched those reported in the literature.<sup>11</sup>

**<sup>1</sup>H NMR** (400 MHz, CDCl<sub>3</sub>) δ 8.02 – 7.94 (m, 2H), 7.74 – 7.67 (m, 2H), 7.35 – 7.28 (m, 2H), 7.10 – 7.02 (m, 2H), 3.90 (s, 3H), 2.45 (s, 3H).

**<sup>13</sup>C NMR** (101 MHz, CDCl<sub>3</sub>) δ 166.4, 153.0, 145.8, 132.0, 131.3, 129.9, 128.9, 128.5, 122.4, 52.3, 21.7.

**HRMS (ESI<sup>+</sup>)** Calc: [M+H]<sup>+</sup> (C<sub>15</sub>H<sub>15</sub>O<sub>5</sub>S) 307.0635; measured: 307.0630 = 1.6 ppm difference.

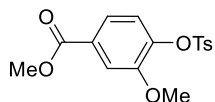
methyl 3-methoxy-4-((methylsulfonyl)oxy)benzoate (**G-OMs**)

From methyl 4-hydroxy-3-methoxybenzoate (9.1 g, 50 mmol) and methanesulfonyl chloride (9.9 mL, 60 mmol), the title compound was prepared following **GP 1** as a white powder (12.2 g, 94% yield). The spectroscopic data matched those reported in the literature.<sup>12</sup>

**<sup>1</sup>H NMR** (600 MHz, CDCl<sub>3</sub>) δ 7.71 – 7.65 (m, 2H), 7.37 (d, *J* = 8.1 Hz, 1H), 3.96 (s, 3H), 3.93 (s, 3H), 3.22 (s, 3H).

**<sup>13</sup>C NMR** (101 MHz, CDCl<sub>3</sub>) δ 166.0, 151.4, 141.7, 130.1, 124.4, 122.8, 114.0, 56.3, 52.5, 38.7.

**HRMS (ESI<sup>+</sup>)** Calc: [M+H]<sup>+</sup> (C<sub>10</sub>H<sub>13</sub>O<sub>6</sub>S) 261.0427; measured: 261.0426 = 0.4 ppm difference.

methyl 3-methoxy-4-(tosyloxy)benzoate (**G-OTs**)

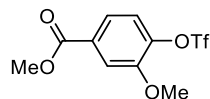
From methyl 4-hydroxy-3-methoxybenzoate (9.1 g, 50 mmol) and *p*-toluenesulfonyl chloride (11.4 g, 60 mmol), the title compound was prepared following **GP 1** as a white powder (16 g, 95% yield). The spectroscopic data matched those reported in the literature.<sup>12</sup>

**<sup>1</sup>H NMR** (400 MHz, CDCl<sub>3</sub>) δ 7.79 – 7.71 (m, 2H), 7.60 (dd, *J* = 8.4, 2.0 Hz, 1H), 7.51 (d, *J* = 1.9 Hz, 1H), 7.30 (d, *J* = 7.9 Hz, 2H), 7.22 (d, *J* = 8.4 Hz, 1H), 3.91 (s, 3H), 3.62 (s, 3H), 2.45 (s, 3H).

**<sup>13</sup>C NMR** (101 MHz, CDCl<sub>3</sub>) δ 166.1, 151.7, 145.3, 141.9, 133.0, 129.8, 129.5, 128.6, 123.9, 122.3, 113.6, 55.8, 52.4, 21.7.

**HRMS (ESI<sup>+</sup>)** Calc: [M+H]<sup>+</sup> (C<sub>16</sub>H<sub>17</sub>O<sub>6</sub>S) 337.0740; measured: 337.0736 = 1.2 ppm difference.

methyl 3-methoxy-4-(((trifluoromethyl)sulfonyl)oxy)benzoate (**G-OTf**)



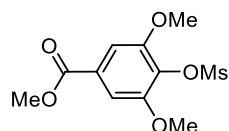
From methyl 4-hydroxy-3-methoxybenzoate (9.1 g, 50 mmol) and trifluoromethanesulfonic anhydride (10.1 mL, 60 mmol), the title compound was prepared following **GP 1** as a yellow liquid (14.4 g, 92% yield). The spectroscopic data matched those reported in the literature.<sup>1</sup>

**<sup>1</sup>H NMR** (400 MHz, CDCl<sub>3</sub>) δ 7.72 (d, *J* = 1.9 Hz, 1H), 7.68 (dd, *J* = 8.4, 1.9 Hz, 1H), 7.28 (d, *J* = 8.5 Hz, 1H), 3.98 (s, 3H), 3.94 (s, 3H).

**<sup>13</sup>C NMR** (101 MHz, CDCl<sub>3</sub>) δ 165.6, 151.3, 141.8, 131.1, 122.8, 122.4, 120.3, 117.1, 114.2, 56.4, 52.6.

**HRMS (ESI<sup>+</sup>)** Calc: [M+H]<sup>+</sup> (C<sub>10</sub>H<sub>10</sub>F<sub>3</sub>O<sub>6</sub>S) 315.0145; measured: 315.0141 = 1.3 ppm difference.

methyl 3,5-dimethoxy-4-((methylsulfonyl)oxy)benzoate (**S-OMs**)



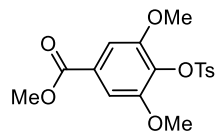
From methyl 4-hydroxy-3,5-dimethoxybenzoate (10.6 g, 50 mmol) and methanesulfonyl chloride (9.9 mL, 60 mmol), the title compound was prepared following **GP 1** as a white powder (13 g, 89% yield).

**<sup>1</sup>H NMR** (400 MHz, CDCl<sub>3</sub>) δ 7.34 (s, 2H), 3.95 (s, 6H), 3.93 (s, 3H), 3.33 (s, 3H).

**<sup>13</sup>C NMR** (101 MHz, CDCl<sub>3</sub>) δ 166.1, 153.1, 131.6, 129.1, 106.4, 56.5, 52.6, 40.2.

**HRMS (ESI<sup>+</sup>)** Calc: [M+NH<sub>4</sub>]<sup>+</sup> (C<sub>11</sub>NH<sub>18</sub>O<sub>7</sub>S) 308.0799; measured: 308.0796 = 1.0 ppm difference.

methyl 3,5-dimethoxy-4-(tosyloxy)benzoate (**S-OTs**)



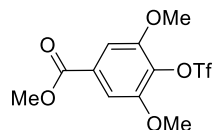
From methyl 4-hydroxy-3,5-dimethoxybenzoate (10.6 g, 50 mmol) and *p*-toluenesulfonyl chloride (11.4 g, 60 mmol), the title compound was prepared following **GP 1** as a white powder (16.5 g, 90% yield).

**<sup>1</sup>H NMR** (400 MHz, CDCl<sub>3</sub>) δ 7.89 – 7.82 (m, 2H), 7.34 (d, *J* = 8.0 Hz, 2H), 7.26 (s, 2H), 3.91 (s, 3H), 3.73 (s, 6H), 2.46 (s, 3H).

**<sup>13</sup>C NMR** (101 MHz, CDCl<sub>3</sub>) δ 166.1, 153.3, 144.8, 134.7, 131.6, 129.2, 129.0, 128.4, 106.3, 56.2, 52.5, 21.7.

**HRMS (ESI<sup>+</sup>)** Calc: [M+NH<sub>4</sub>]<sup>+</sup> (C<sub>17</sub>NH<sub>22</sub>O<sub>7</sub>S) 384.1112; measured: 384.1110 = 0.5 ppm difference.

methyl 3,5-dimethoxy-4-(((trifluoromethyl)sulfonyl)oxy)benzoate (**S-OTf**)



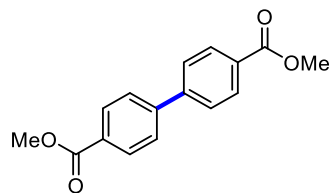
From methyl 4-hydroxy-3,5-dimethoxybenzoate (10.6 g, 50 mmol) and trifluoromethanesulfonic anhydride (10.1 mL, 60 mmol), the title compound was prepared following **GP 1** as a white powder (16 g, 93% yield).

**<sup>1</sup>H NMR** (400 MHz, CDCl<sub>3</sub>) δ 7.34 (s, 2H), 3.95 (s, 6H), 3.94 (s, 3H).

**<sup>13</sup>C NMR** (101 MHz, CDCl<sub>3</sub>) δ 165.8, 152.3, 131.0, 130.2, 120.2, 117.0, 106.3, 56.6, 52.7.

**HRMS (ESI<sup>+</sup>)** Calc: [M+H]<sup>+</sup> (C<sub>11</sub>H<sub>12</sub>F<sub>3</sub>O<sub>7</sub>S) 345.0250; measured: 345.0246 = 1.2 ppm difference.

dimethyl [1,1'-biphenyl]-4,4'-dicarboxylate (**H-H**)



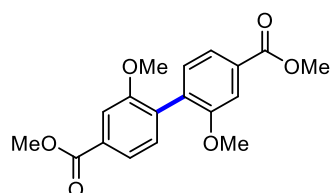
**GP 2** was followed using **H-OMs** (460 mg, 2.0 mmol), NiCl<sub>2</sub>(dme) (4.4 mg, 1 mol%), 2,2'-bipyridyl (9.4 mg, 3 mol%), which furnished the title compound as a white powder (262 mg, 97% yield). The spectroscopic data matched those reported in the literature.<sup>13</sup>

**<sup>1</sup>H NMR** (400 MHz, CDCl<sub>3</sub>) δ 8.13 (d, *J* = 8.2 Hz, 4H), 7.69 (d, *J* = 8.2 Hz, 4H), 3.95 (s, 6H).

**<sup>13</sup>C NMR** (126 MHz, CDCl<sub>3</sub>) δ 166.8, 144.4, 130.2, 129.7, 127.3, 52.2.

**HRMS (ESI<sup>+</sup>)** Calc: [M+H]<sup>+</sup> (C<sub>16</sub>H<sub>15</sub>O<sub>4</sub>) 271.0965; measured: 271.0973 = 0.7 ppm difference.

dimethyl 2,2',6,6'-tetramethoxy-[1,1'-biphenyl]-4,4'-dicarboxylate (**G-G**)



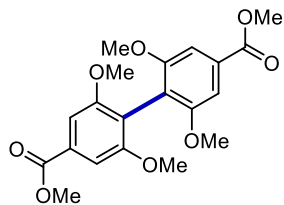
**GP 2** was followed using **G-OMs** (520 mg, 2.0 mmol), NiCl<sub>2</sub>(dme) (22 mg, 5 mol%), 2,2'-bipyridyl (47 mg, 15 mol%), which furnished the title compound as a white powder (297 mg, 90% yield). The spectroscopic data matched those reported in the literature.<sup>14</sup>

**<sup>1</sup>H NMR** (400 MHz, CDCl<sub>3</sub>) δ 7.70 (dd, *J* = 7.8, 1.6 Hz, 2H), 7.64 (d, *J* = 1.5 Hz, 2H), 7.30 (d, *J* = 7.8 Hz, 2H), 3.94 (s, 6H), 3.83 (s, 6H).

**<sup>13</sup>C NMR** (126 MHz, CDCl<sub>3</sub>) δ 166.9, 156.9, 131.8, 131.1, 130.9, 121.8, 111.9, 55.4, 52.2.

**HRMS (ESI<sup>+</sup>)** Calc: [M+H]<sup>+</sup> (C<sub>18</sub>H<sub>19</sub>O<sub>6</sub>) 331.1176; measured: 331.1174 = 0.6 ppm difference.

dimethyl 2,2',6,6'-tetramethoxy-[1,1'-biphenyl]-4,4'-dicarboxylate (**S-S**)



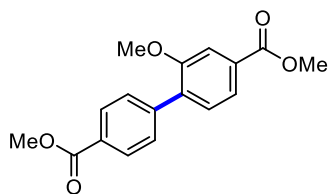
**GP 3** was followed to furnish the title compound as a pale-yellow powder (293 mg, 75% yield).

**<sup>1</sup>H NMR** (400 MHz, CDCl<sub>3</sub>) δ 7.34 (s, 4H), 3.94 (s, 6H), 3.77 (s, 12H).

**<sup>13</sup>C NMR** (151 MHz, CDCl<sub>3</sub>) δ 167.0, 158.5, 131.0, 116.9, 105.6, 56.2, 52.2.

**HRMS (ESI<sup>+</sup>)** Calc: [M+H]<sup>+</sup> (C<sub>20</sub>H<sub>23</sub>O<sub>8</sub>) 391.1387; measured: 391.1382 = 1.3 ppm difference.

dimethyl 2-methoxy-[1,1'-biphenyl]-4,4'-dicarboxylate (**H-G**)



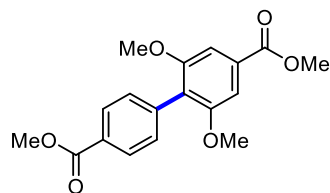
**GP 4** at 60 °C was followed using **H-OMs** (460 mg, 2.0 mmol), **G-OTs** (841 mg, 2.5 mmol), NiCl<sub>2</sub>(dme) (44 mg, 10 mol%), 4,4'-dPhbpy (74 mg, 12 mol%), PdCl<sub>2</sub>(MeCN)<sub>2</sub> (15.6 mg, 3 mol%), dppb (30.6 mg, 3.6 mol%), DMA (5 mL), a Ni foam cathode, which furnished the title compound as a white powder (420 mg, 70% yield). The spectroscopic data matched those reported in the literature.<sup>15</sup>

**<sup>1</sup>H NMR** (400 MHz, CDCl<sub>3</sub>) δ 8.12 – 8.05 (m, 2H), 7.72 (dd, *J* = 7.9, 1.6 Hz, 1H), 7.66 (d, *J* = 1.5 Hz, 1H), 7.64 – 7.59 (m, 2H), 7.39 (d, *J* = 7.9 Hz, 1H), 3.95 (s, 3H), 3.94 (s, 3H), 3.88 (s, 3H).

**<sup>13</sup>C NMR** (101 MHz, CDCl<sub>3</sub>) δ 167.0, 166.8, 156.4, 142.2, 134.1, 131.0, 130.7, 129.5, 129.4, 129.1, 122.3, 112.1, 55.8, 52.3, 52.2.

**HRMS (ESI<sup>+</sup>)** Calc: [M+H]<sup>+</sup> (C<sub>17</sub>H<sub>17</sub>O<sub>5</sub>) 301.1071; measured: 301.1071 < 0.1 ppm difference.

dimethyl 2,6-dimethoxy-[1,1'-biphenyl]-4,4'-dicarboxylate (**H-S**)



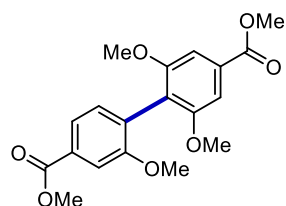
**GP 4** at 80 °C was followed using **H-OTs** (612 mg, 2.0 mmol), **S-OTf** (688 mg, 2.0 mmol), NiCl<sub>2</sub>(dme) (44 mg, 10 mol%), phen (43 mg, 12 mol%), PdCl<sub>2</sub>(MeCN)<sub>2</sub> (10.4 mg, 2 mol%), SPhos (33 mg, 4 mol%), DMSO (5 mL), a RVC cathode, which furnished the title compound as a white powder (468 mg, 71% yield).

**<sup>1</sup>H NMR** (400 MHz, CDCl<sub>3</sub>) δ 8.12 – 8.05 (m, 2H), 7.45 – 7.38 (m, 2H), 7.34 (s, 2H), 3.96 (s, 3H), 3.93 (s, 3H), 3.79 (s, 6H).

**<sup>13</sup>C NMR** (151 MHz, CDCl<sub>3</sub>) δ 167.1, 166.8, 157.3, 138.5, 131.0, 130.8, 129.0, 128.9, 123.0, 105.4, 56.1, 52.4, 52.1.

**HRMS (ESI<sup>+</sup>)** Calc: [M+H]<sup>+</sup> (C<sub>18</sub>H<sub>19</sub>O<sub>5</sub>) 331.1176; measured: 331.1172 = 1.2 ppm difference.

dimethyl 2,2',6-trimethoxy-[1,1'-biphenyl]-4,4'-dicarboxylate (**G-S**)



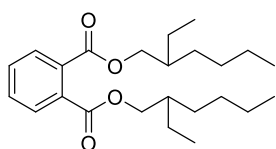
**GP 4** at 80 °C was followed using **G-OTs** (841 mg, 2.5 mmol), **S-OTf** (688 mg, 2.0 mmol), NiCl<sub>2</sub>(dme) (44 mg, 10 mol%), phen (43 mg, 12 mol%), PdCl<sub>2</sub>(MeCN)<sub>2</sub> (15.6 mg, 3 mol%), SPhos (49 mg, 6 mol%), DMSO (5 mL), a Ni foam cathode, which furnished the title compound as a white powder (504 mg, 70% yield).

**$^1\text{H}$  NMR** (400 MHz,  $\text{CDCl}_3$ )  $\delta$  7.71 (dd,  $J = 7.8, 1.6$  Hz, 1H), 7.65 (d,  $J = 1.6$  Hz, 1H), 7.34 (s, 2H), 7.22 (d,  $J = 7.8$  Hz, 1H), 3.95 (s, 3H), 3.93 (s, 3H), 3.80 (s, 3H), 3.78 (s, 6H).

**$^{13}\text{C}$  NMR** (151 MHz,  $\text{CDCl}_3$ )  $\delta$  167.1, 166.9, 157.7, 157.3, 131.8, 131.0, 130.7, 128.1, 121.7, 120.1, 111.9, 105.4, 56.2, 56.0, 52.3, 52.2.

**HRMS (ESI<sup>+</sup>)** Calc:  $[\text{M}+\text{H}]^+$  ( $\text{C}_{19}\text{H}_{21}\text{O}_7$ ) 361.1282; measured: 361.1278 = 1.1 ppm difference.

### Bis(2-ethylhexyl) phthalate (**DEHP**)



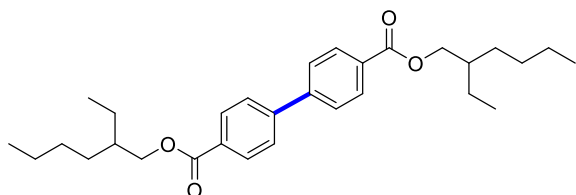
From phthalic anhydride (500 mg, 1 equiv) and 2-ethyl hexanol (2.41 g, 10 equiv), using methane sulfonic acid (1.5 wt%) instead of titanium butoxide, the title compound was prepared following **GP 5** at 130 °C as a transparent viscous oil (1.05 g, 80% yield).

**$^1\text{H}$  NMR** (400 MHz,  $\text{CDCl}_3$ , ppm):  $\delta$  7.71 (dd,  $J = 5.6, 3.2$  Hz, 2H), 7.53 (dd,  $J = 5.6, 3.2$  Hz, 2H), 4.26 – 4.18 (m, 4H), 1.71 – 1.65 (m, 2H), 1.43 – 1.28 (m, 16H), 0.94-0.88 (m, 12H).

**$^{13}\text{C}$  NMR** (101 MHz,  $\text{CDCl}_3$ , ppm):  $\delta$  11.5, 14.6, 23.5, 24.3, 29.4, 30.9, 39.2, 68.7, 129.3, 131.4, 133.0, 168.3.

**HRMS (ESI<sup>+</sup>)** Calc:  $[2\text{M}+\text{Na}]^+$  ( $\text{C}_{48}\text{H}_{76}\text{O}_8\text{Na}$ ) 803.5432; measured: 803.5422 = 1.2 ppm difference.

### Bis(2-ethylhexyl)[1,1'-biphenyl]-4,4'-dicarboxylate (**H-H<sup>PL</sup>**)



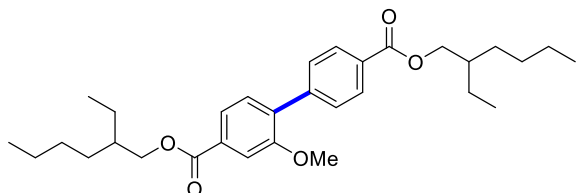
From dimethyl [1,1'-biphenyl]-4,4'-dicarboxylate (500 mg, 1 equiv) and 2-ethyl hexanol (2.41 g, 10 equiv), the title compound was prepared following **GP 5** as a translucent viscous oil (794 mg, 92% yield).

**<sup>1</sup>H NMR** (400 MHz, CDCl<sub>3</sub>, ppm): δ 8.13 (d, *J* = 8.4 Hz, 2H), 7.69 (d, *J* = 8.4 Hz, 2H), 4.31 – 4.23 (m, 4H), 1.77 – 1.71 (m, 2H), 1.50 – 1.33 (m, 16H), 0.964 (t, *J* = 7.2 Hz, 6H), 0.913 (t, *J* = 6.8 Hz, 6H).

**<sup>13</sup>C NMR** (101 MHz, CDCl<sub>3</sub>, ppm): δ 11.2, 14.0, 23.0, 24.0, 29.0, 30.6, 38.9, 67.4, 127.2, 130.1, 144.3, 166.4.

**HRMS (ESI<sup>+</sup>)** Calc: [M+H]<sup>+</sup> (C<sub>30</sub>H<sub>43</sub>O<sub>4</sub>) 467.3156; measured: 467.3149 = 1.5 ppm difference.

Bis(2-ethylhexyl) 2-methoxy-[1,1'-biphenyl]-4,4'-dicarboxylate (**H-G<sup>PL</sup>**)



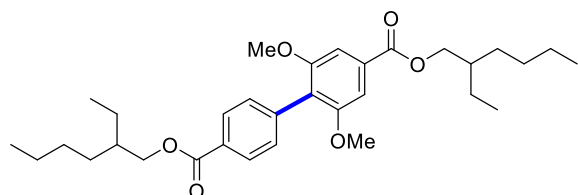
From dimethyl 2-methoxy-[1,1'-biphenyl]-4,4'-dicarboxylate (500 mg, 1 equiv) and 2-ethyl hexanol (2.17 g, 10 equiv), the title compound was prepared following **GP 5** as a translucent viscous oil (777 mg, 94% yield).

**<sup>1</sup>H NMR** (400 MHz, CDCl<sub>3</sub>, ppm): δ 8.09 (d, *J* = 11.3 Hz, 2H), 7.72 (dd, *J* = 2, 10.5 Hz, 1H), 7.68 (d, *J* = 1.8 Hz, 1H), 7.60 (d, *J* = 11.32 Hz, 2H), 7.38 (d, *J* = 10.4 Hz, 1H), 4.29 – 4.25 (m, 4H), 3.87 (s, 3H) 1.79 – 1.70 (m, 2H), 1.50 – 1.33 (m, 16H), 0.994 – 0.891 (m, 12H).

**<sup>13</sup>C NMR** (101 MHz, CDCl<sub>3</sub>, ppm): δ 11.07, 11.00, 14.02, 22.96, 23.98, 24.04, 28.98, 30.58, 30.62, 38.93, 55.71, 67.25, 67.56, 112.05, 122.09, 129.36, 129.43, 129.52, 130.58, 131.39, 134.05, 142.13, 156.37, 166.36, 166.53.

**HRMS (ESI<sup>+</sup>)** Calc: [M+H]<sup>+</sup> (C<sub>31</sub>H<sub>45</sub>O<sub>5</sub>) 497.3262; measured: 497.3252 = 2.0 ppm difference.

Bis(2-ethylhexyl) 2,6-dimethoxy-[1,1'-biphenyl]-4,4'-dicarboxylate (**H-S<sup>PL</sup>**)



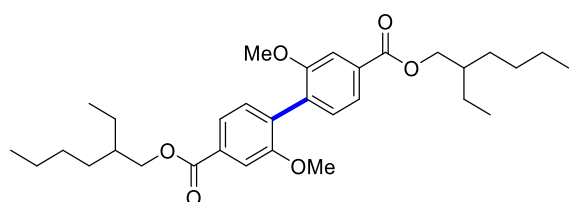
From dimethyl 2,6-dimethoxy-[1,1'-biphenyl]-4,4'-dicarboxylate (500 mg, 1 equiv) and 2-ethyl hexanol (1.97 g, 10 equiv), the title compound was prepared following **GP 5** as a translucent viscous oil (733 mg, 92% yield).

**<sup>1</sup>H NMR** (400 MHz, CDCl<sub>3</sub>, ppm): δ 8.12 – 8.05 (m, 2H), 7.45 – 7.38 (m, 2H), 7.35 (s, 2H), 4.29-4.25 (m, 4H), 3.79 (s, 6H), 1.79 – 1.69 (m, 2H), 1.49 – 1.29 (m, 16H), 0.994 – 0.954 (m, 12H).

**<sup>13</sup>C NMR** (101 MHz, CDCl<sub>3</sub>, ppm): δ 11.06, 14.58, 23.52, 24.52, 24.68, 29.54, 29.54, 31.14, 31.25, 39.48, 56.53, 65.85, 67.63, 68.31, 105.84, 123.46, 129.48, 129.81, 131.25, 131.92, 138.88, 157.85, 166.85, 167.22.

**HRMS (ESI<sup>+</sup>)** Calc: [M+H]<sup>+</sup> (C<sub>32</sub>H<sub>47</sub>O<sub>6</sub>) 527.3367; measured: 527.3357 = 1.9 ppm difference.

Bis(2-ethylhexyl) 2,2'-dimethoxy-[1,1'-biphenyl]-4,4'-dicarboxylate (**G-G<sup>PL</sup>**)



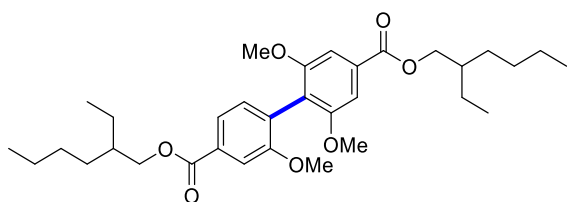
From dimethyl 2,2'-dimethoxy-[1,1'-biphenyl]-4,4'-dicarboxylate (500 mg, 1 equiv) and 2-ethyl hexanol (1.97 g, 10 equiv), the title compound was prepared following **GP 5** as a translucent viscous oil (741 mg, 93% yield).

**<sup>1</sup>H NMR** (400 MHz, CDCl<sub>3</sub>, ppm): δ 7.72 (dd, *J* = 2, 10.4 Hz, 2H), 7.66 (d, *J* = 1.8 Hz, 2H), 7.29 (d, *J* = 10.4 Hz, 2H), 4.28 – 4.26 (m, 4H), 3.83 (s, 6H), 1.78 – 1.68 (m, 2H), 1.53 – 1.33 (m, 16H), 0.990 – 0.893 (m, 12H).

**<sup>13</sup>C NMR** (101 MHz, CDCl<sub>3</sub>, ppm): δ 11.1, 14.1, 23.0, 24.1, 29.0, 30.7, 39.0, 55.8, 67.5, 111.9, 121.7, 131.1, 131.3, 131.7, 156.9, 166.6.

**HRMS (ESI<sup>+</sup>)** Calc: [M+H]<sup>+</sup> (C<sub>32</sub>H<sub>47</sub>O<sub>6</sub>) 527.3367; measured: 527.3358 = 1.7 ppm difference.

Bis(2-ethylhexyl) 2,2',6-trimethoxy-[1,1'-biphenyl]-4,4'-dicarboxylate (**G-S<sup>PL</sup>**)



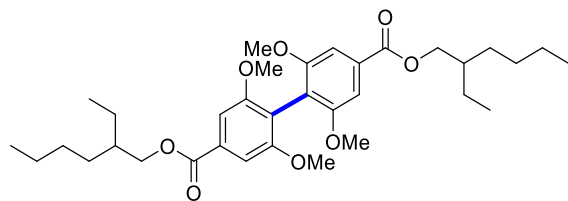
From dimethyl 2,2',6-trimethoxy-[1,1'-biphenyl]-4,4'-dicarboxylate (500 mg, 1 equiv) and 2-ethyl hexanol (1.81 g, 10 equiv), the title compound was prepared following **GP 5** as a translucent viscous oil (695 mg, 90% yield).

**<sup>1</sup>H NMR** (400 MHz, CDCl<sub>3</sub>, ppm): δ 7.70 (d, *J* = 7.8 Hz, 1H), 7.67 (d, *J* = 1.6 Hz, 1H), 7.35 (s, 2H), 7.22 (d, *J* = 7.8 Hz, 1H), 4.28 – 4.25 (m, 4H), 3.81 (s, 3H), 3.77 (s, 6H), 1.79 – 1.70 (m, 2H), 1.49 – 1.32 (m, 16H), 0.991 – 0.959 (m, 6H), 0.940 – 0.899 (m, 6H).

**<sup>13</sup>C NMR** (101 MHz, CDCl<sub>3</sub>, ppm): δ 11.1, 14.0, 23.0, 24.0, 24.1, 29.0, 30.6, 30.7, 39.0, 55.9, 56.1, 67.2, 67.6, 105.3, 111.9, 120.0, 121.6, 128.0, 131.1, 131.4, 131.7, 157.2, 157.7, 166.5, 166.7.

**HRMS (ESI<sup>+</sup>)** Calc: [M+H]<sup>+</sup> (C<sub>33</sub>H<sub>49</sub>O<sub>7</sub>) 557.3473; measured: 557.3469 = 0.7 ppm difference.

Bis(2-ethylhexyl) 2,2',6,6'-tetramethoxy-[1,1'-biphenyl]-4,4'-dicarboxylate (**S-S<sup>PL</sup>**)



From dimethyl 2,2',6,6'-tetramethoxy-[1,1'-biphenyl]-4,4'-dicarboxylate (500 mg, 1 equiv) and 2-ethyl hexanol (1.67 g, 10 equiv), the title compound was prepared following **GP 5** as a slightly yellow viscous oil (677 mg, 90% yield).

**<sup>1</sup>H NMR** (400 MHz, CDCl<sub>3</sub>, ppm): δ 7.36 (s, 4H), 4.29 – 4.23 (m, 4H), 3.78 (s, 12H), 1.76 – 1.72 (m, 2H), 1.49 – 1.32 (m, 16H), 0.99 – 0.90 (m, 12H).

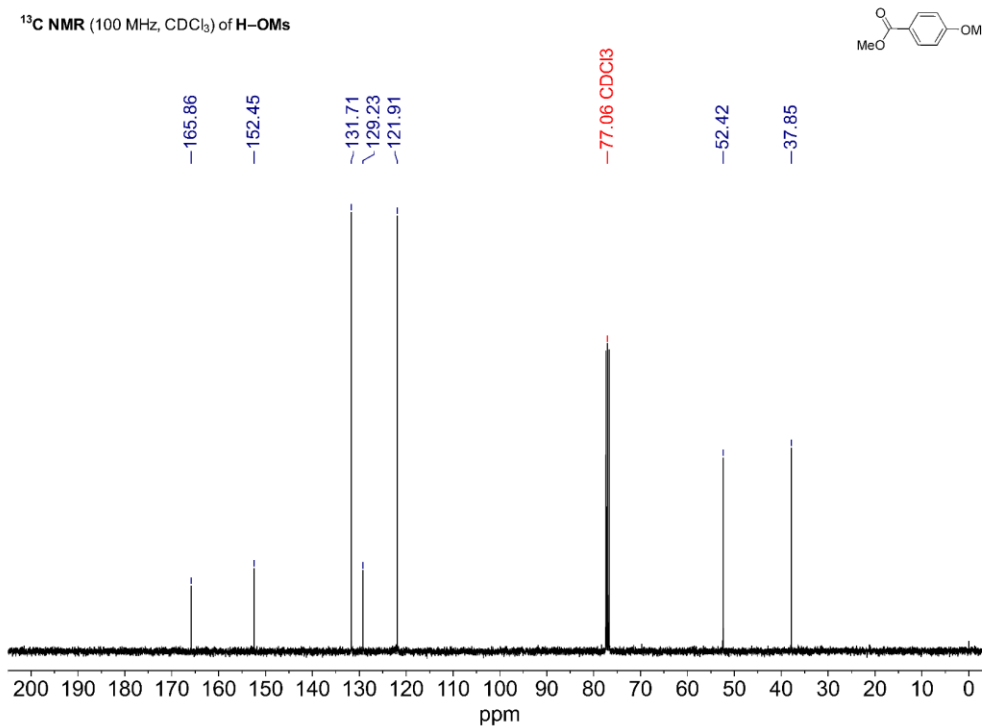
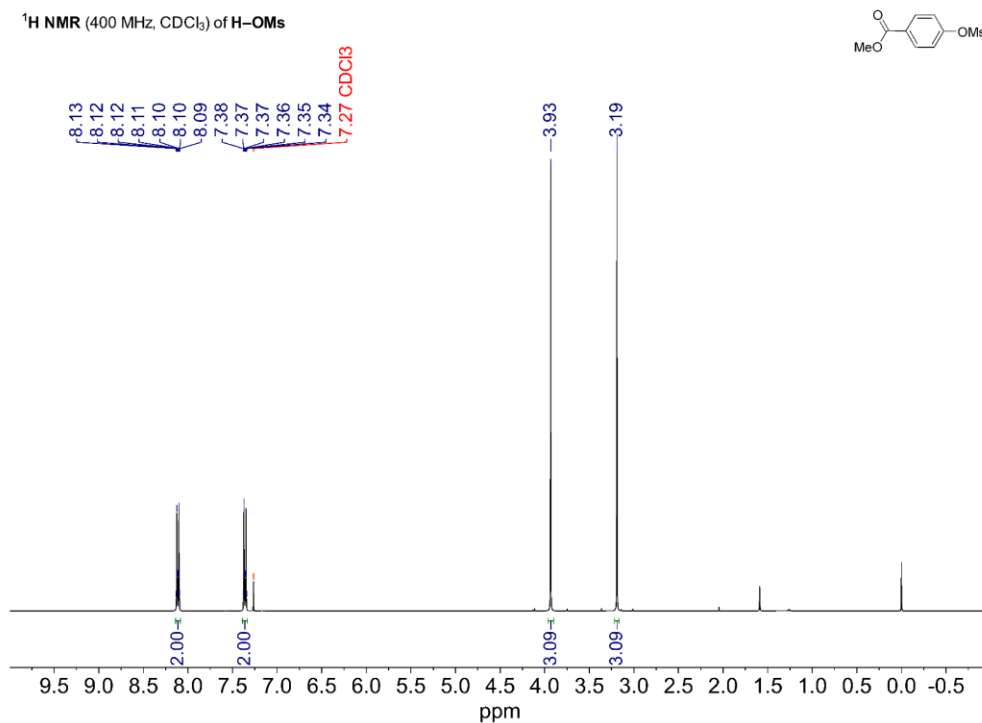
**<sup>13</sup>C NMR** (101 MHz, CDCl<sub>3</sub>, ppm): δ 166.6, 158.0, 131.4, 116.7, 105.5, 67.5, 56.2, 39.0, 30.8, 29.0, 24.2, 23.0, 14.1, 11.2.

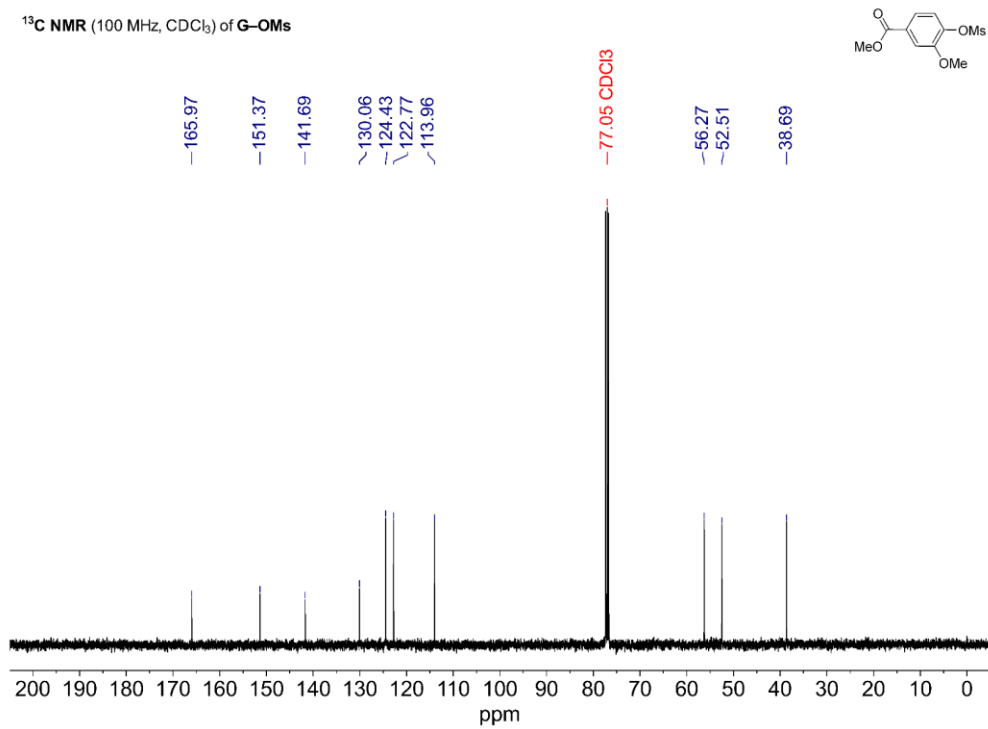
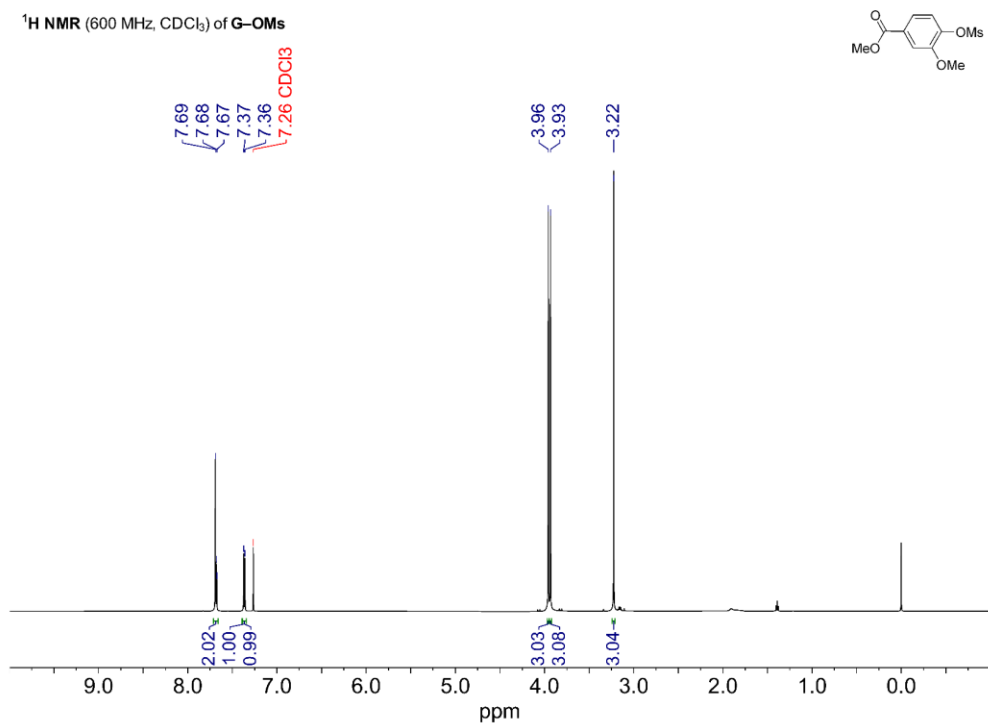
**HRMS (ESI<sup>+</sup>)** Calc: [M+H]<sup>+</sup> (C<sub>34</sub>H<sub>51</sub>O<sub>8</sub>) 587.3579; measured: 587.3573 = 1.0 ppm difference.

## 2A.IX. References

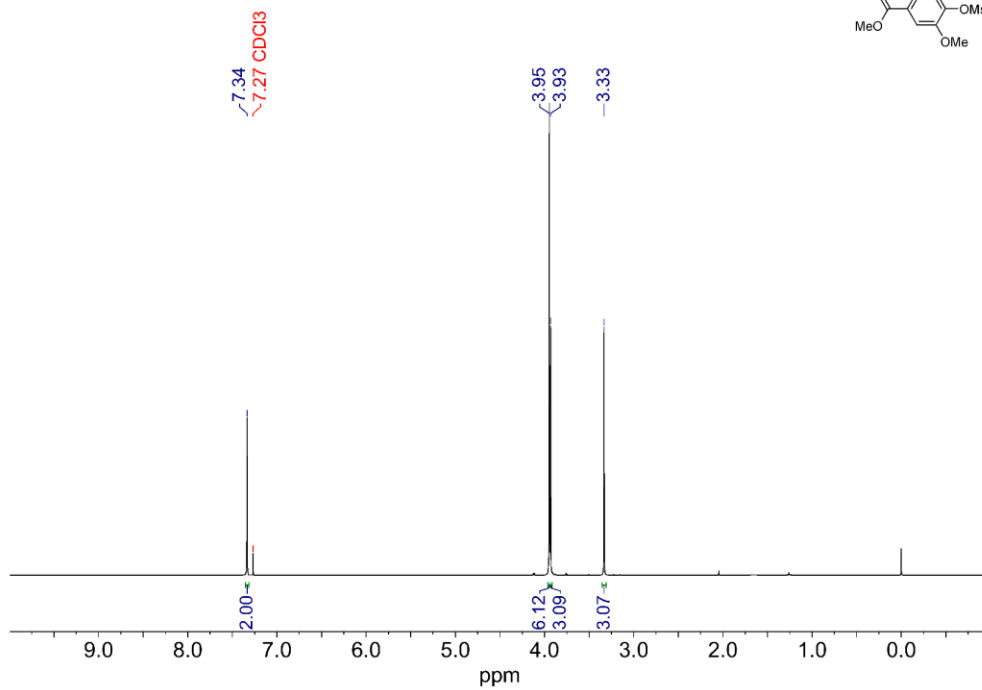
1. Mori, A.; Mizusaki, T.; Ikawa, T.; Maegawa, T.; Monguchi, Y.; Sajiki, H. Mechanistic Study of a Pd/C-Catalyzed Reduction of Aryl Sulfonates Using the Mg–MeOH–NH<sub>4</sub>OAc System. *Chem. Eur. J.* **2007**, *13*, 1432–1441.
2. Boehm, P.; Roediger, S.; Bismuto, A.; Morandi, B. Palladium-Catalyzed Chlorocarbonylation of Aryl (Pseudo)Halides Through In Situ Generation of Carbon Monoxide. *Angew. Chem. Int. Ed.* **2020**, *59*, 17887–17896.
3. Zhong, X.; Hoque, M. A.; Graaf, M. D.; Harper, K. C.; Wang, F.; Genders, J. D.; Stahl, S. S. Scalable Flow Electrochemical Alcohol Oxidation: Maintaining High Stereochemical Fidelity in the Synthesis of Levetiracetam. *Org. Process Res. Dev.* **2021**, *25*, 2601–2607.
4. Percec, V.; Bae, J.-Y.; Zhao, M.; Hill, D. H. Aryl Mesylates in Metal-Catalyzed Homocoupling and Cross-Coupling Reactions. 1. Functional Symmetrical Biaryls from Phenols via Nickel-Catalyzed Homocoupling of Their Mesylates. *J. Org. Chem.* **1995**, *60*, 176.
5. Zackasee, J. L. S.; Al Zubaydi, S.; Truesdell, B. L.; Sevov, C. S. Synergistic Catalyst–Mediator Pairings for Electroreductive Cross-Electrophile Coupling Reactions. *ACS Catal.* **2022**, 1161–1166.
6. Kawamata, Y.; Vantourout, J. C.; Hickey, D. P.; Bai, P.; Chen, L.; Hou, Q.; Qiao, W.; Barman, K.; Edwards, M. A.; Garrido-Castro, A. F.; deGruyter, J. N.; Nakamura, H.; Knouse, K.; Qin, C.; Clay, K. J.; Bao, D.; Li, C.; Starr, J. T.; Garcia-Irizarry, C.; Sach, N.; White, H. S.; Neurock, M.; Minter, S. D.; Baran, P. S. Electrochemically Driven, Ni-Catalyzed Aryl Amination: Scope, Mechanism, and Applications. *J. Am. Chem. Soc.* **2019**, *141*, 6392–6402.
7. Skrzypek, J.; Lachowska, M.; Kulawska, M.; Moroz, H. Synthesis of Bis(2-Ethylhexyl) Phthalate over Methane Sulfonic Acid Catalyst. Kinetic Investigations. *React Kinet Catal Lett* **2008**, *93*, 281–286.
8. Gubbels, E.; Drijfhout, J. P.; Posthuma-van Tent, C.; Jasinska-Walc, L.; Noordover, B. A. J.; Koning, C. E. Bio-Based Semi-Aromatic Polyesters for Coating Applications. *Prog. Org. Coat.* **2014**, *77*, 277–284.
9. Martin, T. M. *T. E. S. T. (Toxicity Estimation Software Tool) Version 5.1*, 5.1; United State Environmental Protection Agency: 2020.
10. EPA, U. S., Chemical Transformation Simulator (CTS), Version 1.0. *Chemical Transformation Simulator (CTS), Version 1.0* 2019.
11. Wilson, D. A.; Wilson, C. J.; Moldoveanu, C.; Resmerita, A.-M.; Corcoran, P.; Hoang, L. M.; Rosen, B. M.; Percec, V. Neopentylglycolborylation of Aryl Mesylates and Tosylates Catalyzed by Ni-Based Mixed-Ligand Systems Activated with Zn. *J. Am. Chem. Soc.* **2010**, *132*, 1800–1801.
12. Yanagita, H.; Yamamoto, N.; Fuji, H.; Liu, X.; Ogata, M.; Yokota, M.; Takaku, H.; Hasegawa, H.; Odagiri, T.; Tashiro, M.; Hoshino, T. Mechanism of Drug Resistance of Hemagglutinin of Influenza Virus and Potent Scaffolds Inhibiting Its Function. *ACS Chem. Biol.* **2012**, *7*, 552–562.
13. Malineni, J.; Jezorek, R. L.; Zhang, N.; Percec, V. An Indefinitely Air-Stable  $\sigma$ -Ni(II) Precatalyst for Quantitative Cross-Coupling of Unreactive Aryl Halides and Mesylates with Aryl Neopentylglycolboronates. *Synthesis* **2016**, *48*, 2795–2807.
14. Rankine, D.; Avellaneda, A.; Hill, M. R.; Doonan, C. J.; Sumbly, C. J. Control of Framework Interpenetration for in Situ Modified Hydroxyl Functionalised IRMOFs. *Chem. Commun.* **2012**, *48*, 10328–10330.
15. Burrows, A. D.; Frost, C. G.; Mahon, M. F.; Richardson, C. Post-Synthetic Modification of Tagged Metal–Organic Frameworks. *Angew. Chem. Int. Ed.* **2008**, *47*, 8482–8486.

## 2A.X. NMR Spectra of Compounds

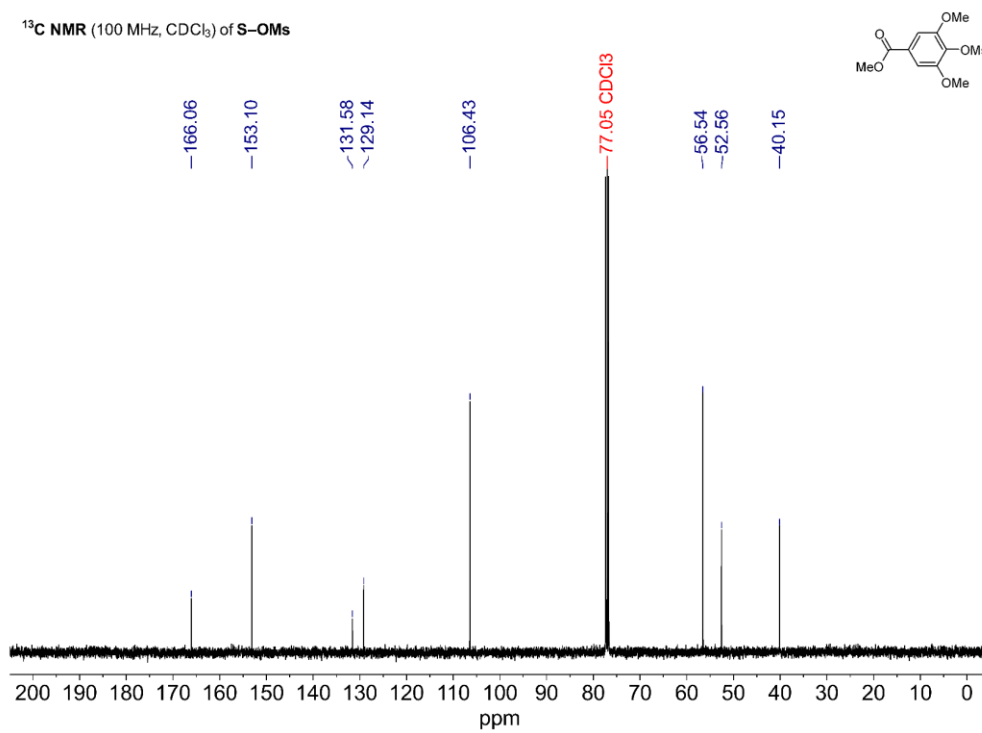


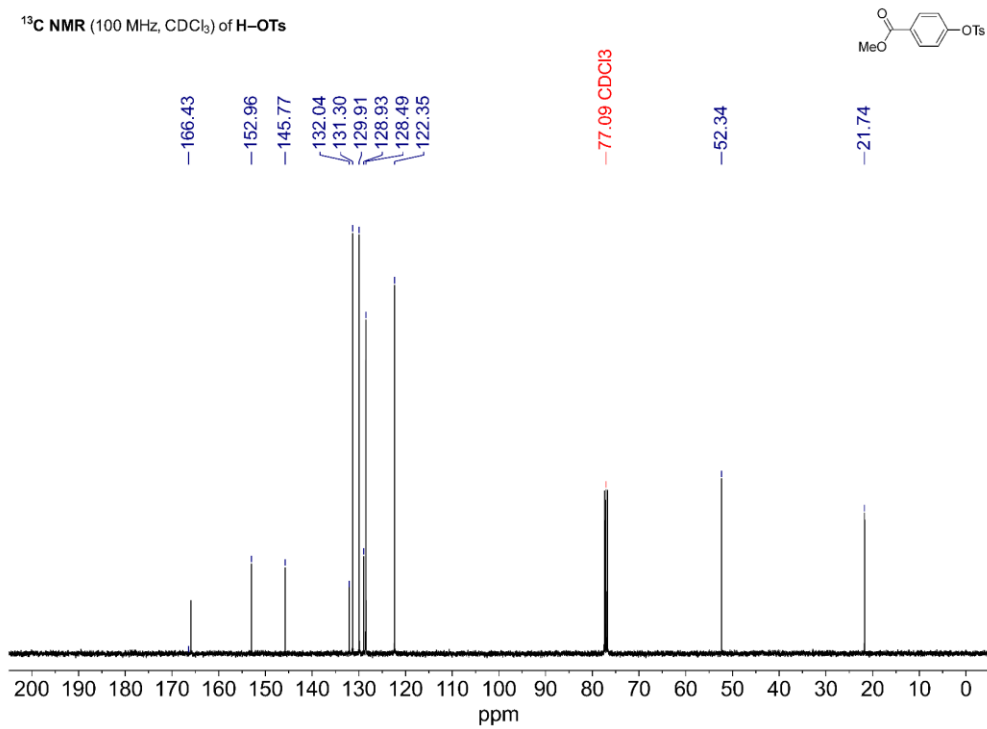
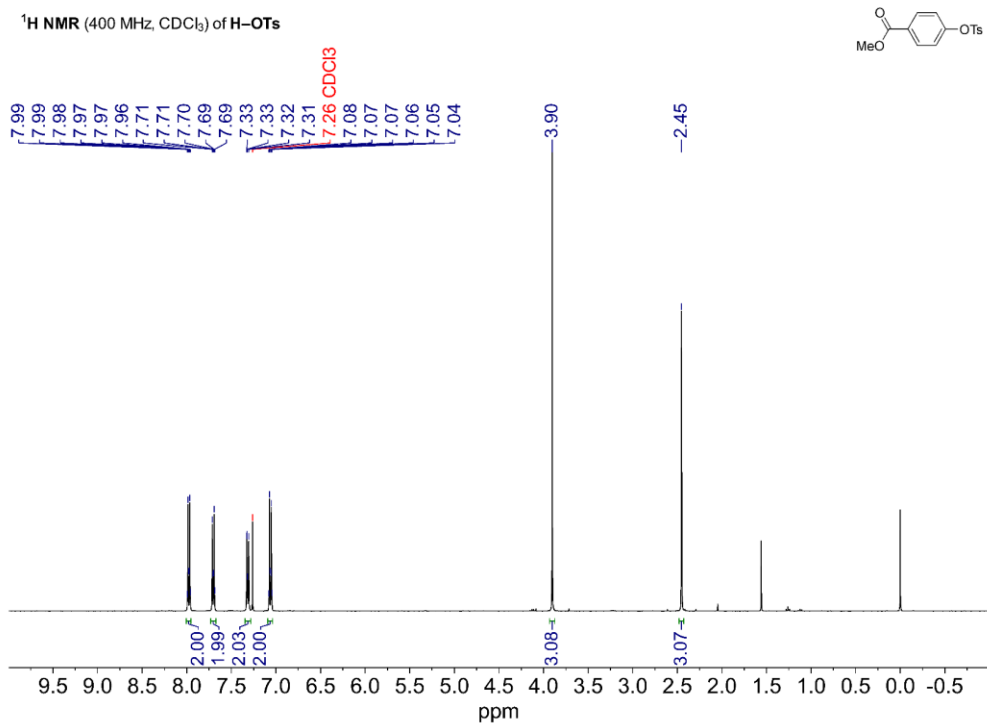


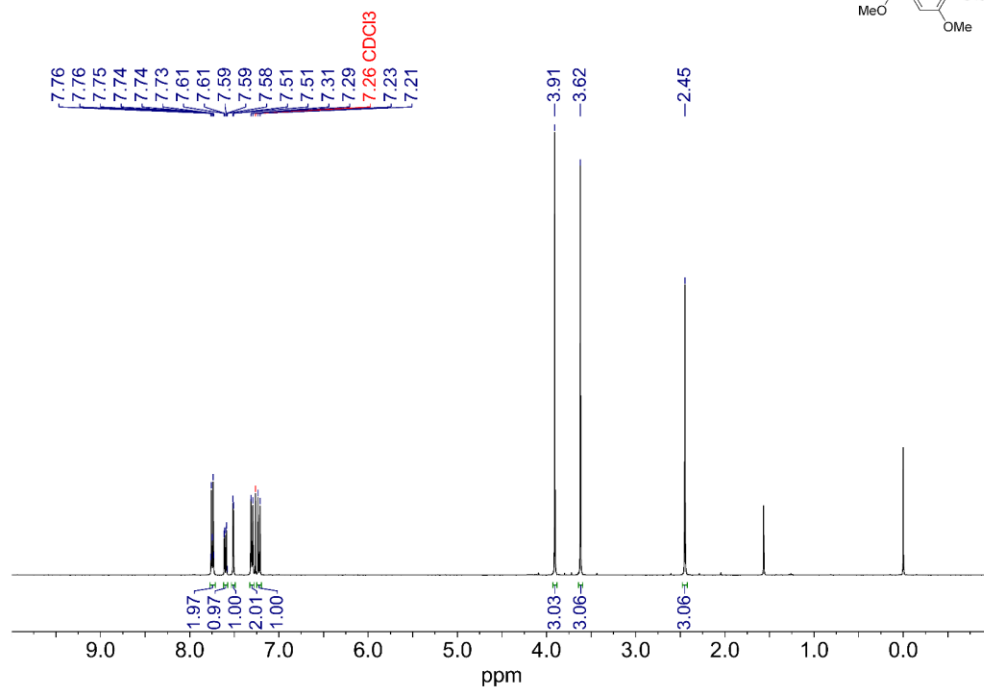
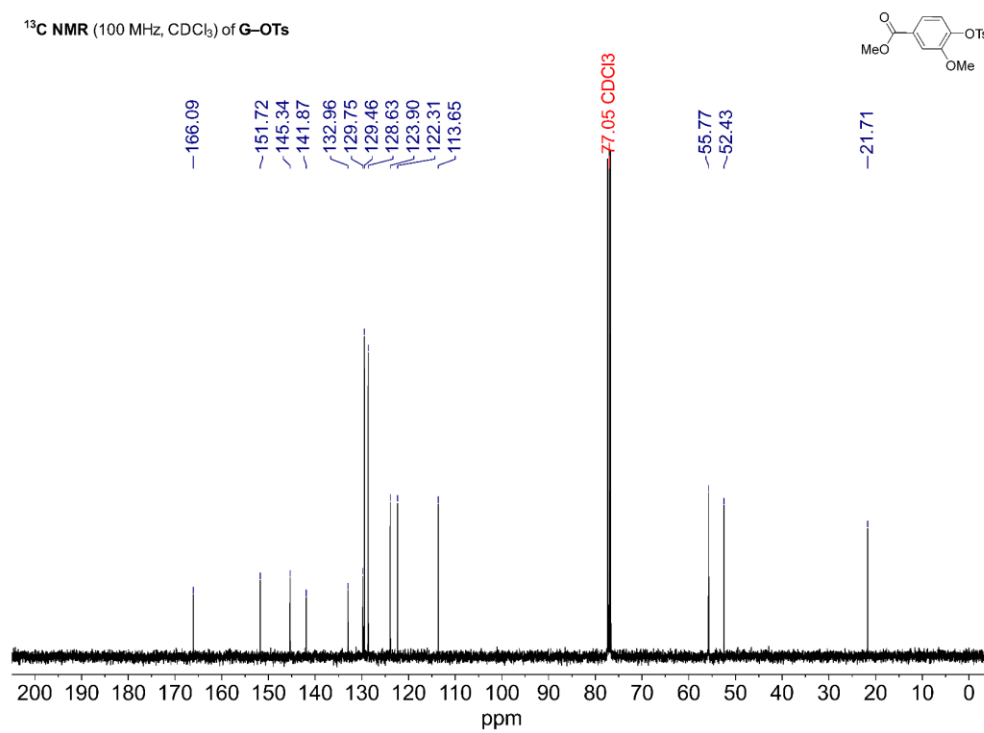
<sup>1</sup>H NMR (400 MHz, CDCl<sub>3</sub>) of S-OMs

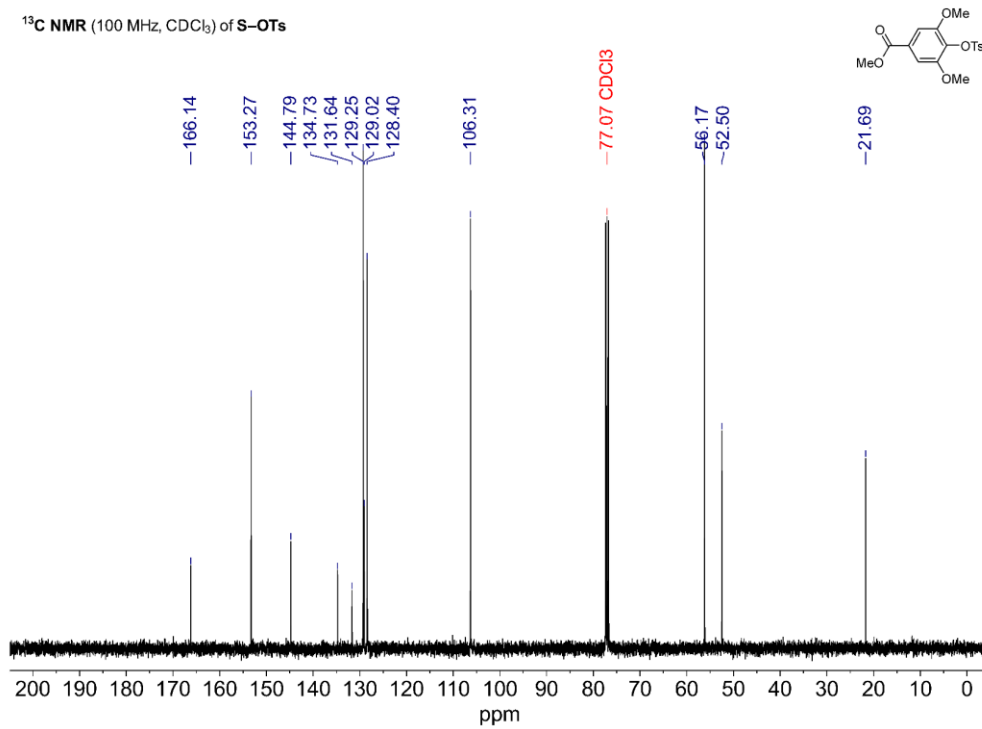
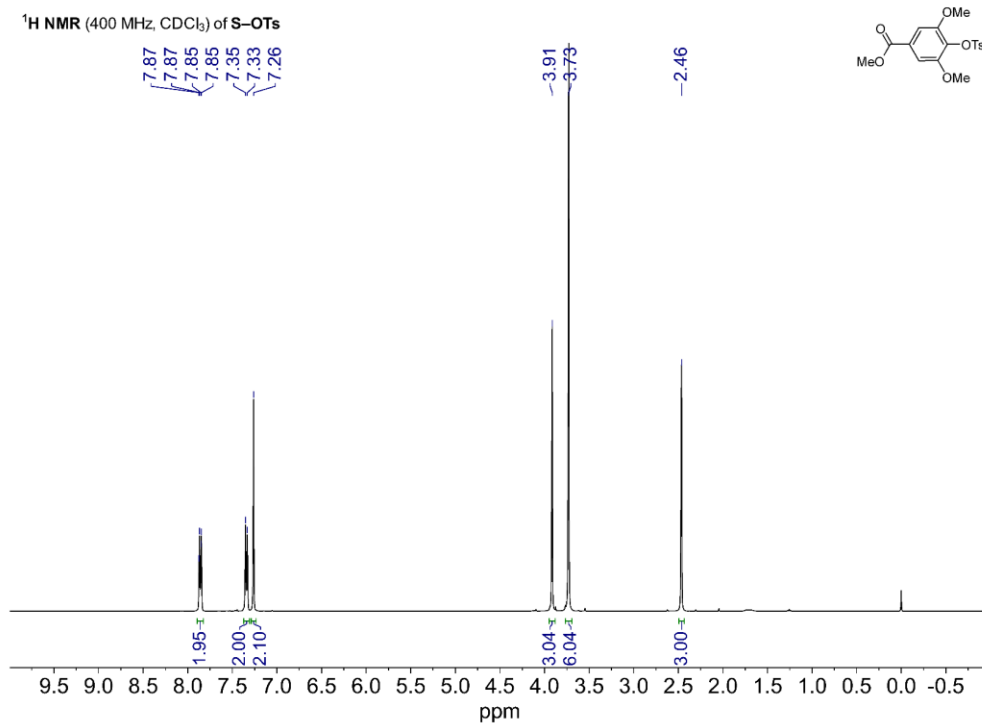


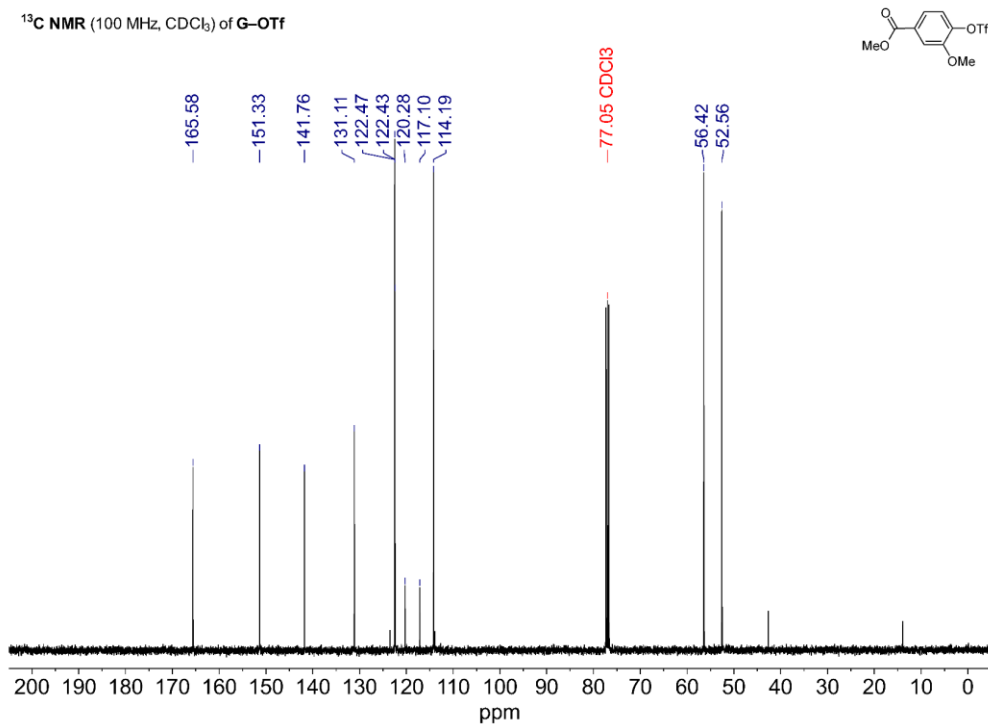
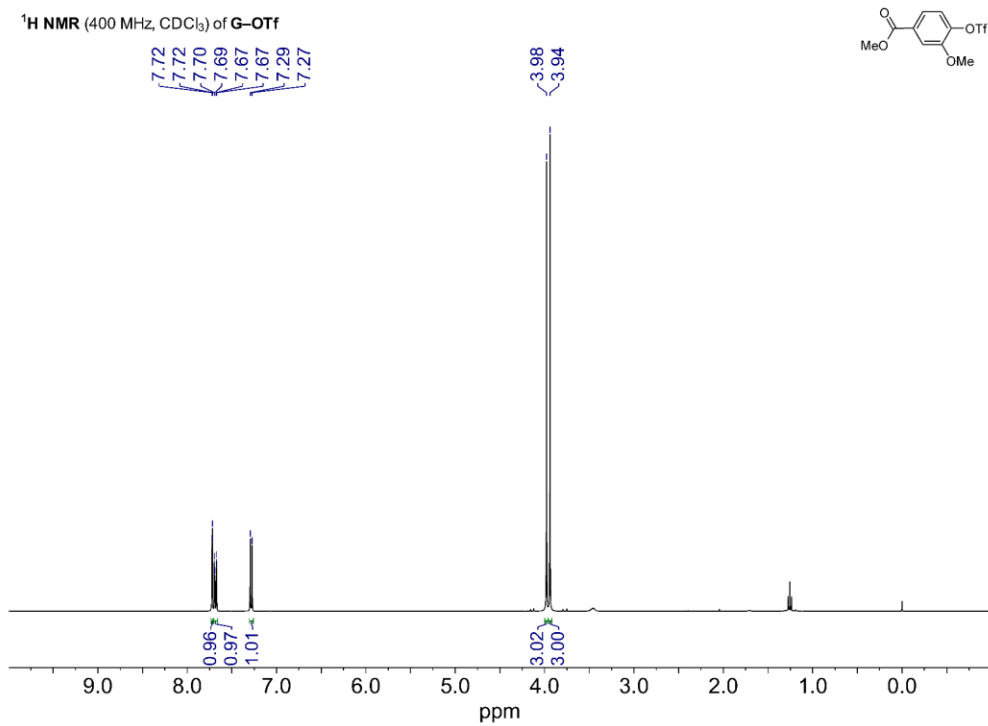
<sup>13</sup>C NMR (100 MHz, CDCl<sub>3</sub>) of S-OMs



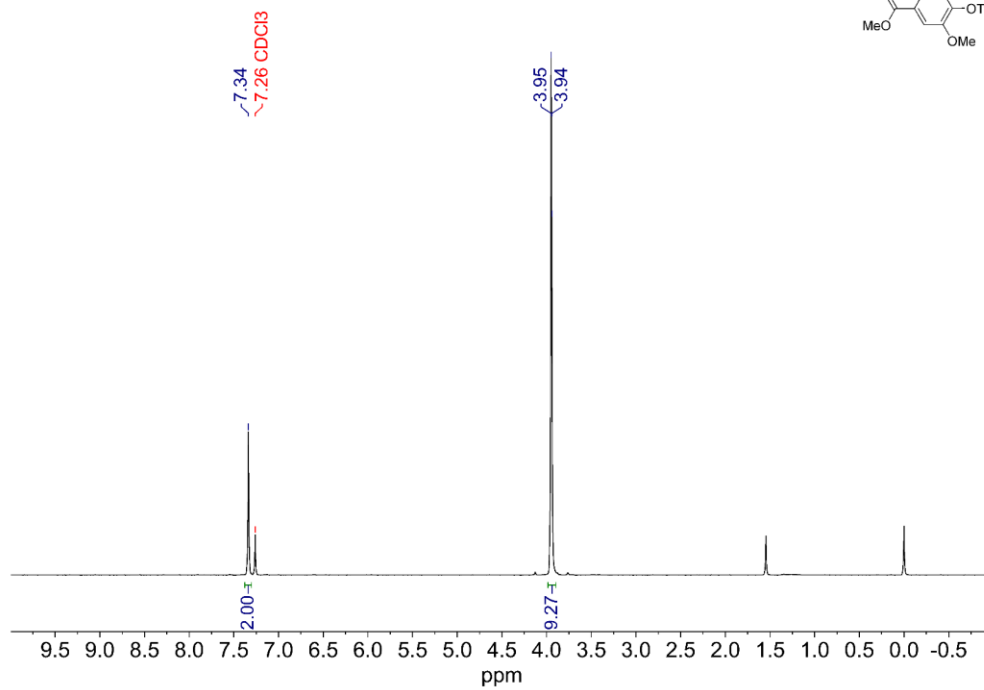


<sup>1</sup>H NMR (400 MHz, CDCl<sub>3</sub>) of G-OTs<sup>13</sup>C NMR (100 MHz, CDCl<sub>3</sub>) of G-OTs

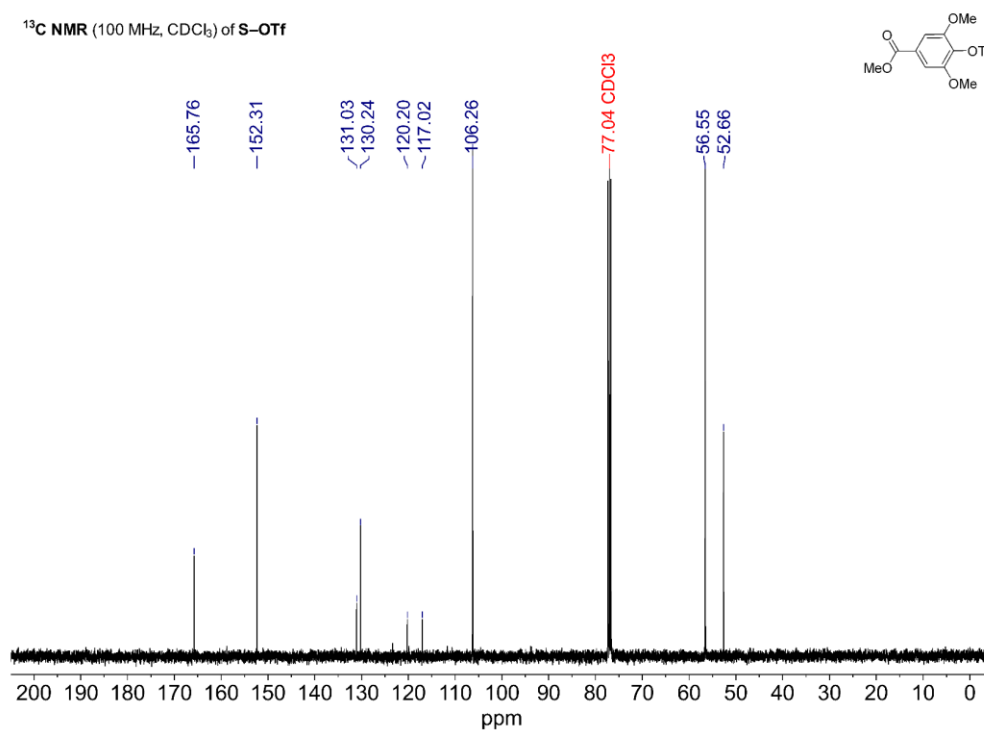


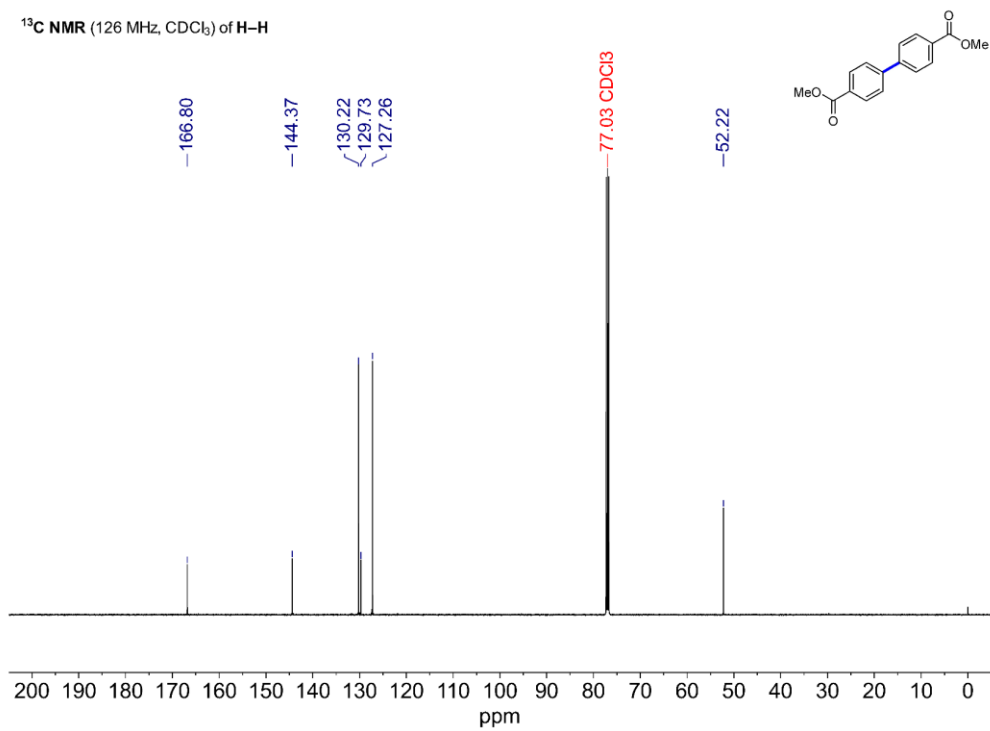
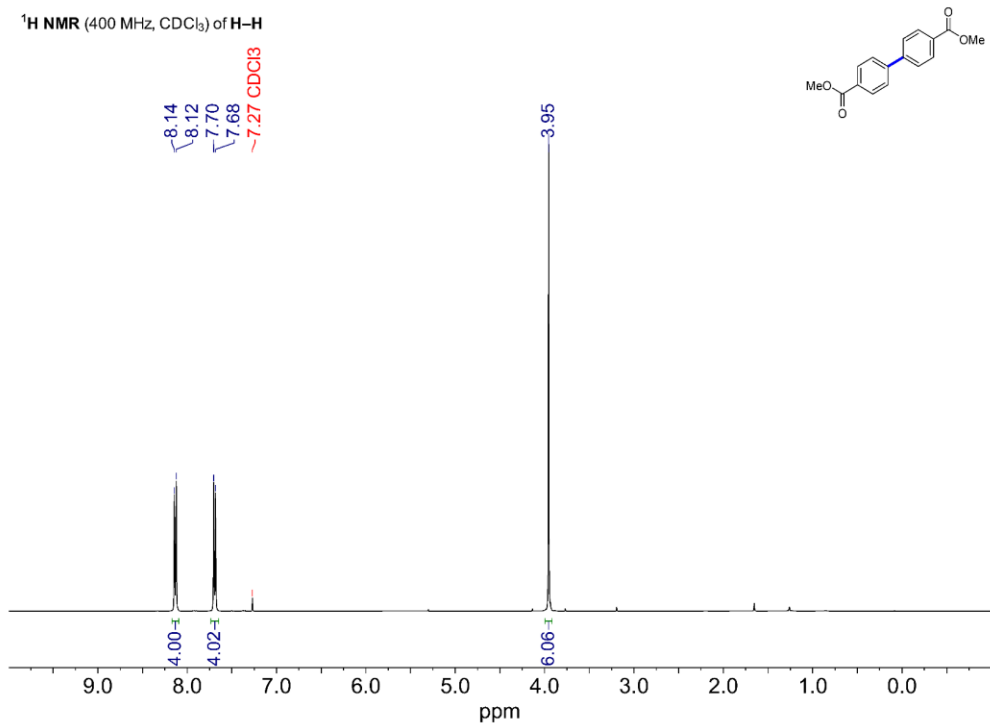


<sup>1</sup>H NMR (400 MHz, CDCl<sub>3</sub>) of S-OTf

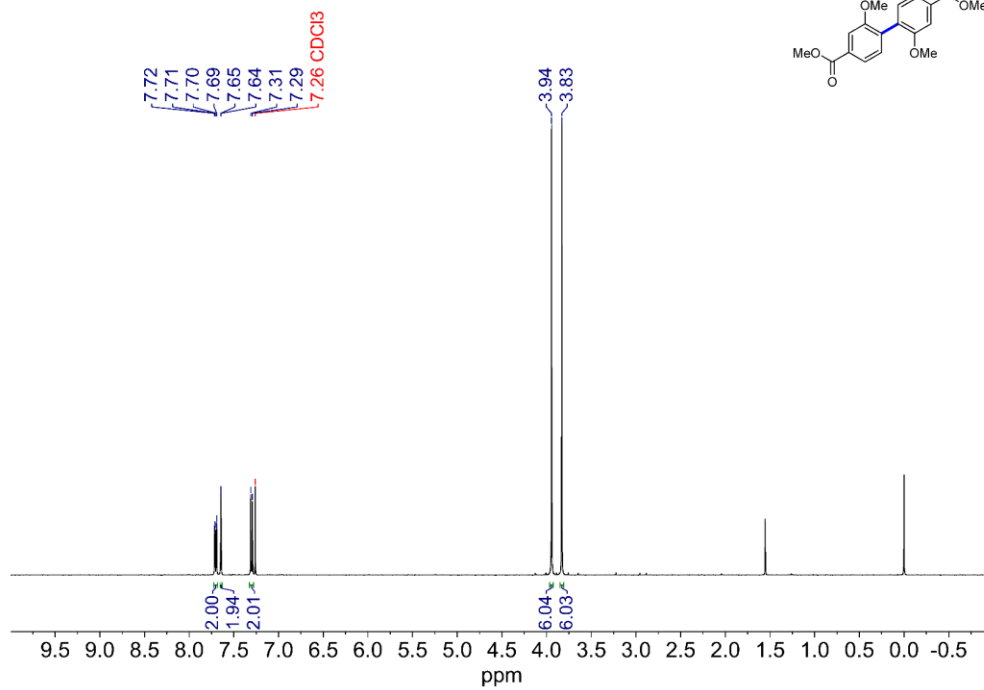


<sup>13</sup>C NMR (100 MHz, CDCl<sub>3</sub>) of S-OTf

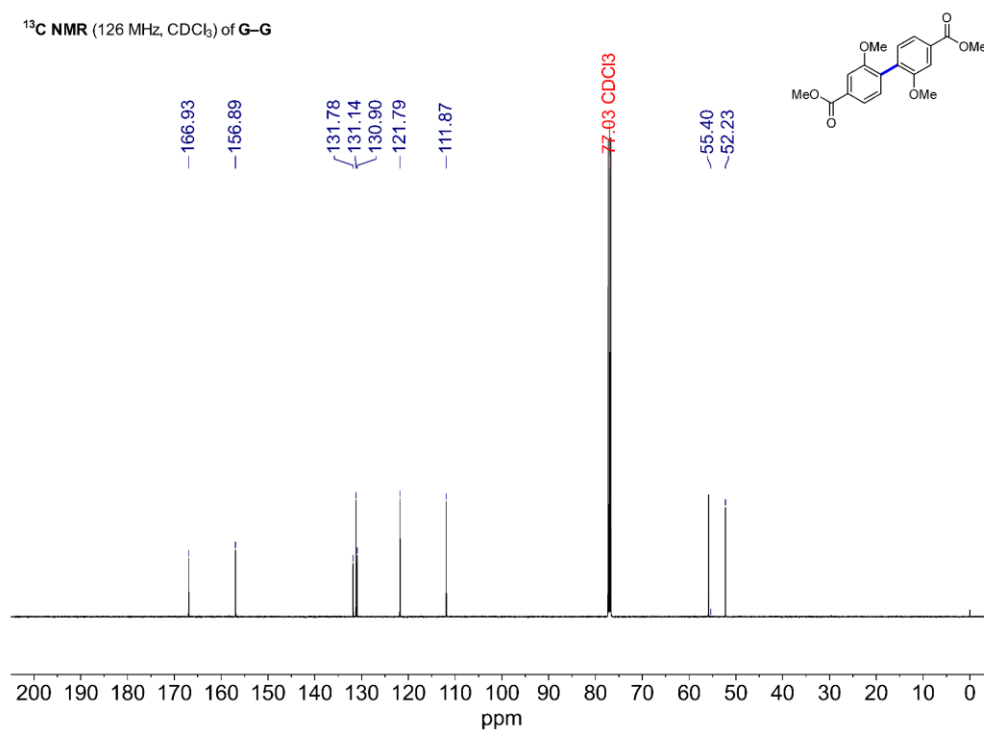




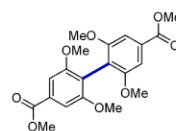
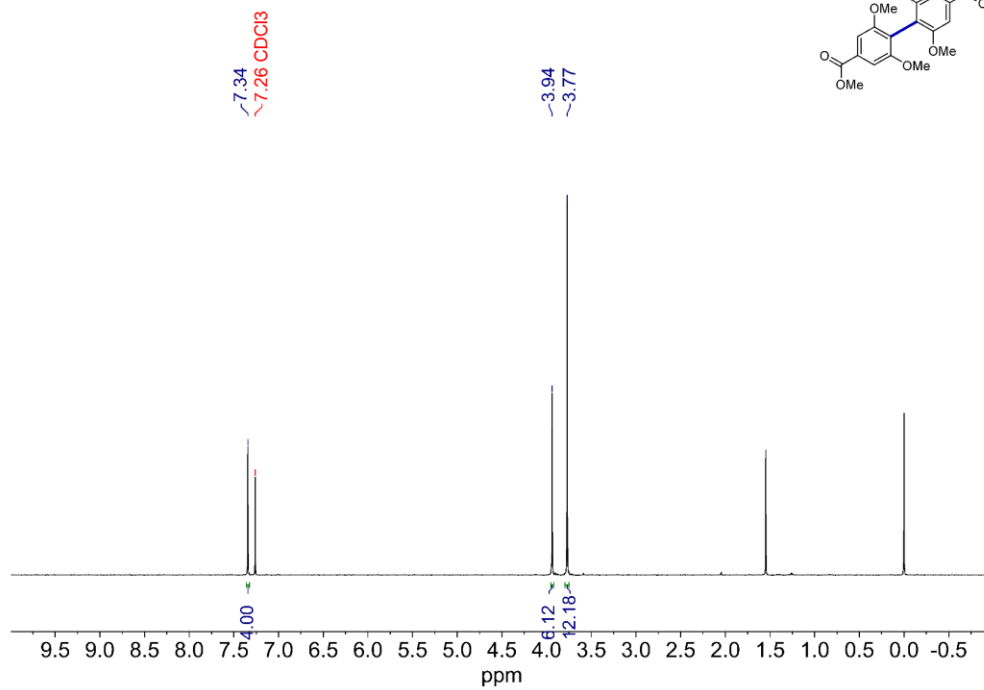
<sup>1</sup>H NMR (400 MHz, CDCl<sub>3</sub>) of G-G



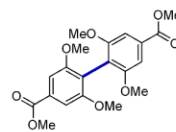
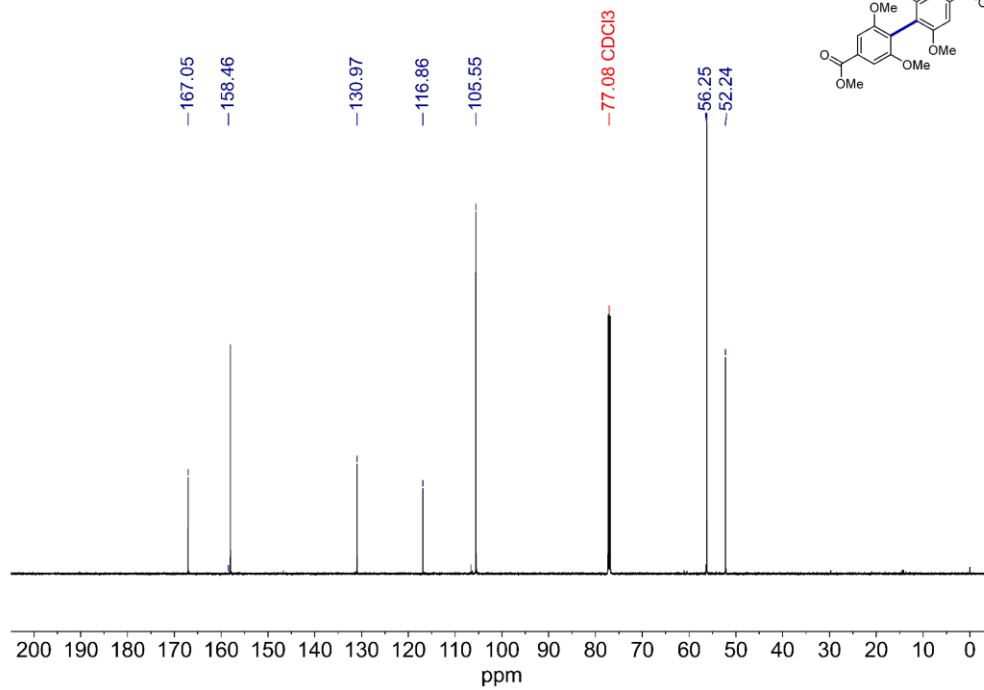
<sup>13</sup>C NMR (126 MHz, CDCl<sub>3</sub>) of G-G

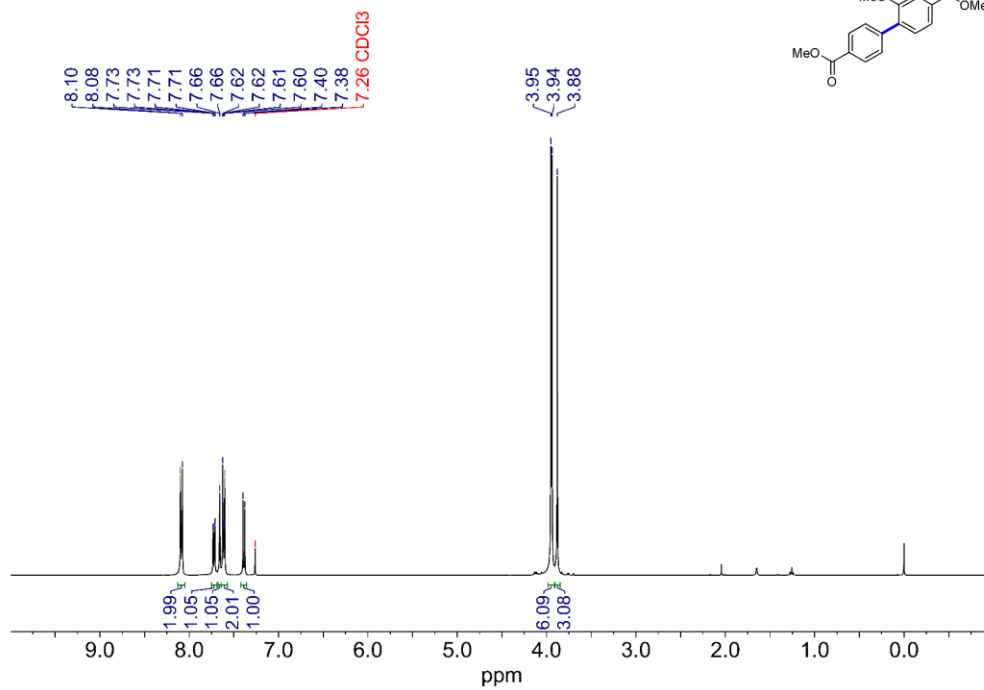
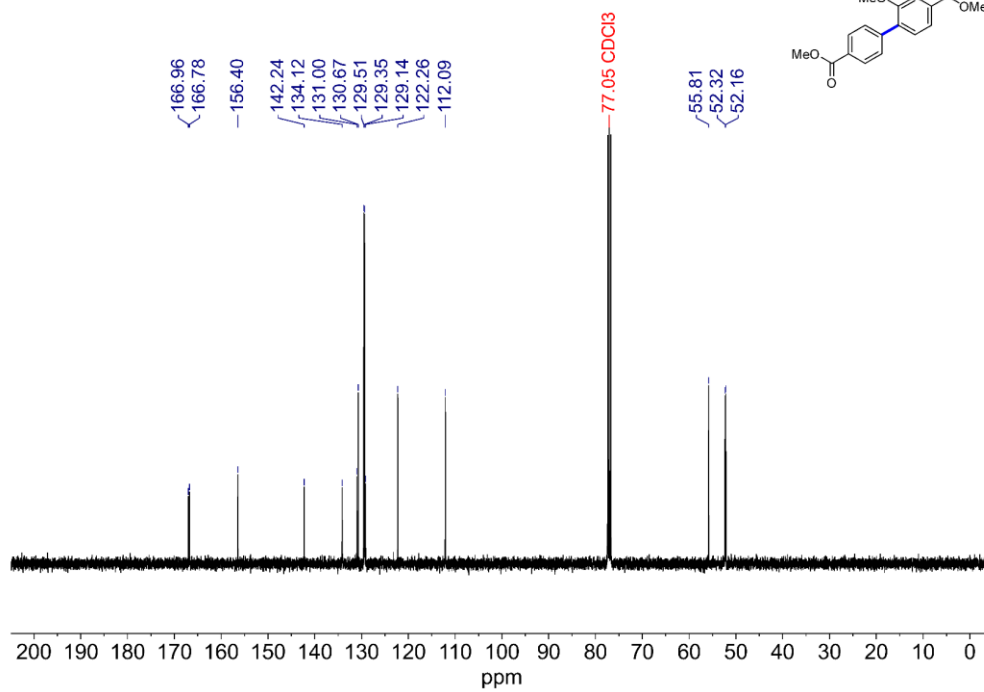


<sup>1</sup>H NMR (400 MHz, CDCl<sub>3</sub>) of S-S

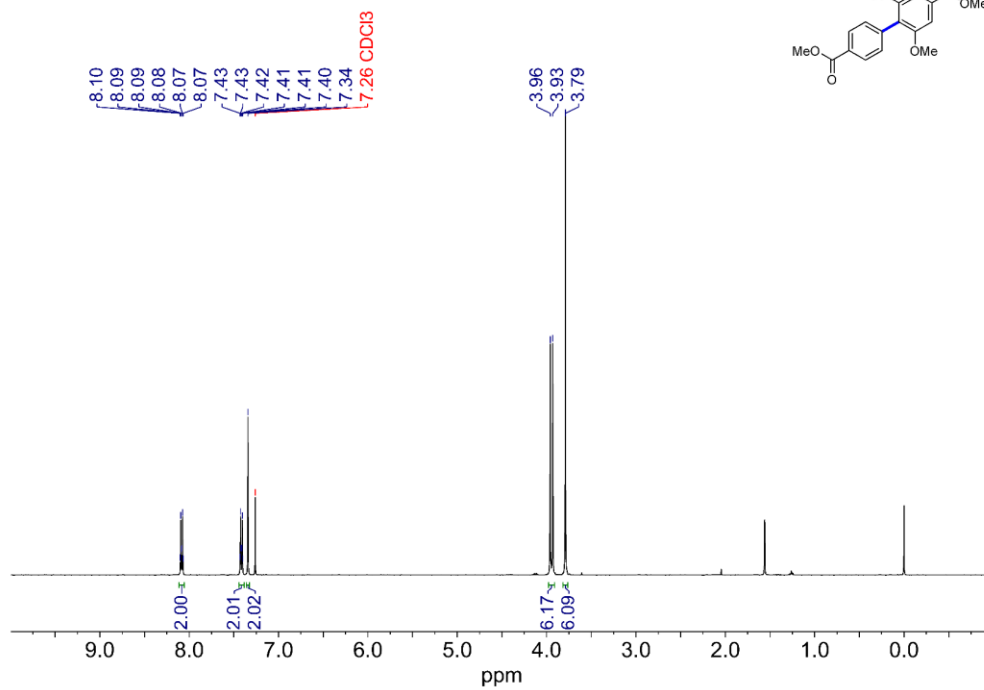


<sup>13</sup>C NMR (151 MHz, CDCl<sub>3</sub>) of S-S

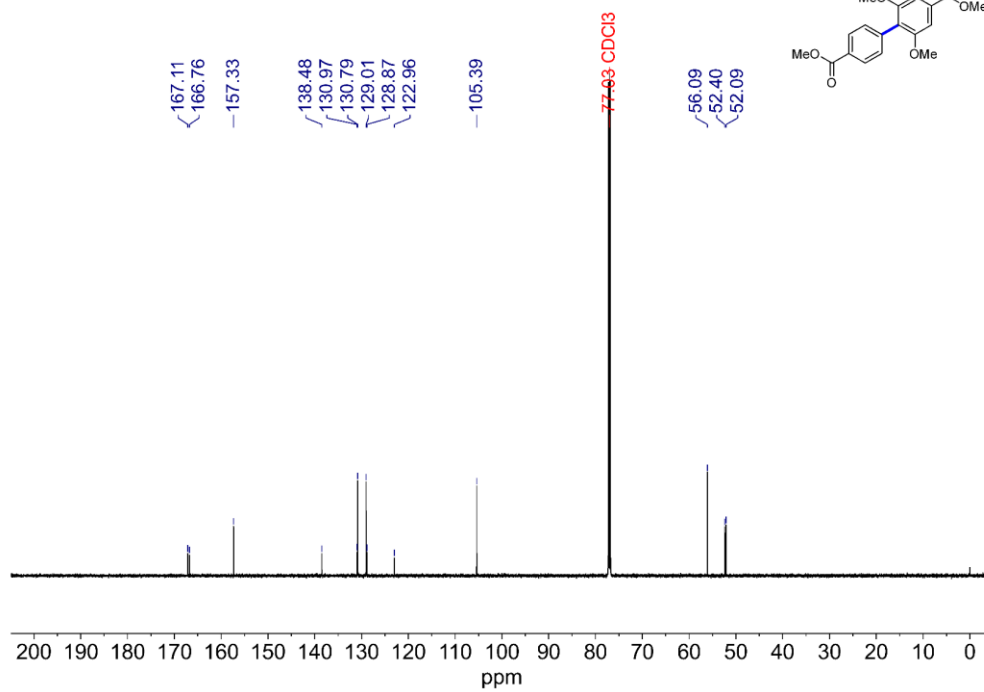


<sup>1</sup>H NMR (400 MHz, CDCl<sub>3</sub>) of H-G<sup>13</sup>C NMR (100 MHz, CDCl<sub>3</sub>) of H-G

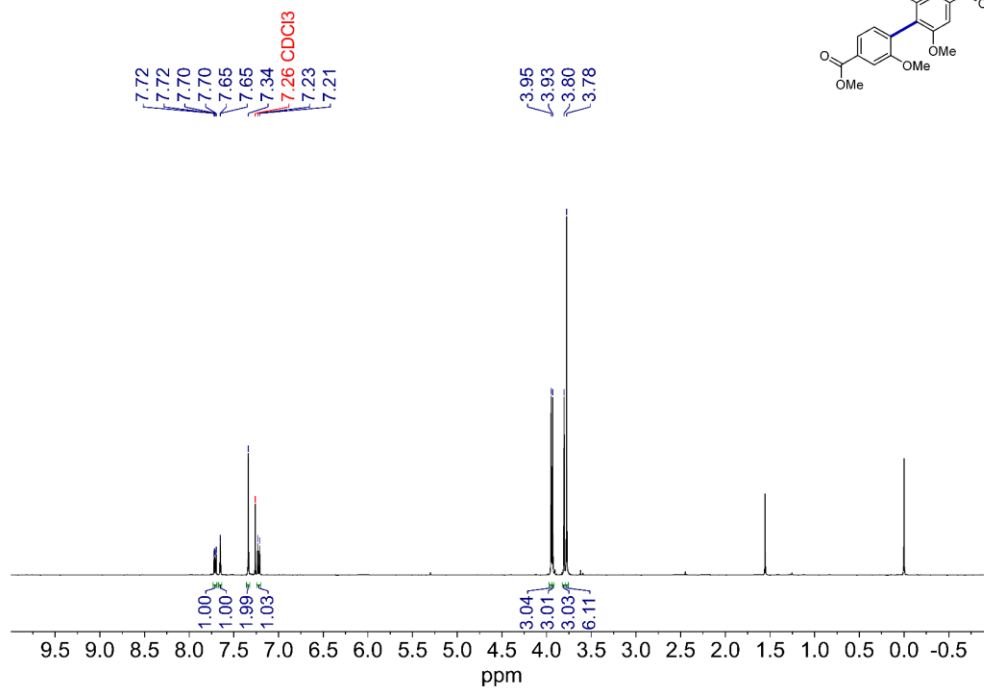
<sup>1</sup>H NMR (400 MHz, CDCl<sub>3</sub>) of H-S



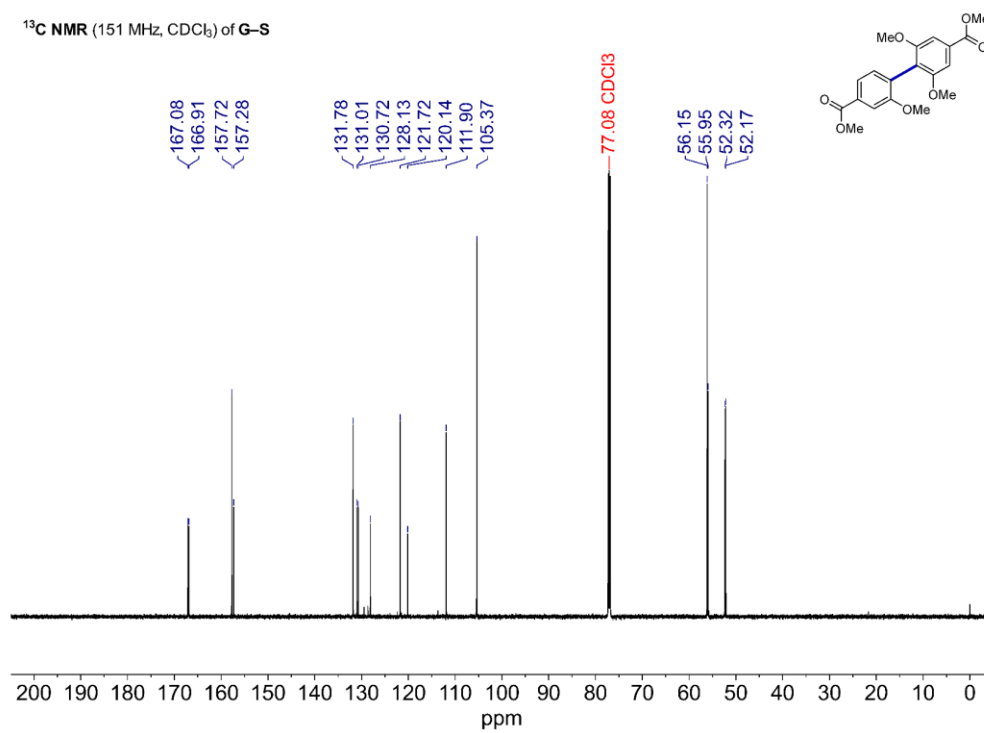
<sup>13</sup>C NMR (151 MHz, CDCl<sub>3</sub>) of H-S

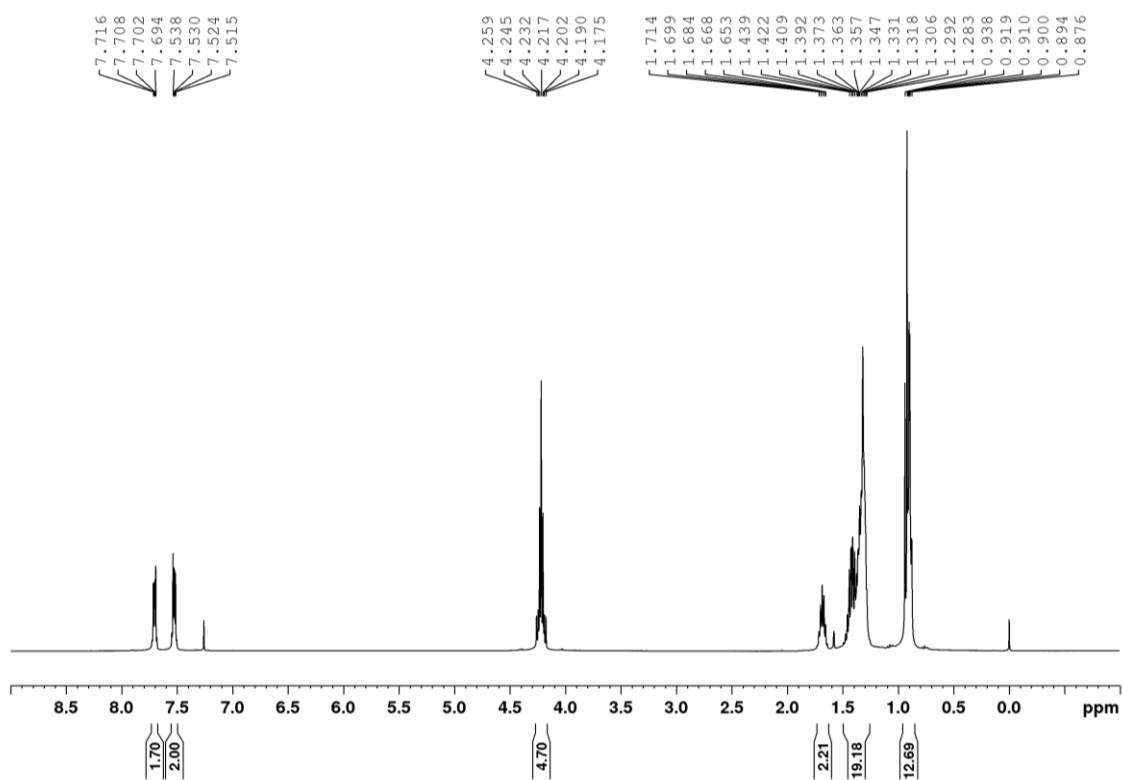
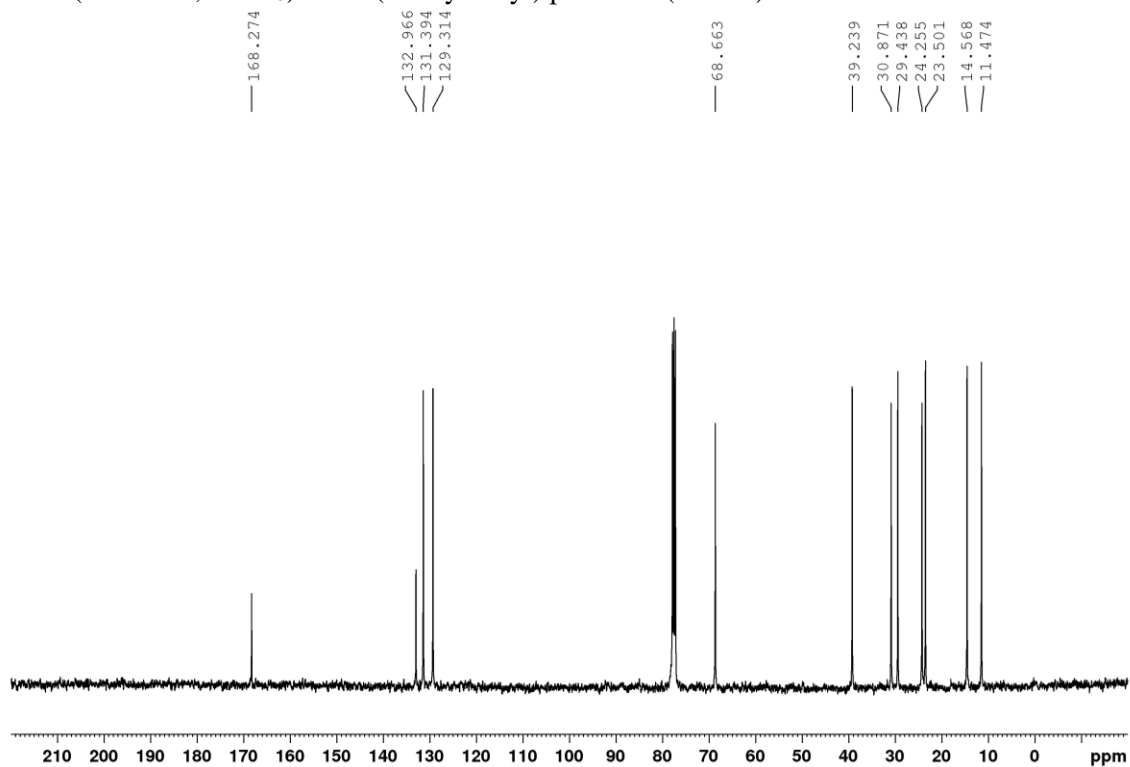


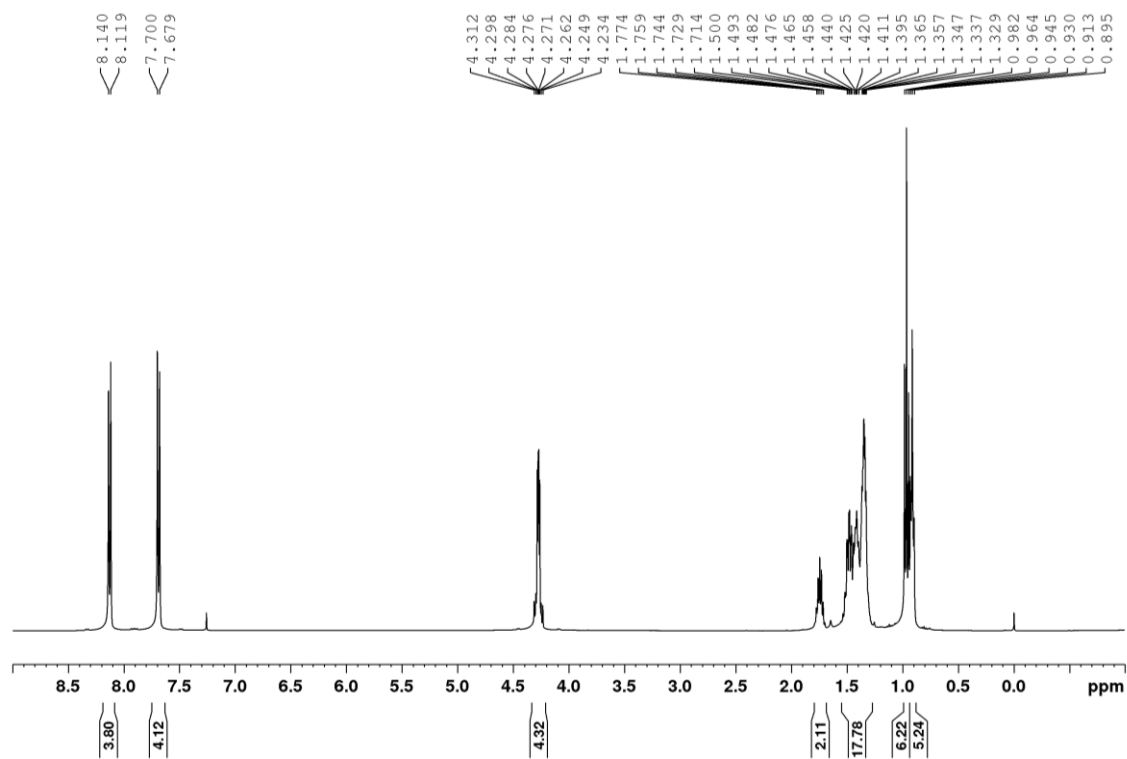
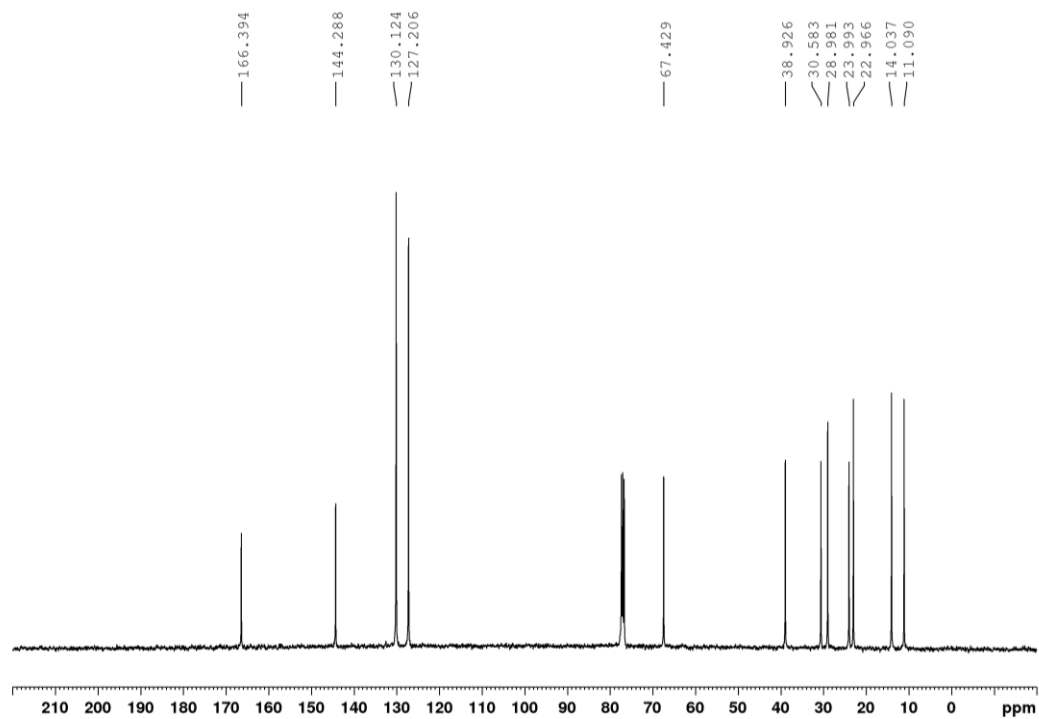
<sup>1</sup>H NMR (400 MHz, CDCl<sub>3</sub>) of G-S

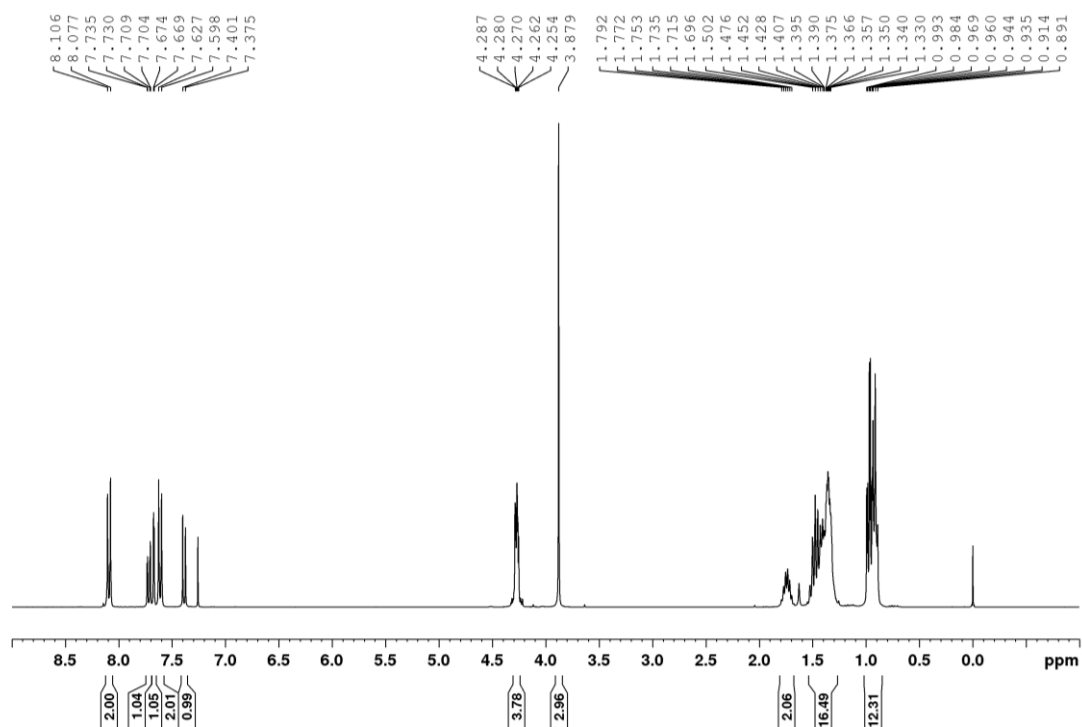
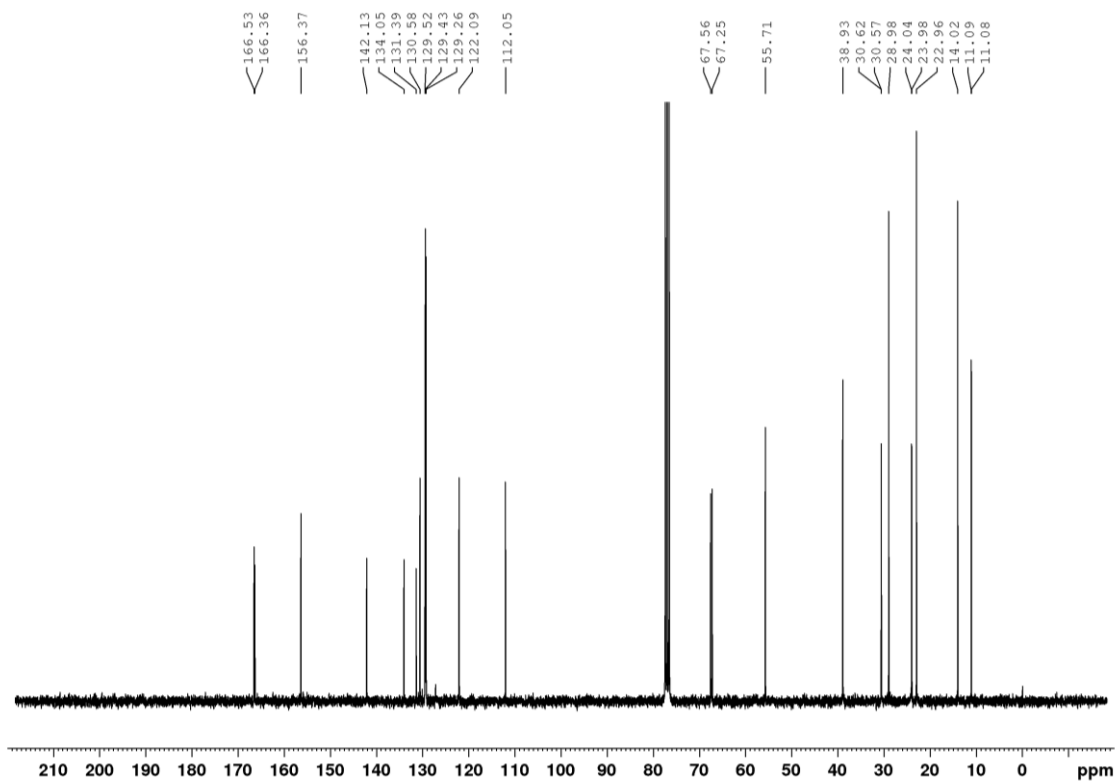


<sup>13</sup>C NMR (151 MHz, CDCl<sub>3</sub>) of G-S

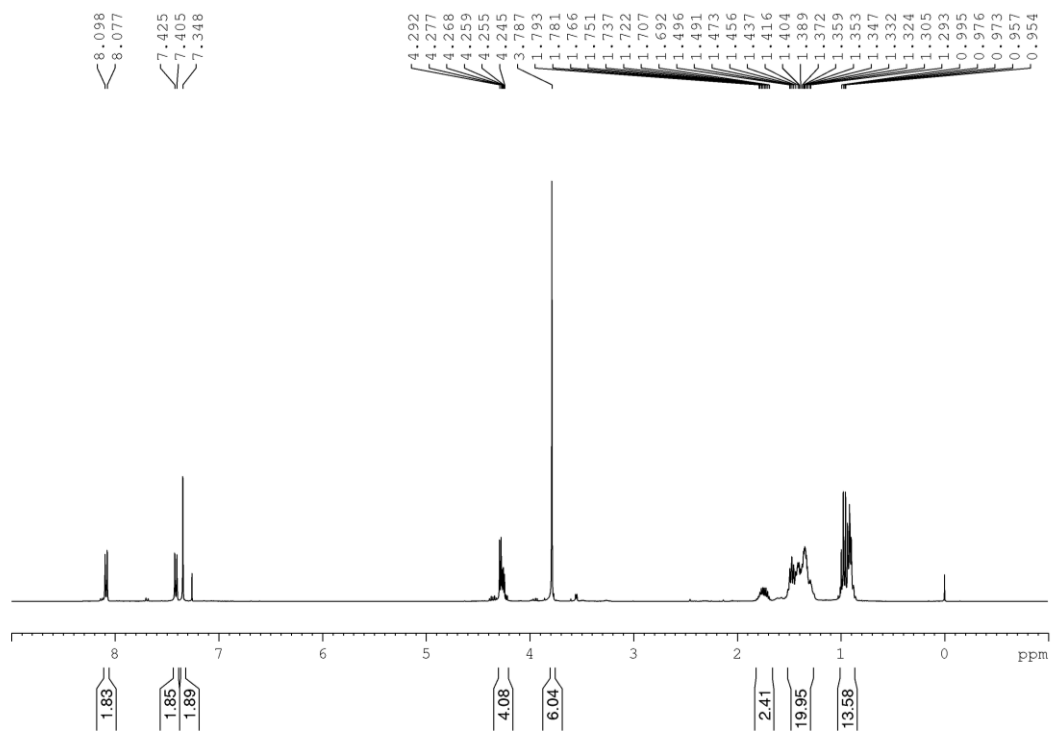


**<sup>1</sup>H NMR (400 MHz, CDCl<sub>3</sub>) of Bis(2-ethylhexyl) phthalate (DEHP)****<sup>13</sup>C NMR (101 MHz, CDCl<sub>3</sub>) of Bis(2-ethylhexyl) phthalate (DEHP)**

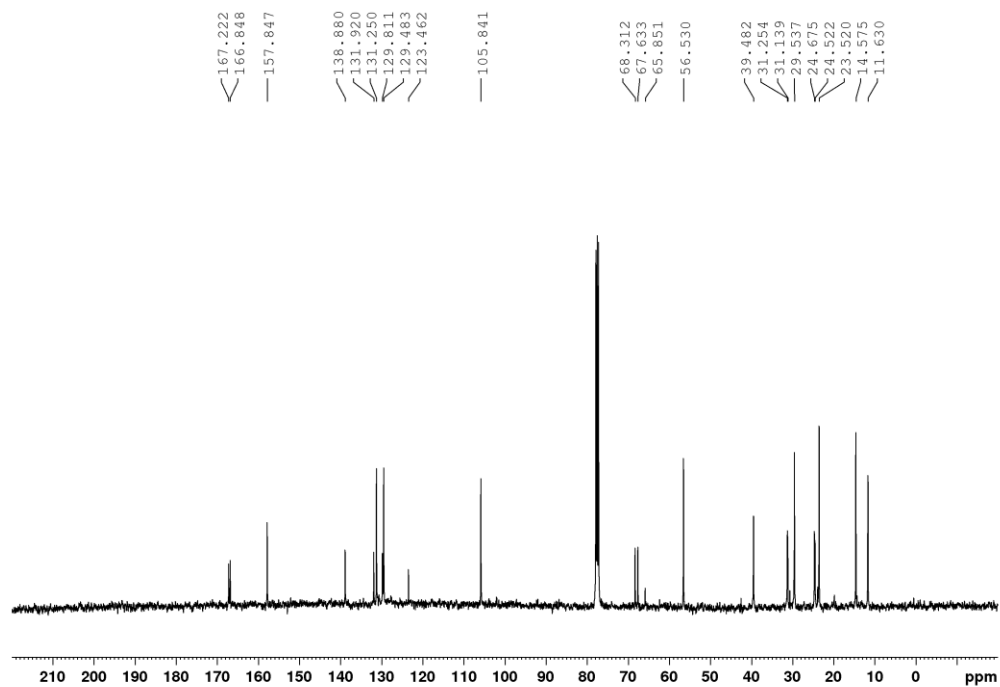
**$^1\text{H}$  NMR (400MHz,  $\text{CDCl}_3$ ) of Bis(2-ethylhexyl)[1,1'-biphenyl]-4,4'-dicarboxylate (**H-H<sup>PL</sup>**)** **$^{13}\text{C}$  NMR (101 MHz,  $\text{CDCl}_3$ ) of Bis(2-ethylhexyl)[1,1'-biphenyl]-4,4'-dicarboxylate (**H-H<sup>PL</sup>**)**

**$^1\text{H}$  NMR (400 MHz,  $\text{CDCl}_3$ ) of Bis(2-ethylhexyl) 2-methoxy-[1,1'-biphenyl]-4,4'-dicarboxylate (**H-G<sup>PL</sup>**)** **$^{13}\text{C}$  NMR (101 MHz,  $\text{CDCl}_3$ ) of Bis(2-ethylhexyl) 2-methoxy-[1,1'-biphenyl]-4,4'-dicarboxylate (**H-G<sup>PL</sup>**)**

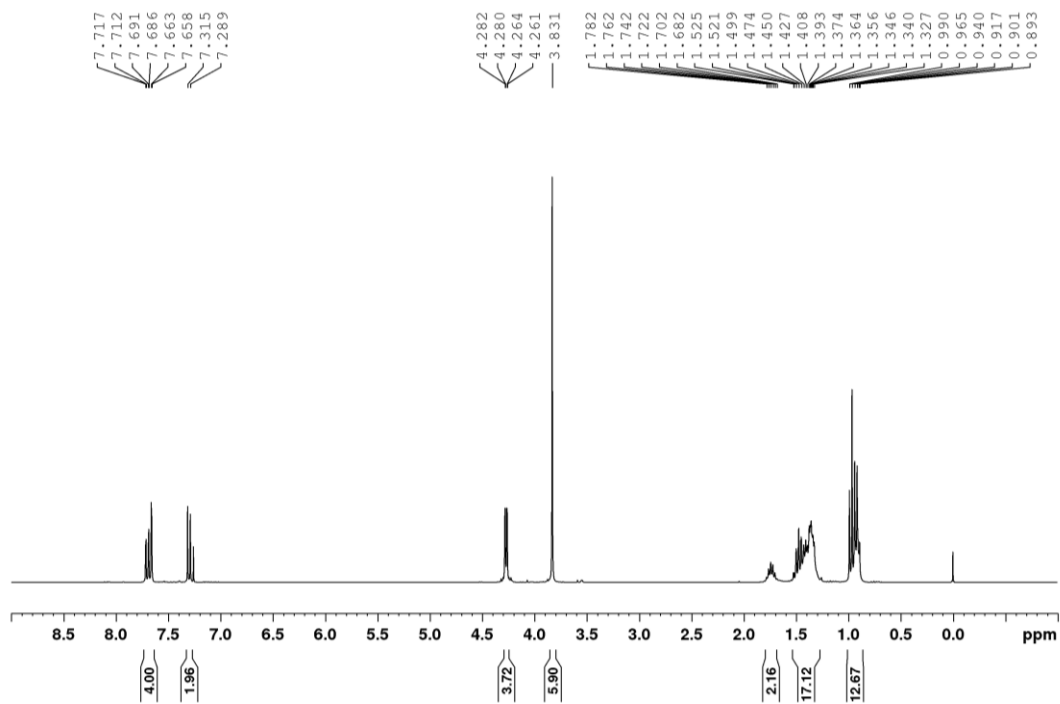
$^1\text{H}$  NMR (400 MHz,  $\text{CDCl}_3$ ) of Bis(2-ethylhexyl) 2,6-dimethoxy-[1,1'-biphenyl]-4,4'-dicarboxylate (**H-S<sup>PL</sup>**)



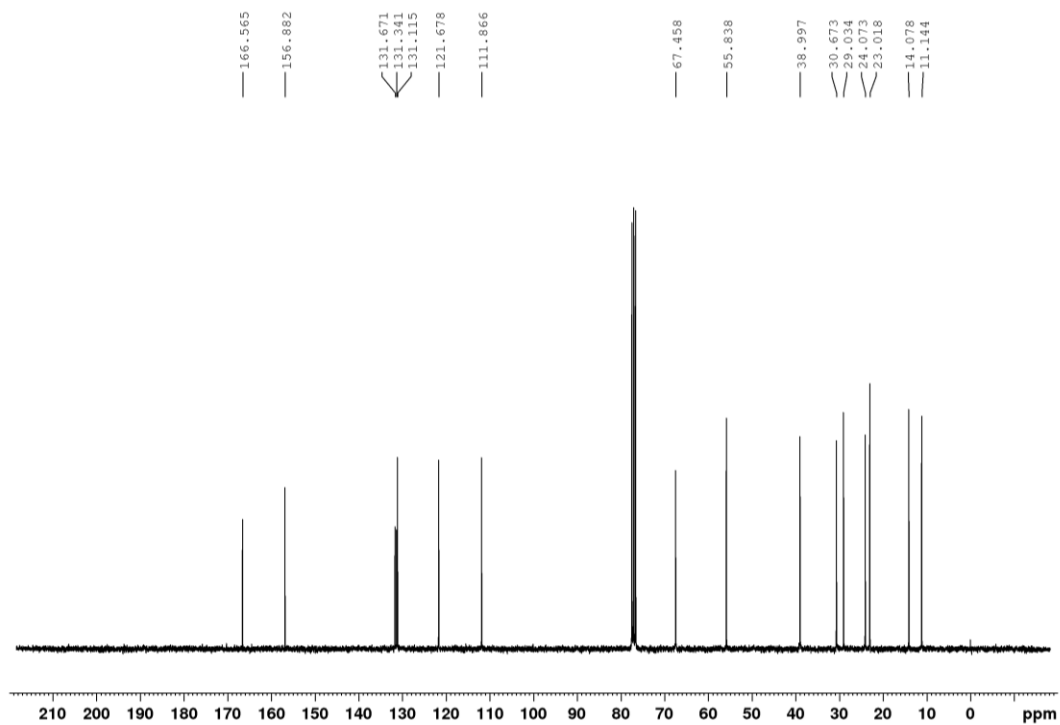
$^{13}\text{C}$  NMR (101 MHz,  $\text{CDCl}_3$ ) of Bis(2-ethylhexyl) 2,6-dimethoxy-[1,1'-biphenyl]-4,4'-dicarboxylate (**H-S<sup>PL</sup>**)



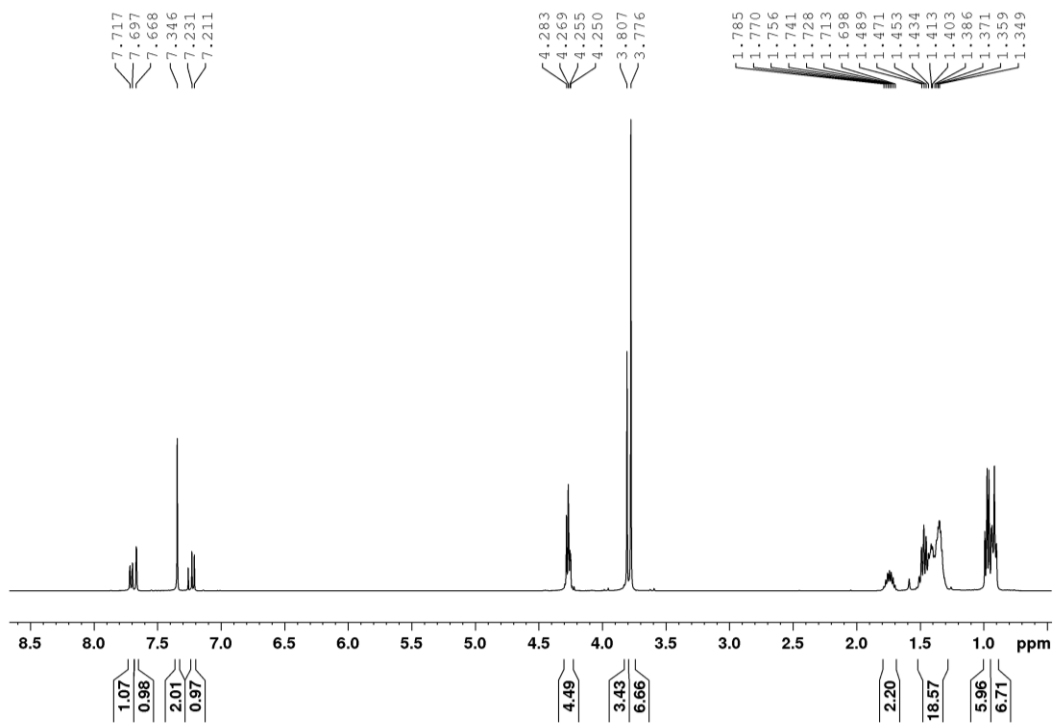
$^1\text{H}$  NMR (400 MHz,  $\text{CDCl}_3$ ) of Bis(2-ethylhexyl) 2,2'-dimethoxy-[1,1'-biphenyl]-4,4'-dicarboxylate ( $\text{G}^{\text{PL}}$ )



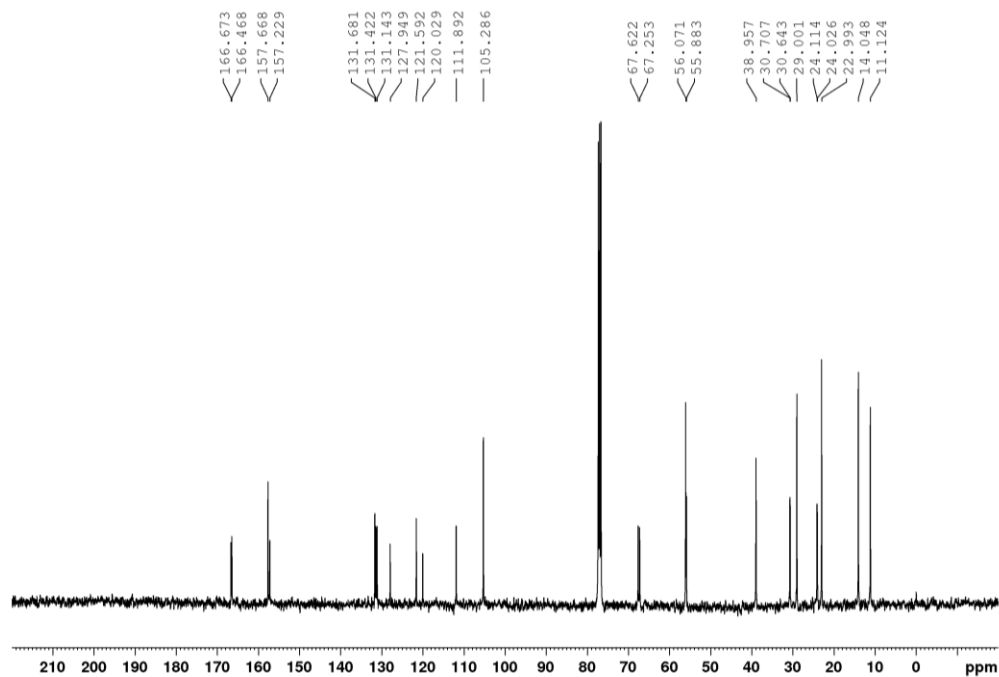
$^{13}\text{C}$  NMR (101 MHz,  $\text{CDCl}_3$ ) of Bis(2-ethylhexyl) 2,2'-dimethoxy-[1,1'-biphenyl]-4,4'-dicarboxylate ( $\text{G}^{\text{PL}}$ )



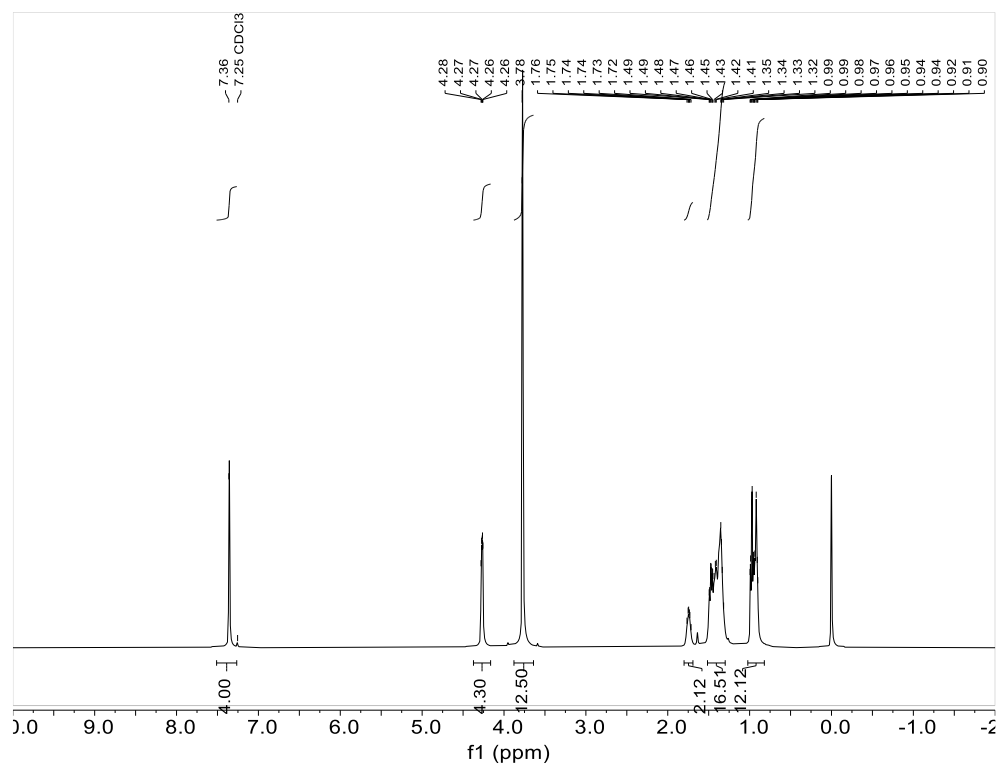
$^1\text{H NMR}$  (400 MHz,  $\text{CDCl}_3$ ) of Bis(2-ethylhexyl) 2,2',6-trimethoxy-[1,1'-biphenyl]-4,4'-dicarboxylate (**G-S<sup>PL</sup>**)



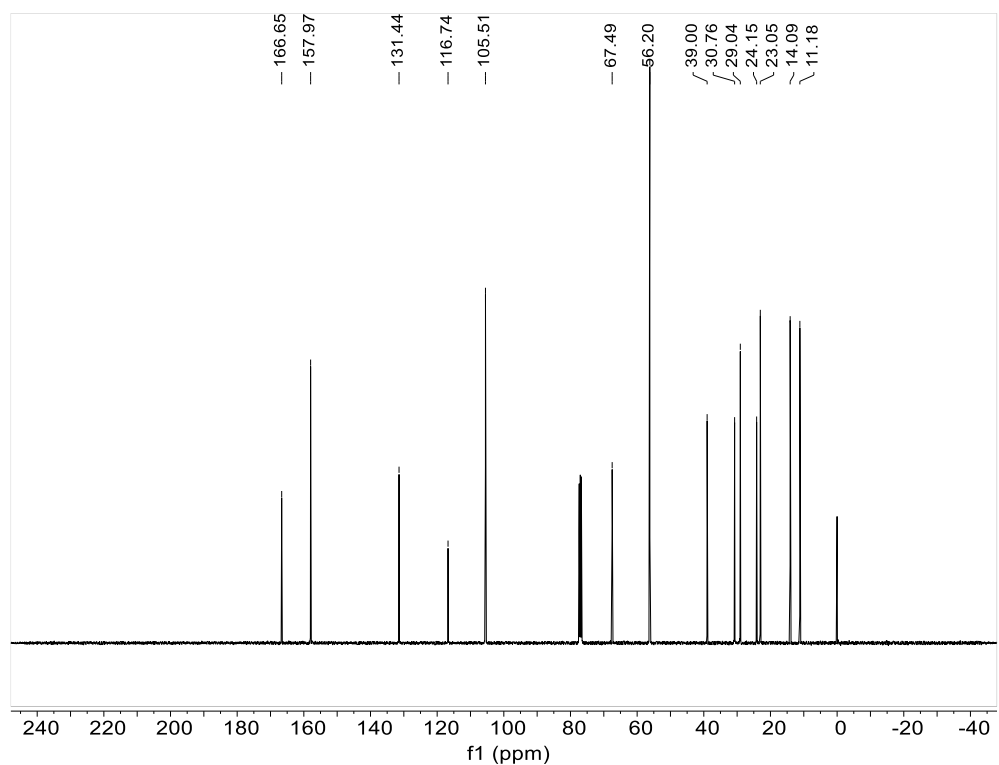
$^{13}\text{C NMR}$  (101 MHz,  $\text{CDCl}_3$ ) of Bis(2-ethylhexyl) 2,2',6-trimethoxy-[1,1'-biphenyl]-4,4'-dicarboxylate (**G-S<sup>PL</sup>**)



$^1\text{H NMR}$  (400 MHz,  $\text{CDCl}_3$ ) of Bis(2-ethylhexyl) 2,2',6,6'-tetramethoxy-[1,1'-biphenyl]-4,4'-dicarboxylate ( $\text{S-S}^{\text{PL}}$ )



$^{13}\text{C NMR}$  (101 MHz,  $\text{CDCl}_3$ ) of Bis(2-ethylhexyl) 2,2',6,6'-tetramethoxy-[1,1'-biphenyl]-4,4'-dicarboxylate ( $\text{S-S}^{\text{PL}}$ )



## Appendix B. Supporting Information for Chapter 3

### 3B.I. General Experimental Considerations

#### *Solvents and reagents*

All reagents were purchased from commercial sources and used as received without further purification. Starting materials (amines and aryl halides) were purchased from MilliporeSigma, Alfa Aesar, Thermo Scientific, TCI America, and Combi-Blocks. Zn powder (average 4–7 micron) and Mn powder (~325 mesh) were purchased from Alfa Aesar. Electrolytes and additives (LiCl, LiBr, LiI, LiPF<sub>6</sub>, NaBr, KPF<sub>6</sub>, <sup>n</sup>Bu<sub>4</sub>NCl, <sup>n</sup>Bu<sub>4</sub>NBr, <sup>n</sup>Bu<sub>4</sub>NI, <sup>n</sup>Bu<sub>4</sub>NPF<sub>6</sub>, <sup>n</sup>Bu<sub>4</sub>NBF<sub>4</sub>, ZnBr<sub>2</sub>, MnBr<sub>2</sub>, MgBr<sub>2</sub>, FeBr<sub>2</sub>, AlBr<sub>3</sub>) were purchased from MilliporeSigma, TCI America, and Thermo Scientific and handled in a nitrogen-filled glove box, unless otherwise noted. Nickel salts and ligands were purchased from MilliporeSigma or Alfa Aesar. Anhydrous solvents (DMF, DMA, DMSO, NMP, MeCN, THF, DMPU, DMI) were purchased from MilliporeSigma and stored over activated 4 Å molecular sieves in a nitrogen-filled glove box.

#### *Electrodes*

All electrode materials were purchased from commercial sources and used as received. Ni foams (1.6 mm thickness, 80–110 pores per inch, average hole diameter 0.25 mm, > 99.9 wt% purity) were purchased from MTI. Fe rods (5 mm diameter, 99.8 wt% purity) were purchased from American-Scientific. Zn foil (99.99% metals basis) was purchased from MilliporeSigma. Mn pieces (99.95% metals basis) were purchased from Thermo Scientific. Mg plates (99.95% metals basis) and Al plates (99.95% metals basis) were purchased from American-Scientific. Glassy carbon working electrodes (MF-2012) and non-aqueous reference electrodes (MW-1085) were purchased from BASi. Pt wires (0.5 mm diameter, 99.99% metals basis) were purchased from MilliporeSigma and custom-made as Pt counter electrodes (~ 4 cm, 5–7 spiral coils).

### *Characterization of products*

All proton ( $^1\text{H}$ ), carbon ( $^{13}\text{C}$ ), and fluorine ( $^{19}\text{F}$ ) nuclear magnetic resonance (NMR) spectra were recorded on a Bruker 400 MHz at 25 °C ( $^1\text{H}$  400.1 MHz,  $^{13}\text{C}$  100.6 MHz,  $^{19}\text{F}$  376.5 MHz) or a Bruker 500 MHz at 25 °C ( $^1\text{H}$  500.1 MHz,  $^{13}\text{C}$  125.7 MHz,  $^{19}\text{F}$  470.6 MHz). Chemical shifts are given in parts per million (ppm) relative to residual solvent peaks in the  $^1\text{H}$  and  $^{13}\text{C}$  NMR spectra or are referenced as noted. An absolute referencing method was used for  $^{19}\text{F}$  NMR chemical shifts, based on the frequency of solvent peaks in the  $^1\text{H}$  NMR spectra. The following abbreviations (and their combinations) are used to label the multiplicities: s (singlet), d (doublet), t (triplet), m (multiplet) and br (broad). High-resolution mass spectra were obtained using a Thermo Q Exactive<sup>TM</sup> Plus in the mass spectrometry facility at the University of Wisconsin (data were collected by facility staff). Automatic normal phase column chromatography was performed using reusable Silicycle SiliaSep premium cartridges (25 or 40 g, 25  $\mu\text{m}$ ) on a Biotage<sup>®</sup> Isolera. Thin-layer chromatography (TLC) was performed on Silicycle silica gel UV254 pre-coated plates (0.25 mm). Visualization of the developed chromatogram was performed by using UV lamps (254 nm) or  $\text{KMnO}_4$  stain.

### *Electrochemical experiments*

Cyclic Voltammetry (CV) experiments: All CV experiments were performed using a Pine WaveNow PGstat without IR compensation under an  $\text{N}_2$  atmosphere. The experiments were carried out in a three-electrode cell configuration with a glassy carbon (GC) working electrode, a platinum wire counter electrode, and a  $\text{Ag}/\text{AgNO}_3$  non-aqueous reference electrode (internal solution, 0.1 M  $^n\text{Bu}_4\text{NPF}_6$  and 0.01 M  $\text{AgNO}_3$  in DMF). The redox potential of ferrocene/ferrocenium ( $\text{Fc}/\text{Fc}^+$ ) was measured (under same experimental conditions) and used to provide an internal reference. The potential values recorded versus  $\text{Ag}/\text{AgNO}_3$  were then adjusted

relative to  $\text{Fc}/\text{Fc}^+$ , and electrochemical studies in organic solvents were reported accordingly. The GC working electrode was polished with alumina powder (5  $\mu\text{m}$ ) before each experiment. The resultant voltammograms were plotted following IUPAC convention.

Open-Circuit Potential (OCP) measurements: All OCP measurements were performed using a CH-600E potentiostat under an  $\text{N}_2$  atmosphere. The experiments were carried out in a three-electrode cell configuration with a metal (Zn, Mn, Mg, Fe, or Al) as the working electrode, a platinum wire counter electrode, and a  $\text{Ag}/\text{AgNO}_3$  reference electrode (internal solution, 0.1 M  $^n\text{Bu}_4\text{NPF}_6$  and 0.01 M  $\text{AgNO}_3$  in DMF). The redox potential of ferrocene/ferrocenium ( $\text{Fc}/\text{Fc}^+$ ) was measured (under same experimental conditions; when bromide or iodide salts were used as the electrolyte,  $^n\text{Bu}_4\text{NPF}_6$  was used instead for measuring  $\text{Fc}/\text{Fc}^+$  potential, as  $\text{Br}_2/\text{Br}^-$  and  $\text{I}_2/\text{I}_3^-$  redox waves overlap with  $\text{Fc}/\text{Fc}^+$  redox wave) and used to provide an internal reference. The potential values recorded versus  $\text{Ag}/\text{AgNO}_3$  were then adjusted relative to  $\text{Fc}/\text{Fc}^+$ , and electrochemical studies in organic solvents were reported accordingly. The working electrodes were polished using a smooth file before each experiment under nitrogen atmosphere. All solvents were rigorously purged with nitrogen for 15 min before preparation of the solutions for OCP analysis. The prepared solutions were stirred for 15 min under nitrogen atmosphere to allow full dissolution of all reagents.

Bulk Electrolysis: All bulk electrolysis experiments were performed using a Pine WaveNow PGstat. The experiments were performed in custom-built undivided cells, with Ni foam as a working electrode, Fe rod as a counter electrode and  $\text{Ag}/\text{AgNO}_3$  (internal solution, 0.1 M  $^n\text{Bu}_4\text{NPF}_6$  and 0.01 M  $\text{AgNO}_3$  in DMF) as a reference electrode.

### 3B.II. General Procedure for Open-Circuit Potential (OCP) Measurements

In a solution containing ZnBr<sub>2</sub> (11.2 mg, 10 mM), MnBr<sub>2</sub> (10.7 mg, 10 mM), MgBr<sub>2</sub> (9.2 mg, 10 mM), FeBr<sub>2</sub> (10.8 mg, 10 mM), or AlBr<sub>3</sub> (13.3 mg, 10 mM), electrolyte (0.2 M, or otherwise noted), and anhydrous solvent (5 mL), the corresponding metal electrode (polished using a smooth file before every experiment) was used as the working electrode for OCP measurements, with a Pt wire counter electrode and a Ag/AgNO<sub>3</sub> reference electrode. While stirring at 600 rpm, the open-circuit potential was measured and recorded after it remained stable (< 5 mV fluctuation over 1 min) (Figures 3B.1 and 3B.2). The measured potential versus Ag/AgNO<sub>3</sub> was then adjusted to be referenced versus Fc/Fc<sup>+</sup> and converted to the formal thermodynamic potential ( $E^{\circ'}$ ) using the Nernst equation below.

$$E = E^{\circ'} + \frac{RT}{nF} \ln \left( \frac{[M^{n+}]}{[M^0]} \right)$$

Given that the measurements were made at room temperature ( $T = 298 \text{ K}$ ), and the number of electrons involved in the redox process is two for Zn, Mn, Mg, Fe ( $n = 2$ ) and three for Al ( $n = 3$ ),  $F$  is the Faraday constant (96485 C/mol),  $R$  is the universal gas constant (8.3145 J M<sup>-1</sup> K<sup>-1</sup>),  $[M^0]$  is the activity of the reduced form (defined as 1 for solid state),  $[M^{n+}]$  is the activity of the oxidized form (approximately equal to the concentration of the oxidized form in solution, 0.01 M), then the Nernst equation (with all potentials relative to Fc/Fc<sup>+</sup>) becomes:

$$E^{\circ'} = E + 59 \text{ mV} \quad T = 298 \text{ K (for Zn, Mn, Mg, Fe)}$$

$$E^{\circ'} = E + 39 \text{ mV} \quad T = 298 \text{ K (for Al)}$$

Note: Zn and Mn are the most common metal reductants used in Ni-catalyzed cross-electrophile coupling (XEC) reactions.<sup>1</sup> Mg is seldom used as metal reductant, although an *in situ* Grignard reagent formation was proposed for the corresponding XEC reaction.<sup>2,3</sup> Other common reducing metals, such as Fe and Al, were also studied in organic solvents. Mixed solvents have proven

indispensable for achieving optimal outcomes in certain XEC reactions. Therefore, redox potentials of Zn and Mn in mixed solvents were also measured. The results are tabulated in Tables 3B.1 and 3B.2.

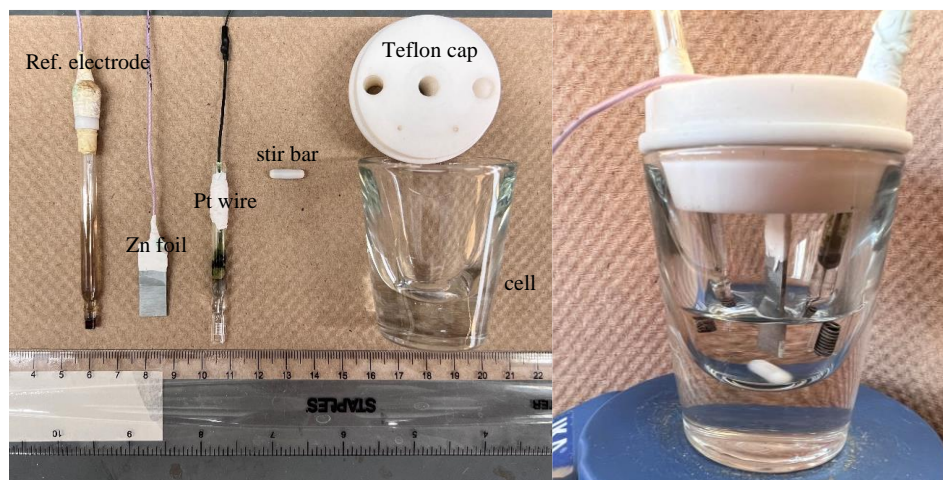


**Figure 3B.1.** Picture of the undivided cell for OCP and CV experiments before (left) and after (right) assembly (working electrode varies based on each experiment, shown is with Zn plate).

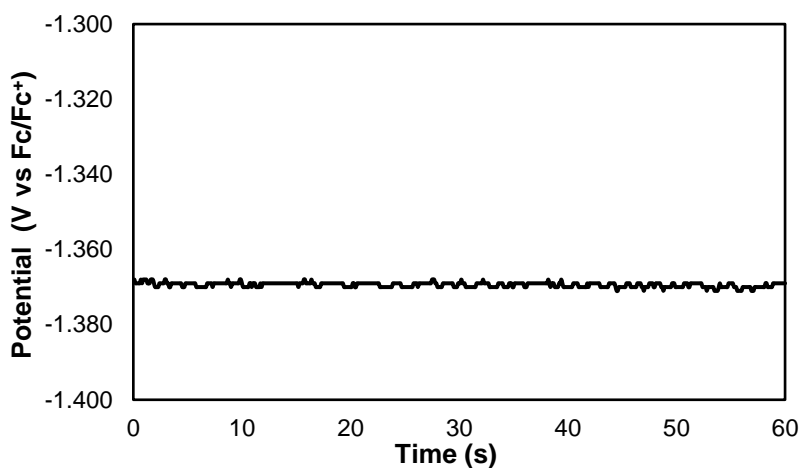


**Figure 3B.2.** A typical trace obtained in OCP measurements (after conversion using the Nernst equation). Conditions: Zn working electrode, 10 mM  $\text{ZnBr}_2$ , 0.2 M  ${}^n\text{Bu}_4\text{NPF}_6$ , DMF.

**Table 3B.1. Formal thermodynamic potentials of Zn, Mn, Mg, Fe, and Al.**

Entry	Solvent	Metal	Additive	$E^{\circ'}$ (V vs Fc/Fc <sup>+</sup> )
1	DMF	Zn	${}^n\text{Bu}_4\text{NPF}_6$	-1.37
2	DMA	Zn	${}^n\text{Bu}_4\text{NPF}_6$	-1.36
3	DMSO	Zn	${}^n\text{Bu}_4\text{NPF}_6$	-1.43
4	NMP	Zn	${}^n\text{Bu}_4\text{NPF}_6$	-1.36

5	MeCN	Zn	<sup>n</sup> Bu <sub>4</sub> NPF <sub>6</sub>	-1.07
6	THF	Zn	<sup>n</sup> Bu <sub>4</sub> NPF <sub>6</sub>	-1.25
7	DMPU	Zn	<sup>n</sup> Bu <sub>4</sub> NPF <sub>6</sub>	-1.32
8	DMI	Zn	<sup>n</sup> Bu <sub>4</sub> NPF <sub>6</sub>	-1.33
9	DMF	Mn	<sup>n</sup> Bu <sub>4</sub> NPF <sub>6</sub>	-1.55
10	DMA	Mn	<sup>n</sup> Bu <sub>4</sub> NPF <sub>6</sub>	-1.56
11	DMSO	Mn	<sup>n</sup> Bu <sub>4</sub> NPF <sub>6</sub>	-1.53
12	NMP	Mn	<sup>n</sup> Bu <sub>4</sub> NPF <sub>6</sub>	-1.50
13	MeCN	Mn	<sup>n</sup> Bu <sub>4</sub> NPF <sub>6</sub>	-1.19
14	THF	Mn	<sup>n</sup> Bu <sub>4</sub> NPF <sub>6</sub>	-1.54
15	DMPU	Mn	<sup>n</sup> Bu <sub>4</sub> NPF <sub>6</sub>	-1.48
16	DMI	Mn	<sup>n</sup> Bu <sub>4</sub> NPF <sub>6</sub>	-1.50
17	DMF	Zn	LiCl	-1.65
18 <sup>b</sup>	DMF	Zn	LiCl	-1.68
19 <sup>c</sup>	DMF	Zn	LiCl	-1.72
20 <sup>d</sup>	DMF	Zn	LiCl	-1.72
21	DMF	Zn	LiBr	-1.53
22	DMF	Zn	LiI	-1.43
23	DMF	Zn	LiPF <sub>6</sub>	-1.36
24	DMF	Zn	NaBr	-1.52
25	DMF	Zn	KPF <sub>6</sub>	-1.36
26 <sup>a</sup>	DMA	Zn	KPF <sub>6</sub>	-1.31
27 <sup>a</sup>	DMF	Zn	<sup>n</sup> Bu <sub>4</sub> NCl	-1.60
28	DMF	Zn	<sup>n</sup> Bu <sub>4</sub> NCl	-1.64
29 <sup>b</sup>	DMF	Zn	<sup>n</sup> Bu <sub>4</sub> NCl	-1.67
30 <sup>c</sup>	DMF	Zn	<sup>n</sup> Bu <sub>4</sub> NCl	-1.70
31 <sup>d</sup>	DMF	Zn	<sup>n</sup> Bu <sub>4</sub> NCl	-1.72
32 <sup>e</sup>	DMF	Zn	<sup>n</sup> Bu <sub>4</sub> NCl	-1.72
33	DMF	Zn	<sup>n</sup> Bu <sub>4</sub> NBr	-1.52
34	DMF	Zn	<sup>n</sup> Bu <sub>4</sub> NI	-1.41
35	DMF	Zn	<sup>n</sup> Bu <sub>4</sub> NPF <sub>6</sub>	-1.37
36	DMF	Zn	<sup>n</sup> Bu <sub>4</sub> NBF <sub>4</sub>	-1.37
37	DMA	Zn	ZnBr <sub>2</sub>	-1.33
38 <sup>f</sup>	DMPU	Zn	<sup>n</sup> Bu <sub>4</sub> NPF <sub>6</sub>	-1.46
39 <sup>g</sup>	DMPU	Zn	<sup>n</sup> Bu <sub>4</sub> NPF <sub>6</sub>	-1.47
40	DMF	Mn	LiCl	-1.75
41	DMF	Mn	LiBr	-1.63
42	DMF	Mn	LiI	-1.59
43	DMF	Mn	LiPF <sub>6</sub>	-1.58
44	DMF	Mn	NaBr	-1.62

45	DMF	Mn	KPF <sub>6</sub>	-1.55
46 <sup>a</sup>	DMA	Mn	KPF <sub>6</sub>	-1.55
47	DMF	Mn	<sup>n</sup> Bu <sub>4</sub> NCl	-1.76
48	DMF	Mn	<sup>n</sup> Bu <sub>4</sub> NBr	-1.66
49	DMF	Mn	<sup>n</sup> Bu <sub>4</sub> NI	-1.61
50	DMF	Mn	<sup>n</sup> Bu <sub>4</sub> NPF <sub>6</sub>	-1.55
51	DMF	Mn	<sup>n</sup> Bu <sub>4</sub> NBF <sub>4</sub>	-1.57
52 <sup>f</sup>	DMPU	Mn	<sup>n</sup> Bu <sub>4</sub> NPF <sub>6</sub>	-1.65
53	DMF	Mg	<sup>n</sup> Bu <sub>4</sub> NPF <sub>6</sub>	-2.19
54	MeCN	Mg	<sup>n</sup> Bu <sub>4</sub> NPF <sub>6</sub>	-2.01
55	DMF	Mg	LiCl	-2.45
56	DMF	Mg	LiBr	-2.22
57	DMF	Mg	Lil	-2.14
58	DMF	Mg	<sup>n</sup> Bu <sub>4</sub> NCl	-2.39
59	DMF	Fe	<sup>n</sup> Bu <sub>4</sub> NPF <sub>6</sub>	-0.81
60	MeCN	Fe	<sup>n</sup> Bu <sub>4</sub> NPF <sub>6</sub>	-0.54
61	DMF	Fe	LiCl	-1.04
62	DMF	Fe	LiBr	-0.95
63	DMF	Fe	Lil	-0.97
64	DMF	Fe	<sup>n</sup> Bu <sub>4</sub> NCl	-1.00
65	DMF	Al	<sup>n</sup> Bu <sub>4</sub> NPF <sub>6</sub>	-1.28
66	MeCN	Al	<sup>n</sup> Bu <sub>4</sub> NPF <sub>6</sub>	-1.07
67	DMF	Al	LiCl	-1.47
68	DMF	Al	LiBr	-1.32
69	DMF	Al	Lil	-1.31
70	DMF	Al	<sup>n</sup> Bu <sub>4</sub> NCl	-1.51
71	MeCN	Zn	<sup>n</sup> Bu <sub>4</sub> NCl	-1.60
72	MeCN	Zn	<sup>n</sup> Bu <sub>4</sub> NBr	-1.47
73	MeCN	Zn	<sup>n</sup> Bu <sub>4</sub> NI	-1.34
74	MeCN	Mn	<sup>n</sup> Bu <sub>4</sub> NCl	-1.64
75	MeCN	Mn	<sup>n</sup> Bu <sub>4</sub> NBr	-1.52
76	MeCN	Mn	<sup>n</sup> Bu <sub>4</sub> NI	-1.32
77	THF	Zn	LiCl	-1.62
78	THF	Zn	LiBr	-1.61
79	THF	Zn	Lil	-1.58
80	THF	Mn	LiCl	-1.72
81	THF	Mn	LiBr	-1.64
82	THF	Mn	Lil	-1.52

<sup>a</sup> 0.1 M additive. <sup>b</sup> 0.4 M additive. <sup>c</sup> 0.8 M additive. <sup>d</sup> 1.0 M additive. <sup>e</sup> 1.2 M additive.

<sup>f</sup> Added 10 mM Me<sub>3</sub>SiCl. <sup>g</sup> Added 20 mM Me<sub>3</sub>SiCl.

**Table 3B.2. Formal thermodynamic potentials of Zn and Mn in mixed solvents.**

Entry	Solvent	Metal	Additive	$E^{\circ}$ (V vs Fc/Fc <sup>+</sup> )
1	DMF/THF (1:1)	Zn	<sup>n</sup> Bu <sub>4</sub> NPF <sub>6</sub>	-1.29
2	DMA/THF (1:1)	Zn	<sup>n</sup> Bu <sub>4</sub> NPF <sub>6</sub>	-1.30
3	DMF/THF (1:1)	Mn	<sup>n</sup> Bu <sub>4</sub> NPF <sub>6</sub>	-1.48
4	DMA/THF (1:1)	Mn	<sup>n</sup> Bu <sub>4</sub> NPF <sub>6</sub>	-1.52

Note: Other common additives (NaCl, NaI, KCl, KBr, KI) were less soluble in DMF and not included in this study.

The OCP measurements can be sensitive to trace oxygen dissolved in the electrolyte solution (Table 3B.3). Therefore, rigorous N<sub>2</sub> purging of the solvents before the preparation of the electrolyte solution is required for OCP measurements.

**Table 3B.3. The impact of dissolved oxygen to measured OCP.**

Entry	Additive/Solvent	Metal	Treatment	Measured potential <sup>a</sup> (V vs Fc/Fc <sup>+</sup> )
1	LiCl/DMF (0.2 M)	Zn	purged the solution with N <sub>2</sub> for 15 min in glovebox, then measured OCP	-1.71
2	LiCl/DMF (0.2 M)	Zn	the same solution was brought out of glovebox, then measured OCP	-1.64
3	LiCl/DMF (0.2 M)	Zn	the same solution was left in ambient atmosphere for 1 h, then measured OCP	-1.53

<sup>a</sup> Note that a Nernstian conversion was not applied here.

Discussion: For a well-defined, fully reversible redox couple Fc/Fc<sup>+</sup>, Dempsey et al. determined its  $E_{1/2}$  to be -0.003 V (vs. Fc/Fc<sup>+</sup>) in MeCN via OCP measurement, which is consistent with the theoretical value of 0 V. This  $E_{1/2}$  was acquired by extracting the intercept value from the linear fit of the measured OCP data against  $\ln\left(\frac{[Fc^+]}{[Fc]}\right)$  (see Nernst equation) for multiple solutions containing different concentrations of Fc and Fc<sup>+</sup>.<sup>4</sup> This corroborates the validity of OCP measurement in determining thermodynamic potentials of redox couples in organic solvents.

However, this exact method was not applicable to this study as (a) limited solubility of the metal salts prevents measurements at high concentration, (b) the anions of the salts may affect the thermodynamic potentials in a non-Nernstian way (see discussions in the main text and Figure 3B.3), and (c) the OCP measurement technique has a  $\pm 5$  mV inaccuracy while a ten-fold change in concentration only results in a theoretical change of  $E$  by 29 mV.

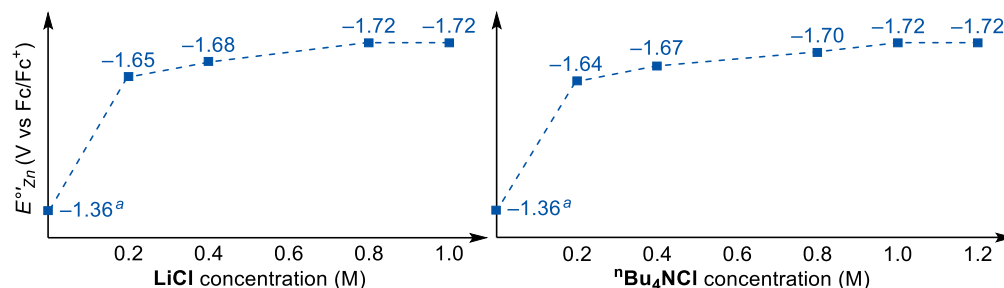
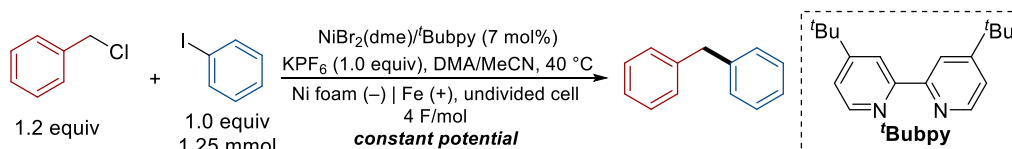


**Figure 3B.3.** Chloride concentration effect on Zn reduction potential in DMF. <sup>a</sup> 0.2 M <sup>t</sup>Bu<sub>4</sub>NPF<sub>6</sub> as electrolyte.

### 3B.III. General Procedures for Reductive Coupling of Benzyl Chloride with Iodobenzene

#### *Electrochemical reductive coupling of benzyl chloride with iodobenzene*

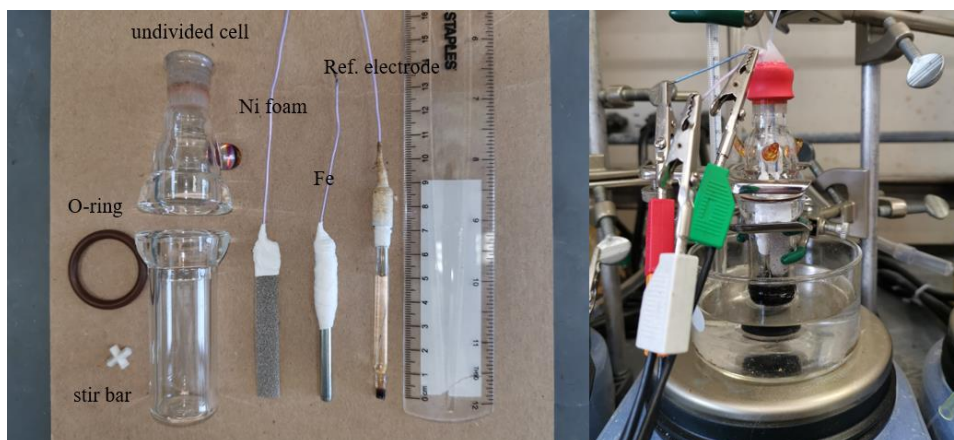


In a nitrogen-filled glove box, NiBr<sub>2</sub>(dme) (27 mg, 7 mol%), <sup>t</sup>Bubpy (23.5 mg, 7 mol%), and DMA or MeCN (5 mL) were added to a 2-dram vial. This solution was stirred at 800 rpm in the glove box for 30 min to allow complexation of Ni with the ligand. To an undivided cell (Figure 3B.4) fitted with a cross-shaped stir bar was added KPF<sub>6</sub> (230 mg, 1.25 mmol, 1.0 equiv), iodobenzene (139  $\mu$ L, 1.25 mmol, 1.0 equiv), and benzyl chloride (172.5  $\mu$ L, 1.5 mmol, 1.2 equiv) under air. The cell was transferred into the glove box, followed by addition of the catalyst solution and installation of a Ni foam cathode, a Ag/AgNO<sub>3</sub> reference electrode, and an Fe rod anode. The cell was then sealed with a rubber septum before being removed from the glove box. A thin Teflon

tube was introduced immediately into the cell to allow continuous nitrogen bubbling. The reaction mixture was stirred at 1000 rpm for 10 min to allow full dissolution of all reagents and exclusion of adventitious oxygen. After that, the Teflon tube was removed, and the top of the rubber septum was sealed with silicone gel. The reaction mixture was electrolyzed under a constant potential ( $-1.07$  V to  $-1.40$  V vs.  $\text{Fc}/\text{Fc}^+$ ) at the desired temperature (25 to 80 °C) until 4 F/mol of charge was passed or otherwise noted.

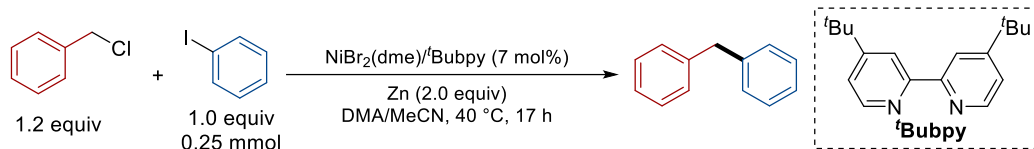
Work-up for condition screening: Upon completion of the reaction, the reaction mixture was cooled to room temperature and diluted with DMA or MeCN (10 mL). Mesitylene (57.9  $\mu\text{L}$ , 0.42 mmol, 0.33 equiv) was added to the crude material. Then a 100  $\mu\text{L}$  aliquot of the solution was filtered through a 2-cm silica gel plug in a Pasteur pipette into a vial. 400  $\mu\text{L}$   $\text{CDCl}_3$  was also added to the pipette and eluted into the same vial. The resultant sample was analyzed by  $^1\text{H}$  NMR spectroscopy and yields were determined using mesitylene as the internal standard.

Work-up for product isolation: Upon reaction completion, the reaction mixture was cooled to room temperature and diluted with water (25 mL). The solution was extracted with ethyl acetate (50 mL  $\times$  2) and the organic layers were combined and washed with brine (50 mL). The resultant organic solution was dried over anhydrous  $\text{Na}_2\text{SO}_4$ , then concentrated *in vacuo*. The obtained residue was purified by flash column chromatography.

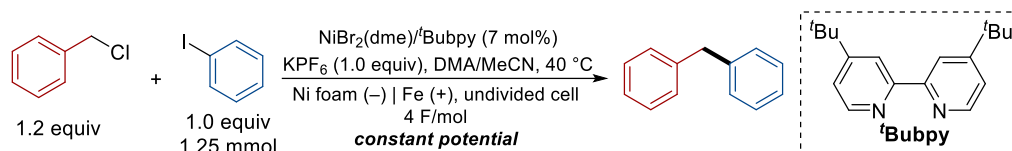


**Figure 3B.4.** Picture of the undivided cell before (left) and after (right) assembly.

*Reductive coupling of benzyl chloride with iodobenzene using Zn reductant*



In a nitrogen-filled glove box,  $\text{NiBr}_2(\text{dme})$  (5.4 mg, 7 mol%),  $t\text{BuBupy}$  (4.7 mg, 7 mol%), and DMA or MeCN (1 mL) were added to a 1-dram vial. This solution was stirred at 800 rpm in the glove box for 30 min to allow complexation of Ni with the ligand, followed by sequential addition of iodobenzene (27.8  $\mu\text{L}$ , 0.25 mmol, 1.0 equiv), benzyl chloride (34.5  $\mu\text{L}$ , 0.3 mmol, 1.2 equiv) and Zn powder (33 mg, 0.5 mmol, 2.0 equiv). The vial was capped with a screw cap fitted with a PTFE-faced silicone septum, then removed from the glove box and heated in a sand bath to 40 °C with stirring (1000 rpm) for 17 h. The reaction mixture was then cooled to room temperature and diluted with DMA or MeCN (2 mL). Mesitylene (19.3  $\mu\text{L}$ , 0.083 mmol, 0.33 equiv) was added to the crude material. Then a 100  $\mu\text{L}$  aliquot of the solution was filtered through a 2-cm silica gel plug in a Pasteur pipette into a vial. 400  $\mu\text{L}$   $\text{CDCl}_3$  was also added to the pipette and eluted into the same vial. The resultant sample was analyzed by  $^1\text{H}$  NMR spectroscopy and the yields were determined using mesitylene as the internal standard.

**Table 3B.4. Optimization of (electro)chemical reductive coupling of benzyl chloride with iodobenzene.<sup>a</sup>**

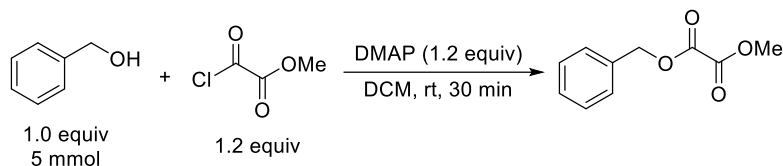
Entry	Solvent	Applied potential (V vs Fc/Fc <sup>+</sup> )	Temp. (°C)	Yield (%)
1	MeCN	-1.20	80	34
2	MeCN	-1.30	80	40
3	MeCN	-1.35	80	58
4	MeCN	-1.40	80	50
<b>5</b>	<b>MeCN</b>	<b>-1.35</b>	<b>40</b>	<b>78</b>
6	MeCN	-1.35	25	74
7 <sup>b</sup>	MeCN	-1.07	80	11
8 <sup>c</sup>	MeCN	-1.07	40	23
9	DMA	-1.35	80	24
10	DMA	-1.35	60	28
<b>11</b>	<b>DMA</b>	<b>-1.35</b>	<b>40</b>	<b>50</b>
12 <sup>d</sup>	DMA	-1.35	25	50
13 <sup>e</sup>	DMA	-1.07	80	12
14 <sup>f</sup>	DMA	-1.07	40	0
15 <sup>g</sup>	MeCN	Zn instead of e-chem	40	12
16 <sup>g</sup>	DMA	Zn instead of e-chem	40	46

<sup>a</sup> Yields were determined by <sup>1</sup>H NMR spectroscopy using mesitylene as the internal standard. <sup>b</sup> 88% iodobenzene remained unreacted. <sup>c</sup> 51% iodobenzene remained unreacted. <sup>d</sup> Reaction time = 72 h. <sup>e</sup> 71% iodobenzene remained unreacted. <sup>f</sup> >90% benzyl chloride and iodobenzene remained unreacted; the reaction was stopped after 36 h. <sup>g</sup> No  $\text{KPF}_6$ , the reaction was conducted at 0.25 mmol scale using Zn (2 equiv) as the reductant.

**Discussion:** The initial conditions are adapted from previous literature.<sup>5</sup> The thermochemical coupling of benzyl chloride with iodobenzene was conducted using 2 equiv of Zn reductant, which provide 4 equiv of e<sup>-</sup> to the reaction medium. A total charge of 4 F/mol (of product) was chosen for electrolysis to mimic the thermochemical reaction, even though only 2 F/mol should be needed. We suspect that the surplus charge reduces Fe<sup>2+</sup> ions (from the sacrificial anode oxidation) at the



### Synthesis of benzyl methyl oxalate



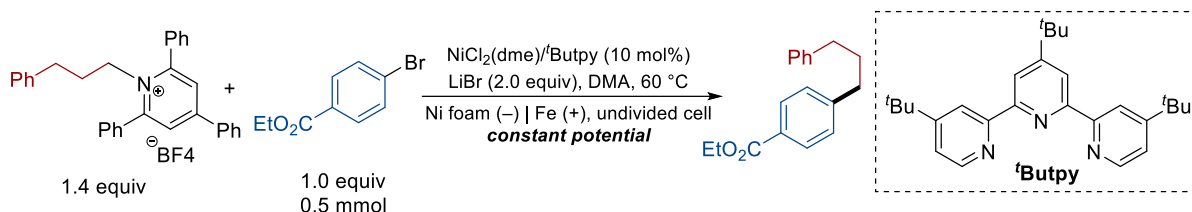
Benzyl methyl oxalate was synthesized according to a procedure described previously in the literature.<sup>7</sup> To a solution of DMAP (733 mg, 6 mmol, 1.2 equiv) in CH<sub>2</sub>Cl<sub>2</sub> (20 mL) was dropwise added methyl chlorooxoacetate (552 μL, 6 mmol, 1.2 equiv) at 0 °C. After stirring at room temperature for 5 min, a solution of benzyl alcohol (519 μL, 5 mmol, 1.0 equiv) in CH<sub>2</sub>Cl<sub>2</sub> (10 mL) was dropwise added and stirred for 30 min. Upon reaction completion, the reaction mixture was diluted with water (20 mL), extracted with CH<sub>2</sub>Cl<sub>2</sub> (20 mL × 2) and the organic layers were combined and washed with brine (30 mL). The resultant organic solution was dried over anhydrous Na<sub>2</sub>SO<sub>4</sub>, then concentrated *in vacuo*. The obtained residue was purified by flash column chromatography (10:90 ethyl acetate:pentane) to afford the product as a white solid (892 mg, 92% yield). The spectroscopic data matched those reported in the literature.<sup>8</sup>

### 3B.V. Optimization of Electrochemical Reductive Coupling of Katritzky Salts with Aryl Halides

In a nitrogen-filled glove box, NiCl<sub>2</sub>(dme), <sup>t</sup>Butpy, and DMA (5 mL) were added to a 2-dram vial. This solution was stirred at 800 rpm in the glove box for 30 min to allow complexation of Ni with the ligand. To an undivided cell (Figure 3B.4) fitted with a cross-shaped stir bar was added electrolyte, 2,4,6-triphenyl-1-(3-phenylpropyl)pyridin-1-ium tetrafluoroborate (360 mg, 0.7 mmol, 1.4 equiv), and aryl bromide (0.5 mmol, 1.0 equiv) under air. The cell was transferred into the glove box, followed by addition of the catalyst solution and installation of a Ni foam cathode, a Ag/AgNO<sub>3</sub> reference electrode, and a sacrificial anode. The cell was then sealed with a rubber septum before removing from the glove box. A thin Teflon tube was introduced immediately into

the cell to allow continuous nitrogen bubbling. The reaction mixture was stirred at 1000 rpm for 10 min to allow full dissolution of all reagents and exclusion of adventitious oxygen. After that, the Teflon tube was removed, and the top of the rubber septum was sealed with silicone gel. The reaction mixture was electrolyzed under constant potential for 10–17 h at 60 °C with stirring (800 rpm). The reaction was automatically stopped by the potentiostat after 2.5 F/mol of charge was passed to ensure full consumption of the aryl halides. The reaction mixture was then cooled to room temperature and diluted with DMA (10 mL). 1,3,5-Trimethoxybenzene (28 mg, 0.17 mmol, 0.33 equiv) was added to the crude material. Then a 100  $\mu$ L aliquot of the solution was filtered through a 2-cm silica gel plug in a Pasteur pipette into a vial. 400  $\mu$ L  $\text{CDCl}_3$  was also added to the pipette and eluted into the same vial. The resultant sample was analyzed by  $^1\text{H}$  NMR spectroscopy and the yields were determined using 1,3,5-trimethoxybenzene as the internal standard.

**Table 3B.5. An example of optimization of electrochemical reductive coupling of Katritzky salts with aryl halides.<sup>a</sup>**



Entry	Applied potential (V vs Fc/Fc <sup>+</sup> )	Mass balance of ArBr (%)	Ar–Ar (%)	Yield (%)
1	–1.20	83	6	45
2	–1.25	103	14	75
3	–1.30	108	34	40
4	–1.50	100	33	33
5	–1.55	110	55	0
6 <sup>b</sup>	–1.25	110	12	70
7 <sup>c</sup>	–1.25	92	6	50
8 <sup>d</sup>	–1.25	110	9	20
9 <sup>e</sup>	–1.25	93	35	23
<b>10<sup>f</sup></b>	<b>–1.25</b>	<b>102</b>	<b>7</b>	<b>81</b>
11 <sup>g</sup>	–1.25	89	4	6

<sup>a</sup> Yields were determined by <sup>1</sup>H NMR spectroscopy using 1,3,5-trimethoxybenzene as the internal standard. <sup>b</sup> 7 mol% Ni catalyst. <sup>c</sup> Al anode. <sup>d</sup> Zn anode. <sup>e</sup> <sup>n</sup>Bu<sub>4</sub>NPF<sub>6</sub> (1.0 equiv) instead of LiBr. <sup>f</sup> KPF<sub>6</sub> (1.0 equiv) instead of LiBr. <sup>g</sup> Divided cell with glass frit separator.

Discussion: The initial conditions were adapted from previous literature.<sup>6</sup> Note that although using LiBr gave a comparable yield as KPF<sub>6</sub>, bromide anions may participate in the catalytic process instead of just serving as the supporting electrolyte. KPF<sub>6</sub> is considered as a more appropriate electrolyte, due to its non-coordinating anion. For the coupling of secondary alkyl Katritzky salts with aryl halides, we continued using KPF<sub>6</sub> as the electrolyte.

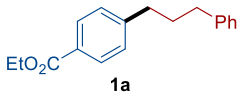
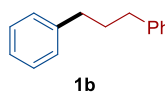
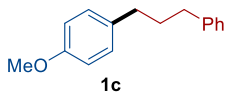
The optimization for the coupling of each pair of substrates generally proceeded according to the following sequence:

(1) Reactions were first performed at the applied potentials corresponding to  $E^{\circ'}_{\text{Zn}}$  and  $E^{\circ'}_{\text{Mn}}$ , and the potential that led to the higher yield was then used as a starting point for further optimization (entries 1 and 2 in each table).

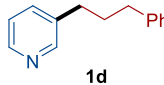
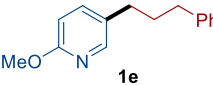
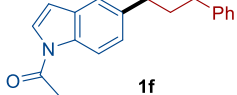
(2) Two experiments were then conducted, one 0.05–0.1 V above and one 0.05–0.1 V below, the  $E^{\circ'}_{\text{Zn}}$  and  $E^{\circ'}_{\text{Mn}}$  potential (whichever led to the higher yield in step 1) (entries 3 and 4 of each table, in most cases).

(3) The potential was incremented further in the direction that led to improved yield in step 2. Optimization efforts were discontinued after yields appeared to be optimized within  $\pm 50$  mV (entry 5, if present).

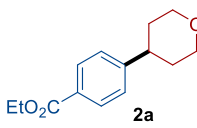
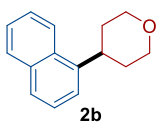
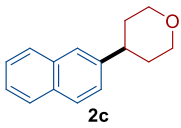
Optimization details for each of the products are summarized in Figures 3B.5 and 3B.6.

 1a			 1b			 1c		
Entry	Applied potential (V vs Fc/Fc <sup>+</sup> )	Yield (%)	Entry	Applied potential (V vs Fc/Fc <sup>+</sup> )	Yield (%)	Entry	Applied potential (V vs Fc/Fc <sup>+</sup> )	Yield (%)
1	-1.31 ( $E^{\circ}_{Zn}$ )	62	1	-1.31 ( $E^{\circ}_{Zn}$ )	61	1	-1.31 ( $E^{\circ}_{Zn}$ )	52
2	-1.55 ( $E^{\circ}_{Mn}$ )	0	2	-1.55 ( $E^{\circ}_{Mn}$ )	54	2	-1.55 ( $E^{\circ}_{Mn}$ )	73
3	<b>-1.25</b>	<b>81</b>	3	-1.25	69	3	<b>-1.50</b>	<b>92</b>
4	-1.40	45	4	-1.35	76	4	-1.60	55
5	-1.20	62	5	<b>-1.40</b>	<b>88</b>	5	-1.45	75

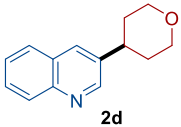
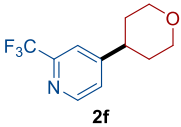
  

 1d			 1e			 1f		
Entry	Applied potential (V vs Fc/Fc <sup>+</sup> )	Yield (%)	Entry	Applied potential (V vs Fc/Fc <sup>+</sup> )	Yield (%)	Entry	Applied potential (V vs Fc/Fc <sup>+</sup> )	Yield (%)
1	-1.31 ( $E^{\circ}_{Zn}$ )	0	1	-1.31 ( $E^{\circ}_{Zn}$ )	61	1	-1.31 ( $E^{\circ}_{Zn}$ )	57
2	-1.55 ( $E^{\circ}_{Mn}$ )	35	2	-1.55 ( $E^{\circ}_{Mn}$ )	54	2	-1.55 ( $E^{\circ}_{Mn}$ )	50
3	-1.60	50	3	-1.25	51	3	-1.25	30
4	<b>-1.65</b>	<b>67</b>	4	<b>-1.40</b>	<b>78</b>	4	<b>-1.40</b>	<b>90</b>
5	-1.70	40	5	-1.45	72	5	-1.50	59

**Figure 3B.5.** Optimization for electrochemical XEC reactions of alkyl Katritzky salt **1** with aryl bromides. Yields were determined by <sup>1</sup>H NMR spectroscopy using 1,3,5-trimethoxybenzene as the internal standard.

 2a			 2b			 2c		
Entry	Applied potential (V vs Fc/Fc <sup>+</sup> )	Yield (%)	Entry	Applied potential (V vs Fc/Fc <sup>+</sup> )	Yield (%)	Entry	Applied potential (V vs Fc/Fc <sup>+</sup> )	Yield (%)
1	-1.31 ( $E^{\circ}_{Zn}$ )	99	1	-1.31 ( $E^{\circ}_{Zn}$ )	77	1	-1.31 ( $E^{\circ}_{Zn}$ )	82
2	-1.55 ( $E^{\circ}_{Mn}$ )	99	2	-1.55 ( $E^{\circ}_{Mn}$ )	64	2	-1.55 ( $E^{\circ}_{Mn}$ )	83
3	<b>-1.30</b>	<b>99</b>	3	-1.25	55	3	<b>-1.50</b>	<b>92</b>
			4	<b>-1.40</b>	<b>84</b>			
			5	-1.50	66			

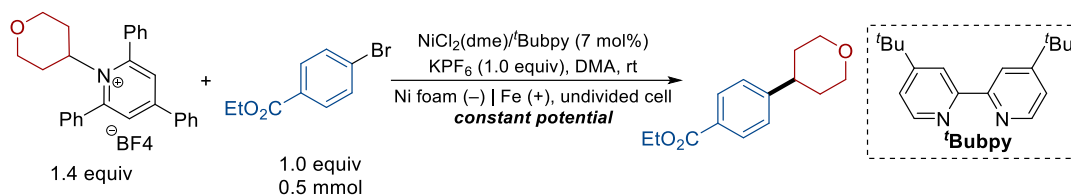
  

 2d			 2e			 2f		
Entry	Applied potential (V vs Fc/Fc <sup>+</sup> )	Yield (%)	Entry	Applied potential (V vs Fc/Fc <sup>+</sup> )	Yield (%)	Entry	Applied potential (V vs Fc/Fc <sup>+</sup> )	Yield (%)
1	-1.31 ( $E^{\circ}_{Zn}$ )	33	1	-1.31 ( $E^{\circ}_{Zn}$ )	19	1	-1.31 ( $E^{\circ}_{Zn}$ )	76
2	-1.55 ( $E^{\circ}_{Mn}$ )	9	2	-1.55 ( $E^{\circ}_{Mn}$ )	16	2	-1.55 ( $E^{\circ}_{Mn}$ )	56
3 <sup>a</sup>	-1.25	31	3	<b>-1.25</b>	<b>46</b>	3	-1.25	88
4	-1.40	38	4	-1.40	20	4	<b>-1.15</b>	<b>92</b>
5	<b>-1.45</b>	<b>44</b>	5	-1.20	26			

**Figure 3B.6.** Optimization for electrochemical XEC reactions of alkyl Katritzky salt **2** with aryl bromides. Yields were determined by <sup>1</sup>H NMR spectroscopy using 1,3,5-trimethoxybenzene as the internal standard.

<sup>a</sup> Current dropped to < 20  $\mu\text{A}$  after 24 h of electrolysis, and the reaction was manually stopped; 2 F/mol of charge was passed.

**Table 3B.6. Zn salt effects in the cross-coupling of Katritzky salts with aryl halides.<sup>a</sup>**

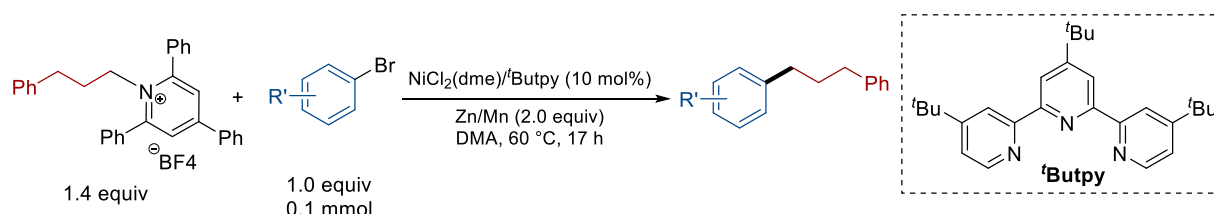


Entry	Applied potential (V vs Fc/Fc <sup>+</sup> )	Mass balance of ArBr (%)	Ar-H (%)	Yield (%)
1	-1.31	102	0	99
2	-1.55	100	0	99
3 <sup>b</sup>	-1.55	98	56	42
4 <sup>c</sup>	Zn instead of e-chem	100	82	0
5 <sup>c</sup>	Mn instead of e-chem	103	0	99
6 <sup>c,d</sup>	Mn instead of e-chem	99	0	99
7 <sup>b,c</sup>	Mn instead of e-chem	101	52	44

<sup>a</sup> Yields were determined by <sup>1</sup>H NMR spectroscopy using 1,3,5-trimethoxybenzene as the internal standard. Ar-H represents the proto-dehalogenation byproduct. <sup>b</sup> ZnCl<sub>2</sub> (1.0 equiv) was added. <sup>c</sup> No KPF<sub>6</sub>, the reaction was conducted at 0.1 mmol scale using Zn or Mn (2 equiv) as the reductant. <sup>d</sup> KPF<sub>6</sub> (1.0 equiv) was added.

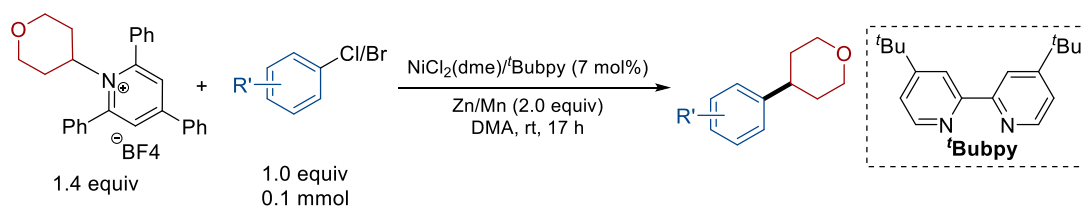
### 3B.VI. General Procedures for Reductive Coupling of Katritzky Salts with Aryl Halides

#### *Reductive coupling of Katritzky salts with aryl halides using Zn or Mn reductant*



In a nitrogen-filled glove box, NiCl<sub>2</sub>(dme) (2.2 mg, 10 mol%), <sup>t</sup>Butpy (4.0 mg, 10 mol%), and DMA (1 mL) were added to a 1-dram vial. This solution was stirred at 800 rpm in the glove box for 30 min to allow complexation of Ni with the ligand, followed by sequential addition of 2,4,6-triphenyl-1-(3-phenylpropyl)pyridinium tetrafluoroborate (72 mg, 0.14 mmol, 1.4 equiv), aryl bromide (0.1 mmol, 1.0 equiv) and Zn powder (13 mg, 0.2 mmol, 2.0 equiv) or Mn powder (11

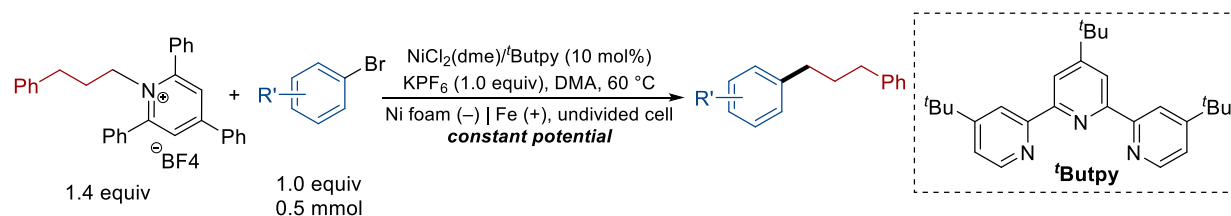
mg, 0.2 mmol, 2.0 equiv). The vial was capped with a screw cap fitted with a PTFE-faced silicone septum, then removed from the glove box and heated in a sand bath to 60 °C with stirring (1000 rpm) for 17 h. The reaction mixture was then cooled to room temperature and diluted with DMA (1 mL). 1,3,5-Trimethoxybenzene (5.6 mg, 0.033 mmol, 0.33 equiv) was added to the crude material. Then a 100  $\mu$ L aliquot of the solution was filtered through a 2-cm silica gel plug in a Pasteur pipette into a vial. 400  $\mu$ L CDCl<sub>3</sub> was also added to the pipette and eluted into the same vial. The resultant sample was analyzed by <sup>1</sup>H NMR spectroscopy and the yields were determined using 1,3,5-trimethoxybenzene as the internal standard.



In a nitrogen-filled glove box, NiCl<sub>2</sub>(dme) (1.54 mg, 7 mol%), <sup>t</sup>Bubpy (1.88 mg, 7 mol%), and DMA (1 mL) were added to a 1-dram vial. This solution was stirred at 800 rpm in the glove box for 30 min to allow complexation of Ni with the ligand, followed by sequential addition of 2,4,6-triphenyl-1-(tetrahydro-2*H*-pyran-4-yl)pyridin-1-ium tetrafluoroborate (67 mg, 0.14 mmol, 1.4 equiv), aryl bromide or aryl chloride (0.1 mmol, 1.0 equiv) and Zn powder (13 mg, 0.2 mmol, 2.0 equiv) or Mn powder (11 mg, 0.2 mmol, 2.0 equiv). The vial was capped with a screw cap fitted with a PTFE-faced silicone septum, then removed from the glove box and stirred (1000 rpm) at room temperature for 17 h. The reaction mixture was then diluted with DMA (1 mL). 1,3,5-Trimethoxybenzene (5.6 mg, 0.033 mmol, 0.33 equiv) was added to the crude material. Then a 100  $\mu$ L aliquot of the solution was filtered through a 2-cm silica gel plug in a Pasteur pipette into a vial. 400  $\mu$ L CDCl<sub>3</sub> was also added to the pipette and eluted into the same vial. The resultant

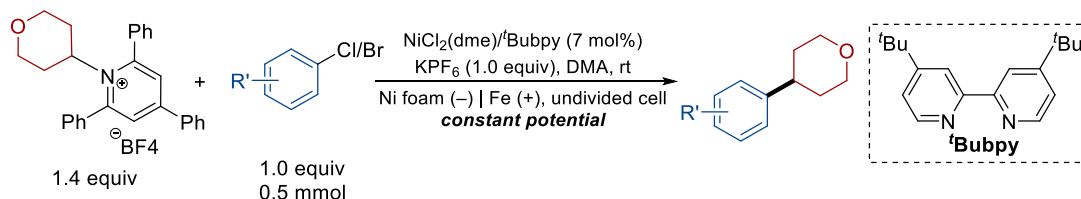
sample was analyzed by  $^1\text{H}$  NMR spectroscopy and the yields were determined using 1,3,5-trimethoxybenzene as the internal standard.

*Electrochemical reductive coupling of Katritzky salts with aryl halides*



**General Procedure 1 (GP 1):** In a nitrogen-filled glove box,  $\text{NiCl}_2(\text{dme})$  (11 mg, 10 mol%),  $t\text{BuPy}$  (20 mg, 10 mol%), and DMA (5 mL) were added to a 2-dram vial. This solution was stirred at 800 rpm in the glove box for 30 min to allow complexation of Ni with the ligand. To an undivided cell (Figure 3B.4) fitted with a cross-shaped stir bar was added  $\text{KPF}_6$  (92 mg, 0.5 mmol, 1.0 equiv, unless otherwise noted), 2,4,6-triphenyl-1-(3-phenylpropyl)pyridin-1-ium tetrafluoroborate (360 mg, 0.7 mmol, 1.4 equiv), and aryl bromide (0.5 mmol, 1.0 equiv) under air. The cell was transferred into the glove box, followed by addition of the catalyst solution and installation of a Ni foam cathode, a  $\text{Ag}/\text{AgNO}_3$  reference electrode, and an Fe rod anode. The cell was then sealed with a rubber septum before removing from the glove box. A thin Teflon tube was introduced immediately into the cell to allow continuous nitrogen bubbling. The reaction mixture was stirred at 1000 rpm for 10 min to allow full dissolution of all reagents and exclusion of adventitious oxygen. After that, the Teflon tube was removed, and the top of the rubber septum was sealed with silicone gel. The reaction mixture was electrolyzed under the desired constant potential for 10–17 h at 60 °C with stirring (800 rpm). The reaction was automatically stopped by the potentiostat after the desired amount of charge (specified in Section 3B.VIII for each product) was passed. Upon reaction completion, the reaction mixture was cooled to room temperature and diluted with water (25 mL). The solution was extracted with ethyl acetate (50 mL  $\times$  2) and the

organic layers were combined and washed with brine (50 mL). The resultant organic solution was dried over anhydrous  $\text{Na}_2\text{SO}_4$ , then concentrated *in vacuo*. The obtained residue was purified by flash column chromatography.



**General Procedure 2 (GP 2):** In a nitrogen-filled glove box,  $\text{NiCl}_2(\text{dme})$  (7.7 mg, 7 mol%),  $t\text{BuBupy}$  (9.4 mg, 7 mol%), and DMA (5 mL) were added to a 2-dram vial. This solution was stirred at 800 rpm in the glove box for 30 min to allow complexation of Ni with the ligand. To an undivided cell (Figure 3B.4) fitted with a cross-shaped stir bar was added  $\text{KPF}_6$  (92 mg, 0.5 mmol, 1.0 equiv, unless otherwise noted), 2,4,6-triphenyl-1-(tetrahydro-2H-pyran-4-yl)pyridin-1-ium tetrafluoroborate (335 mg, 0.7 mmol, 1.4 equiv), and aryl bromide or chloride (0.5 mmol, 1.0 equiv) under air. The cell was transferred into the glove box, followed by addition of the catalyst solution and installation of a Ni foam cathode, a  $\text{Ag}/\text{AgNO}_3$  reference electrode, and an Fe rod anode. The cell was then sealed with a rubber septum before removing from the glove box. A thin Teflon tube was introduced immediately into the cell to allow continuous nitrogen bubbling. The reaction mixture was stirred at 1000 rpm for 10 min to allow full dissolution of all reagents and exclusion of adventitious oxygen. After that, the Teflon tube was removed, and the top of rubber septum was sealed with silicone gel. The reaction mixture was electrolyzed under the desired constant potential for 10–17 h at room temperature with stirring (800 rpm). The reaction was automatically stopped by the potentiostat after the desired amount of charge (specified in Section 3B.VIII for each product) was passed. Upon reaction completion, the reaction mixture was diluted with water (25 mL) and extracted with ethyl acetate (50 mL  $\times$  2). The organic layers were

combined and washed with brine (50 mL). The resultant organic solution was dried over anhydrous  $\text{Na}_2\text{SO}_4$ , then concentrated *in vacuo*. The obtained residue was purified by flash column chromatography.

### 3B.VII. Cyclic Voltammetry Studies

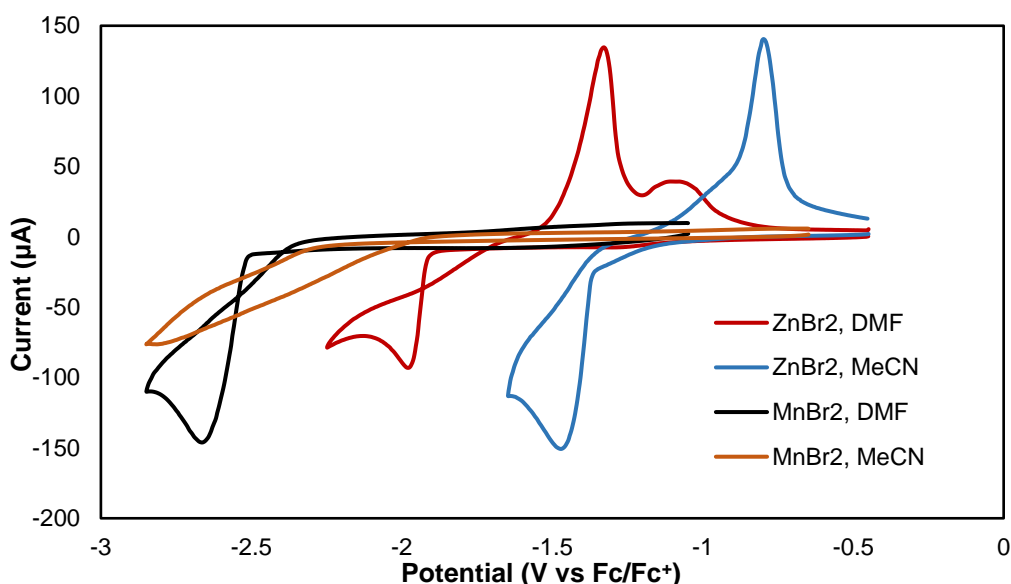


**Figure 3B.7.** CVs of metal salts (10 mM) in DMF (5 mL) or MeCN (5 mL), with  ${}^t\text{Bu}_4\text{NPF}_6$  (0.2 M) as supporting electrolyte, under  $\text{N}_2$  atmosphere, at room temperature, scan rate = 20 mV/s, initially scanning towards a more negative potential.

Discussion: The CV of  $\text{ZnBr}_2$  in DMF or MeCN displays an ill-defined redox couple with a large peak-to-peak separation and a sharp oxidation peak, indicating poor kinetics for the Zn redox and Zn electroplating on the working electrode during the sweep. The CV traces of  $\text{MnBr}_2$  are fully irreversible, again indicating poor kinetics for Mn redox under CV conditions. Overall, these results suggest that CV is not a reliable tool for measuring the thermodynamic potentials of Zn and Mn, and the derived redox potentials thereby may not be appropriate for use in relevant studies.

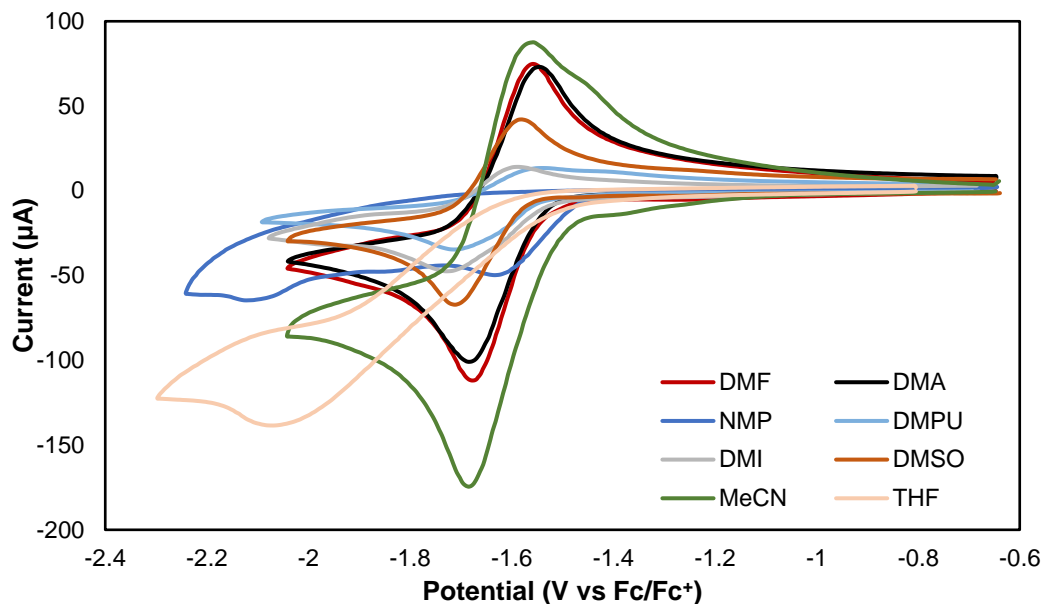


**Figure 3B.8.** CVs of  $[\text{Ni}(\text{bpy})_3]\text{Cl}_2$  (4 mM) in various organic solvents, with  ${}^n\text{Bu}_4\text{NPF}_6$  (0.1 M) as supporting electrolyte, under  $\text{N}_2$  atmosphere, at room temperature, scan rate = 100 mV/s, initially scanning towards a more negative potential.

Discussion:  $[\text{Ni}(\text{bpy})_3]\text{Cl}_2$  displays a fully reversible 2-electron redox couple in DMF, DMA, and DMSO, but a slightly disrupted peak in DMPU, DMI, and MeCN, possibly due to solvent coordination to Ni center. CV traces in NMP and THF are not reversible, which can again be attributed to solvent coordination or a slow re-coordination process of chlorides and ligands back to Ni center. Therefore, no half potentials can be derived from CV traces of  $[\text{Ni}(\text{bpy})_3]\text{Cl}_2$  in NMP and THF. Given these considerations, half-peak potentials instead of half potentials were reported in Figure 3.3B for consistency.

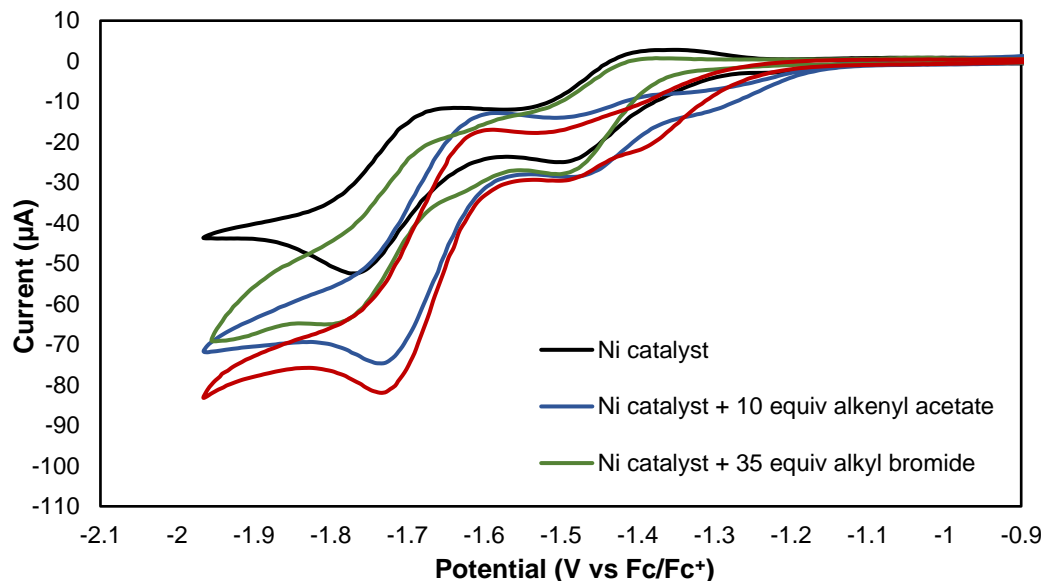


**Figure 3B.9.** CVs of Ni/dmbpy catalyst in the presence or absence of substrates for cross-coupling of alkenyl acetate with alkyl bromide. Black trace: Ni catalyst [5 mM NiBr<sub>2</sub>(dme) + 7.5 mM 5,5'-dimethyl-2,2'-bipyridine]. Blue trace: Ni catalyst + 10 equiv 1-phenylvinyl acetate. Green trace: Ni catalyst + 35 equiv ethyl 4-bromobutanoate. Red trace: Ni catalyst + 10 equiv 1-phenylvinyl acetate + 35 equiv ethyl 4-bromobutanoate. All CVs were recorded in DMA (5 mL), with KPF<sub>6</sub> (0.1 M) as supporting electrolyte, under N<sub>2</sub> atmosphere, at 40 °C, scan rate = 20 mV/s, initially scanning towards a more negative potential.

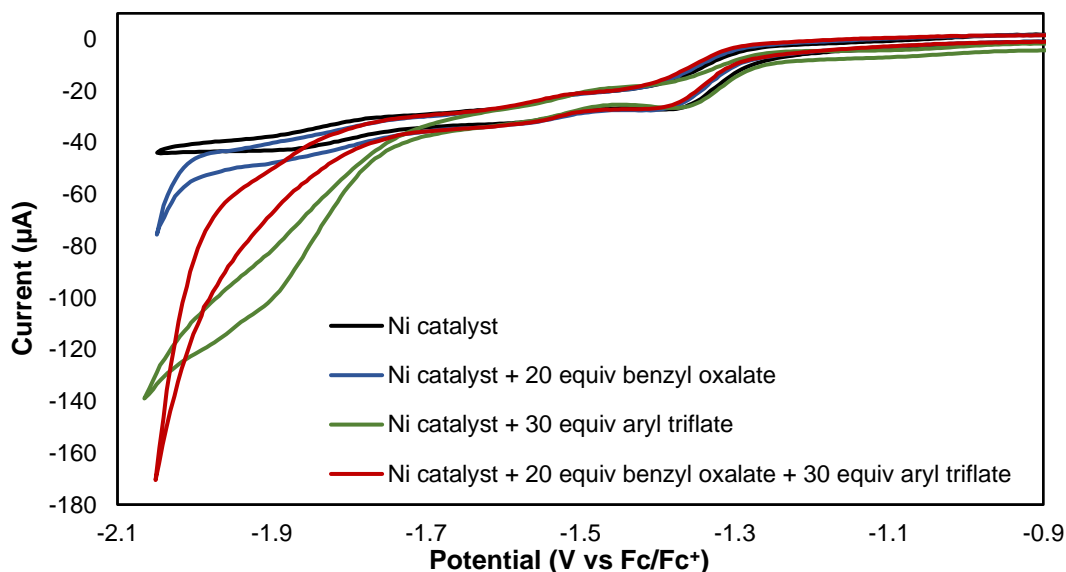
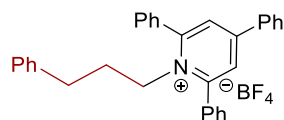


**Figure 3B.10.** CVs of Ni/dppf/phen catalyst system in the presence or absence of substrates for cross-coupling of benzyl oxalate with aryl triflate. Black trace: Ni catalyst [2.5 mM NiCl<sub>2</sub>(dppf) + 2.5 mM dppf + 0.5 mM 1,10-phenanthroline]. Blue trace: Ni catalyst + 20 equiv benzyl methyl oxalate. Green trace: Ni catalyst + 30 equiv methyl 4-(((trifluoromethyl)sulfonyl)oxy)benzoate. Red trace: Ni catalyst + 20 equiv benzyl methyl oxalate + 30 equiv methyl 4-(((trifluoromethyl)sulfonyl)oxy)benzoate. All CVs were recorded in DMF (5 mL), with KPF<sub>6</sub> (0.1 M) as supporting electrolyte, under N<sub>2</sub> atmosphere, at 80 °C, scan rate = 20 mV/s, initially scanning towards a more negative potential.

### 3B.VIII. Compound Characterization Data

#### 2,4,6-triphenyl-1-(3-phenylpropyl)pyridin-1-ium tetrafluoroborate (**1**)



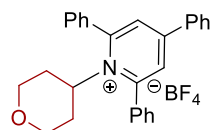
The spectroscopic data matched those reported in the literature.<sup>6</sup>

**<sup>1</sup>H NMR** (500 MHz, CDCl<sub>3</sub>) δ 7.81 (s, 2H), 7.72 (td, *J* = 6.8, 1.3 Hz, 6H), 7.60 – 7.44 (m, 9H), 7.09 – 7.03 (m, 3H), 6.65 – 6.62 (m, 2H), 4.40 – 4.34 (m, 2H), 2.09 (t, *J* = 7.1 Hz, 2H), 1.84 – 1.74 (m, 2H).

**<sup>13</sup>C NMR** (126 MHz, CDCl<sub>3</sub>) δ 156.4, 155.9, 138.8, 134.1, 132.6, 132.0, 131.0, 129.7, 129.3, 128.9, 128.5, 128.2, 127.7, 126.8, 126.2, 54.3, 32.3, 30.7.

**HRMS (ESI<sup>+</sup>)** Calc: [M]<sup>+</sup> (C<sub>32</sub>H<sub>28</sub>N) 426.2216; measured: 426.2206 = 2.3 ppm difference.

#### 2,4,6-triphenyl-1-(tetrahydro-2H-pyran-4-yl)pyridin-1-ium tetrafluoroborate (**2**)



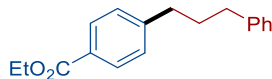
The spectroscopic data matched those reported in the literature.<sup>9</sup>

**<sup>1</sup>H NMR** (500 MHz, CDCl<sub>3</sub>) δ 7.76 – 7.73 (m, 6H), 7.70 – 7.66 (m, 2H), 7.64 – 7.54 (m, 6H), 7.53 – 7.48 (m, 1H), 7.42 (dd, *J* = 8.5, 7.1 Hz, 2H), 4.87 (tt, *J* = 12.4, 3.2 Hz, 1H), 3.74 – 3.68 (m, 2H), 2.79 (td, *J* = 11.7, 1.8 Hz, 2H), 2.06 (dt, *J* = 12.5, 2.4 Hz, 2H), 1.87 (qd, *J* = 12.2, 4.3 Hz, 2H).

**<sup>13</sup>C NMR** (126 MHz, CDCl<sub>3</sub>) δ 157.2, 155.3, 134.0, 133.8, 132.0, 131.1, 129.6, 129.4, 129.0, 128.3, 128.2, 69.1, 67.8, 33.8.

**HRMS (ESI<sup>+</sup>)** Calc: [M]<sup>+</sup> (C<sub>28</sub>H<sub>26</sub>NO) 392.2009; measured: 392.2002 = 1.8 ppm difference.

ethyl 4-(3-phenylpropyl)benzoate (**1a**)



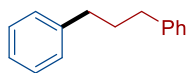
**GP 1** was followed using ethyl 4-bromobenzoate (114 mg, 0.5 mmol, 1.0 equiv) under reductive electrolysis ( $-1.25$  V vs Fc/Fc<sup>+</sup>, 2.5 F/mol), which furnished the title compound following purification by flash column chromatography (2:98 ethyl acetate:pentane) as a colorless oil (105 mg, 78% yield). The spectroscopic data matched those reported in the literature.<sup>10</sup>

**<sup>1</sup>H NMR** (500 MHz, CDCl<sub>3</sub>)  $\delta$  7.96 (d,  $J = 8.3$  Hz, 2H), 7.31 – 7.14 (m, 7H), 4.36 (q,  $J = 7.1$  Hz, 2H), 2.69 (t,  $J = 7.7$  Hz, 2H), 2.64 (t,  $J = 7.7$  Hz, 2H), 2.01 – 1.92 (m, 2H), 1.38 (t,  $J = 7.1$  Hz, 3H).

**<sup>13</sup>C NMR** (126 MHz, CDCl<sub>3</sub>)  $\delta$  166.7, 147.7, 141.9, 129.7, 128.45, 128.39, 125.9, 60.8, 35.44, 35.36, 32.6, 14.4.

**HRMS (ESI<sup>+</sup>)** Calc: [M+H]<sup>+</sup> (C<sub>18</sub>H<sub>21</sub>O<sub>2</sub>) 269.1536; measured: 269.1534 = 0.7 ppm difference.

1,3-diphenylpropane (**1b**)



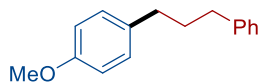
**GP 1** was followed using bromobenzene (78 mg, 0.5 mmol, 1.0 equiv) under reductive electrolysis ( $-1.40$  V vs Fc/Fc<sup>+</sup>, 2.5 F/mol), which furnished the title compound following purification by flash column chromatography (0:100 ethyl acetate:pentane) as a colorless oil (79 mg, 81% yield). This is the corrected yield that excluded the inseparable alkyl dimer byproduct (1.5% with respect to the product based on <sup>1</sup>H NMR). The spectroscopic data matched those reported in the literature.<sup>10</sup>

**<sup>1</sup>H NMR** (500 MHz, CDCl<sub>3</sub>)  $\delta$  7.26 (dd,  $J = 8.1, 6.8$  Hz, 4H), 7.19 – 7.13 (m, 6H), 2.67 – 2.61 (m, 4H), 2.00 – 1.90 (m, 2H).

$^{13}\text{C NMR}$  (126 MHz,  $\text{CDCl}_3$ )  $\delta$  142.4, 128.5, 128.4, 125.8, 35.5, 33.0.

**HRMS (ESI<sup>+</sup>)** Calc:  $[\text{M}+\text{H}]^+$  ( $\text{C}_{16}\text{H}_{17}$ ) 197.1325; measured: 197.1323 = 1.0 ppm difference.

1-methoxy-4-(3-phenylpropyl)benzene (**1c**)



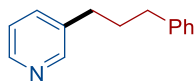
**GP 1** was followed using 1-bromo-4-methoxybenzene (94 mg, 0.5 mmol, 1.0 equiv) under reductive electrolysis ( $-1.50\text{ V}$  vs  $\text{Fc}/\text{Fc}^+$ , 2.5 F/mol), which furnished the title compound following purification by flash column chromatography (1:99 ethyl acetate:pentane) as a colorless oil (98 mg, 87% yield). The spectroscopic data matched those reported in the literature.<sup>10</sup>

$^1\text{H NMR}$  (500 MHz,  $\text{CDCl}_3$ )  $\delta$  7.30 – 7.24 (m, 2H), 7.20 – 7.14 (m, 3H), 7.12 – 7.06 (m, 2H), 6.82 (d,  $J = 8.5\text{ Hz}$ , 2H), 3.78 (s, 3H), 2.63 (t,  $J = 7.7\text{ Hz}$ , 2H), 2.59 (t,  $J = 7.6\text{ Hz}$ , 2H), 1.92 (tt,  $J = 9.3, 6.8\text{ Hz}$ , 2H).

$^{13}\text{C NMR}$  (126 MHz,  $\text{CDCl}_3$ )  $\delta$  157.8, 142.4, 134.4, 129.3, 128.5, 128.3, 125.7, 113.8, 55.3, 35.4, 34.5, 33.2.

**HRMS (ESI<sup>+</sup>)** Calc:  $[\text{M}+\text{H}]^+$  ( $\text{C}_{16}\text{H}_{19}\text{O}$ ) 227.1430; measured: 227.1427 = 1.3 ppm difference.

3-(3-phenylpropyl)pyridine (**1d**)



**GP 1** was followed using 3-bromopyridine (79 mg, 0.5 mmol, 1.0 equiv), LiBr (87 mg, 1.0 mmol, 2.0 equiv) instead of  $\text{KPF}_6$  as electrolyte, under reductive electrolysis ( $-1.65\text{ V}$  vs  $\text{Fc}/\text{Fc}^+$ , 3.0 F/mol), which furnished the title compound following purification by flash column

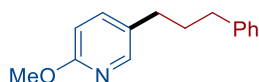
chromatography (20:80 ethyl acetate:pentane) as a pale-yellow oil (59 mg, 60% yield). The spectroscopic data matched those reported in the literature.<sup>11</sup>

**<sup>1</sup>H NMR** (500 MHz, CDCl<sub>3</sub>) δ 8.44 (s, 2H), 7.46 (dt, *J* = 7.8, 2.0 Hz, 1H), 7.27 (dd, *J* = 8.2, 6.9 Hz, 2H), 7.21 – 7.14 (m, 4H), 2.63 (dt, *J* = 10.5, 7.7 Hz, 4H), 1.95 (tt, *J* = 9.3, 6.9 Hz, 2H).

**<sup>13</sup>C NMR** (126 MHz, CDCl<sub>3</sub>) δ 150.0, 147.3, 141.7, 137.5, 135.8, 128.4, 126.0, 123.3, 35.3, 32.6, 32.5.

**HRMS (ESI<sup>+</sup>)** Calc: [M+H]<sup>+</sup> (C<sub>14</sub>H<sub>16</sub>N) 198.1277; measured: 198.1275 = 1.0 ppm difference.

2-methoxy-5-(3-phenylpropyl)pyridine (**1e**)



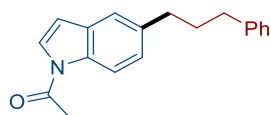
**GP 1** was followed using 5-bromo-2-methoxypyridine (94 mg, 0.5 mmol, 1.0 equiv) under reductive electrolysis (−1.40 V vs Fc/Fc<sup>+</sup>, 3.0 F/mol), which furnished the title compound following purification by flash column chromatography (30:70 ethyl acetate:pentane) as a pale-yellow oil (85 mg, 75% yield). The spectroscopic data matched those reported in the literature.<sup>12</sup>

**<sup>1</sup>H NMR** (500 MHz, CDCl<sub>3</sub>) δ 7.99 (d, *J* = 2.5 Hz, 1H), 7.41 (dd, *J* = 8.4, 2.5 Hz, 1H), 7.32 – 7.23 (m, 2H), 7.23 – 7.15 (m, 3H), 6.69 (d, *J* = 8.3 Hz, 1H), 3.93 (s, 3H), 2.65 (t, 2H), 2.57 (t, *J* = 7.6 Hz, 2H), 1.96 – 1.87 (m, 2H).

**<sup>13</sup>C NMR** (126 MHz, CDCl<sub>3</sub>) δ 162.7, 146.0, 141.9, 139.0, 130.0, 128.44, 128.39, 125.9, 110.5, 53.4, 35.2, 32.8, 31.5.

**HRMS (ESI<sup>+</sup>)** Calc: [M+H]<sup>+</sup> (C<sub>15</sub>H<sub>18</sub>NO) 228.1383; measured: 228.1379 = 1.8 ppm difference.

1-(5-(3-phenylpropyl)-1H-indol-1-yl)ethan-1-one (**1f**)



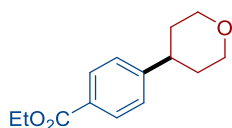
**GP 1** was followed using 1-(5-bromo-1H-indol-1-yl)ethan-1-one (119 mg, 0.5 mmol, 1.0 equiv) under reductive electrolysis ( $-1.40$  V vs Fc/Fc<sup>+</sup>, 2.5 F/mol), which furnished the title compound following purification by flash column chromatography (10:90 ethyl acetate:pentane) as a yellow oil (118 mg, 85% yield). The spectroscopic data matched those reported in the literature.<sup>10</sup>

**<sup>1</sup>H NMR** (500 MHz, CDCl<sub>3</sub>)  $\delta$  8.32 (d,  $J = 8.6$  Hz, 1H), 7.38 (d,  $J = 3.7$  Hz, 1H), 7.36 (s, 1H), 7.30 – 7.25 (m, 2H), 7.21 – 7.15 (m, 4H), 6.57 (d,  $J = 3.7$  Hz, 1H), 2.74 (t,  $J = 7.7$  Hz, 2H), 2.66 (t,  $J = 7.6$  Hz, 2H), 2.61 (s, 3H), 2.03 – 1.96 (m, 2H).

**<sup>13</sup>C NMR** (126 MHz, CDCl<sub>3</sub>)  $\delta$  168.5, 142.4, 137.8, 134.0, 130.7, 128.5, 128.3, 125.9, 125.8, 125.3, 120.3, 116.3, 109.1, 35.43, 35.37, 33.4, 23.9.

**HRMS (ESI<sup>+</sup>)** Calc: [M+H]<sup>+</sup> (C<sub>19</sub>H<sub>19</sub>NONa) 300.1359; measured: 300.1354 = 1.7 ppm difference.

ethyl 4-(tetrahydro-2H-pyran-4-yl)benzoate (**2a**)



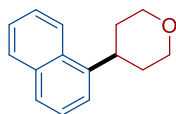
**GP 2** was followed using ethyl 4-bromobenzoate (114 mg, 0.5 mmol, 1.0 equiv) under reductive electrolysis ( $-1.30$  V vs Fc/Fc<sup>+</sup>, 2.5 F/mol), which furnished the title compound following purification by flash column chromatography (4:96 ethyl acetate:pentane) as a white solid (111 mg, 95% yield). The spectroscopic data matched those reported in the literature.<sup>13</sup>

**<sup>1</sup>H NMR** (500 MHz, CDCl<sub>3</sub>)  $\delta$  7.99 (d,  $J = 8.4$  Hz, 2H), 7.29 (d,  $J = 8.4$  Hz, 2H), 4.36 (q,  $J = 7.1$  Hz, 2H), 4.12 – 4.05 (m, 2H), 3.53 (td,  $J = 11.6, 2.4$  Hz, 3H), 2.82 (tt,  $J = 11.8, 4.2$  Hz, 1H), 1.89 – 1.73 (m, 4H), 1.38 (t,  $J = 7.1$  Hz, 3H).

$^{13}\text{C}$  NMR (126 MHz,  $\text{CDCl}_3$ )  $\delta$  166.5, 151.0, 129.9, 128.7, 126.8, 68.2, 60.8, 41.7, 33.6, 14.4.

**HRMS (ESI<sup>+</sup>)** Calc:  $[\text{M}+\text{H}]^+$  ( $\text{C}_{14}\text{H}_{19}\text{O}_3$ ) 235.1329; measured: 235.1326 = 1.3 ppm difference.

4-(naphthalen-1-yl)tetrahydro-2H-pyran (**2b**)



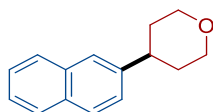
**GP 2** was followed using ethyl 1-bromonaphthalene (104 mg, 0.5 mmol, 1.0 equiv) under reductive electrolysis ( $-1.40$  V vs  $\text{Fc}/\text{Fc}^+$ , 2.5 F/mol), which furnished the title compound following purification by flash column chromatography (5:95 ethyl acetate:pentane) as a white powder (87 mg, 82% yield). The spectroscopic data matched those reported in the literature.<sup>13</sup>

$^1\text{H}$  NMR (500 MHz,  $\text{CDCl}_3$ )  $\delta$  8.12 (d,  $J = 8.4$  Hz, 1H), 7.88 (dd,  $J = 8.0, 1.5$  Hz, 1H), 7.74 (d,  $J = 8.0$  Hz, 1H), 7.55 – 7.44 (m, 3H), 7.41 (dd,  $J = 7.2, 1.3$  Hz, 1H), 4.20 – 4.13 (m, 2H), 3.71 (td,  $J = 11.5, 2.5$  Hz, 2H), 3.60 (tt,  $J = 11.5, 4.0$  Hz, 1H), 2.04 – 1.88 (m, 4H).

$^{13}\text{C}$  NMR (126 MHz,  $\text{CDCl}_3$ )  $\delta$  141.5, 134.0, 131.1, 129.1, 126.8, 125.9, 125.7, 125.4, 122.8, 122.6, 68.7, 36.7, 33.8.

**HRMS (ESI<sup>+</sup>)** Calc:  $[\text{M}+\text{H}]^+$  ( $\text{C}_{15}\text{H}_{17}\text{O}$ ) 213.1274; measured: 213.1272 = 0.9 ppm difference.

4-(naphthalen-2-yl)tetrahydro-2H-pyran (**2c**)



**GP 2** was followed using ethyl 1-bromonaphthalene (104 mg, 0.5 mmol, 1.0 equiv) under reductive electrolysis ( $-1.50$  V vs  $\text{Fc}/\text{Fc}^+$ , 2.5 F/mol), which furnished the title compound

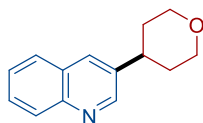
following purification by flash column chromatography (10:90 ethyl acetate:pentane) as a white solid (94 mg, 89% yield). The spectroscopic data matched those reported in the literature.<sup>13</sup>

**<sup>1</sup>H NMR** (500 MHz, CDCl<sub>3</sub>)  $\delta$  7.79 (dd,  $J$  = 8.9, 2.9 Hz, 3H), 7.63 (s, 1H), 7.43 (dq,  $J$  = 8.0, 6.8, 1.5 Hz, 2H), 7.36 (dd,  $J$  = 8.5, 1.8 Hz, 1H), 4.14 – 4.08 (m, 2H), 3.56 (td,  $J$  = 11.7, 2.2 Hz, 2H), 2.90 (tt,  $J$  = 11.9, 4.0 Hz, 1H), 1.97 – 1.80 (m, 4H).

**<sup>13</sup>C NMR** (126 MHz, CDCl<sub>3</sub>)  $\delta$  143.3, 133.7, 132.3, 128.1, 127.7, 127.6, 126.0, 125.7, 125.4, 124.8, 68.5, 41.7, 33.9.

**HRMS (ESI<sup>+</sup>)** Calc: [M+H]<sup>+</sup> (C<sub>15</sub>H<sub>17</sub>O) 213.1274; measured: 213.1273 = 0.5 ppm difference.

3-(tetrahydro-2*H*-pyran-4-yl)quinoline (**2d**)



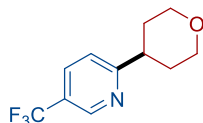
**GP 2** was followed using 3-bromoquinoline (104 mg, 0.5 mmol, 1.0 equiv) under reductive electrolysis (–1.45 V vs Fc/Fc<sup>+</sup>, 2.5 F/mol), which furnished the title compound following purification by flash column chromatography (50:50 ethyl acetate:pentane) as a white solid (41 mg, 38% yield). This is the corrected yield that excluded the inseparable aryl dimer byproduct (6% with respect to the product based on <sup>1</sup>H NMR). The spectroscopic data matched those reported in the literature.<sup>14</sup>

**<sup>1</sup>H NMR** (500 MHz, CDCl<sub>3</sub>)  $\delta$  8.84 (d,  $J$  = 2.2 Hz, 1H), 8.09 (d,  $J$  = 8.4 Hz, 1H), 7.94 (d,  $J$  = 2.2 Hz, 1H), 7.80 (dd,  $J$  = 8.1, 1.4 Hz, 1H), 7.68 (ddd,  $J$  = 8.5, 6.8, 1.4 Hz, 1H), 7.54 (t,  $J$  = 7.5 Hz, 1H), 4.18 – 4.11 (m, 2H), 3.60 (td,  $J$  = 11.5, 2.7 Hz, 2H), 2.99 (tt,  $J$  = 11.6, 4.4 Hz, 1H), 2.00 – 1.85 (m, 4H).

$^{13}\text{C}$  NMR (126 MHz,  $\text{CDCl}_3$ )  $\delta$  150.9, 147.2, 138.2, 132.5, 129.2, 128.9, 128.2, 127.6, 126.7, 68.2, 39.2, 33.6.

**HRMS (ESI<sup>+</sup>)** Calc:  $[\text{M}+\text{H}]^+$  ( $\text{C}_{14}\text{H}_{16}\text{NO}$ ) 214.1226; measured: 214.1224 = 0.9 ppm difference.

2-(tetrahydro-2*H*-pyran-4-yl)-5-(trifluoromethyl)pyridine (**2e**)



**GP 2** was followed using 2-bromo-5-(trifluoromethyl)pyridine (113 mg, 0.5 mmol, 1.0 equiv), LiBr (87 mg, 1.0 mmol, 2.0 equiv) instead of  $\text{KPF}_6$  as electrolyte, under reductive electrolysis (–1.25 V vs  $\text{Fc}/\text{Fc}^+$ , 2.5 F/mol), which furnished the title compound following purification by flash column chromatography (33:67 ethyl acetate:pentane) as a pale-yellow oil (39 mg, 42% yield).

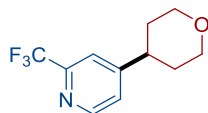
$^1\text{H}$  NMR (400 MHz,  $\text{CDCl}_3$ )  $\delta$  8.83 – 8.79 (m, 1H), 7.89 – 7.84 (m, 1H), 7.30 (d,  $J = 8.2$  Hz, 1H), 4.15 – 4.07 (m, 2H), 3.56 (td,  $J = 11.5, 2.8$  Hz, 2H), 3.04 (tt,  $J = 11.2, 4.5$  Hz, 1H), 1.98 – 1.83 (m, 4H).

$^{13}\text{C}$  NMR (126 MHz,  $\text{CDCl}_3$ )  $\delta$  168.3 (d,  $J = 1.5$  Hz), 146.3 (q,  $J = 4.1$  Hz), 133.7 (q,  $J = 3.5$  Hz), 124.6 (q,  $J = 33.0$  Hz), 123.7 (q,  $J = 272.1$  Hz), 120.6, 67.9, 43.5, 32.1.

$^{19}\text{F}$  NMR (377 MHz,  $\text{CDCl}_3$ )  $\delta$  -62.28.

**HRMS (ESI<sup>+</sup>)** Calc:  $[\text{M}+\text{H}]^+$  ( $\text{C}_{11}\text{H}_{13}\text{F}_3\text{NO}$ ) 232.0944; measured: 232.0941 = 1.3 ppm difference.

4-(tetrahydro-2*H*-pyran-4-yl)-2-(trifluoromethyl)pyridine (**2f**)



**GP 2** was followed using 4-chloro-2-(trifluoromethyl)pyridine (91 mg, 0.5 mmol, 1.0 equiv) under reductive electrolysis ( $-1.15$  V vs Fc/Fc<sup>+</sup>, 2.5 F/mol), which furnished the title compound following purification by flash column chromatography (33:67 ethyl acetate:pentane) as a colorless oil (102 mg, 88% yield).

**<sup>1</sup>H NMR** (400 MHz, CDCl<sub>3</sub>)  $\delta$  8.65 (d,  $J = 5.0$  Hz, 1H), 7.55 (s, 1H), 7.36 (d,  $J = 5.1$  Hz, 1H), 4.16 – 4.07 (m, 2H), 3.62 – 3.49 (m, 2H), 2.95 – 2.82 (m, 1H), 1.90 – 1.77 (m, 4H).

**<sup>13</sup>C NMR** (126 MHz, CDCl<sub>3</sub>)  $\delta$  156.4, 150.2, 148.5 (q,  $J = 34.1$  Hz), 124.7, 121.6 (q,  $J = 274.3$  Hz), 119.0 (q,  $J = 2.8$  Hz), 67.8, 40.9, 32.8.

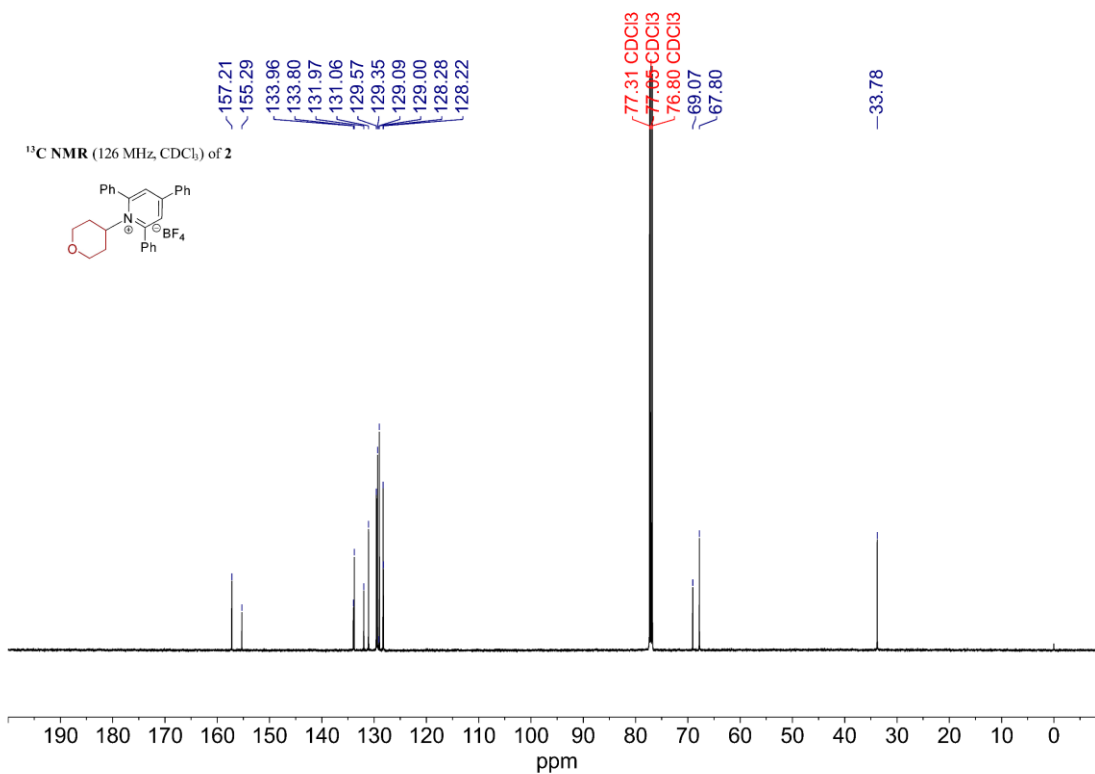
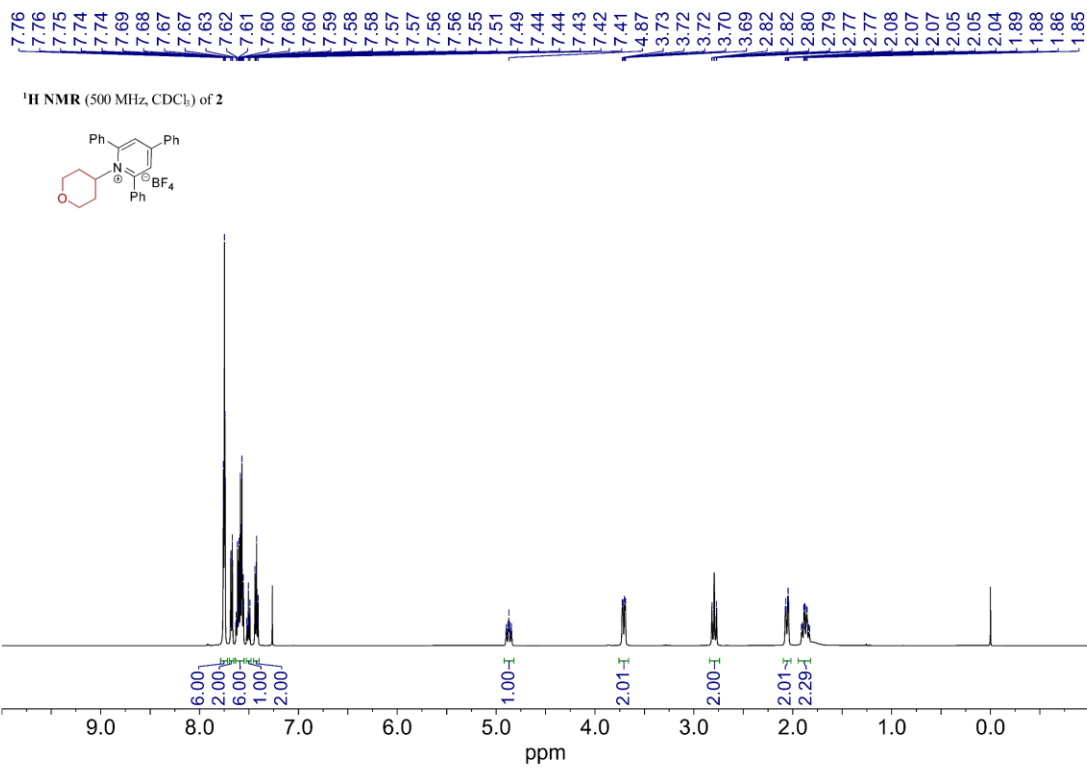
**<sup>19</sup>F NMR** (377 MHz, CDCl<sub>3</sub>)  $\delta$  -67.96.

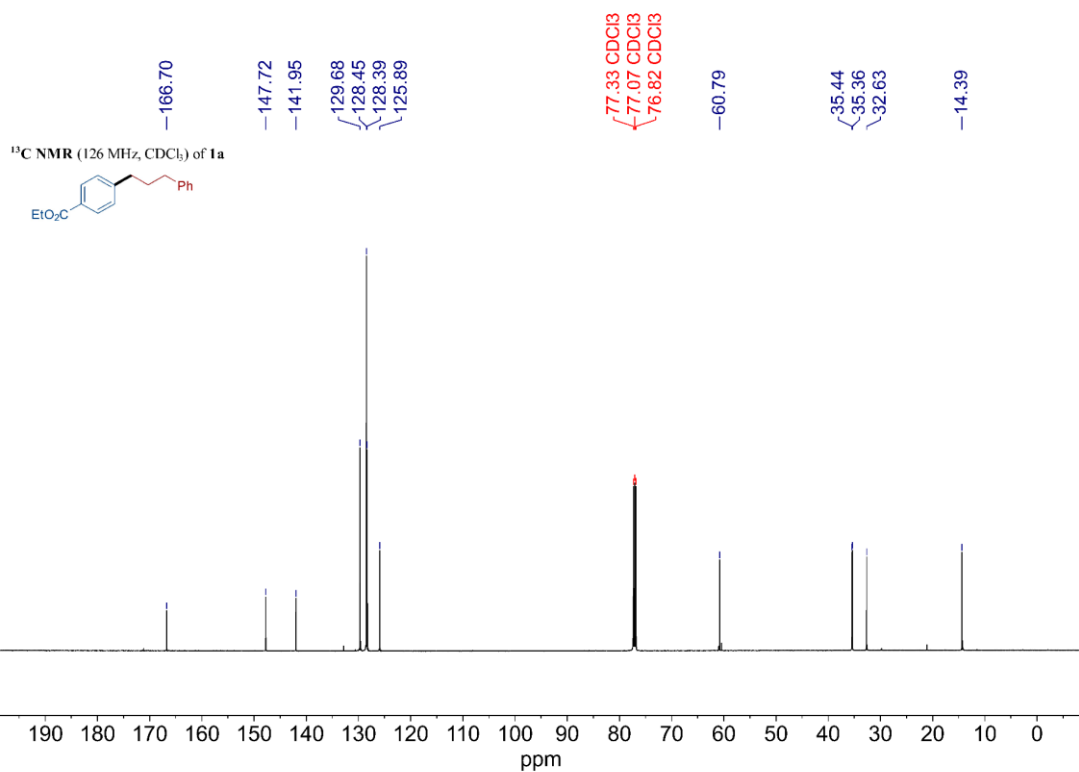
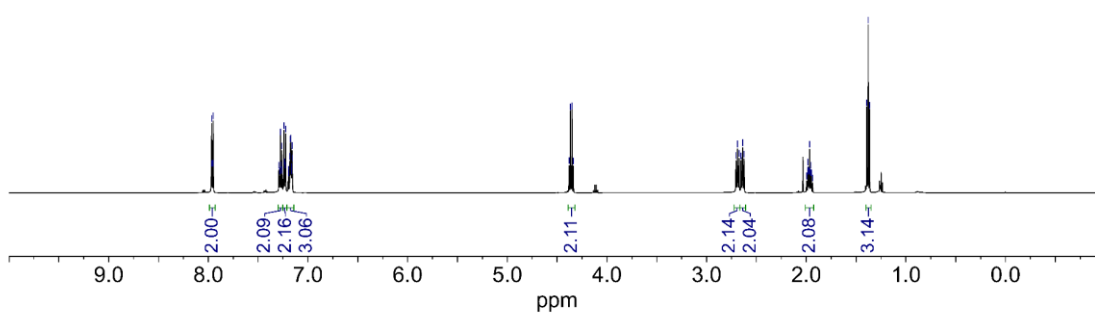
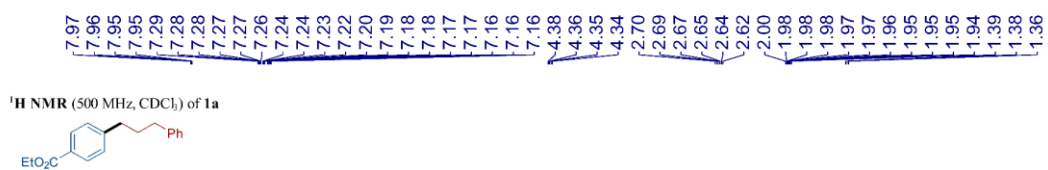
**HRMS (ESI<sup>+</sup>)** Calc: [M+H]<sup>+</sup> (C<sub>11</sub>H<sub>13</sub>F<sub>3</sub>NO) 232.0944; measured: 232.0941 = 1.3 ppm difference.

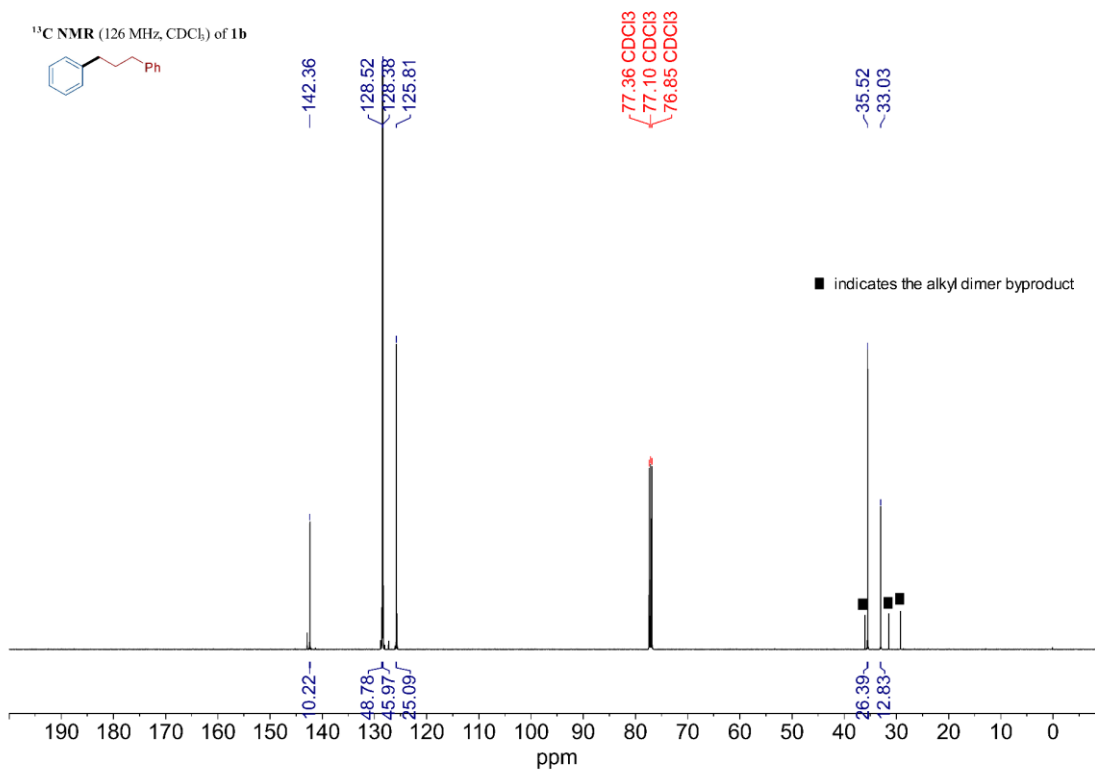
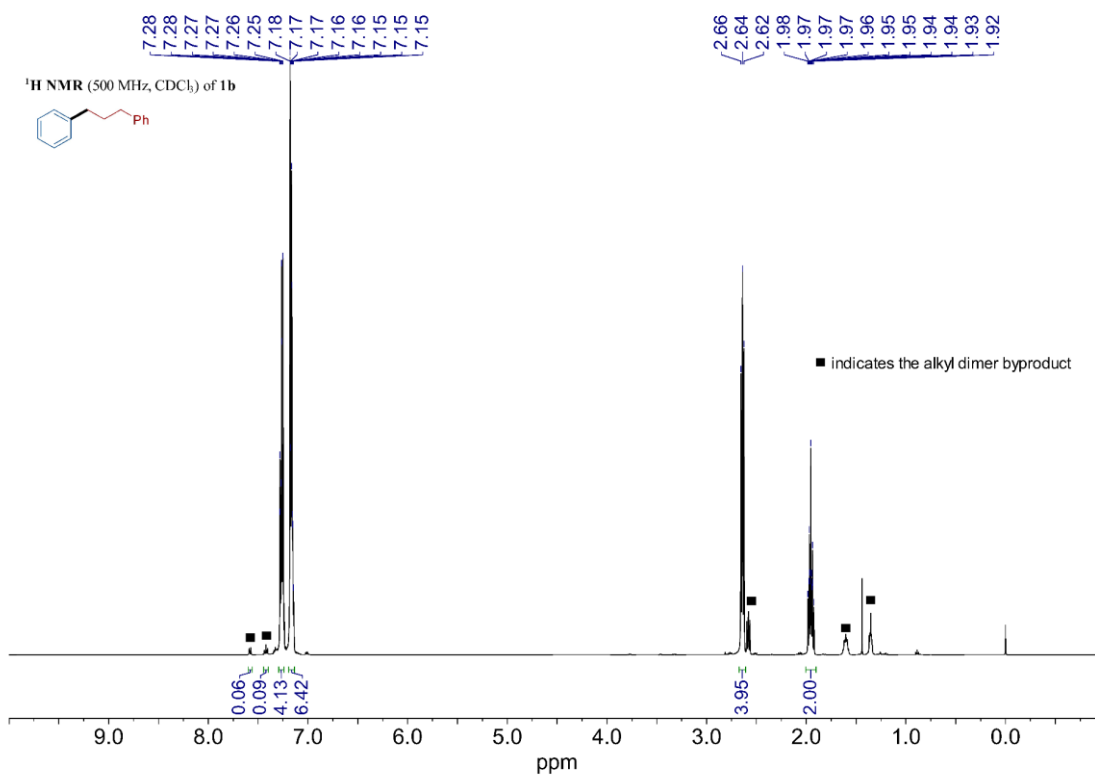
### 3B.IX. References

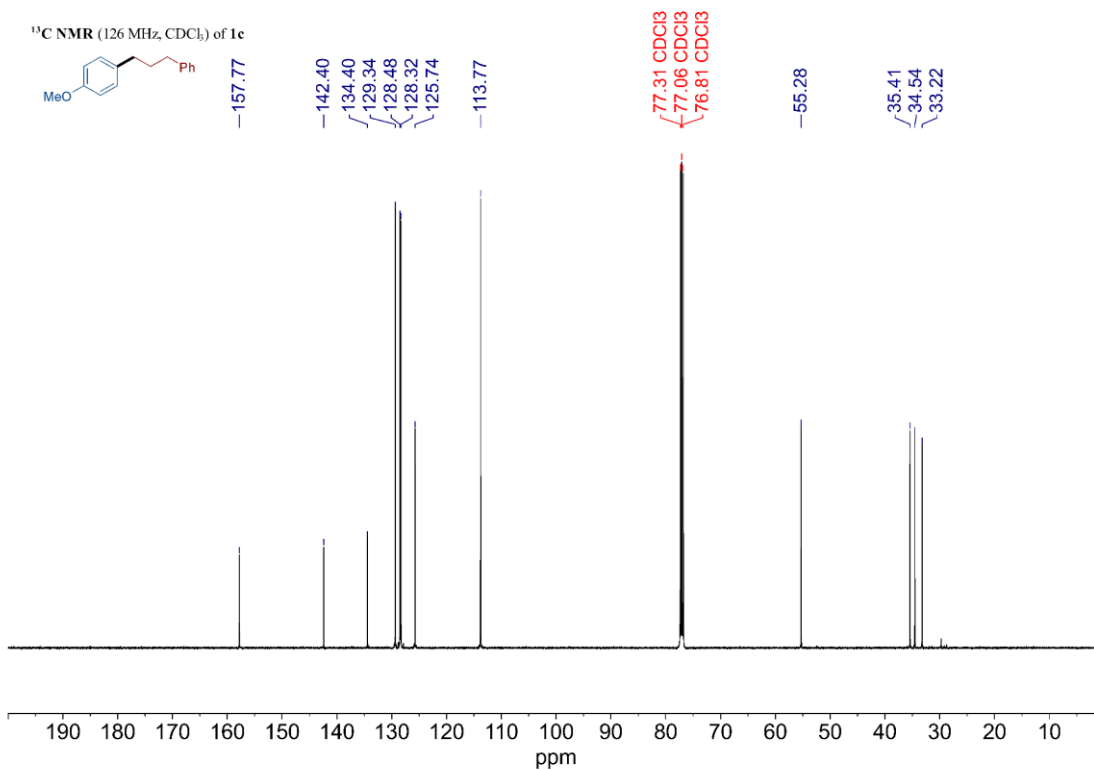
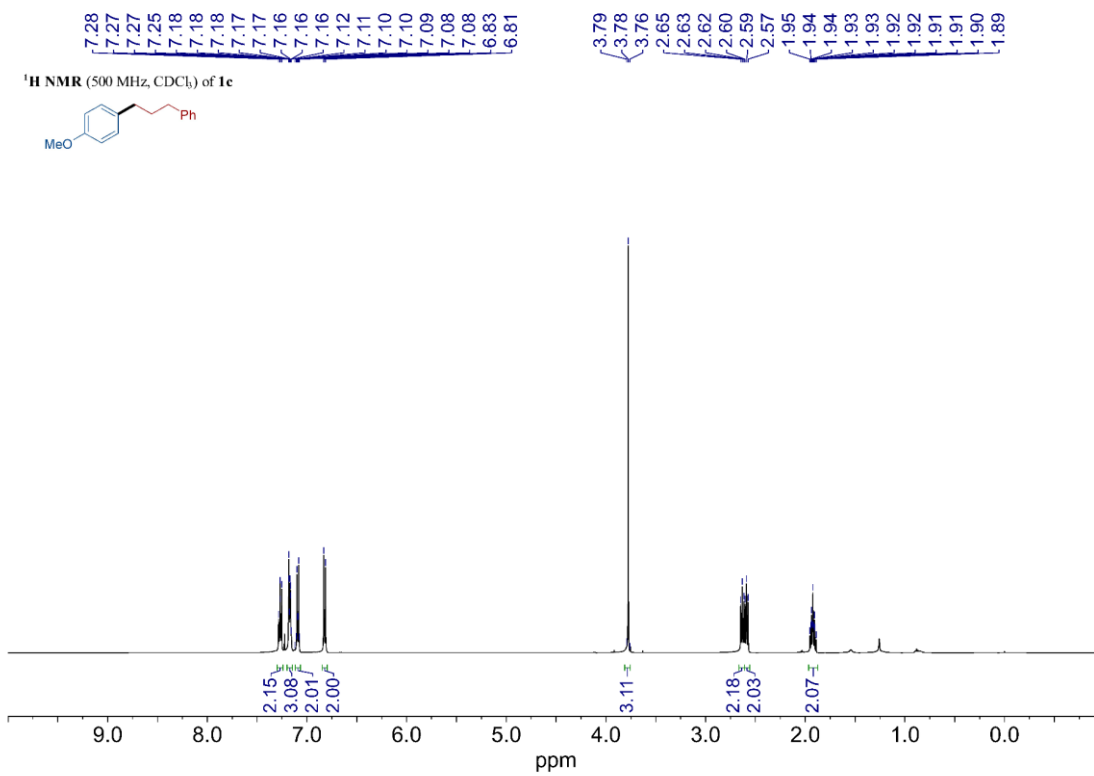
1. Goldfogel, M. J., Huang, L. & Weix, D. J. Cross-Electrophile Coupling. in *Nickel Catalysis in Organic Synthesis* 183–222 (John Wiley & Sons, Ltd, 2020).
2. Zhang, J., Lu, G., Xu, J., Sun, H. & Shen, Q. Nickel-Catalyzed Reductive Cross-Coupling of Benzyl Chlorides with Aryl Chlorides/Fluorides: A One-Pot Synthesis of Diarylmethanes. *Org. Lett.* **18**, 2860–2863 (2016).
3. Ma, N.-N. *et al.* Nickel-Catalyzed Direct Cross-Coupling of Aryl Thioether with Aryl Bromide. *Org. Lett.* **25**, 1771–1775. (2023)
4. Elgrishi, N. *et al.* A Practical Beginner's Guide to Cyclic Voltammetry. *J. Chem. Educ.* **95**, 197–206 (2018).
5. Anka-Lufford, L. L., Huihui, K. M. M., Gower, N. J., Ackerman, L. K. G. & Weix, D. J. Nickel-Catalyzed Cross-Electrophile Coupling with Organic Reductants in Non-Amide Solvents. *Chem. Eur. J.* **22**, 11564–11567 (2016).
6. Yue, H. *et al.* Nickel-catalyzed C–N bond activation: activated primary amines as alkylating reagents in reductive cross-coupling. *Chem. Sci.* **10**, 4430–4435 (2019).
7. Yan, X.-B., Li, C.-L., Jin, W.-J., Guo, P. & Shu, X.-Z. Reductive coupling of benzyl oxalates with highly functionalized alkyl bromides by nickel catalysis. *Chem. Sci.* **9**, 4529–4534 (2018).
8. Wang, L. *et al.* Visible-Light-Promoted  $\alpha$ -Benzylation of N-Phenyl  $\alpha$ -Amino Acids to  $\alpha$ -Amino Phenylpropanoids. *J. Org. Chem.* **88**, 11924–11934 (2023).
9. Plunkett, S., Basch, C. H., Santana, S. O. & Watson, M. P. Harnessing Alkylpyridinium Salts as Electrophiles in Deaminative Alkyl–Alkyl Cross-Couplings. *J. Am. Chem. Soc.* **141**, 2257–2262 (2019).
10. Perkins, R. J., Hughes, A. J., Weix, D. J. & Hansen, E. C. Metal-Reductant-Free Electrochemical Nickel-Catalyzed Couplings of Aryl and Alkyl Bromides in Acetonitrile. *Org. Process Res. Dev.* **23**, 1746–1751 (2019).
11. Figula, B. C., Kane, D. L., Balaraman, K. & Wolf, C. Organocuprate Cross-Coupling Reactions with Alkyl Fluorides. *Org. Lett.* **24**, 8719–8723 (2022).
12. Hansen, E. C., Li, C., Yang, S., Pedro, D. & Weix, D. J. Coupling of Challenging Heteroaryl Halides with Alkyl Halides via Nickel-Catalyzed Cross-Electrophile Coupling. *J. Org. Chem.* **82**, 7085–7092 (2017).
13. Hamby, T. B., LaLama, M. J. & Sevov, C. S. Controlling Ni redox states by dynamic ligand exchange for electroreductive  $\text{Csp}^3$ – $\text{Csp}^2$  coupling. *Science* **376**, 410–416 (2022).
14. Yi, J., Badir, S. O., Kammer, L. M., Ribagorda, M. & Molander, G. A. Deaminative Reductive Arylation Enabled by Nickel/Photoredox Dual Catalysis. *Org. Lett.* **21**, 3346–3351 (2019).

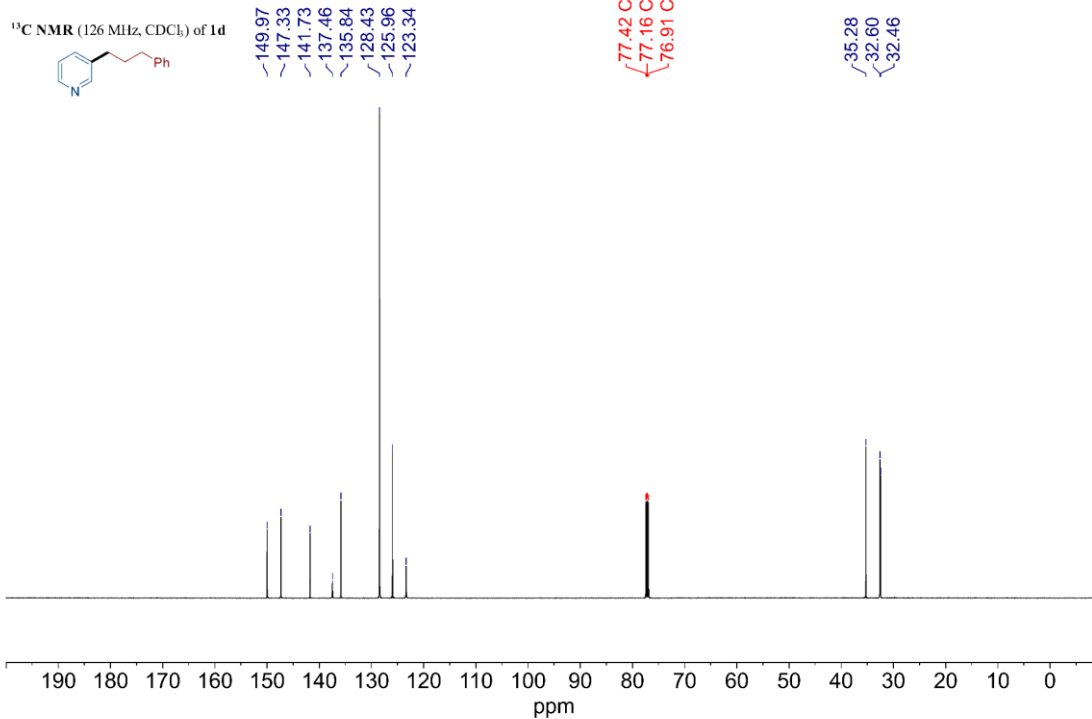
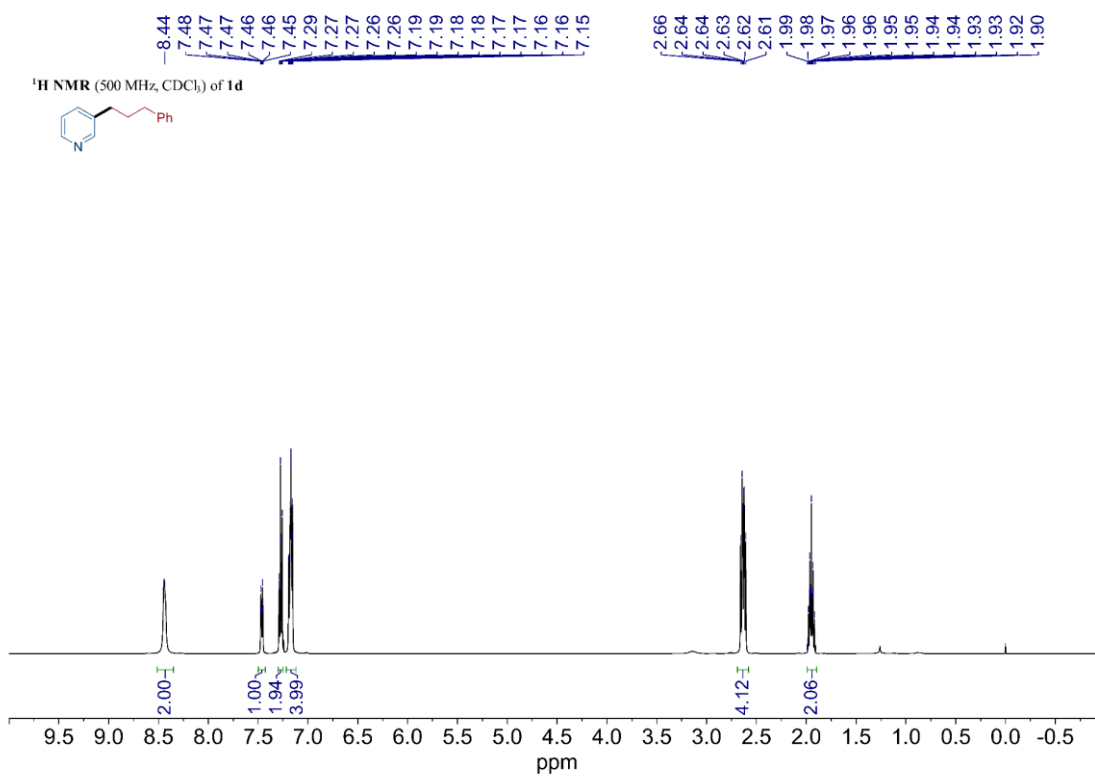


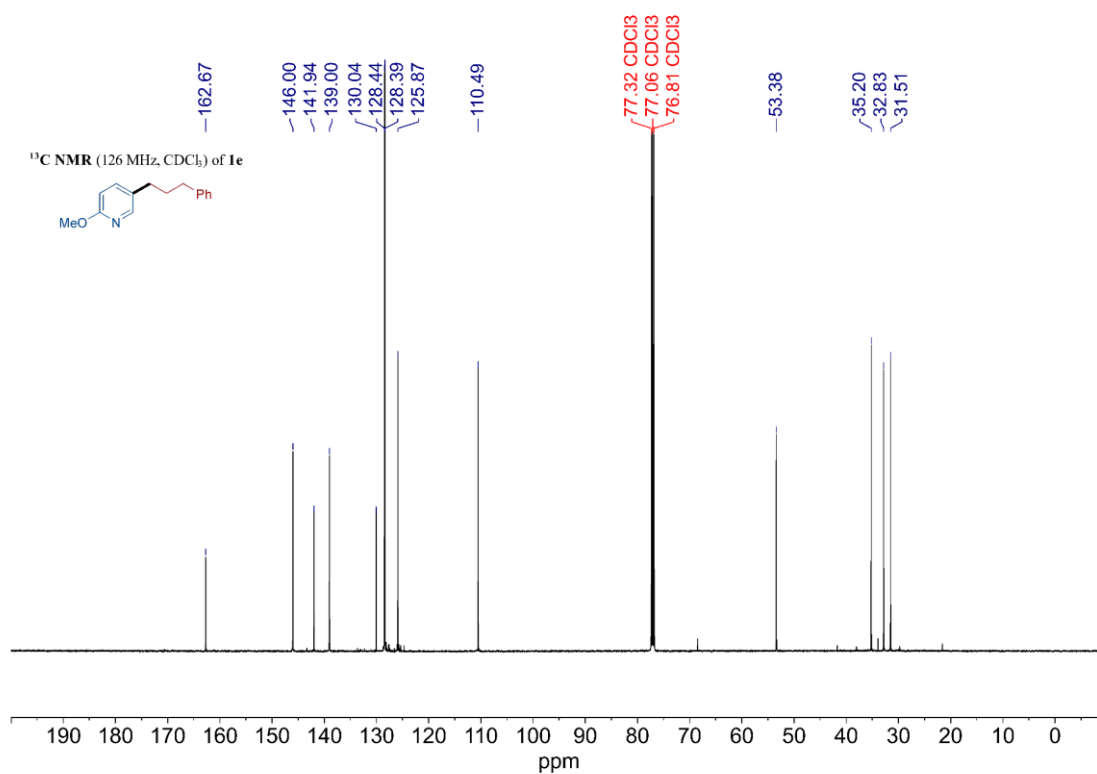
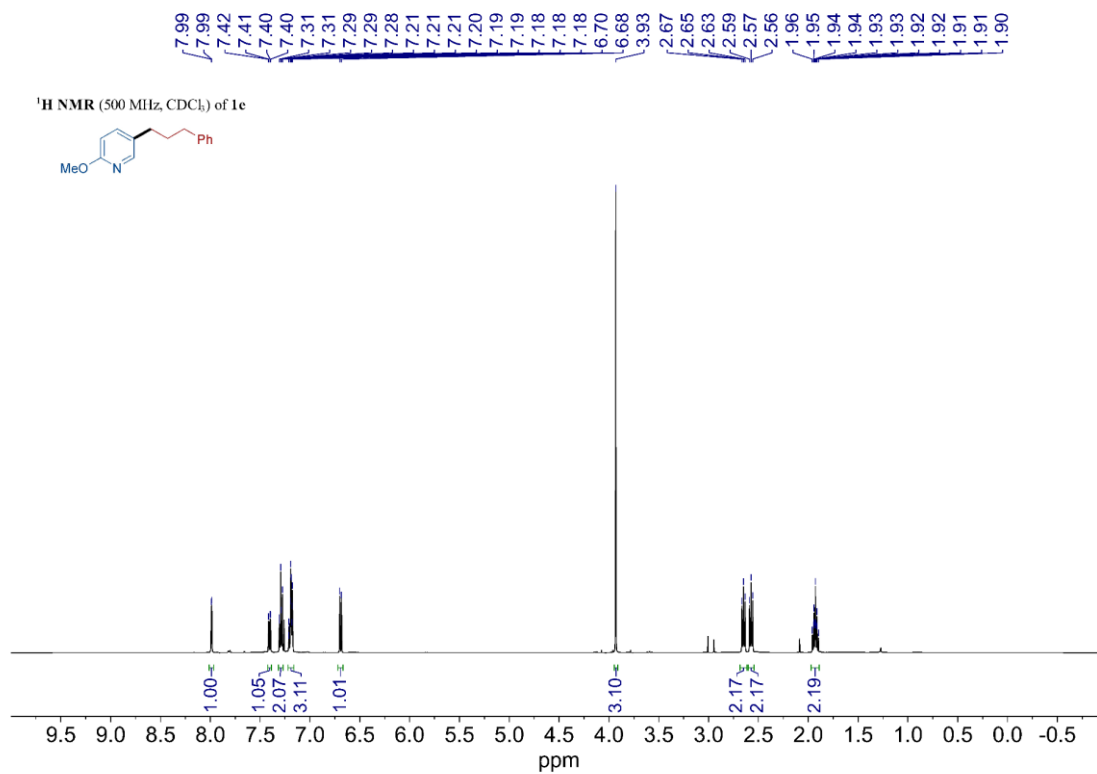


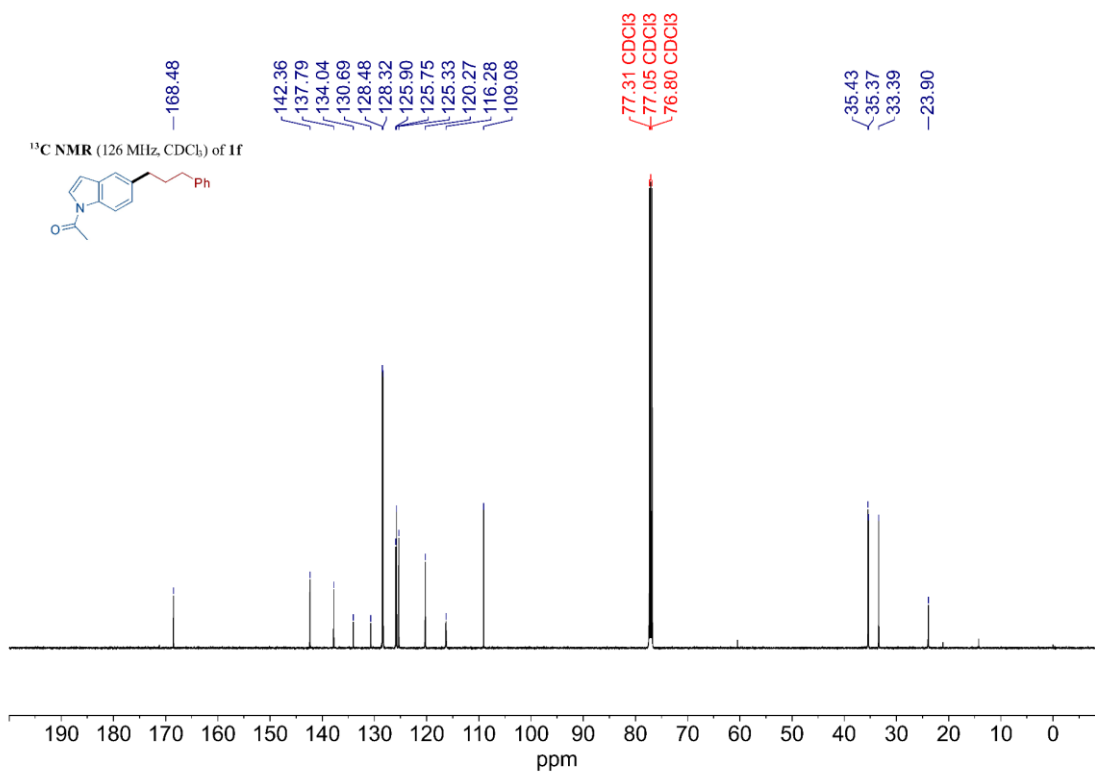
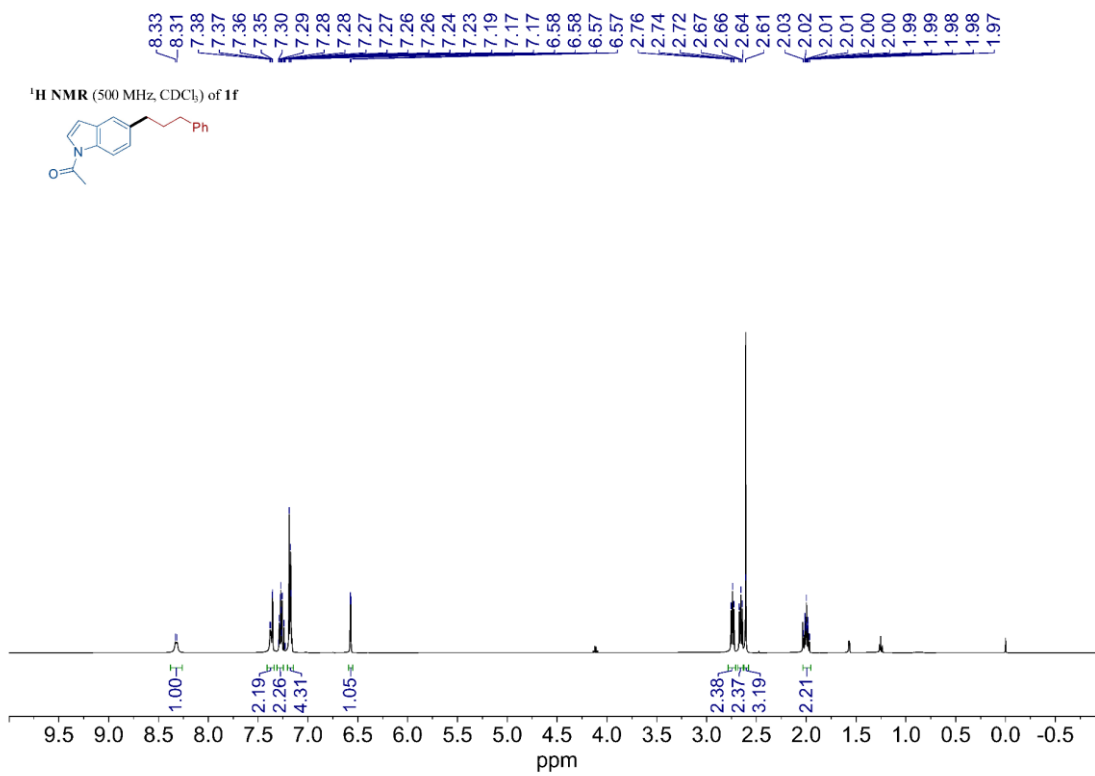


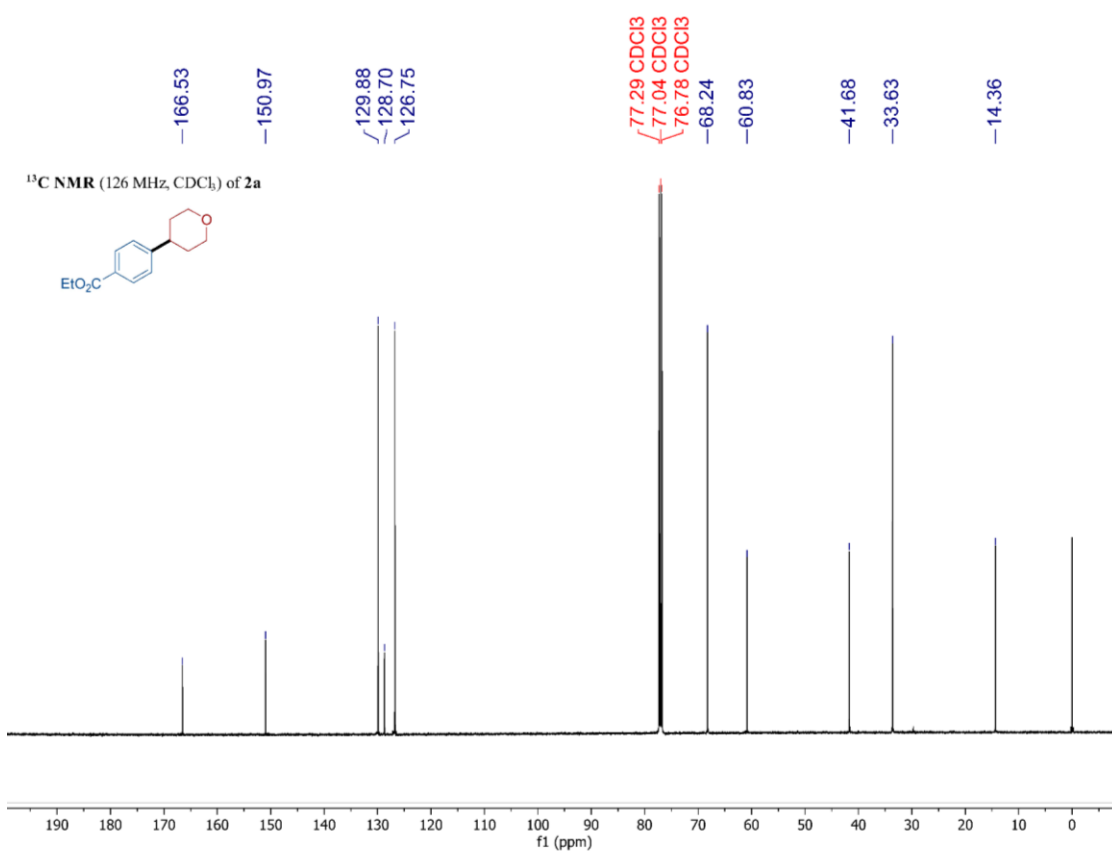
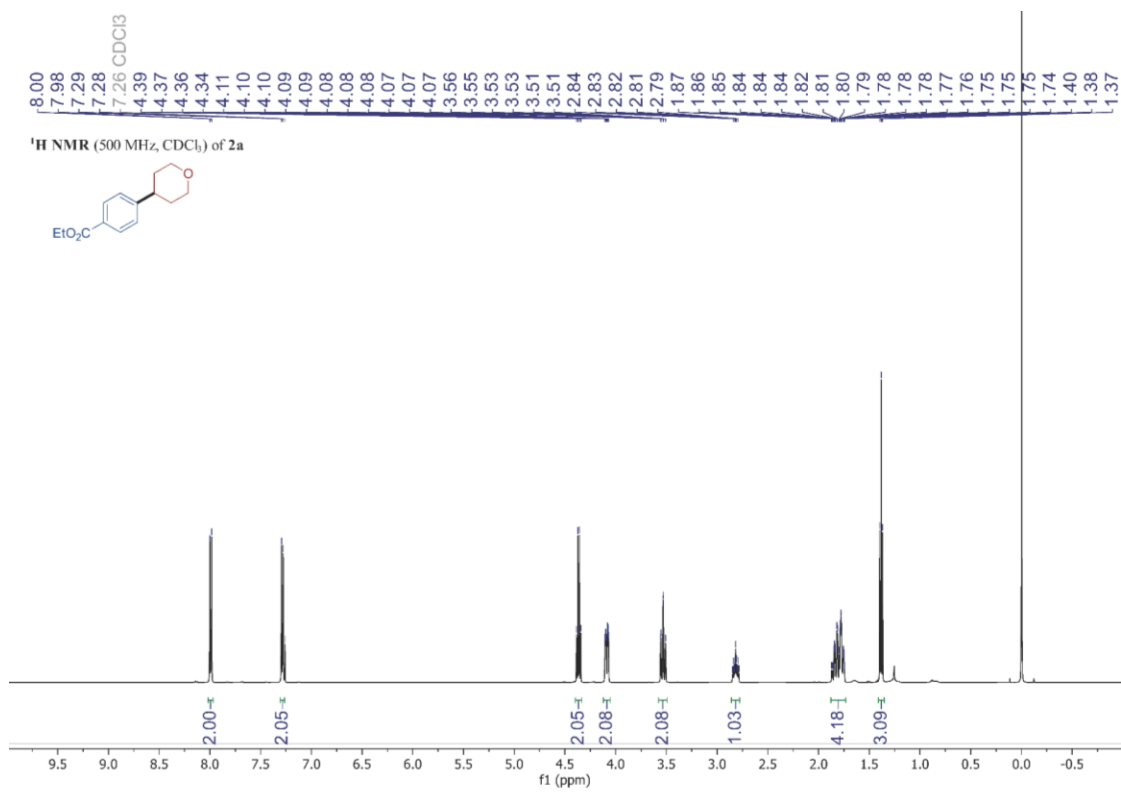


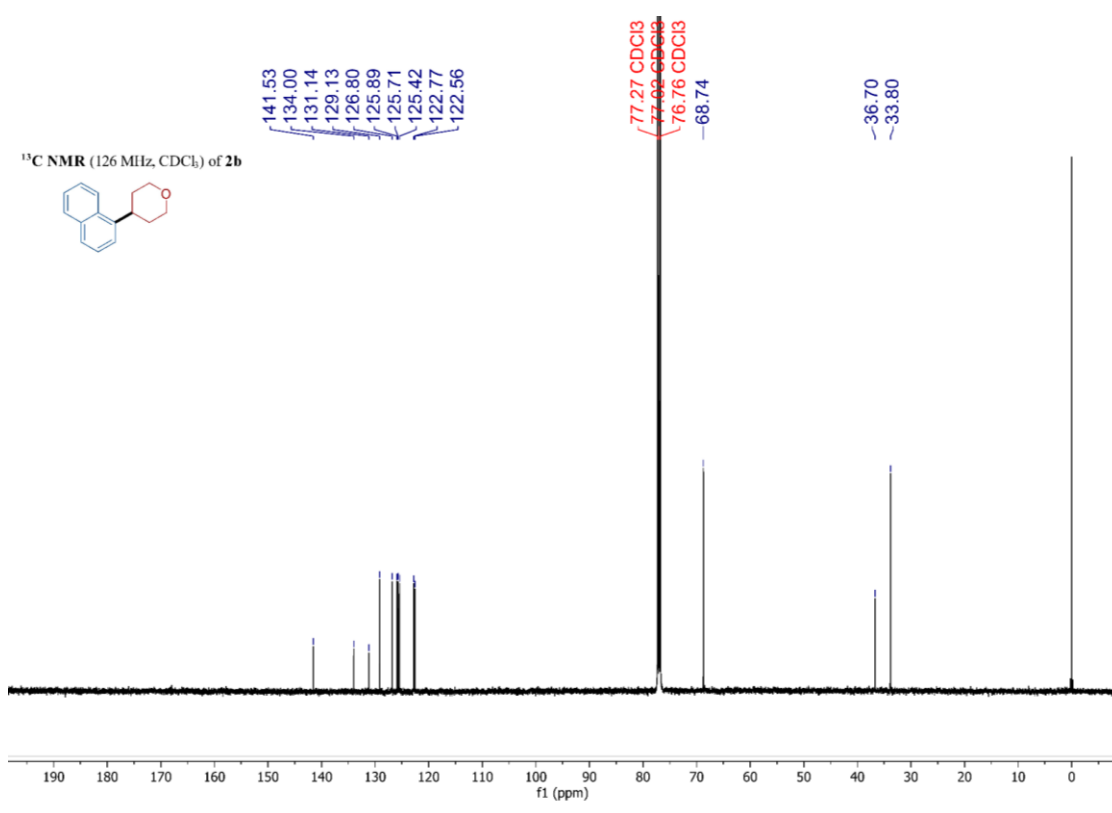
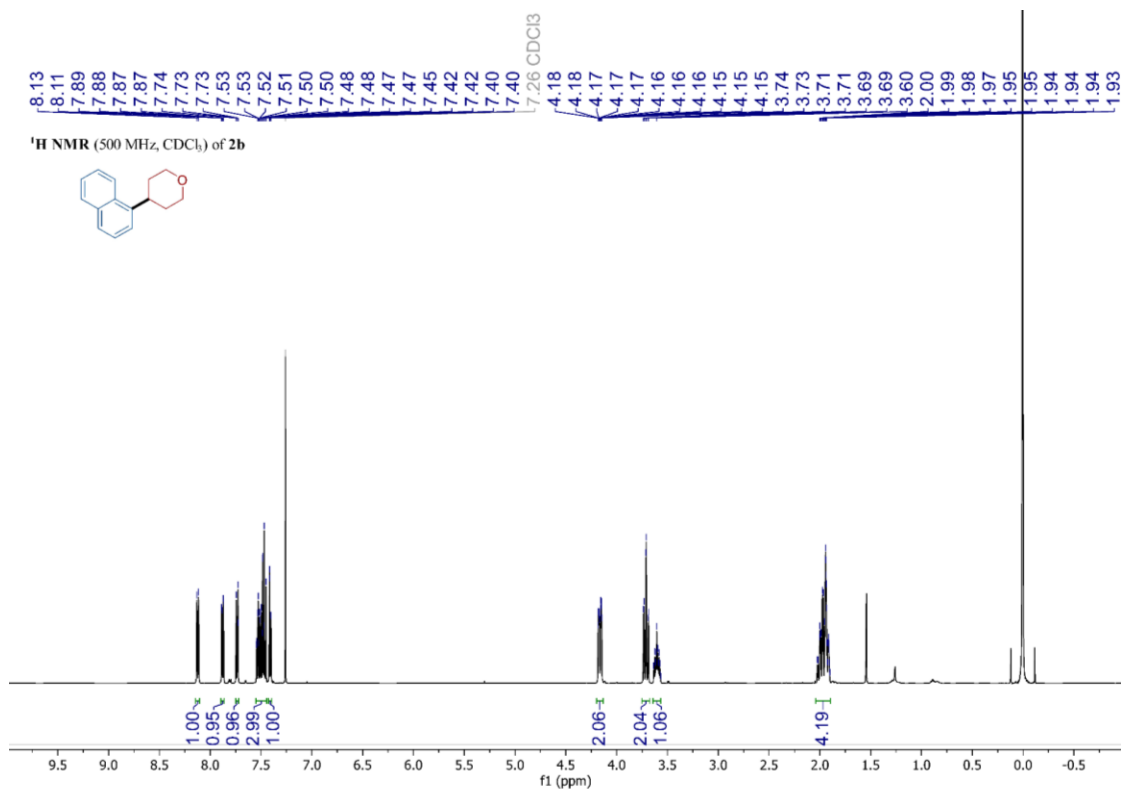


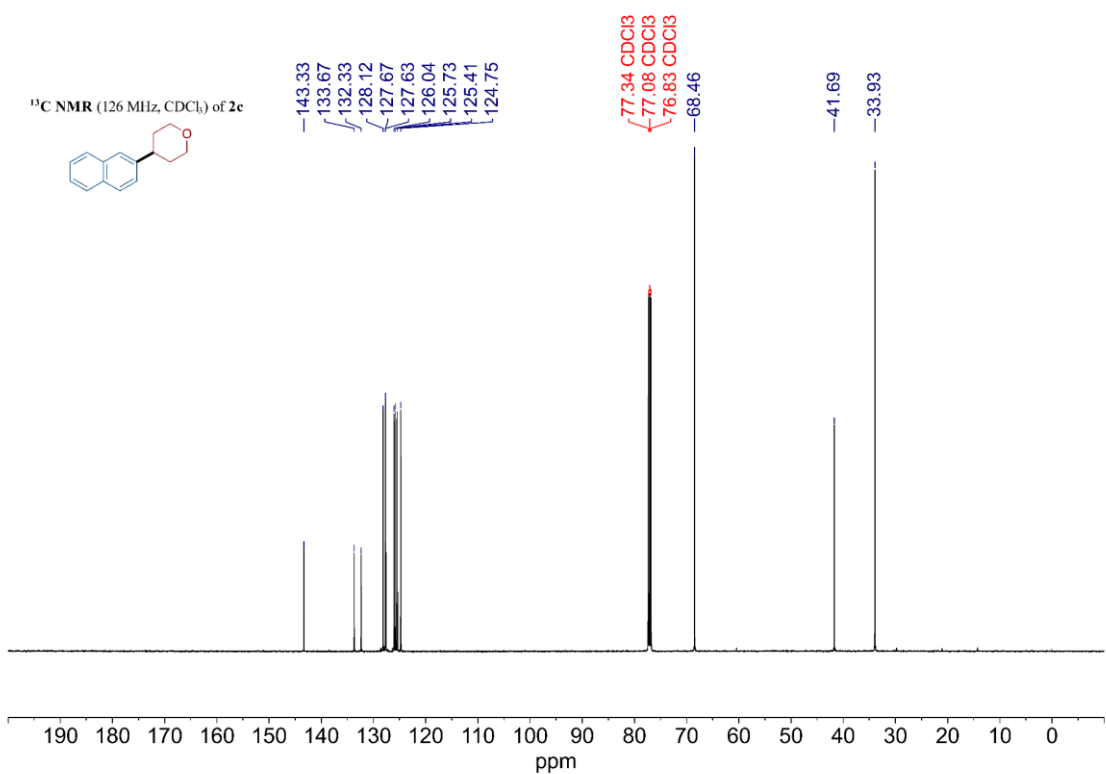
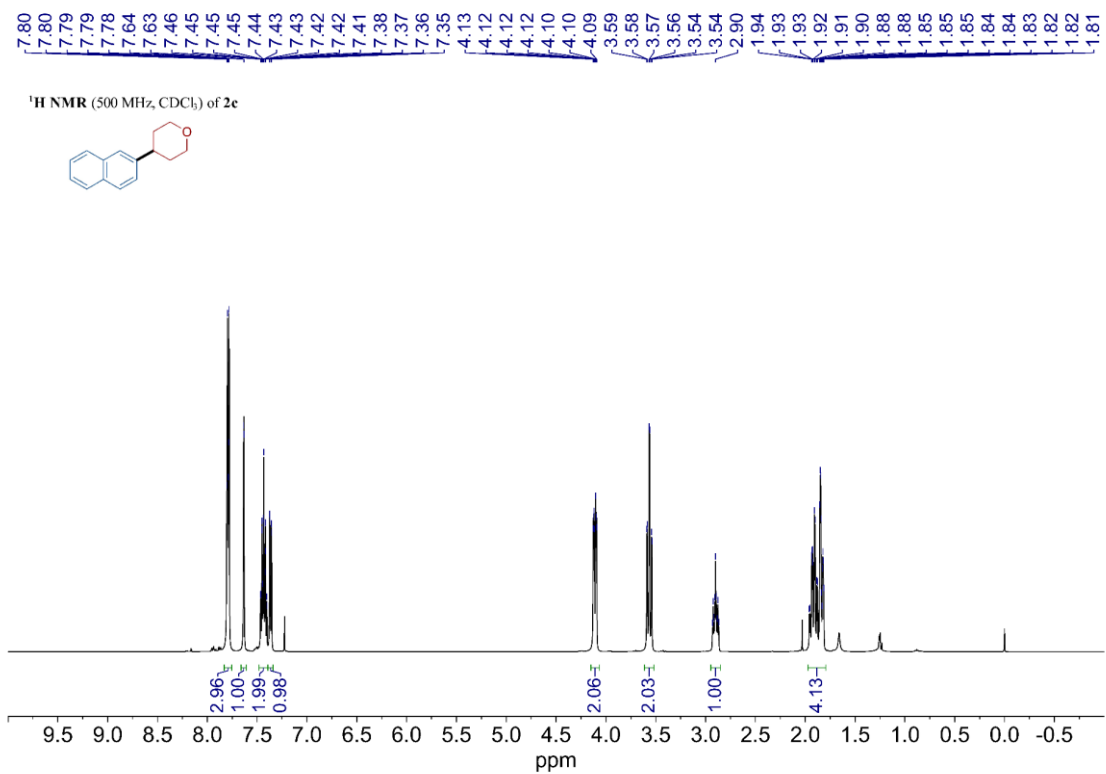


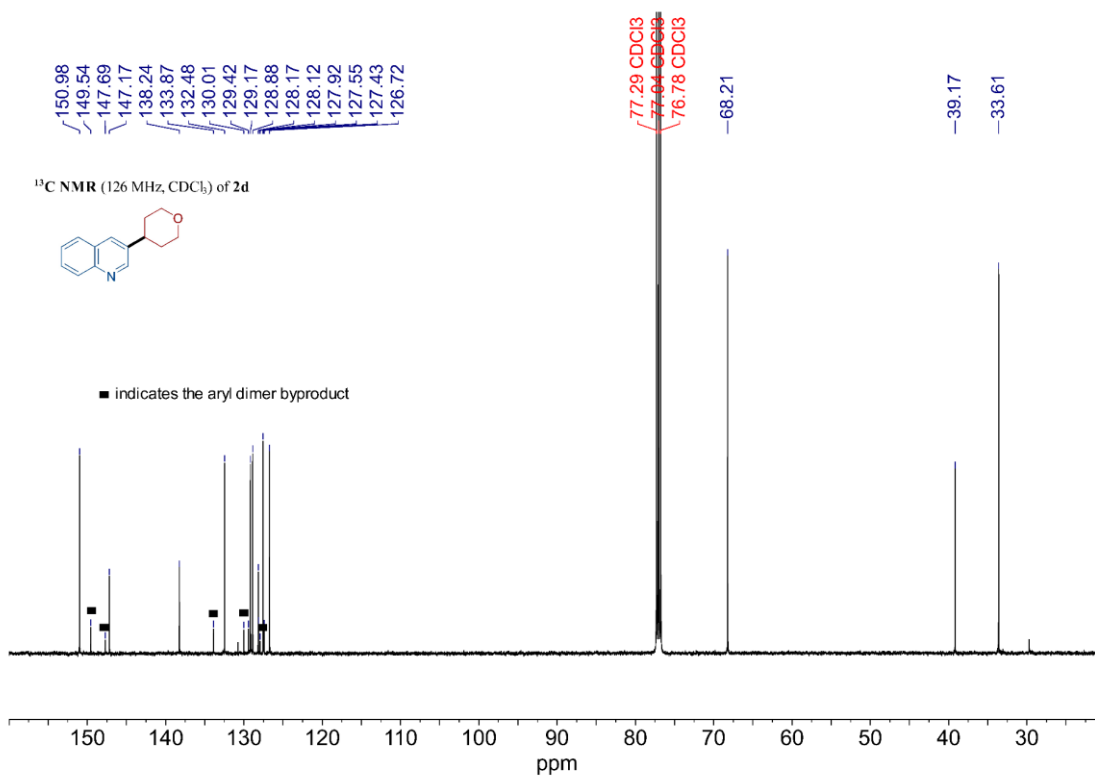
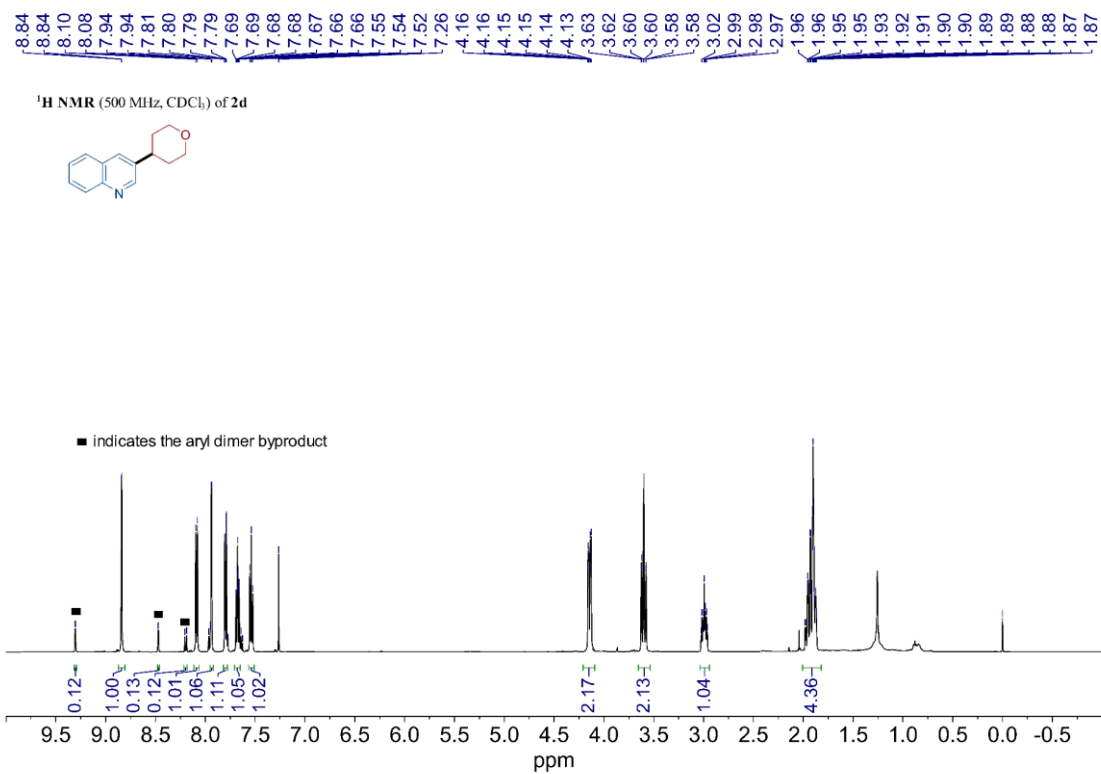


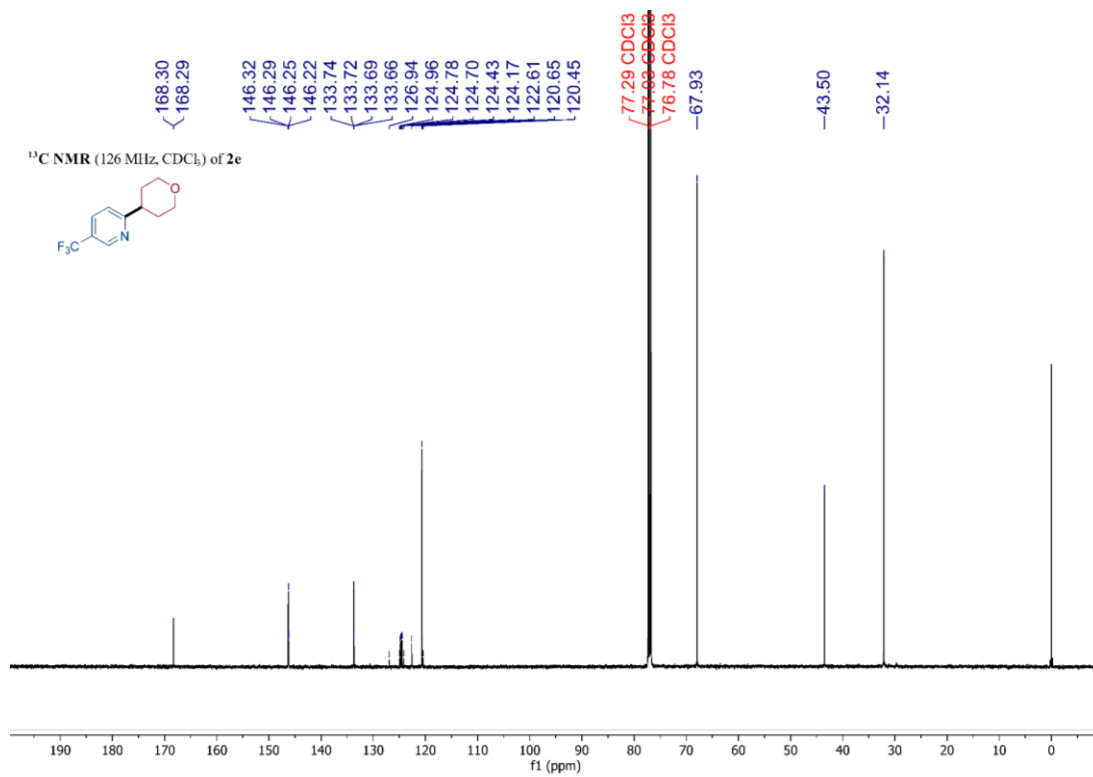
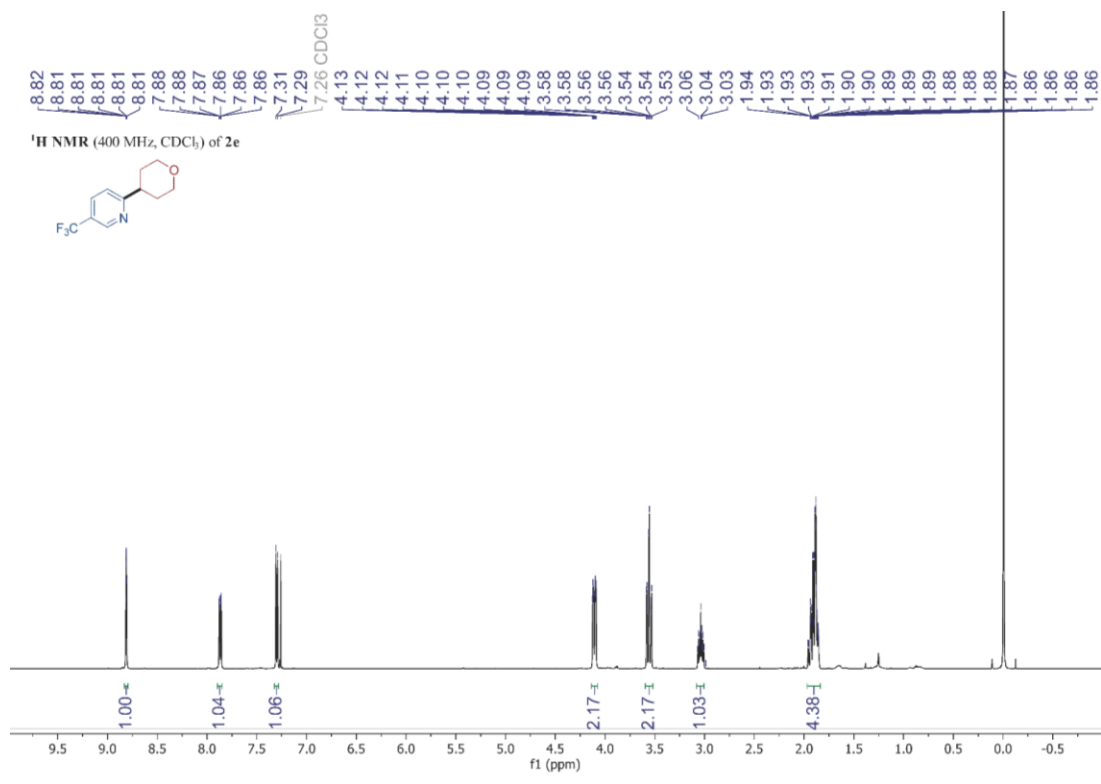




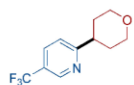




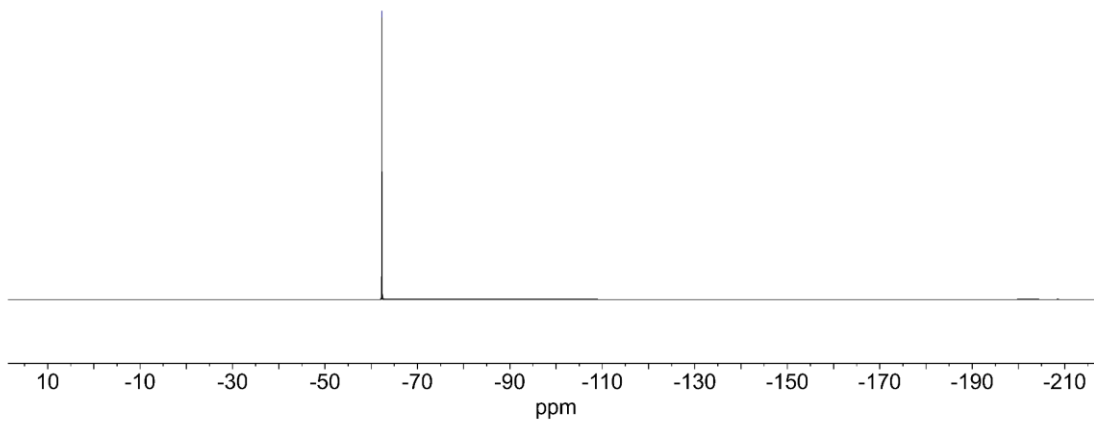




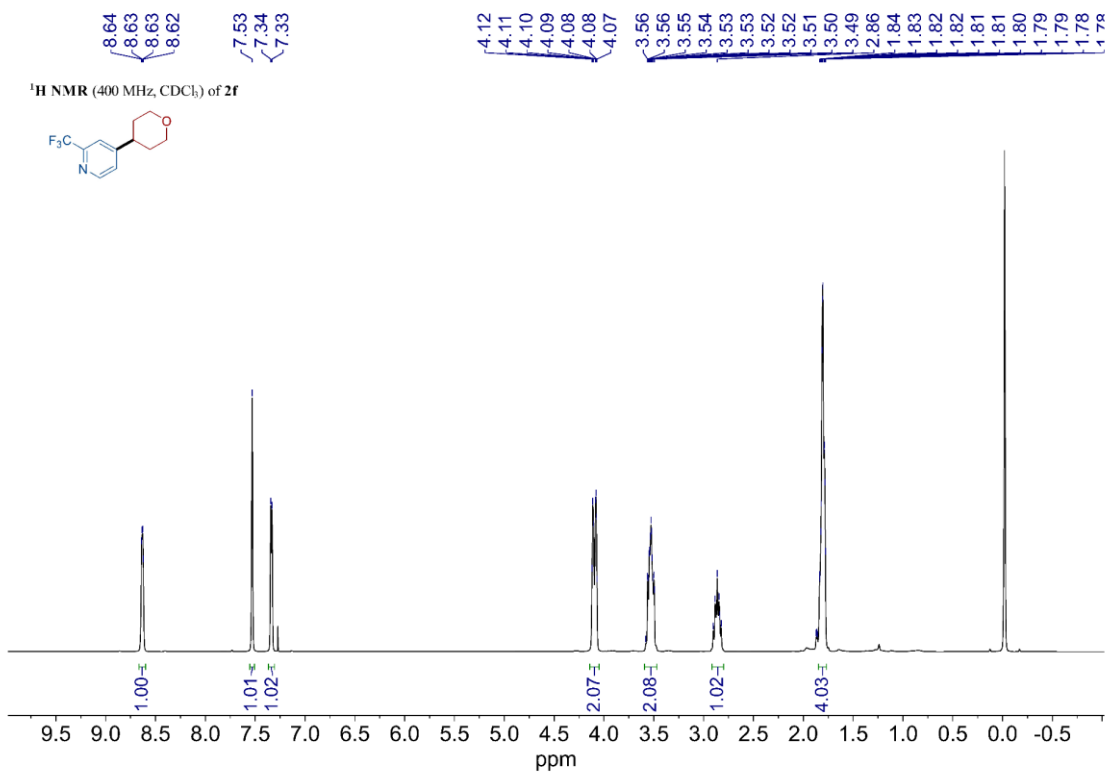
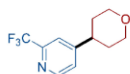
<sup>19</sup>F NMR (377 MHz, CDCl<sub>3</sub>) of 2e

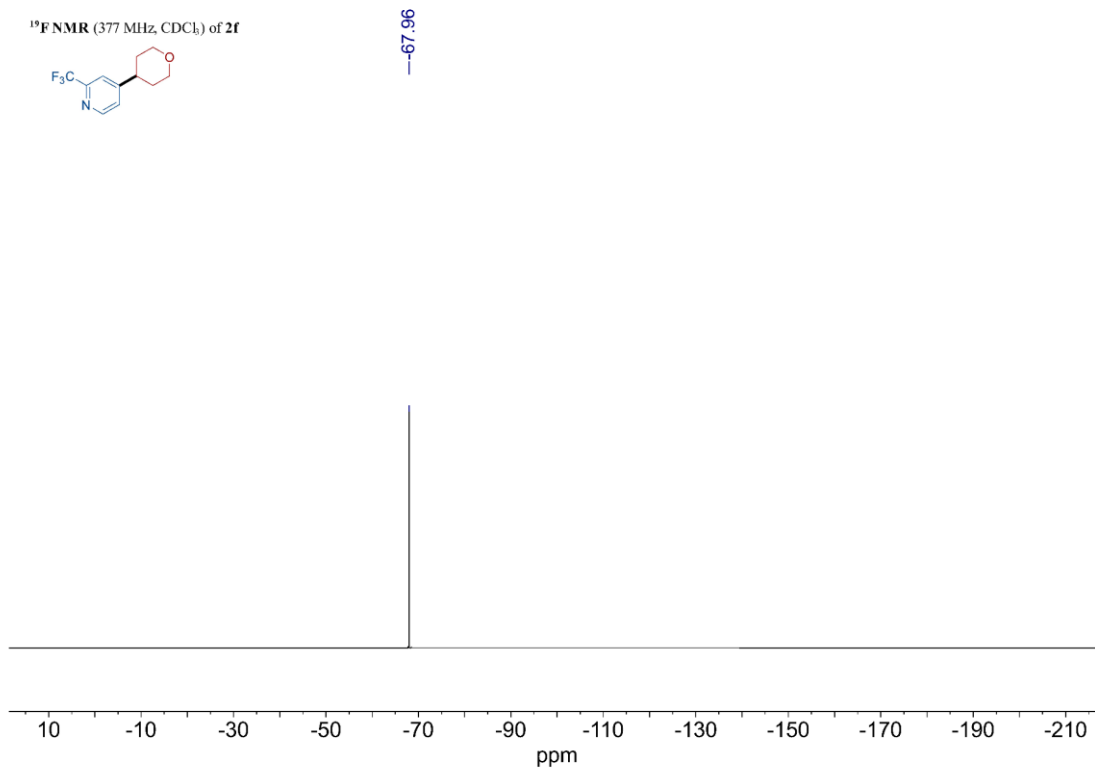
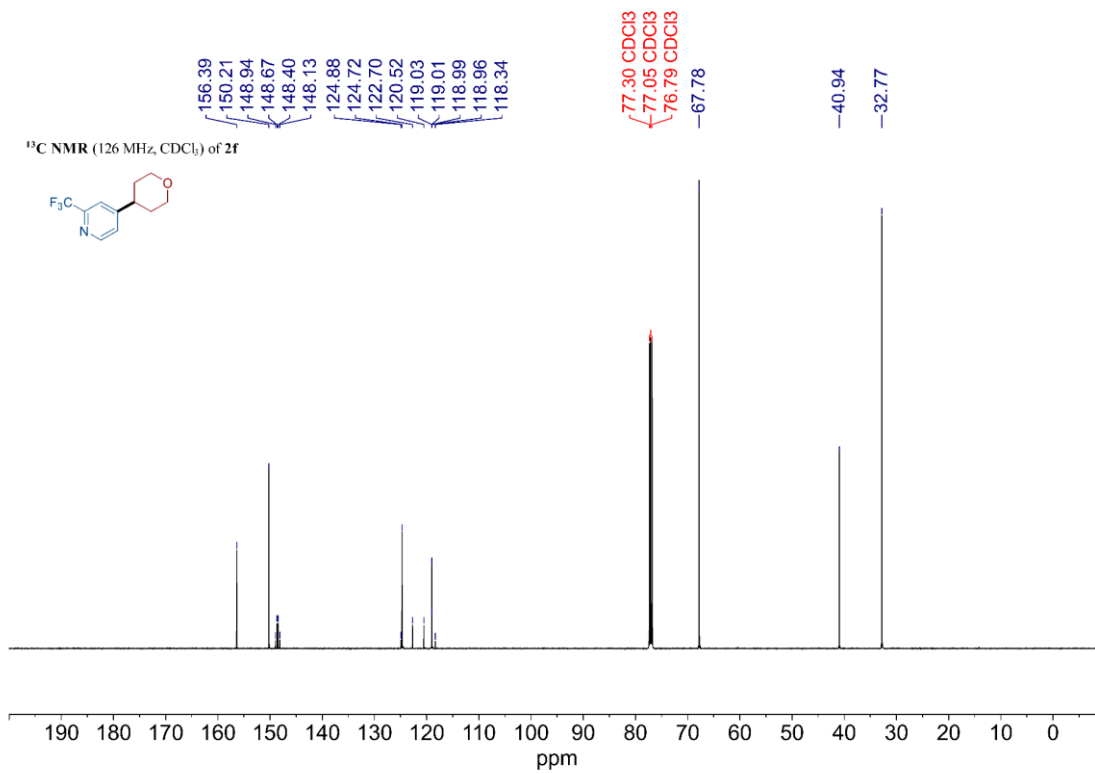


-62.28



<sup>1</sup>H NMR (400 MHz, CDCl<sub>3</sub>) of 2f





## Appendix C. Supporting Information for Chapter 4

### 4C.I. General Experimental Considerations

#### *Solvents and reagents*

All reagents were purchased from commercial sources and used as received without further purification. Starting materials (heteroaryl and aryl halides) were purchased from MilliporeSigma, Alfa Aesar, Thermo Scientific, Ambeed, AstaTech, and Combi-Blocks, or supplied by GSK. Nickel(II) bromide ethylene glycol dimethyl ether complex ( $\text{NiBr}_2(\text{dme})$ ) was purchased from MilliporeSigma. (2,2'-Bipyridine)nickel(II) dibromide ( $(\text{bpy})\text{NiBr}_2$ ) was purchased from AstaTech. Ligands were purchased from MilliporeSigma, TCI America, and Alfa Aesar. Ammonia solution (2.0 M in methanol) was purchased from Thermo Scientific. The Turbo Grignard reagent ( ${}^i\text{PrMgCl}\cdot\text{LiCl}$ , 1.3 M in THF) was purchased from MilliporeSigma. Metal reductants, Zn powder (average 4–7 micron), Mn powder (–325 mesh), and Mg powder (–325 mesh), were purchased from MilliporeSigma or Alfa Aesar. Organic reductant, tetrakis(dimethylamino)ethylene (TDAE), was purchased from MilliporeSigma. Anhydrous salt additives ( $\text{LiCl}$ ,  $\text{LiBr}$ ,  $\text{LiI}$ ,  $\text{NaI}$ ,  $\text{MgCl}_2$ ,  $\text{FeBr}_2$ ,  $\text{ZnCl}_2$ ,  $\text{ZnBr}_2$ ) were purchased from MilliporeSigma or Thermo Scientific. All reductants and metal salts were stored and handled in a nitrogen-filled glove box and used as-is. Anhydrous solvents (DMF, DMA, NMP, DMI, DMSO, 1,4-dioxane, THF) were purchased from MilliporeSigma and stored over activated 4 Å molecular sieves in a nitrogen-filled glove box.

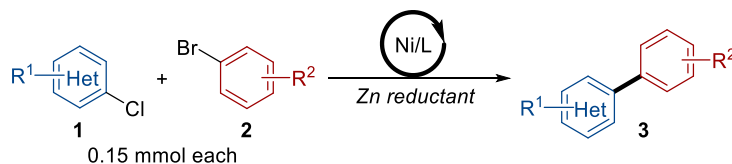
#### *Characterization of products*

All proton ( ${}^1\text{H}$ ), carbon ( ${}^{13}\text{C}$ ), and fluorine ( ${}^{19}\text{F}$ ) nuclear magnetic resonance (NMR) spectra were recorded on a Bruker 400 MHz at 25 °C ( ${}^1\text{H}$  400.1 MHz,  ${}^{13}\text{C}$  100.6 MHz,  ${}^{19}\text{F}$  376.5 MHz) or a Bruker 500 MHz at 25 °C ( ${}^1\text{H}$  500.1 MHz,  ${}^{13}\text{C}$  125.7 MHz,  ${}^{19}\text{F}$  470.6 MHz), using  $\text{CDCl}_3$  (99.8 atoms% D, contains 0.03–1% (v/v) TMS) as the solvent. Chemical shifts are given in parts per

million (ppm) relative to residual solvent peaks in the  $^1\text{H}$  and  $^{13}\text{C}$  NMR spectra or are referenced as noted. An absolute referencing method was used for  $^{19}\text{F}$  NMR chemical shifts, based on the frequency of solvent peaks in the  $^1\text{H}$  NMR spectra. The following abbreviations (and their combinations) are used to label the multiplicities: s (singlet), d (doublet), t (triplet), m (multiplet) and br (broad). High-resolution mass spectra were obtained using a Thermo Q Exactive<sup>TM</sup> Plus in the mass spectrometry facility at the University of Wisconsin (data were collected by facility staff). Automatic normal phase column chromatography was performed using reusable Silicycle SiliaSep premium cartridges (40 g, 25  $\mu\text{m}$ ) on a Biotage<sup>®</sup> Selekt. Thin-layer chromatography (TLC) was performed on Silicycle silica gel UV254 pre-coated plates (0.25 mm). Visualization of the developed chromatogram was performed by using UV lamps (254 nm) or  $\text{KMnO}_4$  stain.

#### 4C.II. Reaction Optimization

*Evaluation of Ni-catalyzed heteroaryl-aryl XEC with informer library*

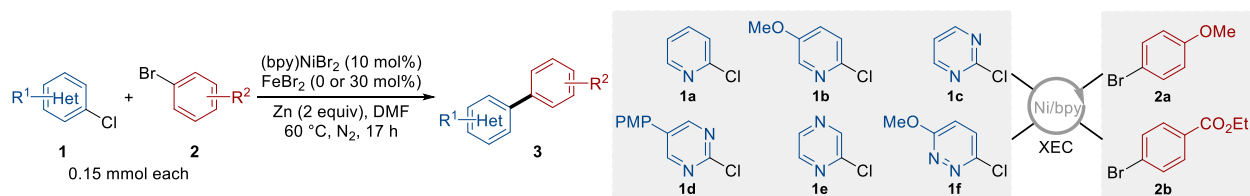


**Reaction setup:** In a nitrogen-filled glove box,  $\text{NiBr}_2(\text{bpy})$  (5.6 mg, 10 mol%), heteroaryl chloride **1** (0.15 mmol, 1.0 equiv), aryl bromide **2** (0.15 mmol, 1.0 equiv), DMF (1 mL), and Zn powder (19.5 mg, 0.30 mmol, 2.0 equiv) were sequentially added to a 1-dram vial equipped with a PTFE-coated stir-bar. The vial was capped with a screw cap fitted with a PTFE-faced silicone septum, then removed from the glove box and heated in a sand bath at 60  $^\circ\text{C}$  with stirring (1100 rpm) for 17 h.

For reactions using heteroaryl chlorides containing more than one nitrogen atom in the ring,  $\text{FeBr}_2$  (9.7 mg, 0.075 mmol, 0.30 equiv) was added before the addition of Zn powder.

Work-up for NMR analysis: After 17 h, the reaction mixture was cooled to room temperature and quenched with 2 M NH<sub>3</sub>/methanol solution (1 mL). The resultant mixture was stirred at 800 rpm for 30 min. A stock solution of 1,3,5-trimethoxybenzene was prepared (0.5 M), and 100  $\mu$ L of this stock solution (0.33 equiv relative to substrate) was added to the crude material. Then a 100  $\mu$ L aliquot of the solution was diluted with 600  $\mu$ L CDCl<sub>3</sub> and filtered through a syringe filter (PVDF membrane, 0.22  $\mu$ m pore size, 13 mm diameter) into an NMR sample tube. The resultant sample was analyzed by <sup>1</sup>H NMR spectroscopy and yields were determined using 1,3,5-trimethoxybenzene as the internal standard.

**Table 4C.1. Results of XEC reactions under adapted literature condition using informer library substrates.<sup>a</sup>**



Entry	1	2	Conversion of 1/2 (%)	Dimer of 1 (%)	Dimer of 2 (%)	Cross-coupled product (%)
1	<b>1a</b>	<b>2a</b>	100/100	20	22	62
2	<b>1a</b>	<b>2b</b>	100/100	32	33	35
3	<b>1b</b>	<b>2a</b>	100/100	45	46	10
4	<b>1b</b>	<b>2b</b>	100/100	42	43	14
5 <sup>b</sup>	<b>1c</b>	<b>2a</b>	95/100	30	9	19
6	<b>1c</b>	<b>2b</b>	97/100	22	25	40
7 <sup>b</sup>	<b>1d</b>	<b>2a</b>	100/100	23	10	12
8 <sup>b</sup>	<b>1d</b>	<b>2b</b>	100/100	11	18	44
9 <sup>b</sup>	<b>1e</b>	<b>2a</b>	65/64	10	6	13
10	<b>1e</b>	<b>2b</b>	100/100	15	24	49
11 <sup>b,c</sup>	<b>1f</b>	<b>2a</b>	N.A./56	\	2.5	3
12 <sup>b,c</sup>	<b>1f</b>	<b>2b</b>	N.A./100	\	3	10

<sup>a</sup> Yields are determined by <sup>1</sup>H NMR spectroscopy of the crude reaction mixture using 1,3,5-trimethoxybenzene as an internal standard. Yields of homo-coupled dimers are reported with respect to the stoichiometry of the reaction, i.e., the maximal theoretical yield is 50%. Added 30 mol% FeBr<sub>2</sub> in entries 5–12. <sup>b</sup> Proto-dehalogenation products accounted for the remaining mass of **2**. <sup>c</sup> NMR signals of **1f** and its dimer overlap with solvent peaks in the crude NMR.

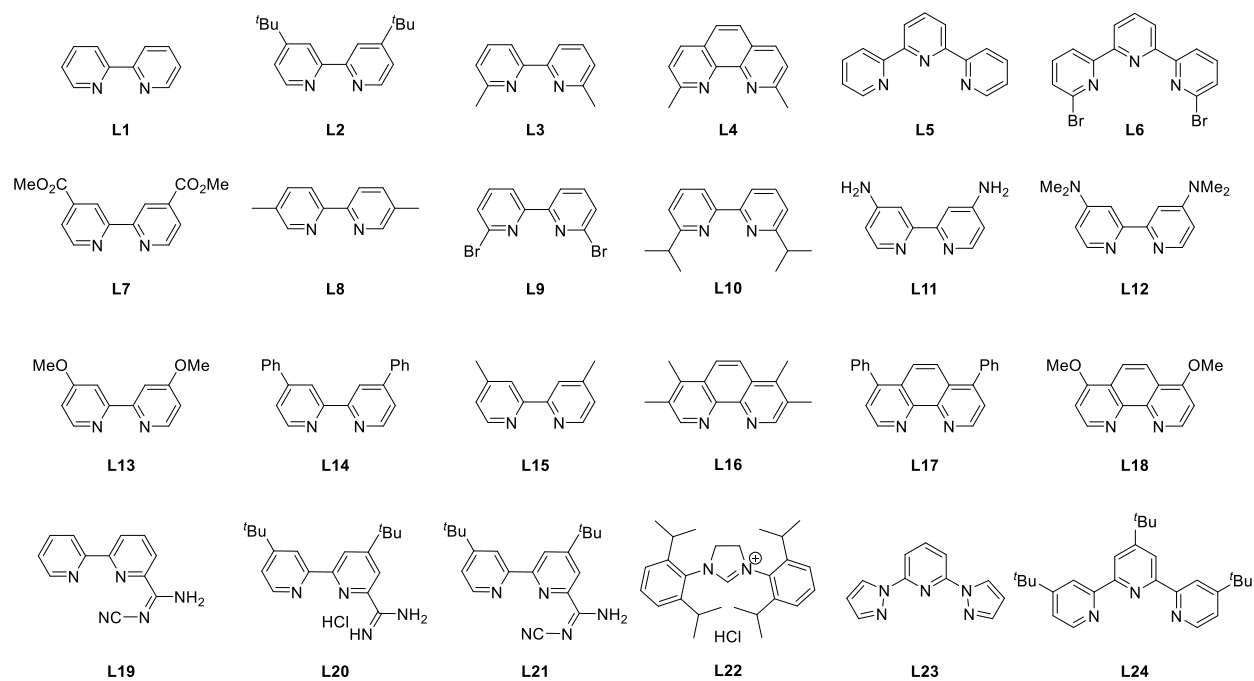
Discussion: Dimers and/or proto-dehalogenation products from **1c–1e** may be ligated to Ni or Zn ions in the reaction mixture and may not be completely extracted by the NH<sub>3</sub>/methanol solution during work-up. Prolonged stirring of the reaction mixture after the addition of NH<sub>3</sub>/methanol solution may result in displacement of –Cl with –NH<sub>2</sub> on the heteroaryl chloride due to NH<sub>3</sub> attack, likely via a nucleophilic aromatic substitution pathway. Additionally, control experiments in the absence of the Ni catalyst showed that certain heteroaryl chlorides slowly decomposed at 60 °C in the reaction mixture. Together, these factors may account for the poor mass balances of the heteroaryl chlorides in some cases. Similar phenomena were observed in the experiments described in the following sections.

*General Procedure for optimization of condition A*

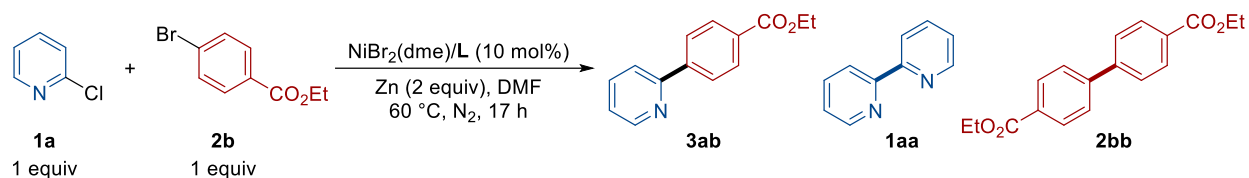
Reaction setup: In a nitrogen-filled glove box, NiBr<sub>2</sub>(dme) (4.6 mg, 10 mol%, or otherwise noted), ligand (10 mol%, or otherwise noted), and DMF (1 mL, or otherwise noted) were added to a 1-dram vial equipped with a PTFE-coated stir-bar. This solution was stirred at 800 rpm in the glove box for 30 min to allow complexation of Ni with the ligand, followed by sequential addition of 2-chloropyridine (13.8 μL, 0.15 mmol, 1.0 equiv), ethyl 4-bromobenzoate (24 μL, 0.15 mmol, 1.0 equiv) and Zn powder (19.5 mg, 0.30 mmol, 2.0 equiv). The vial was capped with a screw cap fitted with a PTFE-faced silicone septum, then removed from the glove box and heated in a sand bath at 60 °C with stirring (1100 rpm) for 17 h.

Work-up for NMR analysis: After 17 h, the reaction mixture was cooled to room temperature and quenched with 2 M NH<sub>3</sub>/methanol solution (1 mL). The resultant mixture was stirred at 800 rpm for 30 min. A stock solution of 1,3,5-trimethoxybenzene in DMF was prepared (0.5 M), and 100 μL of this stock solution (0.33 equiv relative to substrate) was added to the crude material. Then a 100 μL aliquot of the solution was diluted with 600 μL CDCl<sub>3</sub> and filtered through a syringe

filter (PVDF membrane, 0.22  $\mu\text{m}$  pore size, 13 mm diameter) into an NMR sample tube. The resultant sample was analyzed by  $^1\text{H}$  NMR spectroscopy and yields were determined using 1,3,5-trimethoxybenzene as the internal standard.

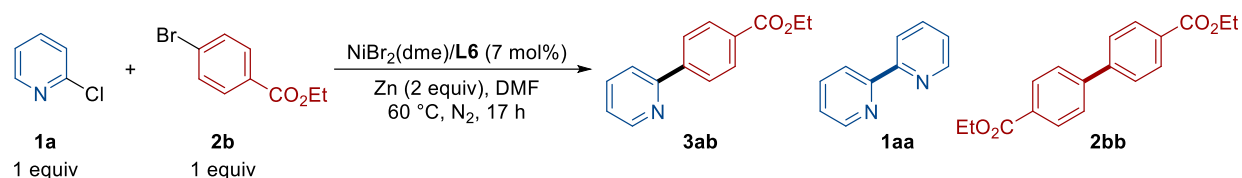


**Figure 4C.1.** Ligands used for optimization of conditions A and B.

Table 4C.2. Ligand evaluation for condition A.<sup>a</sup>

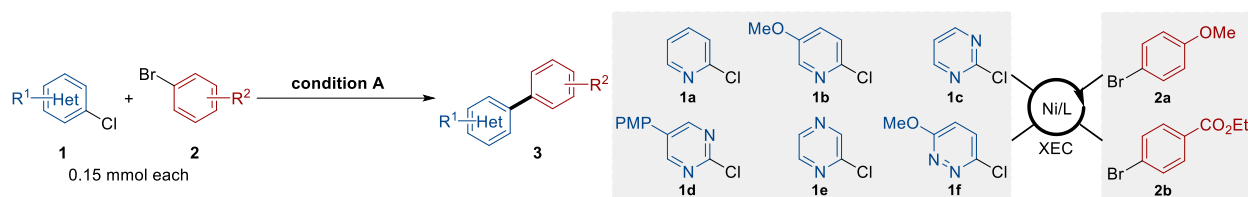
Entry	Ligand	<b>1aa</b> (%)	<b>2bb</b> (%)	<b>3ab</b> (%)	Cross-selectivity
1	<b>L1</b>	34	34	35	1:2.0
2	<b>L2</b>	33	32	37	1:1.8
3	<b>L3</b>	29	27	47	1:1.2
4	<b>L4</b>	22.5	25	37	1:1.3
5	<b>L5</b>	31	30	39	1:1.6
6	<b>L6</b>	17	15	62	1.9:1
7	<b>L7</b>	33	39	17	1:4.2
8	<b>L8</b>	32	29	34	1:1.8
9	<b>L9</b>	25	17	50	1.2:1
10	<b>L10</b>	27	27	48	1:1.1
11	<b>L16</b>	36	35	18	1:4.0
12	<b>L17</b>	37	38	19	1:4.0
13	<b>L19</b>	20	12.5	53	1.6:1
14	<b>L23</b>	45	40	15	1:5.7
15	<b>L24</b>	30	25	40	1:1.4

<sup>a</sup> Yields are determined by <sup>1</sup>H NMR spectroscopy of the crude reaction mixture using 1,3,5-trimethoxybenzene as an internal standard. Cross-selectivity is defined as **3ab** NMR yield:(**1aa** NMR yield + **2bb** NMR yield). Yields of homo-coupled dimers are reported with respect to the stoichiometry of the reaction, i.e., the maximal theoretical yield is 50%.

Table 4C.3. Further optimization and control reactions for condition A.<sup>a</sup>

Entry	Variation from above	<b>1aa</b> (%)	<b>2bb</b> (%)	<b>3ab</b> (%)	Cross-selectivity
1	none	9	5.5	83	5.7:1
2	10 mol% Ni catalyst, 2 mL DMF	9	8	73	4.3:1
3	5 mol% Ni catalyst	12	9	78	3.7:1
4 <sup>b</sup>	w/o ligand, 48 h	0	0	0	/
5 <sup>c</sup>	w/o Ni salt, 48 h	0	0	0	/
6 <sup>c</sup>	w/o Ni salt and ligand, 48 h	0	0	0	/
7 <sup>d</sup>	w/o Ni salt; 7 mol% ZnBr <sub>2</sub> , 48 h	0	0	0	/
8 <sup>e</sup>	added 1 equiv BHT	12	7	82	4.3:1
9 <sup>e</sup>	added 1 equiv 1,1'-diphenylethylene	8.5	3	86	7.4:1

<sup>a</sup> Yields are determined by <sup>1</sup>H NMR spectroscopy of the crude reaction mixture using 1,3,5-trimethoxybenzene as an internal standard. Cross-selectivity is defined as **3ab** NMR yield:(**1aa** NMR yield + **2bb** NMR yield). Yields of homo-coupled dimers are reported with respect to the stoichiometry of the reaction, i.e., the maximal theoretical yield is 50%. <sup>b</sup> 20% ethyl benzoate observed, 80% **2b** and 100% **1a** remained unreacted. <sup>c</sup> No conversion. <sup>d</sup> 3% ethyl benzoate observed, 97% **2b** and 100% **1a** remained unreacted. <sup>e</sup> 100% of the added radical scavenger remained intact after reaction.

**Table 4C.4. Results of XEC reactions under condition A using informer library substrates.<sup>a</sup>**

Entry	1	2	Conversion of 1/2 (%)	Dimer of 1 (%)	Dimer of 2 (%)	Cross-coupled product (%)
1	<b>1a</b>	<b>2a</b>	100/100	1.5	2	92
2	<b>1a</b>	<b>2b</b>	100/100	9	5.5	83
3	<b>1b</b>	<b>2a</b>	100/100	1	2.5	76
4	<b>1b</b>	<b>2b</b>	100/100	13	11	68
5 <sup>b</sup>	<b>1c</b>	<b>2a</b>	70/62	4	4	2
6 <sup>c</sup>	<b>1c</b>	<b>2b</b>	100/100	3.5	1.5	68
7 <sup>d</sup>	<b>1d</b>	<b>2a</b>	100/100	22	10	11
8 <sup>d</sup>	<b>1d</b>	<b>2b</b>	100/100	19	16	17
9 <sup>d</sup>	<b>1e</b>	<b>2a</b>	25/30	10	2	0
10	<b>1e</b>	<b>2b</b>	100/100	0	7	82
11 <sup>c,e</sup>	<b>1f</b>	<b>2a</b>	N.A./54	N.A.	0	17
12 <sup>c,e</sup>	<b>1f</b>	<b>2b</b>	N.A./100	N.A.	1.5	65

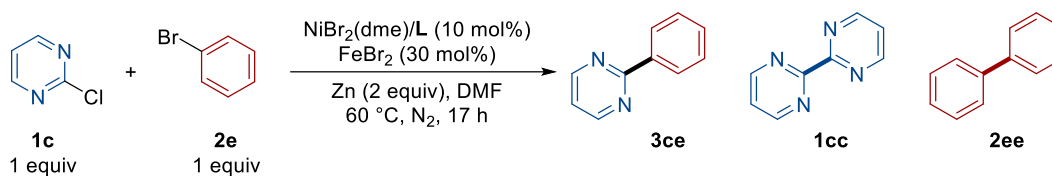
<sup>a</sup> Yields are determined by <sup>1</sup>H NMR spectroscopy of the crude reaction mixture using 1,3,5-trimethoxybenzene as an internal standard. Used 10 mol% Ni catalyst and added 30 mol% FeBr<sub>2</sub> in entries 5–12. <sup>b</sup> 28% pyrimidine byproduct was observed. <sup>c</sup> Proto-dehalogenation products accounted for the remaining mass of **2**. <sup>d</sup> Proto-dehalogenation products accounted for the remaining mass of both substrates. <sup>e</sup> NMR signals of **1f** and its dimer overlap with solvent peaks in the crude NMR.

#### General Procedure for optimization of Condition B

**Reaction setup:** In a nitrogen-filled glove box, NiBr<sub>2</sub>(dme) (4.6 mg, 10 mol%), ligand (10 mol%), and solvent (1 mL, or otherwise noted) were added to a 1-dram vial equipped with a PTFE-coated stir-bar. This solution was stirred at 800 rpm in the glove box for 30 min to allow complexation of Ni with the ligand, followed by sequential addition of 2-chloropyrimidine (17.2 mg, 0.15 mmol, 1.0 equiv), bromobenzene (15.7 μL, 0.15 mmol, 1.0 equiv) or 4-bromoanisole (18.8 μL, 0.15 mmol, 1.0 equiv), FeBr<sub>2</sub> (9.7 mg, 0.075 mmol, 0.30 equiv), salt additive, and the

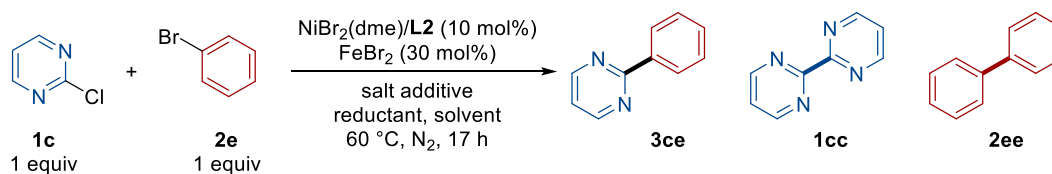
reductant. The vial was capped with a screw cap fitted with a PTFE-faced silicone septum, then removed from the glove box and heated in a sand bath at 60 °C with stirring (1100 rpm) for 17 h.

Work-up for NMR analysis: After 17 h, the reaction mixture was cooled to room temperature and quenched with 2 M NH<sub>3</sub>/methanol solution (1 mL). The resultant mixture was stirred at 800 rpm for 30 min. A stock solution of 1,3,5-trimethoxybenzene was prepared (0.5 M), and 100 μL of this stock solution (0.33 equiv relative to substrate) was added to the crude material. Then a 100 μL aliquot of the solution was diluted with 600 μL CDCl<sub>3</sub> and filtered through a syringe filter (PVDF membrane, 0.22 μm pore size, 13 mm diameter) into an NMR sample tube. The resultant sample was analyzed by <sup>1</sup>H NMR spectroscopy and the yields were determined using 1,3,5-trimethoxybenzene as the internal standard.

Table 4C.5. Ligand evaluation for condition B.<sup>a</sup>

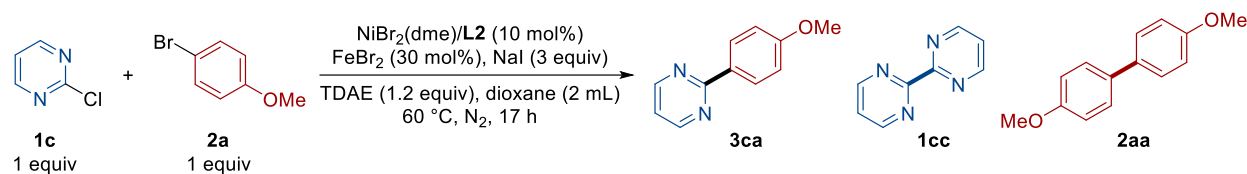
Entry	Ligand	<b>1cc</b> (%)	<b>2ee</b> (%)	<b>3ce</b> (%)	Cross-selectivity
1	<b>L1</b>	7	6	30	/
2	<b>L2</b>	5	7	42	/
3	<b>L3</b>	11	3.5	13	/
4	<b>L6</b>	20	20	2	/
5	<b>L11</b>	7	0	25	/
6	<b>L12</b>	11	\	21	/
7	<b>L13</b>	6.5	4	40	/
8	<b>L14</b>	1	24	39	/
9	<b>L15</b>	9	6	32	/
10	<b>L17</b>	2	7	37	/
11	<b>L18</b>	7	2	26	/
12	<b>L20</b>	3	0	18	/
13	<b>L21</b>	0	0	2	/
14	<b>L22</b>	2.5	2	24	/
15	<b>L24</b>	3	3.5	30	/

<sup>a</sup> Yields are determined by <sup>1</sup>H NMR spectroscopy of the crude reaction mixture using 1,3,5-trimethoxybenzene as an internal standard. Yields of homo-coupled dimers are reported with respect to the stoichiometry of the reaction, i.e., the maximal theoretical yield is 50%. 30–80% **2e** and 0–55% **1c** remained unreacted, varying due to different ligands used. Proto-dehalogenation side products also accounted for some of the mass balance. Therefore, cross-selectivity is not reported.

Table 4C.6. Screening of reductants, additives, and solvents for condition B.<sup>a</sup>

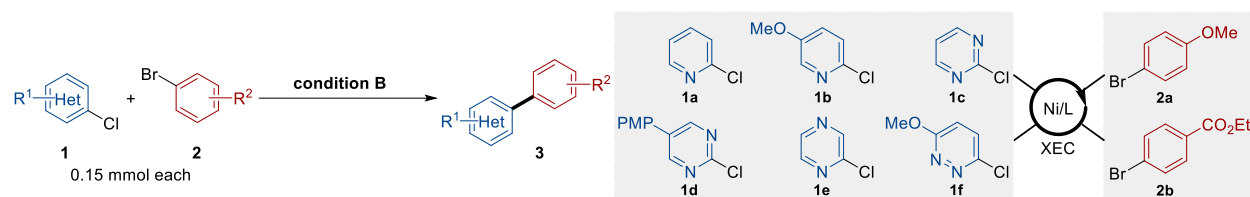
Entry	Additive (equiv)	Reductant (equiv)	Solvent	<b>1c</b> (%)	<b>1cc</b> (%)	<b>2e</b> (%)	<b>2ee</b> (%)	<b>3ce</b> (%)
1	none	Zn (2)	DMF	0	5	33	7	42
2	none	Mn (2)	DMF	0	3	30	16	40
3	none	TDAE (1.4)	DMF	50	6.5	53	2	36
4	none	TDAE (2.0)	DMF	50	6	52	5	31
5 <sup>b</sup>	LiCl (2)	TDAE (1.4)	DMF	78	2.5	N.A.	0	5
6 <sup>b</sup>	LiBr (2)	TDAE (1.4)	DMF	35	6	N.A.	0	40
7 <sup>b</sup>	$\text{MgCl}_2$ (2)	TDAE (1.4)	DMF	58	0	57	0	0
8	NaI (2)	TDAE (1.4)	DMF	29	11	48	6	44
9 <sup>c</sup>	NaI (2)	TDAE (2.4)	DMF	20	7.5	36	7	50
10	NaI (3)	TDAE (1.4)	DMF	20	9.5	32	7.5	54
11	NaI (3)	TDAE (1.4)	DMA	15	10	40	8	54
12	NaI (3)	TDAE (1.4)	NMP	11.5	11	15	10	63
13	NaI (3)	TDAE (1.4)	DMI	10.5	12.5	10	13.5	56
14	NaI (3)	TDAE (1.4)	DMSO	69	5	55	0	8
15 <sup>b</sup>	NaI (3)	Zn (2)	DMF	0	17	0	13	51
16	NaI (3)	TDAE (1.4)	1,4-dioxane	0	2.5	0	4	88
17 <sup>d</sup>	NaI (3)	TDAE (1.2)	1,4-dioxane	0	2	0	3	90

<sup>a</sup> Yields are determined by  $^1\text{H}$  NMR spectroscopy of the crude reaction mixture using 1,3,5-trimethoxybenzene as an internal standard. Yields of homo-coupled dimers are reported with respect to the stoichiometry of the reaction, i.e., the maximal theoretical yield is 50%. <sup>b</sup> Benzene as the major side product from **2e**. <sup>c</sup> Injected 1 equiv TDAE after 17 h and stirred for an additional 7 h. <sup>d</sup> Used 2 mL dioxane instead of 1 mL.

Table 4C.7. Further optimization and control reactions for condition B.<sup>a</sup>

Entry	Variation from above	<b>1c</b> (%)	<b>1cc</b> (%)	<b>2a</b> (%)	<b>2aa</b> (%)	<b>3ca</b> (%)	Cross-selectivity
1	none	0	2	0	5	91	13:1
2	4 equiv NaI	0	1.5	0	7.5	86	9.6:1
3	2 equiv NaI	0	3.5	0	5	90	10.6:1
4	1 equiv NaI	29	4.5	46	0	45	/
5	w/o NaI	65	4.5	86	0	15	/
6	w/o FeBr <sub>2</sub>	55	3.5	78	0	24	/
7	TDAE (1.4 equiv), dioxane (1 mL)	0	3	0	8	85	7.7:1
8	TDAE (1.4 equiv), DMF (1 mL)	37	7.5	57	0	38	5.1:1
9	THF instead of dioxane	0	7	0	16	75	3.3:1
10	Mn (2 equiv) instead of TDAE	95	0	93	0	0	/
11	Zn (2 equiv) instead of TDAE	80	0	93	0	0	/
12 <sup>b</sup>	Zn (2 equiv) instead of TDAE, DMF (1 mL) instead of dioxane	4	9	0	4	43	/
13	Lil instead of NaI	0	2	0	7.5	84	8.8:1
14	<b>L6</b> instead of <b>L2</b>	85	0	100	0	0	/
15	4-iodoanisole instead of <b>2a</b> , w/o NaI	30	2	0	16	64	/
16	2-iodopyrimidine instead of <b>1c</b> , w/o NaI	0	40	100	0	0	/
17	7 mol% Ni catalyst	0	4	0	7.5	81	7.0:1

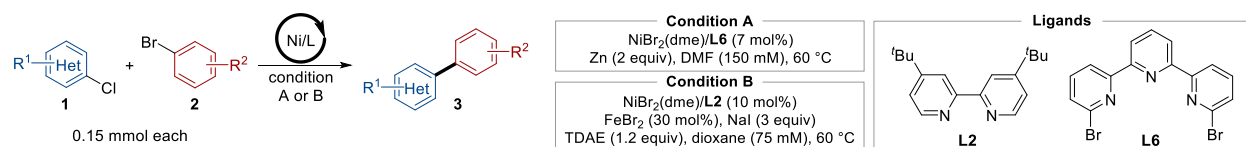
<sup>a</sup> Yields are determined by <sup>1</sup>H NMR spectroscopy of the crude reaction mixture using 1,3,5-trimethoxybenzene as an internal standard. Cross-selectivity is defined as **3ca** NMR yield:(**1cc** NMR yield + **2aa** NMR yield). Yields of homo-coupled dimers are reported with respect to the stoichiometry of the reaction, i.e., the maximal theoretical yield is 50%. <sup>b</sup> 47% anisole (proto-dehalogenation product from **2a**) was observed.

**Table 4C.8. Results of XEC reactions under condition B using informer library substrates.<sup>a</sup>**

Entry	1	2	Conversion of 1/2 (%)	Dimer of 1 (%)	Dimer of 2 (%)	Cross-coupled product (%)
1	<b>1a</b>	<b>2a</b>	57/100	3.5	25	50
2	<b>1a</b>	<b>2b</b>	35/100	5	42	14
3 <sup>b</sup>	<b>1b</b>	<b>2a</b>	80/100	0	32	17
4 <sup>b</sup>	<b>1b</b>	<b>2b</b>	46/40	0	20	0
5	<b>1c</b>	<b>2a</b>	100/100	2	5	91
6	<b>1c</b>	<b>2b</b>	100/100	1.5	5.5	88
7	<b>1d</b>	<b>2a</b>	100/100	0	7.5	76
8	<b>1d</b>	<b>2b</b>	100/100	0	8	65
9	<b>1e</b>	<b>2a</b>	100/100	14	13	75
10	<b>1e</b>	<b>2b</b>	100/100	20	28	47
11	<b>1f</b>	<b>2a</b>	100/100	17	21	55
12 <sup>b</sup>	<b>1f</b>	<b>2b</b>	100/100	40	24	17

<sup>a</sup> Yields are determined by <sup>1</sup>H NMR spectroscopy of the crude reaction mixture using 1,3,5-trimethoxybenzene as an internal standard. Yields of homo-coupled dimers are reported with respect to the stoichiometry of the reaction, i.e., the maximal theoretical yield is 50%. <sup>b</sup> Proto-dehalogenation products accounted for the remaining mass of **2**.

### 4C.III. General Procedures for Scope Investigation



#### General procedure for XEC reaction under condition A (GP 1)

**Reaction setup:** In a nitrogen-filled glove box, NiBr<sub>2</sub>(dme) (3.2 mg, 7 mol%), 6,6''-dibromo-2,2':6',2''-terpyridine (**L6**, 4.1 mg, 7 mol%), and DMF (1 mL) were added to a 1-dram vial equipped with a PTFE-coated stir-bar. This solution was stirred at 800 rpm in the glove box for 30 min to allow complexation of Ni with the ligand, followed by sequential addition of heteroaryl

chloride **1** (0.15 mmol, 1.0 equiv), aryl bromide **2** (0.15 mmol, 1.0 equiv), and Zn powder (19.5 mg, 0.30 mmol, 2.0 equiv). The vial was capped with a screw cap fitted with a PTFE-faced silicone septum, then removed from the glove box and heated in a sand bath at 60 °C with stirring (1100 rpm) for 17 h.

**GP 1-1:** For reactions using heteroaryl chlorides containing more than one nitrogen in the ring, NiBr<sub>2</sub>(dme) (6.4 mg, 10 mol%), 6,6''-dibromo-2,2':6',2''-terpyridine (**L6**, 5.9 mg, 10 mol%) was used as the catalyst. FeBr<sub>2</sub> (9.7 mg, 0.075 mmol, 0.30 equiv) was added before the addition of Zn powder.

Work-up for NMR analysis: After 17 h, the reaction mixture was cooled to room temperature and quenched with 2 M NH<sub>3</sub>/methanol solution (1 mL). The resultant mixture was stirred at 800 rpm for 30 min. A stock solution of 1,3,5-trimethoxybenzene was prepared (0.5 M), and 100 μL of this stock solution (0.33 equiv relative to substrate) was added to the crude material. Then a 100 μL aliquot of the solution was diluted with 600 μL CDCl<sub>3</sub> and filtered through a syringe filter (PVDF membrane, 0.22 μm pore size, 13 mm diameter) into an NMR sample tube. The resultant sample was analyzed by <sup>1</sup>H NMR spectroscopy and yields were determined using 1,3,5-trimethoxybenzene as the internal standard.

Work-up for product isolation: The NMR sample was combined with the rest of the reaction mixture, and the resultant solution was diluted with water (3 mL). The solution was extracted with ethyl acetate (20 mL × 3) and the organic layers were combined and dried over anhydrous Na<sub>2</sub>SO<sub>4</sub>, then concentrated *in vacuo*. The obtained residue was purified by flash column chromatography.

### **General procedure for XEC reaction under condition B (GP 2)**

Reaction setup: In a nitrogen-filled glove box, NiBr<sub>2</sub>(dme) (4.6 mg, 10 mol%), 4,4'-di-*tert*-butyl-2,2'-bipyridine (**L2**, 4.0 mg, 10 mol%), and 1,4-dioxane (2 mL) were added to a 1-dram vial

equipped with a PTFE-coated stir-bar. This solution was stirred at 800 rpm in the glove box for 30 min to allow complexation of Ni with the ligand, followed by sequential addition of heteroaryl chloride **1** (0.15 mmol, 1.0 equiv), aryl bromide **2** (0.15 mmol, 1.0 equiv), FeBr<sub>2</sub> (9.7 mg, 0.075 mmol, 0.30 equiv), NaI (67.5 mg, 0.45 mmol, 3.0 equiv), and TDAE (41.8 μL, 0.18 mmol, 1.2 equiv). The vial was capped with a screw cap fitted with a PTFE-faced silicone septum, then removed from the glove box and heated in a sand bath at 60 °C with stirring (1100 rpm) for 17 h.

Work-up for NMR analysis: After 17 h, the reaction mixture was cooled to room temperature and quenched with 2 M NH<sub>3</sub>/methanol solution (1 mL). The resultant mixture was stirred at 800 rpm for 30 min. A stock solution of 1,3,5-trimethoxybenzene was prepared (0.5 M), and 100 μL of this stock solution (0.33 equiv relative to substrate) was added to the crude material. Then a 100 μL aliquot of the solution was diluted with 600 μL CDCl<sub>3</sub> and filtered through a syringe filter (PVDF membrane, 0.22 μm pore size, 13 mm diameter) into an NMR sample tube. The resultant sample was analyzed by <sup>1</sup>H NMR spectroscopy and yields were determined using 1,3,5-trimethoxybenzene as the internal standard.

Work-up for product isolation: The NMR sample was combined with the rest of the reaction mixture, and the resultant solution was diluted with water (3 mL). The solution was extracted with ethyl acetate (20 mL × 3) and the organic layers were combined and dried over anhydrous Na<sub>2</sub>SO<sub>4</sub>, then concentrated *in vacuo*. The obtained residue was purified by flash column chromatography.

#### 4C.IV. Mechanistic Studies

##### *Time-course experiments under condition A*

Preparation of iodine quenching solution:<sup>1</sup> In a nitrogen-filled glove box, LiCl (127 mg, 3.0 mmol) and THF (6 mL) were added to a 4-dram vial equipped with a PTFE-coated stir-bar. The

solution was stirred at room temperature overnight until all solids were dissolved. I<sub>2</sub> (381 mg, 1.5 mmol) was then added, and the brown solution was stirred at room temperature for 1 h before use.

Reaction setup: In a nitrogen-filled glove box, NiBr<sub>2</sub>(dme) (3.2 mg, 7 mol%), 6,6''-dibromo-2,2':6',2''-terpyridine (**L6**, 4.1 mg, 7 mol%), and DMF (1 mL) were added to a 2-dram vial equipped with a PTFE-coated stir-bar. This solution was stirred at 800 rpm in the glove box for 30 min to allow complexation of Ni with the ligand, followed by sequential addition of 2-chloropyridine (13.8 μL, 0.15 mmol, 1.0 equiv), or ethyl 4-bromobenzoate (24 μL, 0.15 mmol, 1.0 equiv), or both electrophiles, and Zn powder (19.5 mg, 0.30 mmol, 2.0 equiv). Finally, 1,3,5-trimethoxybenzene (8.4 mg, 0.05 mmol, 0.33 equiv) was added to the solution. The vial was capped with a screw cap fitted with a PTFE-faced silicone septum, then removed from the glove box and heated in a sand bath at 60 °C with stirring (1100 rpm) for 3 h.

Iodine quenching and NMR analysis: At each time point, a reaction aliquot (66.7 μL) was extracted via a Hamilton syringe under positive N<sub>2</sub> pressure, transferred into a 1-dram vial equipped with a PTFE-coated stir-bar, and *immediately* quenched with iodine/LiCl solution (200 μL). The resultant mixture was stirred at room temperature for 15 min, at which point 2 M NH<sub>3</sub>/methanol solution (100 μL) was added and the mixture was stirred for an additional 30 min. Then a 100 μL aliquot of the solution was diluted with 600 μL CDCl<sub>3</sub> and filtered through a syringe filter (PVDF membrane, 0.22 μm pore size, 13 mm diameter) into an NMR sample tube. The resultant sample was analyzed by <sup>1</sup>H NMR spectroscopy and yields were determined using 1,3,5-trimethoxybenzene as the internal standard.

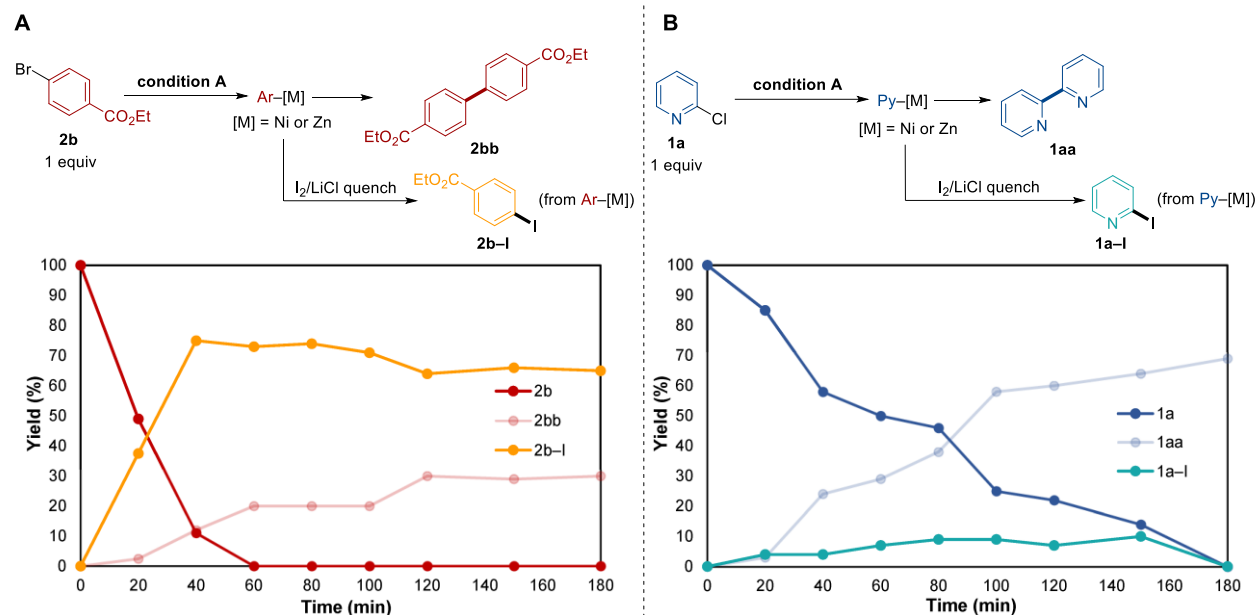
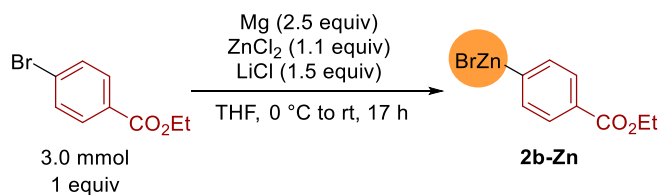


**Figure 4C.2.** Time-course studies using only **2b** (A) or only **1a** (B) under condition A. Yields are determined by  $^1\text{H}$  NMR spectroscopy of the crude reaction mixture using 1,3,5-trimethoxybenzene as an internal standard.

### Preparation of organozinc reagents

The organozinc reagents were prepared according to procedures described previously in the literature.

### Synthesis of arylzinc bromide **2b-Zn**<sup>2</sup>



Under nitrogen,  $\text{ZnCl}_2$  (450 mg, 3.3 mmol, 1.1 equiv),  $\text{LiCl}$  (191 mg, 4.5 mmol, 1.5 equiv),  $\text{Mg}$  powder (180 mg, 7.5 mmol, 2.5 equiv), and anhydrous THF (6 mL) were added into an oven-dried Schlenk flask equipped with a PTFE-coated stir-bar and stirred at room temperature for 30 min. To this mixture was added dropwise ethyl 4-bromobenzoate (480  $\mu\text{L}$ , 3.0 mmol, 1.0 equiv) via a Hamilton syringe under positive  $\text{N}_2$  pressure at 0  $^\circ\text{C}$ , and the mixture was warmed to room temperature and stirred for 17 h. The reaction was monitored by NMR (the reaction aliquots were



The reaction was carried out following **GP 1** with the following modifications: The organozinc **1a-Zn** (0.45 M in THF, 333  $\mu$ L, 0.15 mmol) was used instead of **1a**, with no or catalytic amount of Zn powder (0 or 2.9 mg, 0 or 15 mol%).

#### **Stoichiometric reaction of 2b-Zn with NiBr<sub>2</sub>(dme)/L6**

The reaction was carried out following **GP 1** with the following modifications: Substrate **1a** was omitted, and a stoichiometric amount of NiBr<sub>2</sub>(dme)/**L6** was used. The organozinc **2b-Zn** (0.48 M in THF, 312  $\mu$ L, 0.15 mmol) was used instead of **2b**.

#### **Stoichiometric reaction of 1a-Zn with NiBr<sub>2</sub>(dme)/L6**

The reaction was carried out following **GP 1** with the following modifications: Substrate **2b** was omitted, and a stoichiometric amount of NiBr<sub>2</sub>(dme)/**L6** was used. The organozinc **1a-Zn** (0.45 M in THF, 333  $\mu$ L, 0.15 mmol) was used instead of **1a**.

#### **Decoupled aryl-zinc formation/cross-coupling reaction**

In a nitrogen-filled glove box, NiBr<sub>2</sub>(dme) (3.2 mg, 7 mol%), 6,6''-dibromo-2,2':6',2''-terpyridine (**L6**, 4.1 mg, 7 mol%), and DMF (1 mL) were added to a 1-dram vial equipped with a PTFE-coated stir-bar. This solution was stirred at 800 rpm in the glove box for 30 min to allow complexation of Ni with the ligand, followed by sequential addition of 1,3,5-trimethoxybenzene (8.4 mg, 0.05 mmol, 0.33 equiv), ethyl 4-bromobenzoate (24  $\mu$ L, 0.15 mmol, 1.0 equiv), and Zn powder (19.5 mg, 0.30 mmol, 2.0 equiv). The vial was capped with a screw cap fitted with a PTFE-faced silicone septum, then removed from the glove box and heated in a sand bath at 60 °C with stirring (1100 rpm) for 40 min. A reaction aliquot (66.7  $\mu$ L) was extracted via a Hamilton syringe under positive N<sub>2</sub> pressure and subjected to the iodine quenching and NMR analysis procedure described in *Section 4.1*. Substrate 2-chloropyridine (13.8  $\mu$ L, 0.15 mmol, 1.0 equiv) was injected into the mixture via a Hamilton syringe under positive N<sub>2</sub> pressure. The reaction mixture was

stirred at 60 °C for an additional 3 h, then subjected to the work-up for NMR analysis procedure as described in **GP 1**, except that the stock solution of 1,3,5-trimethoxybenzene was not added.

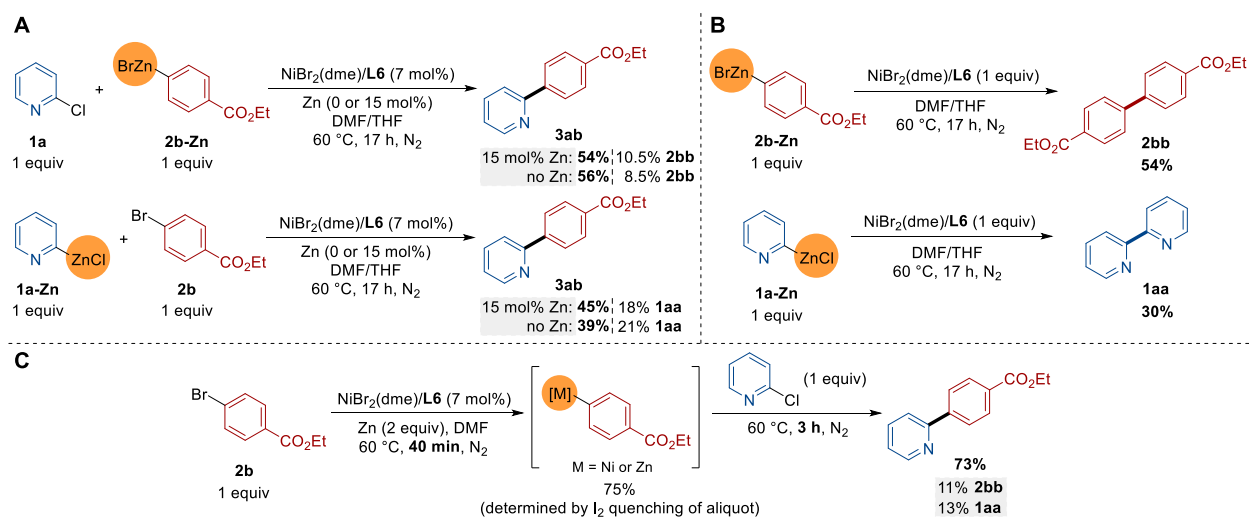


**Figure 4C.3.** Reactions of organozinc reagents with substrates or Ni catalyst. Yields are determined by <sup>1</sup>H NMR spectroscopy of the crude reaction mixture using 1,3,5-trimethoxybenzene as an internal standard. Yields of homo-coupled dimers are reported with respect to the stoichiometry of the reaction, i.e., the maximal theoretical yield is 50%. (A) Reactions of **1a** with **2b-Zn** (top) and **1a-Zn** with **2b** (bottom) catalyzed by NiBr<sub>2</sub>(dme)/L6. (B) Stoichiometric reactions of **2b-Zn** (top) or **1a-Zn** (bottom) with NiBr<sub>2</sub>(dme)/L6. (C) Decoupled aryl-zinc formation/cross-coupling reaction catalyzed by NiBr<sub>2</sub>(dme)/L6.

**Discussion:** As shown in Figure 4C.3A, external reductant is not needed for NiBr<sub>2</sub>(dme)/L6-catalyzed Negishi coupling when organozinc is directly used. In the absence of reductant, the reaction may be initiated by reduction of the Ni catalyst by organozinc, which eventually generates low-valent Ni species and the corresponding (hetero)aryl dimers.<sup>4</sup> This is supported by the generation of homocoupling dimers in the catalytic (Figure 4C.3A) and stoichiometric (Figure 4C.3B) reactions. The lower **3ab** yields may be contributed to (a) the halide salts and THF solvents introduced by the organozinc/THF solution and (b) decomposition and/or homocoupling of the organozinc under reaction conditions.

The cross-coupling of pyridyl-zinc (**1a-Zn**) with **2b** is also viable, albeit resulting in even lower yields. Combining the results from Figure 4C.2B and 4C.3A, it seems that Ni/L6 is not capable of

converting 2-chloropyridine to pyridyl-zinc but can be a catalyst for the direct coupling of **1a-Zn** and **2b**.

*Time-course experiments under condition B*

Preparation of iodine quenching solution:<sup>1</sup> In a nitrogen-filled glove box, LiCl (127 mg, 3.0 mmol) and THF (6 mL) were added to a 4-dram vial equipped with a PTFE-coated stir-bar. The solution was stirred at room temperature overnight until all solids were dissolved. I<sub>2</sub> (381 mg, 1.5 mmol) was then added, and the brown solution was stirred at room temperature for 1 h before use.

Reaction setup: In a nitrogen-filled glove box, NiBr<sub>2</sub>(dme) (4.6 mg, 10 mol%), 4,4'-di-*tert*-butyl-2,2'-bipyridine (**L2**, 4.0 mg, 10 mol%), and 1,4-dioxane (2 mL) were added to a 1-dram vial equipped with a PTFE-coated stir-bar. This solution was stirred at 800 rpm in the glove box for 30 min to allow complexation of Ni with the ligand, followed by sequential addition of 2-chloropyrimidine (17.2 mg, 0.15 mmol, 1.0 equiv), 4-bromoanisole or 4-iodoanisole (28 or 35.1 mg, 0.15 mmol, 1.0 equiv), FeBr<sub>2</sub> (none, or 9.7 mg, 0.075 mmol, 0.30 equiv), NaI (none, or 67.5 mg, 0.45 mmol, 3.0 equiv) and TDAE (41.8 μL, 0.18 mmol, 1.2 equiv). Finally, 1,3,5-trimethoxybenzene (8.4 mg, 0.05 mmol, 0.33 equiv) was added to the solution. The vial was capped with a screw cap fitted with a PTFE-faced silicone septum, then removed from the glove box and heated in a sand bath at 60 °C with stirring (1100 rpm) for 4 h.

Iodine quenching and NMR analysis: At each time point, a reaction aliquot (133 μL) was extracted via a Hamilton syringe under positive N<sub>2</sub> pressure, transferred into a 1-dram vial equipped with a PTFE-coated stir-bar, and *immediately* quenched with iodine/LiCl solution (200 μL). The resultant mixture was stirred at room temperature for 15 min, at which point 2 M NH<sub>3</sub>/methanol solution (100 μL) was added and the mixture was stirred for an additional 30 min. Then a 100 μL aliquot of the solution was diluted with 600 μL CDCl<sub>3</sub> and filtered through a syringe

filter (PVDF membrane, 0.22  $\mu\text{m}$  pore size, 13 mm diameter) into an NMR sample tube. The resultant sample was analyzed by  $^1\text{H}$  NMR spectroscopy and yields were determined using 1,3,5-trimethoxybenzene as the internal standard.

Note: For reactions using 4-iodoanisole as the coupling partner, iodine quenching was not performed; instead, the reaction aliquot was directly quenched by 2 M  $\text{NH}_3$ /methanol solution. The rest of the procedure remains the same.

#### *The role of $\text{FeBr}_2$*

XEC reactions were carried out under Condition A or B, in the presence or absence of  $\text{FeBr}_2$ , following **GP 1** or **2**. The results are summarized in Figure 4C.4.

Discussion: The results in Figure 4C.4 show that the role of  $\text{FeBr}_2$  in the developed heteroaryl-aryl XEC reactions may be more than just limiting heteroaryl ligation to the Ni catalyst. For condition A, 30 mol%  $\text{FeBr}_2$  is added when the heteroaryl chloride contains more than one nitrogen in the ring. Comparing entries 3 and 4 in Figure 4C.4, omitting  $\text{FeBr}_2$  in the coupling of **1e** and **2b** resulted in significant aryl bromide proto-dehalogenation (42% **2b-H**), which seems to suggest that  $\text{FeBr}_2$  could modulate the transmetalation between aryl-[M] and Ni species; without  $\text{FeBr}_2$ , some amount of aryl-[M] remained unreacted in the solution and underwent protonolysis upon reaction quenching. In the coupling of **1a** and **2b**, the inclusion of  $\text{FeBr}_2$  promoted the homocoupling dimer formation. For condition B,  $\text{FeBr}_2$  seems not to have significant impact on the reaction outcomes in the coupling of **1c** with electron-neutral **2e** or electron-deficient **2b** (entries 7–10, Figure 4C.4); however, omitting  $\text{FeBr}_2$  in the coupling of **1c** with electron-rich **2a** resulted in low conversion of both substrates and significantly decreased yield (entries 5 and 6, Figure 4C.4).

Overall, these differences imply a more dynamic role of FeBr<sub>2</sub> under conditions A and B, and in-depth investigations are ongoing in our laboratory.

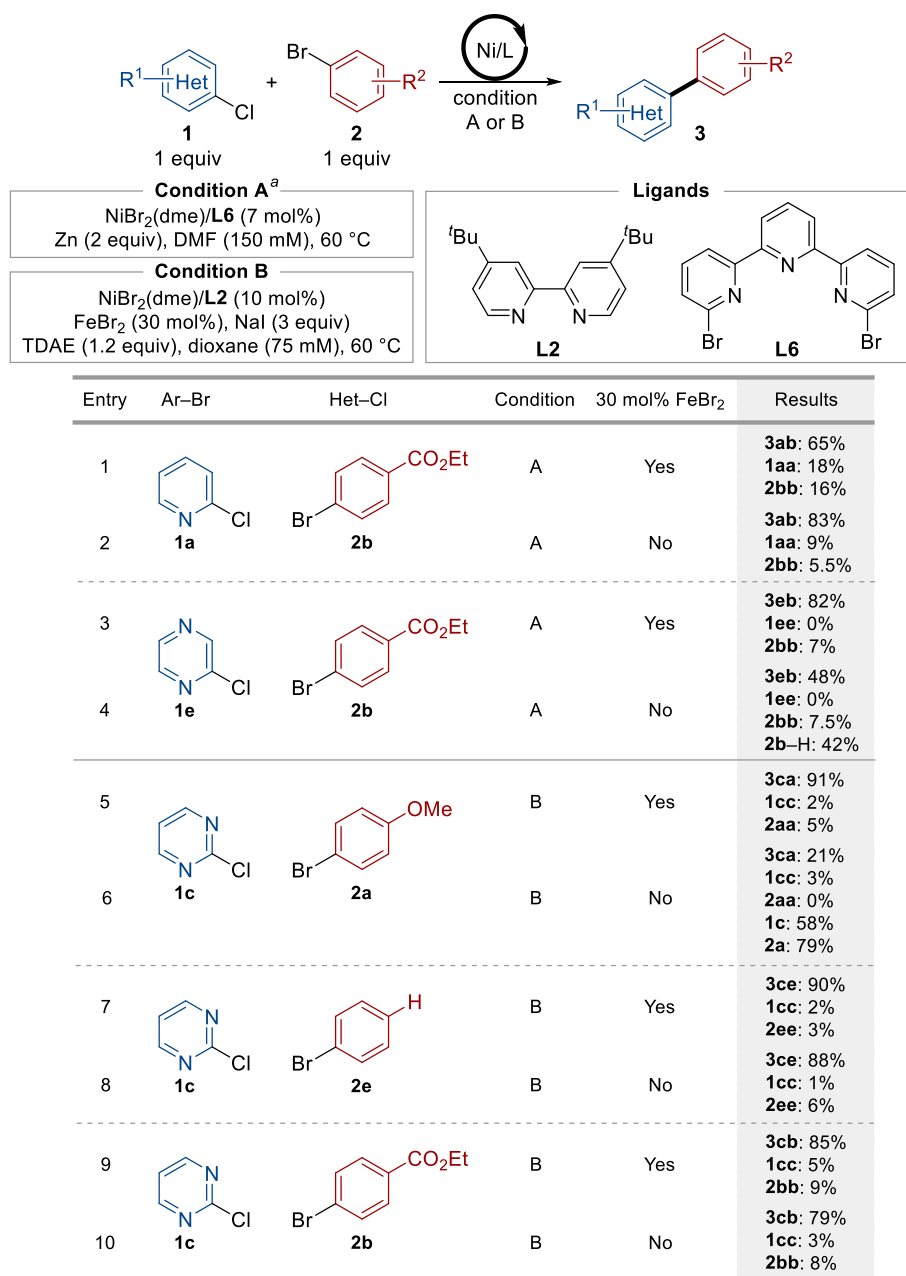
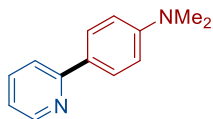


**Figure 4C.4.** XEC reactions in the presence or absence of 30 mol% FeBr<sub>2</sub>. Yields are determined by <sup>1</sup>H NMR spectroscopy of the crude reaction mixture using 1,3,5-trimethoxybenzene as an internal standard. Yields of homo-coupled dimers are reported with respect to the stoichiometry of the reaction, i.e., the maximal theoretical yield is 50%. <sup>a</sup> Used 10 mol% Ni catalyst in entries 3 and 4.

#### 4C.V. Compound Characterization Data

*N,N*-dimethyl-4-(pyridin-2-yl)aniline (**3ac**)

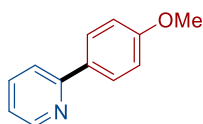


**GP 1** was followed using 2-chloropyridine (13.8  $\mu$ L, 0.15 mmol, 1.0 equiv) and 4-bromo-*N,N*-dimethylaniline (30 mg, 0.15 mmol, 1.0 equiv) as starting materials, which furnished the title compound following purification by flash column chromatography (20:80 ethyl acetate:pentane) as a yellow solid (22.9 mg, 77% yield). The spectroscopic data matched those reported in the literature.<sup>5</sup>

**<sup>1</sup>H NMR** (500 MHz, CDCl<sub>3</sub>)  $\delta$  8.62 (d,  $J$  = 4.9 Hz, 1H), 7.95 – 7.90 (m, 2H), 7.69 – 7.62 (m, 2H), 7.09 (ddd,  $J$  = 6.6, 4.8, 1.9 Hz, 1H), 6.83 – 6.77 (m, 2H), 3.02 (s, 6H).

**<sup>13</sup>C NMR** (126 MHz, CDCl<sub>3</sub>)  $\delta$  157.7, 151.2, 149.5, 136.6, 127.8, 127.4, 120.7, 119.3, 112.4, 40.5.

2-(4-methoxyphenyl)pyridine (**3aa**)

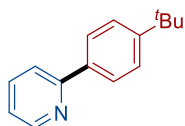


**GP 1** was followed using 2-chloropyridine (13.8  $\mu$ L, 0.15 mmol, 1.0 equiv) and 1-bromo-4-methoxybenzene (28 mg, 0.15 mmol, 1.0 equiv) as starting materials, which furnished the title compound following purification by flash column chromatography (20:80 ethyl acetate:pentane) as a white solid (24.2 mg, 87% yield). The spectroscopic data matched those reported in the literature.<sup>6</sup>

**<sup>1</sup>H NMR** (500 MHz, CDCl<sub>3</sub>)  $\delta$  8.65 (d,  $J$  = 4.9 Hz, 1H), 7.98 – 7.93 (m, 2H), 7.73 – 7.63 (m, 2H), 7.16 (ddd,  $J$  = 7.2, 4.9, 1.4 Hz, 1H), 7.02 – 6.97 (m, 2H), 3.86 (s, 3H).

$^{13}\text{C}$  NMR (126 MHz,  $\text{CDCl}_3$ )  $\delta$  160.6, 157.2, 149.7, 136.8, 132.2, 128.3, 121.5, 119.9, 114.2, 55.5.

2-(4-(*tert*-butyl)phenyl)pyridine (**3ad**)

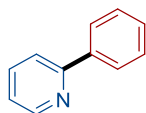


**GP 1** was followed using 2-chloropyridine (13.8  $\mu\text{L}$ , 0.15 mmol, 1.0 equiv) and 1-bromo-4-(*tert*-butyl)benzene (32 mg, 0.15 mmol, 1.0 equiv) as starting materials, which furnished the title compound following purification by flash column chromatography (10:90 ethyl acetate:pentane) as a colorless liquid (26 mg, 82% yield). The spectroscopic data matched those reported in the literature.<sup>6</sup>

$^1\text{H}$  NMR (500 MHz,  $\text{CDCl}_3$ )  $\delta$  8.68 (d,  $J = 4.8$  Hz, 1H), 7.96 – 7.91 (m, 2H), 7.75 – 7.69 (m, 2H), 7.53 – 7.48 (m, 2H), 7.22 – 7.17 (m, 1H), 1.37 (s, 9H).

$^{13}\text{C}$  NMR (126 MHz,  $\text{CDCl}_3$ )  $\delta$  157.6, 152.2, 149.8, 136.7, 126.7, 125.8, 121.9, 120.4, 34.8, 31.4.

2-phenylpyridine (**3ae**)

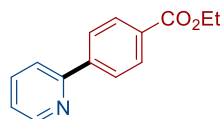


**GP 1** was followed using 2-chloropyridine (13.8  $\mu\text{L}$ , 0.15 mmol, 1.0 equiv) and bromobenzene (23.6 mg, 0.15 mmol, 1.0 equiv) as starting materials, which furnished the title compound following purification by flash column chromatography (5:95 ethyl acetate:pentane) as a colorless liquid (16.5 mg, 71% yield). The spectroscopic data matched those reported in the literature.<sup>6</sup>

$^1\text{H}$  NMR (400 MHz,  $\text{CDCl}_3$ )  $\delta$  8.75 (d,  $J = 5.1$  Hz, 1H), 8.08 – 8.01 (m, 2H), 7.83 – 7.74 (m, 2H), 7.56 – 7.49 (m, 2H), 7.49 – 7.43 (m, 1H), 7.29 – 7.23 (m, 1H).

$^{13}\text{C}$  NMR (101 MHz,  $\text{CDCl}_3$ )  $\delta$  157.6, 149.8, 139.5, 136.8, 129.0, 128.8, 127.0, 122.2, 120.6.

ethyl 4-(pyridin-2-yl)benzoate (**3ab**)

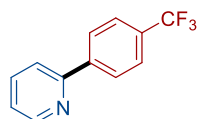


**GP 1** was followed using 2-chloropyridine (13.8  $\mu\text{L}$ , 0.15 mmol, 1.0 equiv) and ethyl 4-bromobenzoate (34.4 mg, 0.15 mmol, 1.0 equiv) as starting materials, which furnished the title compound following purification by flash column chromatography (20:80 ethyl acetate:pentane) as a white solid (26.9 mg, 79% yield). The spectroscopic data matched those reported in the literature.<sup>6</sup>

$^1\text{H}$  NMR (400 MHz,  $\text{CDCl}_3$ )  $\delta$  8.72 (d,  $J = 4.8$  Hz, 1H), 8.17 – 8.12 (m, 2H), 8.10 – 8.04 (m, 2H), 7.80 – 7.75 (m, 2H), 7.31 – 7.23 (m, 1H), 4.40 (q,  $J = 7.1$  Hz, 2H), 1.42 (t,  $J = 7.1$  Hz, 3H).

$^{13}\text{C}$  NMR (101 MHz,  $\text{CDCl}_3$ )  $\delta$  166.6, 156.4, 150.0, 143.5, 137.0, 130.8, 130.1, 126.9, 122.9, 121.1, 61.2, 14.5.

2-(4-(trifluoromethyl)phenyl)pyridine (**3af**)



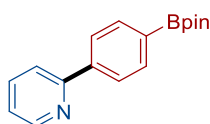
**GP 1** was followed using 2-chloropyridine (13.8  $\mu\text{L}$ , 0.15 mmol, 1.0 equiv) and 1-bromo-4-(trifluoromethyl)benzene (33.8 mg, 0.15 mmol, 1.0 equiv) as starting materials, which furnished the title compound following purification by flash column chromatography (15:85 ethyl acetate:pentane) as a white solid (23.8 mg, 71% yield). The spectroscopic data matched those reported in the literature.<sup>6</sup>

**<sup>1</sup>H NMR** (400 MHz, CDCl<sub>3</sub>) δ 8.73 (d, *J* = 4.8 Hz, 1H), 8.15 – 8.08 (m, 2H), 7.84 – 7.75 (m, 2H), 7.73 (d, *J* = 8.2 Hz, 2H), 7.30 (ddd, *J* = 6.7, 4.8, 1.6 Hz, 1H).

**<sup>13</sup>C NMR** (126 MHz, CDCl<sub>3</sub>) δ 156.1, 150.1, 142.8, 137.1, 130.9 (q, *J* = 32.4 Hz), 127.3, 125.8 (q, *J* = 3.9 Hz), 124.3 (q, *J* = 272.0 Hz), 123.1, 121.0.

**<sup>19</sup>F NMR** (377 MHz, CDCl<sub>3</sub>) δ –62.57.

2-[4-(4,4,5,5-tetramethyl-1,3,2-dioxaborolan-2-yl)phenyl]pyridine (**3ag**)

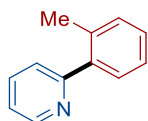


**GP 1** was followed using 2-chloropyridine (13.8 μL, 0.15 mmol, 1.0 equiv) and 2-(4-bromophenyl)-4,4,5,5-tetramethyl-1,3,2-dioxaborolane (42.4 mg, 0.15 mmol, 1.0 equiv) as starting materials, which furnished the title compound following purification by flash column chromatography (10:90 ethyl acetate:pentane) as a white solid (27.8 mg, 66% yield). The spectroscopic data matched those reported in the literature.<sup>7</sup>

**<sup>1</sup>H NMR** (500 MHz, CDCl<sub>3</sub>) δ 8.71 (d, *J* = 4.8 Hz, 1H), 8.03 – 7.98 (m, 2H), 7.94 – 7.90 (m, 2H), 7.79 – 7.72 (m, 2H), 7.24 (ddd, *J* = 6.7, 4.8, 2.1 Hz, 1H), 1.37 (s, 12H).

**<sup>13</sup>C NMR** (126 MHz, CDCl<sub>3</sub>) δ 157.4, 149.9, 142.0, 136.9, 135.4, 126.2, 122.5, 120.9, 84.0, 25.0.

2-(*o*-tolyl)pyridine (**3ah**)



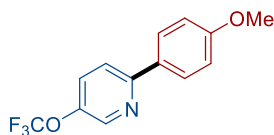
**GP 1** was followed using 2-chloropyridine (13.8 μL, 0.15 mmol, 1.0 equiv) and 1-bromo-2-methylbenzene (25.6 mg, 0.15 mmol, 1.0 equiv) as starting materials, NiBr<sub>2</sub>(dme) (6.43 mg, 10

mol%) complexed with 6,6'-dimethyl-2,2'-bipyridine (2.76 mg, 10 mol%) as the catalyst, which furnished the title compound following purification by flash column chromatography (25:75 ethyl acetate:pentane) as a colorless liquid (21.3 mg, 84% yield). The spectroscopic data matched those reported in the literature.<sup>8</sup>

**<sup>1</sup>H NMR** (400 MHz, CDCl<sub>3</sub>) δ 8.67 (d, *J* = 4.9 Hz, 1H), 7.71 (td, *J* = 7.7, 1.8 Hz, 1H), 7.40 – 7.34 (m, 2H), 7.31 – 7.18 (m, 4H), 2.34 (s, 3H).

**<sup>13</sup>C NMR** (101 MHz, CDCl<sub>3</sub>) δ 160.2, 149.4, 140.6, 136.2, 135.9, 130.9, 129.8, 128.4, 126.0, 124.2, 121.8, 20.4.

2-(4-methoxyphenyl)-5-(trifluoromethoxy)pyridine (**3ga**)



**GP 1** was followed using 2-chloro-5-(trifluoromethoxy)pyridine (29.6 mg, 0.15 mmol, 1.0 equiv) and 1-bromo-4-methoxybenzene (28 mg, 0.15 mmol, 1.0 equiv) as starting materials, NiBr<sub>2</sub>(dme) (6.43 mg, 10 mol%) complexed with 6,6'-dimethyl-2,2'-bipyridine (2.76 mg, 10 mol%) as the catalyst, which furnished the title compound following purification by flash column chromatography (2:98 ethyl acetate:pentane) as a white solid (31.1 mg, 77% yield).

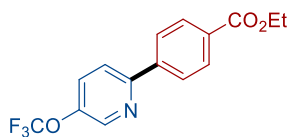
**<sup>1</sup>H NMR** (400 MHz, CDCl<sub>3</sub>) δ 8.57 (d, *J* = 2.8 Hz, 1H), 7.96 – 7.91 (m, 2H), 7.70 (d, *J* = 8.7 Hz, 1H), 7.61 – 7.56 (m, 1H), 7.03 – 6.97 (m, 2H), 3.87 (s, 3H).

**<sup>13</sup>C NMR** (126 MHz, CDCl<sub>3</sub>) δ 160.9, 156.0, 144.7 – 144.6 (m), 142.7, 130.8, 129.3, 128.4, 120.6 (q, *J* = 258.3 Hz), 119.6, 114.4, 55.5.

**<sup>19</sup>F NMR** (377 MHz, CDCl<sub>3</sub>) δ –58.23.

**HRMS (ESI<sup>+</sup>)** Calc: [M+H]<sup>+</sup> (C<sub>13</sub>H<sub>11</sub>F<sub>3</sub>NO<sub>2</sub>) 270.0376; measured: 270.0733 = 1.1 ppm difference.

ethyl 4-(5-(trifluoromethoxy)pyridin-2-yl)benzoate (**3gb**)



**GP 1** was followed using 2-chloro-5-(trifluoromethoxy)pyridine (29.6 mg, 0.15 mmol, 1.0 equiv) and ethyl 4-bromobenzoate (34.4 mg, 0.15 mmol, 1.0 equiv) as starting materials, which furnished the title compound following purification by flash column chromatography (5:95 ethyl acetate:pentane) as a white solid (25.2 mg, 54% yield).

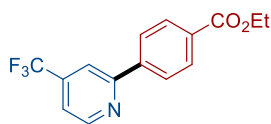
**<sup>1</sup>H NMR** (400 MHz, CDCl<sub>3</sub>) δ 8.65 (d, *J* = 2.8 Hz, 1H), 8.19 – 8.12 (m, 2H), 8.09 – 8.01 (m, 2H), 7.86 – 7.81 (m, 1H), 7.68 – 7.62 (m, 1H), 4.41 (q, *J* = 7.1 Hz, 2H), 1.42 (t, *J* = 7.1 Hz, 3H).

**<sup>13</sup>C NMR** (126 MHz, CDCl<sub>3</sub>) δ 166.4, 155.0, 145.6 (q, *J* = 1.8 Hz), 143.0, 142.1, 131.3, 130.3, 129.2, 127.0, 121.6, 120.6 (q, *J* = 259.0 Hz), 61.3, 14.5.

**<sup>19</sup>F NMR** (377 MHz, CDCl<sub>3</sub>) δ –58.14.

**HRMS (ESI<sup>+</sup>)** Calc: [M+H]<sup>+</sup> (C<sub>15</sub>H<sub>13</sub>F<sub>3</sub>NO<sub>3</sub>) 312.0842; measured: 312.0838 = 1.3 ppm difference.

ethyl 4-(4-(trifluoromethyl)pyridin-2-yl)benzoate (**3hb**)



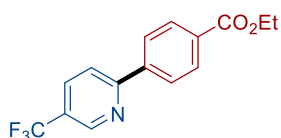
**GP 1** was followed using 2-chloro-4-(trifluoromethyl)pyridine (27.2 mg, 0.15 mmol, 1.0 equiv) and ethyl 4-bromobenzoate (34.4 mg, 0.15 mmol, 1.0 equiv) as starting materials, which furnished the title compound following purification by flash column chromatography (10:90 ethyl acetate:pentane) as a white solid (31.9 mg, 72% yield). The spectroscopic data matched those reported in the literature.<sup>9</sup>

**<sup>1</sup>H NMR** (400 MHz, CDCl<sub>3</sub>) δ 8.91 (d, *J* = 5.0 Hz, 1H), 8.21 – 8.15 (m, 2H), 8.14 – 8.08 (m, 2H), 7.98 (s, 1H), 7.53 – 7.48 (m, 1H), 4.42 (q, *J* = 7.1 Hz, 2H), 1.43 (t, *J* = 7.1 Hz, 3H).

**<sup>13</sup>C NMR** (126 MHz, CDCl<sub>3</sub>) δ 166.4, 157.8, 151.0, 142.1, 139.5 (q, *J* = 34.0 Hz), 131.8, 130.3, 127.1, 123.0 (q, *J* = 273.3 Hz), 118.4 (q, *J* = 3.5 Hz), 116.7 – 116.6 (m), 61.3, 14.5.

**<sup>19</sup>F NMR** (377 MHz, CDCl<sub>3</sub>) δ –64.82.

ethyl 4-(5-(trifluoromethyl)pyridin-2-yl)benzoate (**3ib**)



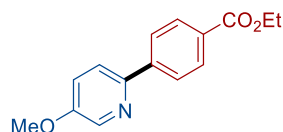
**GP 1** was followed using 2-chloro-5-(trifluoromethyl)pyridine (27.2 mg, 0.15 mmol, 1.0 equiv) and ethyl 4-bromobenzoate (34.4 mg, 0.15 mmol, 1.0 equiv) as starting materials, which furnished the title compound following purification by flash column chromatography (5:95 ethyl acetate:pentane) as a white solid (35.4 mg, 80% yield). This is the corrected yield that excluded the inseparable aryl dimer byproduct (3% with respect to the product based on <sup>1</sup>H NMR). The spectroscopic data matched those reported in the literature.<sup>10</sup>

**<sup>1</sup>H NMR** (400 MHz, CDCl<sub>3</sub>) δ 9.00 – 8.95 (m, 1H), 8.21 – 8.15 (m, 2H), 8.14 – 8.08 (m, 2H), 8.05 – 7.99 (m, 1H), 7.90 (dt, *J* = 8.3, 0.8 Hz, 1H), 4.42 (q, *J* = 7.1 Hz, 2H), 1.43 (t, *J* = 7.1 Hz, 3H).

**<sup>13</sup>C NMR** (126 MHz, CDCl<sub>3</sub>) δ 166.3, 159.6 (d, *J* = 1.7 Hz), 146.9 (q, *J* = 4.0 Hz), 142.0, 134.2 (q, *J* = 3.5 Hz), 131.9, 130.3, 127.3, 125.7 (q, *J* = 33.2 Hz), 123.8 (d, *J* = 271.7 Hz), 120.6, 61.4, 14.5.

**<sup>19</sup>F NMR** (377 MHz, CDCl<sub>3</sub>) δ –62.35.

ethyl 4-(5-methoxypyridin-2-yl)benzoate (**3bb**)



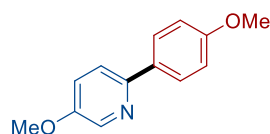
**GP 1** was followed using 2-chloro-5-methoxypyridine (21.5 mg, 0.15 mmol, 1.0 equiv) and ethyl 4-bromobenzoate (34.4 mg, 0.15 mmol, 1.0 equiv) as starting materials, which furnished the title compound following purification by flash column chromatography (20:80 ethyl acetate:pentane) as a white solid (25.1 mg, 65% yield).

**<sup>1</sup>H NMR** (500 MHz, CDCl<sub>3</sub>) δ 8.41 (d, *J* = 2.9 Hz, 1H), 8.14 – 8.07 (m, 2H), 8.03 – 7.96 (m, 2H), 7.71 (d, *J* = 8.7 Hz, 1H), 7.27 (dd, *J* = 8.8, 3.0 Hz, 1H), 4.39 (q, *J* = 7.1 Hz, 2H), 3.90 (s, 3H), 1.40 (t, *J* = 7.1 Hz, 3H).

**<sup>13</sup>C NMR** (126 MHz, CDCl<sub>3</sub>) δ 166.6, 155.5, 148.9, 143.3, 137.7, 130.1, 130.0, 126.3, 121.4, 121.2, 61.1, 55.8, 14.5.

**HRMS (ESI<sup>+</sup>)** Calc: [M+H]<sup>+</sup> (C<sub>15</sub>H<sub>16</sub>NO<sub>3</sub>) 258.1125; measured: 258.1123 = 0.8 ppm difference.

#### 5-methoxy-2-(4-methoxyphenyl)pyridine (**3ba**)

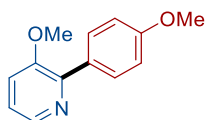


**GP 1** was followed using 2-chloro-5-methoxypyridine (21.5 mg, 0.15 mmol, 1.0 equiv) and 1-bromo-4-methoxybenzene (28 mg, 0.15 mmol, 1.0 equiv) as starting materials, which furnished the title compound following purification by flash column chromatography (15:85 ethyl acetate:pentane) as a white solid (23.2 mg, 72% yield). The spectroscopic data matched those reported in the literature.<sup>11</sup>

**<sup>1</sup>H NMR** (500 MHz, CDCl<sub>3</sub>) δ 8.36 (d, *J* = 3.0 Hz, 1H), 7.91 – 7.84 (m, 2H), 7.59 (d, *J* = 8.7 Hz, 1H), 7.23 (dd, *J* = 8.7, 3.0 Hz, 1H), 7.01 – 6.94 (m, 2H), 3.88 (s, 3H), 3.85 (s, 3H).

$^{13}\text{C NMR}$  (126 MHz,  $\text{CDCl}_3$ )  $\delta$  160.0, 154.5, 150.1, 136.9, 132.0, 127.7, 121.6, 120.2, 114.2, 55.8, 55.5.

3-methoxy-2-(4-methoxyphenyl)pyridine (**3ja**)

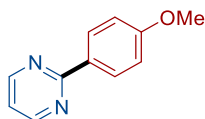


**GP 1** was followed using 2-chloro-3-methoxypyridine (21.5 mg, 0.15 mmol, 1.0 equiv) and 1-bromo-4-methoxybenzene (28 mg, 0.15 mmol, 1.0 equiv) as starting materials,  $\text{NiBr}_2(\text{dme})$  (6.43 mg, 10 mol%) complexed with 6,6'-dimethyl-2,2'-bipyridine (2.76 mg, 10 mol%) as the catalyst, which furnished the title compound following purification by flash column chromatography (50:50 ethyl acetate:pentane) as a colorless liquid (27.4 mg, 85% yield). The spectroscopic data matched those reported in the literature.<sup>12</sup>

$^1\text{H NMR}$  (500 MHz,  $\text{CDCl}_3$ )  $\delta$  8.30 (dd,  $J = 4.7, 1.3$  Hz, 1H), 7.96 – 7.89 (m, 2H), 7.30 – 7.24 (m, 1H), 7.20 (dd,  $J = 8.3, 4.6$  Hz, 1H), 7.02 – 6.96 (m, 2H), 3.89 – 3.86 (m, 6H).

$^{13}\text{C NMR}$  (126 MHz,  $\text{CDCl}_3$ )  $\delta$  159.8, 153.5, 147.9, 141.4, 130.8, 130.4, 122.4, 118.5, 113.5, 55.6, 55.4.

2-(4-methoxyphenyl)pyrimidine (**3ca**)



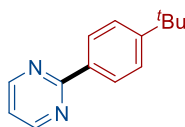
**GP 2** was followed using 2-chloropyrimidine (17.2 mg, 0.15 mmol, 1.0 equiv) and 1-bromo-4-methoxybenzene (28 mg, 0.15 mmol, 1.0 equiv) as starting materials, which furnished the title compound following purification by flash column chromatography (20:80 ethyl acetate:pentane)

as a white solid (23.2 mg, 83% yield). The spectroscopic data matched those reported in the literature.<sup>13</sup>

**<sup>1</sup>H NMR** (500 MHz, CDCl<sub>3</sub>) δ 8.74 (d, *J* = 4.8 Hz, 2H), 8.43 – 8.36 (m, 2H), 7.10 (t, *J* = 4.8 Hz, 1H), 7.03 – 6.97 (m, 2H), 3.87 (s, 3H).

**<sup>13</sup>C NMR** (126 MHz, CDCl<sub>3</sub>) δ 165.1, 162.5, 157.7, 130.8, 130.3, 118.9, 114.5, 55.9.

2-(4-(*tert*-butyl)phenyl)pyrimidine (**3cd**)

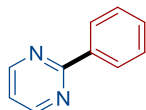


**GP 2** was followed using 2-chloropyrimidine (17.2 mg, 0.15 mmol, 1.0 equiv) and 1-bromo-4-(*tert*-butyl)benzene (32 mg, 0.15 mmol, 1.0 equiv) as starting materials, which furnished the title compound following purification by flash column chromatography (10:90 ethyl acetate:pentane) as a white solid (25.8 mg, 81% yield). The spectroscopic data matched those reported in the literature.<sup>14</sup>

**<sup>1</sup>H NMR** (500 MHz, CDCl<sub>3</sub>) δ 8.78 (d, *J* = 4.8 Hz, 2H), 8.40 – 8.34 (m, 2H), 7.55 – 7.49 (m, 2H), 7.14 (t, *J* = 4.8 Hz, 1H), 1.37 (s, 9H).

**<sup>13</sup>C NMR** (126 MHz, CDCl<sub>3</sub>) δ 164.9, 157.3, 154.3, 135.0, 128.1, 125.7, 118.9, 35.0, 31.4.

2-phenylpyrimidine (**3ce**)



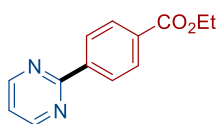
**GP 2** was followed using 2-chloropyrimidine (17.2 mg, 0.15 mmol, 1.0 equiv) and bromobenzene (23.6 mg, 0.15 mmol, 1.0 equiv) as starting materials, which furnished the title compound

following purification by flash column chromatography (5:95 ethyl acetate:pentane) as a white solid (19.7 mg, 84% yield). The spectroscopic data matched those reported in the literature.<sup>13</sup>

**<sup>1</sup>H NMR** (500 MHz, CDCl<sub>3</sub>) δ 8.81 (d, *J* = 4.8 Hz, 2H), 8.49 – 8.41 (m, 2H), 7.54 – 7.46 (m, 3H), 7.19 (t, *J* = 4.8 Hz, 1H).

**<sup>13</sup>C NMR** (126 MHz, CDCl<sub>3</sub>) δ 164.9, 157.4, 137.7, 130.9, 128.8, 128.3, 119.2.

ethyl 4-(pyrimidin-2-yl)benzoate (**3cb**)

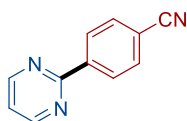


**GP 2** was followed using 2-chloropyrimidine (17.2 mg, 0.15 mmol, 1.0 equiv) and ethyl 4-bromobenzoate (34.4 mg, 0.15 mmol, 1.0 equiv) as starting materials, which furnished the title compound following purification by flash column chromatography (20:80 ethyl acetate:pentane) as a white solid (28.1 mg, 82% yield). The spectroscopic data matched those reported in the literature.<sup>13</sup>

**<sup>1</sup>H NMR** (500 MHz, CDCl<sub>3</sub>) δ 8.83 (d, *J* = 4.8 Hz, 2H), 8.54 – 8.48 (m, 2H), 8.19 – 8.12 (m, 2H), 7.23 (t, *J* = 4.8 Hz, 1H), 4.41 (q, *J* = 7.1 Hz, 2H), 1.42 (t, *J* = 7.1 Hz, 3H).

**<sup>13</sup>C NMR** (126 MHz, CDCl<sub>3</sub>) δ 166.5, 164.0, 157.5, 141.6, 132.4, 129.9, 128.2, 119.8, 61.3, 14.5.

4-(pyrimidin-2-yl)benzotrile (**3ci**)



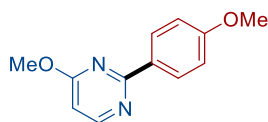
**GP 1-1** was followed using 2-chloropyrimidine (17.2 mg, 0.15 mmol, 1.0 equiv) and 4-bromobenzotrile (27.3 mg, 0.15 mmol, 1.0 equiv) as starting materials, which furnished the title

compound following purification by flash column chromatography (67:33 ethyl acetate:pentane) as a white solid (17.4 mg, 64% yield). The spectroscopic data matched those reported in the literature.<sup>13</sup>

**<sup>1</sup>H NMR** (500 MHz, CDCl<sub>3</sub>) δ 8.85 (d, *J* = 4.9 Hz, 2H), 8.59 – 8.55 (m, 2H), 7.79 – 7.76 (m, 2H), 7.27 (t, *J* = 4.9 Hz, 1H).

**<sup>13</sup>C NMR** (126 MHz, CDCl<sub>3</sub>) δ 163.1, 157.6, 141.7, 132.5, 128.8, 120.2, 118.9, 114.2.

4-methoxy-2-(4-methoxyphenyl)pyrimidine (**3ka**)

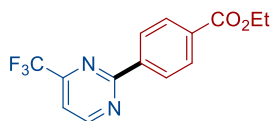


**GP 2** was followed using 2-chloro-4-methoxypyrimidine (21.7 mg, 0.15 mmol, 1.0 equiv) and 1-bromo-4-methoxybenzene (28 mg, 0.15 mmol, 1.0 equiv) as starting materials, which furnished the title compound following purification by flash column chromatography (20:80 ethyl acetate:pentane) as a white solid (24.0 mg, 74% yield). The spectroscopic data matched those reported in the literature.<sup>15</sup>

**<sup>1</sup>H NMR** (500 MHz, CDCl<sub>3</sub>) δ 8.45 (d, *J* = 5.7 Hz, 1H), 8.43 – 8.37 (m, 2H), 7.02 – 6.95 (m, 2H), 6.56 (d, *J* = 5.7 Hz, 1H), 4.07 (s, 3H), 3.87 (s, 3H).

**<sup>13</sup>C NMR** (126 MHz, CDCl<sub>3</sub>) δ 169.5, 164.3, 162.0, 157.4, 130.4, 129.9, 113.9, 105.5, 55.5, 53.5.

ethyl 4-(4-(trifluoromethyl)pyrimidin-2-yl)benzoate (**31b**)



**GP 2** was followed using 2-chloro-4-(trifluoromethyl)pyrimidine (27.4 mg, 0.15 mmol, 1.0 equiv) and ethyl 4-bromobenzoate (34.4 mg, 0.15 mmol, 1.0 equiv) as starting materials, which furnished the title compound following purification by flash column chromatography (10:90 ethyl acetate:pentane) as a white solid (37.3 mg, 84% yield).

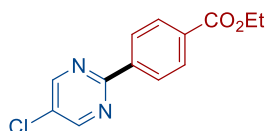
**<sup>1</sup>H NMR** (500 MHz, CDCl<sub>3</sub>) δ 9.07 (d, *J* = 5.0 Hz, 1H), 8.61 – 8.55 (m, 2H), 8.20 – 8.14 (m, 2H), 7.55 (d, *J* = 5.0 Hz, 1H), 4.42 (q, *J* = 7.1 Hz, 2H), 1.43 (t, *J* = 7.1 Hz, 3H).

**<sup>13</sup>C NMR** (126 MHz, CDCl<sub>3</sub>) δ 166.3, 164.7, 159.8, 156.3 (q, *J* = 36.5 Hz), 140.1, 133.3, 130.0, 128.6, 120.6 (q, *J* = 275.3 Hz), 115.2 (q, *J* = 2.6 Hz), 61.4, 14.5.

**<sup>19</sup>F NMR** (377 MHz, CDCl<sub>3</sub>) δ –70.09.

**HRMS (ESI<sup>+</sup>)** Calc: [M+H]<sup>+</sup> (C<sub>14</sub>H<sub>12</sub>F<sub>3</sub>N<sub>2</sub>O<sub>2</sub>) 297.0845; measured: 297.0844 = 0.3 ppm difference.

ethyl 4-(5-chloropyrimidin-2-yl)benzoate (**3mb**)

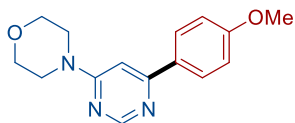


**GP 2** was followed using 2,5-dichloropyrimidine (22.2 mg, 0.15 mmol, 1.0 equiv) and ethyl 4-bromobenzoate (34.4 mg, 0.15 mmol, 1.0 equiv) as starting materials, which furnished the title compound following purification by flash column chromatography (5:95 ethyl acetate:pentane) as a white solid (23.6 mg, 60% yield).

**<sup>1</sup>H NMR** (500 MHz, CDCl<sub>3</sub>) δ 8.77 (s, 2H), 8.51 – 8.44 (m, 2H), 8.18 – 8.12 (m, 2H), 4.41 (q, *J* = 7.1 Hz, 2H), 1.42 (t, *J* = 7.1 Hz, 3H).

**<sup>13</sup>C NMR** (126 MHz, CDCl<sub>3</sub>) δ 166.9, 162.3, 156.4, 141.0, 133.2, 130.6, 130.5, 128.7, 61.8, 15.0.

**HRMS (ESI<sup>+</sup>)** Calc: [M+H]<sup>+</sup> (C<sub>13</sub>H<sub>12</sub>ClN<sub>2</sub>O<sub>2</sub>) 263.0582; measured: 263.0581 = 0.4 ppm difference.

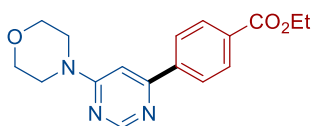
4-(6-(4-methoxyphenyl)pyrimidin-4-yl)morpholine (**3na**)

**GP 2** was followed using 4-(6-chloropyrimidin-4-yl)morpholine (29.9 mg, 0.15 mmol, 1.0 equiv) and 1-bromo-4-methoxybenzene (28 mg, 0.15 mmol, 1.0 equiv) as starting materials, which furnished the title compound following purification by flash column chromatography (75:25 ethyl acetate:pentane) as a white solid (32.6 mg, 80% yield).

**<sup>1</sup>H NMR** (500 MHz, CDCl<sub>3</sub>) δ 8.66 (d, *J* = 1.2 Hz, 1H), 7.97 – 7.90 (m, 2H), 7.00 – 6.93 (m, 2H), 6.79 (d, *J* = 1.2 Hz, 1H), 3.85 (s, 3H), 3.81 – 3.78 (m, 4H), 3.67 (m, 4H).

**<sup>13</sup>C NMR** (126 MHz, CDCl<sub>3</sub>) δ 163.5, 163.2, 161.9, 158.7, 130.8, 128.8, 114.6, 97.8, 67.0, 55.8, 44.7.

**HRMS (ESI<sup>+</sup>)** Calc: [M+H]<sup>+</sup> (C<sub>15</sub>H<sub>18</sub>N<sub>3</sub>O<sub>2</sub>) 272.1394; measured: 272.1392 = 0.7 ppm difference.

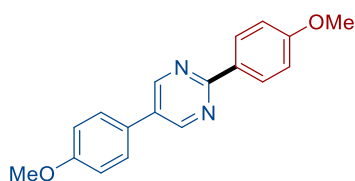
ethyl 4-(6-morpholinopyrimidin-4-yl)benzoate (**3nb**)

**GP 1-1** was followed using 4-(6-chloropyrimidin-4-yl)morpholine (29.9 mg, 0.15 mmol, 1.0 equiv) and ethyl 4-bromobenzoate (34.4 mg, 0.15 mmol, 1.0 equiv) as starting materials, which furnished the title compound following purification by flash column chromatography (90:10 ethyl acetate:pentane) as a white solid (33.8 mg, 80% yield). The spectroscopic data matched those reported in the literature.<sup>16</sup>

**$^1\text{H NMR}$**  (500 MHz,  $\text{CDCl}_3$ )  $\delta$  8.71 (d,  $J = 1.1$  Hz, 1H), 8.15 – 8.09 (m, 2H), 8.05 – 7.99 (m, 2H), 6.89 (d,  $J = 1.2$  Hz, 1H), 4.39 (q,  $J = 7.1$  Hz, 2H), 3.83 – 3.78 (m, 4H), 3.72 – 3.68 (m, 4H), 1.40 (t,  $J = 7.1$  Hz, 3H).

**$^{13}\text{C NMR}$**  (126 MHz,  $\text{CDCl}_3$ )  $\delta$  166.9, 163.2, 162.9, 159.0, 142.6, 132.3, 130.4, 127.4, 99.5, 67.0, 61.7, 44.7, 14.8.

2,5-bis(4-methoxyphenyl)pyrimidine (**3da**)



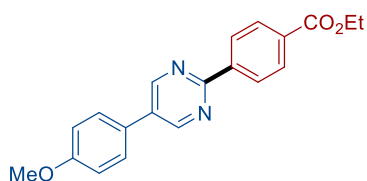
**GP 2** was followed using 2-chloro-5-(4-methoxyphenyl)pyrimidine (33.1 mg, 0.15 mmol, 1.0 equiv) and 1-bromo-4-methoxybenzene (28 mg, 0.15 mmol, 1.0 equiv) as starting materials, which furnished the title compound following purification by flash column chromatography (20:80 ethyl acetate:pentane) as a white solid (32.9 mg, 75% yield).

**$^1\text{H NMR}$**  (500 MHz,  $\text{CDCl}_3$ )  $\delta$  8.93 (s, 2H), 8.46 – 8.39 (m, 2H), 7.59 – 7.52 (m, 2H), 7.08 – 6.98 (m, 4H), 3.89 (s, 3H), 3.87 (s, 3H).

**$^{13}\text{C NMR}$**  (126 MHz,  $\text{CDCl}_3$ )  $\delta$  162.7, 161.8, 160.2, 154.7, 130.6, 130.1, 129.6, 127.8, 127.1, 114.9, 114.0, 55.43, 55.39.

**HRMS (ESI<sup>+</sup>)** Calc:  $[\text{M}+\text{H}]^+$  ( $\text{C}_{18}\text{H}_{17}\text{N}_2\text{O}_2$ ) 293.1285; measured: 293.1283 = 0.7 ppm difference.

ethyl 4-(5-(4-methoxyphenyl)pyrimidin-2-yl)benzoate (**3db**)



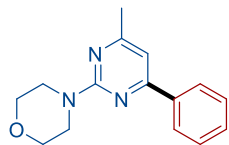
**GP 2** was followed using 2-chloro-5-(4-methoxyphenyl)pyrimidine (33.1 mg, 0.15 mmol, 1.0 equiv) and ethyl 4-bromobenzoate (34.4 mg, 0.15 mmol, 1.0 equiv) as starting materials, which furnished the title compound following purification by flash column chromatography (20:80 ethyl acetate:pentane) as a white solid (31.1 mg, 62% yield).

**<sup>1</sup>H NMR** (500 MHz, CDCl<sub>3</sub>) δ 9.01 (s, 2H), 8.58 – 8.52 (m, 2H), 8.21 – 8.15 (m, 2H), 7.62 – 7.55 (m, 2H), 7.10 – 7.03 (m, 2H), 4.42 (q, *J* = 7.1 Hz, 2H), 3.88 (s, 3H), 1.43 (t, *J* = 7.1 Hz, 3H).

**<sup>13</sup>C NMR** (126 MHz, CDCl<sub>3</sub>) δ 166.4, 161.9, 160.5, 154.8, 141.4, 132.1, 131.9, 129.9, 128.0, 127.9, 126.6, 115.0, 61.1, 55.5, 14.4.

**HRMS (ESI<sup>+</sup>)** Calc: [M+H]<sup>+</sup> (C<sub>20</sub>H<sub>18</sub>N<sub>2</sub>O<sub>3</sub>) 335.1390; measured: 335.1388 = 0.6 ppm difference.

4-(4-methyl-6-phenylpyrimidin-2-yl)morpholine (**3oe**)

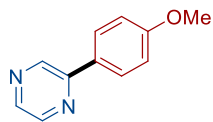


**GP 2** was followed using 4-(4-chloro-6-methylpyrimidin-2-yl)morpholine (32.1 mg, 0.15 mmol, 1.0 equiv) and bromobenzene (23.6 mg, 0.15 mmol, 1.0 equiv) as starting materials, which furnished the title compound following purification by flash column chromatography (20:80 ethyl acetate:pentane) as a white solid (27.6 mg, 72% yield).

**<sup>1</sup>H NMR** (500 MHz, CDCl<sub>3</sub>) δ 8.07 – 7.99 (m, 2H), 7.49 – 7.42 (m, 3H), 6.87 (s, 1H), 3.91 (dd, *J* = 5.6, 4.0 Hz, 4H), 3.80 (dd, *J* = 5.6, 4.1 Hz, 4H), 2.41 (s, 3H).

**<sup>13</sup>C NMR** (126 MHz, CDCl<sub>3</sub>) δ 168.2, 164.1, 162.1, 137.9, 130.2, 128.6, 127.0, 105.7, 67.0, 44.4, 24.5.

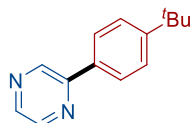
**HRMS (ESI<sup>+</sup>)** Calc: [M+H]<sup>+</sup> (C<sub>15</sub>H<sub>18</sub>N<sub>3</sub>O) 256.1444; measured: 256.1443 = 0.4 ppm difference.

2-(4-methoxyphenyl)pyrazine (**3ea**)

**GP 2** was followed using 2-chloropyrazine (17.2 mg, 0.15 mmol, 1.0 equiv) and 1-bromo-4-methoxybenzene (28 mg, 0.15 mmol, 1.0 equiv) as starting materials, which furnished the title compound following purification by flash column chromatography (20:80 ethyl acetate:pentane) as a white solid (20.1 mg, 72% yield). The spectroscopic data matched those reported in the literature.<sup>13</sup>

**<sup>1</sup>H NMR** (500 MHz, CDCl<sub>3</sub>) δ 8.97 (d, *J* = 1.5 Hz, 1H), 8.57 (dd, *J* = 2.5, 1.6 Hz, 1H), 8.43 (d, *J* = 2.5 Hz, 1H), 8.01 – 7.95 (m, 2H), 7.06 – 6.99 (m, 2H), 3.87 (s, 3H).

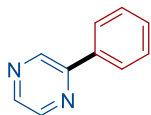
**<sup>13</sup>C NMR** (126 MHz, CDCl<sub>3</sub>) δ 161.3, 152.7, 144.1, 142.2, 141.8, 129.0, 128.4, 114.6, 55.5.

2-(4-(*tert*-butyl)phenyl)pyrazine (**3ed**)

**GP 2** was followed using 2-chloropyrazine (17.2 mg, 0.15 mmol, 1.0 equiv) and 1-bromo-4-(*tert*-butyl)benzene (32 mg, 0.15 mmol, 1.0 equiv) as starting materials, which furnished the title compound following purification by flash column chromatography (10:90 ethyl acetate:pentane) as a white solid (24.8 mg, 78% yield). The spectroscopic data matched those reported in the literature.<sup>17</sup>

**<sup>1</sup>H NMR** (500 MHz, CDCl<sub>3</sub>) δ 9.02 (d, *J* = 1.6 Hz, 1H), 8.61 (dd, *J* = 2.5, 1.6 Hz, 1H), 8.47 (d, *J* = 2.5 Hz, 1H), 7.99 – 7.93 (m, 2H), 7.57 – 7.51 (m, 2H), 1.37 (s, 9H).

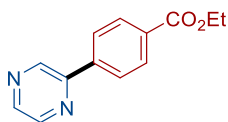
**<sup>13</sup>C NMR** (126 MHz, CDCl<sub>3</sub>) δ 153.4, 153.0, 144.3, 142.7, 142.2, 133.7, 126.8, 126.2, 34.9, 31.4.

2-phenylpyrazine (**3ee**)

**GP 2** was followed using 2-chloropyrazine (17.2 mg, 0.15 mmol, 1.0 equiv) and bromobenzene (23.6 mg, 0.15 mmol, 1.0 equiv) as starting materials, which furnished the title compound following purification by flash column chromatography (10:90 ethyl acetate:pentane) as a white solid (18.0 mg, 77% yield). The spectroscopic data matched those reported in the literature.<sup>18</sup>

**<sup>1</sup>H NMR** (500 MHz, CDCl<sub>3</sub>) δ 9.04 (d, *J* = 1.5 Hz, 1H), 8.64 (dd, *J* = 2.5, 1.5 Hz, 1H), 8.51 (d, *J* = 2.5 Hz, 1H), 8.05 – 7.99 (m, 2H), 7.56 – 7.45 (m, 3H).

**<sup>13</sup>C NMR** (126 MHz, CDCl<sub>3</sub>) δ 153.0, 144.3, 143.1, 142.4, 136.5, 130.1, 129.2, 127.1.

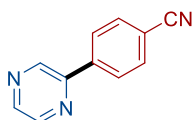
ethyl 4-(pyrazin-2-yl)benzoate (**3eb**)

**GP 1-1** was followed using 2-chloropyrazine (17.2 mg, 0.15 mmol, 1.0 equiv) and ethyl 4-bromobenzoate (34.4 mg, 0.15 mmol, 1.0 equiv) as starting materials, which furnished the title compound following purification by flash column chromatography (20:80 ethyl acetate:pentane) as a white solid (27.0 mg, 79% yield). The spectroscopic data matched those reported in the literature.<sup>13</sup>

**<sup>1</sup>H NMR** (500 MHz, CDCl<sub>3</sub>) δ 9.08 (d, *J* = 1.5 Hz, 1H), 8.67 (dd, *J* = 2.5, 1.5 Hz, 1H), 8.56 (d, *J* = 2.5 Hz, 1H), 8.21 – 8.15 (m, 2H), 8.13 – 8.06 (m, 2H), 4.42 (q, *J* = 7.1 Hz, 2H), 1.42 (t, *J* = 7.1 Hz, 3H).

$^{13}\text{C NMR}$  (126 MHz,  $\text{CDCl}_3$ )  $\delta$  166.3, 151.8, 144.5, 143.8, 142.6, 140.5, 131.8, 130.4, 127.0, 61.4, 14.5.

4-(pyrazin-2-yl)benzotrile (**3ei**)

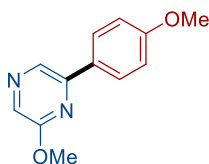


**GP 1-1** was followed using 2-chloropyrazine (17.2 mg, 0.15 mmol, 1.0 equiv) and 4-bromobenzotrile (27.3 mg, 0.15 mmol, 1.0 equiv) as starting materials, which furnished the title compound following purification by flash column chromatography (50:50 ethyl acetate:pentane) as a white solid (17.9 mg, 66% yield). The spectroscopic data matched those reported in the literature.<sup>13</sup>

$^1\text{H NMR}$  (500 MHz,  $\text{CDCl}_3$ )  $\delta$  9.07 (d,  $J$  = 1.6 Hz, 1H), 8.69 (dd,  $J$  = 2.5, 1.5 Hz, 1H), 8.60 (d,  $J$  = 2.4 Hz, 1H), 8.19 – 8.12 (m, 2H), 7.84 – 7.77 (m, 2H).

$^{13}\text{C NMR}$  (126 MHz,  $\text{CDCl}_3$ )  $\delta$  150.8, 144.6, 144.4, 142.5, 140.6, 132.9, 127.6, 118.6, 113.7.

2-methoxy-6-(4-methoxyphenyl)pyrazine (**3pa**)



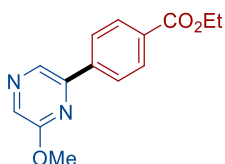
**GP 2** was followed using 2-chloro-6-methoxypyrazine (21.7 mg, 0.15 mmol, 1.0 equiv) and 1-bromo-4-methoxybenzene (28 mg, 0.15 mmol, 1.0 equiv) as starting materials, which furnished the title compound following purification by flash column chromatography (15:85 ethyl acetate:pentane) as a white solid (26.9 mg, 83% yield).

**<sup>1</sup>H NMR** (500 MHz, CDCl<sub>3</sub>) δ 8.54 (s, 1H), 8.09 (s, 1H), 8.03 – 7.96 (m, 2H), 7.04 – 6.97 (m, 2H), 4.05 (s, 3H), 3.87 (s, 3H).

**<sup>13</sup>C NMR** (126 MHz, CDCl<sub>3</sub>) δ 161.1, 159.9, 148.8, 132.8, 132.5, 128.9, 128.3, 114.4, 55.5, 53.4.

**HRMS (ESI<sup>+</sup>)** Calc: [M+H]<sup>+</sup> (C<sub>12</sub>H<sub>13</sub>N<sub>2</sub>O<sub>2</sub>) 217.0972; measured: 217.0972 < 0.1 ppm difference.

ethyl 4-(6-methoxypyrazin-2-yl)benzoate (**3pb**)



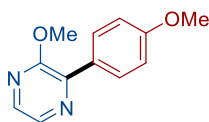
**GP 1-1** was followed using 2-chloro-6-methoxypyrazine (21.7 mg, 0.15 mmol, 1.0 equiv) and ethyl 4-bromobenzoate (34.4 mg, 0.15 mmol, 1.0 equiv) as starting materials, which furnished the title compound following purification by flash column chromatography (20:80 ethyl acetate:pentane) as a white solid (18.6 mg, 48% yield).

**<sup>1</sup>H NMR** (500 MHz, CDCl<sub>3</sub>) δ 8.64 (s, 1H), 8.21 (s, 1H), 8.17 – 8.13 (m, 2H), 8.12 – 8.08 (m, 2H), 4.41 (q, *J* = 7.1 Hz, 2H), 4.08 (s, 3H), 1.42 (t, *J* = 7.1 Hz, 3H).

**<sup>13</sup>C NMR** (126 MHz, CDCl<sub>3</sub>) δ 166.3, 160.0, 147.8, 140.4, 134.8, 133.6, 131.5, 130.2, 126.8, 61.3, 53.6, 14.5.

**HRMS (ESI<sup>+</sup>)** Calc: [M+H]<sup>+</sup> (C<sub>14</sub>H<sub>15</sub>N<sub>2</sub>O<sub>3</sub>) 259.1077; measured: 259.1076 = 0.4 ppm difference.

2-methoxy-3-(4-methoxyphenyl)pyrazine (**3qa**)



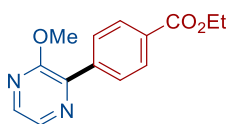
**GP 2** was followed using 2-chloro-3-methoxypyrazine (21.7 mg, 0.15 mmol, 1.0 equiv) and 1-bromo-4-methoxybenzene (28 mg, 0.15 mmol, 1.0 equiv) as starting materials, which furnished

the title compound following purification by flash column chromatography (15:85 ethyl acetate:pentane) as a white solid (25.6 mg, 79% yield). The spectroscopic data matched those reported in the literature.<sup>19</sup>

**<sup>1</sup>H NMR** (500 MHz, CDCl<sub>3</sub>) δ 8.20 (d, *J* = 2.6 Hz, 1H), 8.10 – 8.03 (m, 2H), 8.00 (d, *J* = 2.7 Hz, 1H), 7.02 – 6.96 (m, 2H), 4.04 (s, 3H), 3.86 (s, 3H).

**<sup>13</sup>C NMR** (126 MHz, CDCl<sub>3</sub>) δ 160.6, 157.9, 143.3, 138.4, 136.3, 130.8, 128.5, 113.7, 55.4, 53.8.

ethyl 4-(6-methoxypyrazin-2-yl)benzoate (**3qb**)



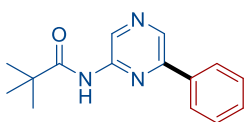
**GP 1-1** was followed using 2-chloro-3-methoxypyrazine (21.7 mg, 0.15 mmol, 1.0 equiv) and ethyl 4-bromobenzoate (34.4 mg, 0.15 mmol, 1.0 equiv) as starting materials, which furnished the title compound following purification by flash column chromatography (20:80 ethyl acetate:pentane) as a white solid (29.0 mg, 75% yield).

**<sup>1</sup>H NMR** (500 MHz, CDCl<sub>3</sub>) δ 8.26 (d, *J* = 2.6 Hz, 1H), 8.16 – 8.11 (m, 4H), 8.10 (d, *J* = 2.6 Hz, 1H), 4.40 (q, *J* = 7.1 Hz, 2H), 4.05 (s, 3H), 1.41 (t, *J* = 7.1 Hz, 3H).

**<sup>13</sup>C NMR** (126 MHz, CDCl<sub>3</sub>) δ 166.5, 158.4, 142.2, 140.2, 140.0, 136.6, 130.9, 129.4, 129.2, 61.2, 53.9, 14.5.

**HRMS (ESI<sup>+</sup>)** Calc: [M+H]<sup>+</sup> (C<sub>14</sub>H<sub>15</sub>N<sub>2</sub>O<sub>3</sub>) 259.1077; measured: 259.1075 = 0.8 ppm difference.

*N*-(6-phenylpyrazin-2-yl)pivalamide (**3re**)



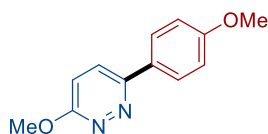
**GP 2** with additional LiCl (12.7 mg, 0.30 mmol, 2.0 equiv) was followed using *N*-(6-chloropyrazin-2-yl)pivalamide (32.0 mg, 0.15 mmol, 1.0 equiv) and bromobenzene (23.6 mg, 0.15 mmol, 1.0 equiv) as starting materials, which furnished the title compound following purification by flash column chromatography (50:50 ethyl acetate:pentane, containing 0.5% v/v triethylamine) as a white solid (24.5 mg, 66% yield).

**<sup>1</sup>H NMR** (500 MHz, CDCl<sub>3</sub>) δ 9.51 (s, 1H), 8.78 (s, 1H), 8.01 (s, 1H), 7.99 – 7.95 (m, 2H), 7.54 – 7.43 (m, 3H), 1.38 (s, 9H).

**<sup>13</sup>C NMR** (126 MHz, CDCl<sub>3</sub>) δ 177.1, 150.4, 147.6, 137.3, 136.0, 134.9, 130.1, 129.2, 127.0, 40.0, 27.6.

**HRMS (ESI<sup>+</sup>)** Calc: [M+H]<sup>+</sup> (C<sub>15</sub>H<sub>18</sub>N<sub>3</sub>O) 256.1444; measured: 256.1443 = 0.4 ppm difference.

3-methoxy-6-(4-methoxyphenyl)pyridazine (**3fa**)

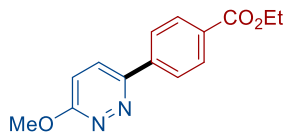


**GP 2** was followed using 3-chloro-6-methoxypyridazine (21.7 mg, 0.15 mmol, 1.0 equiv) and 1-bromo-4-methoxybenzene (28 mg, 0.15 mmol, 1.0 equiv) as starting materials, which furnished the title compound following purification by flash column chromatography (20:80 ethyl acetate:pentane) as a white solid (17.2 mg, 53% yield). The spectroscopic data matched those reported in the literature.<sup>20</sup>

**<sup>1</sup>H NMR** (500 MHz, CDCl<sub>3</sub>) δ 7.99 – 7.93 (m, 2H), 7.72 (d, *J* = 9.2 Hz, 1H), 7.04 – 6.98 (m, 3H), 4.17 (s, 3H), 3.86 (s, 3H).

**<sup>13</sup>C NMR** (126 MHz, CDCl<sub>3</sub>) δ 164.1, 160.9, 155.0, 128.9, 127.9, 126.7, 117.8, 114.5, 55.5, 54.9.

ethyl 4-(6-methoxypyridazin-3-yl)benzoate (**3fb**)

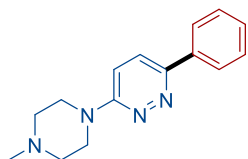


**GP 1-1** was followed using 2-chloro-3-methoxypyrazine (21.7 mg, 0.15 mmol, 1.0 equiv) and ethyl 4-bromobenzoate (34.4 mg, 0.15 mmol, 1.0 equiv) as starting materials, which furnished the title compound following purification by flash column chromatography (20:80 ethyl acetate:pentane) as a white solid (24.0 mg, 62% yield). The spectroscopic data matched those reported in the literature.<sup>20</sup>

**<sup>1</sup>H NMR** (500 MHz, CDCl<sub>3</sub>) δ 8.36 (d, *J* = 8.5 Hz, 2H), 8.28 (d, *J* = 8.4 Hz, 2H), 8.02 (d, *J* = 9.2 Hz, 1H), 7.27 (d, *J* = 9.2 Hz, 1H), 4.61 (q, *J* = 7.1 Hz, 2H), 4.40 (s, 3H), 1.62 (t, *J* = 7.1 Hz, 3H).

**<sup>13</sup>C NMR** (126 MHz, CDCl<sub>3</sub>) δ 166.4, 164.7, 154.4, 140.4, 131.3, 130.3, 127.3, 126.5, 117.8, 61.3, 55.1, 14.5.

3-(4-methylpiperazin-1-yl)-6-phenylpyridazine (**3se**)



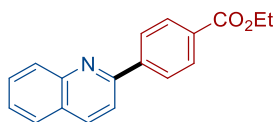
**GP 2** was followed using 3-chloro-6-(4-methylpiperazin-1-yl)pyridazine (31.9 mg, 0.15 mmol, 1.0 equiv) and bromobenzene (23.6 mg, 0.15 mmol, 1.0 equiv) as starting materials, which furnished the title compound following purification by flash column chromatography (10:90 methanol:ethyl acetate) as a white solid (17.2 mg, 45% yield). This is the corrected yield that excluded the inseparable heteroaryl dimer byproduct (2% with respect to the product based on <sup>1</sup>H NMR).

**<sup>1</sup>H NMR** (500 MHz, CDCl<sub>3</sub>) δ 8.03 – 7.96 (m, 2H), 7.65 (d, *J* = 9.6 Hz, 1H), 7.50 – 7.43 (m, 2H), 7.43 – 7.37 (m, 1H), 6.98 (d, *J* = 9.5 Hz, 1H), 3.78 – 3.73 (m, 4H), 2.62 – 2.55 (m, 4H), 2.38 (s, 3H).

**<sup>13</sup>C NMR** (126 MHz, CDCl<sub>3</sub>) δ 159.1, 151.3, 136.9, 129.0, 128.8, 126.1, 125.3, 113.0, 54.8, 46.3, 45.1.

**HRMS (ESI<sup>+</sup>)** Calc: [M+H]<sup>+</sup> (C<sub>15</sub>H<sub>19</sub>N<sub>4</sub>) 255.1604; measured: 255.1601 = 1.2 ppm difference.

ethyl 4-(quinolin-2-yl)benzoate (**3tb**)

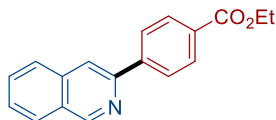


**GP 1** was followed using 2-chloroquinoline (24.5 mg, 0.15 mmol, 1.0 equiv) and ethyl 4-bromobenzoate (34.4 mg, 0.15 mmol, 1.0 equiv) as starting materials, which furnished the title compound following purification by flash column chromatography (10:90 ethyl acetate:pentane) as a white solid (20.8 mg, 50% yield). The spectroscopic data matched those reported in the literature.<sup>21</sup>

**<sup>1</sup>H NMR** (500 MHz, CDCl<sub>3</sub>) δ 8.25 (d, *J* = 8.5 Hz, 3H), 8.20 (s, 0H), 7.91 (d, *J* = 8.6 Hz, 1H), 7.87 – 7.81 (m, 1H), 7.75 (ddd, *J* = 8.4, 6.8, 1.5 Hz, 1H), 7.56 (ddd, *J* = 8.1, 6.9, 1.2 Hz, 1H), 4.43 (q, *J* = 7.1 Hz, 2H), 1.44 (t, *J* = 7.1 Hz, 3H).

**<sup>13</sup>C NMR** (126 MHz, CDCl<sub>3</sub>) δ 166.6, 156.2, 148.4, 143.8, 137.1, 131.2, 130.2, 130.04, 130.03, 127.64, 127.58, 127.56, 126.9, 119.1, 61.2, 14.5.

ethyl 4-(isoquinolin-3-yl)benzoate (**3ub**)



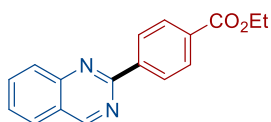
**GP 1** was followed using 3-chloroisoquinoline (24.5 mg, 0.15 mmol, 1.0 equiv) and ethyl 4-bromobenzoate (34.4 mg, 0.15 mmol, 1.0 equiv) as starting materials, which furnished the title compound following purification by flash column chromatography (5:95 ethyl acetate:pentane) as a white solid (27.0 mg, 65% yield).

**<sup>1</sup>H NMR** (500 MHz, CDCl<sub>3</sub>) δ 9.35 (d, *J* = 1.0 Hz, 1H), 8.23 – 8.19 (m, 2H), 8.19 – 8.15 (m, 2H), 8.13 (s, 1H), 8.00 (dt, *J* = 8.1, 1.0 Hz, 1H), 7.89 (dd, *J* = 8.3, 1.1 Hz, 1H), 7.72 (ddd, *J* = 8.2, 6.9, 1.2 Hz, 1H), 7.62 (ddd, *J* = 8.1, 6.9, 1.1 Hz, 1H), 4.42 (q, *J* = 7.1 Hz, 2H), 1.43 (t, *J* = 7.1 Hz, 3H).

**<sup>13</sup>C NMR** (126 MHz, CDCl<sub>3</sub>) δ 166.7, 152.7, 150.2, 143.8, 136.6, 130.9, 130.4, 130.2, 128.2, 127.74, 127.72, 127.2, 126.9, 117.5, 61.2, 14.5.

**HRMS (ESI<sup>+</sup>)** Calc: [M+H]<sup>+</sup> (C<sub>18</sub>H<sub>16</sub>NO<sub>2</sub>) 278.1176; measured: 278.1173 = 1.1 ppm difference.

ethyl 4-(quinazolin-2-yl)benzoate (**3vb**)



**GP 2** was followed using 2-chloroquinazoline (24.7 mg, 0.15 mmol, 1.0 equiv) and ethyl 4-bromobenzoate (34.4 mg, 0.15 mmol, 1.0 equiv) as starting materials, which furnished the title compound following purification by flash column chromatography (10:90 ethyl acetate:pentane) as a white solid (16.3 mg, 39% yield).

**<sup>1</sup>H NMR** (500 MHz, CDCl<sub>3</sub>) δ 9.49 (d, *J* = 0.9 Hz, 1H), 8.73 – 8.66 (m, 2H), 8.23 – 8.17 (m, 2H), 8.12 (dq, *J* = 8.4, 0.9 Hz, 1H), 7.98 – 7.90 (m, 2H), 7.65 (ddd, *J* = 8.1, 6.9, 1.1 Hz, 1H), 4.43 (q, *J* = 7.1 Hz, 2H), 1.44 (t, *J* = 7.1 Hz, 3H).

$^{13}\text{C}$  NMR (126 MHz,  $\text{CDCl}_3$ )  $\delta$  166.6, 160.7, 160.2, 150.9, 142.2, 134.5, 132.2, 130.0, 129.0, 128.6, 127.9, 127.3, 123.9, 61.3, 14.5.

HRMS (ESI<sup>+</sup>) Calc:  $[\text{M}+\text{H}]^+$  ( $\text{C}_{17}\text{H}_{15}\text{N}_2\text{O}_2$ ) 279.1128; measured: 279.1127 = 0.4 ppm difference.

ethyl 4-(quinoxalin-2-yl)benzoate (**3wb**)

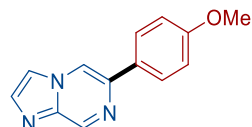


**GP 2** was followed using 2-chloroquinoxaline (24.7 mg, 0.15 mmol, 1.0 equiv) and ethyl 4-bromobenzoate (34.4 mg, 0.15 mmol, 1.0 equiv) as starting materials, which furnished the title compound following purification by flash column chromatography (15:85 ethyl acetate:pentane) as a white solid (32.1 mg, 77% yield). The spectroscopic data matched those reported in the literature.<sup>22</sup>

$^1\text{H}$  NMR (500 MHz,  $\text{CDCl}_3$ )  $\delta$  9.36 (s, 1H), 8.31 – 8.26 (m, 2H), 8.26 – 8.20 (m, 2H), 8.20 – 8.16 (m, 1H), 8.16 – 8.11 (m, 1H), 7.83 – 7.75 (m, 2H), 4.43 (q,  $J = 7.1$  Hz, 2H), 1.44 (t,  $J = 7.1$  Hz, 3H).

$^{13}\text{C}$  NMR (126 MHz,  $\text{CDCl}_3$ )  $\delta$  166.3, 150.8, 143.3, 142.4, 142.0, 140.9, 132.0, 130.7, 130.4, 130.2, 129.9, 129.4, 127.6, 61.4, 14.5.

6-(4-methoxyphenyl)imidazo[1,2-*a*]pyrazine (**3xa**)



**GP 2** with additional LiCl (12.7 mg, 0.30 mmol, 2.0 equiv) was followed using 6-chloroimidazo[1,2-*a*]pyrazine (23.0 mg, 0.15 mmol, 1.0 equiv) and 1-bromo-4-methoxybenzene

(28 mg, 0.15 mmol, 1.0 equiv) as starting materials, which furnished the title compound following purification by flash column chromatography (100% ethyl acetate) as a pale brown solid (20.9 mg, 62% yield).

**<sup>1</sup>H NMR** (500 MHz, CDCl<sub>3</sub>) δ 9.15 (d, *J* = 1.5 Hz, 1H), 8.36 (d, *J* = 1.5 Hz, 1H), 7.88 – 7.82 (m, 2H), 7.80 (d, *J* = 1.1 Hz, 1H), 7.71 (d, *J* = 0.9 Hz, 1H), 7.05 – 6.97 (m, 2H), 3.86 (s, 3H).

**<sup>13</sup>C NMR** (126 MHz, CDCl<sub>3</sub>) δ 160.4, 143.2, 140.2, 139.8, 136.1, 129.0, 127.7, 114.5, 114.1, 113.9, 55.5.

**HRMS (ESI<sup>+</sup>)** Calc: [M+H]<sup>+</sup> (C<sub>13</sub>H<sub>12</sub>N<sub>3</sub>O) 226.0975; measured: 226.0974 = 0.4 ppm difference.

2-(quinolin-6-yl)quinoxaline (**3wj**)



**GP 2** was followed using 2-chloroquinoxaline (24.7 mg, 0.15 mmol, 1.0 equiv) and 6-bromoquinoline (31.2 mg, 0.15 mmol, 1.0 equiv) as starting materials, which furnished the title compound following purification by flash column chromatography (100% ethyl acetate) as a white solid (25.8 mg, 67% yield).

**<sup>1</sup>H NMR** (500 MHz, CDCl<sub>3</sub>) δ 9.48 (s, 1H), 8.99 (dd, *J* = 4.2, 1.7 Hz, 1H), 8.65 (d, *J* = 2.0 Hz, 1H), 8.61 (dd, *J* = 8.8, 2.1 Hz, 1H), 8.32 (dd, *J* = 8.2, 1.5 Hz, 1H), 8.29 (d, *J* = 8.8 Hz, 1H), 8.23 – 8.18 (m, 1H), 8.17 – 8.13 (m, 1H), 7.80 (dddd, *J* = 20.2, 8.4, 6.9, 1.6 Hz, 2H), 7.49 (dd, *J* = 8.3, 4.2 Hz, 1H).

**<sup>13</sup>C NMR** (126 MHz, CDCl<sub>3</sub>) δ 151.7, 151.0, 149.2, 143.4, 142.5, 141.9, 137.0, 135.0, 130.74, 130.67, 130.0, 129.8, 129.4, 128.46, 128.35, 127.4, 122.0.

**HRMS (ESI<sup>+</sup>)** Calc: [M+H]<sup>+</sup> (C<sub>17</sub>H<sub>12</sub>N<sub>3</sub>) 258.1026; measured: 258.1025 = 0.4 ppm difference.

methyl 2-methoxy-6-(1-methyl-1*H*-indol-3-yl)isonicotinate (**3yk**)



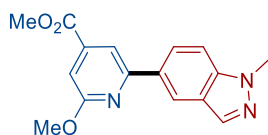
**GP 1** was followed using methyl 2-chloro-6-methoxyisonicotinate (30.2 mg, 0.15 mmol, 1.0 equiv) and 3-bromo-1-methyl-1*H*-indole (31.5 mg, 0.15 mmol, 1.0 equiv) as starting materials, which furnished the title compound following purification by flash column chromatography (25:75 ethyl acetate:pentane) as a pale brown solid (26.2 mg, 59% yield).

**<sup>1</sup>H NMR** (500 MHz, CDCl<sub>3</sub>) δ 8.48 – 8.42 (m, 1H), 7.75 (d, *J* = 1.1 Hz, 1H), 7.69 (s, 1H), 7.35 – 7.30 (m, 1H), 7.29 – 7.24 (m, 1H), 7.24 – 7.19 (m, 1H), 7.04 (d, *J* = 1.2 Hz, 1H), 4.08 (s, 3H), 3.92 (s, 3H), 3.82 (s, 3H).

**<sup>13</sup>C NMR** (126 MHz, CDCl<sub>3</sub>) δ 166.3, 164.6, 154.0, 140.5, 138.0, 129.6, 126.2, 122.5, 122.0, 120.9, 115.4, 111.5, 109.7, 106.4, 54.1, 52.7, 33.3.

**HRMS (ESI<sup>+</sup>)** Calc: [M+H]<sup>+</sup> (C<sub>17</sub>H<sub>17</sub>N<sub>2</sub>O<sub>3</sub>) 297.1234; measured: 297.1232 = 0.7 ppm difference.

methyl 2-methoxy-6-(1-methyl-1*H*-indazol-5-yl)isonicotinate (**3yl**)



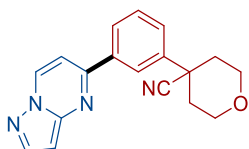
**GP 1** was followed using methyl 2-chloro-6-methoxyisonicotinate (30.2 mg, 0.15 mmol, 1.0 equiv) and 5-bromo-1-methyl-1*H*-indazole (31.7 mg, 0.15 mmol, 1.0 equiv) as starting materials, which furnished the title compound following purification by flash column chromatography (50:50 ethyl acetate:pentane) as a white solid (18.3 mg, 41% yield).

**<sup>1</sup>H NMR** (500 MHz, CDCl<sub>3</sub>) δ 8.49 (dd, *J* = 1.7, 0.8 Hz, 1H), 8.17 (dd, *J* = 8.8, 1.6 Hz, 1H), 8.07 (d, *J* = 1.0 Hz, 1H), 7.94 (d, *J* = 1.2 Hz, 1H), 7.47 (dt, *J* = 8.8, 0.9 Hz, 1H), 7.23 (d, *J* = 1.1 Hz, 1H), 4.12 (s, 3H), 4.11 (s, 3H), 3.98 (s, 3H).

**<sup>13</sup>C NMR** (126 MHz, CDCl<sub>3</sub>) δ 166.0, 164.6, 156.1, 141.1, 140.5, 134.0, 131.4, 125.7, 124.7, 120.0, 111.9, 109.2, 108.9, 53.9, 52.8, 35.8.

**HRMS (ESI<sup>+</sup>)** Calc: [M+H]<sup>+</sup> (C<sub>16</sub>H<sub>16</sub>N<sub>3</sub>O<sub>3</sub>) 298.1186; measured: 298.1185 = 0.3 ppm difference.

4-(3-(pyrazolo[1,5-*a*]pyrimidin-5-yl)phenyl)tetrahydro-2*H*-pyran-4-carbonitrile (**3zm**)



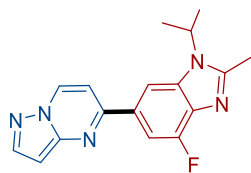
**GP 2** was followed using methyl 5-chloropyrazolo[1,5-*a*]pyrimidine (23.0 mg, 0.15 mmol, 1.0 equiv) and 4-(3-bromophenyl)tetrahydro-2*H*-pyran-4-carbonitrile (39.9 mg, 0.15 mmol, 1.0 equiv) as starting materials, which furnished the title compound following purification by flash column chromatography (100% ethyl acetate) as a white solid (32.0 mg, 70% yield).

**<sup>1</sup>H NMR** (500 MHz, CDCl<sub>3</sub>) δ 8.74 (dd, *J* = 7.3, 0.9 Hz, 1H), 8.29 (t, *J* = 1.9 Hz, 1H), 8.15 (d, *J* = 2.4 Hz, 1H), 8.02 (dt, *J* = 7.9, 1.3 Hz, 1H), 7.64 (ddd, *J* = 7.9, 2.1, 1.1 Hz, 1H), 7.58 (t, *J* = 7.8 Hz, 1H), 7.28 (d, *J* = 7.4 Hz, 1H), 6.75 (dd, *J* = 2.3, 0.9 Hz, 1H), 4.17 – 4.09 (m, 2H), 3.99 – 3.90 (m, 2H), 2.30 – 2.20 (m, 2H), 2.14 (m, 2H).

**<sup>13</sup>C NMR** (126 MHz, CDCl<sub>3</sub>) δ 155.3, 148.6, 145.9, 141.0, 138.3, 135.4, 129.9, 127.7, 127.3, 124.6, 121.7, 105.4, 97.4, 65.2, 42.2, 36.8.

**HRMS (ESI<sup>+</sup>)** Calc: [M+H]<sup>+</sup> (C<sub>18</sub>H<sub>17</sub>N<sub>4</sub>O) 305.1397; measured: 305.1394 = 1.0 ppm difference.

5-(4-fluoro-1-isopropyl-2-methyl-1*H*-benzo[*d*]imidazol-6-yl)pyrazolo[1,5-*a*]pyrimidine (**3zn**)



**GP 2** was followed using methyl 5-chloropyrazolo[1,5-*a*]pyrimidine (23.0 mg, 0.15 mmol, 1.0 equiv) and 6-bromo-4-fluoro-1-isopropyl-2-methyl-1*H*-benzo[*d*]imidazole (40.7 mg, 0.15 mmol, 1.0 equiv) as starting materials, which furnished the title compound following purification by flash column chromatography (100% ethyl acetate) as a white solid (20.9 mg, 45% yield).

**<sup>1</sup>H NMR** (400 MHz, CDCl<sub>3</sub>) δ 8.69 (dd, *J* = 7.4, 0.9 Hz, 1H), 8.10 (dd, *J* = 15.0, 1.9 Hz, 2H), 7.59 (dd, *J* = 11.4, 1.4 Hz, 1H), 7.25 (d, *J* = 7.5 Hz, 1H), 6.70 (dd, *J* = 2.3, 0.9 Hz, 1H), 4.74 (hept, *J* = 7.0 Hz, 1H), 2.67 (s, 3H), 1.70 (d, *J* = 7.0 Hz, 6H).

**<sup>13</sup>C NMR** (126 MHz, CDCl<sub>3</sub>) δ 155.9 (d, *J* = 2.6 Hz), 153.7 (d, *J* = 252.1 Hz), 153.5, 148.6, 145.8, 137.3 (d, *J* = 9.3 Hz), 135.2, 133.7 (d, *J* = 17.0 Hz), 131.9 (d, *J* = 6.8 Hz), 106.8 (d, *J* = 19.5 Hz), 106.4 (d, *J* = 3.5 Hz), 105.6, 97.0, 48.7, 21.7, 15.4.

**<sup>19</sup>F NMR** (377 MHz, CDCl<sub>3</sub>) δ -128.27.

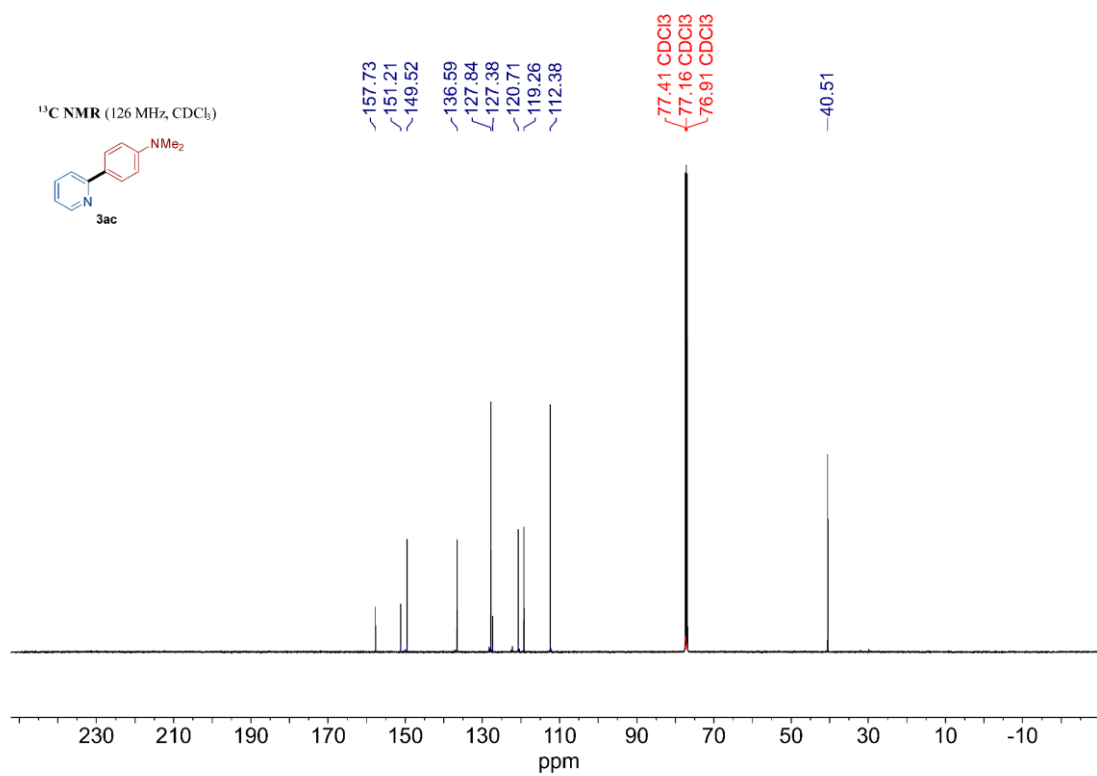
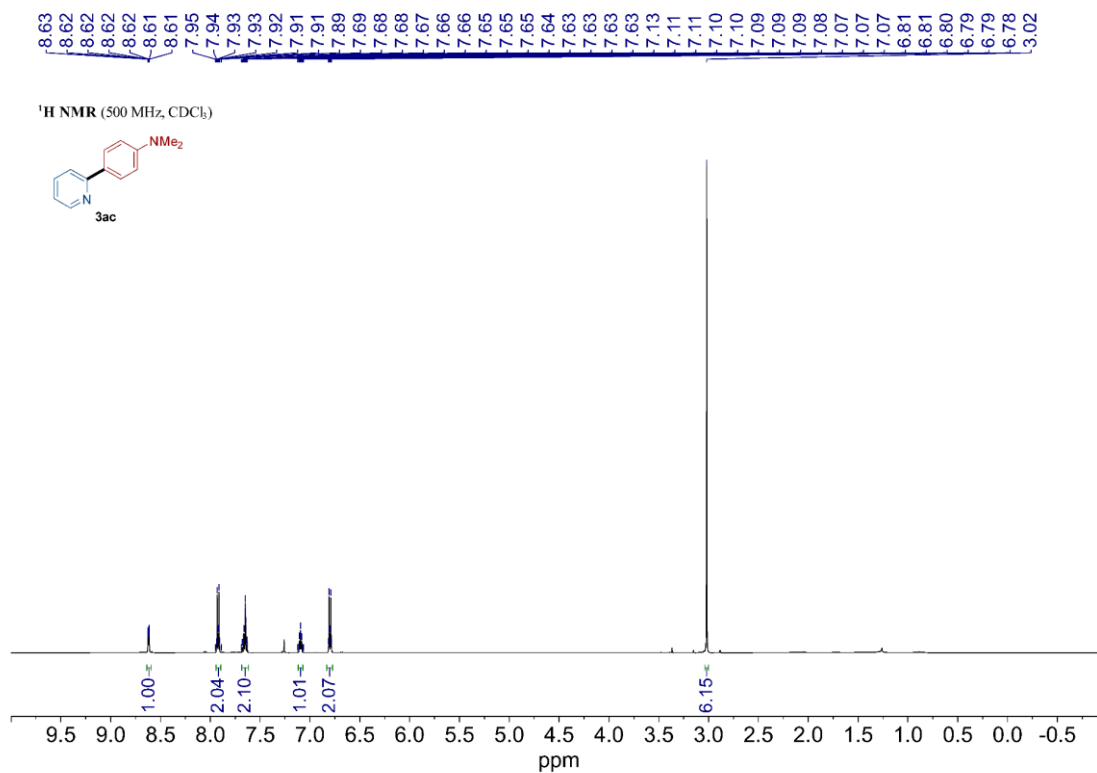
**HRMS (ESI<sup>+</sup>)** Calc: [M+H]<sup>+</sup> (C<sub>17</sub>H<sub>17</sub>N<sub>5</sub>F) 310.1463; measured: 310.1460 = 1.0 ppm difference.

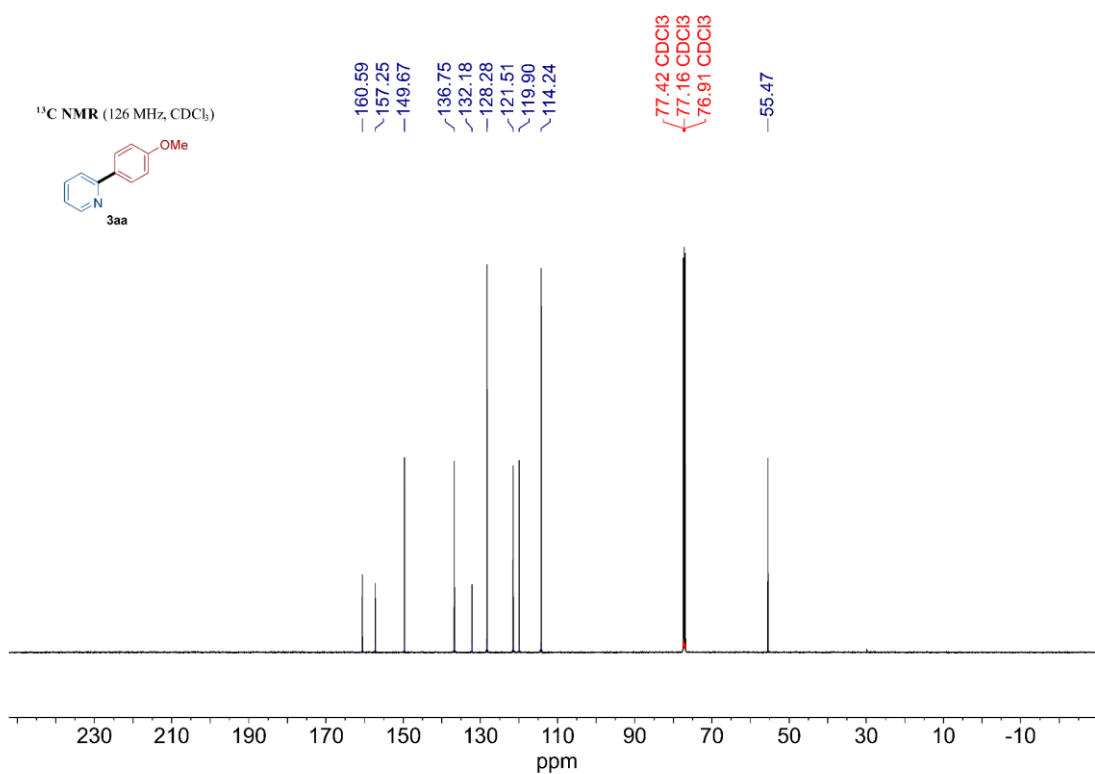
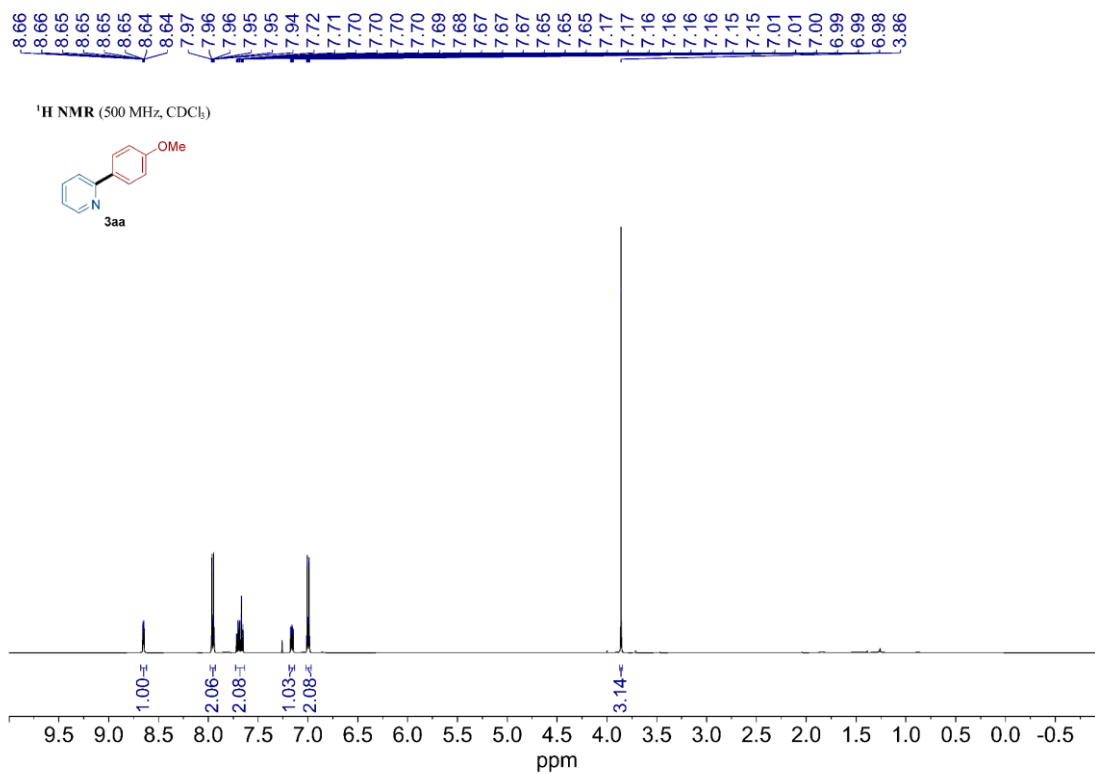
#### 4C.VI. References

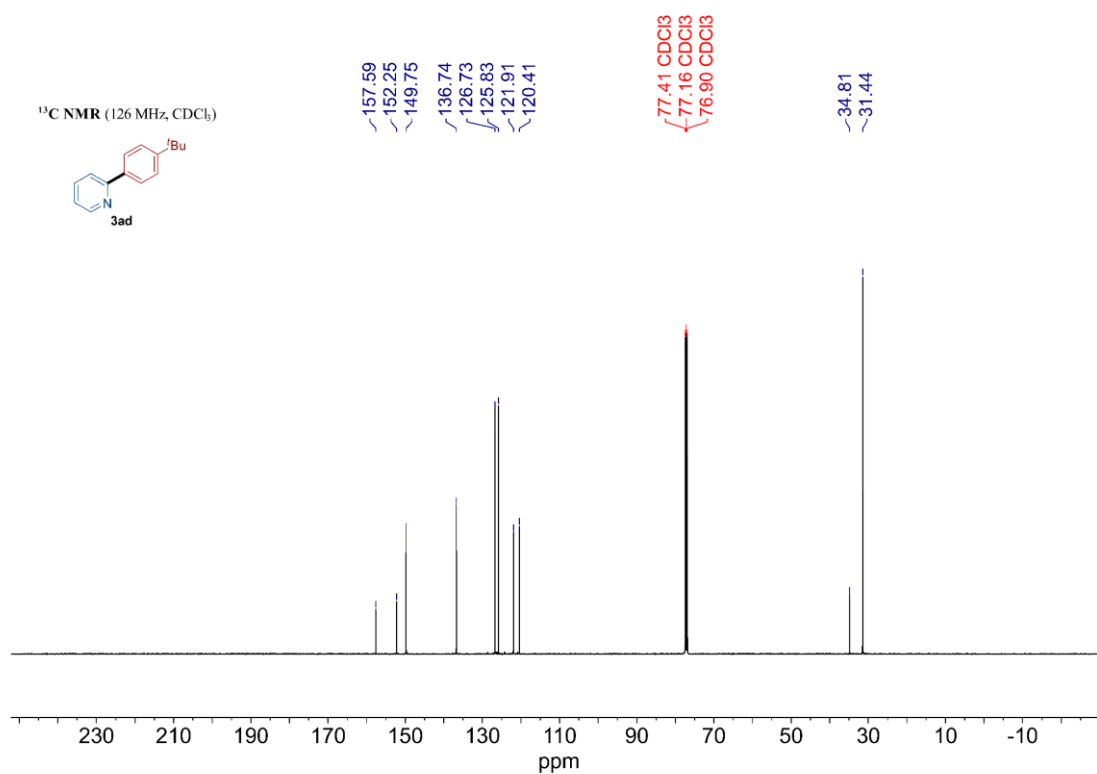
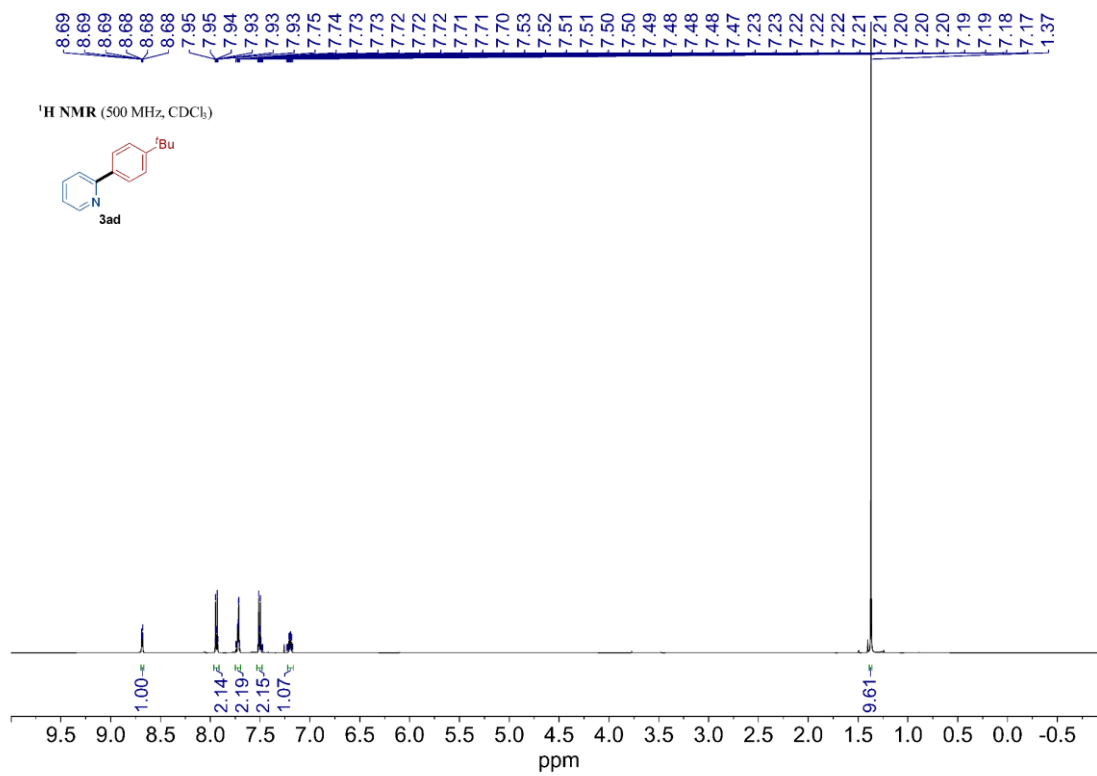
1. Krasovskiy, A.; Knochel, P. Convenient Titration Method for Organometallic Zinc, Magnesium, and Lanthanide- Reagents. *Synthesis* **2006**, *2006*, 890–891.
2. Peng, Z.; Wang, Y.; Yu, Z.; Zhao, D.; Song, L.; Jiang, C. Direct Arylation of Benzyl Ethers with Organozinc Reagents. *J. Org. Chem.* **2018**, *83*, 7900–7906.
3. Downs, R. P.; Chin, A. L.; Dean, K. M.; Carrick, J. D. Synthesis of Functionalized Hemi-1,2,4-Triazinyl-[2,2']-Bipyridines via Telescoped Condensation of [2,2']-Bipyridinyl-6-Carbonitrile. *J. Heterocycl. Chem.* **2017**, *54*, 3008–3014.
4. Gilbert, M. M.; Trenerry, M. J.; Longley, V. R.; Castro, A. J.; Berry, J. F.; Weix, D. J. Ligand–Metal Cooperation Enables Net Ring-Opening C–C Activation/Difunctionalization of Cyclopropyl Ketones. *ACS Catal.* **2023**, *13*, 11277–11290.
5. Guo, W.-J.; Wang, Z.-X. Cross-Coupling of ArX with ArMgBr Catalyzed by N-Heterocyclic Carbene-Based Nickel Complexes. *J. Org. Chem.* **2013**, *78*, 1054–1061.
6. Miao, W.; Ni, C.; Xiao, P.; Jia, R.; Zhang, W.; Hu, J. Nickel-Catalyzed Reductive 2-Pyridination of Aryl Iodides with Difluoromethyl 2-Pyridyl Sulfone. *Org. Lett.* **2021**, *23*, 711–715.
7. Wang, J.; Lu, H.; He, Y.; Jing, C.; Wei, H. Cobalt-Catalyzed Nitrogen Atom Insertion in Arylcycloalkenes. *J. Am. Chem. Soc.* **2022**, *144*, 22433–22439.
8. Hu, Y.; Gao, Y.; Ye, J.; Ma, Z.; Feng, J.; Liu, X.; Lei, P.; Szostak, M. Suzuki–Miyaura Cross-Coupling of 2-Pyridyl Trimethylammonium Salts by N–C Activation Catalyzed by Air- and Moisture-Stable Pd–NHC Precatalysts: Application to the Discovery of Agrochemicals. *Org. Lett.* **2023**, *25*, 2975–2980.
9. Xue, D.; Jia, Z.-H.; Zhao, C.-J.; Zhang, Y.-Y.; Wang, C.; Xiao, J. Direct Arylation of N-Heteroarenes with Aryldiazonium Salts by Photoredox Catalysis in Water. *Chem. – Eur. J.* **2014**, *20*, 2960–2965.
10. Linke, S.; Manolikakès, S.; Auffrant, A.; Gosmini, C. Cobalt-Catalyzed Formation of 2-Pyridylzinc Reagents and Their Subsequent Coupling. *Synthesis* **2018**, *50*, 2595–2600.
11. Cook, X. A. F.; Pantaine, L. R. E.; Blakemore, D. C.; Moses, I. B.; Sach, N. W.; Shavnya, A.; Willis, M. C. Base-Activated Latent Heteroaromatic Sulfinates as Nucleophilic Coupling Partners in Palladium-Catalyzed Cross-Coupling Reactions. *Angew. Chem. Int. Ed.* **2021**, *60*, 22461–22468.
12. Huang, L.; Ackerman, L. K. G.; Kang, K.; Parsons, A. M.; Weix, D. J. LiCl-Accelerated Multimetallic Cross-Coupling of Aryl Chlorides with Aryl Triflates. *J. Am. Chem. Soc.* **2019**, *141*, 10978–10983.
13. Bégouin, J.-M.; Gosmini, C. Cobalt-Catalyzed Cross-Coupling Between In Situ Prepared Arylzinc Halides and 2-Chloropyrimidine or 2-Chloropyrazine. *J. Org. Chem.* **2009**, *74*, 3221–3224.
14. Mo, S.; Zhu, Y.; Shen, Z. Copper-Catalyzed Aromatic C–H Bond Halogenation with Lithium Halides under Aerobic Conditions. *Org. Biomol. Chem.* **2013**, *11*, 2756–2760.
15. Smith, C. L.; Hirschhäuser, C.; Malcolm, G. K.; Nasrallah, D. J.; Gallagher, T. Synthesis of Mono- and Diaza-'Pyridones' via Stille Coupling of Alkoxyastannanes. *Synlett* **2014**, *25*, 1904–1908.
16. Sengmany, S.; Le Gall, E.; Léonel, E. An Electrochemical Synthesis of Functionalized Arylpyrimidines from 4-Amino-6-Chloropyrimidines and Aryl Halides. *Molecules* **2011**, *16*, 5550–5560.
17. Singh, B.; Paira, R.; Biswas, G.; Shaw, B. K.; Mandal, S. K. Graphene Oxide–Phenalenyl Composite: Transition Metal-Free Recyclable and Catalytic C–H Functionalization. *Chem. Commun.* **2018**, *54*, 13220–13223.
18. Goebel, J. F.; Löffler, J.; Zeng, Z.; Handelsmann, J.; Hermann, A.; Rodstein, I.; Gensch, T.; Gessner, V. H.; Gooßen, L. J. Computer-Driven Development of Ylide Functionalized Phosphines for Palladium-Catalyzed Hiyama Couplings. *Angew. Chem. Int. Ed.* **2023**, *62*, e202216160.
19. Cervantes-Reyes, A.; Smith, A. C.; Chinigo, G. M.; Blakemore, D. C.; Szostak, M. Decarbonylative Pd-Catalyzed Suzuki Cross-Coupling for the Synthesis of Structurally Diverse Heterobiaryls. *Org. Lett.* **2022**, *24*, 1678–1683.
20. Sengmany, S.; Léonel, E.; Polissaint, F.; Nédélec, J.-Y.; Pipelier, M.; Thobie-Gautier, C.; Dubreuil, D. Preparation of Functionalized Aryl- and Heteroarylpyridazines by Nickel-Catalyzed Electrochemical Cross-Coupling Reactions. *J. Org. Chem.* **2007**, *72*, 5631–5636.

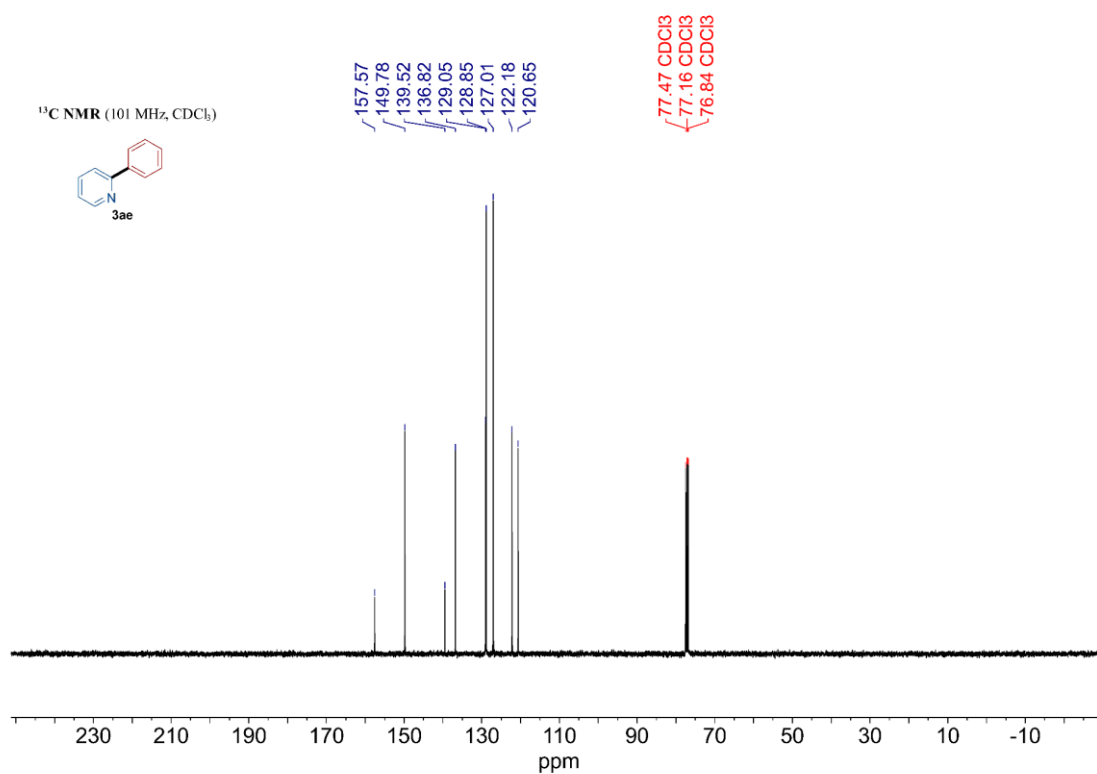
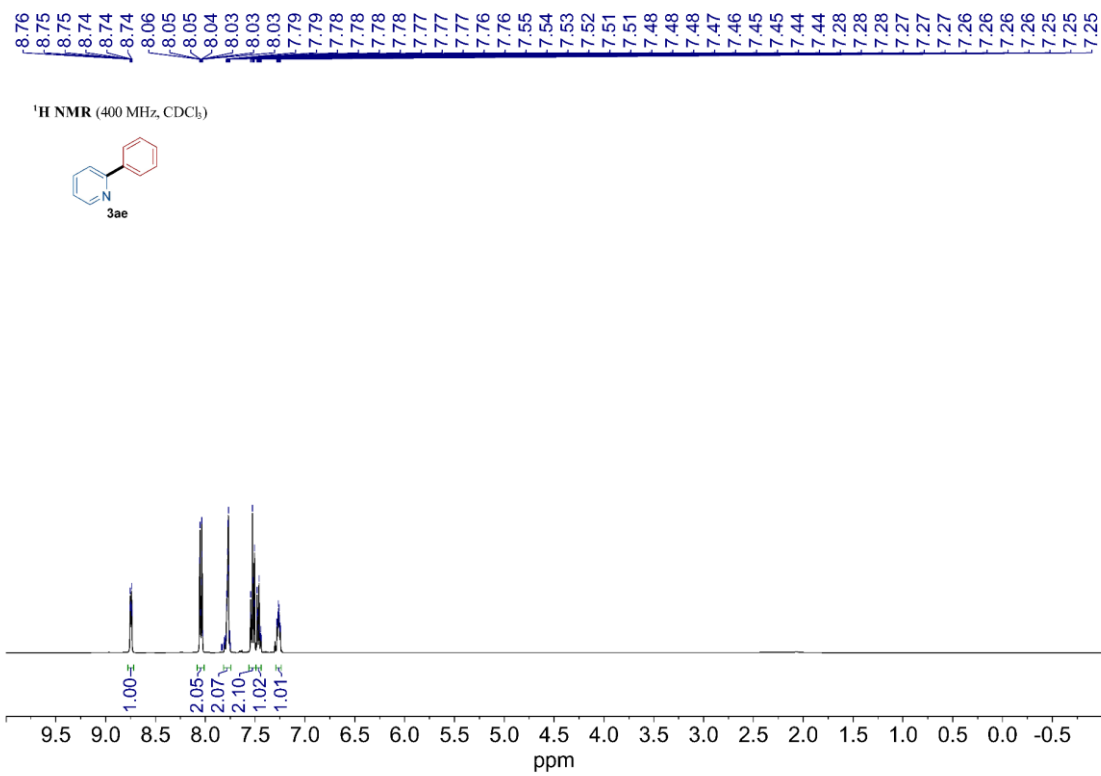
21. Takahashi, F.; Nogi, K.; Yorimitsu, H. Intramolecular Desulfinitative Coupling: Nickel-Catalyzed Transformation of Diaryl Sulfones into Biaryls via Extrusion of SO<sub>2</sub>. *Org. Lett.* **2018**, *20*, 6601–6605.
22. Wang, P.; Yang, Z.; Wang, Z.; Xu, C.; Huang, L.; Wang, S.; Zhang, H.; Lei, A. Electrochemical Arylation of Electron-Deficient Arenes through Reductive Activation. *Angew. Chem. Int. Ed.* **2019**, *58*, 15747–15751.

## 4C.VII. NMR Spectra of Compounds



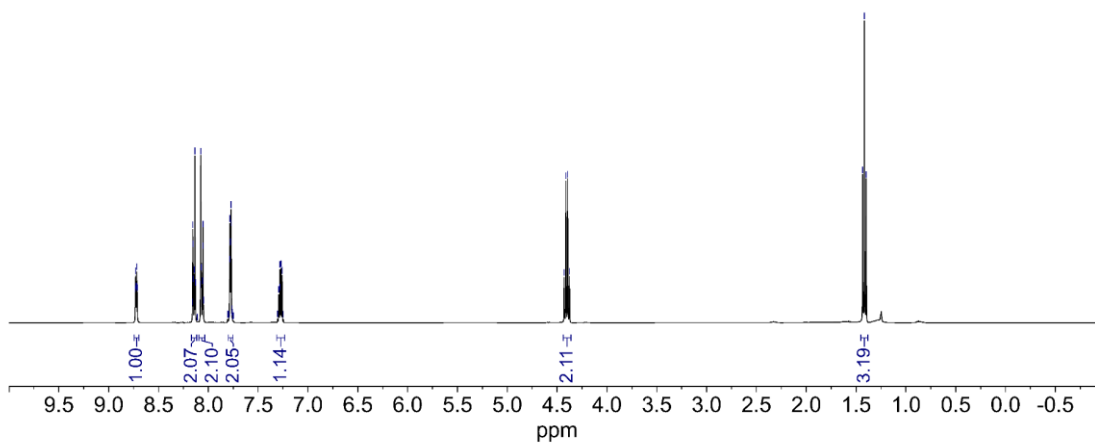
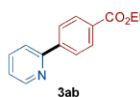




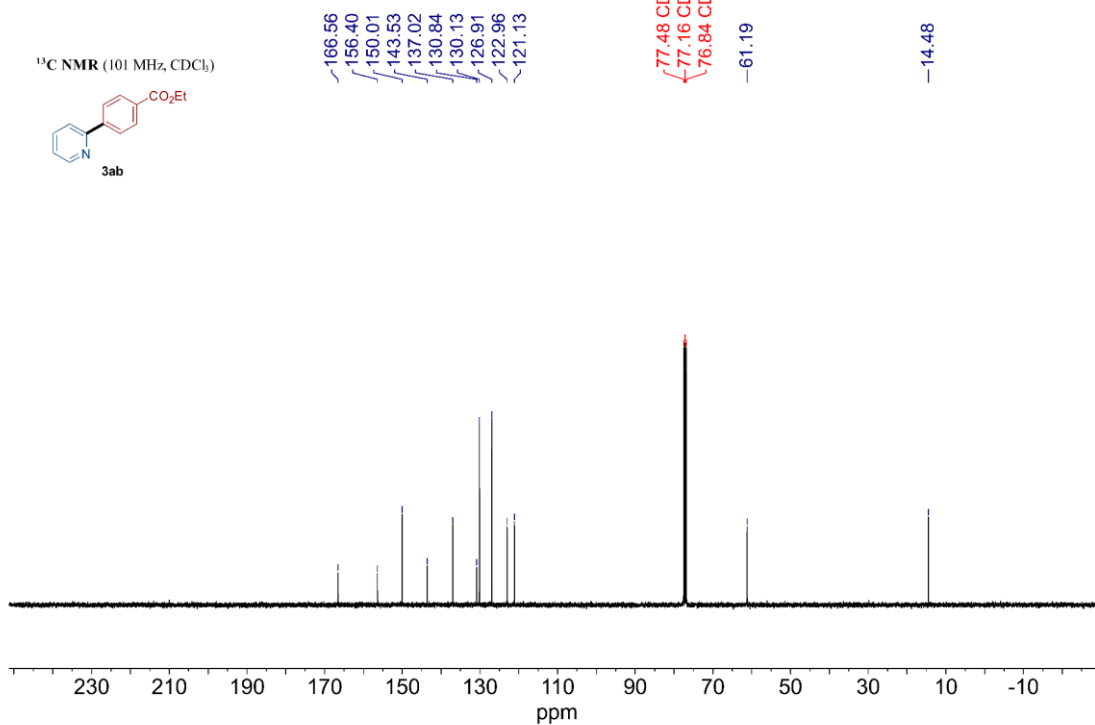
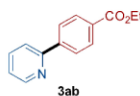


8.73  
8.73  
8.73  
8.72  
8.71  
8.16  
8.16  
8.15  
8.15  
8.14  
8.13  
8.13  
8.11  
8.08  
8.07  
8.07  
8.06  
8.05  
8.05  
8.05  
7.81  
7.80  
7.79  
7.79  
7.78  
7.78  
7.77  
7.77  
7.76  
7.76  
7.75  
7.75  
7.75  
7.30  
7.29  
7.28  
7.28  
7.27  
7.26  
7.26  
7.25  
4.43  
4.41  
4.39  
4.38  
1.43  
1.42  
1.40

<sup>1</sup>H NMR (400 MHz, CDCl<sub>3</sub>)

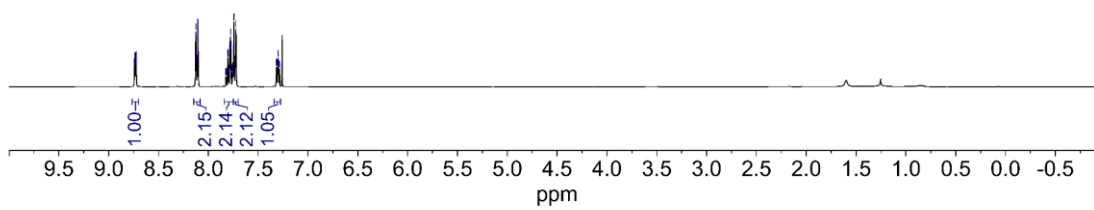
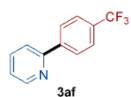


<sup>13</sup>C NMR (101 MHz, CDCl<sub>3</sub>)



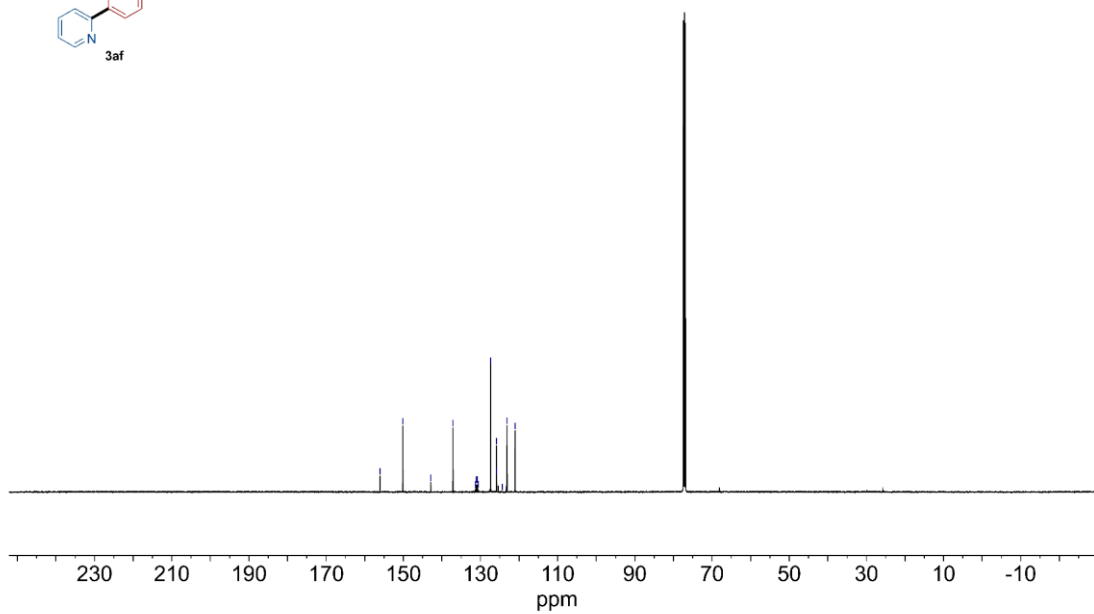
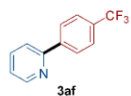
8.74  
8.74  
8.73  
8.73  
8.72  
8.72  
8.13  
8.12  
8.12  
8.11  
8.10  
8.10  
7.82  
7.82  
7.81  
7.80  
7.80  
7.79  
7.78  
7.78  
7.77  
7.76  
7.76  
7.75  
7.74  
7.72  
7.72  
7.32  
7.31  
7.31  
7.30  
7.29  
7.28

<sup>1</sup>H NMR (400 MHz, CDCl<sub>3</sub>)

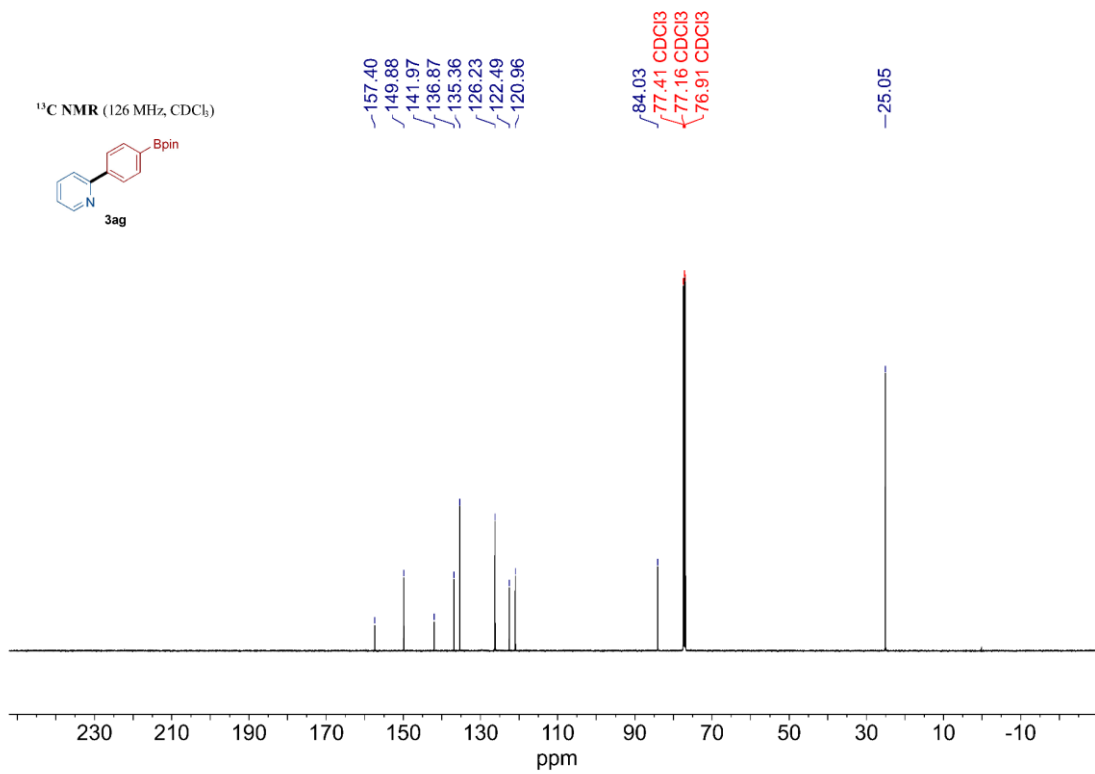
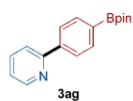


156.07  
150.10  
142.84  
137.12  
131.35  
131.10  
130.84  
130.58  
127.34  
125.89  
125.85  
125.82  
125.79  
124.34  
123.10  
121.01

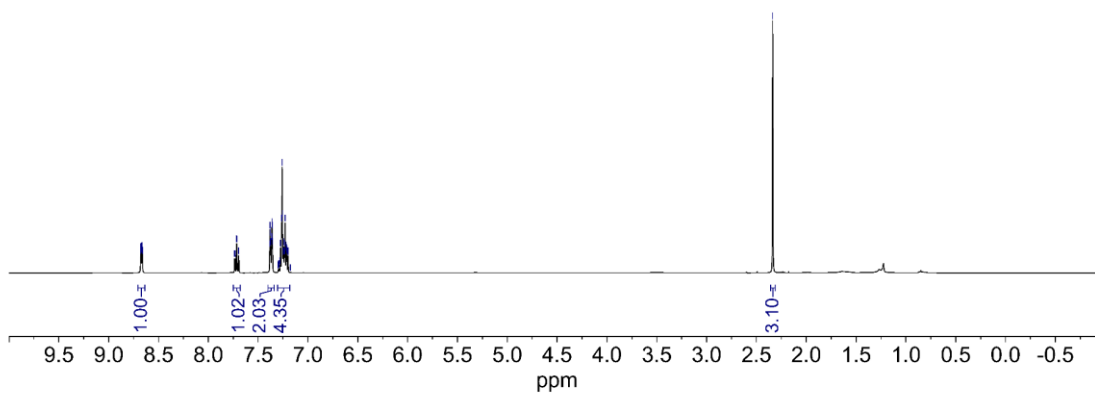
<sup>13</sup>C NMR (126 MHz, CDCl<sub>3</sub>)

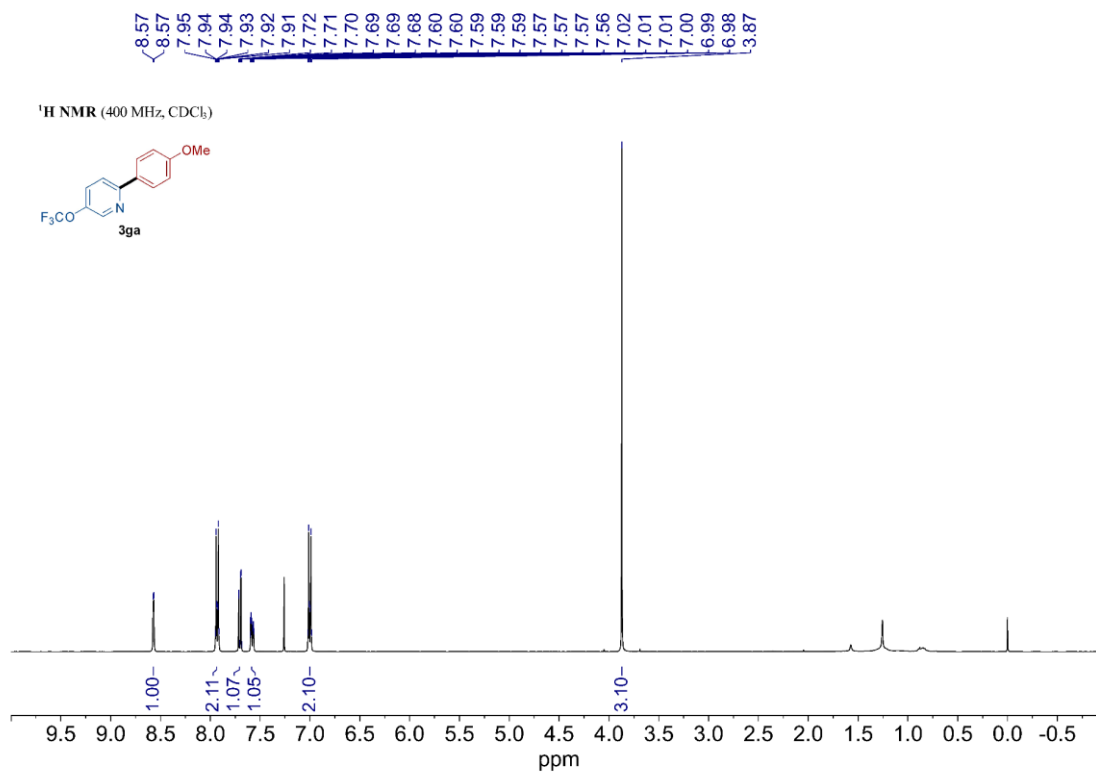
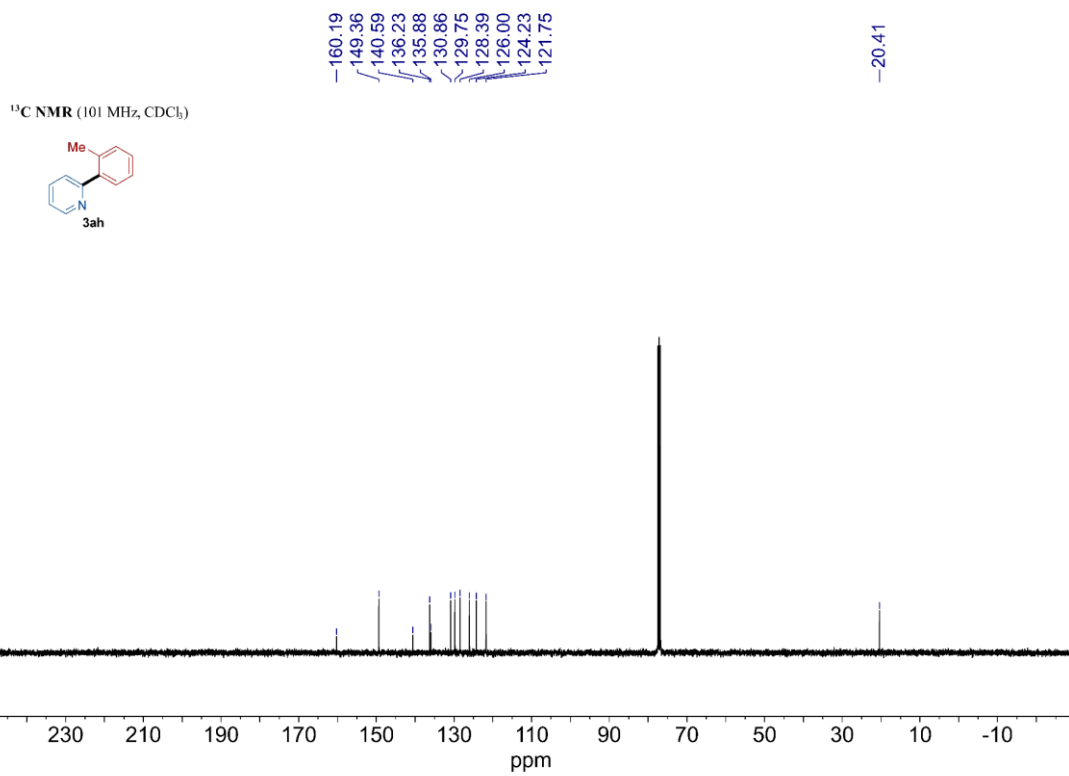


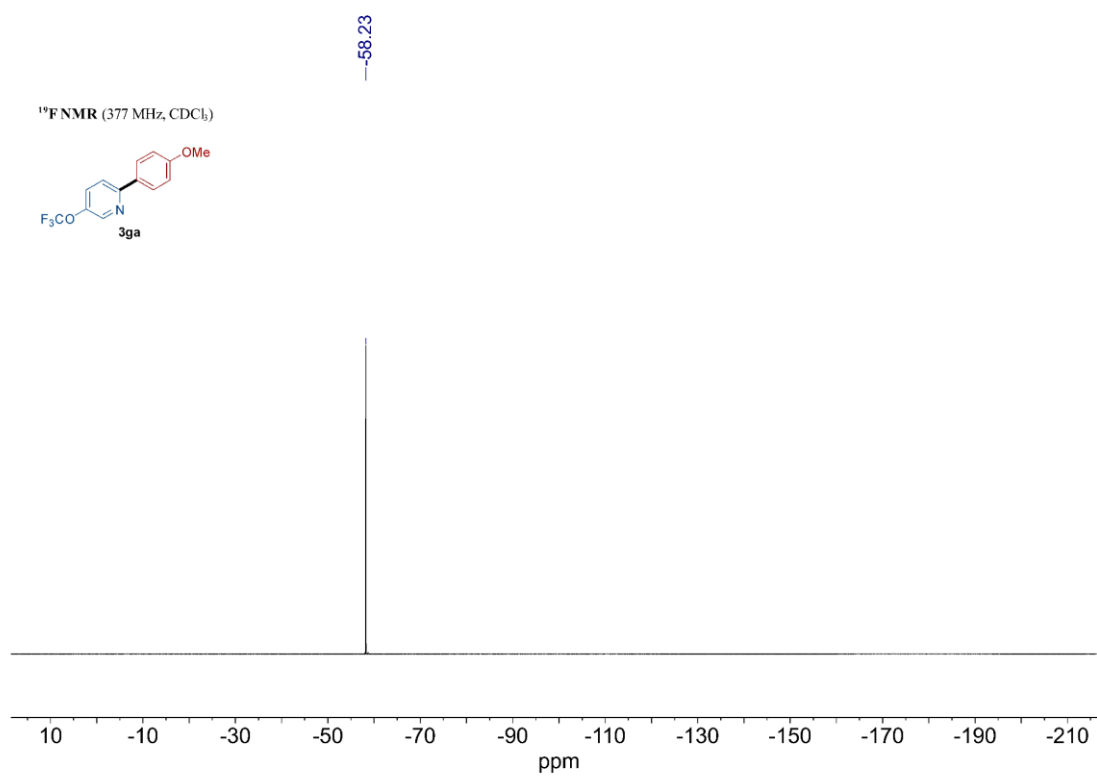
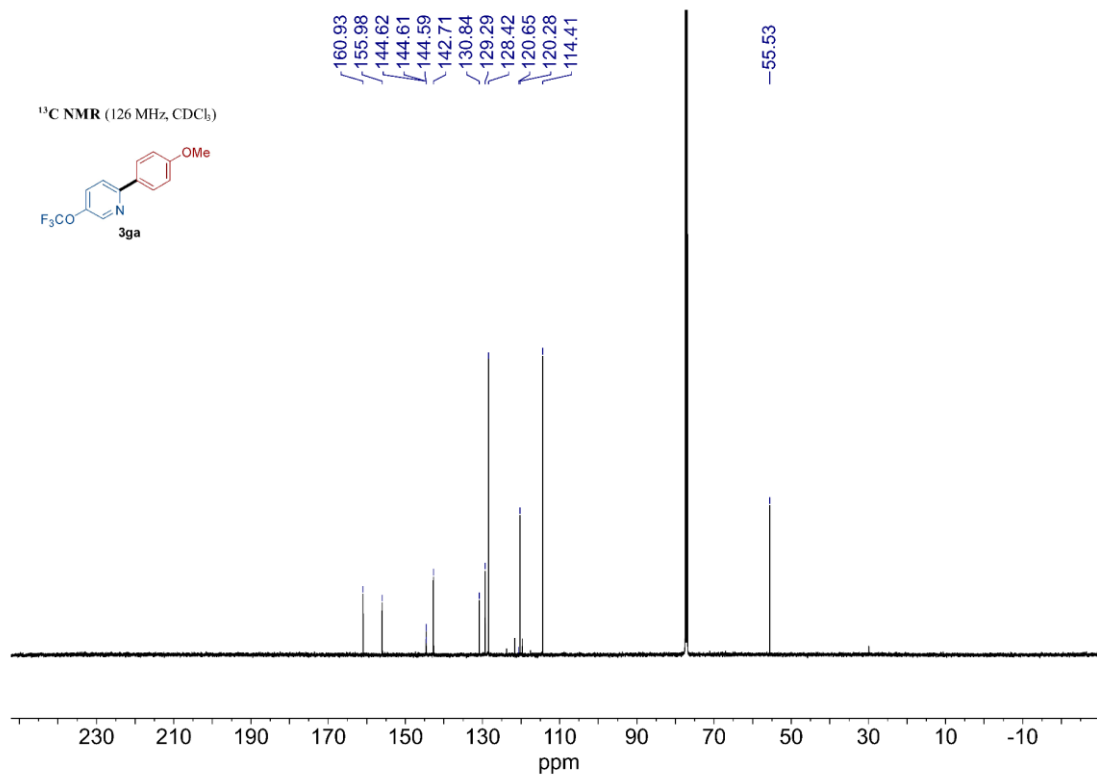


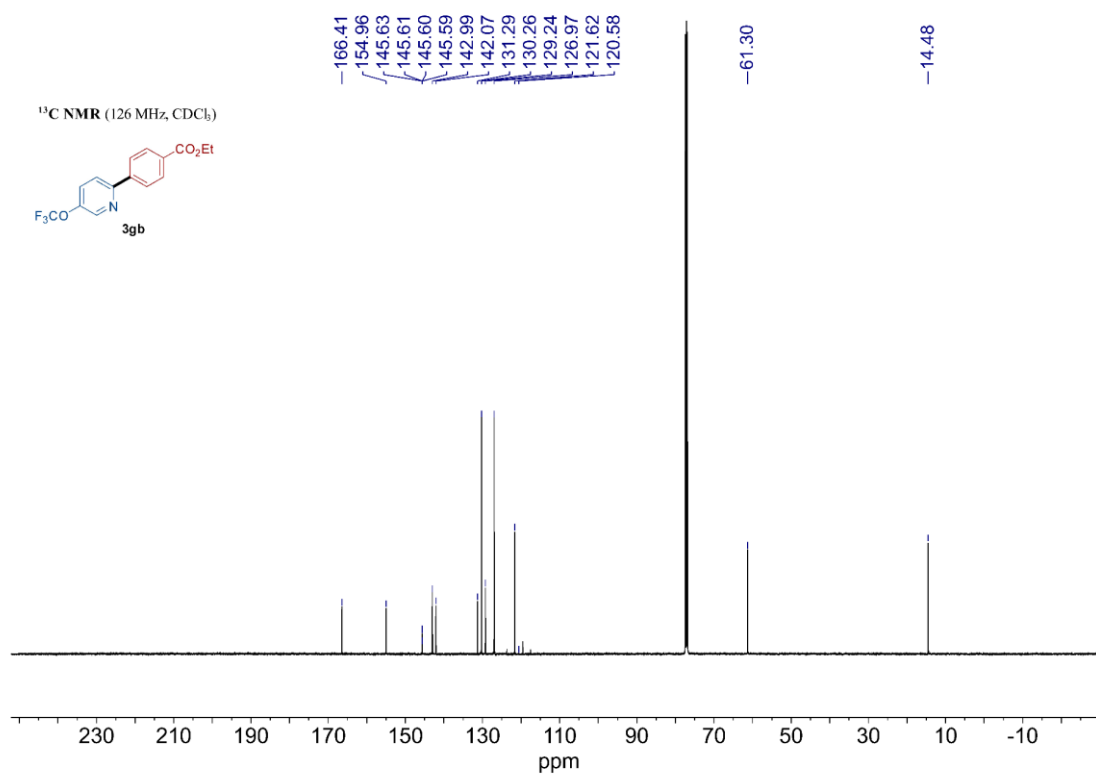
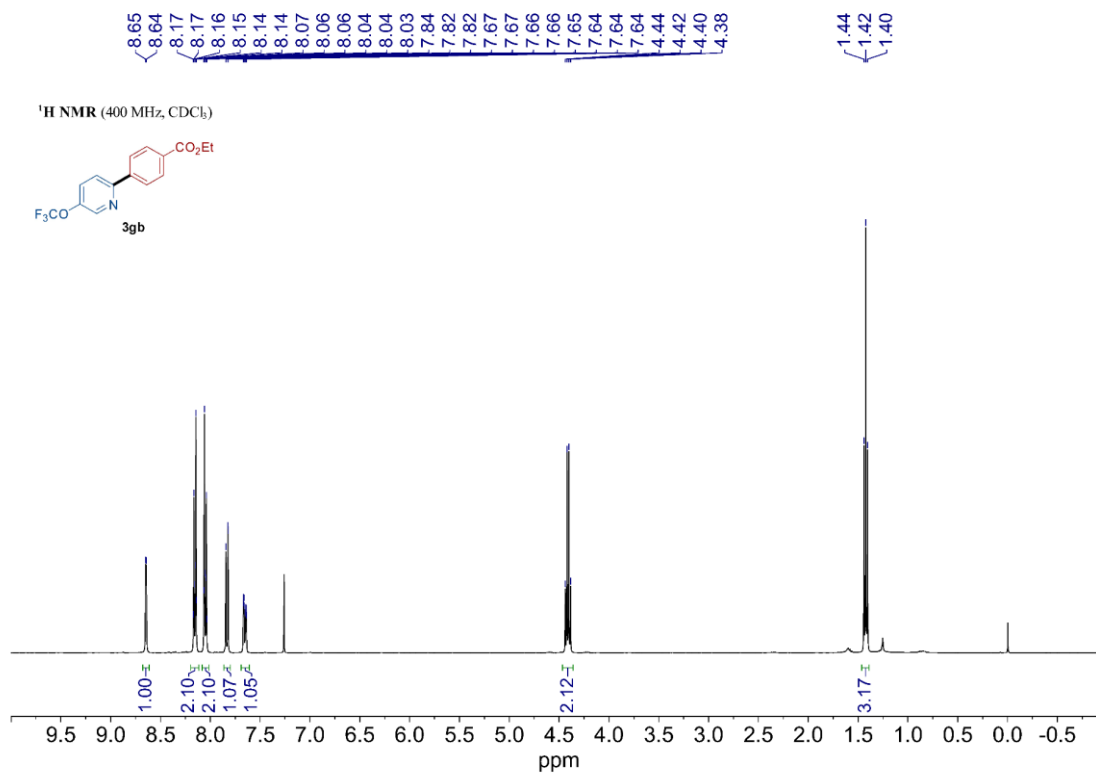
<sup>13</sup>C NMR (126 MHz, CDCl<sub>3</sub>)

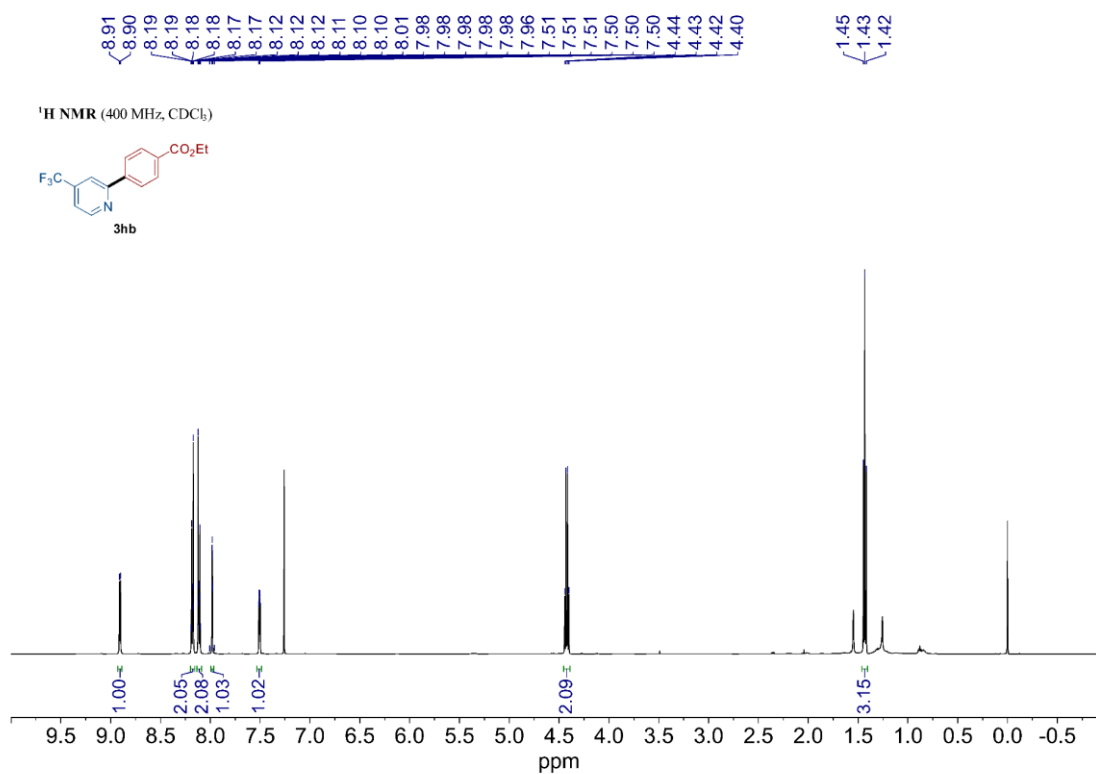
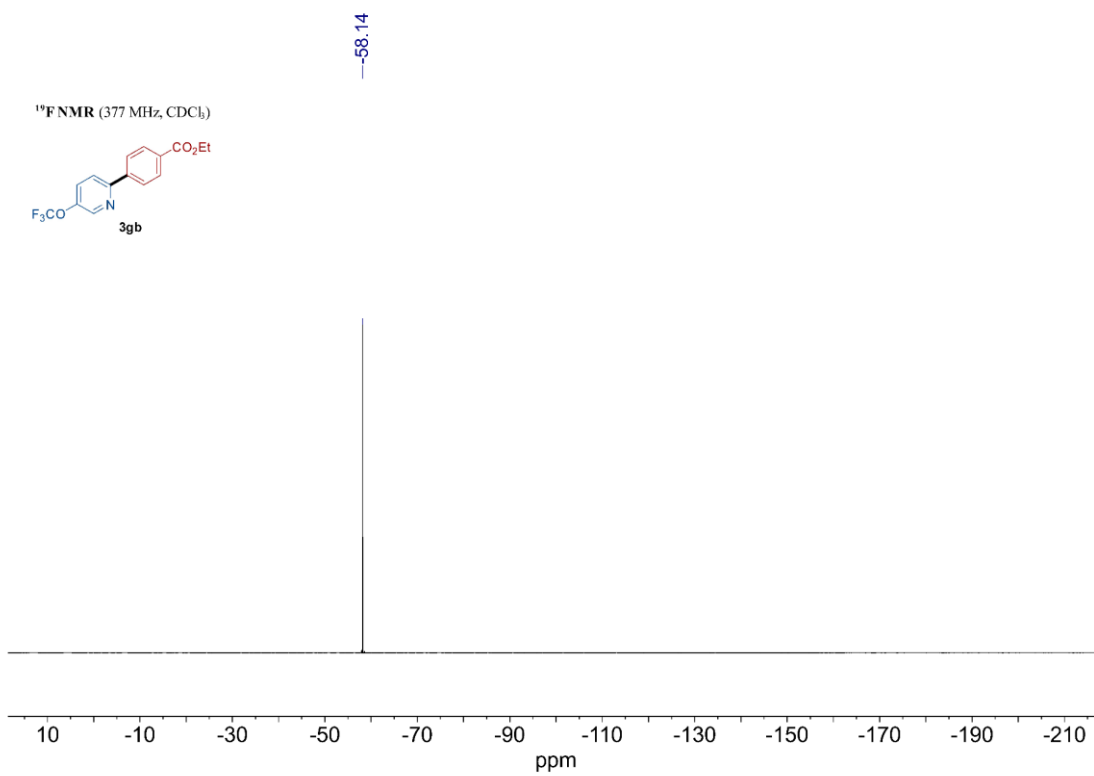
8.68  
8.68  
8.67  
8.67  
8.66  
8.66  
7.74  
7.73  
7.72  
7.71  
7.70  
7.69  
7.38  
7.38  
7.38  
7.37  
7.36  
7.36  
7.36  
7.36  
7.30  
7.29  
7.29  
7.28  
7.28  
7.27  
7.26  
7.26  
7.25  
7.25  
7.24  
7.24  
7.23  
7.23  
7.22  
7.22  
7.21  
7.21  
7.20  
7.20  
7.18  
7.18  
2.34

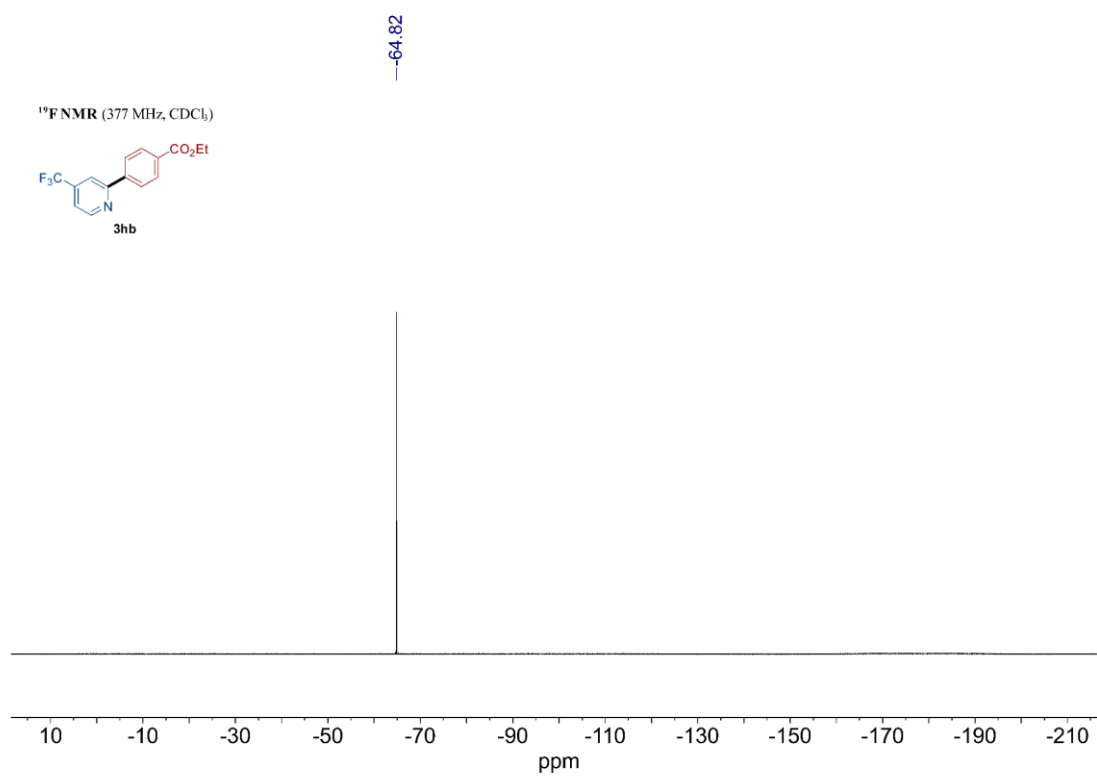
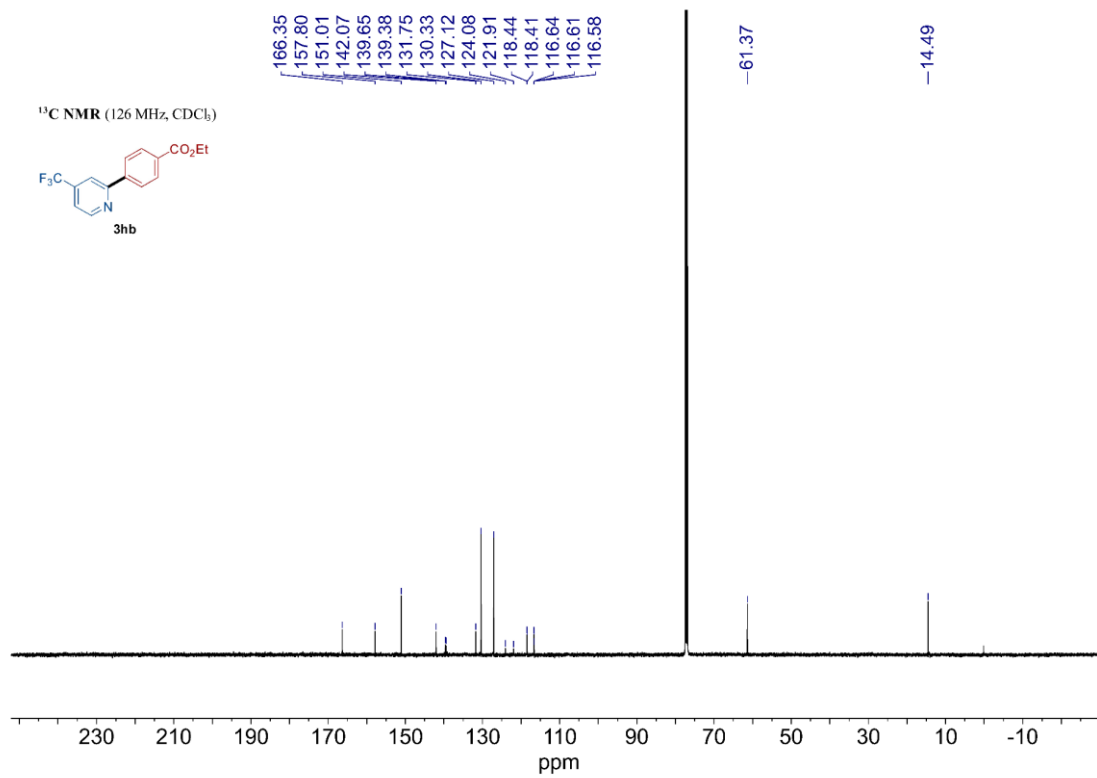
<sup>1</sup>H NMR (400 MHz, CDCl<sub>3</sub>)

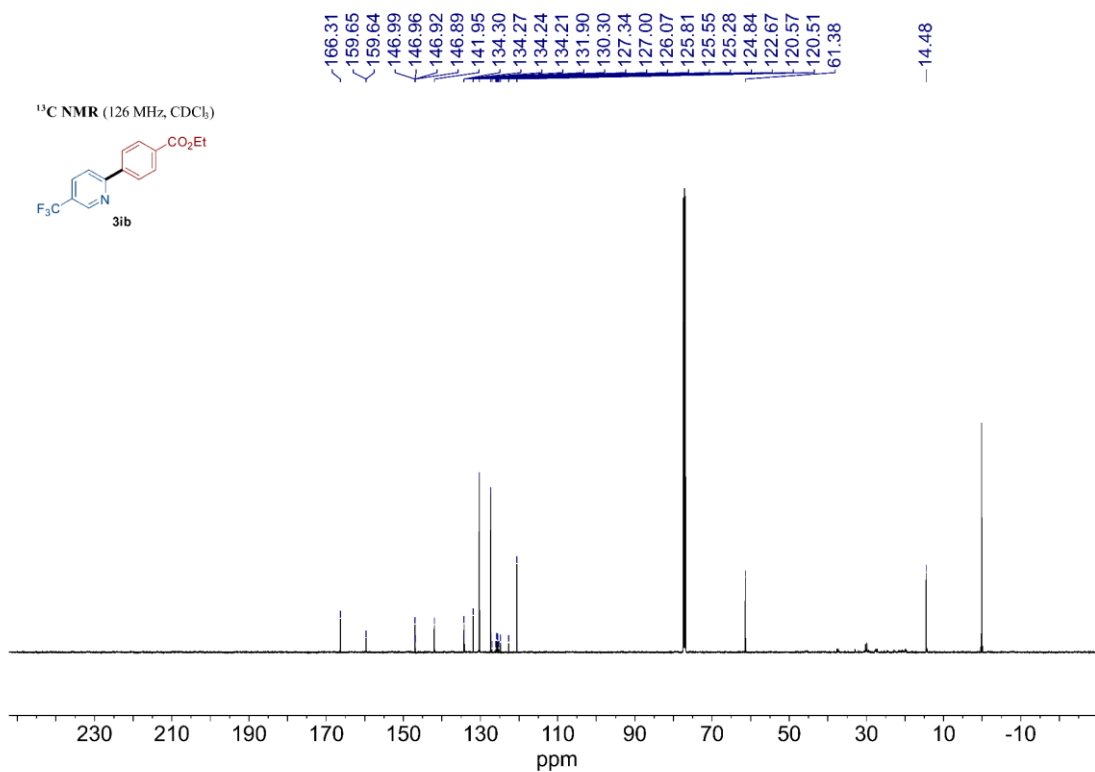
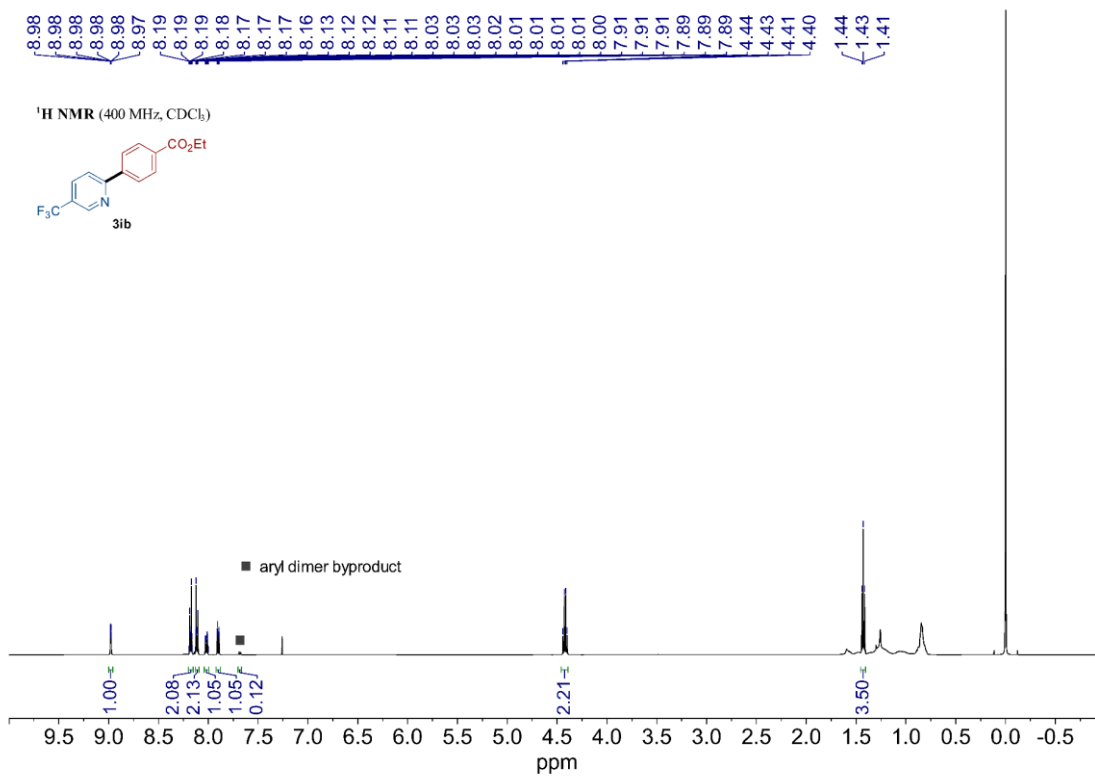


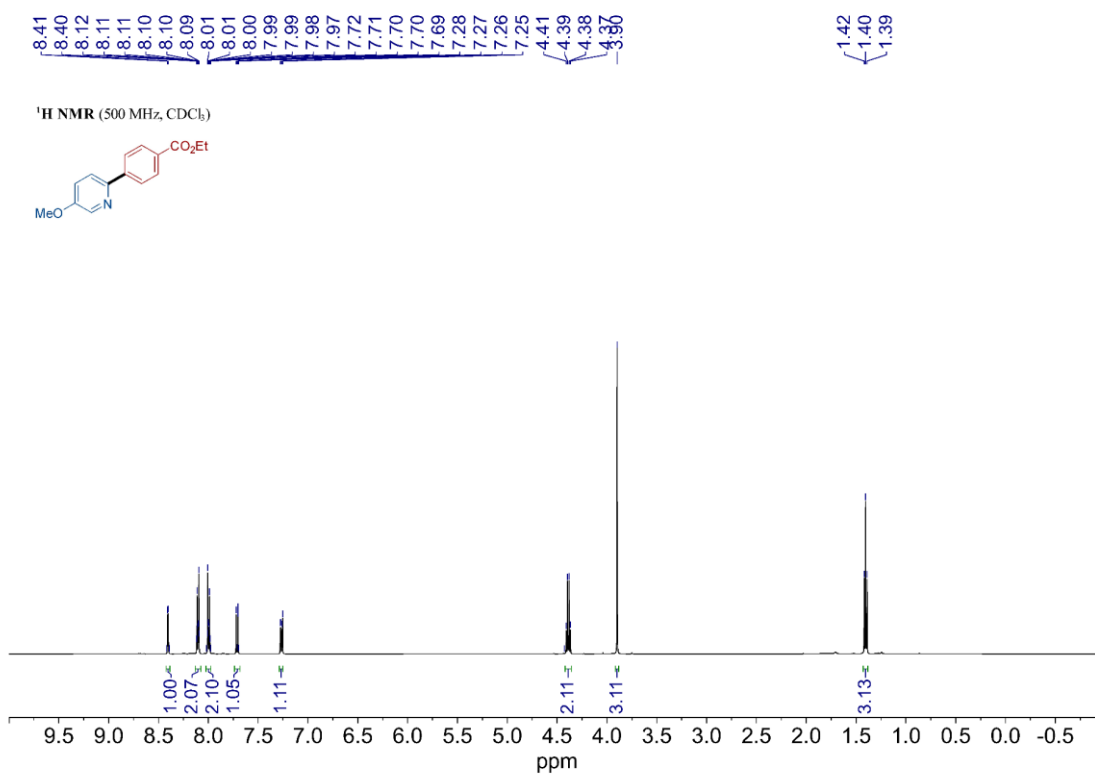
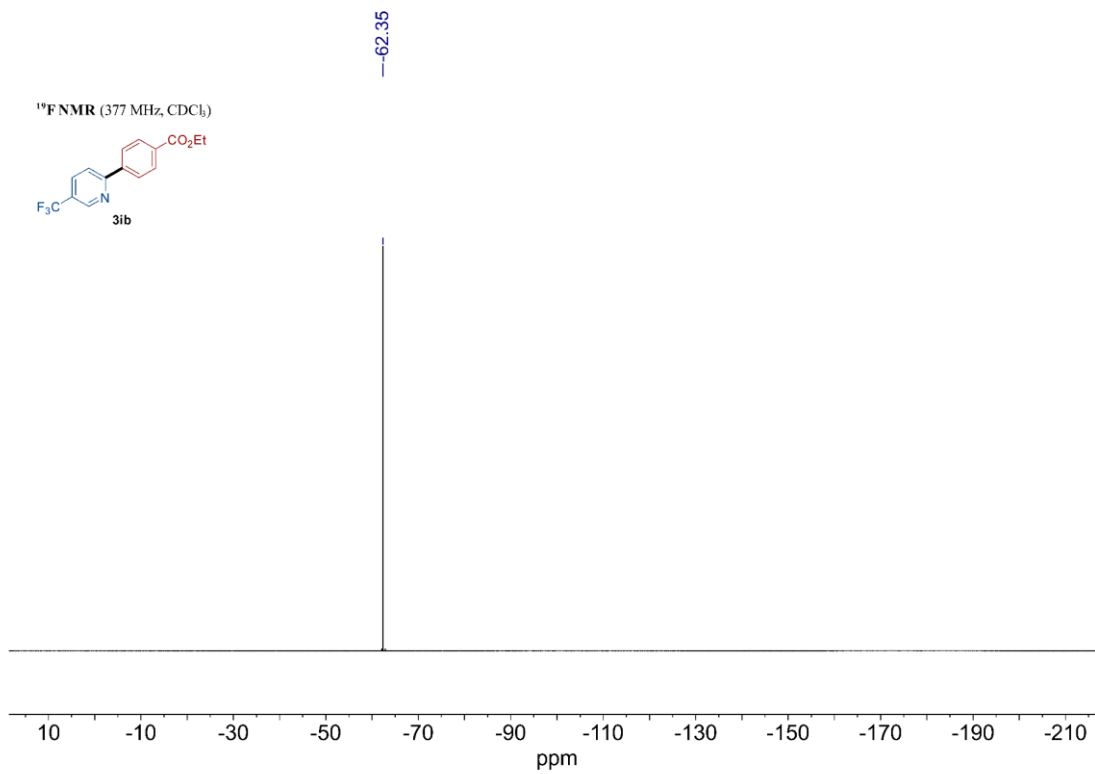


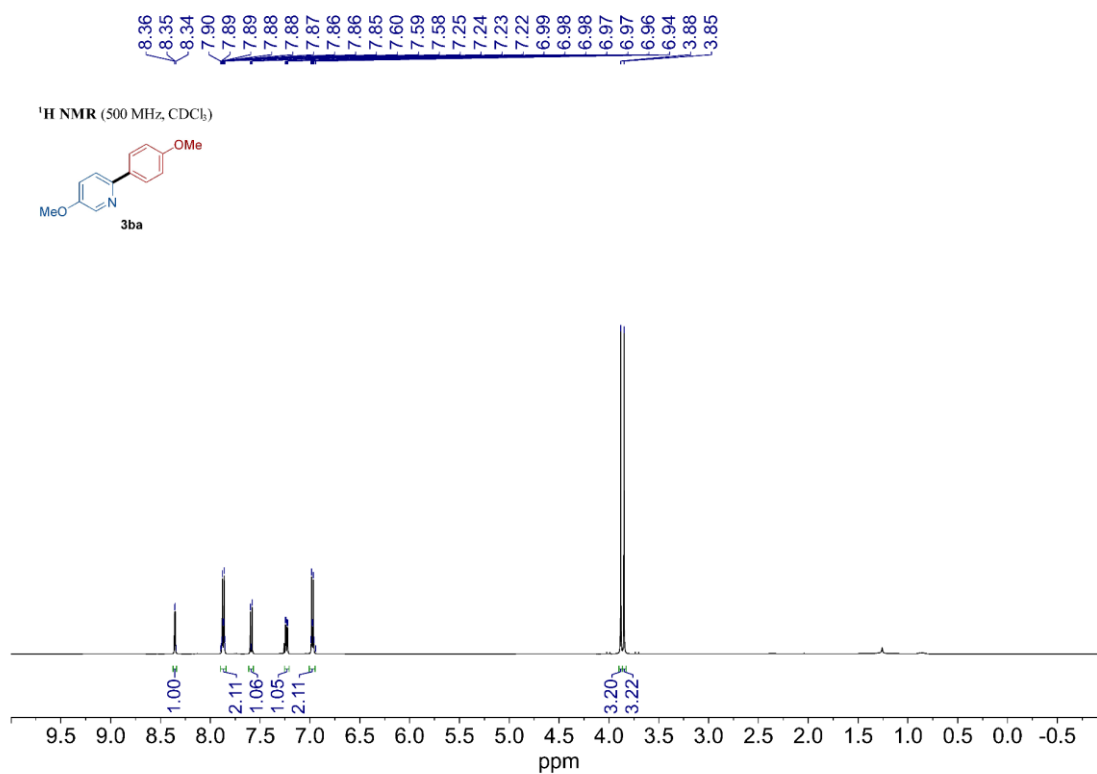
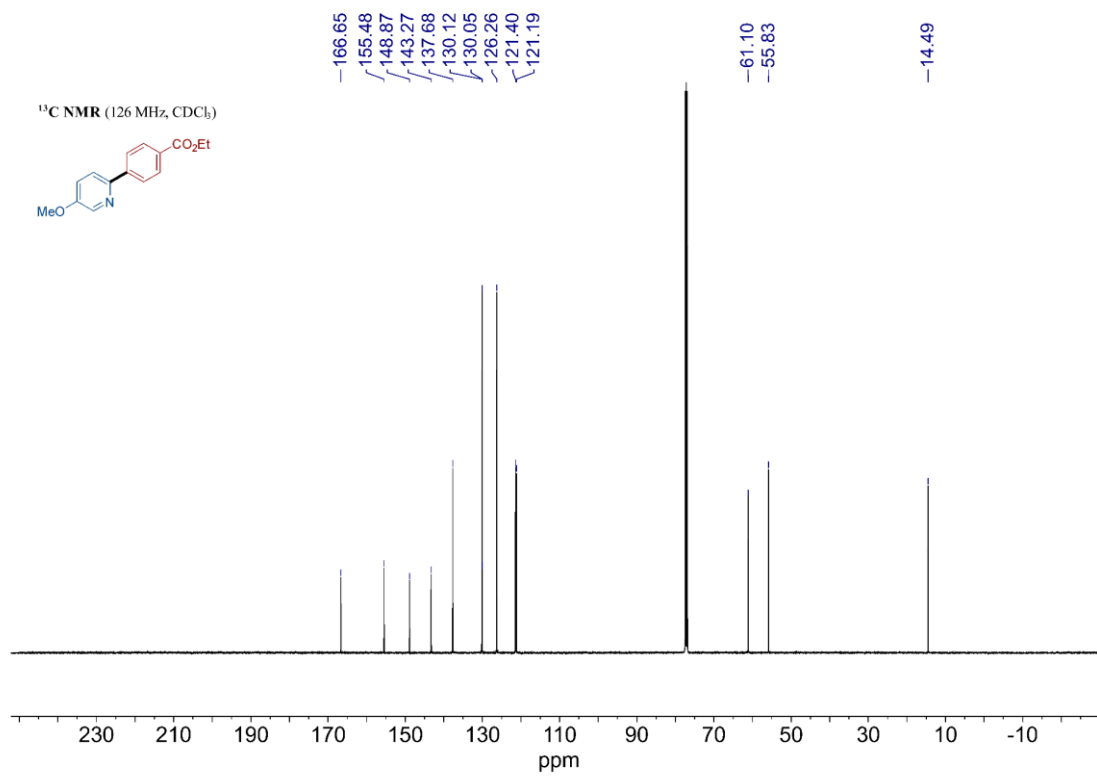


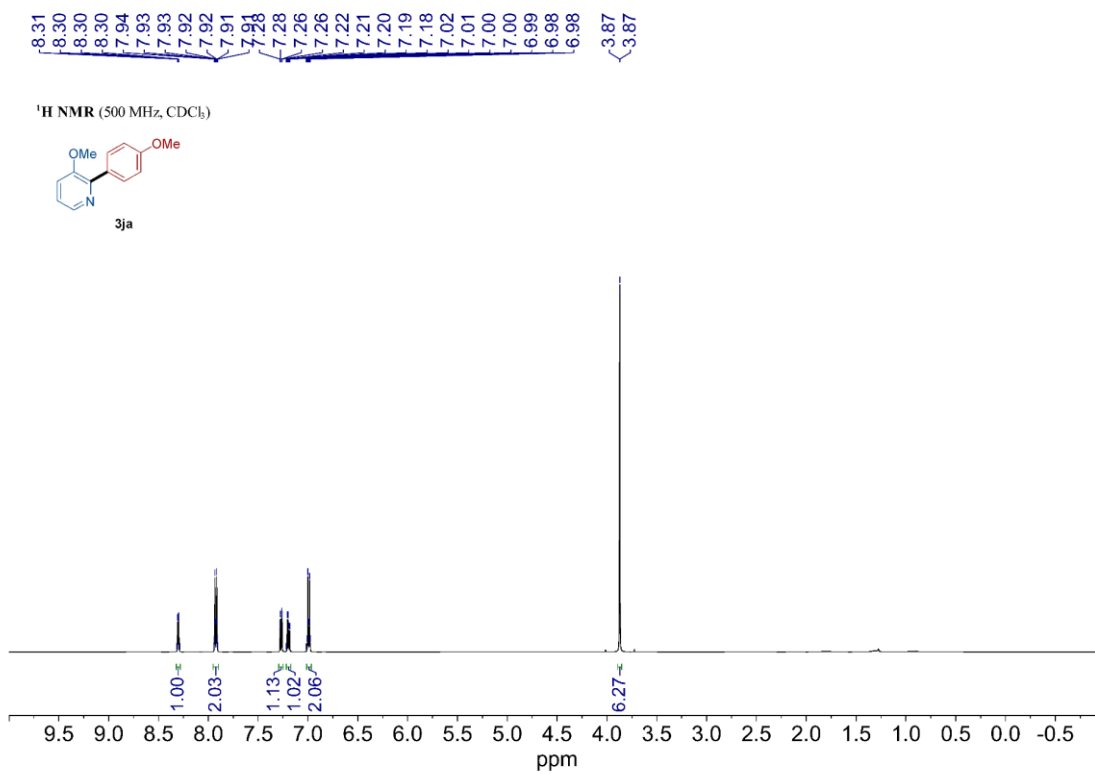
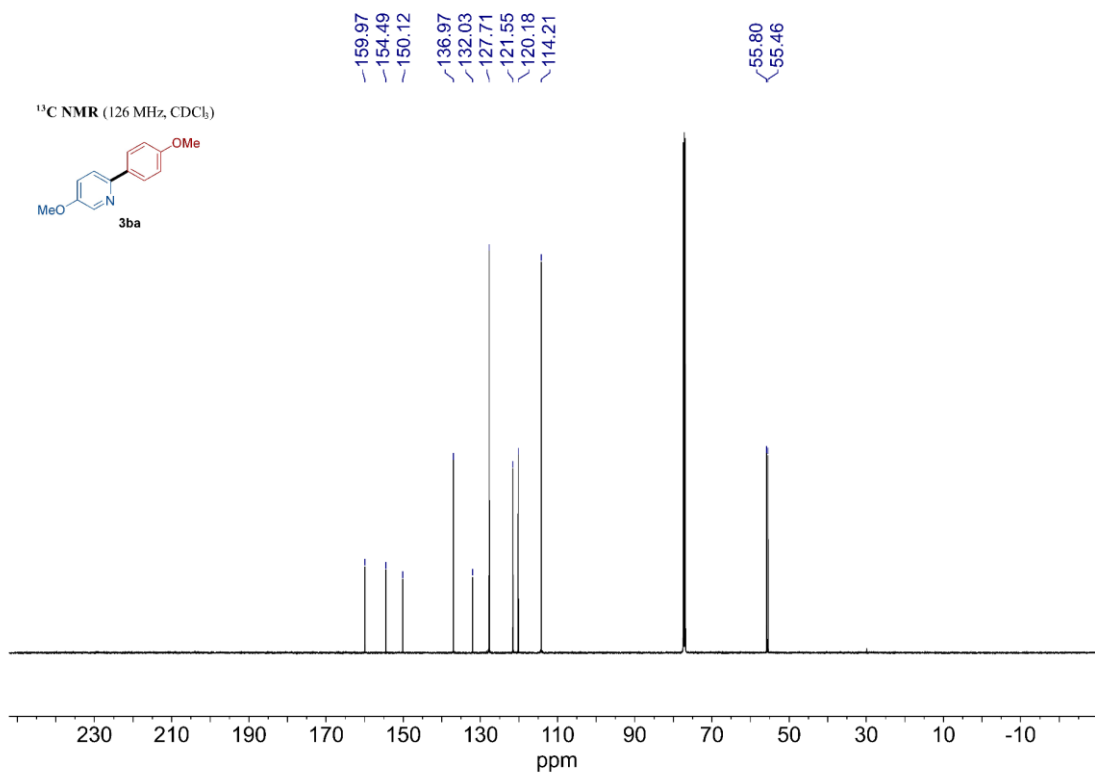


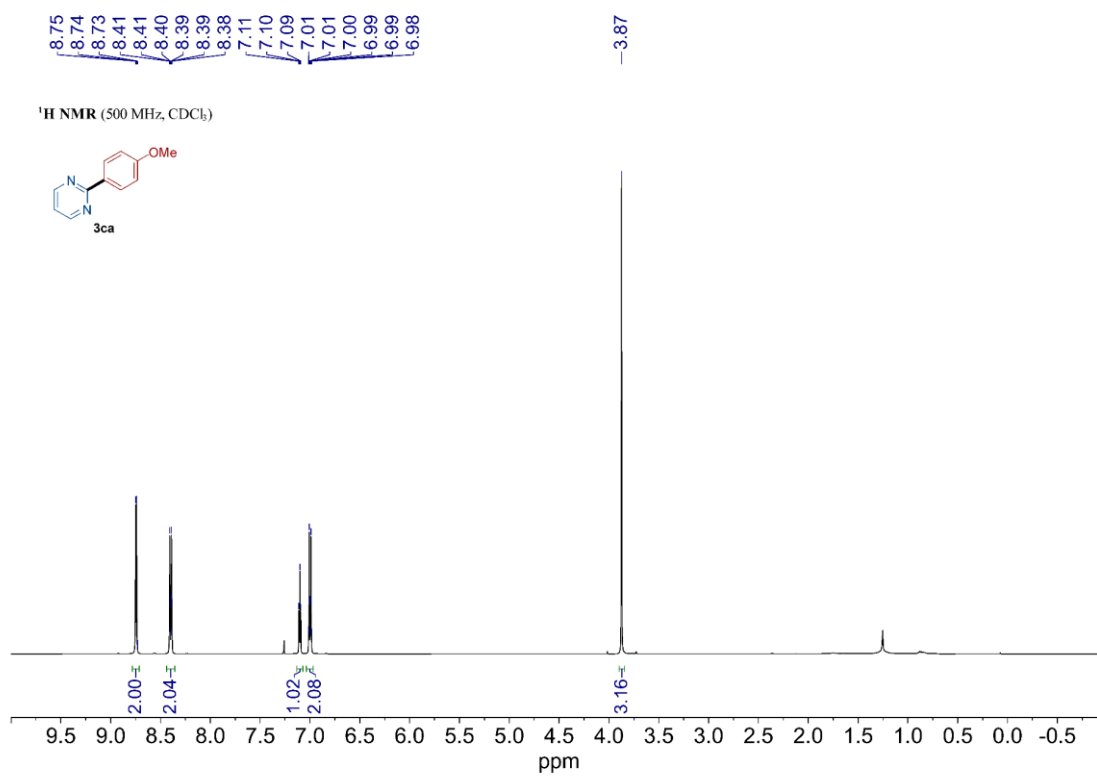
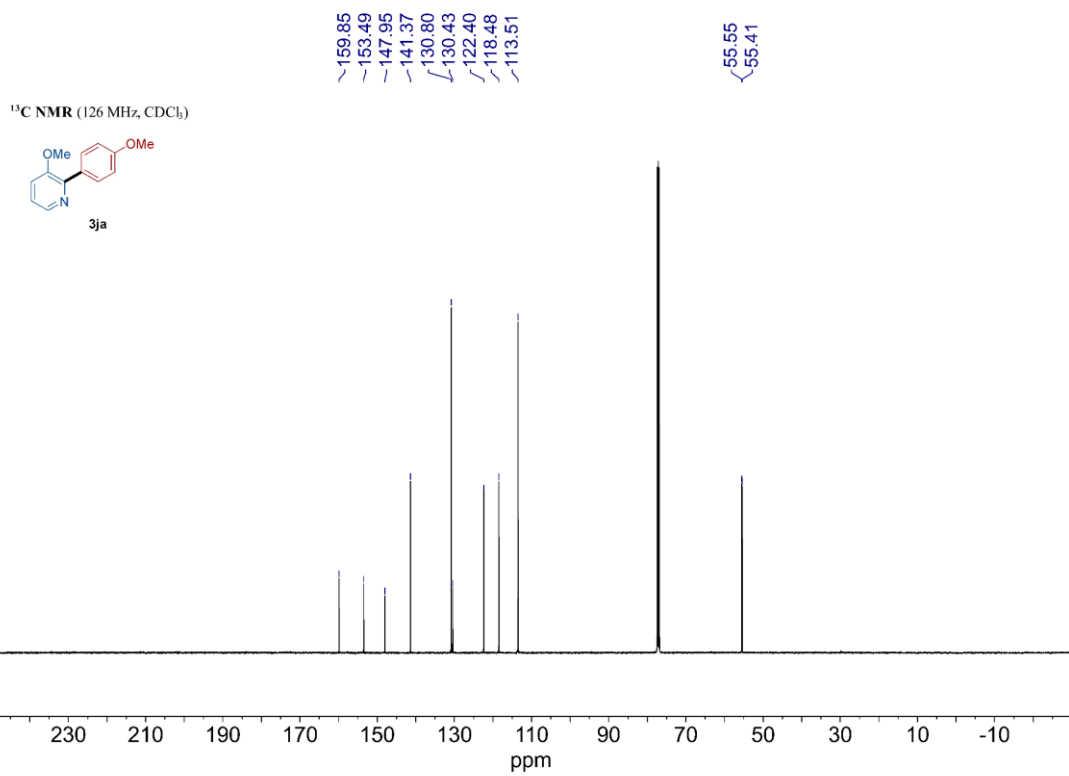


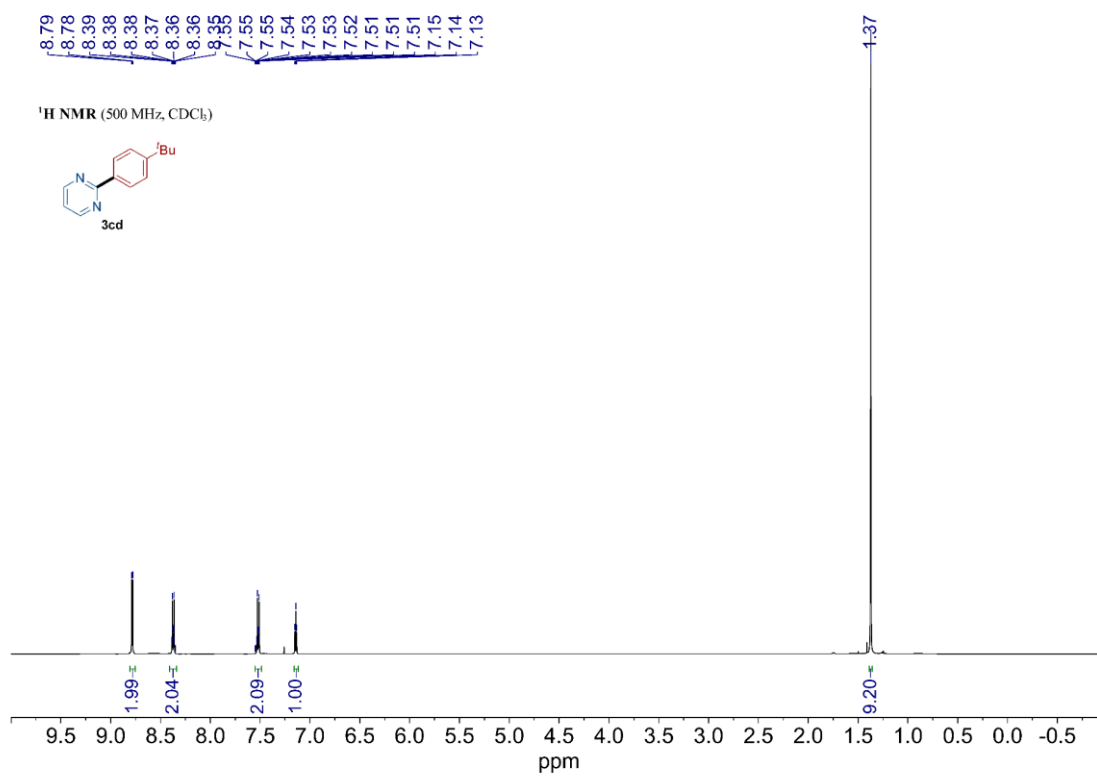
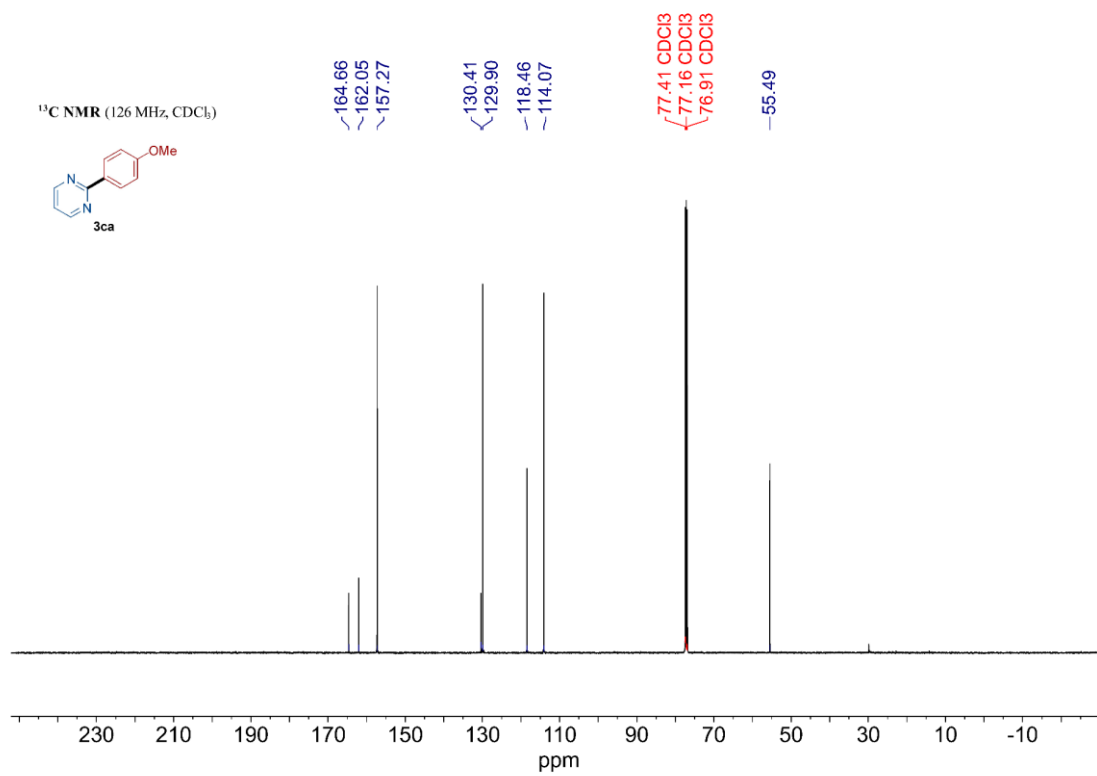


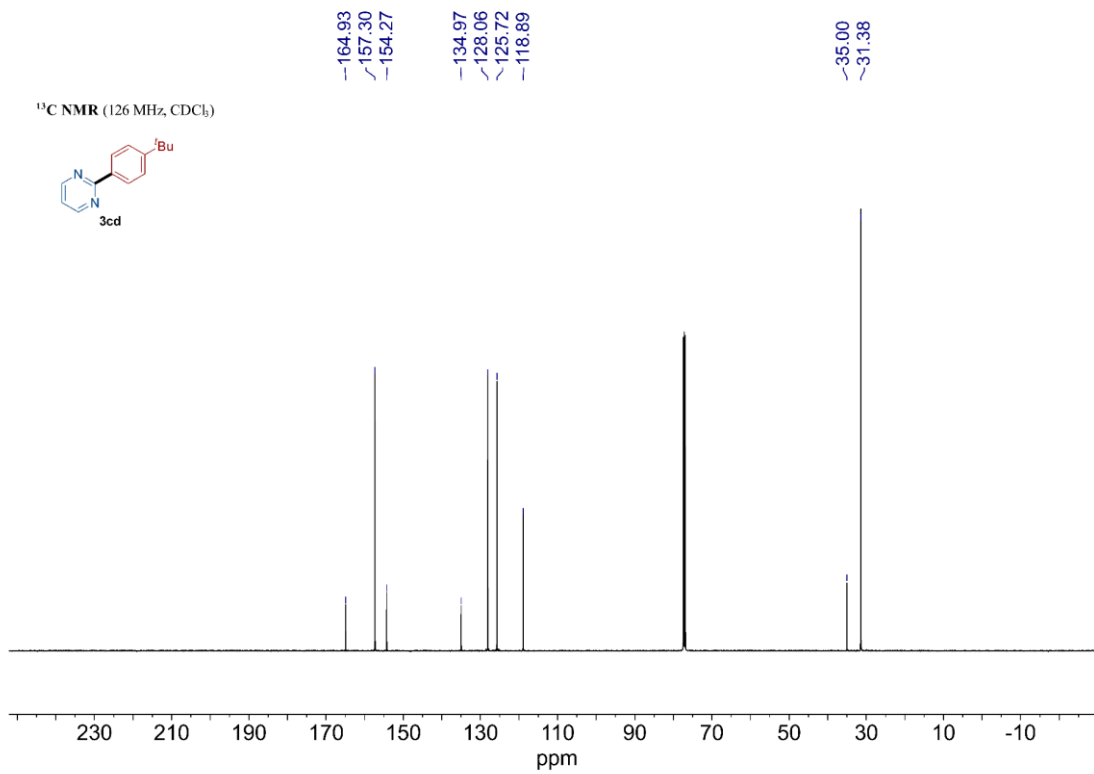
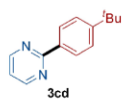




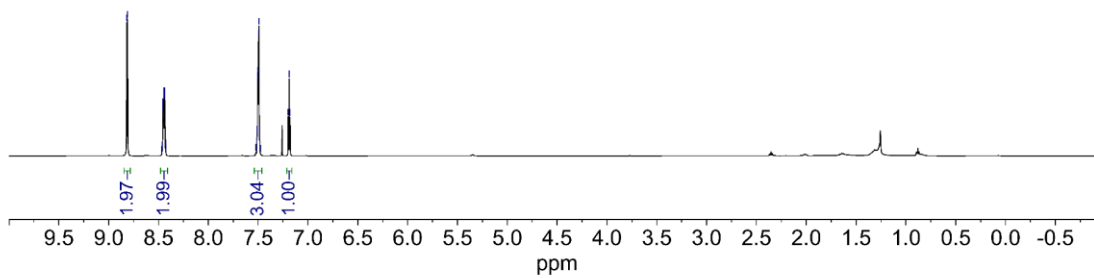


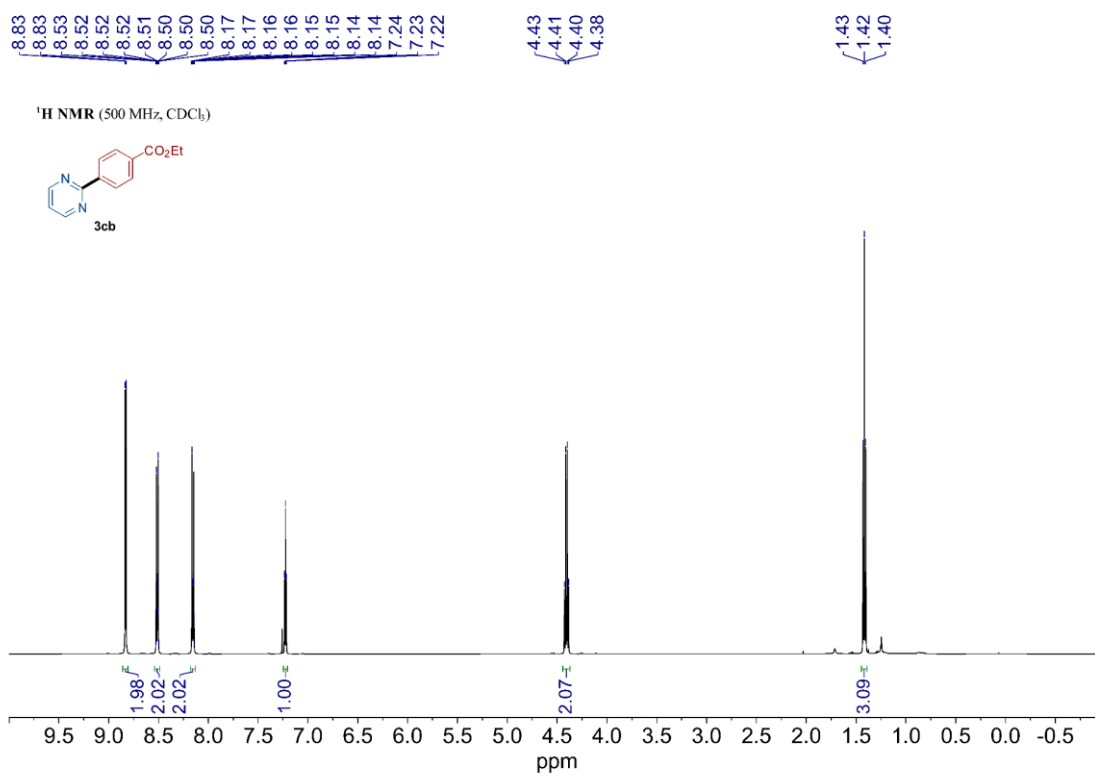
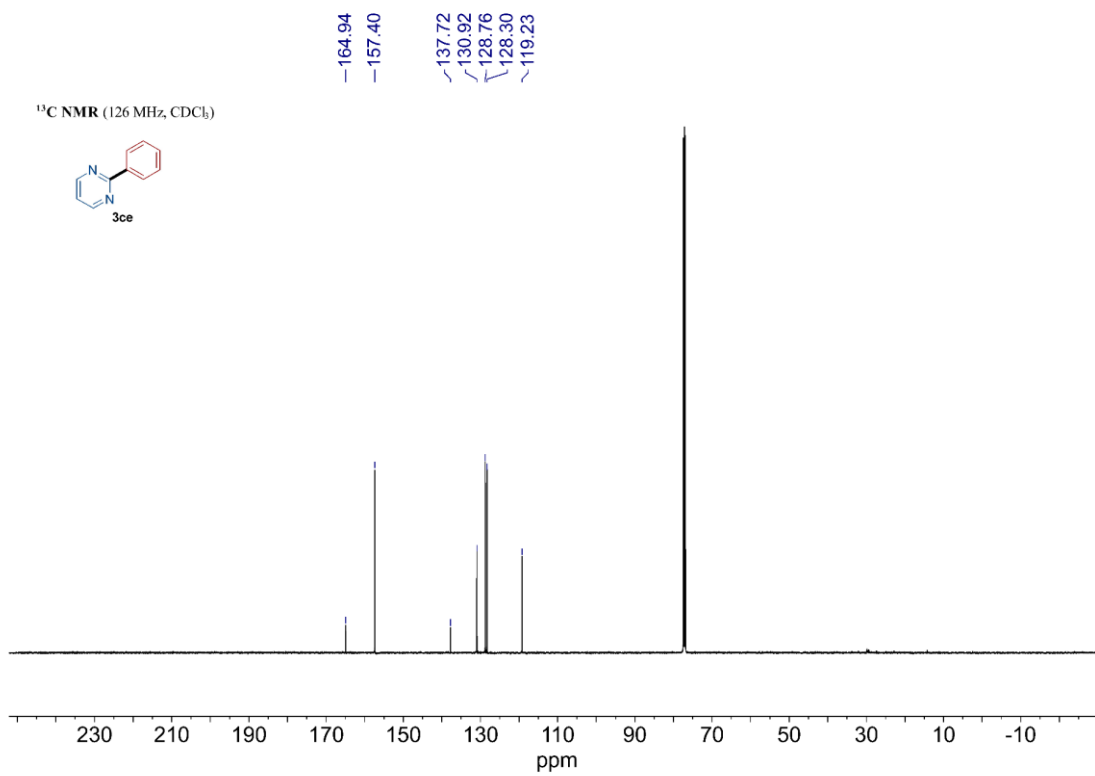


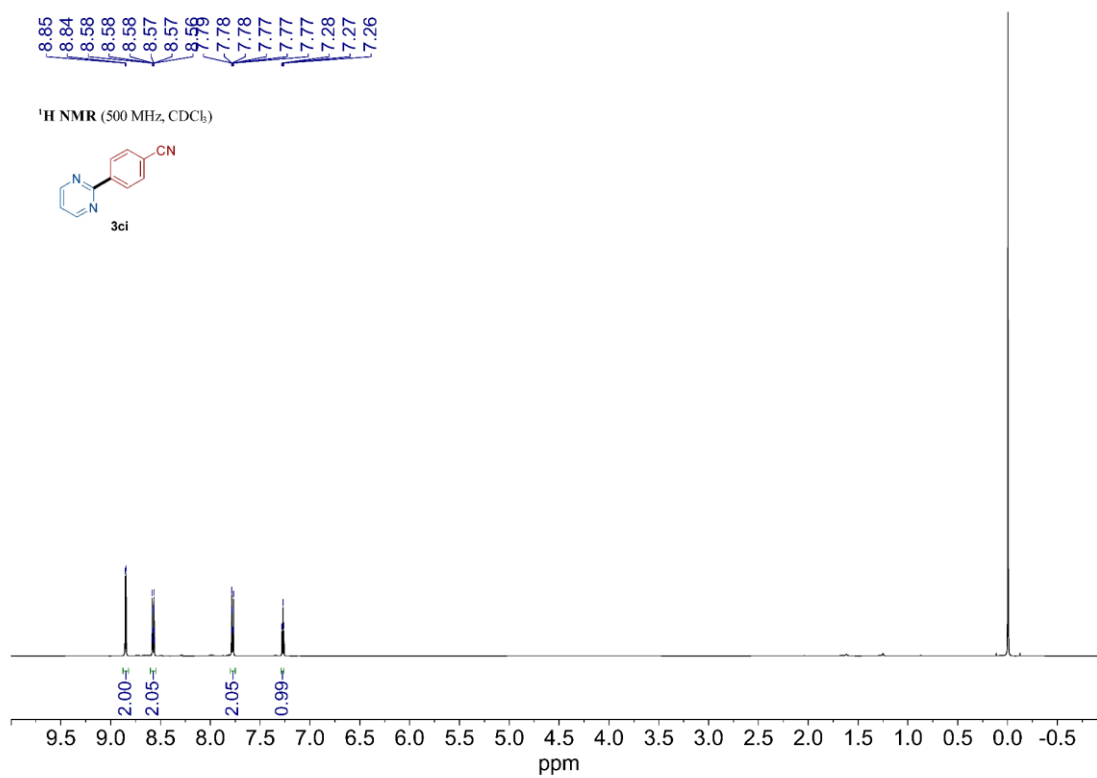
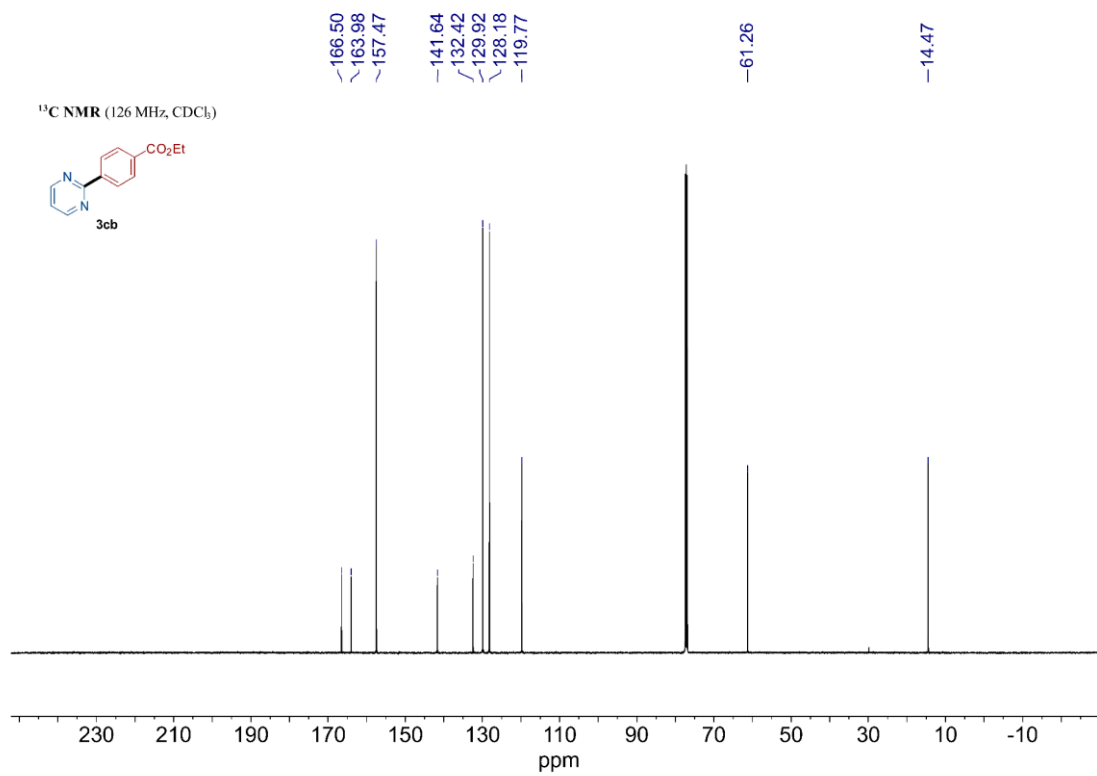


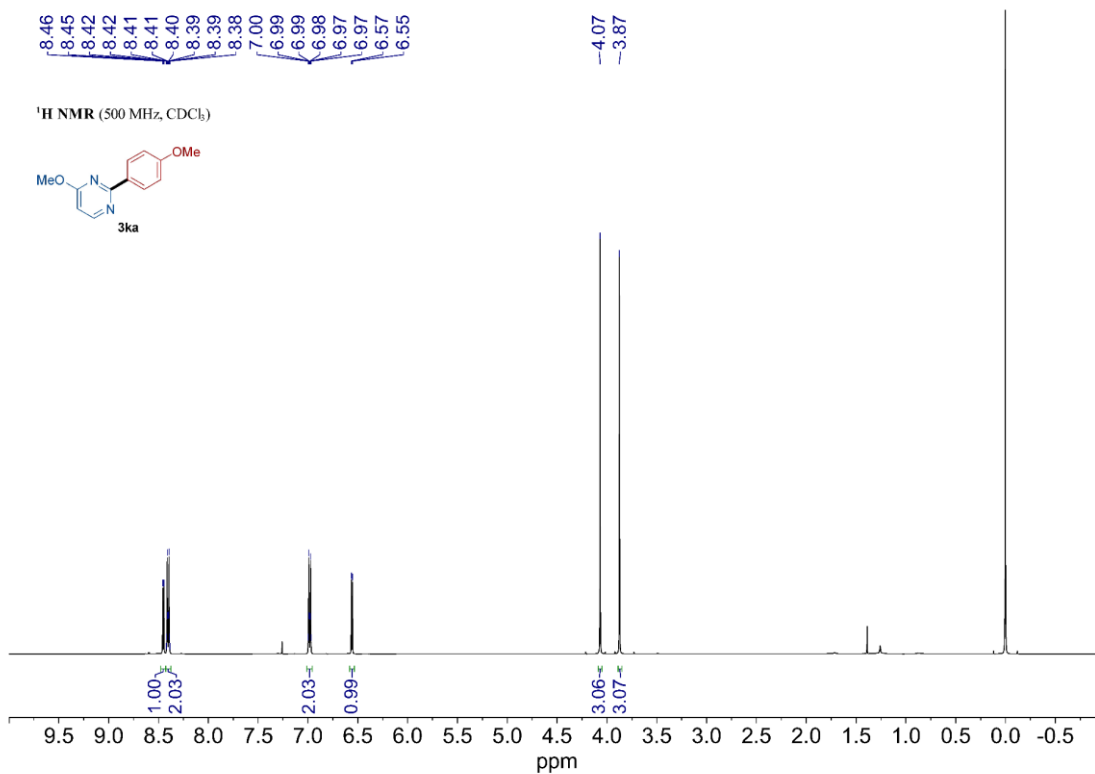
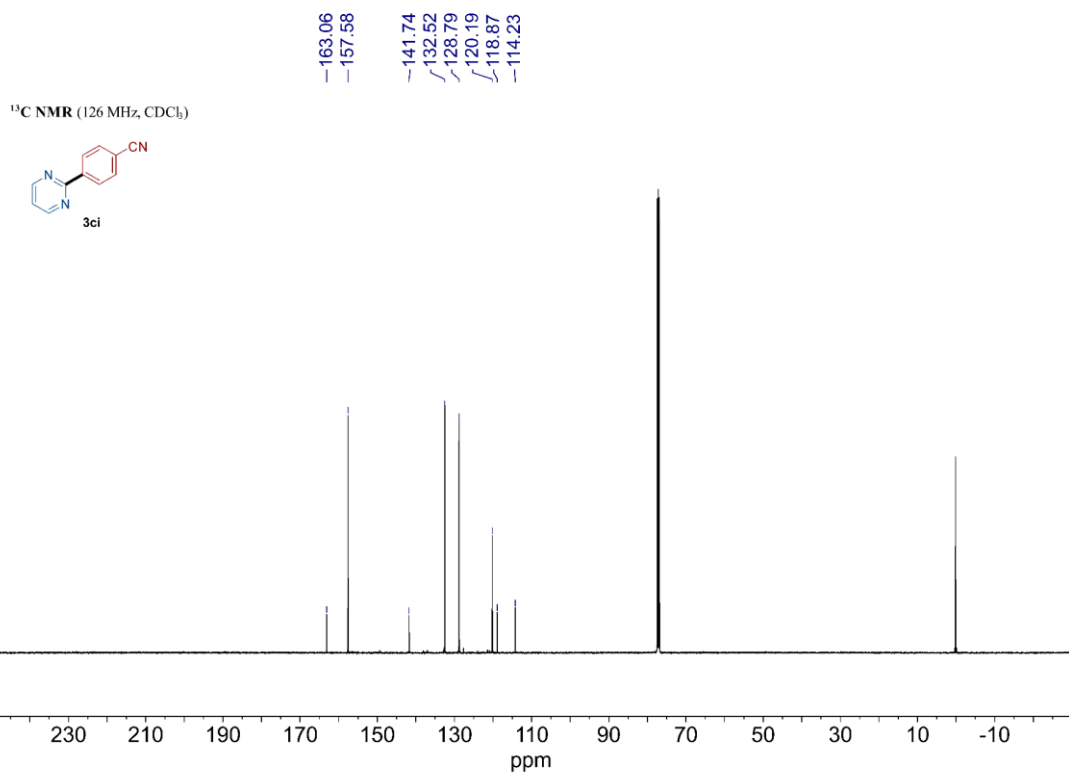
<sup>13</sup>C NMR (126 MHz, CDCl<sub>3</sub>)

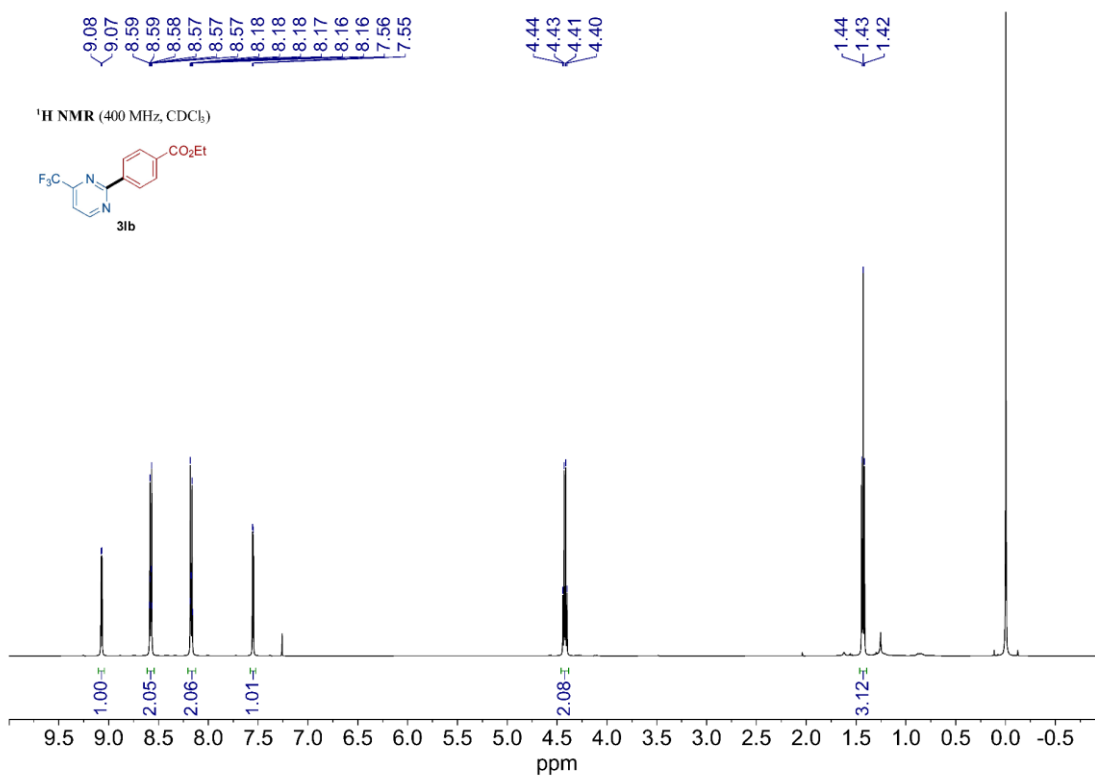
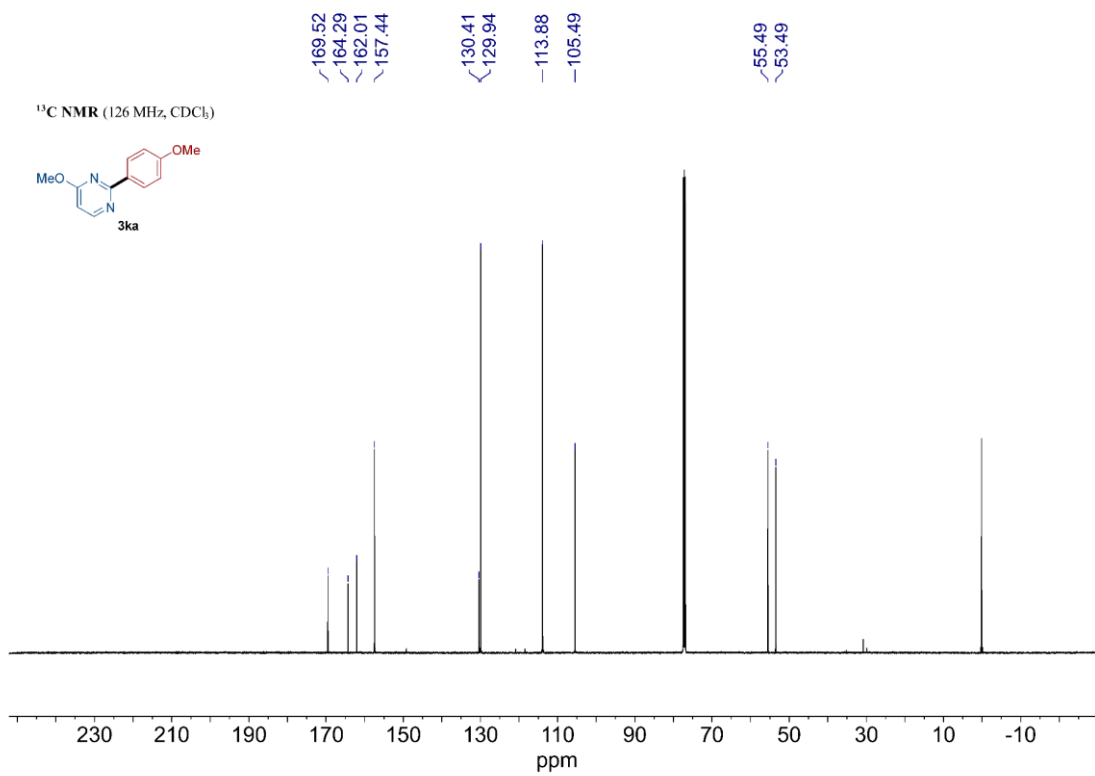
8.82, 8.81, 8.47, 8.46, 8.46, 8.46, 8.45, 8.45, 8.45, 8.44, 8.44, 8.43, 8.42, 7.52, 7.52, 7.51, 7.51, 7.51, 7.51, 7.50, 7.50, 7.49, 7.48, 7.20, 7.19, 7.18

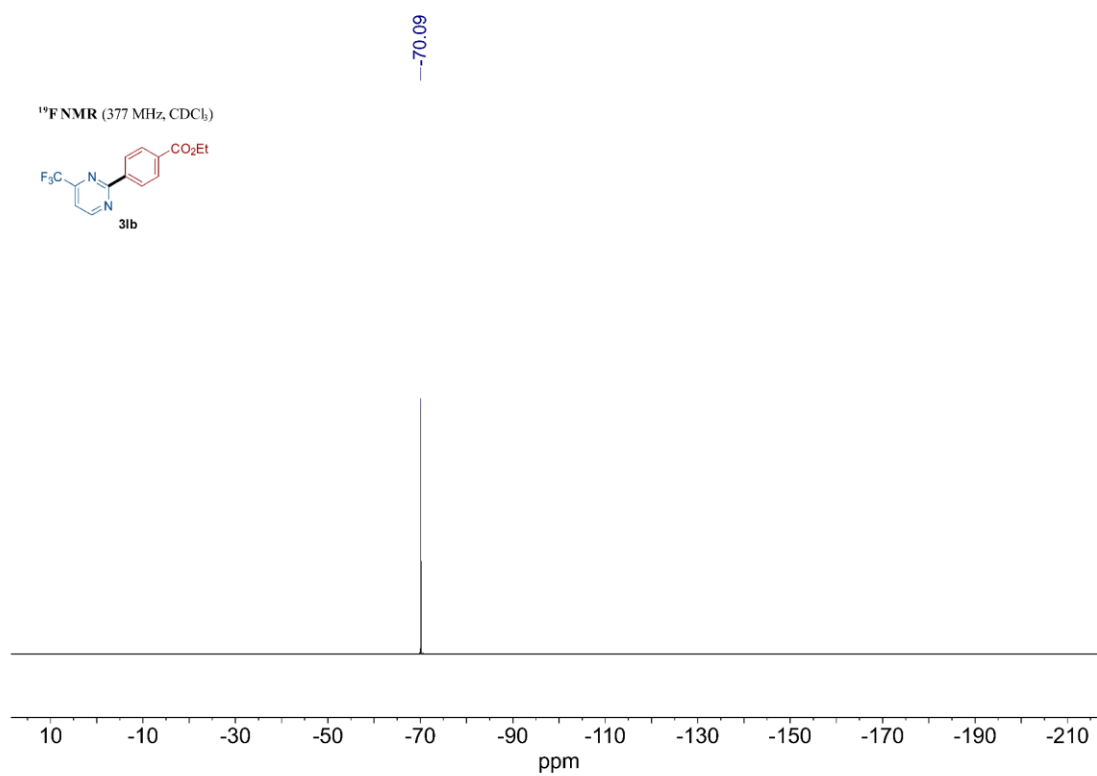
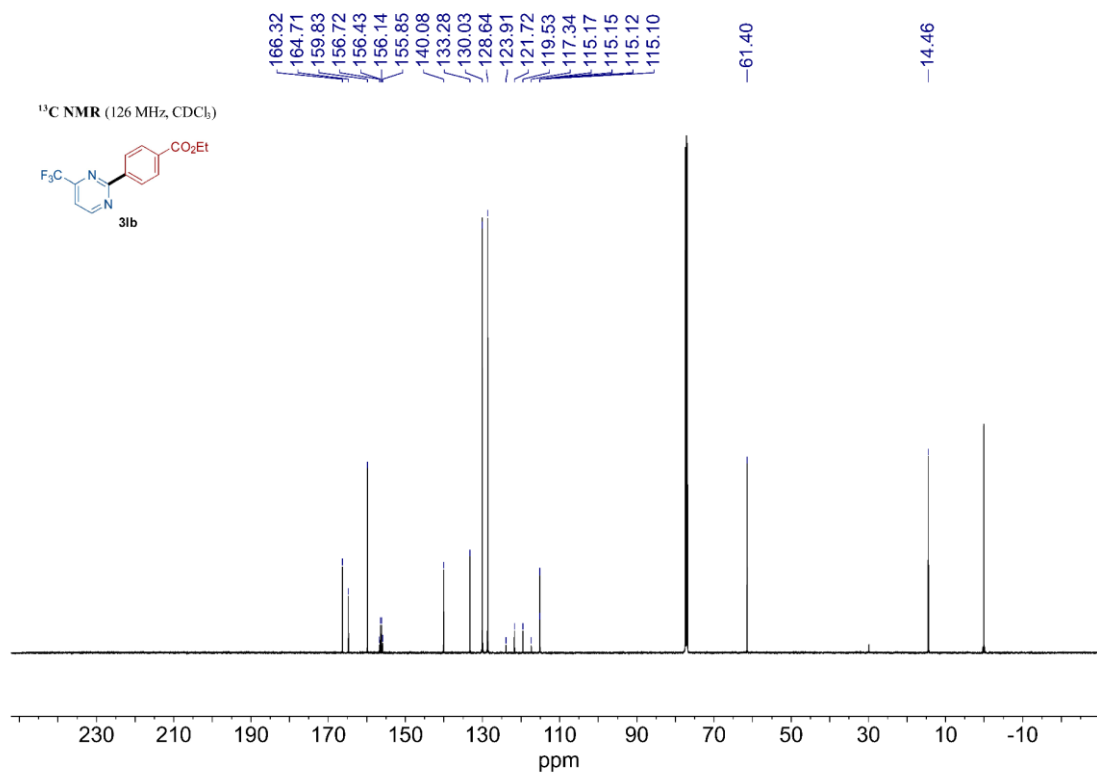
<sup>1</sup>H NMR (500 MHz, CDCl<sub>3</sub>)

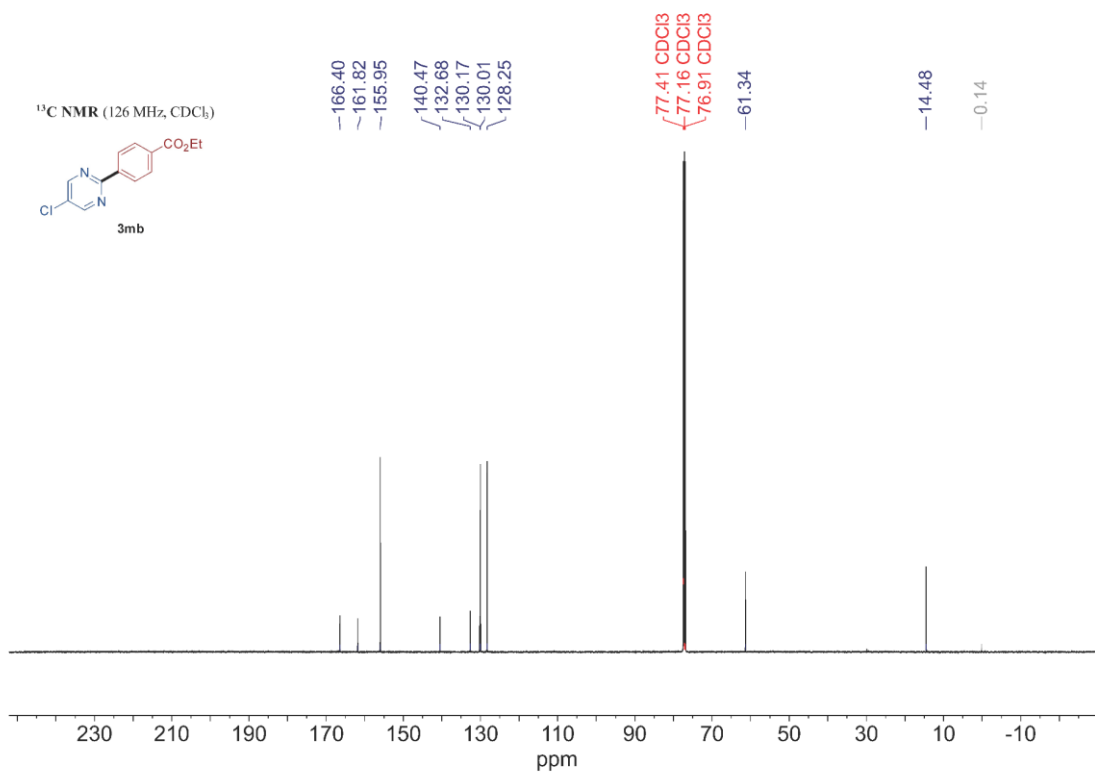
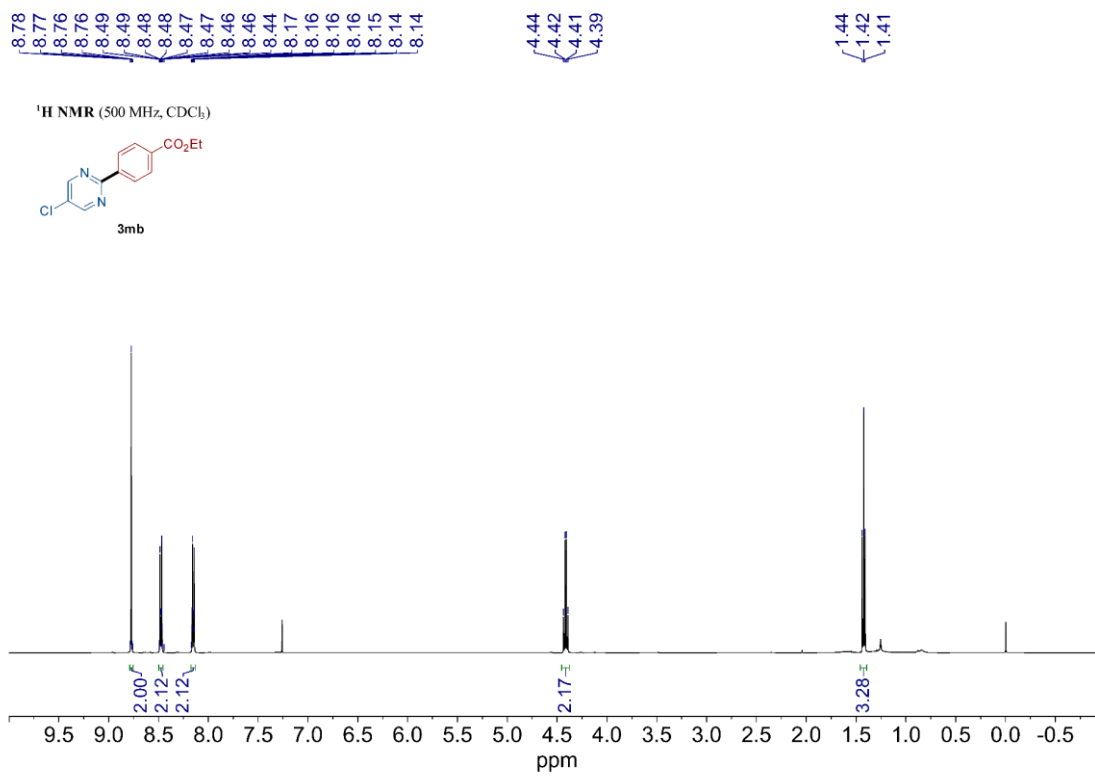


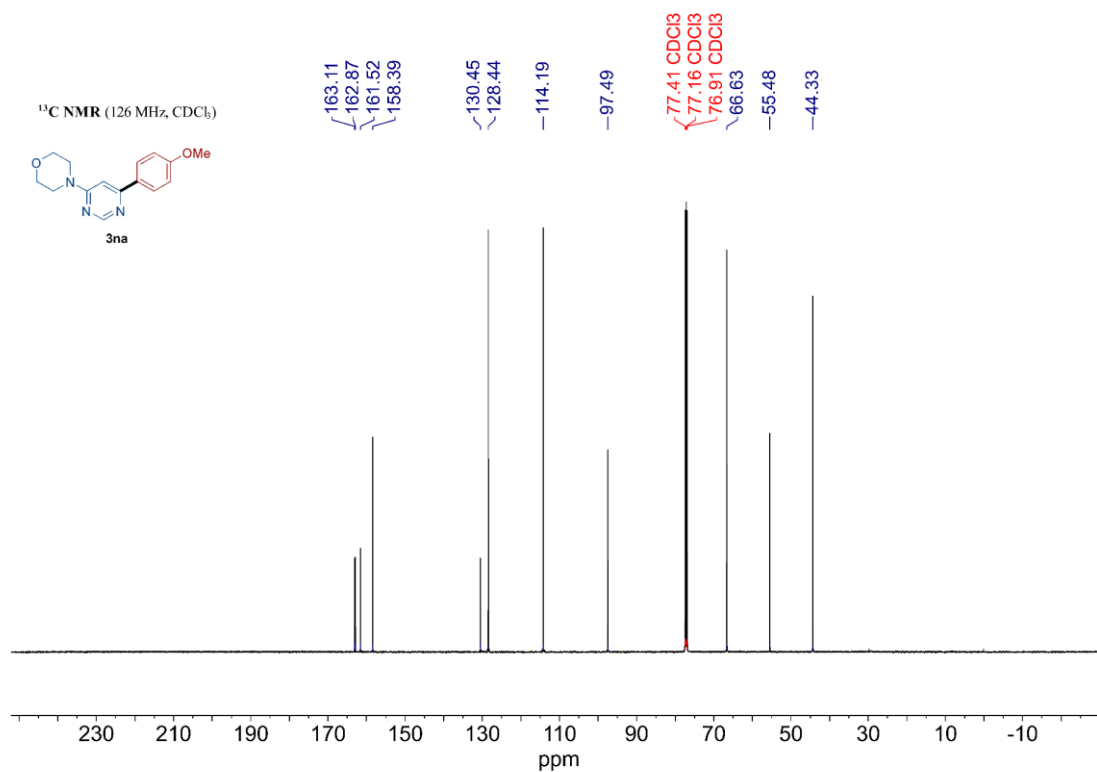
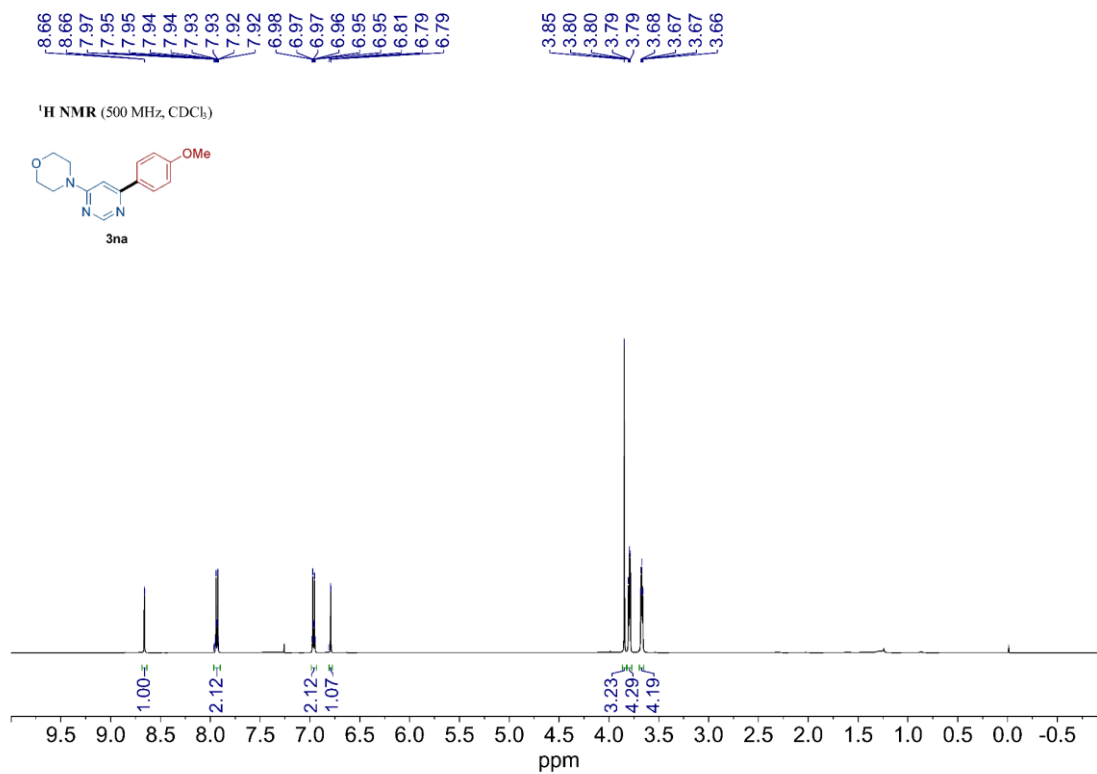


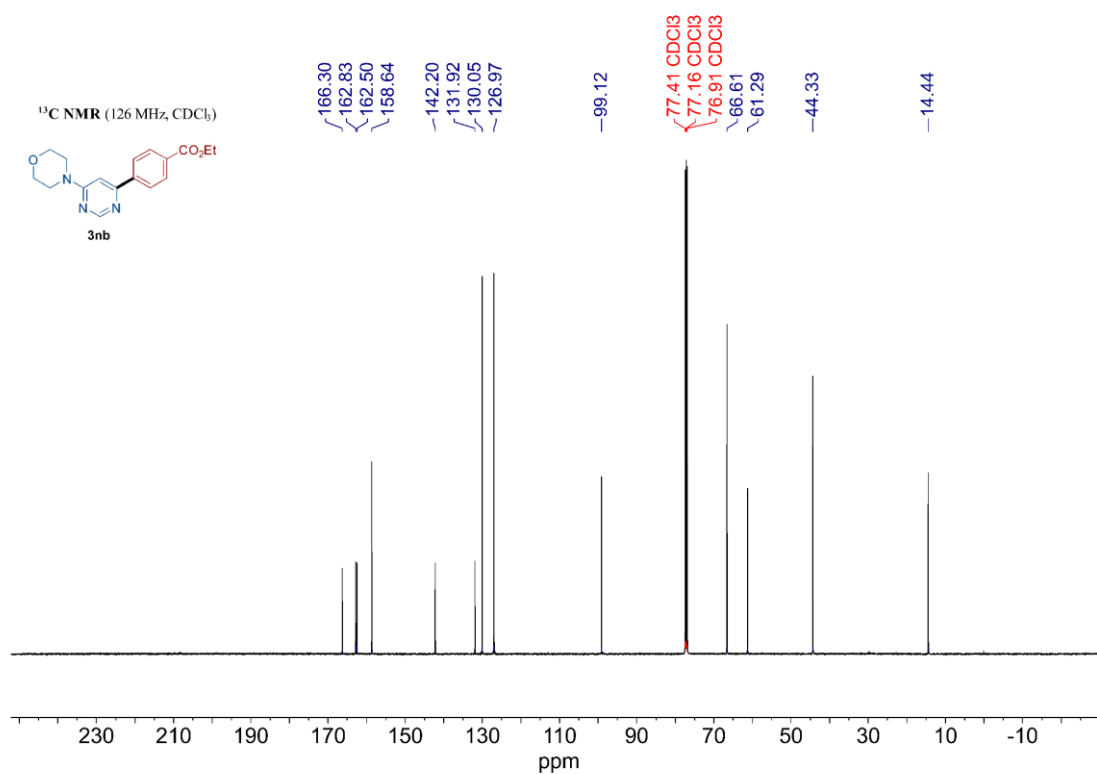
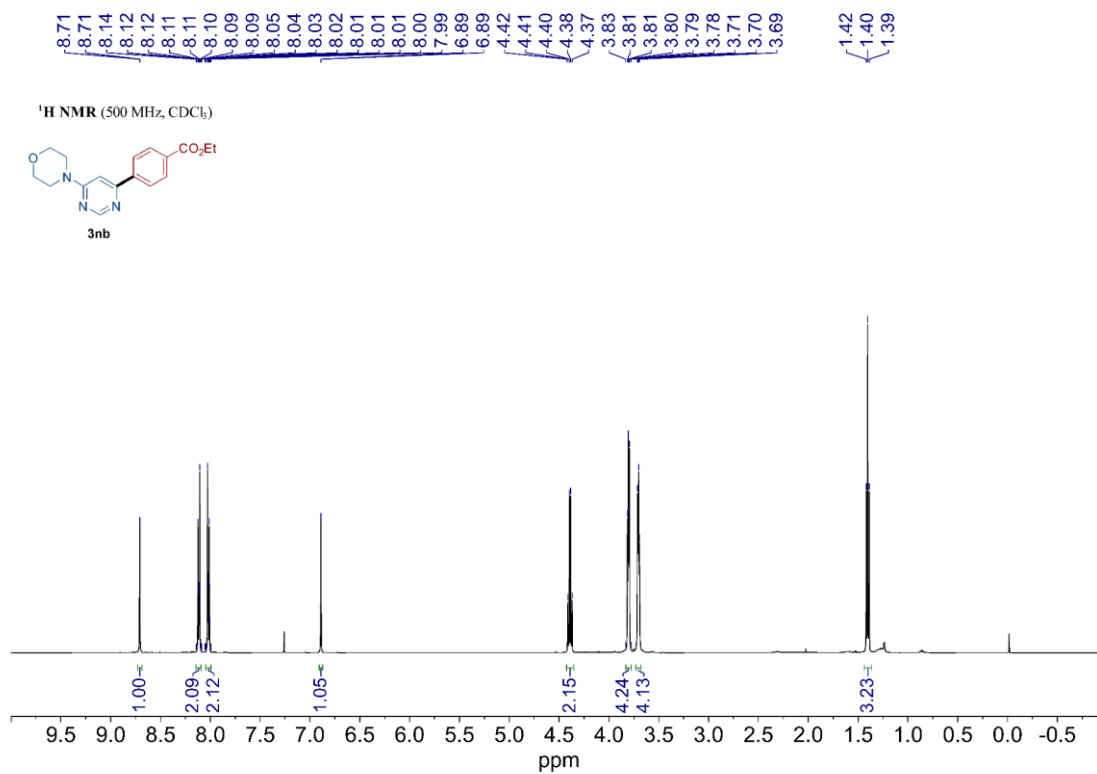


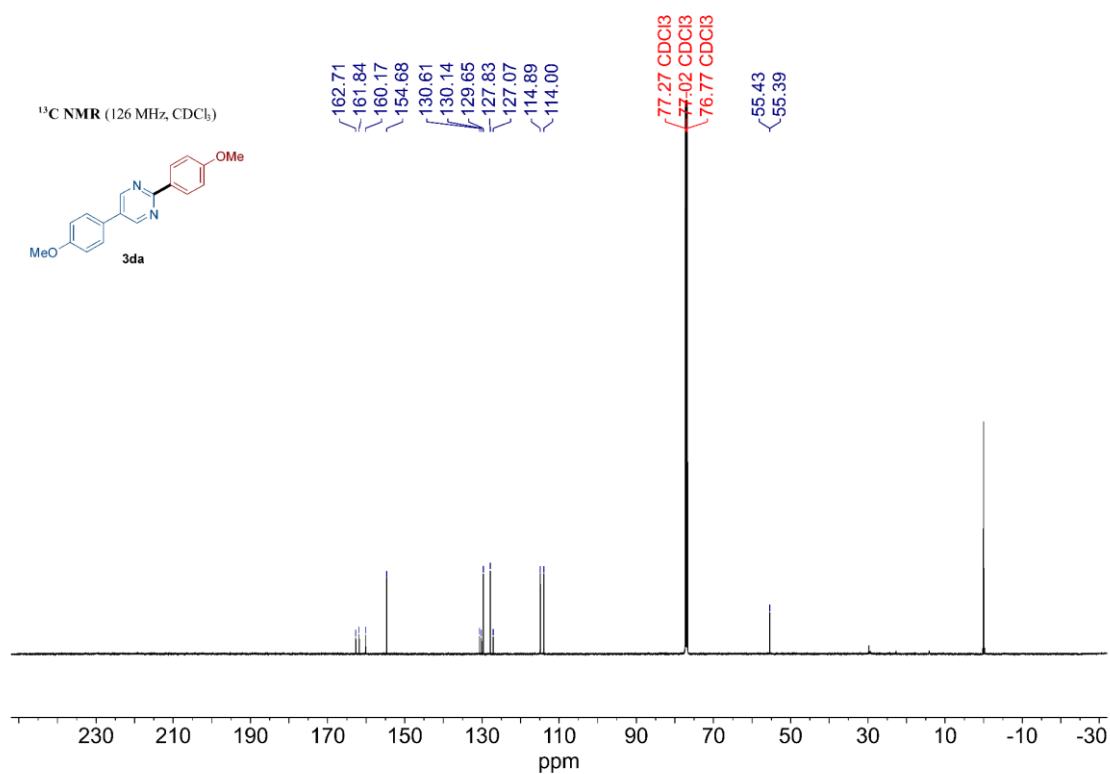
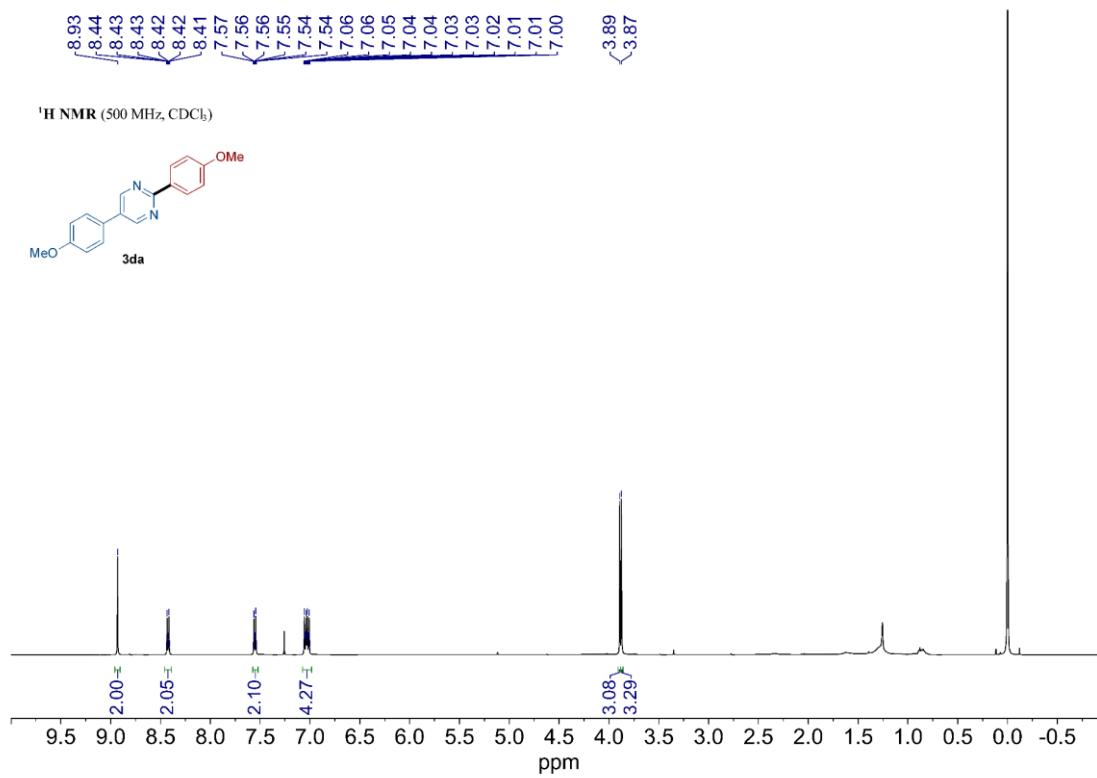


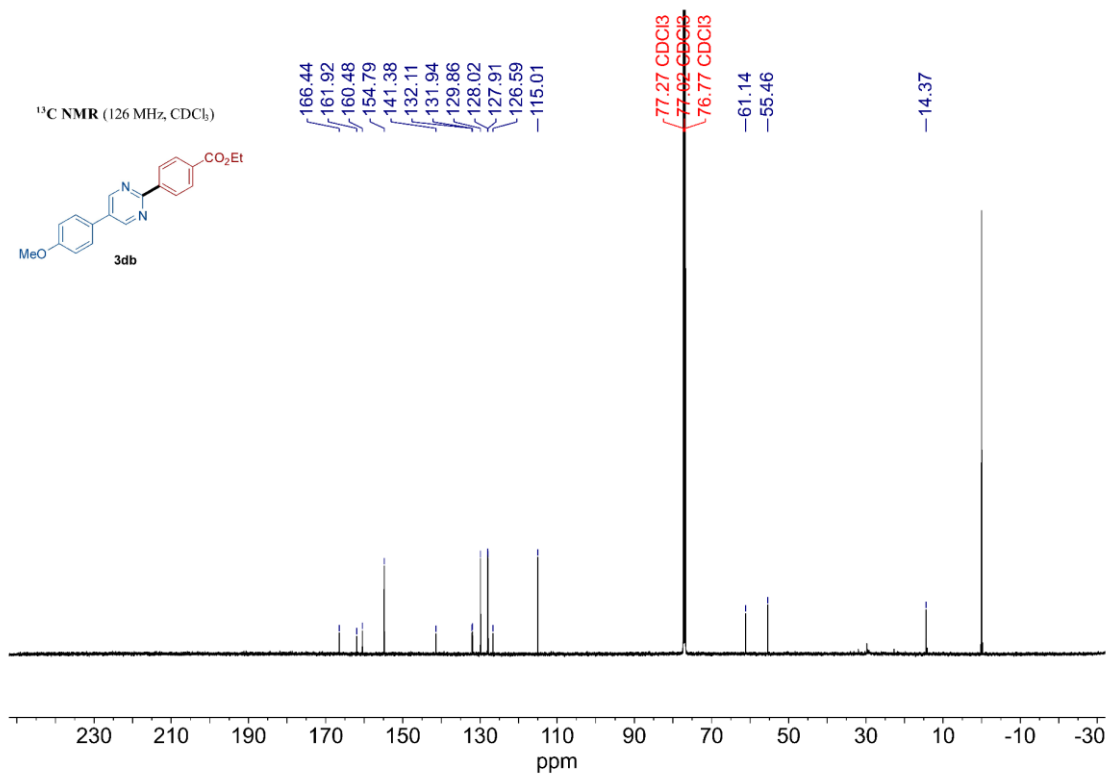
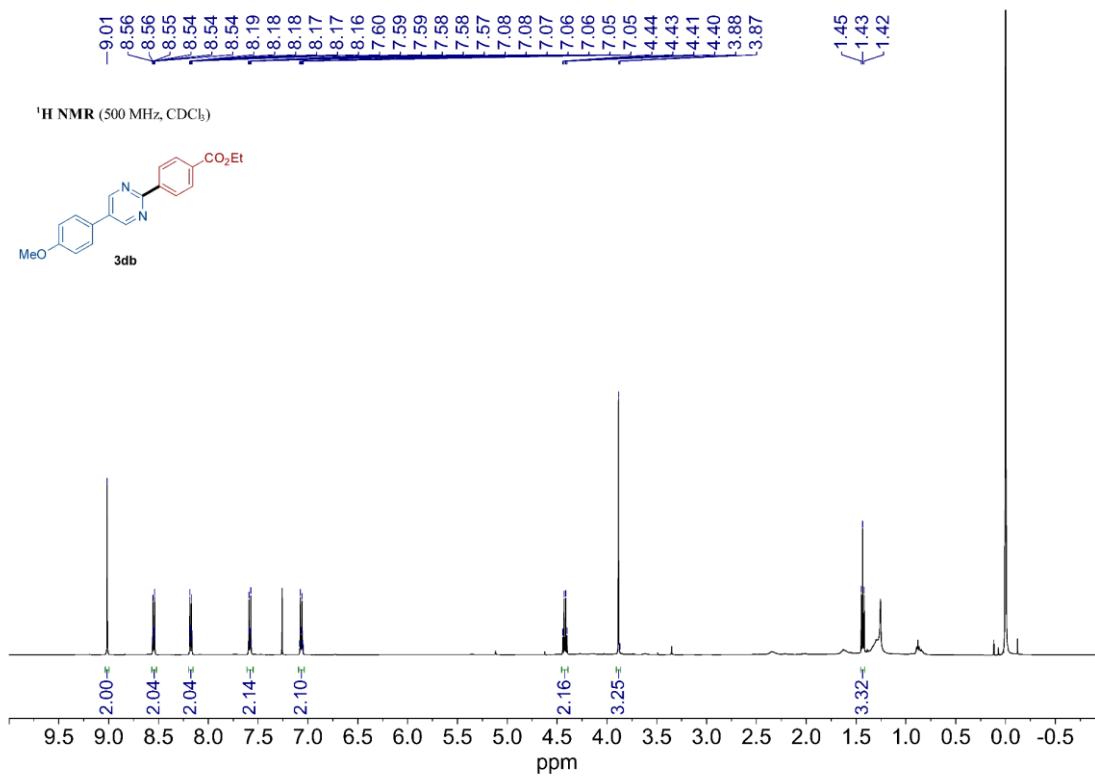


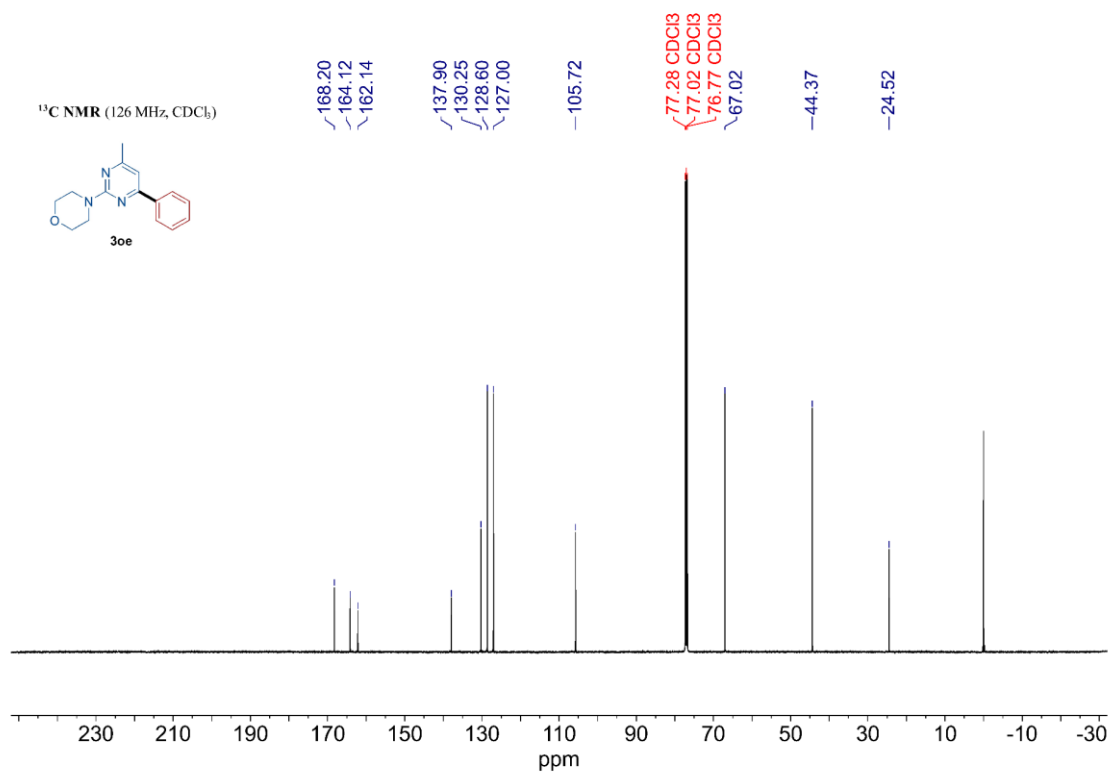
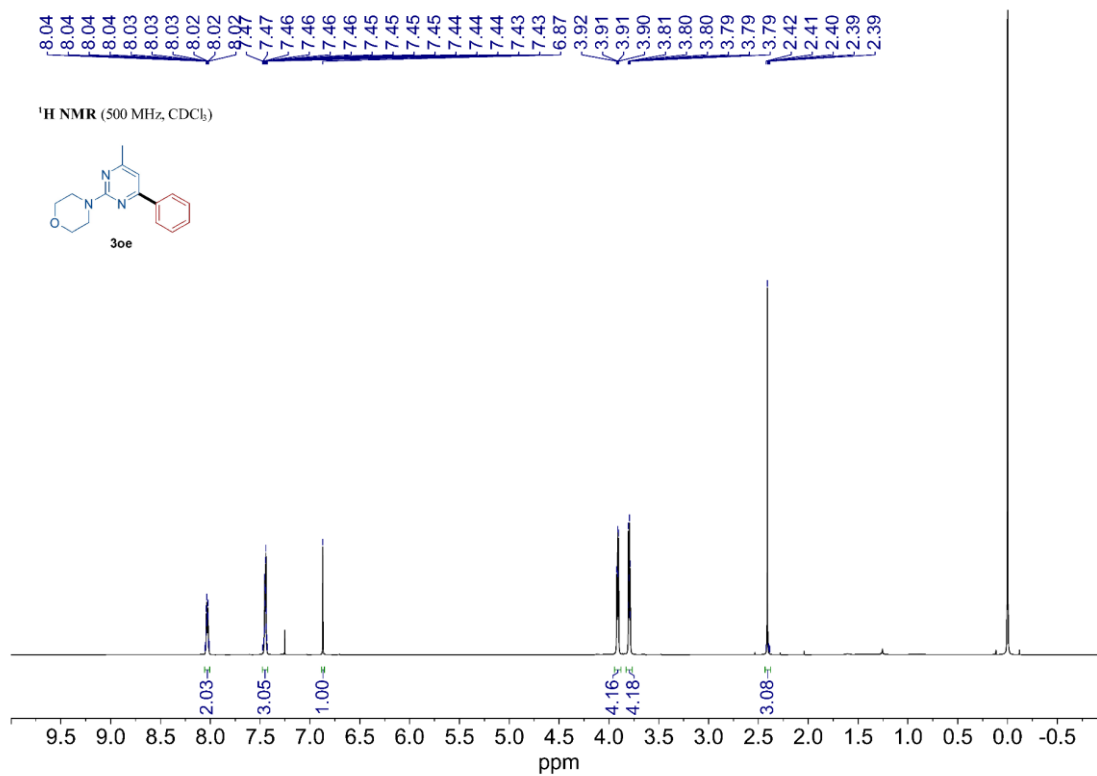


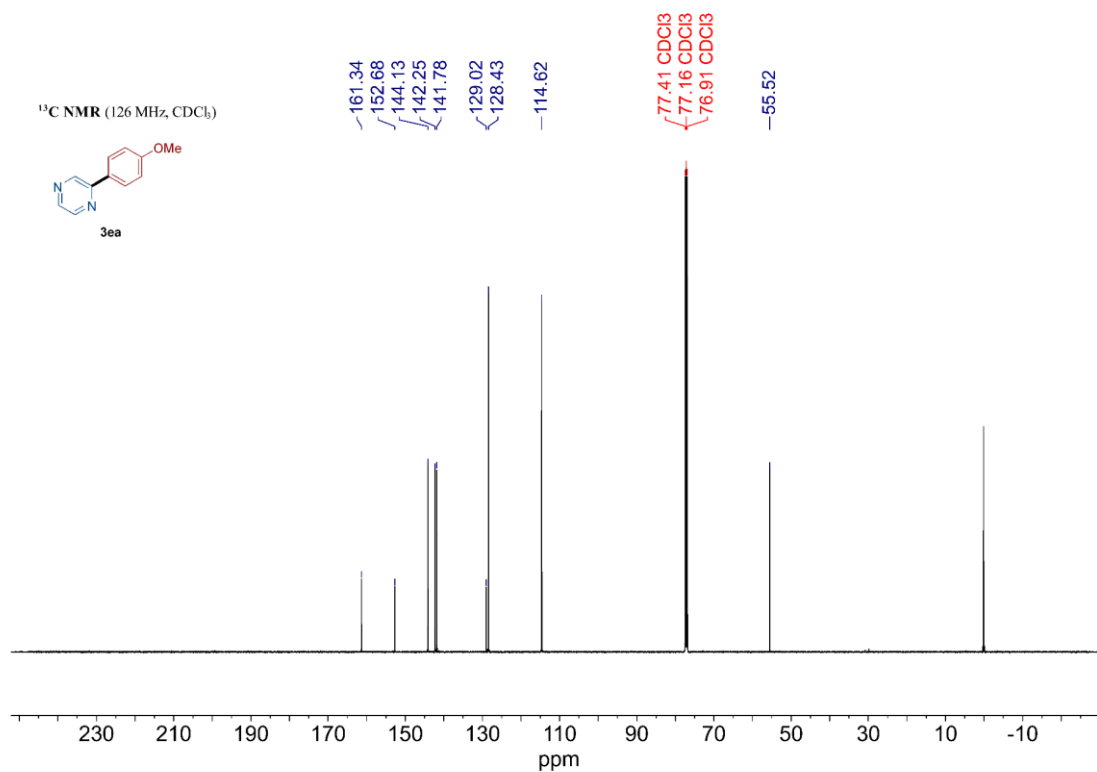
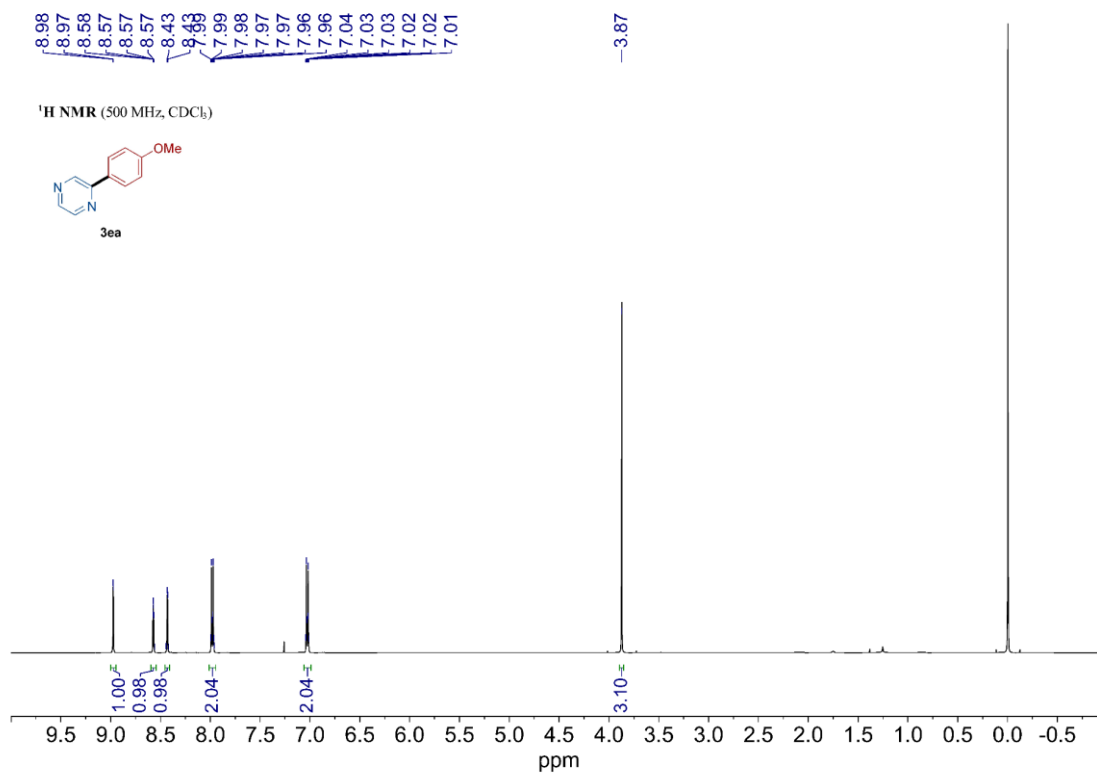


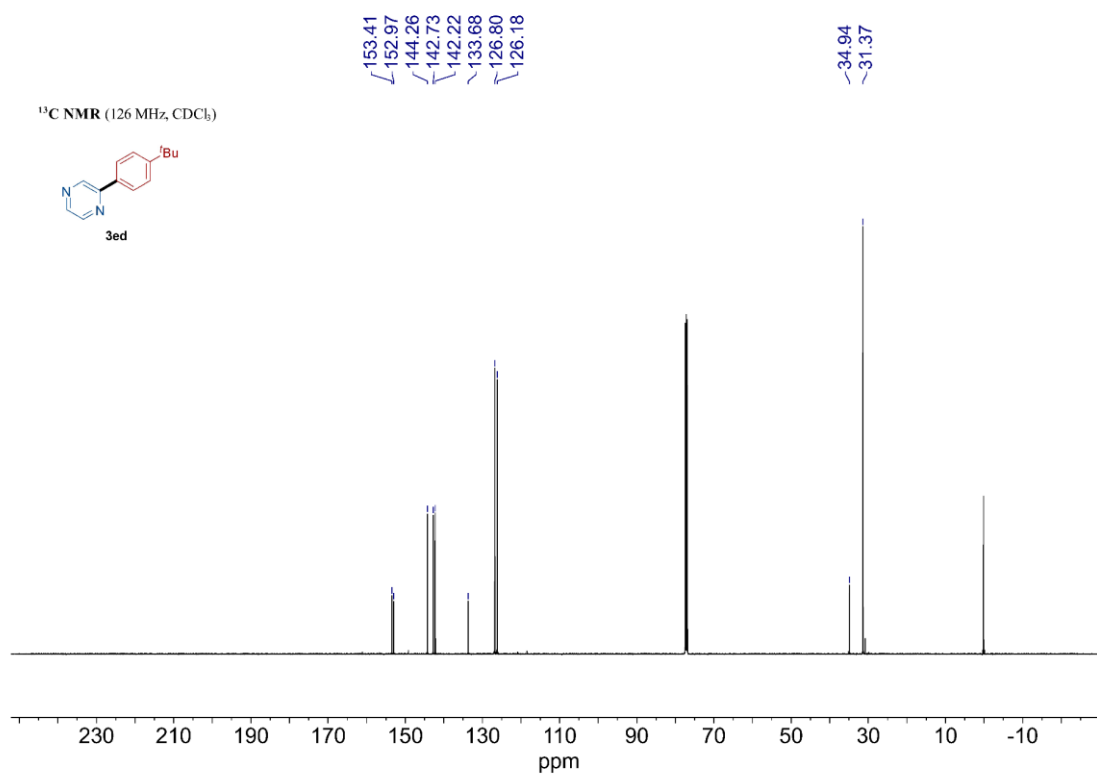
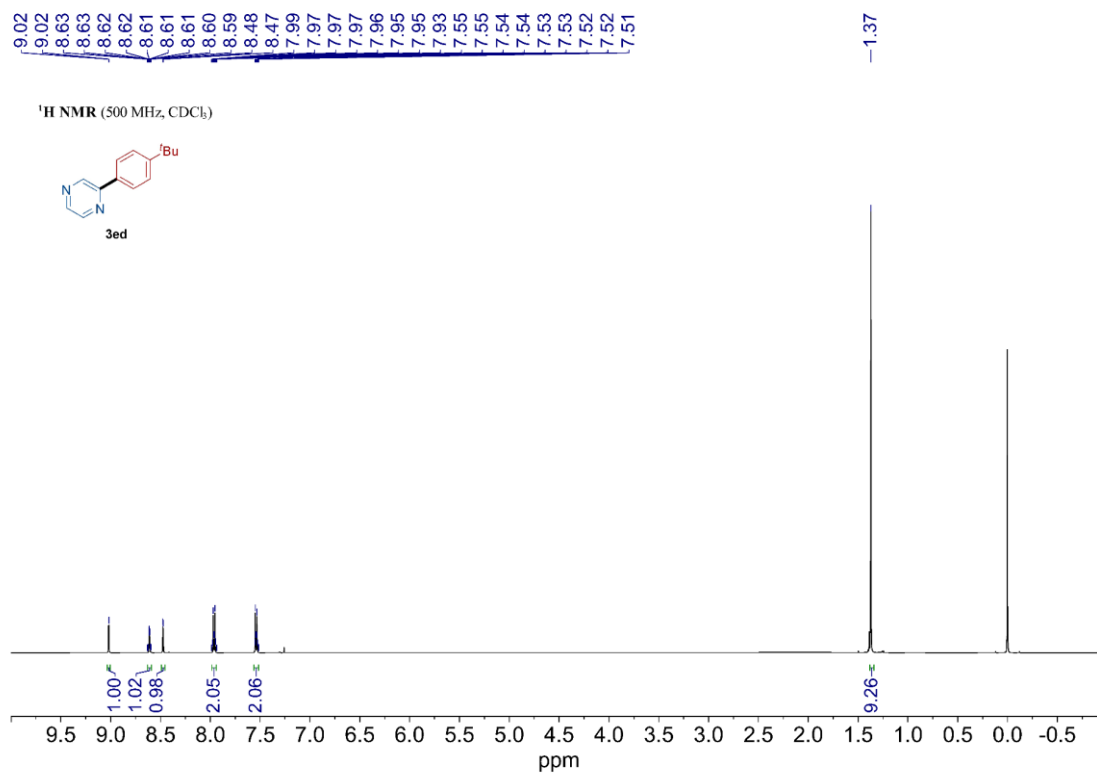


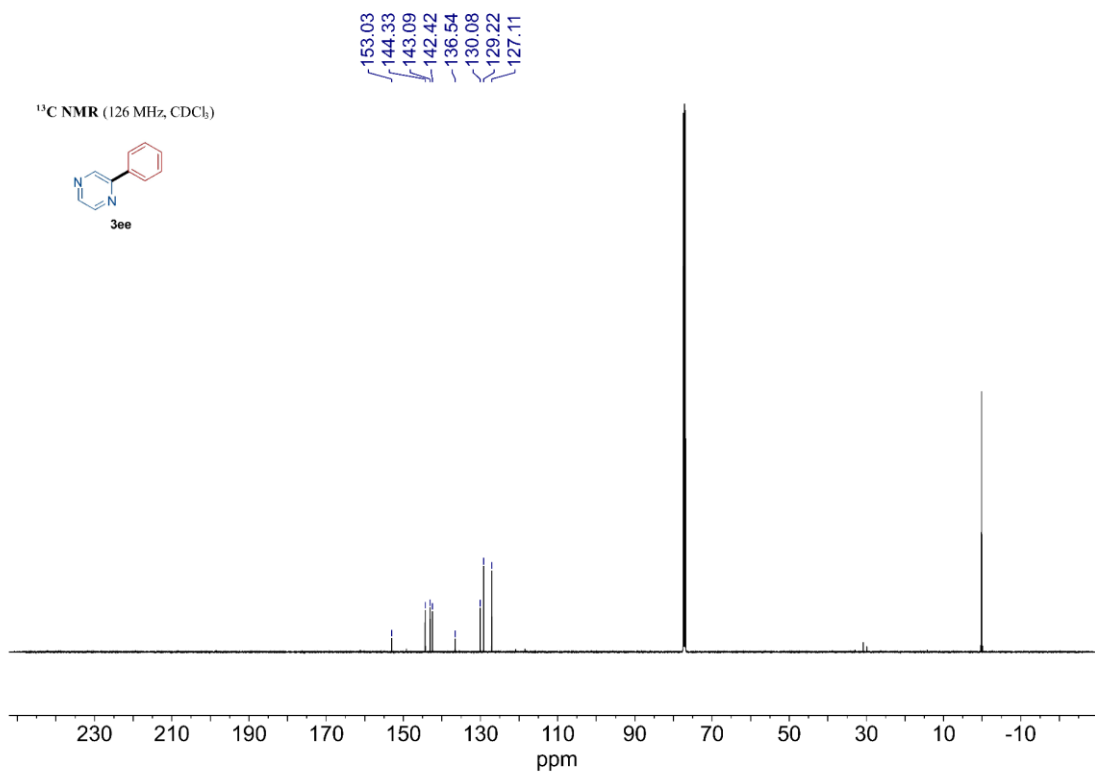
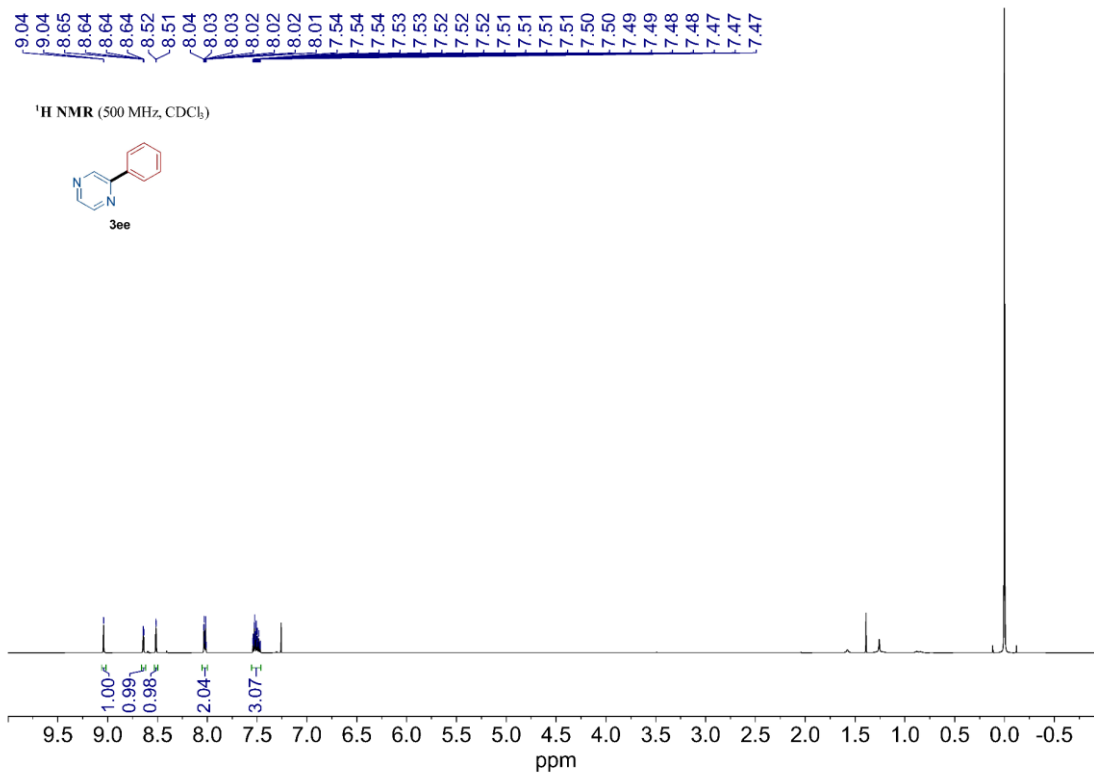


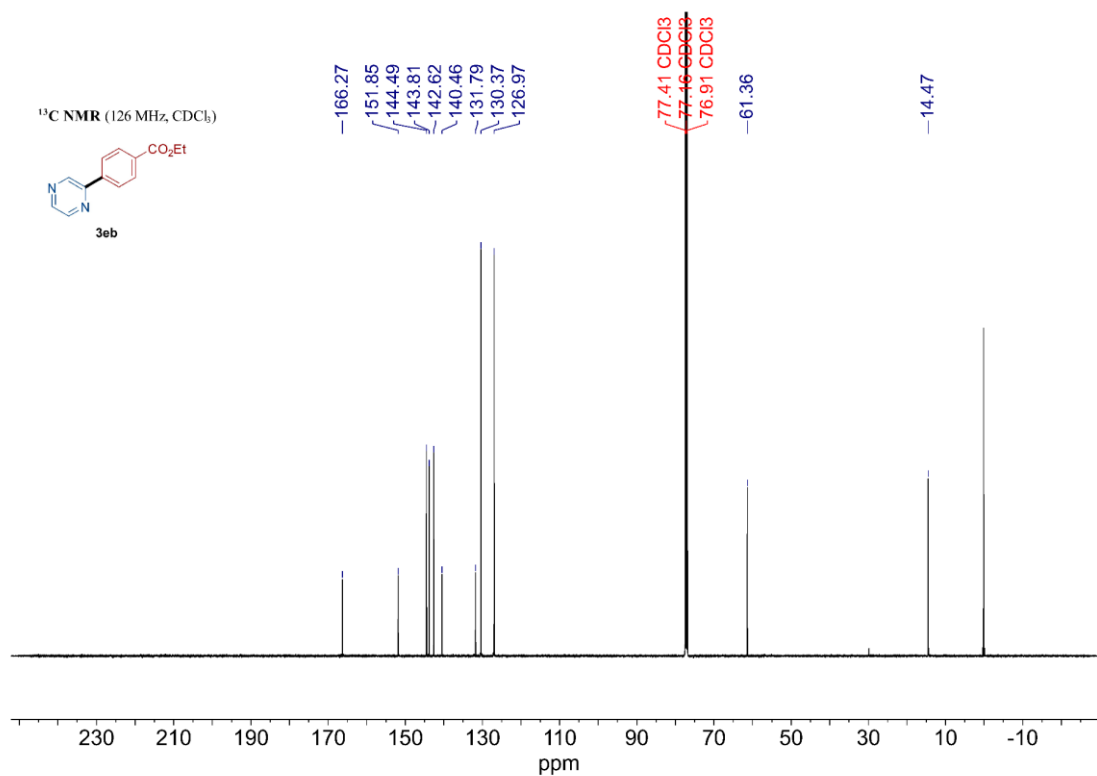
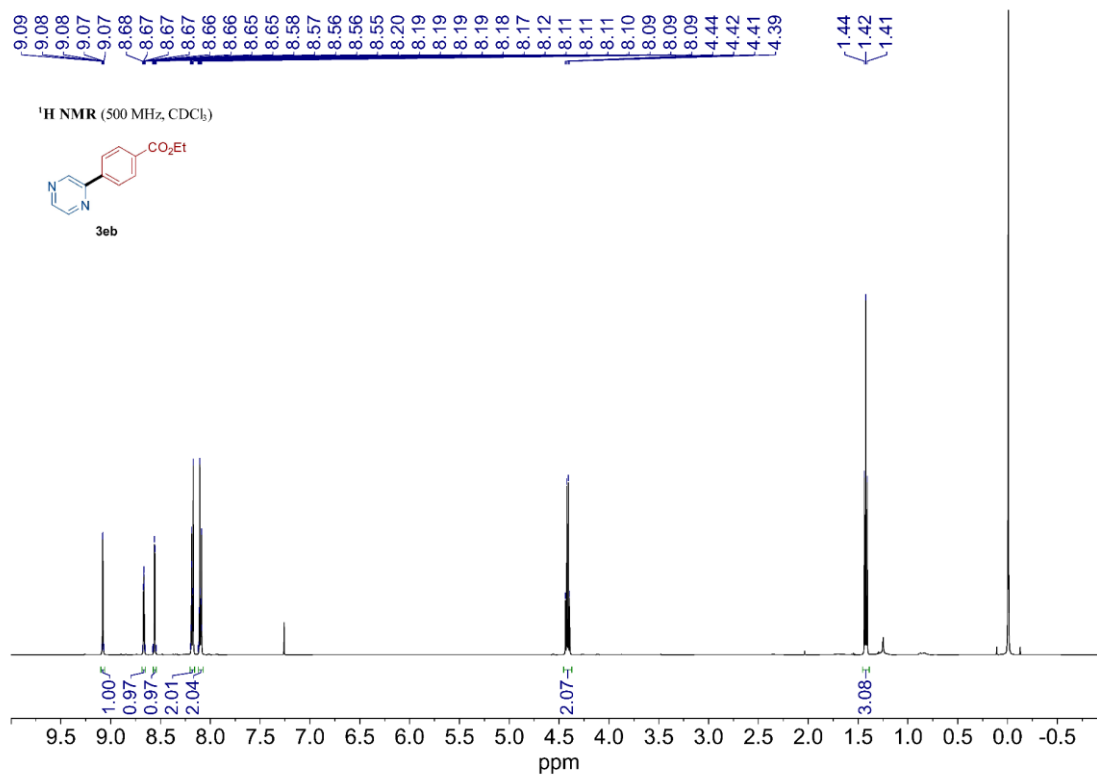


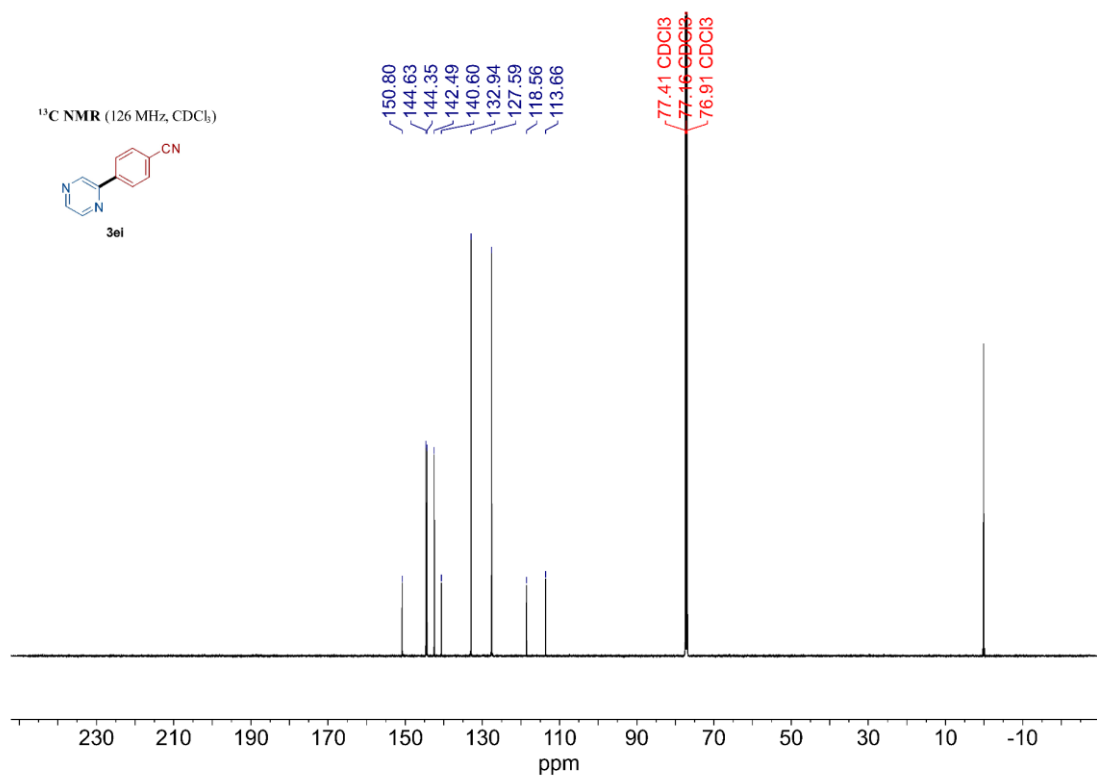
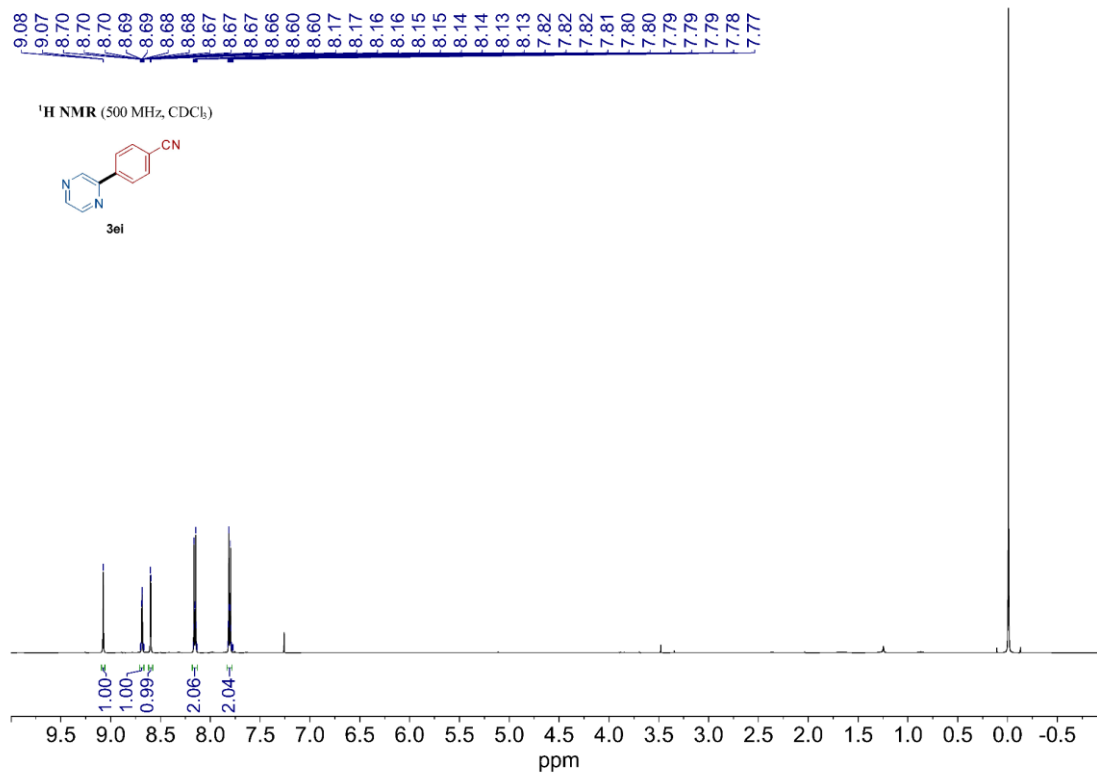


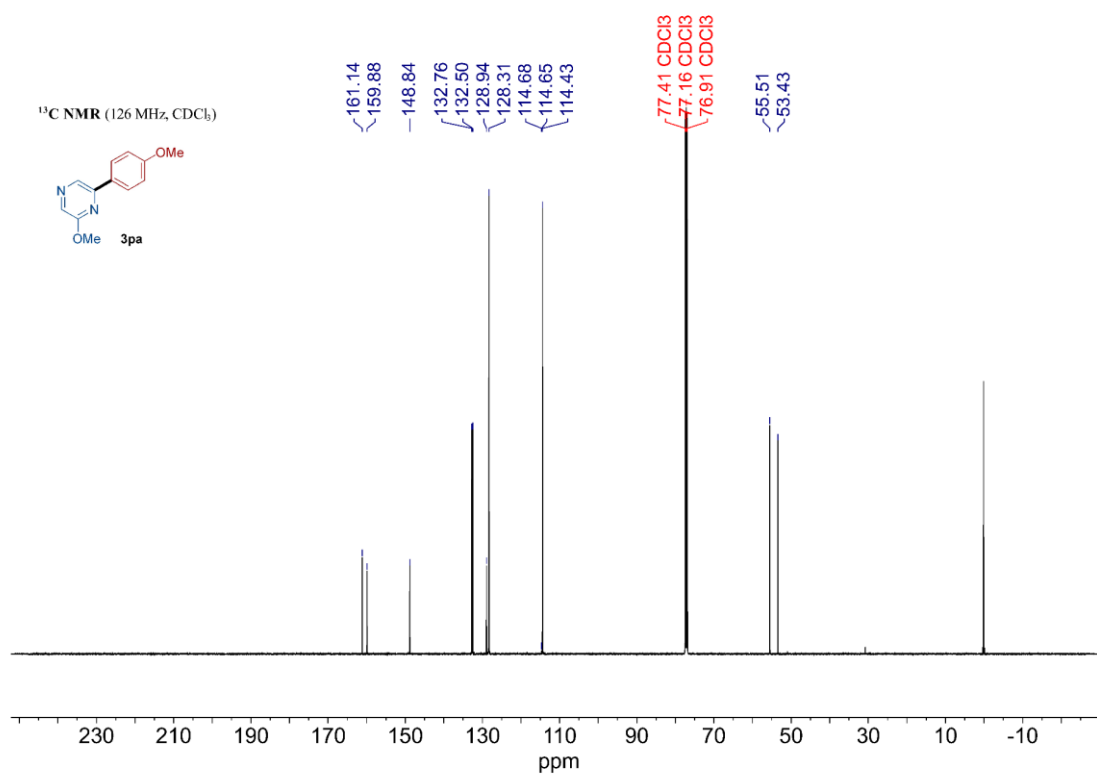
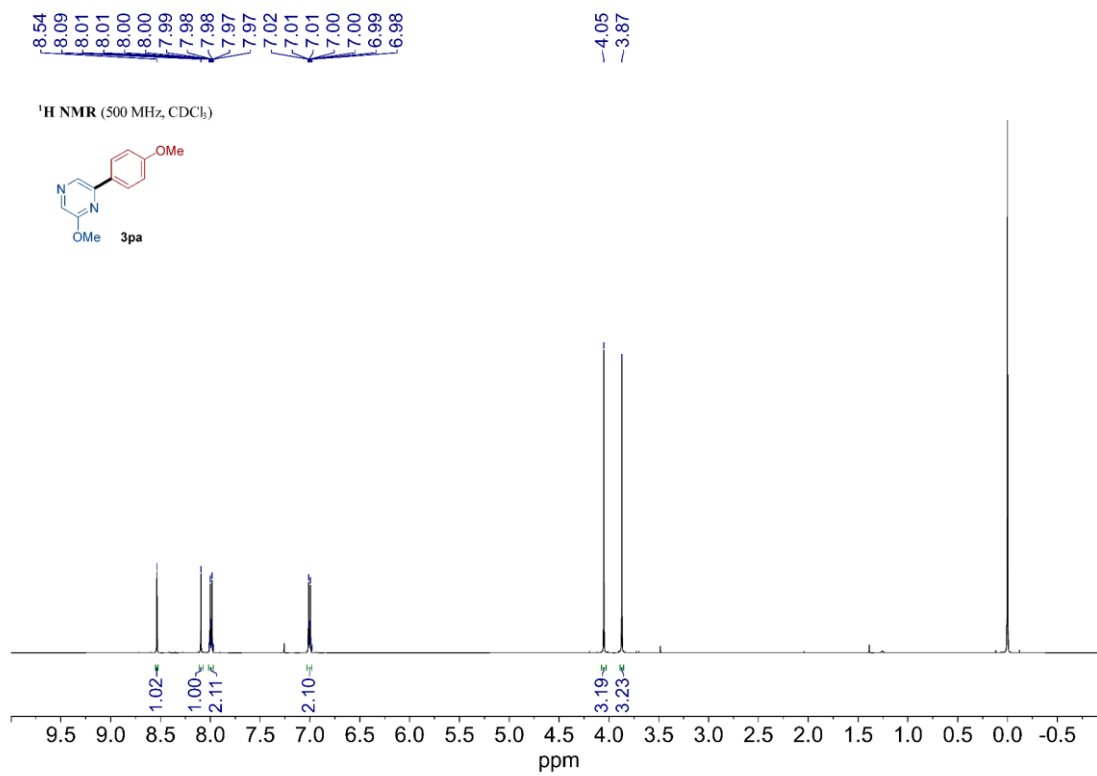


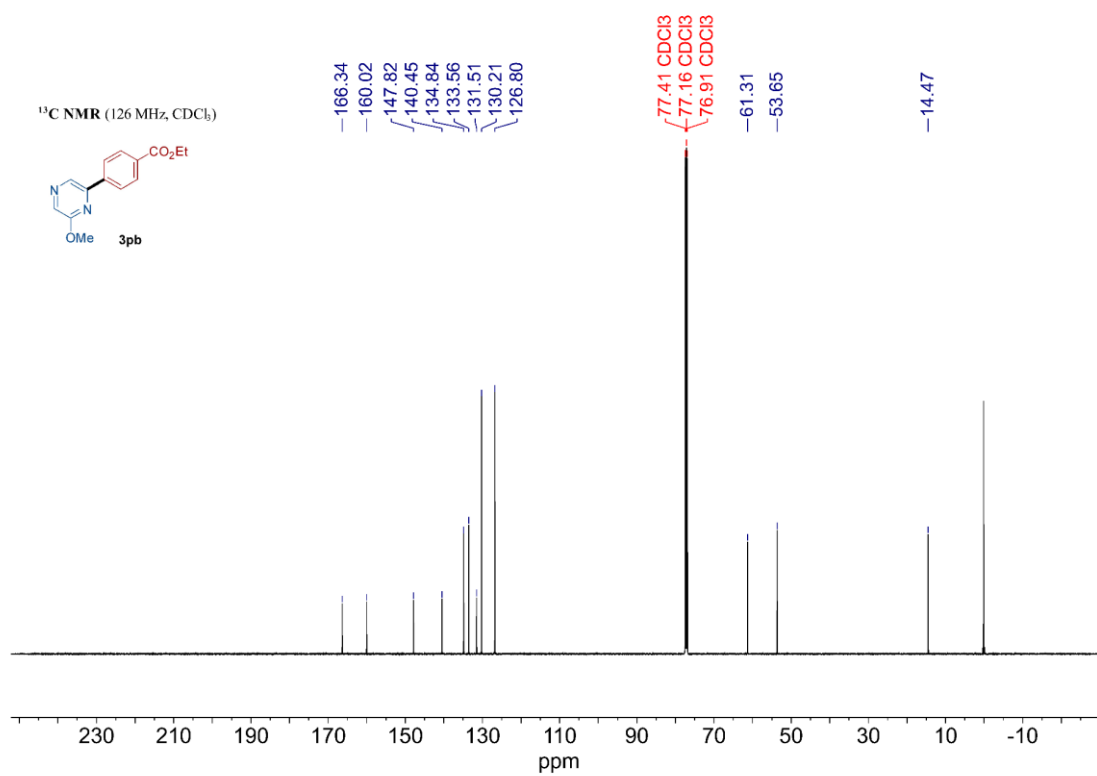
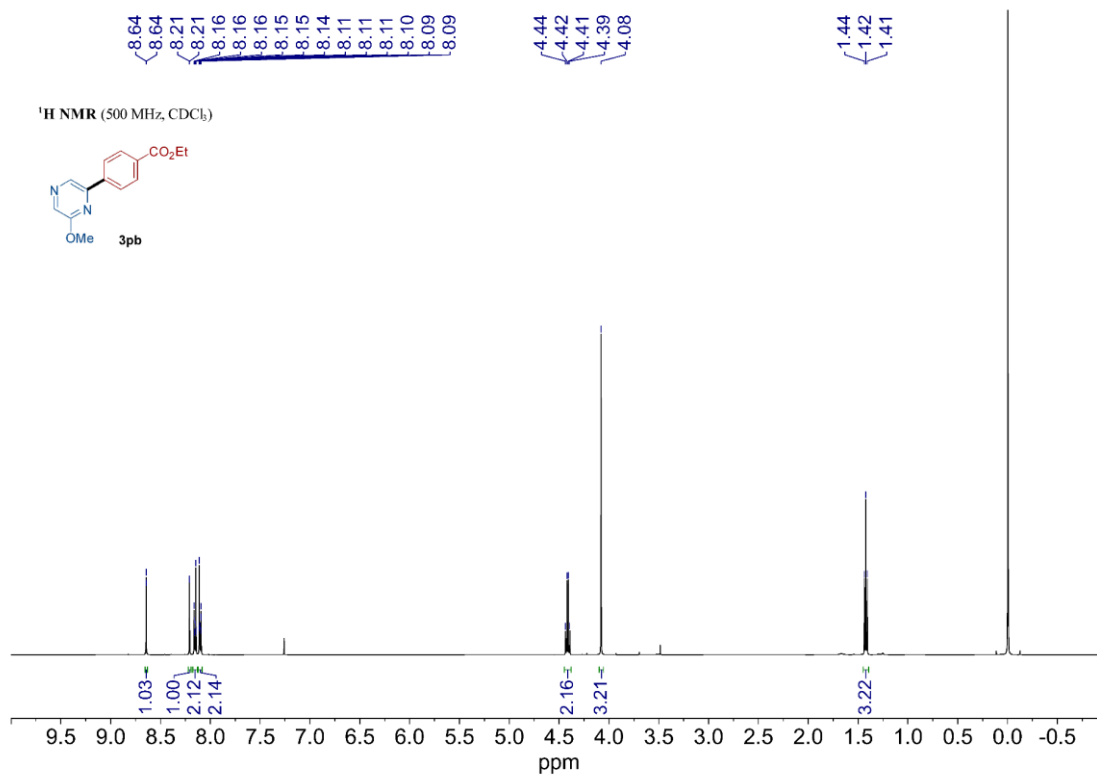


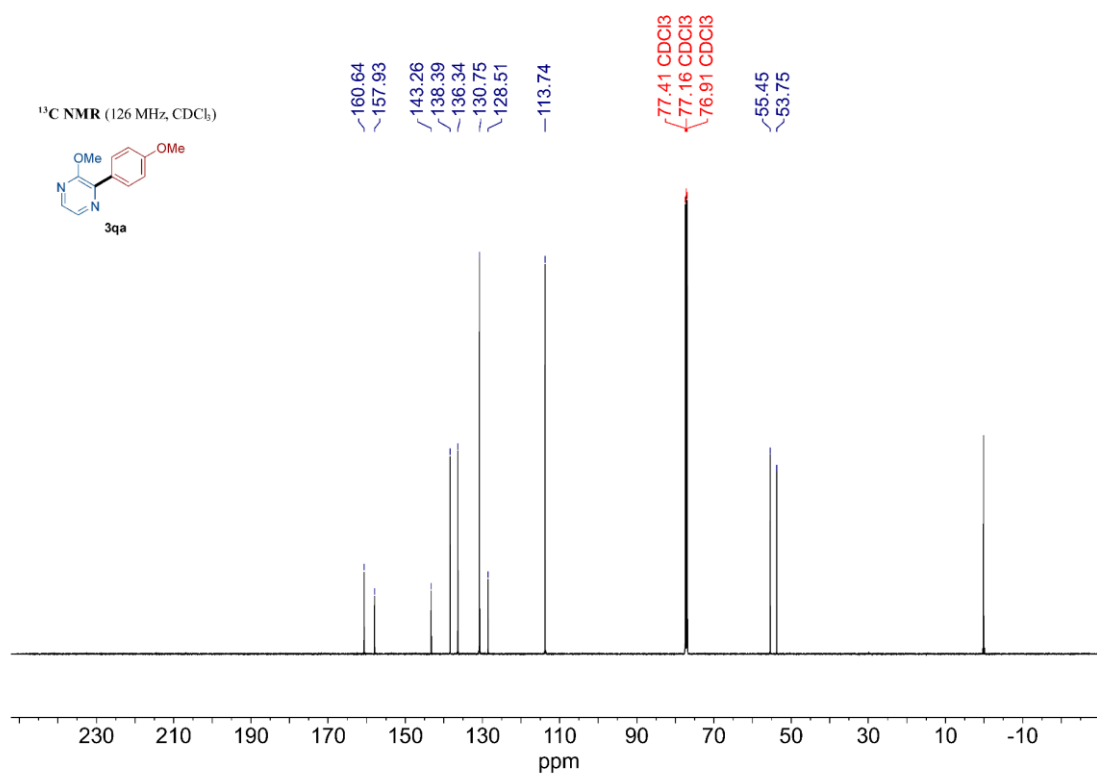
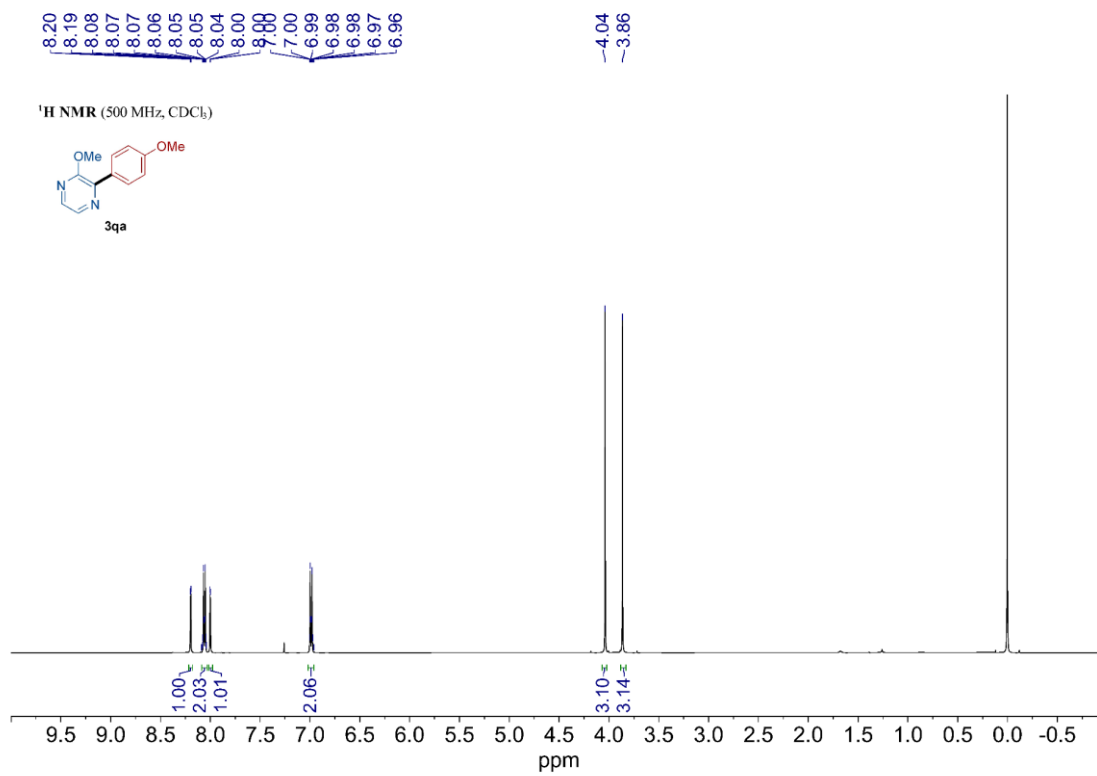


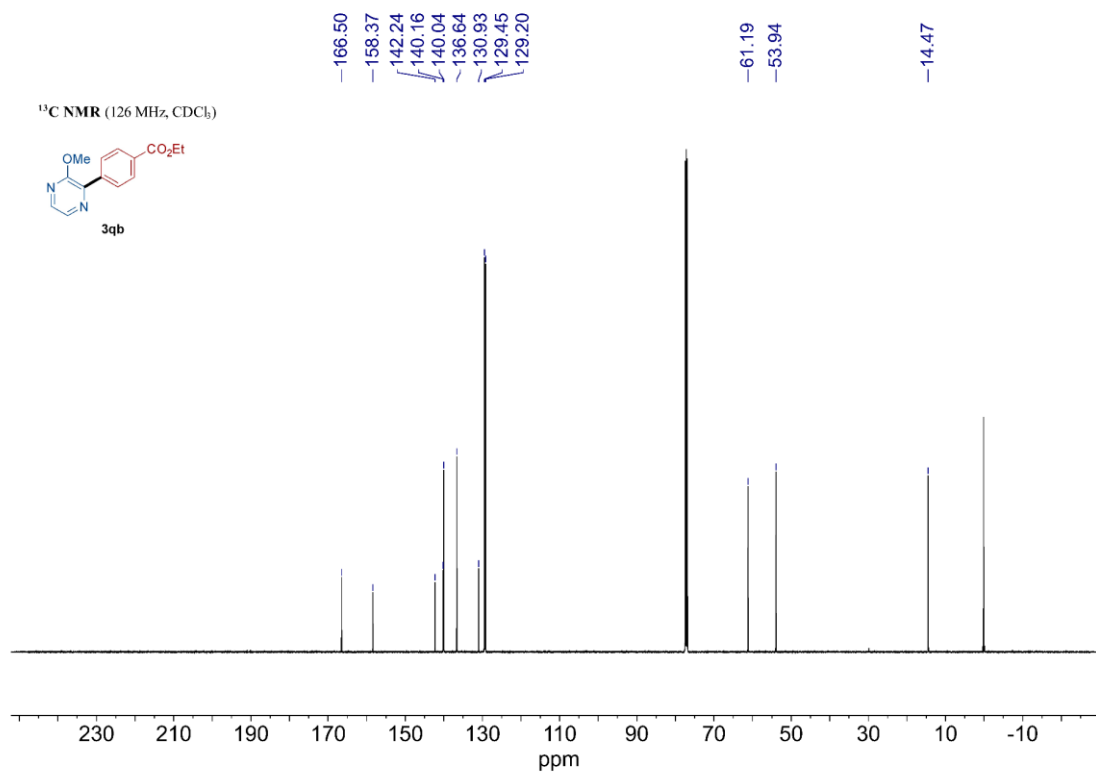
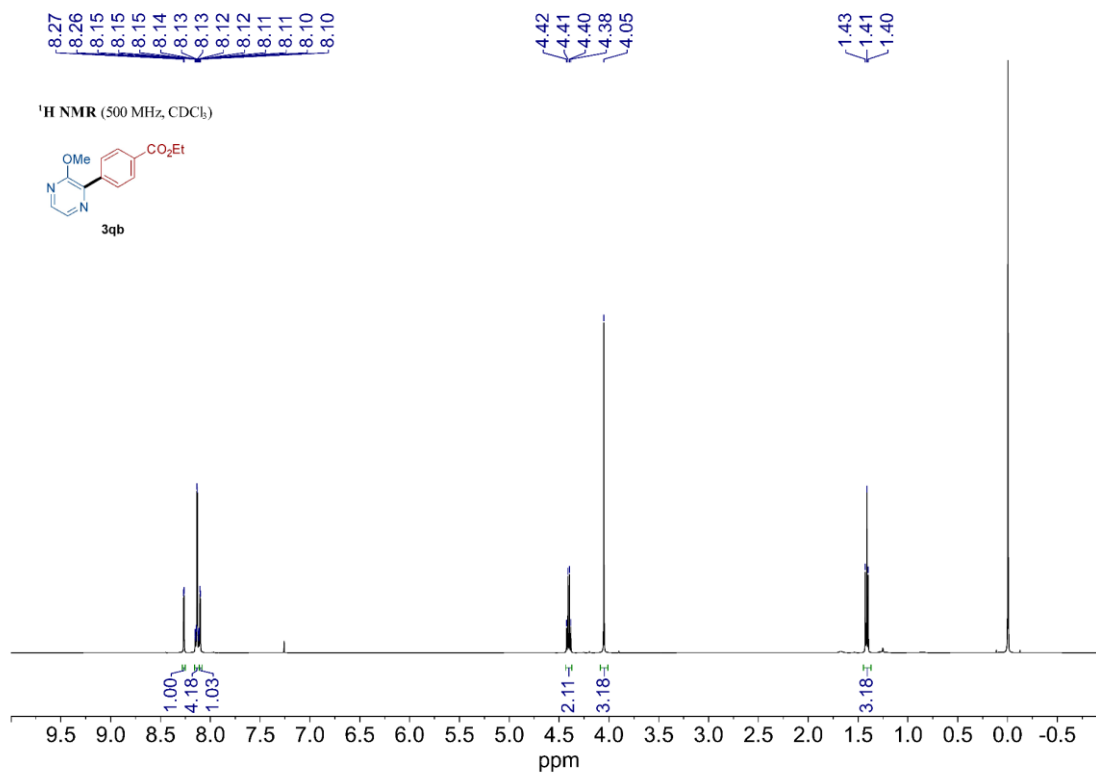


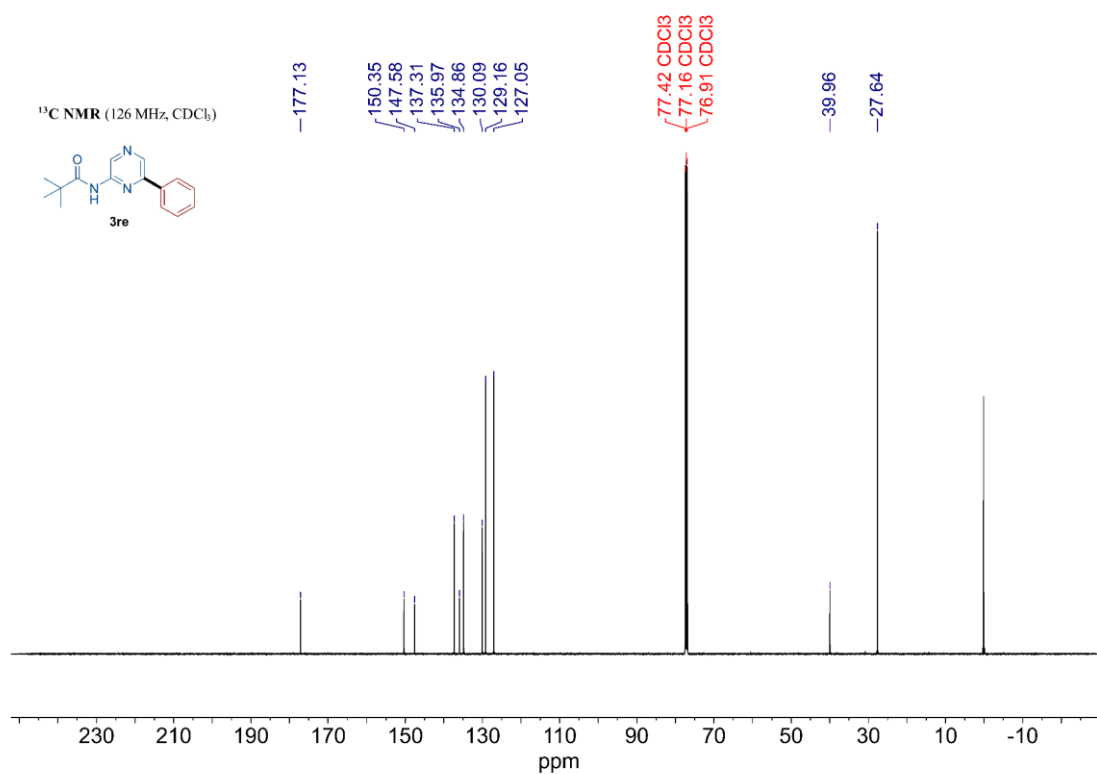
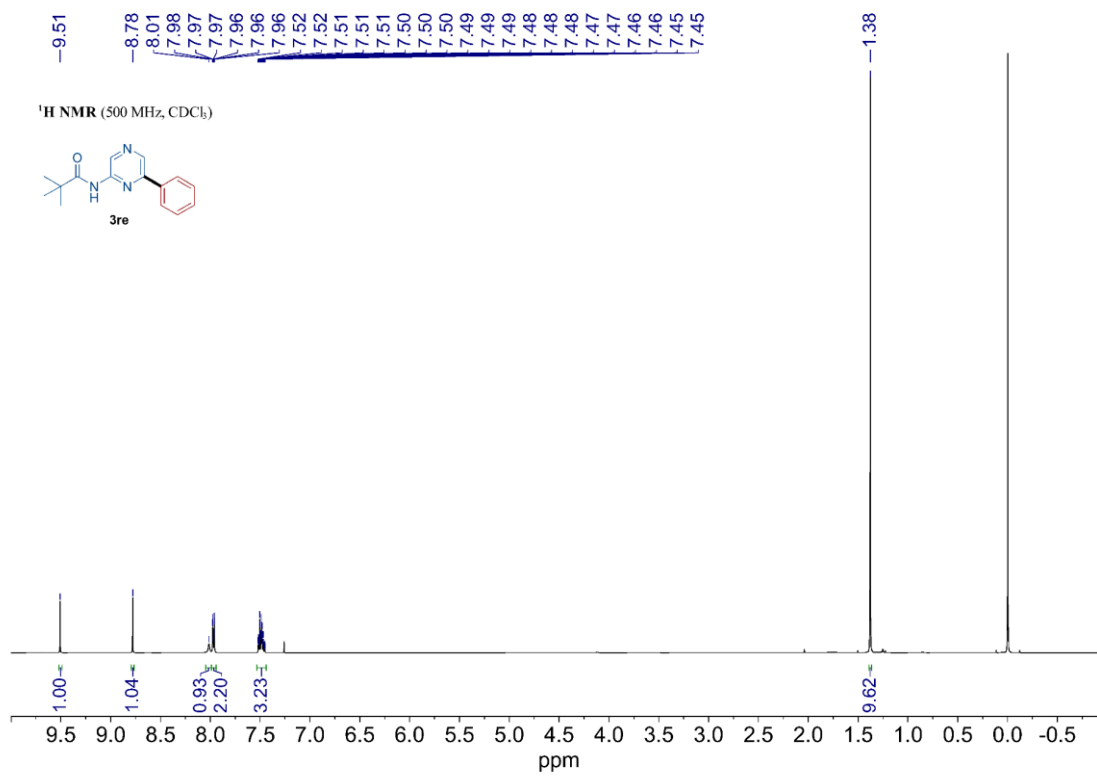


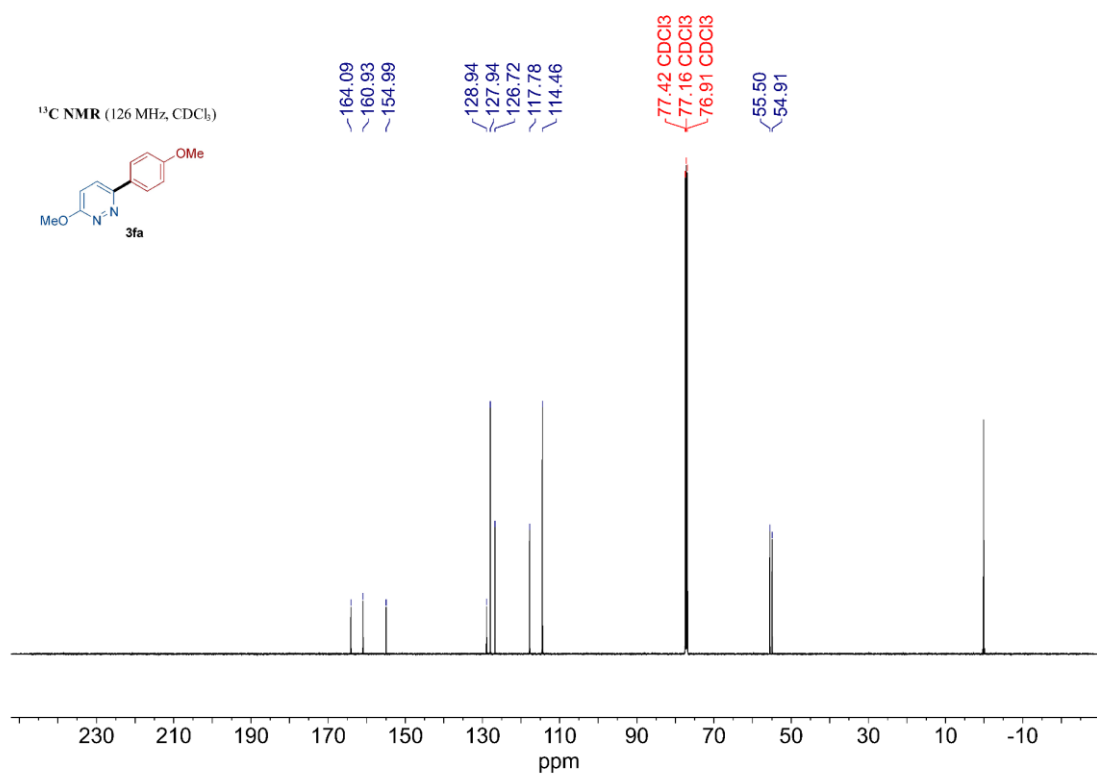
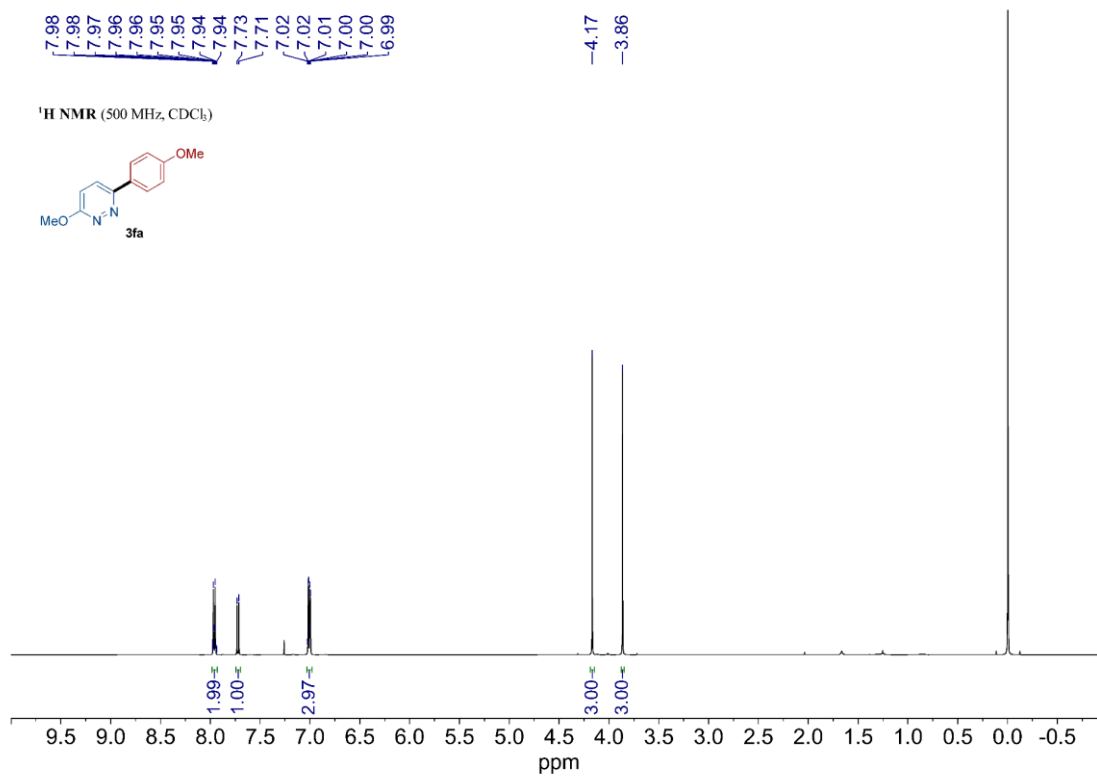


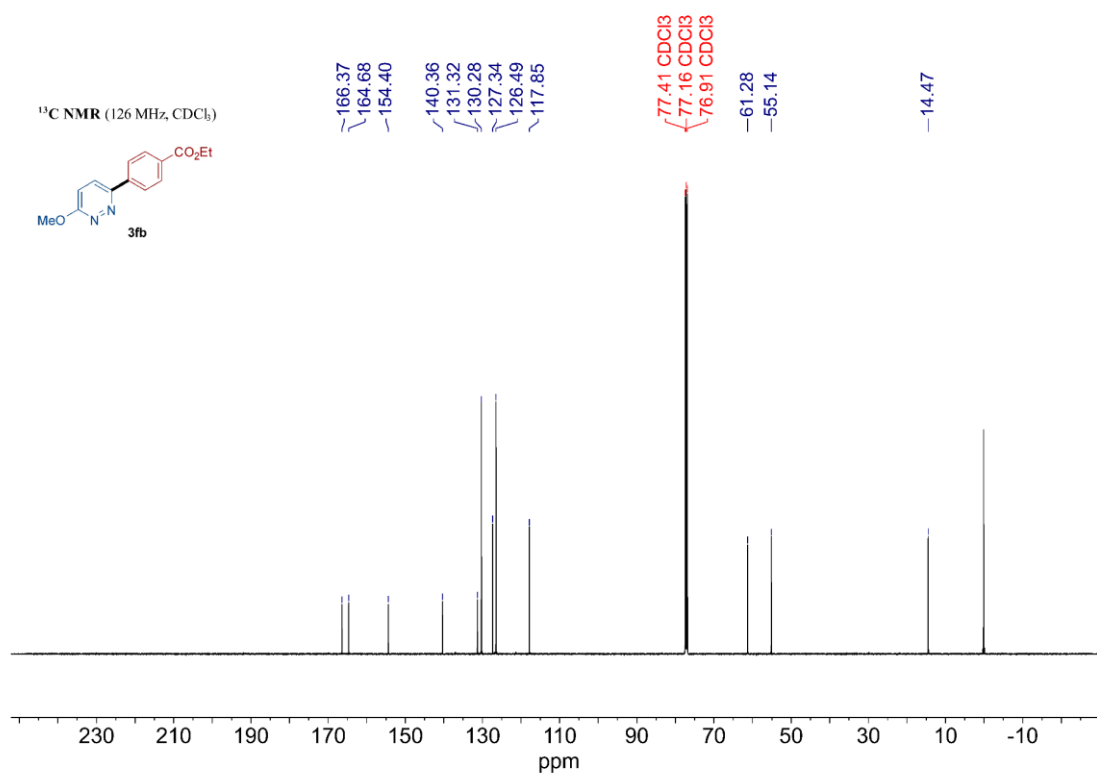
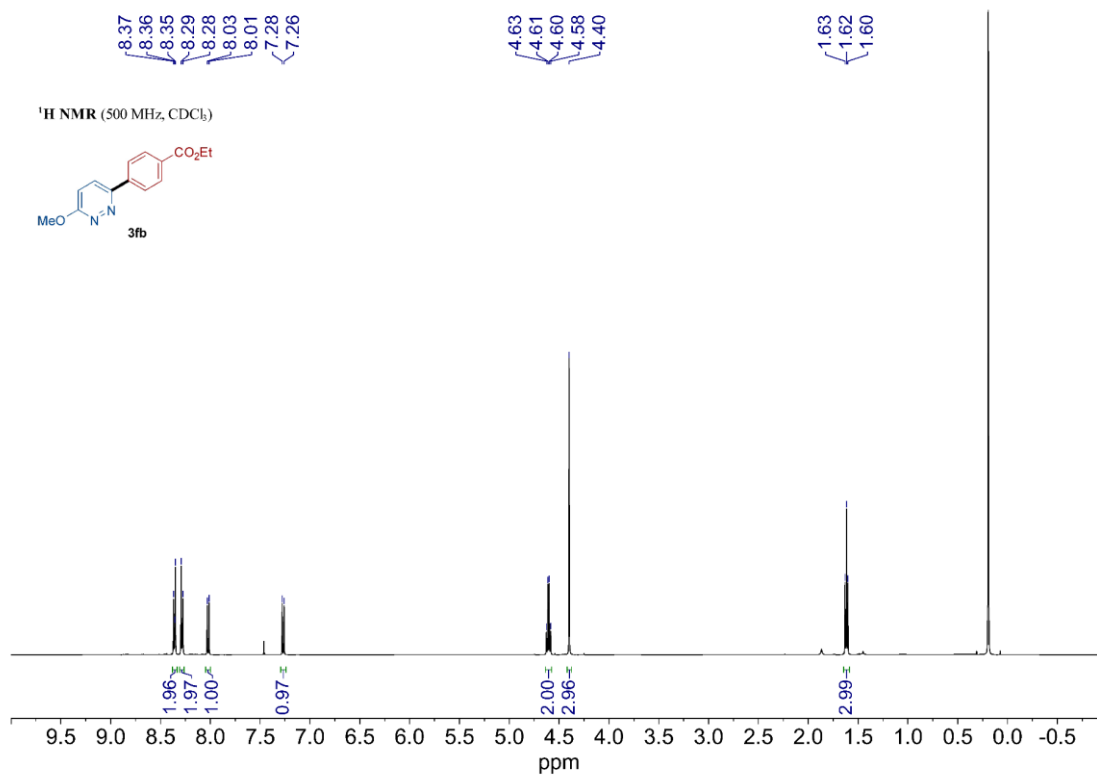


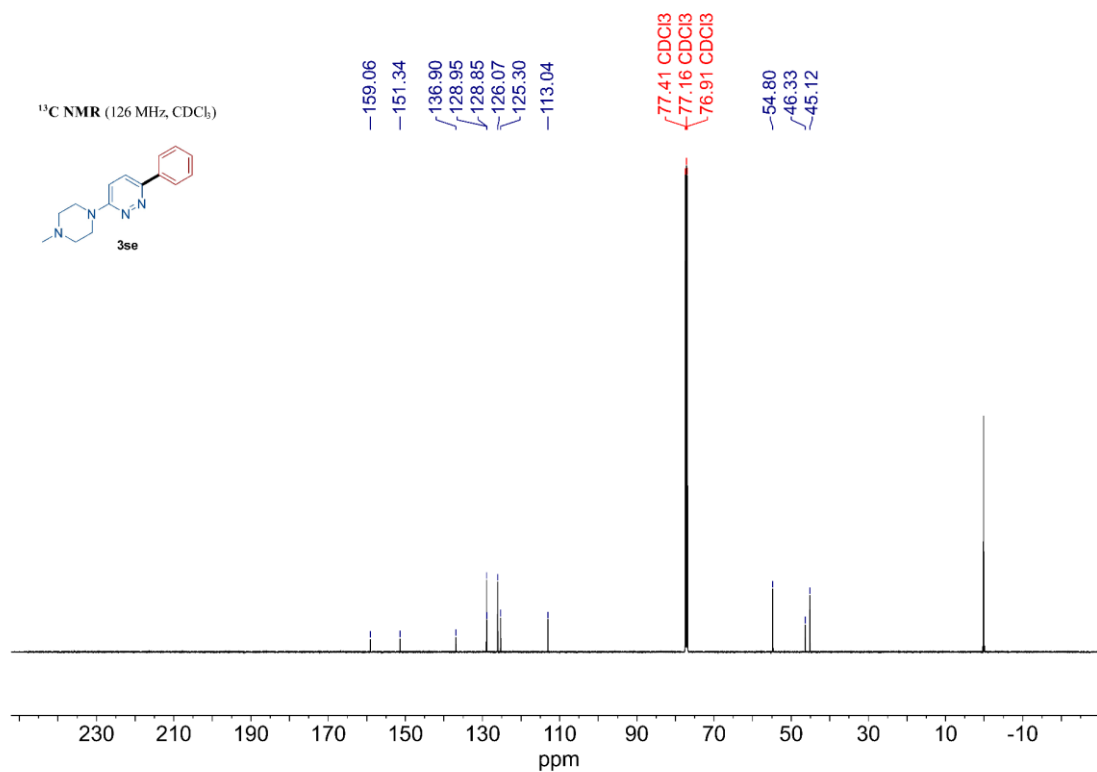
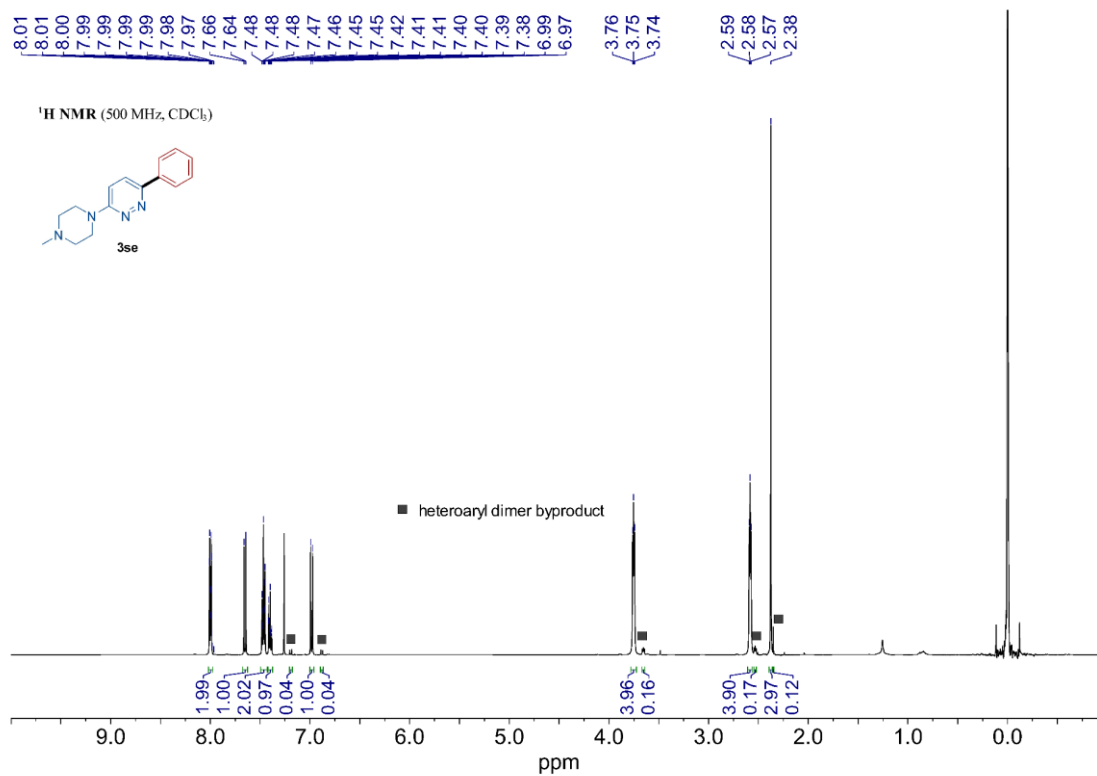


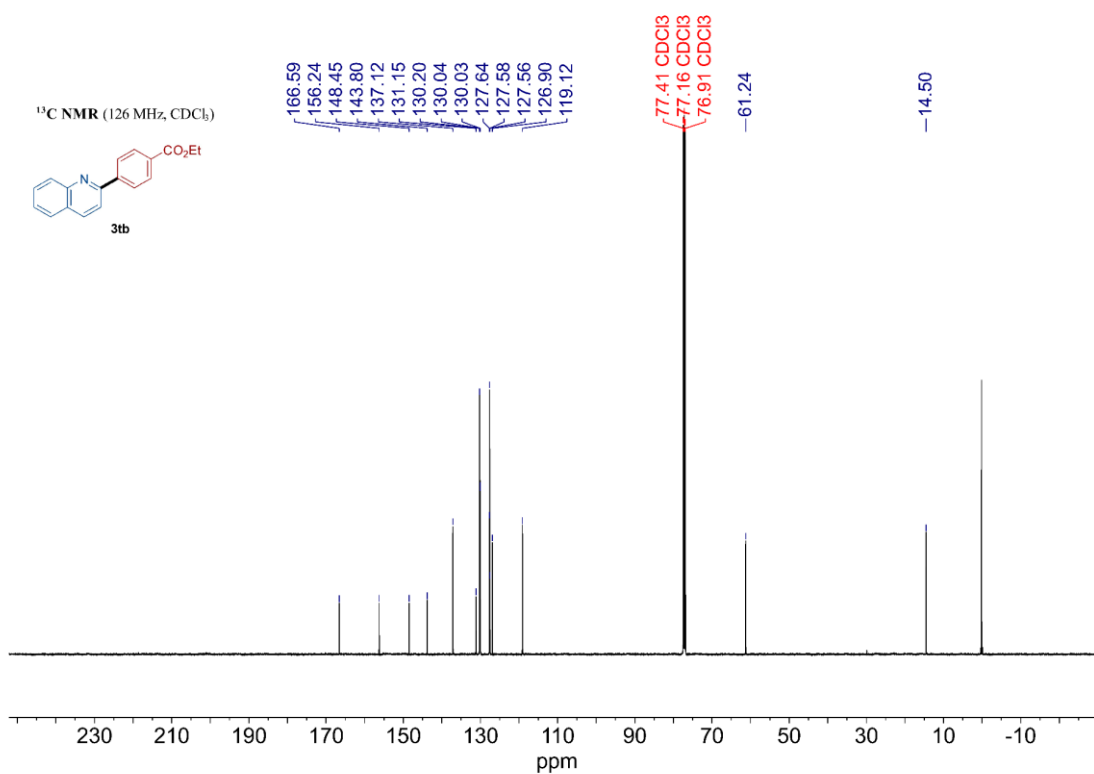
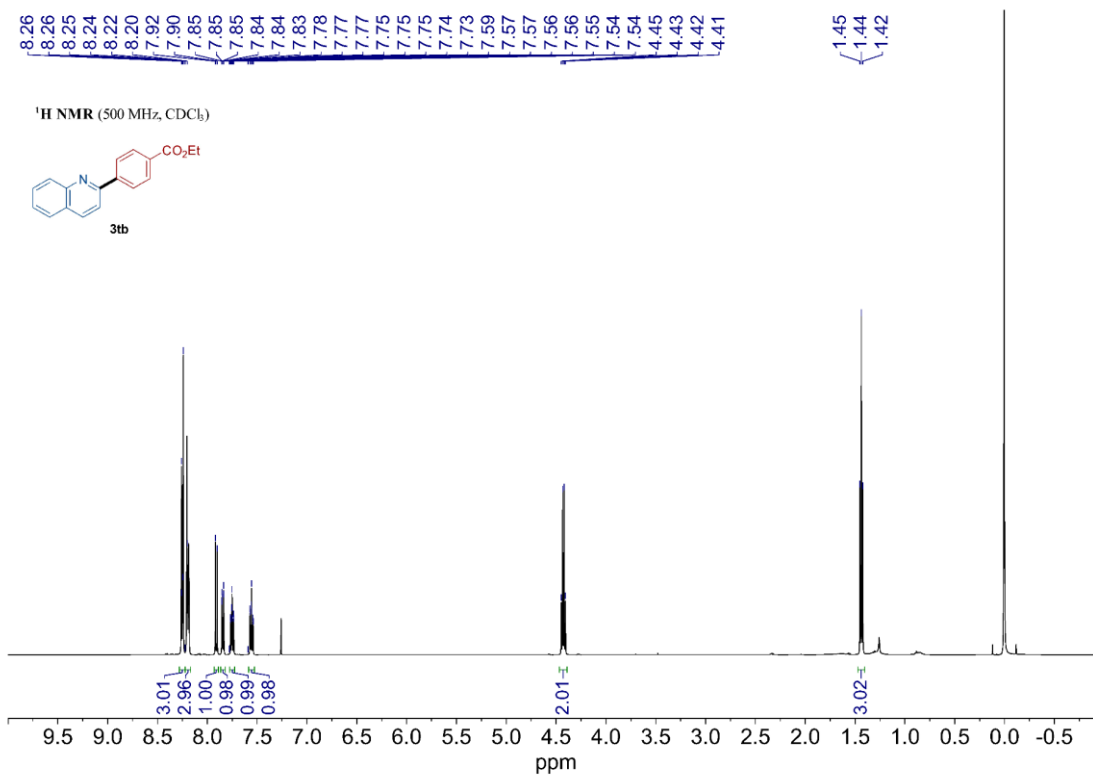


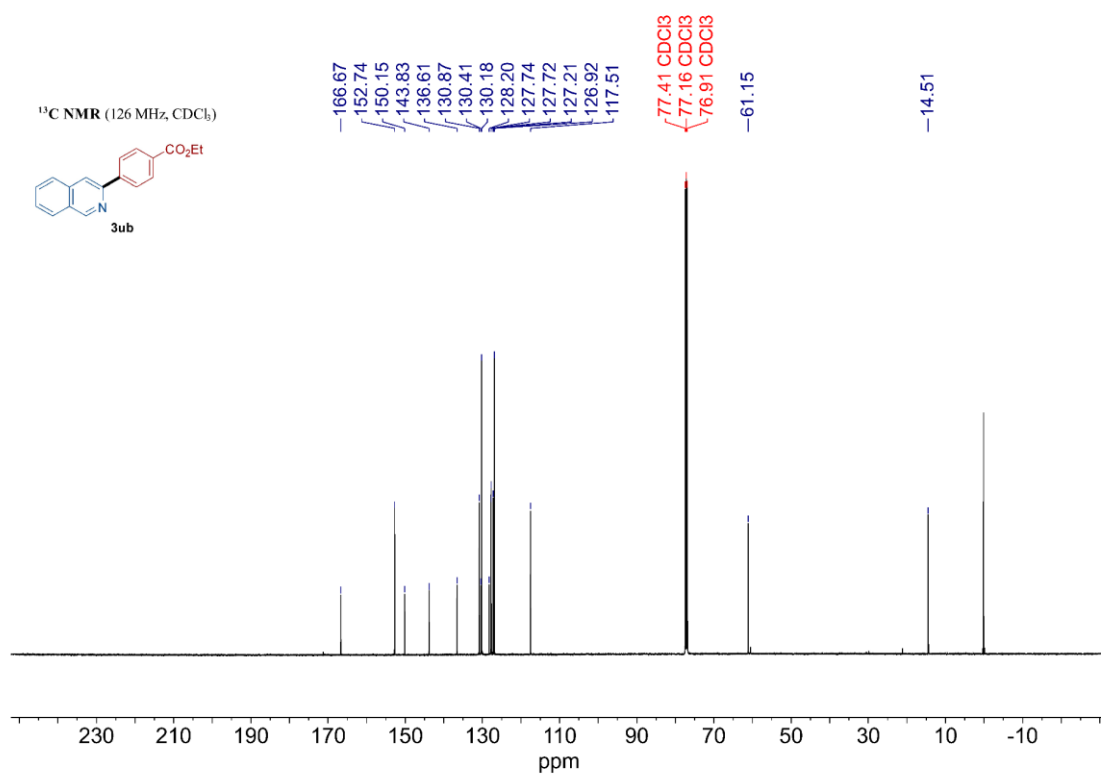
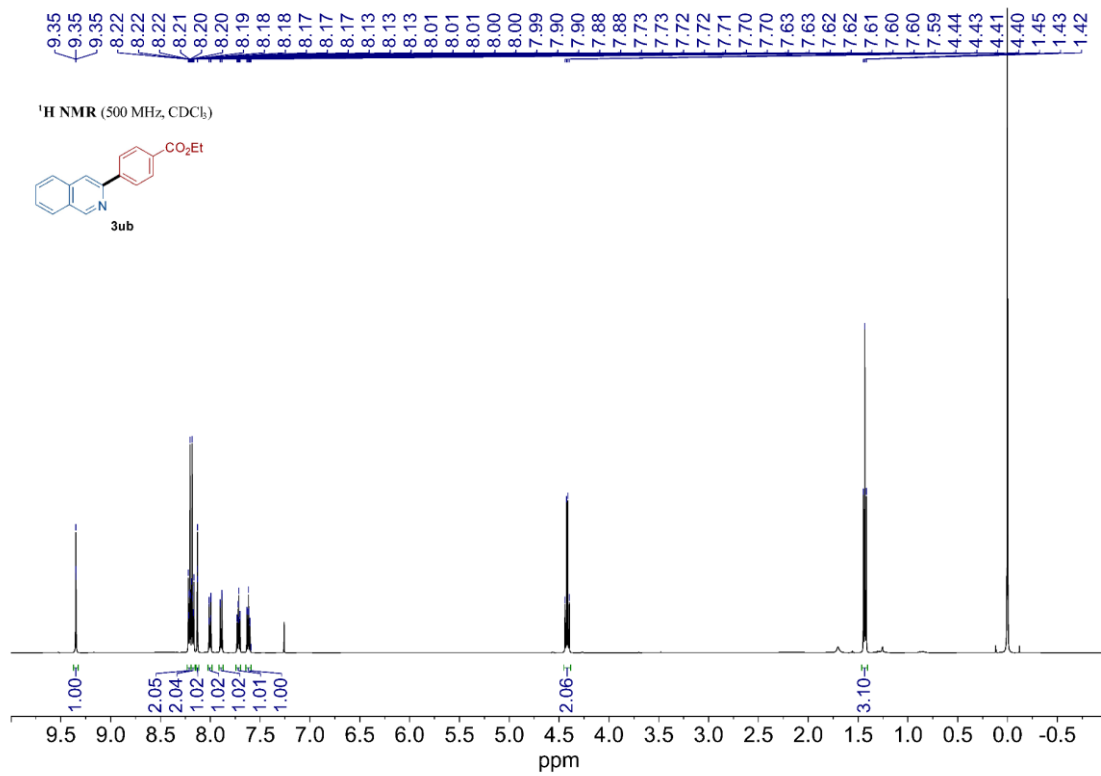


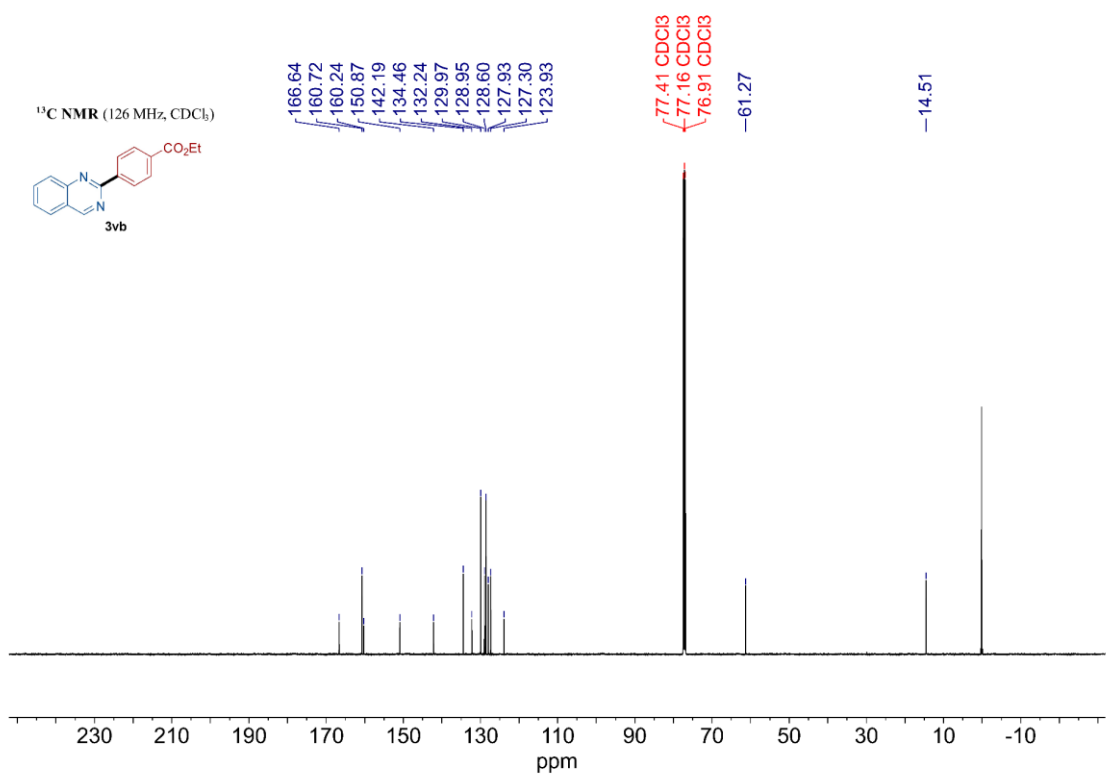
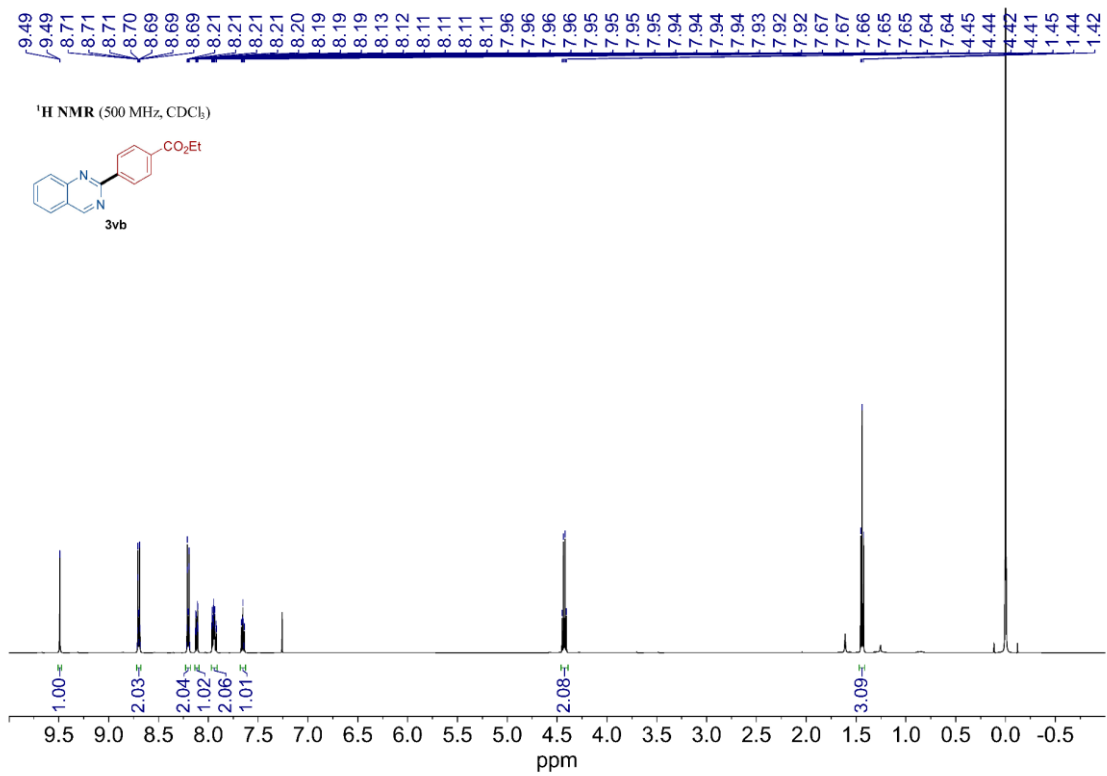


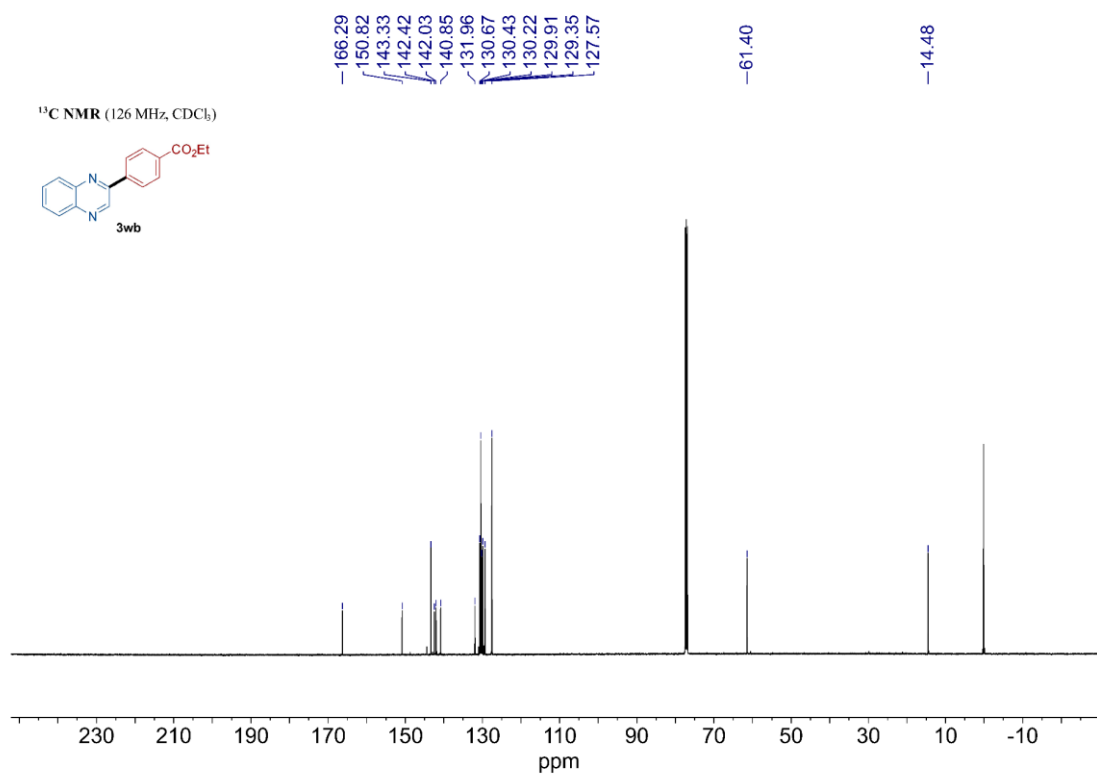
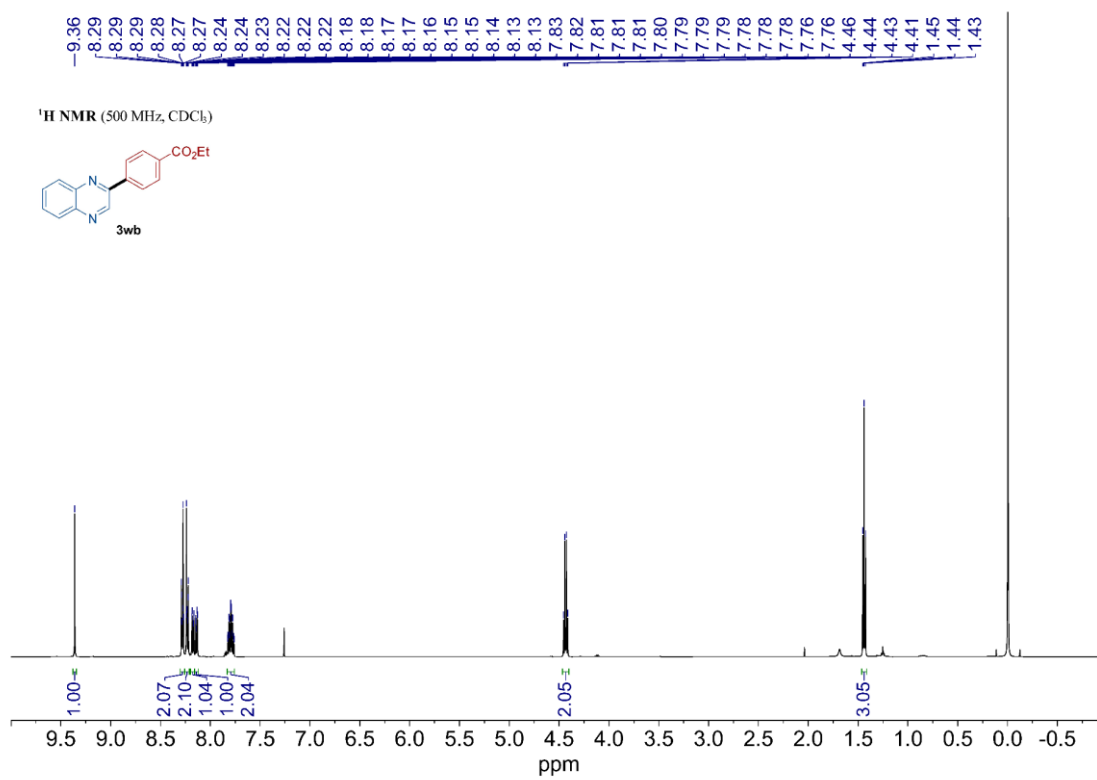


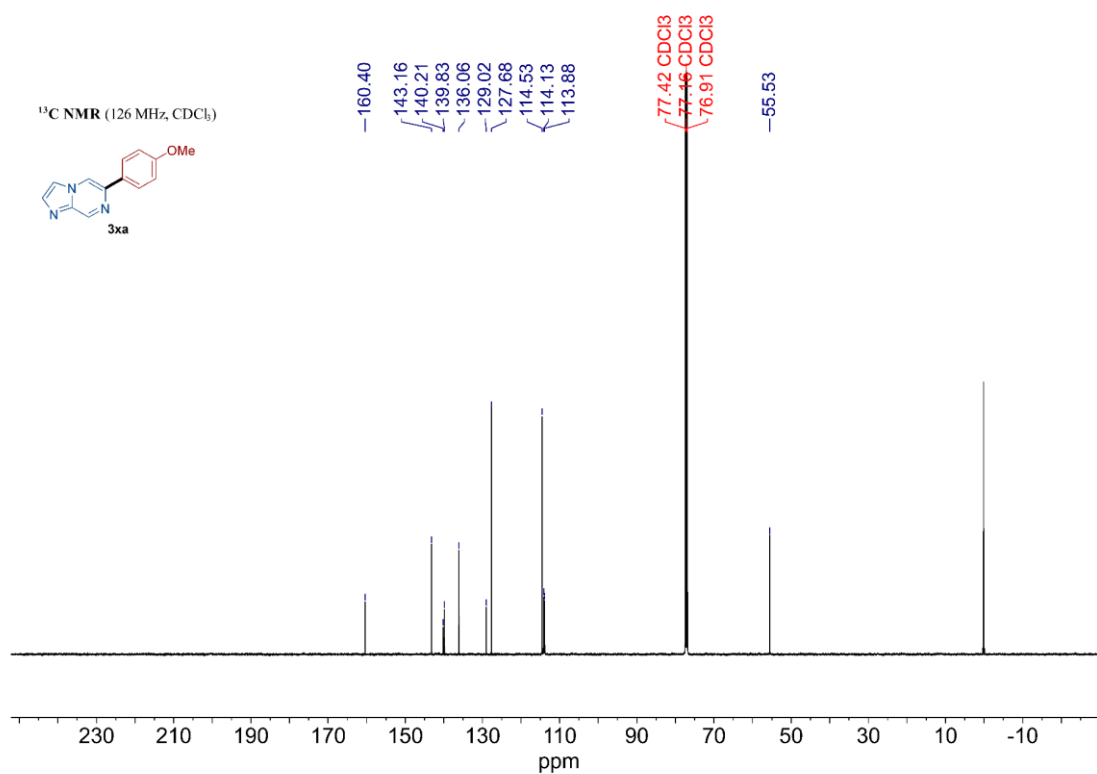
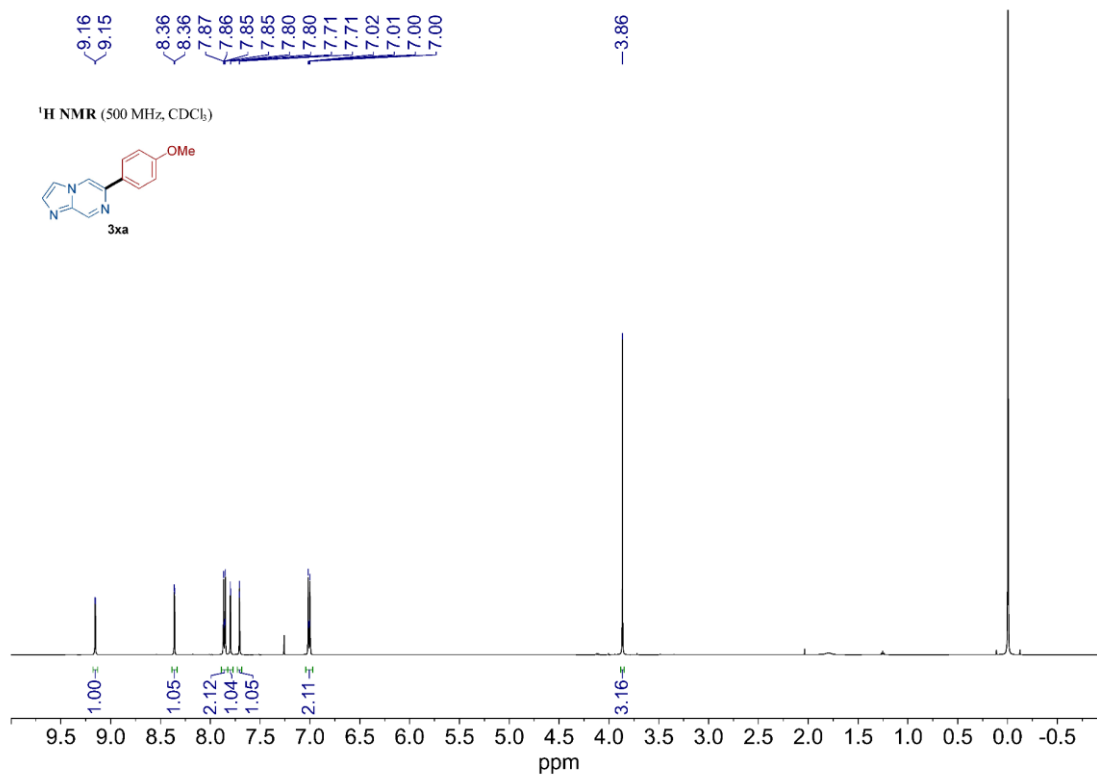


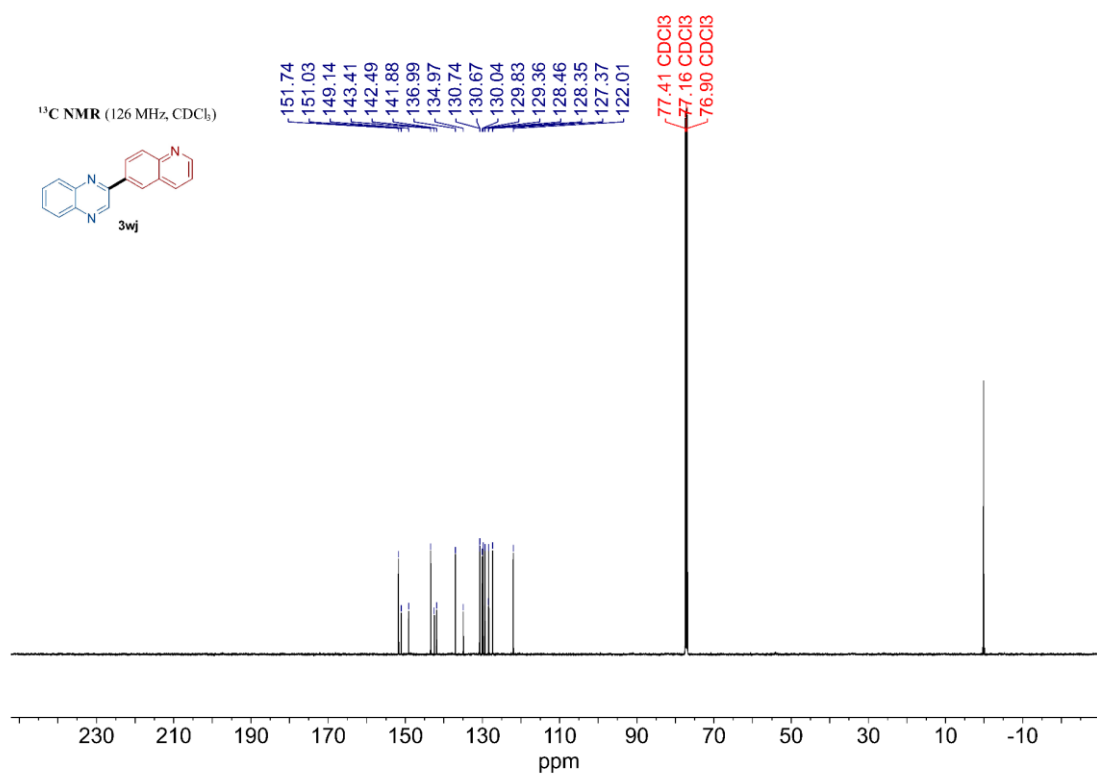
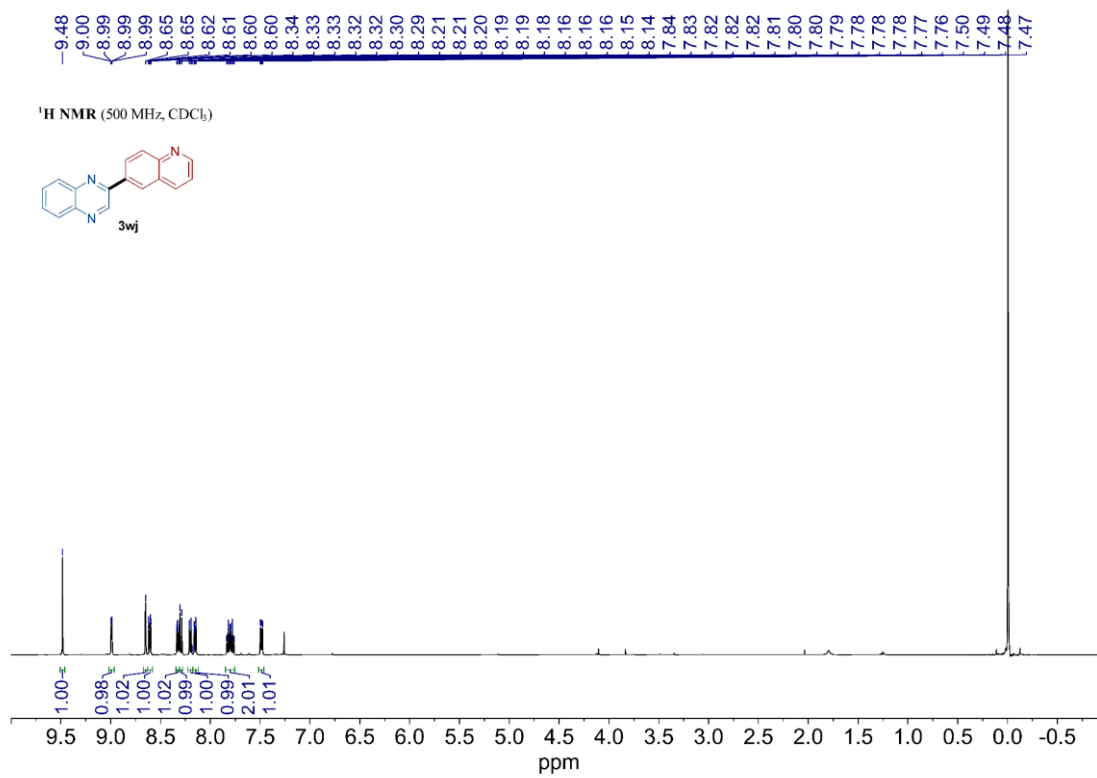


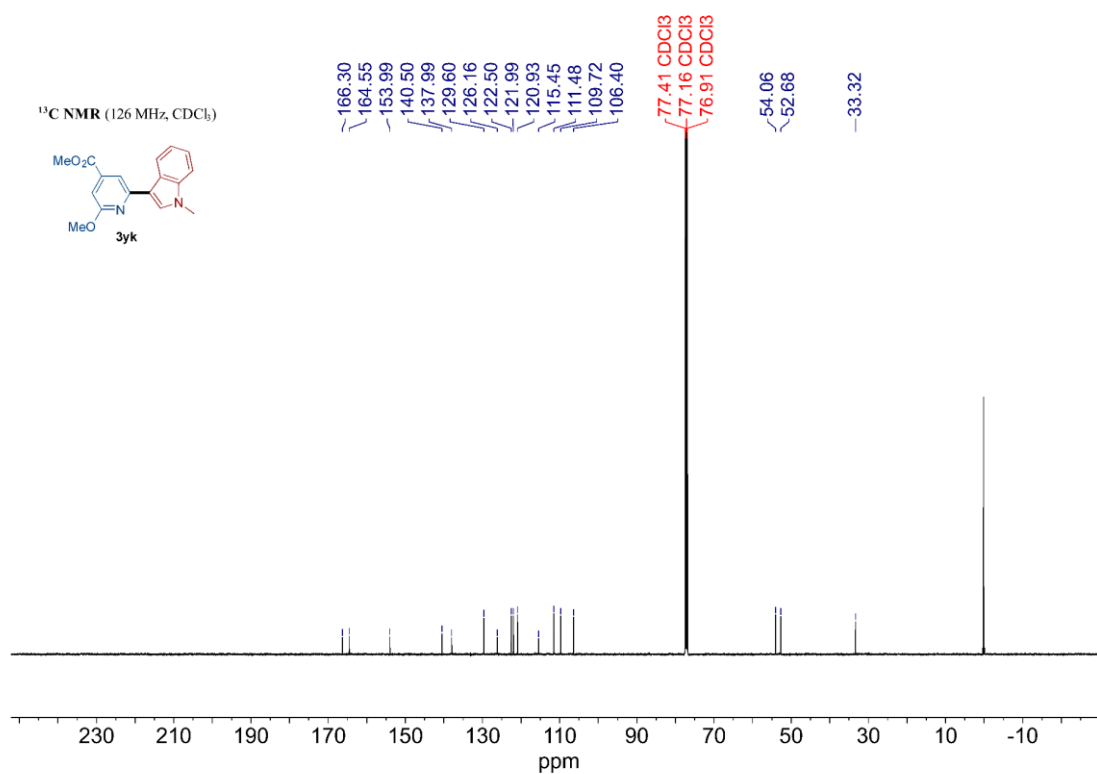
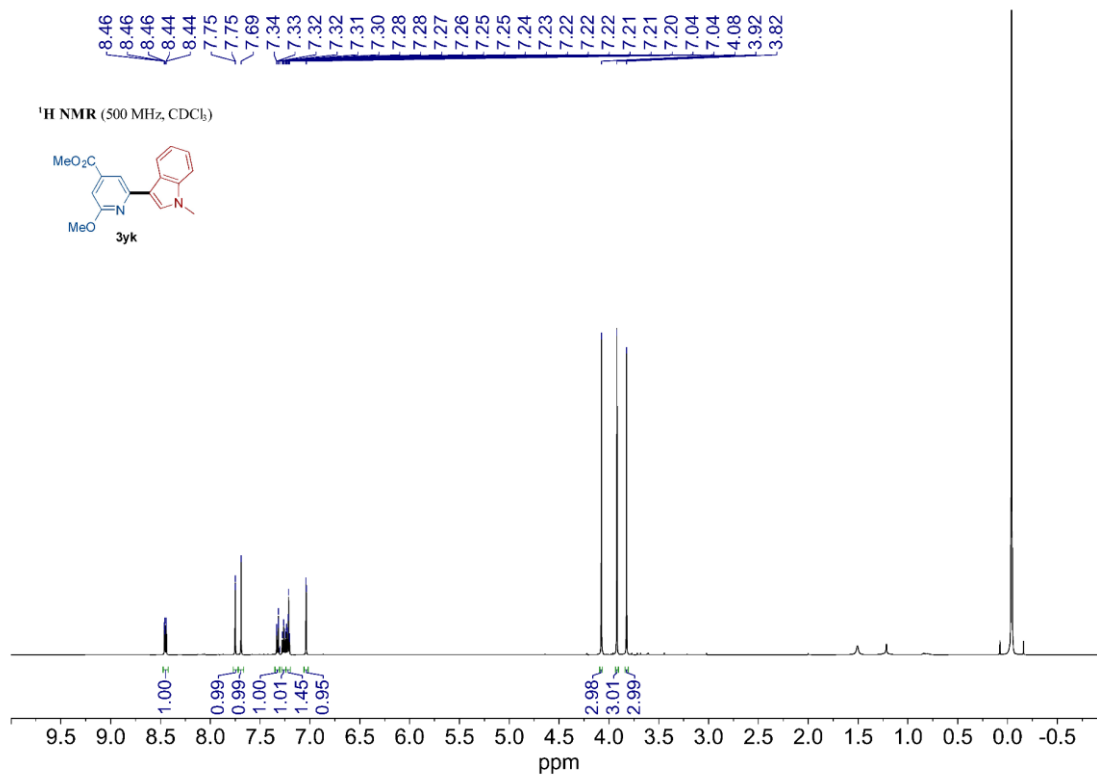


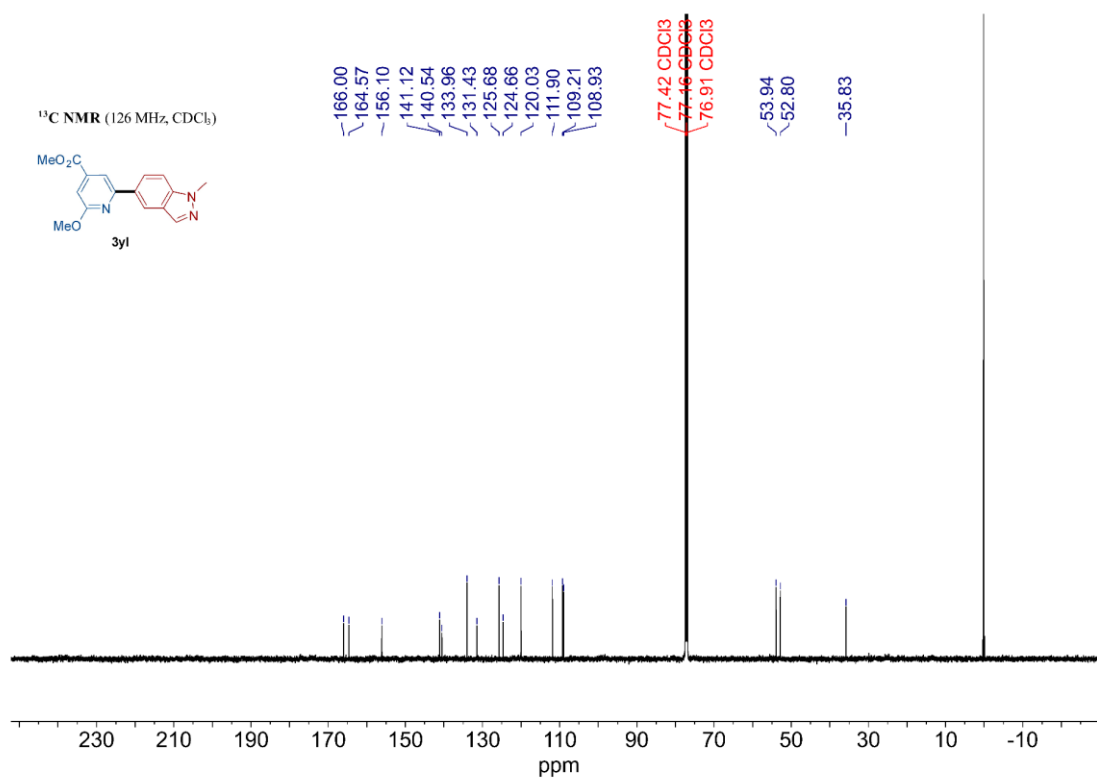
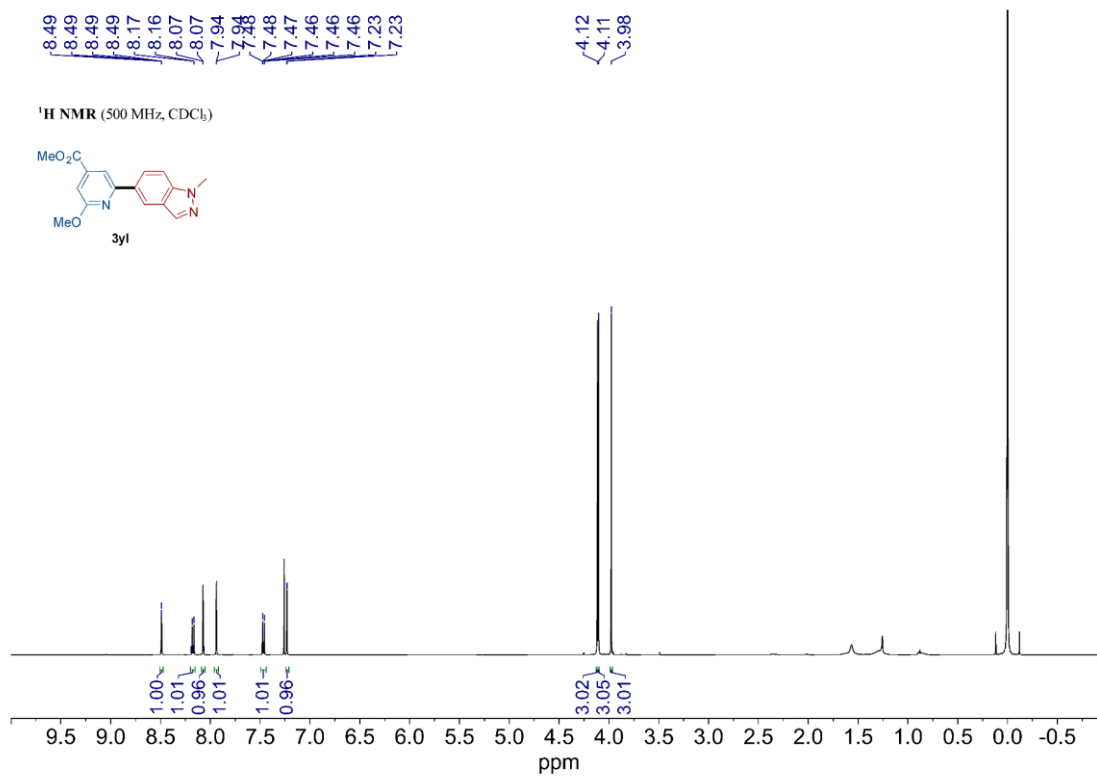


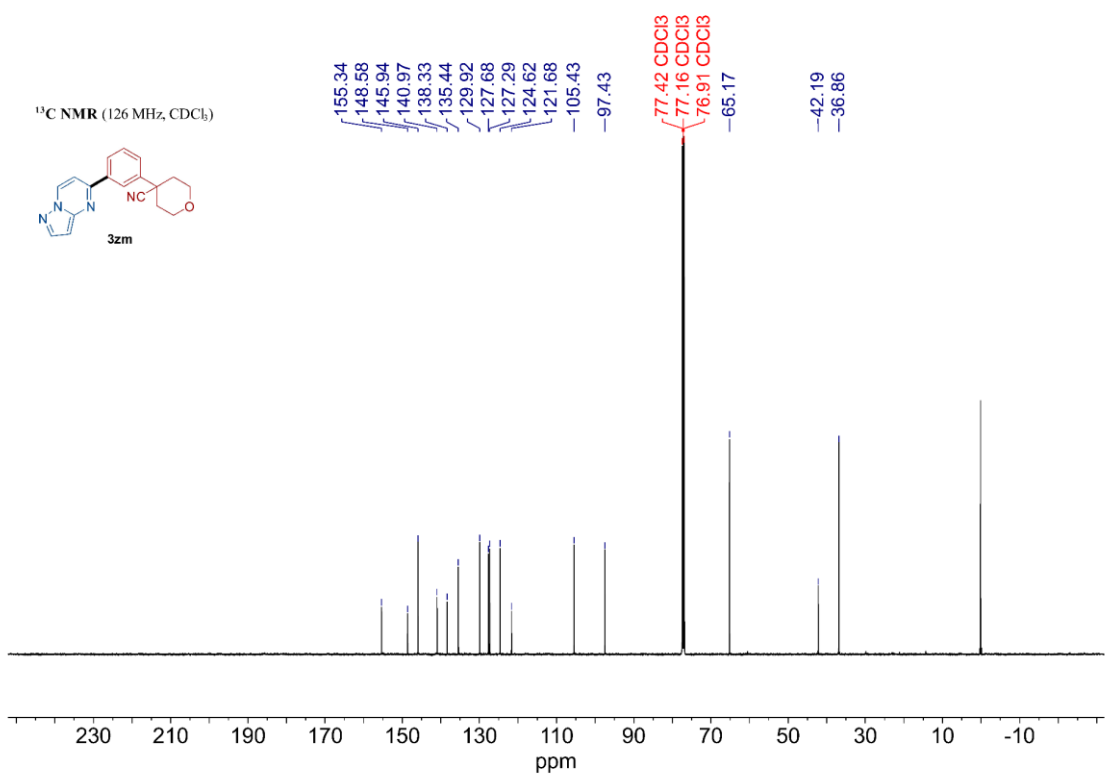
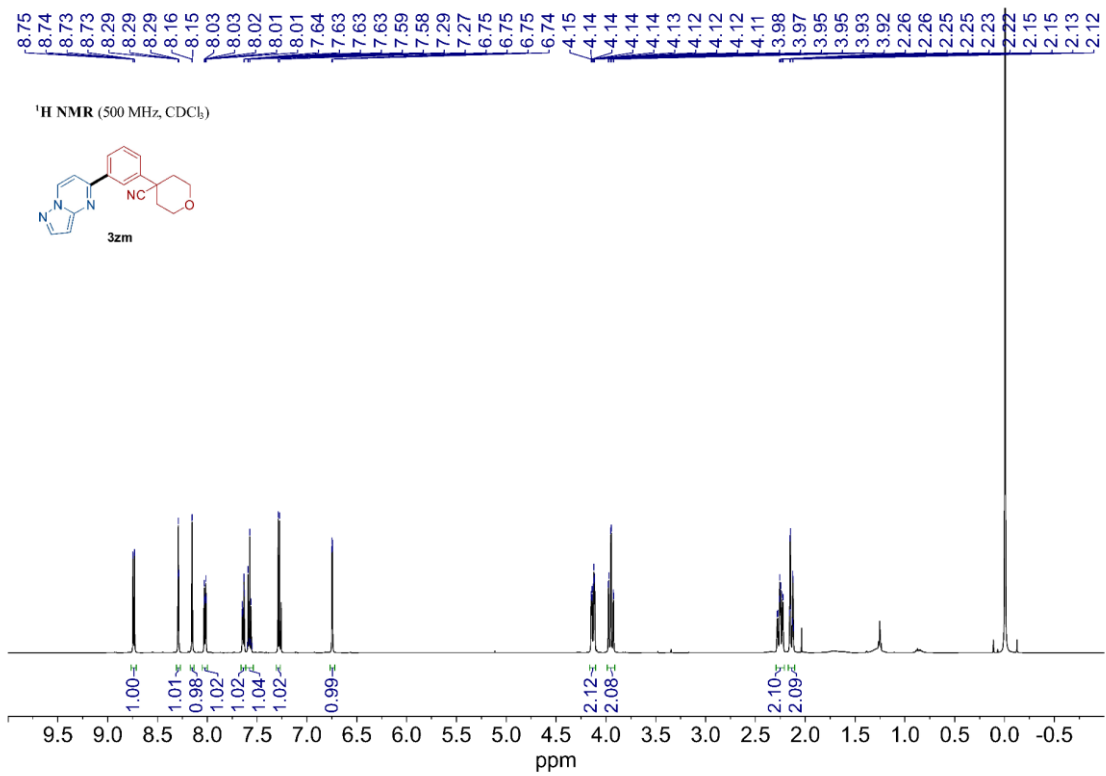


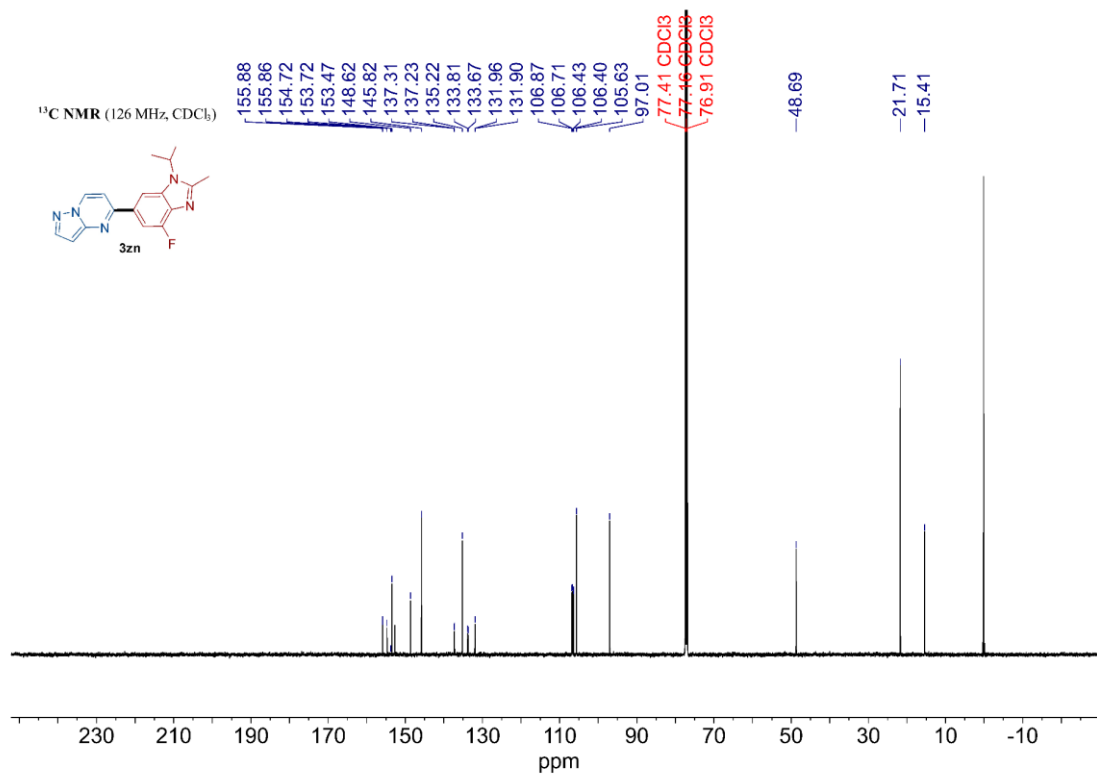
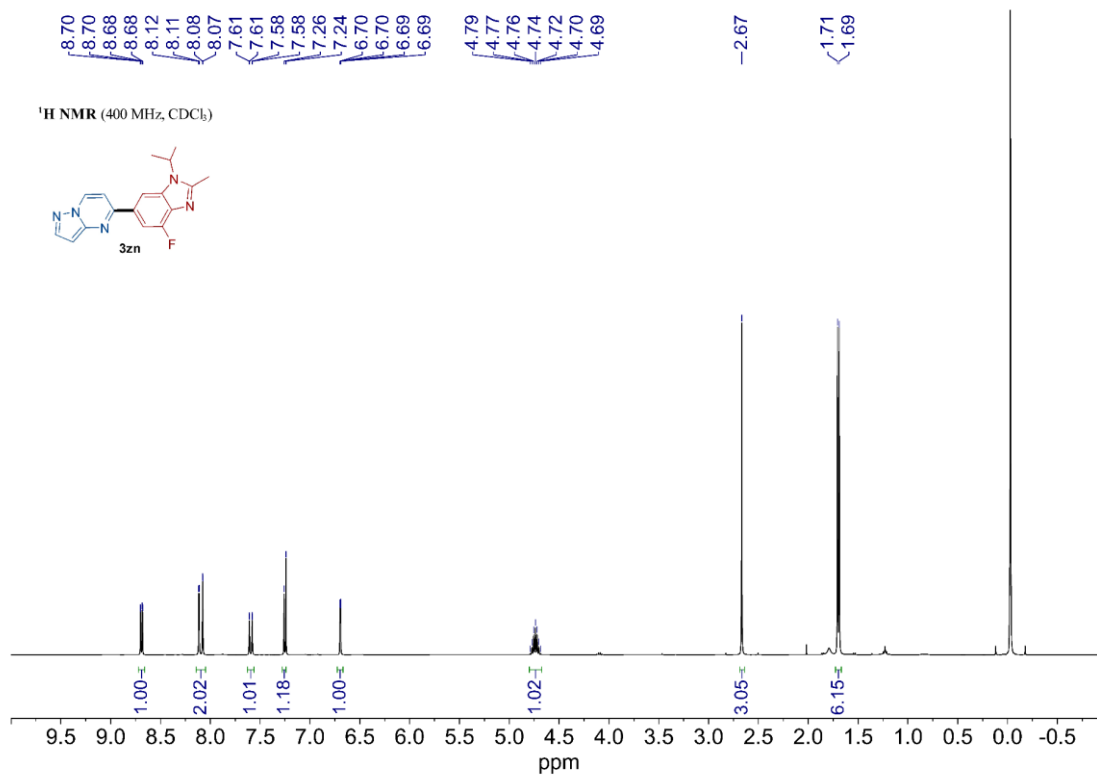




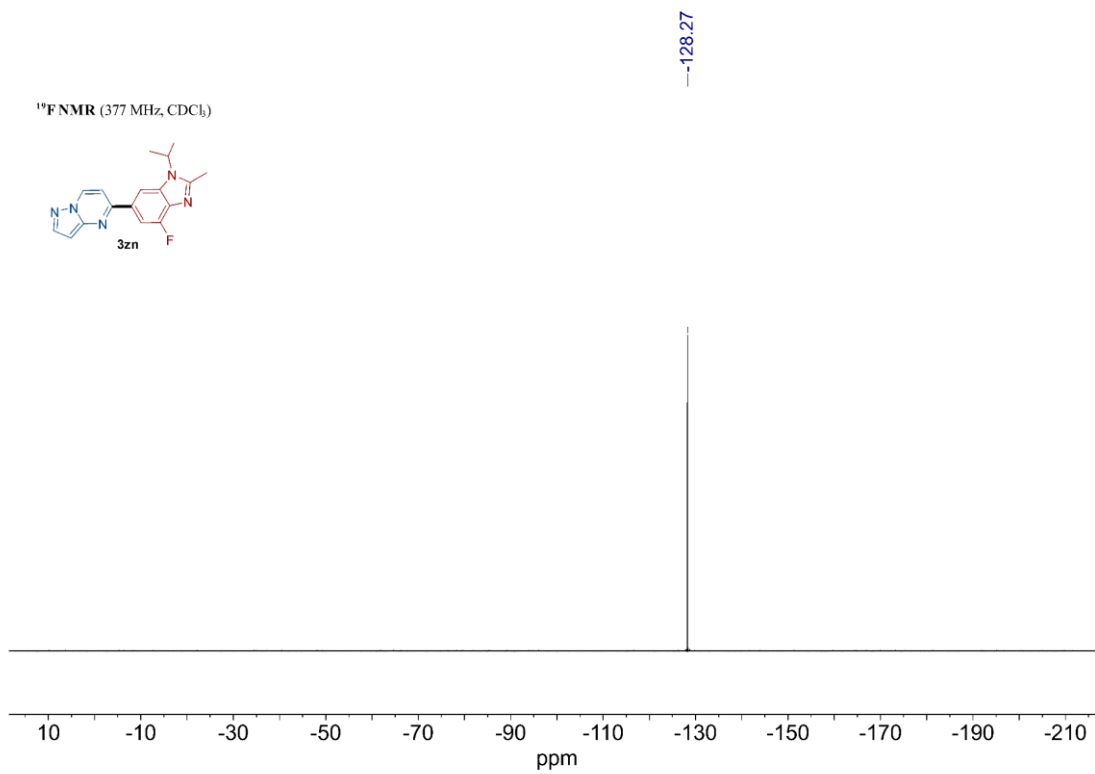








<sup>19</sup>F NMR (377 MHz, CDCl<sub>3</sub>)



## Appendix D. Pairing of Aqueous and Nonaqueous Electrosynthetic Reactions Enabled by a Redox Reservoir Electrode

The content presented in this Appendix is reproduced with permission from a published manuscript: Katelyn H. Michael, **Zhi-Ming Su**, Rui Wang, Hongyuan Sheng, Wenjie Li, Fengmei Wang, Shannon S. Stahl, and Song Jin. Pairing of Aqueous and Nonaqueous Electrosynthetic Reactions Enabled by a Redox Reservoir Electrode. *J. Am. Chem. Soc.* **2022**, *144*, 22641–22650. Copyright 2022 American Chemical Society.

## D.I. Abstract

Paired electrolysis methods are appealing for chemical synthesis because they generate valuable products at both electrodes; however, development of such reactions is complicated by the need for both half-reactions to proceed under mutually compatible conditions. Here, a modular electrochemical synthesis (ModES) strategy bypasses these constraints using a "redox reservoir" (RR) to pair electrochemical half-reactions across aqueous and nonaqueous solvents. Electrochemical oxidation reactions in organic solvents, the conversion of 4-*t*-butyltoluene to benzylic dimethyl acetal and aldehyde in methanol or the oxidative C–H amination of naphthalene in acetonitrile, and the reduction of oxygen to hydrogen peroxide in water were paired using nickel hexacyanoferrate as an RR that can selectively store and release protons (and electrons) while serving as the counter electrode for these reactions. Selective proton transport through the RR is optimized and confirmed to enable the ion balance, and thus the successful pairing, between redox half-reactions that proceed with different rates, on different scales, and in different solvents (methanol, acetonitrile, and water).

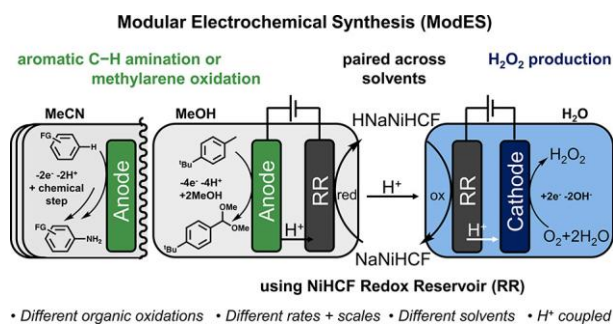


**Figure D.1.** Summary of this work.

## D.II. Introduction

Electrochemical synthesis is the focus of increased attention, owing to its ability to avoid elevated temperatures and pressures, eliminate stoichiometric chemical reagents, and reduce chemical waste.<sup>1-6</sup> In typical electrosynthetic reactions, the desired chemical transformation taking place at the working electrode is balanced by a sacrificial reaction that takes place at the counter/auxiliary electrode. Anodic oxidations, such as conversion of a primary alcohol to a carboxylic acid,<sup>7</sup> are typically balanced by proton reduction to hydrogen gas at the cathode. Cathodic reductions, such as the dimerization of acrylonitrile to adiponitrile,<sup>8</sup> are often balanced by water oxidation to O<sub>2</sub> at the anode. Smaller scale electrosynthetic reductions commonly use a sacrificial metal anode, such as Zn or Fe. The nonproductive counter electrode reactions are designed to balance the charge and avoid interference with the reaction of interest; however, it would be ideal if the nonproductive reaction at the counter electrode could be replaced with a redox reaction that generates a valuable product.<sup>9-11</sup> Such "paired electrolysis" methods can improve the efficiency, sustainability, and/or economics of large-scale applications.<sup>6,9-16</sup> A prominent example of paired electrolysis developed by BASF (Badische Anilin- und Sodafabrik) features the oxidation of 4-*t*-butyltoluene and the reduction of dimethyl-*o*-phthalate in a methanol solvent (Figure D.2a).<sup>5,17,18</sup> The process is formally 100% atom efficient owing to its perfect methanol and electron balance. Both products may be formed at the same rate under identical reaction conditions (temperature, solvent, supporting electrolyte, etc.). This matching of reaction conditions and rates presents a challenge to the development and widespread adoption of paired electrochemical reactions, as the optimal conditions and rates of different reactions are seldom identical.<sup>6,11,19</sup>

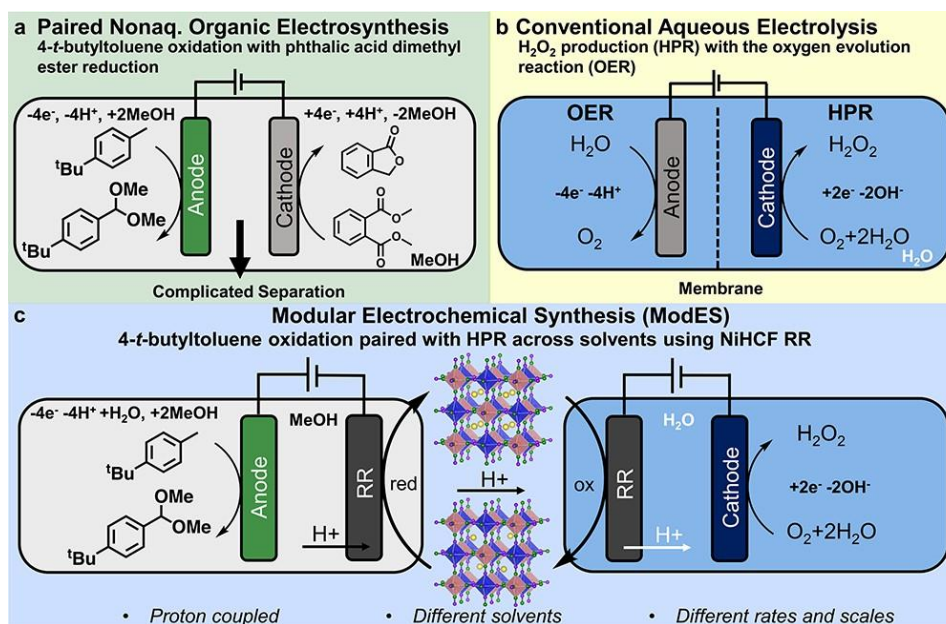
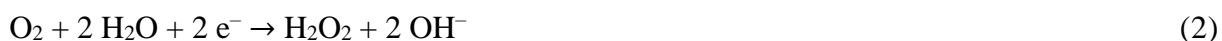


**Figure D.2.** Schematic illustration of RR-enabled ModES for paired oxidation of 4-*t*-butyltoluene in methanol and reduction of oxygen to  $\text{H}_2\text{O}_2$  in water in comparison to conventional electrolysis processes. (a) Schematic of the BASF paired electrolysis that takes place in methanol where two organic products are synthesized simultaneously at both the cathode and anode. (b) In conventional electrochemical  $\text{H}_2\text{O}_2$  production (HPR), the nonproductive OER takes place on the anode to charge balance the cathodic reaction. This process requires a membrane to prevent  $\text{H}_2\text{O}_2$  decomposition on the anode. (c) In the ModES process, the anodic and cathodic processes take place in two undivided cells and an RR electrode serves as the counter electrode for the process of interest, storing ions and charge and ensuring ion balance. This allows the two reactions to take place in different solvents, with different scales and rates and without a complicated separation process.

The challenges for achieving paired electrolyses can be alleviated by the recently described redox reservoir (RR)-enabled modular electrochemical synthesis (ModES) method.<sup>20</sup> RRs are solid-state battery materials that temporarily store/release ions and electrons to balance the ion/electron transfer steps taking place at the working electrode. Therefore, RRs can serve as a universal counter electrode, capable of pairing alternately with both cathodic and anodic half-reactions. Implementation of this RR-based ModES concept relaxes the constraints of paired electrochemical synthesis because the paired half-reactions may be carried out in different cells, and at different times, locations, rates, and/or scales, to align with demand. The promises of the ModES strategy have been demonstrated by the reports on decoupled water splitting, which can

reduce the crossover of oxygen impurity in the produced hydrogen and provide a means to reduce gas purification costs and safety hazards.<sup>21–27</sup> Moreover, RRs can enable the pairing of many incompatible half-reactions to synthesize value-added chemicals such as the coproduction of several high-value oxidants in aqueous media,<sup>20,28</sup> which was not previously possible due to product and membrane incompatibility. RRs could also enable electrosynthetic reactions to take place in an undivided cell instead of the commonly used divided cell, bypassing the need for a membrane or separator. To date, the ModES strategy has only been used to pair two redox half-reactions in aqueous solutions, but it should also be compatible with nonaqueous solvents commonly used in organic electrosynthesis.<sup>3,6,10</sup>

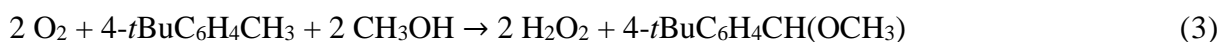
To expand the flexibility and potential utility of ModES, we elected to investigate the use of a solid-state RR to pair two electrosynthetic redox reactions conducted in different solvents. These half-reactions include the methylarene oxidation reaction featured in the BASF process conducted in methanol at the anode (eq 1 and Figure D.2a), and electrochemical hydrogen peroxide production via two-electron reduction of O<sub>2</sub> in water at the cathode (eq 2 and Figure D.2b).



These important reactions are performed on very different scales industrially, 10<sup>3</sup> and 10<sup>6</sup> tons per year for methylarene oxidation and H<sub>2</sub>O<sub>2</sub> production, respectively. Electrochemical production of H<sub>2</sub>O<sub>2</sub> for disinfection, environmental applications, or as an oxidant for chemical synthesis is the focus of growing interest as an alternative for the traditional chemical anthraquinone process that requires high energy consumption, expensive catalysts, and multiple steps.<sup>29–32</sup> The susceptibility of H<sub>2</sub>O<sub>2</sub> to decomposition limits compatible half-reactions; therefore, the H<sub>2</sub>O<sub>2</sub> electrolyzer usually has the oxygen evolution reaction (OER) as the anodic process separated by an expensive ion

exchange membrane (Figure D.2b). The use of RRs in a ModES strategy could eliminate the unproductive counter reactions and the need for ion exchange membranes, but RR electrodes that can transfer the common ions involved in both half-reactions need to be developed to maintain the ion balance and realize the sustained coproduction of chemicals.<sup>28,33</sup>

Here, we demonstrate the pairing of these two half-reactions across aqueous and nonaqueous solvents using a carefully designed RR that results in the following overall ModES reaction (eq 3 and Figure D.2c):



The anodic methylarene oxidation reaction generates  $\text{H}^+$  in the undivided cell and the RR undergoes reduction with  $\text{H}^+$  intercalation (Figure D.1c, left). Then, the RR electrode is transferred to a separate undivided cell where it supports cathodic hydrogen peroxide production by undergoing oxidation and release of  $\text{H}^+$  (Figure D.1c, right), which neutralizes the  $\text{OH}^-$  produced by  $\text{H}_2\text{O}_2$  production (eqs 2 and 4).



The overall process avoids contact between the supporting electrolytes of the two half-reactions, while allowing for ion balance between two incompatible processes. We identify a Prussian blue analogue (PBA) material, nickel hexacyanoferrate (NiHCF), that is compatible with both aqueous and nonaqueous solvents as the RR to ensure selective transport of protons across the electrochemical cells. After optimization of the RR material, reaction electrolytes, and ModES process, continuous proton-balanced ModES cycles with pH stability that yield complete conversion of methylarene in methanol and the production of  $\text{H}_2\text{O}_2$  in water are achieved. To further support the flexibility of the ModES strategy, the amination of naphthalene in acetonitrile is paired with  $\text{H}_2\text{O}_2$  production using the same NiHCF RR.

### D.III. Results and Discussion

**Synthesis and Electrochemical Performance of NiHCF as a Redox Reservoir.** The RR materials for the ModES processes should be selected based on their ability to transport the balancing ion, chemical and electrochemical stability in the appropriate electrolytes, their redox potential, cycling capacity, and kinetics. For the ModES pairing herein, proton is the balancing ion; therefore, we selected PBAs because they have been reported as proton battery materials.<sup>34–36</sup> The rigid open framework and large interstitial sites with a three-dimensional diffusion channel along the  $\langle 110 \rangle$  crystallographic directions in PBAs make them advantageous for intercalation of ions in aqueous and nonaqueous solutions.<sup>36,37</sup> PBAs are also inexpensive and can be synthesized on a larger scale using a simple coprecipitation method. Various PBAs, including NiHCF and CuHCF, were tested for stability in a range of solvents commonly used in batteries and organic electrochemical reactions. First, a small amount of PBA powder was added to the solvents to check for solubility. If there was no visible dissolution, a cyclic voltammogram (CV) was taken to find the formal potential of the PBA followed by cycling tests. NiHCF was found to be the most stable PBA in nonaqueous solvents and undergoes redox in methanol, dimethylformamide, and acetonitrile (Figure D.S1).

We synthesized the rhombohedral NiHCF crystals with occupied  $\text{Na}^+$  following a reported coprecipitation method.<sup>38</sup> Scanning electron microscopy (SEM) images of the as-synthesized crystals show well-faceted microcubes with an average size of approximately  $2 \mu\text{m}$  (Figure D.3a, inset). A powder X-ray diffraction pattern displays the characteristic doublet diffraction peaks of the rhombohedral phase at (220), (440), and (660) compared to the standard pattern that represents the cubic phase (JCPDS no. 52-1907) (Figure D.S2). The as-synthesized rhombohedral phase is preferred due to its slightly higher capacity compared to the cubic (oxidized) phase and its larger

unit cell.<sup>39</sup> Inductively coupled plasma optical emission spectroscopy (Table D.S1) and thermogravimetric analysis (TGA, Figure D.S3) were conducted to determine the compositions of Na, Ni, and Fe elements and the water content in the NaNiHCF sample to confirm the exact formula to be  $\text{Na}_{2.29}\text{Ni}[\text{Fe}(\text{CN})_6]_{1.04} \cdot 2.2 \text{H}_2\text{O}$ .

### MeOH

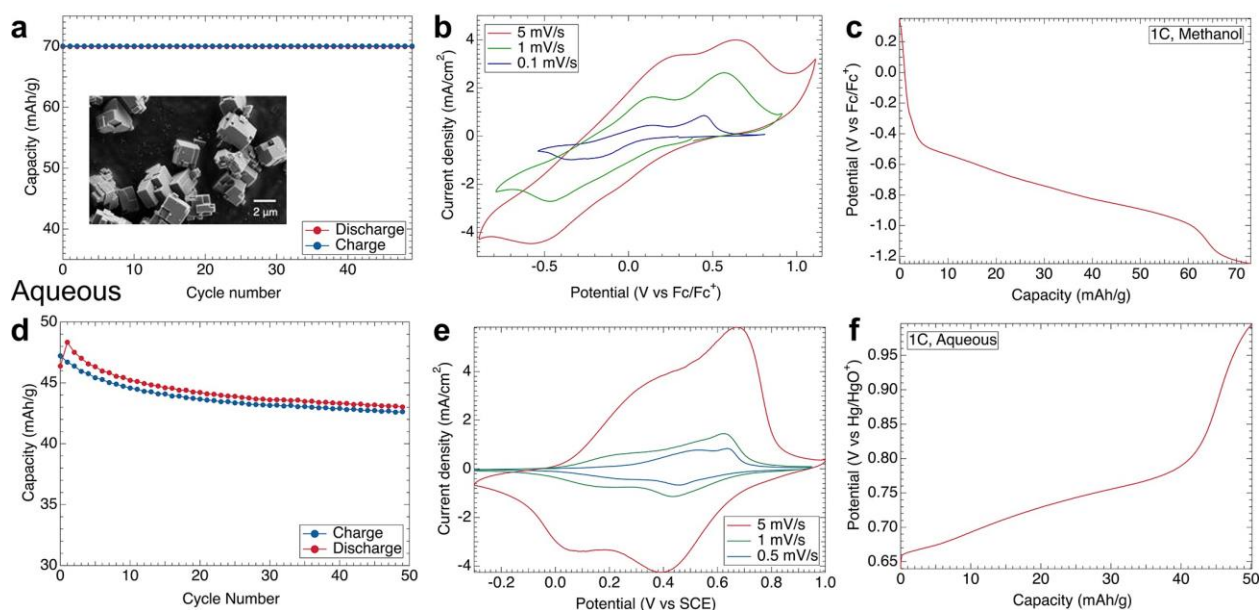


**Figure D.3.** Electrochemical characterizations of the NiHCF RR material in both aqueous and methanol solutions. (a) Galvanostatic charge–discharge tests in a methanol solution containing 0.1 M TBAClO<sub>4</sub>, 20 mM NiNO<sub>3</sub>, and 0.01 M H<sub>2</sub>SO<sub>4</sub> with a NiHCF working electrode (WE) and counter electrode (CE). The inset shows a representative SEM image of NiHCF crystals. (b) CVs of NiHCF in 0.1 M TBAClO<sub>4</sub> and 0.01 M H<sub>2</sub>SO<sub>4</sub> in methanol at a scan rate from 0.1 to 5 mV/s. (c) Galvanostatic discharge curve of NiHCF in methanol with 0.1 M TBAClO<sub>4</sub>, 20 mM NiNO<sub>3</sub>, and 0.01 M H<sub>2</sub>SO<sub>4</sub>. (d) Galvanostatic charge–discharge tests in aqueous 0.5 M H<sub>2</sub>SO<sub>4</sub> with a NiHCF WE and CE. (e) CVs of NiHCF conducted in 0.5 M H<sub>2</sub>SO<sub>4</sub> at a scan rate of 0.5, 1, and 5 mV/s. (f) Galvanostatic charge curve of NiHCF in 1.7 M Na<sub>2</sub>SO<sub>4</sub> and 1 mM NaOH (pH = 11) after discharge in MeOH.

We then studied the electrochemical behaviors of the NiHCF electrode intercalating and deintercalating proton in both methanol and aqueous solutions using a three-electrode setup. The as-synthesized NiHCF was always oxidized before use to allow for intercalation of proton upon reduction. When NiHCF (cubic phase) is reduced with the intercalation of proton rather than an alkali metal cation, the crystal structure remains cubic and does not shift to rhombohedral (Figures D.S4 and D.S5). Before all electrochemical tests, the NiHCF electrode was reduced and oxidized

10 times (Figure D.S6) to activate the electrode. The charge/discharge rate of 1C (meaning the material is fully discharged in 1 h, and a rate of  $nC$  means the battery is fully discharged in  $60/n$  min) was determined based on the capacity of NiHCF in neutral aqueous solutions ( $65 \text{ mAh g}^{-1}$ ). The stability tests show that NiHCF can be cycled repeatedly using protons in methanol with only 1% decay over 50 cycles (Figure D.3a) and in water with a 9.76% decay after 50 cycles (Figure D.3d). CVs of NiHCF at different scan rates show a reversible redox behavior with a NiHCF working and counter electrode in an undivided cell (Figures D.3b and D.3e), following this reaction:



With proton intercalation, it is common to see multiple CV peaks, which is usually attributed to the binding of protons with ligand and zeolitic water molecules.<sup>40,41</sup> The potential window in an acidic aqueous solution is  $-0.3$  to  $1.0$  V vs SCE, and NiHCF has a formal potential of  $0.5$  V (Figure D.3e). In methanol, the potential window is  $-0.9$  to  $1.1$  V vs  $\text{Fc}/\text{Fc}^+$  with a NiHCF counter electrode (Figure D.3b).

With the desired half-reactions in mind, the RR stability bounds were tested. Hydrogen peroxide production can occur over a wide pH range, so the redox performance of the RR electrode was studied under different pH conditions. NiHCF was found to be stable to reduction in acidic to neutral conditions but unstable in alkaline solutions (Figure D.S7). However, NiHCF was stable to oxidation in weakly alkaline solutions. Therefore, we could select an aqueous  $\text{H}_2\text{O}_2$  production supporting electrolyte with a pH from 0 to 11, in which oxidation of NiHCF will take place. For the cell in which NiHCF reduction takes place, the aqueous supporting electrolyte could be acidic to neutral. When undergoing reduction in methanol, NiHCF had more severe dissolution. It was reported that excess Ni ions in solution help stabilize the Prussian blue structure, preventing Ni

dissolution that results in leaching of the redox-active Fe from NiHCF.<sup>42</sup> Therefore, we added 20 mM NiNO<sub>3</sub> into the methanol solution, which improved the cycling performance. Clear improvement of lattice stability is evident by the lack of precipitate formation after 50 cycles of reduction and oxidation in the methanol solution and 23 cycles of ModES (Figures D.S9 and D.S10). Due to potential decomposition of H<sub>2</sub>O<sub>2</sub> in the presence of nickel ions, Ni ions were not added in the aqueous electrolyte, but no color change or precipitate was observed when running H<sub>2</sub>O<sub>2</sub> production.

NiHCF has worse rate capabilities in methanol than aqueous solutions presumably due to the reduced hydrogen bonding network.<sup>43</sup> After studying different cycling currents, keeping the C rate as low as possible during cycling in methanol proved to be essential for maintaining the capacity of NiHCF. A discharging rate not exceeding 1C was selected for this half-reaction (Figure D.S8). In aqueous solutions, the rate capabilities are improved by stronger intermolecular forces as well as higher solution conductivity compared to organic solvents.<sup>20</sup> This means that aqueous half-reactions can be run at a higher rate than the nonaqueous half-reactions. A representative galvanostatic discharge curve of NiHCF (reduction) in methanol from 100 to 25% state of charge (SOC) is shown in Figure D.3c. The corresponding galvanostatic charge curve (oxidation) in a pH = 11 aqueous solution is shown in Figure D.3f.

**Optimization of Half-Reactions.** Literature precedents for the organic half-reaction, the methylarene oxidation reaction, provide an important foundation for the work conducted here.<sup>18,44</sup> CVs, obtained in an acetonitrile solvent, highlight a comparison of redox potentials associated with 4-*t*-butyltoluene and its corresponding intermediate and product relative to that of MeOH (Figure D.4a). The plots show that the methylarene reagent and methyl ether intermediate undergo

oxidation at potentials below that of methanol, while the product dimethylacetal is oxidized at a potential higher than that of methanol.

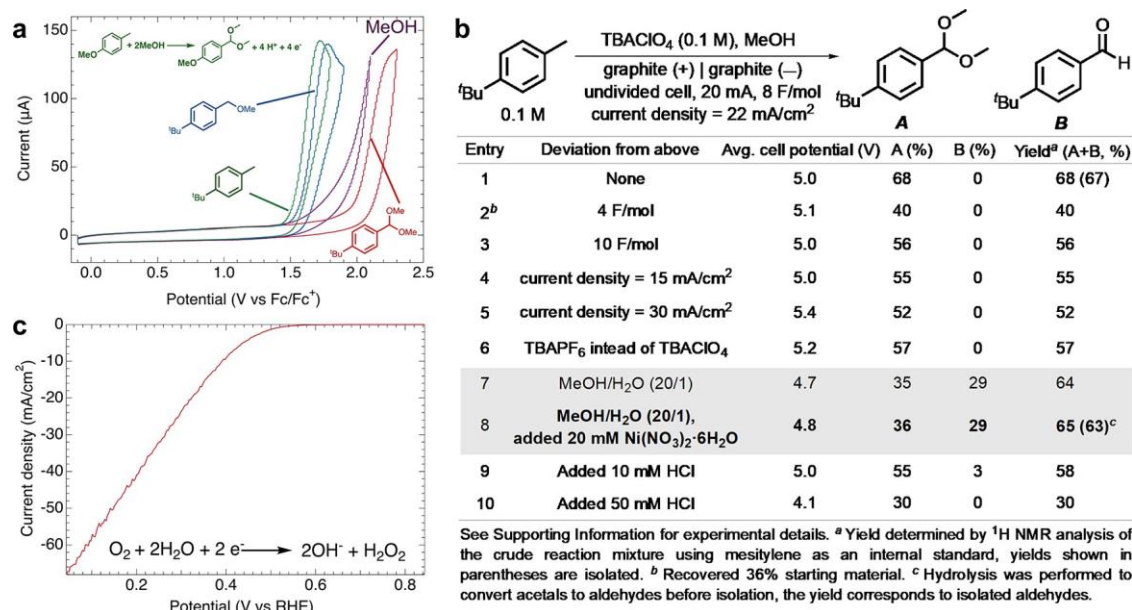


**Figure D.4.** Electrochemical behaviors and product distributions of the separate electrochemical half-reactions. (a) CV data relevant to methylarene oxidation. Conditions: 0.1 M TBAPF<sub>6</sub> in acetonitrile, glassy carbon working electrode, Pt wire counter electrode, reference electrode Ag/AgNO<sub>3</sub> (10 mM AgNO<sub>3</sub> in acetonitrile) corrected vs Fc/Fc<sup>+</sup>. Oxidation of methanol prevents overoxidation of the acetal and aldehyde to the carboxylic acid. (b) Table for optimizing the product yield and distributions of methylarene oxidation with graphite rod working and counter electrodes. Entries 1–6 show optimization of the half-reaction. Entries 7 and 8 reflect conditions used to improve the anticipated performance of the RR. Entries 9 and 10 show the sensitivity of the reaction to excess proton concentration. (c) Linear sweep voltammety (LSV) curve for the cathodic production of H<sub>2</sub>O<sub>2</sub> using an Fe-CNT working electrode with an area of 2 cm<sup>2</sup> at a scan rate of 10 mV/s in O<sub>2</sub>-saturated 1.7 M Na<sub>2</sub>SO<sub>4</sub> (adjusted to pH = 11) with a Pt counter electrode.

By adapting the previously reported conditions, direct oxidation of 4-*t*-butyltoluene delivered a 68% yield of the corresponding dimethyl acetal in an undivided cell using graphite for both the working and auxiliary electrodes (Figure D.4b, entry 1). The reaction was conducted at a constant current of 20 mA, and the optimal yield was obtained after passing 8 F/mol of charge. The reaction did not reach completion when the theoretical charge of 4 F/mol was passed (40% product yield with 36% unreacted starting material, entry 2). A modest drop in yield was observed when more charge was passed (56% yield at 10 F/mol, entry 3), and decreased yields were also observed at

lower and higher current densities (entries 4 and 5). TBAPF<sub>6</sub> was not as effective a supporting electrolyte as TBAClO<sub>4</sub> (entry 6). In anticipation of pairing the methylene oxidation reaction with a proton-exchange RR, a small amount of water was added to the methanol to facilitate proton transport within the RR. This modification resulted in partial hydrolysis of the dimethyl acetal, but a comparable overall acetal/aldehyde yield was obtained (64%, entry 7). The influence of added Ni(NO<sub>3</sub>)<sub>2</sub> was tested to account for the stabilizing effect of Ni<sup>2+</sup> ions on the stability of the NiHCF RR in methanol. The presence of 20 mM Ni(NO<sub>3</sub>)<sub>2</sub> in the electrolyte had minimal impact on the reaction yield (65% yield, entry 8; Figure D.S11). On the other hand, control experiments confirmed that moderate quantities of Brønsted acid in the solution (10 and 50 mol % with respect to the substrate) had a deleterious effect on the reaction, lowering the yield to 58 and 30%, respectively (entries 9 and 10).

For H<sub>2</sub>O<sub>2</sub> production at the cathode, we used carbon-based catalysts as the working electrodes due to their stability and good performance in neutral to alkaline conditions and their low cost.<sup>45</sup> Following previous reports, annealed carbon felt<sup>20,29,46</sup> and iron-decorated carbon nanotubes<sup>47</sup> (10 nm width) (Fe-CNT; Figure D.S12) were prepared and tested in neutral to weakly alkaline solutions (Figures D.S13–D.S.15) with LSV in a divided cell with a Pt counter electrode to measure the current density (Figure D.4c). We chose a solution of 1.7 M Na<sub>2</sub>SO<sub>4</sub> adjusted to pH = 11 with 1 M NaOH for performing H<sub>2</sub>O<sub>2</sub> electrosynthesis due to the high activity of H<sub>2</sub>O<sub>2</sub> production, reduced competition with OER, and the stability of the RR. Under these conditions, the 2 cm<sup>2</sup> Fe-CNT cathode showed a current of –100 mA at 0.16 V vs RHE (reversible hydrogen electrode, Figure D.4c). Various applied potentials were screened using chronoamperometry (Figure D.S16), and the produced H<sub>2</sub>O<sub>2</sub> was quantified chemically using titration (see details in the Supporting Information, Figure D.S17). The best current density and Faradaic efficiency (FE)

were achieved using Fe-CNT electrodes on hydrophobic carbon fiber paper, similar to what was previously reported.<sup>47</sup> A potential of 0.244 V vs RHE was selected to ensure a high FE above 90% when accumulating 200 ppm of H<sub>2</sub>O<sub>2</sub> in a 30 mL cell.

**Proton-Balancing Ability of the RR.** The overall ModES reaction requires protons to be transferred from the methylarene oxidation reaction cell in methanol to the cathodic H<sub>2</sub>O<sub>2</sub> production cell in water by the RR (Figure D.2c). Therefore, it is important to study the ability of the RR electrode to transfer and balance protons. Protons have a smaller mass and ionic radius compared to metal ions and exhibit the fastest diffusion kinetics via the Grotthuss mechanism, which allows protons to be transferred via a hydrogen bonding network (Figure D.5a).<sup>34,48</sup> Under the Grotthuss proton conduction mechanism, zeolitic water in the PBA cages and ligand water in anion vacancies can form a continuous hydrogen bonding network that allows for concerted cleavage and formation of O–H bonds for proton transfer.<sup>35</sup>

In the beginning of the methylarene oxidation reaction process, there is a large excess of the supporting electrolyte cation and an absence of protons in solution. If a metal cation that can be intercalated into NiHCF, such as sodium, is present, it will compete with proton and result in ion imbalance. Unlike conventional batteries in which there is a large excess of the ions causing the redox, this ModES system requires the protons produced during anodic oxidation to be intercalated into the RR electrode. Because the reaction yield of the methylarene oxidation reaction is affected by high proton concentration (Figure D.4b, entries 9 and 10), an acidic electrolyte cannot be used to alleviate ion competition. To manage this competition, we selected a tetrabutylammonium (TBA) cation-based supporting electrolyte, TBAClO<sub>4</sub>, to ensure preferred intercalation of protons based on the cation size (Figure D.5a). TBA<sup>+</sup> has an approximate diameter of 9.9 Å,<sup>49</sup> which is larger

than that of the NiHCF cage (5.1 Å),<sup>50</sup> thus ensuring exclusion from the cage. In contrast, the desolvated ionic diameter of Na<sup>+</sup> is 1.9 Å, allowing it to compete with protons.<sup>51</sup>

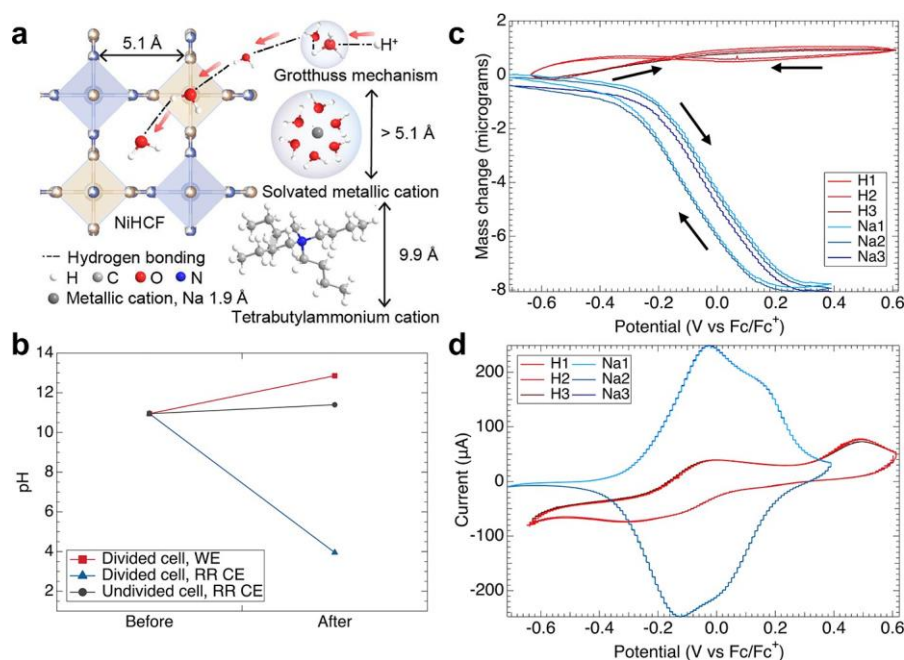


**Figure D.5.** Proton-balancing ability of the NiHCF RR. (a) Schematic of the Grotthuss mechanism, size of ions, and NiHCF cage illustrating the role of hydrogen bonding and the need to minimize ion competition. (b) pH shifts showing the proton intercalation and deintercalation ability of the RR. A pH = 11 solution was used in both the undivided and divided cells. The RR was reduced in 1 M H<sub>2</sub>SO<sub>4</sub> in methanol and then oxidized, releasing protons in the respective cells. H<sub>2</sub>O<sub>2</sub> production was performed at the working electrode to ensure proton release. (c) Electrochemical quartz crystal microbalance measured mass change of proton (d)intercalation of NiHCF in a 1:20 water-to-methanol solution of 1 mM H<sub>2</sub>SO<sub>4</sub>, 20 mM NiNO<sub>3</sub>, and 0.1 M TBAClO<sub>4</sub> in comparison with sodium (de)intercalation in 0.1 M Na<sub>2</sub>SO<sub>4</sub> in methanol. Slope trends are opposite of each other due to their differing (de)intercalation mechanisms. (d) The corresponding CVs during the measurements of the mass changes in panel (c).

To further improve the proton uptake into the RR, we also varied the water-to-methanol ratio as the solvent for the methylarene oxidation reaction. The addition of water enhances the kinetics of proton intercalation by improving the hydrogen bonding network and improves the solution conductivity compared to a purely methanol solution.<sup>52</sup> Even though adding water introduces competition between OER and the methylarene oxidation reaction, the benefits of improved conductivity and kinetics outweigh the slight loss in FE and minimal decrease in product yield (cf.

Figure D.4b). We found that the optimal water-to-methanol ratio is 1:20, which retained the methylene oxidation reaction product yield and FE while improving RR performance.

To evaluate the proton (de)intercalation by the NiHCF RR, we ran hydrogen peroxide production in undivided and divided cells to monitor pH changes with the RR as the counter electrode. In the divided cell, there is a glass frit dividing the working and counter electrode chambers to slow down ion movement, primarily allowing the supporting electrolyte ions to pass between the two chambers to maintain charge balance. As a result, pH shifts can be measured in the two chambers immediately following the electrochemical experiment. The RR was first reduced in methanol with 1 M H<sub>2</sub>SO<sub>4</sub> as the supporting electrolyte. For the RR oxidation, the supporting electrolyte was a 1.7 M Na<sub>2</sub>SO<sub>4</sub> and 1 mM NaOH aqueous solution. In the divided cell, an increase of 1.91 pH units was observed in the working electrode compartment due to the hydroxide released during H<sub>2</sub>O<sub>2</sub> production (Figure D.5b, red trace). In the counter electrode compartment, there was a decrease of 7 pH units from the protons deintercalated from the NiHCF RR (Figure D.5b, blue trace). In an undivided cell, all ions can diffuse through the cell and the same supporting electrolytes were used for the RR reduction and oxidation. Only a small pH shift of 0.45 pH units was observed in the undivided cell (Figure D.5b, gray trace) because the proton deintercalated from the NiHCF neutralizes the hydroxide produced from H<sub>2</sub>O<sub>2</sub> production. This demonstrates that the NiHCF RR is capable of balancing the protons across solvents.

For further support that protons are the ions that are intercalated into the NiHCF RR, we conducted operando electrochemical quartz crystal microbalance (EQCM) measurements during cyclic voltammetry (Figures D.5c and D.5d) to monitor the electrode mass change (see details in the Supporting Information). In PBAs, cation (de)intercalation must be charge balancing the redox process.<sup>53</sup> The EQCM results (Figure D.5c, red trace) show that during reduction (protonation) the

electrode experiences a frequency increase indicating a mass loss according to the Sauerbrey equation.<sup>54</sup>

$$\Delta f_s = -\frac{2*f_0^2*\Delta m*n}{(\mu_q\rho_q)^{\frac{1}{2}}} \quad (6)$$

which simplifies to:

$$\Delta f = -C_f * \Delta m \quad (7)$$

where  $\rho_q$  is the density of the quartz crystal (2.648 g/cm<sup>3</sup>),  $\mu_q$  is the shear modulus of quartz (2.947  $\times 10^{11}$  g/cm s<sup>2</sup>),  $f_0$  is the resonant frequency of the fundamental mode of the crystal in Hz,  $C_f$  is the sensitivity factor,  $n$  is the overtone, and  $\Delta m$  and  $\Delta f$  are the mass change and frequency change, respectively. During oxidation (deprotonation), the frequency change is reversed for a mass gain. This indicates that solvent movement dominates the mass change as it is reversibly inserted into the lattice in a movement opposite to that of proton.<sup>41, 55</sup> Since the mass of a proton is much smaller than that of the solvent molecules assisting with hydrogen bonding, the slopes are the opposite of what is expected.<sup>55</sup> This was also observed when measuring NiHCF in an acidic aqueous solution (Figure D.S18). In contrast, when measuring the frequency and mass change of NiHCF with sodium ions as the intercalating ion in methanol, the expected mass change trend is observed (Figure D.5c, blue trace). This is because sodium ions rely on ionic attraction for movement during (de)intercalation and not a hydrogen bonding network like protons.

In summary, the slope of the mass change curves measured in an acidic methanol solution (Figure D.5c, red trace) indicates that lattice water and solvent molecule rearrangement plays a large role in the ion intercalation process, rather than being dependent on cation–anion attraction as alkali metal ions would be (Figure D.5c, blue trace).<sup>53</sup> This is indicative of proton movement into and out of the NiHCF RR material. This proton (de)intercalation is reversible, indicated by the electrode having the same mass when fully oxidized and reduced over multiple cycles (Figure

D.5c, red trace). Additionally, no mass change was observed when a bare Cr/Au-coated quartz crystal was measured in the same potential range in the same solution (Figure D.S19), indicating that the mass changes were due to the behavior of the NiHCF thin film.

**Proton-Balanced ModES Production of 4-*t*-Butyl Benzyl Acetal/Aldehyde and H<sub>2</sub>O<sub>2</sub>.** The full cycle of ModES involves two half-reactions conducted sequentially in different electrolytes with the RR switched between the two undivided cells (Figure D.6a) with a three-electrode configuration. Before ModES cycling, the RR electrode (Figure D.S20) is fully oxidized in aqueous solution. For the methylarene oxidation reaction step, the RR electrode is washed in water and then in methanol multiple times and then dried (Figure D.6a). A current density of 22 mA/cm<sup>2</sup> is applied to the graphite rod working electrode, while the RR is reduced to 25% SOC based on its capacity in aqueous solution (34 C) in the optimized supporting electrolyte of 0.1 M TBAClO<sub>4</sub> and 20 mM NiNO<sub>3</sub> in a methanol/water mixture (20:1; cf. Figure D.4b). The average potential on the graphite rod is approximately 2.1 V vs Fc/Fc<sup>+</sup>. For the aqueous hydrogen peroxide production step at pH = 11, the applied potential was set at 0.244 V vs RHE and the RR is oxidized back to 100% SOC with an average current density of 39 mA/cm<sup>2</sup>. The same amount of charge was passed for the aqueous and nonaqueous half-reactions.

After 23 cycles of continuous ModES operation, full conversion of 1 mmol 4-*t*-butyltoluene was achieved, producing the aldehyde/acetal products in 52% yield (Figures D.6b, D.6c, and D.S21). This corresponds to an FE of 26%, which is similar to the FE in the control experiment (34%; entry 8, Figure D.4b). Methylarene oxidation occurs progressively within the same 10 mL cell throughout the ModES process. Modest solvent loss over time due to the repeated transfer of the RR electrode between the two reaction cells likely contributes to the yield reduction relative to the single-batch result in Figure D.4b. On the cathodic side, a fresh 30 mL aqueous Na<sub>2</sub>SO<sub>4</sub>

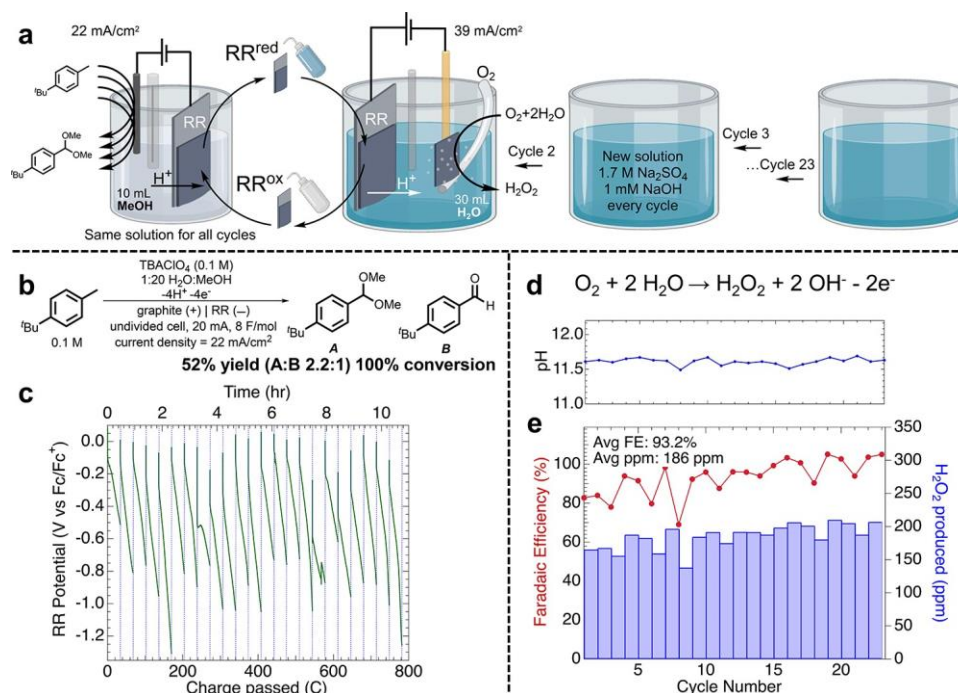


**Figure D.6.** Modular electrosynthesis of 4-*t*-butylbenzaldehyde in methanol and H<sub>2</sub>O<sub>2</sub> in aqueous solution enabled by the proton-selective NiHCF RR. (a) Full schematic of the ModES process for pairing the methylarene oxidation reaction and H<sub>2</sub>O<sub>2</sub> production. (b) Reaction schematic of methylarene oxidation to 4-*t*-butylbenzaldehyde and the acetal product resulting from 23 cycles of ModES with the resulting product yields. (c) Potential of the NiHCF RR electrode during methylarene oxidation at the working electrode over 23 ModES cycles. (d) Reaction equation and pH after H<sub>2</sub>O<sub>2</sub> production for each cycle. The electrolyte had a starting pH of 11 and shifted minimally during the production of 200 ppm H<sub>2</sub>O<sub>2</sub> showing pH stability over the course of the ModES cycling. (e) FE and concentration of H<sub>2</sub>O<sub>2</sub> produced in the aqueous cell for each ModES cycle. A new 30 mL solution was used for each cycle.

solution (1.7 M, adjusted to pH = 11) under continuous bubbling of oxygen gas was used for each ModES cycle at a constant potential, producing an average of 186 ppm H<sub>2</sub>O<sub>2</sub> (5.47 mM) with an FE of 93.2% (Figure D.6e). Such accumulated concentration of H<sub>2</sub>O<sub>2</sub> is already useful for many applications, such as disinfection and water treatment.<sup>32</sup> There was only a 0.4–0.7 pH unit increase per cycle during the cathodic reaction (Figure D.6d). Approximately 10% of protons released during the oxidative reaction are not intercalated into the RR. Due to the sensitivity of the methylarene oxidation reaction to excess protons, a small amount of base *N,N*-diisopropylethylamine (20 μL) was added every four cycles to the organic reaction mixture to neutralize the excess protons. X-ray diffraction confirmed that the phase and crystallinity of the

NiHCF RR did not change after 23 cycles of ModES, ending in the fully oxidized state (Figure D.S22).

**Extension to Another Oxidation Reaction (Arene C–H Amination) and Organic Solvent (Acetonitrile).** With the understanding that the NiHCF RR can be used to balance electrons and protons across half-reactions in different solvents, we pursued pairing another oxidation reaction with a different set of reaction conditions (Figure D.7a). Yoshida and co-workers have reported an arene C–H amination reaction involving oxidative coupling of arenes with pyridine to afford arylpyridinium products, which are then directly converted to the corresponding anilines upon treatment with piperidine.<sup>56</sup> The reported reactions are performed in acetonitrile using a divided cell configuration. We first conducted the Yoshida amination reaction under the reported conditions with a Pt cathode in divided and undivided cells to assess the influence of the cell configuration (see experimental details in the Supporting Information). These reactions afforded 72% and 6% yields of the 1-naphthylamine product, respectively (Figures D.S23 and D.S24). The low yield in the undivided cell is attributed to the facile in situ reduction of the arylpyridinium product at the Pt cathode.

We then repeated the reaction in an undivided cell in which the Pt cathode was replaced with the NiHCF RR as the counter electrode (Figure D.7a, left side). Under otherwise identical conditions, the reaction affords 1-naphthylamine in yields up to 67% (Figures D.7b and D.S25, see full screening details in Table D.S2). It was necessary to include some cations in the acetonitrile solution to facilitate the ion transport and support effective cycling of the RR. Due to the sensitivity of this reaction to water, unlike the methylarene oxidation reaction described above, water could not be used as a source of H<sup>+</sup> cations. Addition of 100 mM acetic acid to the reaction mixture led to a 52% yield of product (Figures D.7b and D.S26). Speculating that acetic acid could hydrogen

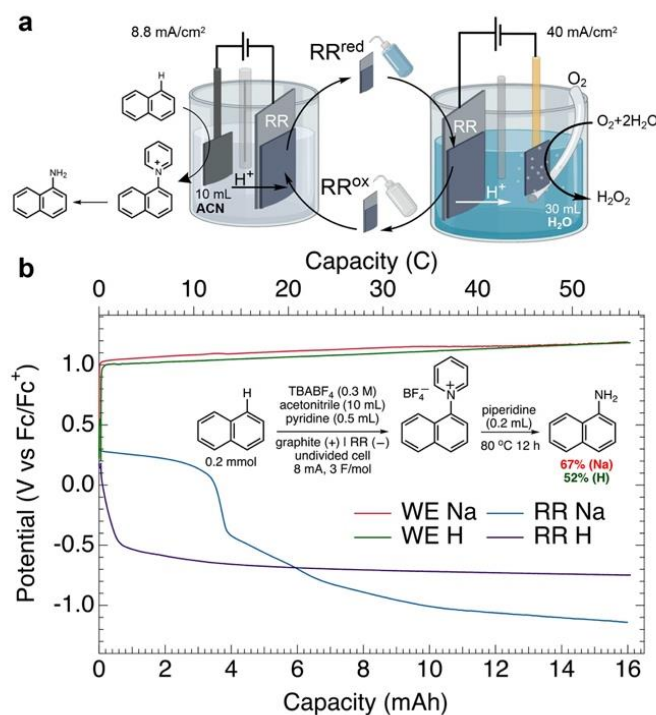


**Figure D.7.** Modular electrosynthesis of 1-naphthylamine in acetonitrile and  $\text{H}_2\text{O}_2$  in aqueous solution enabled by the NiHCF RR. (a) Full schematic of the ModES process for pairing the oxidative C–H amination of naphthalene and  $\text{H}_2\text{O}_2$  production. (b) Potential evolution of the NiHCF RR counter electrode and carbon felt working electrode during naphthalene amination with  $\text{NaClO}_4$  (blue and red traces, respectively) and acetic acid (purple and green traces, respectively) added in the electrolyte. The inset shows the reaction schematic for naphthalene amination and the resulting product yields.

bond with pyridine in solution and limit its effectiveness as a nucleophile, we tested sodium cations for improving the reaction. The optimal yield (66%) was obtained from a reaction mixture initiated with 16 mM  $\text{NaClO}_4$ . The cell potential evolution during the discharge process (Figure D.7b, blue RR Na trace) suggests that sodium ions are readily intercalated into the RR at the early stages of the reaction, after which protons accumulated from oxidation of naphthalene undergo intercalation into the RR. This anodic arene C–H amination can proceed in an undivided cell together with the reduction of the RR electrode because the pyridinium intermediate does not decompose on the RR electrode. This is supported by CVs on platinum that show an onset potential of reduction at  $-0.95$  V vs  $\text{Fc}/\text{Fc}^+$  in the presence of pyridinium (Figure D.S27). Figure D.7b shows that the RR electrode

remains at a potential above  $-0.95$  V for the majority of the electrolysis. In contrast, the reduction of pyridinium has a similar potential to that seen for hydrogen evolution (Figures D.S27–D.S29).

Furthermore, the use of RRs to support the electrosynthesis of  $\text{H}_2\text{O}_2$  in aqueous solution (Figure D.7a, right half), following the oxidative amination of naphthalene in acetonitrile, was successful and proceeded with an FE of 85%. This completes the ModES cycle and demonstrates the pairing of aqueous  $\text{H}_2\text{O}_2$  production with another anodic organic electrosynthetic reaction in another solvent beyond methanol, which was used in the methylarene oxidation reaction discussed above. These results suggest the potential utility of the ModES strategy for general organic electrosynthesis and also highlight the advantage that the use of RR can translate an electrolysis reaction that requires a divided cell under conventional conditions into a reaction that proceeds effectively in an undivided cell.

#### **D.IV. Conclusion**

In conclusion, we demonstrate the pairing of two electrosynthetic reactions across different solvents: methylarene oxidation in methanol or naphthalene C–H amination in acetonitrile with hydrogen peroxide production in water using an ion-balanced ModES strategy. These ModES processes are enabled by a proton-selective NiHCF RR material that (de)intercalates protons to maintain pH stability for the electrochemical cells, allowing for effective methylarene oxidation or arene C–H amination, and the accumulation of  $\text{H}_2\text{O}_2$ . Careful experiments ensure and confirm the selective transport of protons through NiHCF RR electrodes from the nonaqueous anodic cell to the aqueous cathodic cell. Not only would these pairings of electrochemical reactions not be possible without the RR because of the incompatible reaction media, but also the ModES process eliminates the less productive auxiliary counter electrode reactions and the need for expensive and cumbersome ion-selective membranes used in divided electrochemical cells. These pairings show

the utility of ModES by enabling the synthesis of three chemicals (both inorganic and organic) with flexibility in rate, scale, and reaction conditions.

To increase the utility of ModES in general organic electrosynthesis, the development of RR materials that have high stability, solvent compatibility, selectivity for ion transport, and high capacity is crucial. Higher capacity materials improve the practicality of ModES because many organic electrochemical reactions require large amounts of charge. The emerging proton battery materials<sup>35,57</sup> would be suitable candidates, but they are commonly reported in aqueous systems, so their solvent compatibility, stability, and ion selectivity need to be screened and further improved. Flexible pairing of electrochemical syntheses of products that have incompatible reaction conditions, different and variable market demand but similar local applications without sacrificial half-reactions and expensive membranes could enhance the economic viability of distributed electrochemical production.

#### **D.V. Acknowledgements**

This work was supported by the University of Wisconsin-Madison UW2020 grant provided by the Wisconsin Alumni Research Foundation (WARF). Z.-M.S. and S.S.S. were also supported by the NIH (R35 GM134929). Spectroscopic instrumentation was supported by a generous gift from Paul J. and Margaret M. Bender, the NIH (S10 OD020022), and the NSF (CHE-1048642). The authors gratefully acknowledge the use of facilities and instrumentation supported by NSF through the University of Wisconsin-Madison Materials Research Science and Engineering Center (DMR-1720415).

#### **D.VI. Author Contributions**

S.J., K.H.M., H.S., and W.L. conceived the project. S.J. and K.H.M. designed the experiments. K.H.M. led the efforts on synthesis and electrochemical analysis of RR candidates, materials

characterization, optimization of HPR and Yoshida amination as half-reactions, as well as performed all ModES reactions. Z.-M.S. optimized the methylarene oxidation reaction and contributed in part to optimization of Yoshida amination. R.W. provided Fe-CNT materials. F.W. provided the procedure for RR synthesis. S.S.S. served as consultant for this work. S.J., K.H.M., and Z.-M.S. wrote the manuscript.

## D.VII. Supporting Information

### Experimental Section

#### *Chemicals and materials*

All chemicals were used as purchased without further purification. Nickel (II) chloride hexahydrate ( $\text{NiCl}_2 \cdot 6\text{H}_2\text{O}$ , 99.9%), sodium ferrocyanide decahydrate ( $\text{Na}_4\text{Fe}(\text{CN})_6 \cdot 10\text{H}_2\text{O}$ ,  $\geq 99\%$ ), sulfuric acid ( $\text{H}_2\text{SO}_4$ , 95–98%), sodium sulfate ( $\text{Na}_2\text{SO}_4$ , 99%), cerium sulfate ( $\text{Ce}(\text{SO}_4)_2$ , 94%), sodium hydroxide ( $\text{NaOH}$ , 98%), isopropyl alcohol ( $(\text{CH}_3)_2\text{CHOH}$ , 99.5%), tetrabutylammonium perchlorate (98%), 4-*tert*-butylanisole (95%), iron (III) nitrate nonahydrate ( $\text{Fe}(\text{NO}_3)_3 \cdot 9\text{H}_2\text{O}$ , 98%), and multi-walled carbon nanotube (MWCNT, 724769, > 95% carbon) were purchased from Sigma Aldrich. Sodium citrate dihydrate (ACS reagent grade) was purchased from ICN Biomedicals Inc. Carbon black (Super P Conductive, 99.0+%) was purchased from Alfa Aesar. TUBALL BATT NMP 0.4% (a mixture of single-wall carbon nanotubes, 0.4 wt%; polyvinylidene fluoride, 2 wt%; *N*-methyl-2-pyrrolidone, > 96.7 wt%) was purchased from OCSiAl. Type 316 stainless steel (316 SS) mesh and AvCarb 1071 HCB carbon cloth were purchased from Fuel Cell Store. Anhydrous methanol was purchased from Macron Fine Chemicals. Deionized nanopure water (18.2  $\text{M}\Omega \cdot \text{cm}$ ) from Thermo Scientific Barnstead water purification systems was used for all experiments.

### *Synthesis of NiHCF*

Nickel hexacyanoferrate (NiHCF) was synthesized via a coprecipitation method previously reported.<sup>20,38</sup> 100 mL of 0.1 M NiCl<sub>2</sub>·6H<sub>2</sub>O and 1 M sodium citrate dihydrate solution and 100 mL of 0.1 M Na<sub>4</sub>Fe(CN)<sub>6</sub>·10H<sub>2</sub>O were simultaneously added dropwise to 100 mL H<sub>2</sub>O under vigorous stirring. The molar ratio between Ni<sup>2+</sup> and citrate was 1:10. The solution was then stirred for another 24 h at 80 °C to yield a light-green precipitate. This precipitate was centrifuged and then rinsed with deionized water multiple times with a final wash in ethanol, then dried in a vacuum oven at 60 °C overnight.

### *Synthesis of Fe-CNT Catalyst*

The synthesis of Fe-CNT catalyst followed a previously reported impregnation and reduction method with minor modifications.<sup>28,47</sup> In a typical synthesis, a 7.5 mM iron nitrate stock solution was first prepared by dissolving 30.3 mg Fe(NO<sub>3</sub>)<sub>3</sub>·9H<sub>2</sub>O into 10 mL nanopure water. The carbon nanotube (CNT) suspension was prepared by mixing 50 mg multiple walled CNT (MWCNT) with 20 mL of ethanol via sonication for 1 h until a well dispersed suspension was achieved. Then 200 μL of 7.5 mM Fe<sup>3+</sup> solution was added dropwise into the CNT suspension under sonication for 30 min, making a raw atomic ratio of Fe:C around 0.1 at.%. Then the solvent was removed using a rotary evaporator, and the as-prepared material was dried in a vacuum oven at 60 °C for 20 min to further evaporate the residual solvent. The dried Fe(NO<sub>3</sub>)<sub>3</sub>/CNT powder was heated in a tube furnace to 600 °C in 20 min under a flow of 100 sccm Ar gas (UHP, Airgas) and pressure of 1 Torr, and kept at the same temperature for another 40 min before cooling down to room temperature.

### *Fabrication of Redox Reservoir Electrode*

The RR electrodes were prepared using a conventional slurry-casting method. Typically, NiHCF powder (70 wt%) and super P conductive carbon (18 wt%) were ground with a mortar and pestle for 30 min then stirred with SWCNT (2 wt%), and polyvinylidene fluoride (PVDF) (10 wt%) from TUBALL BATT NMP (consisted of 0.4 wt% SWCNT, 2 wt% polyvinylidene fluoride, > 96.7 wt% *N*-methyl-2-pyrrolidone) at 800 rpm overnight at room temperature into a well dispersed slurry. This slurry was cast onto a 316 SS mesh current collector, unless otherwise stated. The prepared electrodes were dried in a vacuum oven at 60 °C for 12 h to remove the residual solvent. The mass loading of active material was approximately 20 mg/cm<sup>2</sup>.

### *Materials Characterization*

The size and morphology of the NiHCF product were characterized using a scanning electron microscope (SEM, Zeiss SUPRA 55VP Scanning Electron Microscope) equipped with an energy dispersive X-ray spectroscopy (EDS) detector. Powder X-ray diffraction (PXRD) patterns were collected on a Bruker D8 Advance X-ray diffractometer with Cu-K $\alpha$  radiation. Inductively coupled plasma-optical emission spectrometer (ICP-OES, Agilent 5110) was utilized to determine the compositions of Na, Ni, and Fe elements, and thermogravimetric analysis (TGA, TA Q500) was used to determine the water content in NiHCF samples. The TGA analysis was done with a ramp rate of 5 °C/min under an N<sub>2</sub> atmosphere. The Fe-CNT catalyst was characterized using a transition electron microscope (TEM, FEI Tecnai T12) operated at 120 keV with a Gatan CCD image system.

### *Electrochemical characterization*

All the electrochemical measurements, except the methylarene oxidation reaction optimization reactions, were carried out using a Bio-Logic SP-200 potentiostat or a Bio-Logic VMP-3 multichannel potentiostat. A three-electrode cell was used for measurements with a Pt or graphite

counter electrode (Figures D.S30a and D.S30b) and an appropriate reference electrode: Ag/AgNO<sub>3</sub> (internal solution, 0.1 M TBAClO<sub>4</sub> and 0.01 M AgNO<sub>3</sub> in methanol from BASi, or leak-free Ag/Ag<sup>+</sup> reference from Innovative Instruments, Inc, Figure D.S30c) for organic conditions, SCE in aqueous acidic/neutral conditions, Hg/HgO in aqueous alkaline solution. For non-aqueous systems, the redox potential of ferrocene/ferrocenium was measured under the same experimental conditions and used to provide an internal reference. Before all electrochemical tests, the NiHCF RR electrodes were activated using a 10- to 15-cycle cyclic voltammogram or galvanostatic charge-discharge tests at 1C rate where 1C is defined as 65 mAh g<sup>-1</sup> based on the demonstrated capacity of NiHCF in 1.7 M Na<sub>2</sub>SO<sub>4</sub>.

#### *Methylarene oxidation reaction optimization and characterization*

All methylarene oxidation reaction optimization experiments were performed using a Pine WaveNow PGstat. The CV experiments were carried out in a three-electrode cell configuration with a glassy carbon (GC) working electrode (3 mm diameter), and a platinum wire counter electrode (~ 1.0 cm, spiral wire, Figure D.S30a). The working electrode potentials were measured versus a Ag/AgNO<sub>3</sub> reference electrode (internal solution, 0.1 M TBANPF<sub>6</sub> and 0.01 M AgNO<sub>3</sub> in MeCN). The GC working electrode was polished with alumina powder (5 μm) before each experiment. Bulk electrolysis experiments were performed in custom-built undivided cells (Figure D.S31a), with graphite rods (3 mm diameter, Figure D.S30b) as working and counter electrodes.

Product characterization: <sup>1</sup>H and <sup>13</sup>C NMR (Nuclear Magnetic Resonance) spectra were recorded on a Bruker 400 MHz spectrometer with a BBFO probe. Chemical shifts are given in parts per million (ppm) relative to residual solvent peaks in the <sup>1</sup>H and <sup>13</sup>C NMR spectra or are referenced as noted. The following abbreviations (and their combinations) are used to label the multiplicities: s (singlet), d (doublet), t (triplet), m (multiplet) and br (broad). Chromatographic

purification of products was accomplished with silica gel 60 M (particle size 40–63  $\mu\text{m}$ , 230–400 mesh) from MACHEREY-NAGEL Inc. Thin-layer chromatography (TLC) was performed on Silicycle silica gel UV254 pre-coated plates (0.25 mm). Visualization of the developed chromatogram was performed by using UV lamps or  $\text{KMnO}_4$  stain.

Condition screening: To the undivided cell was added 4-*tert*-butyltoluene (86  $\mu\text{L}$ , 0.5 mmol, 1.0 equiv), electrolyte (0.5 mmol, 0.1 M), and anhydrous methanol solvent (5 mL). In some cases  $\text{Ni}(\text{NO}_3)_2 \cdot 6\text{H}_2\text{O}$  (29.1 mg, 0.1 mmol, 20 mM), HCl (10 mM or 50 mM), and/or a small fraction of water (water:methanol = 1:20) was added to the methanol solution. Two graphite rods were inserted into the cell and sealed with a rubber septum. The reaction mixture was electrolyzed at a constant current and current density and allowed to pass the required amount of charge while undergoing stirring at 600 rpm. The reaction was stopped automatically by the potentiostat after the set reaction time was achieved, and the resultant solution was directly concentrated *in vacuo* and analyzed by  $^1\text{H}$  NMR using mesitylene as an internal standard to calculate the NMR yield.

Product isolation under optimal condition - acetals: The resultant solution was directly concentrated *in vacuo* and the crude was purified by column chromatography (eluent: hexane/ethyl acetate, 12/1) to furnish the desired product as a yellow oil (70 mg, 67%). Spectroscopic data of the product aligned well with reported literature.<sup>58</sup>

$^1\text{H}$  NMR (400 MHz,  $\text{CDCl}_3$ ):  $\delta$  7.35 – 7.17 (m, 4H), 5.36 (s, 1H), 3.33 (s, 6H), 2.61 (t, 2H), 1.62 – 1.56 (m, 2H), 1.35 (m, 2H), 0.92 (t, 3H).

$^{13}\text{C}$  NMR (101 MHz,  $\text{CDCl}_3$ ):  $\delta$  143.2, 135.4, 128.3, 126.6, 103.4, 52.8, 35.4, 33.6, 22.3, 13.9.

Product isolation under optimal condition - aldehydes: The resultant solution was directly concentrated *in vacuo* before hydrolysis was carried out to convert the acetal to the corresponding aldehyde. The crude was then purified by column chromatography (eluent: hexane/ethyl acetate,

15/1) to furnish the desired product as a pale-yellow oil (51 mg, 63%). Spectroscopic data of the product aligned well with reported literature.<sup>59</sup>

**<sup>1</sup>H NMR** (400 MHz, CDCl<sub>3</sub>): δ 10.01 (s, 1H), 7.86 (d, *J* = 8.3 Hz, 2H), 7.59 (d, *J* = 8.4 Hz, 2H), 1.39 (s, 9H).

**<sup>13</sup>C NMR** (101 MHz, CDCl<sub>3</sub>): δ 192.13, 158.47, 134.08, 129.75, 126.01, 35.35, 31.07.

#### *H<sub>2</sub>O<sub>2</sub> production and detection*

To prepare the Fe-CNT working electrodes, typically, 10 mg of as-prepared Fe-CNT catalyst was mixed with 1 mL of ethanol and 100 μL of Nafion 117 solution (5%), and then sonicated for 2 h to get a well dispersed catalyst ink. Then 40 μL of the catalyst ink was drop-cast onto 4 cm<sup>2</sup> Toray carbon paper (TGP-H-060, Fuel Cell Store) and then dried at room temperature (Figure D.S30d). The mass loading of each electrode was around 0.2 mg.

H<sub>2</sub>O<sub>2</sub> production reaction was optimized in an H-cell with a glass frit (89057-578, ACE glass Incorporated, USA) with Fe-CNT as the working electrode, a Pt wire as the counter electrode, and a Hg/HgO reference electrode in 1.7 M Na<sub>2</sub>SO<sub>4</sub> solution adjusted to pH 11 with 1 M NaOH. Prior to the measurements, the electrolyte was purged with O<sub>2</sub> gas for 15 min. Linear sweep voltammetry (LSV) was conducted with continuous O<sub>2</sub> gas bubbling at 10 mV/s. Chronoamperometry (CA) was conducted at different potentials (0.244 to 0.394 V vs RHE). All potentials measured against Hg/HgO electrode were converted to the reversible hydrogen electrode (RHE) scale using  $E_{\text{RHE}} = E_{\text{Hg/HgO}} + 0.098 \text{ V} + 0.059 \times \text{pH}$ , where the pH values of solutions were determined using an Orion 810 BNUWP ROSS Ultra pH meter. For runs in 1.7 M Na<sub>2</sub>SO<sub>4</sub>, potentials were measured against SCE and converted to the reversible hydrogen electrode scale using  $E_{\text{RHE}} = E_{\text{SCE}} + 0.241 \text{ V} + 0.059 \times \text{pH}$ . For ModES, an undivided cell configuration was used (Figure D.S31b).

Product characterization: To determine the Faradaic efficiency (FE) of the hydrogen peroxide production in weakly alkaline conditions, the concentration of the H<sub>2</sub>O<sub>2</sub> generated from chronoamperometry (CA) was quantified by colorimetric titration with ceric sulfate.<sup>60,61</sup> A 4 mM Ce(SO<sub>4</sub>)<sub>2</sub> solution was prepared by dissolving Ce(SO<sub>4</sub>)<sub>2</sub> in 0.5 M H<sub>2</sub>SO<sub>4</sub> and diluted to 0.4 mM. A calibration curve was constructed with every dilution by measuring the UV-Vis spectroscopy of Ce(SO<sub>4</sub>)<sub>2</sub> solutions using a Cary 50 SCAN spectrometer with different concentrations at a wavelength of 319 nm (Figure D.S17).

An appropriate volume of sample solution containing the produced H<sub>2</sub>O<sub>2</sub> was added into 5.0 mL 0.4 mM Ce(SO<sub>4</sub>)<sub>2</sub> solution and measured by the UV-Vis spectroscopy to determine the concentration of Ce<sup>4+</sup>. The concentration of H<sub>2</sub>O<sub>2</sub> could be determined by the following equations:



$$[\text{H}_2\text{O}_2](\text{mM}) = \frac{V_{\text{before}} * [\text{Ce}_{\text{before}}^{4+}] - (V_{\text{before}} + \Delta V) * [\text{Ce}_{\text{after}}^{4+}]}{\Delta V * 2} \quad \text{Eq. S2}$$

where  $V_{\text{before}}$  is the original volume of the 0.4 mM Ce<sup>4+</sup> solution,  $[\text{Ce}_{\text{before}}^{4+}]$  and  $[\text{Ce}_{\text{after}}^{4+}]$  are the concentrations of Ce<sup>4+</sup> before and after adding the H<sub>2</sub>O<sub>2</sub> solution, and  $\Delta V$  is the amount of H<sub>2</sub>O<sub>2</sub> added to solution. Then, the Faradaic efficiency can be found by comparing these concentrations according to the equation:

$$\text{FE (\%)} = \frac{Q \text{ for H}_2\text{O}_2 \text{ production}}{Q_{\text{input}}} \times 100 = \frac{[\text{H}_2\text{O}_2] \times V \times 2 \times 96485}{Q_{\text{input}}} \times 100 \quad \text{Eq. S3}$$

where V, [H<sub>2</sub>O<sub>2</sub>], and Q<sub>input</sub> are the volume of the solution, the concentration of produced H<sub>2</sub>O<sub>2</sub> and the input charge during the electrosynthesis, respectively.

#### *Yoshida C–H amination reaction*

The oxidative C–H amination of naphthalene was conducted using a procedure adopted from the literature.<sup>56</sup> The reaction was carried out in an undivided cell (4-dram vial; Figure D.S31c)

with one 1 cm<sup>2</sup> carbon felt square at the end of a graphite rod as the working electrode (Figure D.S30e) and four 4 cm<sup>2</sup> RRs as the counter electrode (Figure D.S30f). NaClO<sub>4</sub> (20 mg, 16 mM) or acetic acid (concentration varies, as indicated in Table D.S2) was added to the solution. For control experiments with a platinum counter electrode (Figure D.S30a), the same setup was used with the exception of the replacement of the counter electrode (Figure D.S31d). Bulk electrolysis with a constant current of 8 mA was conducted at 25 °C with magnetic stirring. 16 mAh of charge was passed, equivalent to one cycle of RR reduction. The resulting solution was transferred to a 50 mL round bottom flask and the solvent was removed under reduced pressure. Then piperidine (200 μL) in acetonitrile (10 mL) was added and the mixture was stirred at 80 °C for 12 hours. The reaction mixture was then cooled to room temperature and 1,3,5-trimethoxybenzene (11.2 mg, 0.067 mmol, 0.33 equiv) was added. Then a 100 μL aliquot of the solution was extracted and diluted with 400 μL CD<sub>3</sub>CN. The resultant sample was analyzed by <sup>1</sup>H NMR spectroscopy and the yields were determined using 1,3,5-trimethoxybenzene as the internal standard. The results are summarized in Table D.S2.

Additionally, the reaction was carried out in a divided cell as reported by Yoshida et al.<sup>56</sup> In a divided cell, naphthalene (22.5 μL, 0.2 mmol, 1.0 equiv), pyridine (0.5 mL) and Bu<sub>4</sub>NBF<sub>4</sub> (197 mg, 0.3 M) in acetonitrile (10 mL) was added to the anodic chamber equipped with a carbon felt (1 cm<sup>2</sup>) working electrode. To the cathodic chamber equipped with a Pt counter electrode, trifluoromethanesulfonic acid (200 μL) and Bu<sub>4</sub>NBF<sub>4</sub> (197 mg, 0.3 M) in acetonitrile (10 mL) was added (Figure D.S31e). Bulk electrolysis with a constant current of 8 mA was conducted at 25 °C with magnetic stirring. After 16 mAh of charge was passed, the resulting solution was transferred to a 50 mL round bottom flask and the solvent was removed under reduced pressure. Then piperidine (200 μL) in acetonitrile (10 mL) was added and the mixture was stirred at 80 °C for 12

hours. The reaction mixture was then cooled to room temperature and 1,3,5-trimethoxybenzene (11.2 mg, 0.067 mmol, 0.33 equiv) was added. Then a 100  $\mu$ L aliquot of the solution was extracted and diluted with 400  $\mu$ L  $\text{CD}_3\text{CN}$ . The resultant sample was analyzed by  $^1\text{H}$  NMR spectroscopy and 72% yield was determined using 1,3,5-trimethoxybenzene as the internal standard (Figure D.S23).

Product isolation: The reaction mixture from the optimal condition experiment (entry 7, Table D.S2) was further subjected to purification. The crude product was purified with preparative TLC (Hexane/ethyl acetate = 1/1) to obtain 1-naphthylamine as a brown solid (18.7 mg, 66%). Spectroscopic data of the product align with reported literature.<sup>62</sup>

$^1\text{H}$  NMR (500 MHz,  $\text{CDCl}_3$ )  $\delta$  7.85 – 7.77 (m, 2H), 7.48 – 7.42 (m, 2H), 7.33 – 7.26 (m, 2H), 6.78 (dd,  $J$  = 6.9, 1.5 Hz, 1H), 4.14 (s, 2H).

$^{13}\text{C}$  NMR (126 MHz,  $\text{CDCl}_3$ )  $\delta$  142.1, 134.4, 128.6, 126.3, 125.8, 124.9, 123.7, 120.8, 119.0, 109.7.

#### *Measurements on the ion-balance ability of the RR electrodes*

The proton ion-balancing ability of the NiHCF RRs was evaluated in two different three-electrode electrochemical configurations: an H-cell with a sintered glass frit (89057-758, ACE glass Incorporated, USA) and an undivided cell. Both configurations use an Fe-CNT working electrode, Hg/HgO reference electrode, and a NiHCF RR counter electrode. Before all tests, one 4  $\text{cm}^2$  NiHCF RR was reduced to intercalate protons. Hydrogen peroxide production was paired with the RR oxidation in both set ups. The pH shift was recorded during the undivided electrolysis. In the H-cell, the glass frit separated the RR oxidation and hydrogen peroxide production into different chambers, and the pH shift in both chambers was recorded during the electrolysis.

### *Electrochemical Quartz Crystal Microbalance (EQCM)*

The electrode slurry used above for RR electrode preparation was diluted to 1 mg/mL active material in isopropyl alcohol. A 1.38 cm<sup>2</sup> quartz crystal (Stanford Research Systems O100RX1, p/n 6-613 Cr/Au, 5 MHz) was spray coated with an air brush to achieve an approximately 0.1 mg loading. Operando EQCM measurements were conducted using a QCM200 Stanford Research Systems digital controller during cyclic voltammetry.<sup>55,63</sup> The frequency change of the quartz resonator ( $\Delta f$ ) was converted into a mass change ( $\Delta m$ ) of the slurry coated on the quartz crystal based on the Sauerbrey equation:<sup>54</sup>

$$\Delta f_s = -\frac{2 * f_0^2 * \Delta m * n}{(\mu_q \rho_q)^{\frac{1}{2}}} \quad \text{Eq. S4}$$

which simplifies to:

$$\Delta f = -C_f * \Delta m \quad \text{Eq. S5}$$

where  $\rho_q$  is the density of the quartz crystal (2.648 g/cm<sup>3</sup>),  $\mu_q$  is the shear modulus of quartz (2.947 × 10<sup>11</sup> g/cm·s<sup>2</sup>),  $f_0$  is the resonant frequency of the fundamental mode of the crystal in Hz,  $C_f$  is the sensitivity factor,  $n$  is the overtone, and  $\Delta m$  and  $\Delta f$  are the mass change and frequency change, respectively. An overtone of 1 of was used for all measurements.  $C_f$  was calculated by measuring the mass and frequency of the crystal before and after coating in contact with the supporting electrolyte of the measurement. The value of the calibration constant  $C_f$  used here is 41.0 Hz/μg.

To study the proton de(intercalation) of NiHCF in MeOH, the EQCM measurement was in 0.1 M TBAClO<sub>4</sub> and 0.001 M HClO<sub>4</sub> in 1:20 water:methanol at 29.9 °C and the cyclic voltammogram was measured at 4 mV/s with a leakless Ag/AgCl reference electrode and a NiHCF RR CE that was fully oxidized in 0.5 M H<sub>2</sub>SO<sub>4</sub> before use.

*Demonstration of ion-balanced ModES process enabled by RR*

To demonstrate the co-production of H<sub>2</sub>O<sub>2</sub> and 4-*tert*-butylbenzaldehyde in an ion-balanced ModES system, two electrochemical cells were used: the H<sub>2</sub>O<sub>2</sub> cell (Cell<sub>H<sub>2</sub>O<sub>2</sub></sub>) containing 30 mL 1.7 M Na<sub>2</sub>SO<sub>4</sub> (adjusted to pH 11 using NaOH), and the cell for methylarene oxidation reaction (Cell<sub>MAOR</sub>) with 10 mL of 0.1 M TBAClO<sub>4</sub> solution in methanol (see Figure D.6a in the main text for the relevant scheme, Figures D.S31b and D.S31f for photos of the reaction setups). Four NiHCF RR electrodes (2 × 2 cm<sup>2</sup> each) with a total active material loading of 340 mg (capable of passing 34 Coulombs per ModES cycle) were used as the counter electrodes in both cells. In Cell<sub>H<sub>2</sub>O<sub>2</sub></sub>, two Fe-CNT electrodes (mass loading of each electrode around 0.2 mg) were used back-to-back as the working electrode and a Hg/HgO electrode was used as the reference electrode. A potential of 0.244 V vs. RHE was applied for this half reaction while the electrolyte was continuously bubbled with O<sub>2</sub> gas to ensure the O<sub>2</sub> saturation. In the Cell<sub>MAOR</sub>, a graphite rod with a 3 mm diameter and submerged 9 mm and a leakless Ag/AgCl electrode were used as the working electrode and the reference electrode, respectively. This methylarene oxidation reaction was run at a current density of 22 mA/cm<sup>2</sup> while the solution was stirred at 600 rpm.

In the Cell<sub>H<sub>2</sub>O<sub>2</sub></sub>, the oxidation of RR from RR<sup>red</sup> to RR<sup>ox</sup> deintercalated H<sup>+</sup>, and the oxygen reduction generated H<sub>2</sub>O<sub>2</sub> and OH<sup>-</sup>. After passing 34 Coulombs of charge, the RR<sup>ox</sup> electrode was taken out of the Cell<sub>H<sub>2</sub>O<sub>2</sub></sub>, washed with water, then ethanol and dried, then methanol to remove the residual electrolyte, and then moved to the Cell<sub>MAOR</sub>. In the Cell<sub>MAOR</sub>, the RR<sup>ox</sup> was reduced to RR<sup>red</sup> and intercalated H<sup>+</sup> passing 34 Coulombs of charge, while 4-*tert*-butyltoluene was oxidized on the graphite rod electrode to produce the benzaldehyde. The RR<sup>red</sup> electrode was washed with methanol and the aqueous supporting electrolyte then moved back to Cell<sub>H<sub>2</sub>O<sub>2</sub></sub> to repeat the process. During the ModES co-production, the RR electrode effectively transported the H<sup>+</sup> released during

the methylene oxidation reaction in methanol to balance the  $\text{OH}^-$  generated during hydrogen peroxide production, without appreciable pH swing. During these ModES cycles, the RR electrode's potential was also monitored, and the capacity of the RR electrode was controlled by the potential and capacity restrictions to make sure the RR electrode was operated within the desired potential windows. The pH shift in the  $\text{Cell}_{\text{H}_2\text{O}_2}$  was also recorded after the ModES cycles.

*Quantification of the 4-tertbutyl toluene oxidation products after ModES cycles*

$^1\text{H}$  NMR was used to quantify the products after 23 cycles of the 4-*tert*-butyltoluene oxidation reaction. 40  $\mu\text{L}$  of a 0.5 M trimethoxy benzene in MeOD was used as an internal standard. A sample was prepared by combining 200  $\mu\text{L}$  of the post ModES reaction mixture and 360  $\mu\text{L}$  MeOD to make a 600  $\mu\text{L}$  solution. Each sample was measured with a relaxation time of 16 seconds, a solvent suppression technique of pre-saturation with a composite pulse, and 24 scans. Doublet aromatic peaks at 7.85 and 7.65 ppm were used to quantify the aldehyde, and doublet aromatic peaks at 7.4 and 7.35 ppm were used to quantify the acetal produced (Figure D.S21).

*Quantification of the 1-naphthylamine product after ModES cycles*

11.2 mg (0.33 equiv) of 1,3,5-trimethoxybenzene was added as an internal standard to the reaction mixture after cooling to room temperature. 100  $\mu\text{L}$  of the reaction mixture was diluted with 400  $\mu\text{L}$  deuterated acetonitrile to an NMR tube for  $^1\text{H}$  NMR analysis. A doublet of doublets (equivalent to 1 proton) at 6.78 ppm was used to quantify the yield of the reaction (Figure D.S23). No solvent suppression techniques were used.

## Materials and Electrochemical Characterization of NiHCF

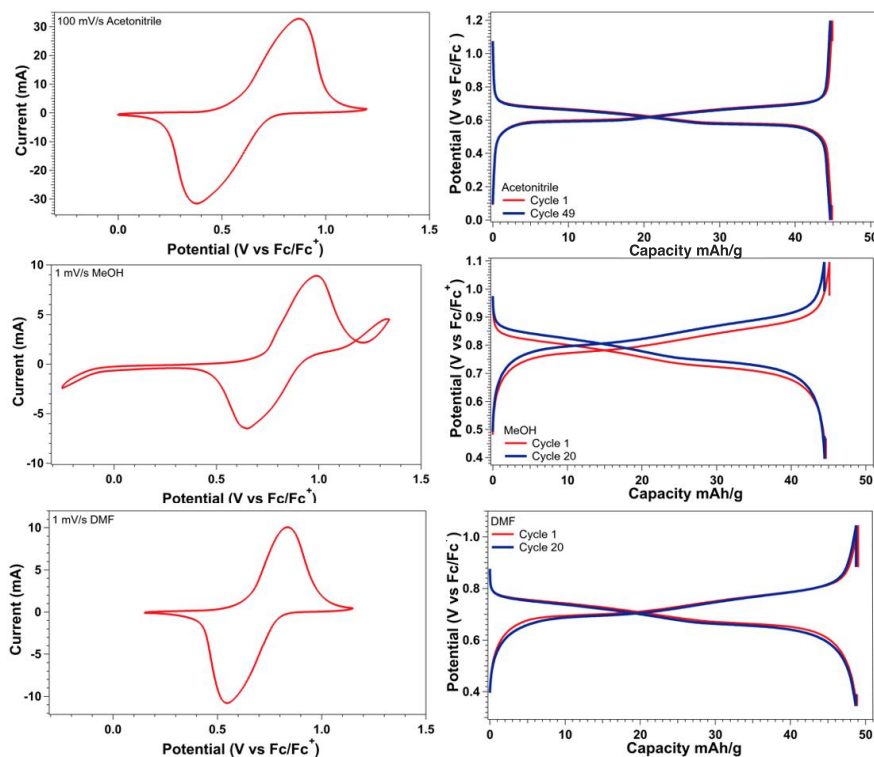


**Figure D.S1.** Cyclic voltammograms (CVs) and galvanostatic charge/discharge (GCD) curves of the NiHCF electrode at a rate of 1C in 1 M NaClO<sub>4</sub> in acetonitrile, methanol, and dimethylformamide.

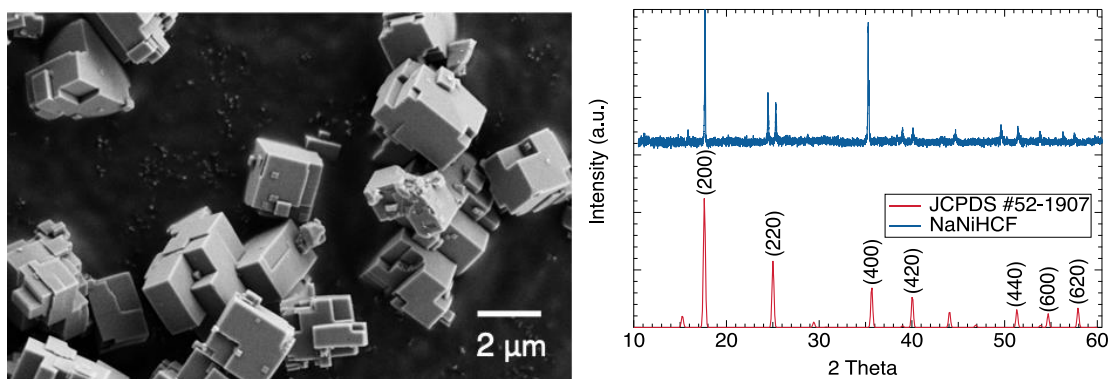


**Figure D.S2.** Structural characterization of the NiHCF product. SEM image (left) and PXRD pattern (right) of the as-synthesized NiHCF powder. The doublets indicate that the as synthesized NiHCF is rhombohedral. The JCPDS standard pattern is of the cubic polymorph.

**Table D.S1.** Weight percentages of metal elements and water content in a NiHCF sample from ICP-OES and TGA. The exact formula is Na<sub>2.29</sub>Ni[Fe(CN)<sub>6</sub>]<sub>1.04</sub>·2.2 H<sub>2</sub>O.

Na	Ni	Fe	H <sub>2</sub> O	(CN) <sub>6</sub>
14.10%	15.97%	15.57%	10.38%	43.53%

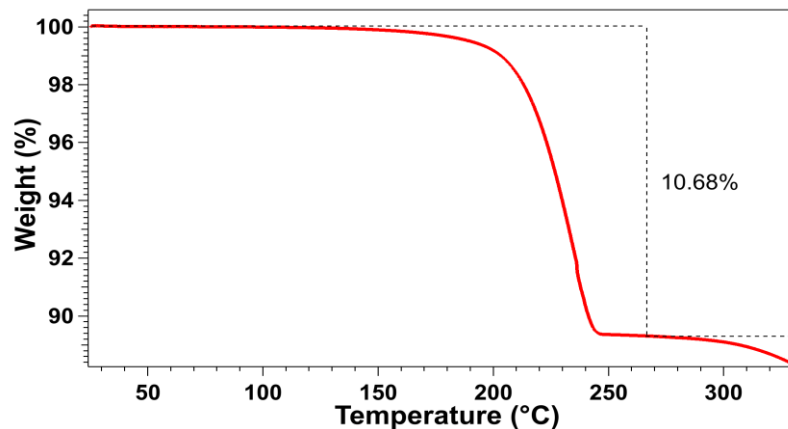


**Figure D.S3.** TGA analysis of a NiHCF sample. The analysis was done with a ramp rate of 5 °C/min under an N<sub>2</sub> atmosphere.

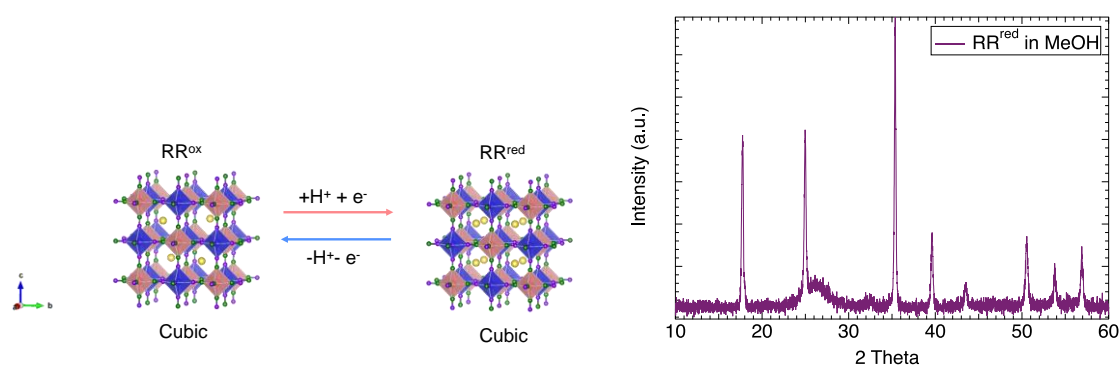


**Figure D.S4.** Illustration of the ion intercalation into NiHCF (left). NiHCF is synthesized in the fully reduced form with sodium present in the interstitial cages. Before use, NiHCF is oxidized to release the sodium ions. Then, protons are reversibly intercalated into NiHCF. The PXRD pattern supports that the NiHCF remains cubic when reduced with proton (right).

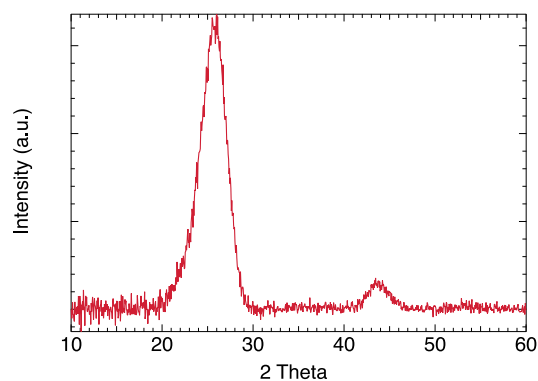


**Figure D.S5.** XRD pattern of the carbon cloth used as the current collector in Figure D.S4.

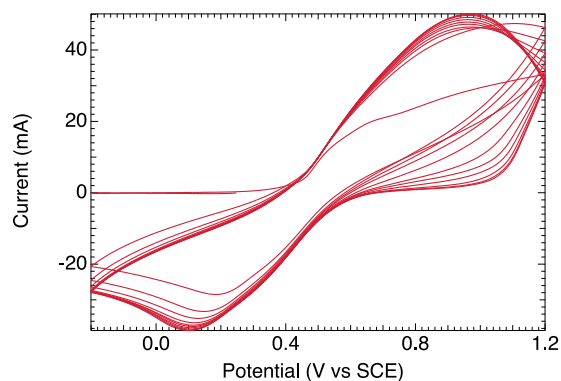


**Figure D.S6.** Activation process of the NiHCF RR electrode. CV for 10 cycles for the redox to stabilize before use.

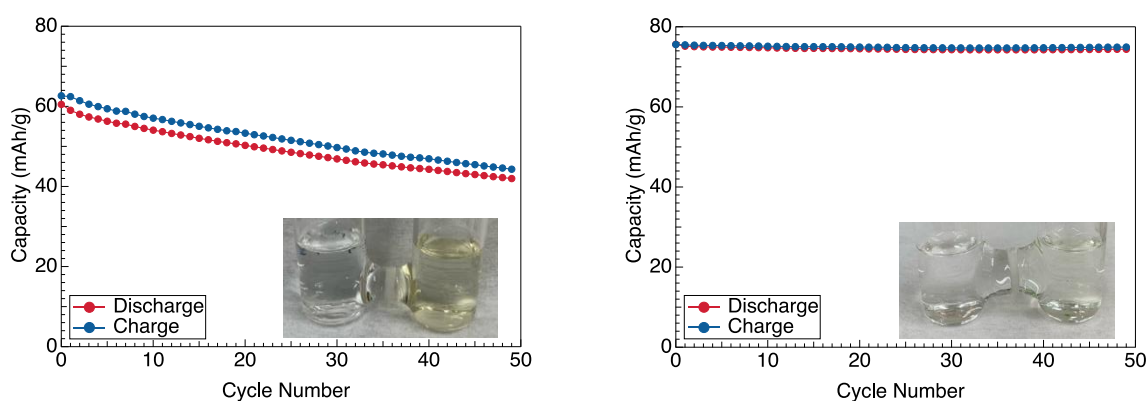


**Figure D.S7.** Cycling performance of the NiHCF RR in 1.7 M  $\text{Na}_2\text{SO}_4$  with pH = 11 (left) and 1.7 M  $\text{Na}_2\text{SO}_4$  with pH = 6 (right) at a rate of 1C. At higher pH, a clear color change was observed over the cycling showing the instability of the RR. At neutral pH, no obvious color change was observed over the cycling showing superior stability. However, when only discharging the RR in pH 11, no obvious color change of the solution was observed.

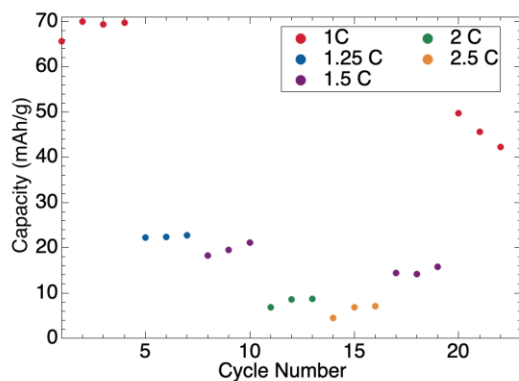


**Figure D.S8.** Rate capabilities of NiHCF RR in 0.1 M  $\text{TBAClO}_4$ , 20 mM  $\text{NiNO}_3$ , and 0.01 M  $\text{H}_2\text{SO}_4$  in MeOH.

### Precipitate Formation in MeOH

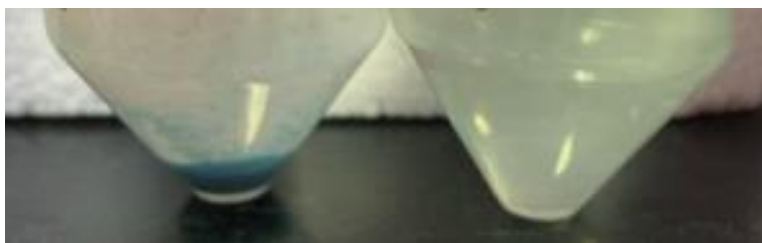


**Figure D.S9.** Photographs of the electrolyte solution after 50 GCD cycles with NiHCF working and counter electrodes without (left) and with (right) 20 mM NiNO<sub>3</sub> added. Clear dissolution of electrode material was observed without the addition of NiNO<sub>3</sub>.



**Figure D.S10.** Photographs of the methylarene oxidation reaction solution without (left) and with (right) 20 mM NiNO<sub>3</sub> and the RR as the counter electrode. A dark blue precipitate was present if NiNO<sub>3</sub> was not added to stabilize the NiHCF crystal structure.

### Methylarene Oxidation Process Using Graphite Rod Electrode

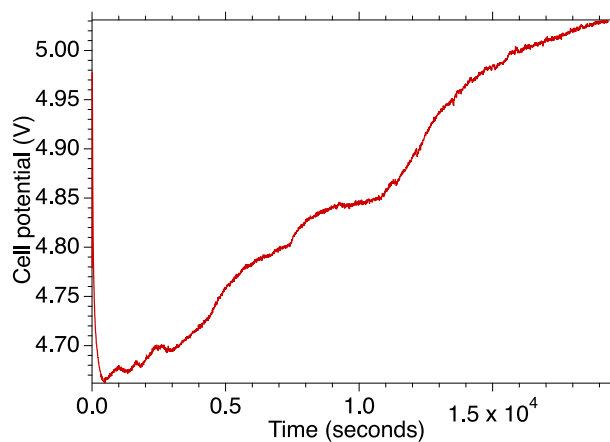


**Figure D.S11.** Cell potential vs. time for the methylarene oxidation reaction with a graphite rod CE.

## Hydrogen Peroxide Production Process Using Fe-CNT

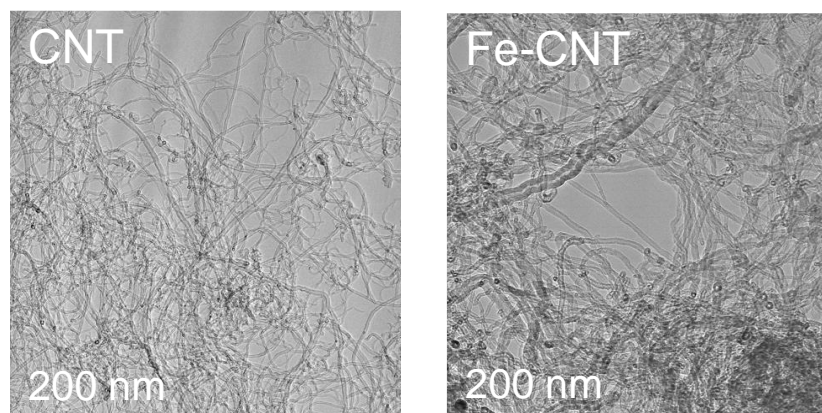


**Figure D.S12.** TEM images of carbon nanotube and Fe-decorated carbon nanotube catalysts for hydrogen peroxide production.

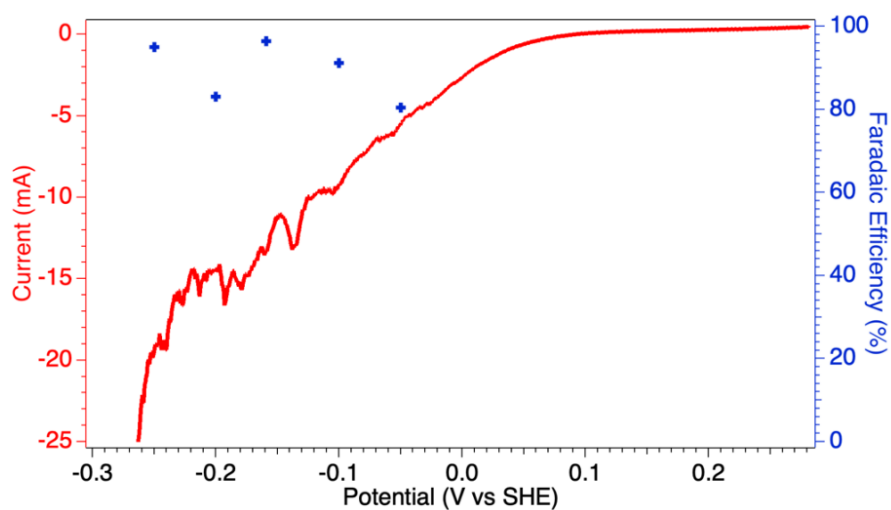


**Figure D.S13.** LSV in 1.7 M  $\text{Na}_2\text{SO}_4$  solution (pH = 6) for hydrogen peroxide production (red) and FE for CA runs at various applied potentials (blue) with carbon felt as the working electrode.

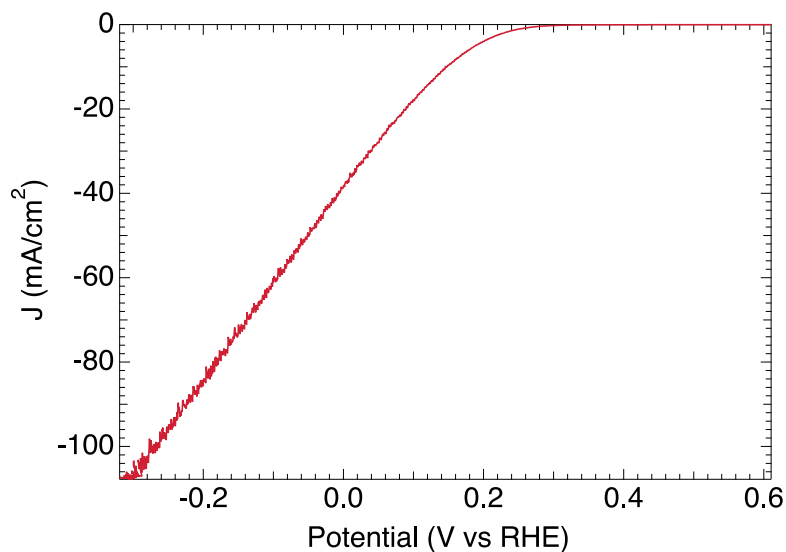


**Figure D.S14.** LSV in 1.7 M  $\text{Na}_2\text{SO}_4$  solution (pH = 6) solution for hydrogen peroxide production with Fe-CNT as the working electrode.

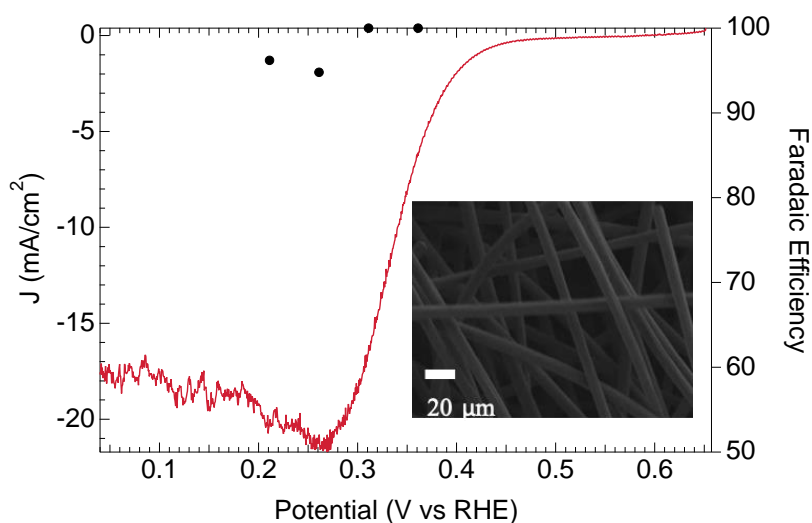


**Figure D.S15.** LSV in 1.7 M  $\text{Na}_2\text{SO}_4$  solution (adjusted to pH = 11) for hydrogen peroxide production (red) and FE for CA runs at various applied potentials (black) with carbon felt as the working electrode (the inset shows a representative SEM image of the carbon felt used). The FE was high for low charge passed but when enough charge was passed to produce 200 ppm  $\text{H}_2\text{O}_2$  the FE was consistently below 30%. Higher current densities were needed for high FE.

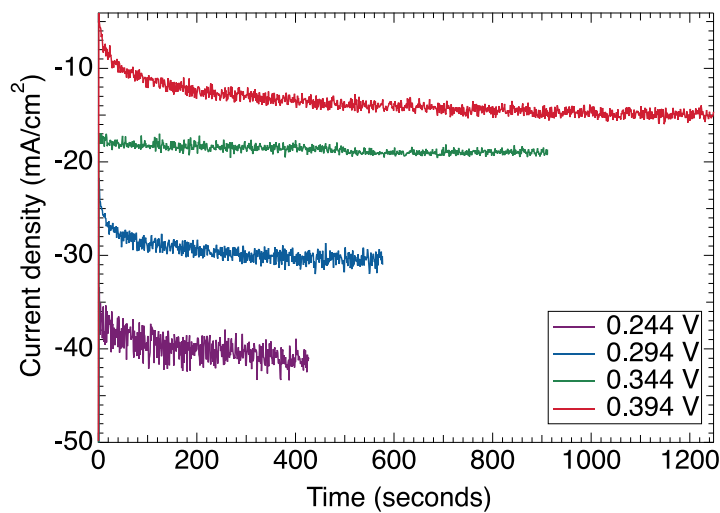


**Figure D.S16.** Chronoamperometry curves for hydrogen peroxide production in 1.7 M Na<sub>2</sub>SO<sub>4</sub> solution (adjusted to pH = 11) at various potentials vs. RHE with a RR CE.

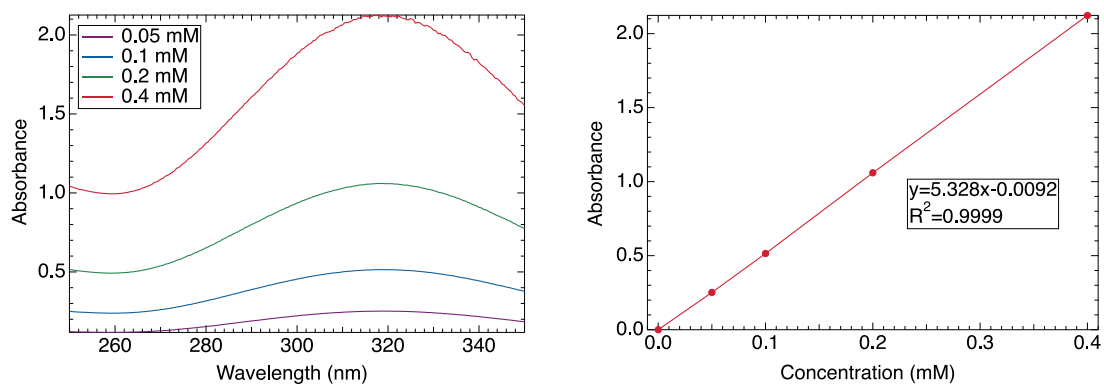


**Figure D.S17.** Absorption spectra of the standard solutions of CeSO<sub>4</sub> in 0.5 M H<sub>2</sub>SO<sub>4</sub> (left) and the resulting calibration curve from the absorbance measured at 319 nm (right).

## EQCM Results

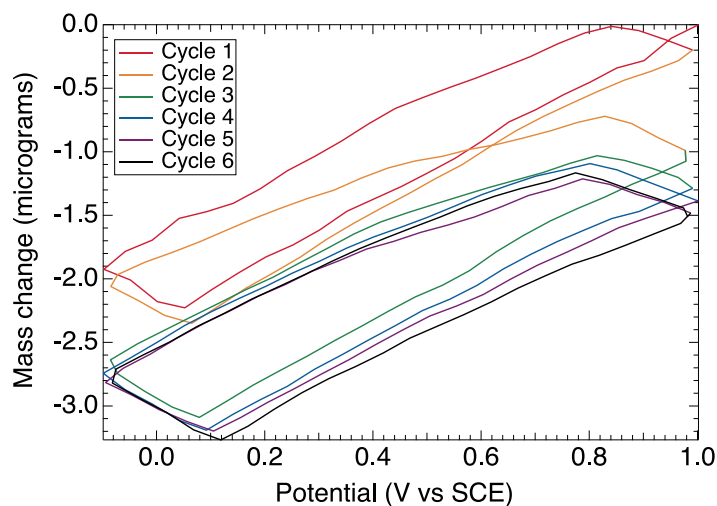


**Figure D.S18.** EQCM measurements in 0.1 M  $\text{Mg}(\text{NO}_3)_2$  and 1 mM  $\text{HNO}_3$  in water.  $\text{Mg}(\text{NO}_3)_2$  was selected as the supporting electrolyte because  $\text{Mg}^{2+}$  ions do not intercalate into  $\text{NiHCF}$ .<sup>14</sup> Each cycle begins with reduction followed by oxidation. The slopes are also opposite of what is expected, with mass loss occurring during reduction instead of mass gain due to the opposite movement of water molecules. During reduction (proton intercalation), the mass increase after a mass decrease may be attributed to the insertion of  $\text{H}_3\text{O}^+$ . During oxidation (proton deintercalation), the mass decrease seen after mass increase may be attributed to the de(insertion) of  $\text{H}_3\text{O}^+$ .

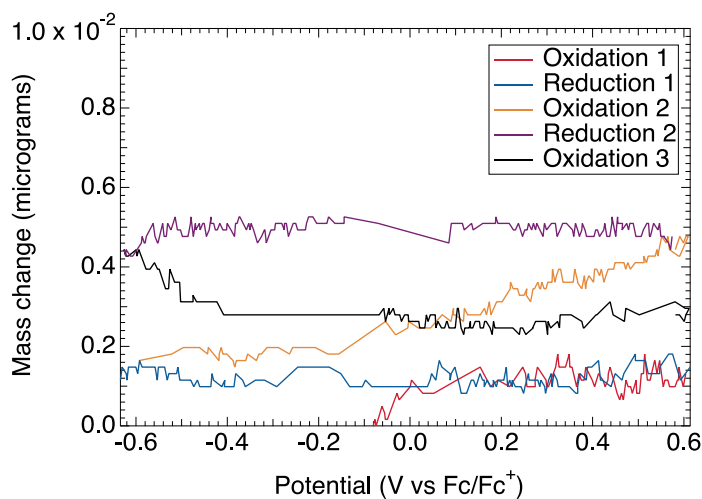


**Figure D.S19.** EQCM measurements in 0.1 M  $\text{TBAClO}_4$  and 1 mM  $\text{H}^+$  in 1:20 water:methanol. Each cycle begins with oxidation followed by reduction. A bare Cr/Au coated quartz crystal was used as the working electrode and no pattern of frequency and mass change was observed as a potential was applied.

## Ion-Balanced ModES Process

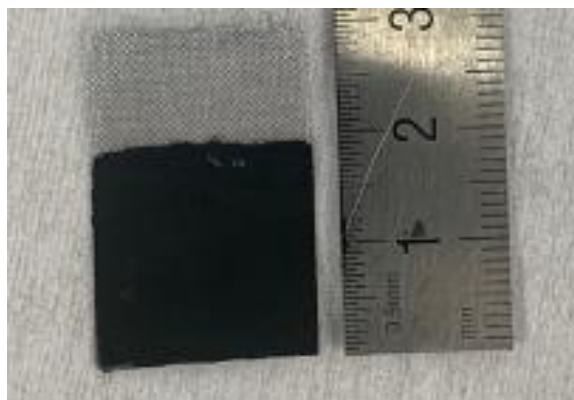


**Figure D.S20.** Photograph of a NiHCF RR electrode. The active material area is  $2 \times 2$  cm<sup>2</sup>.

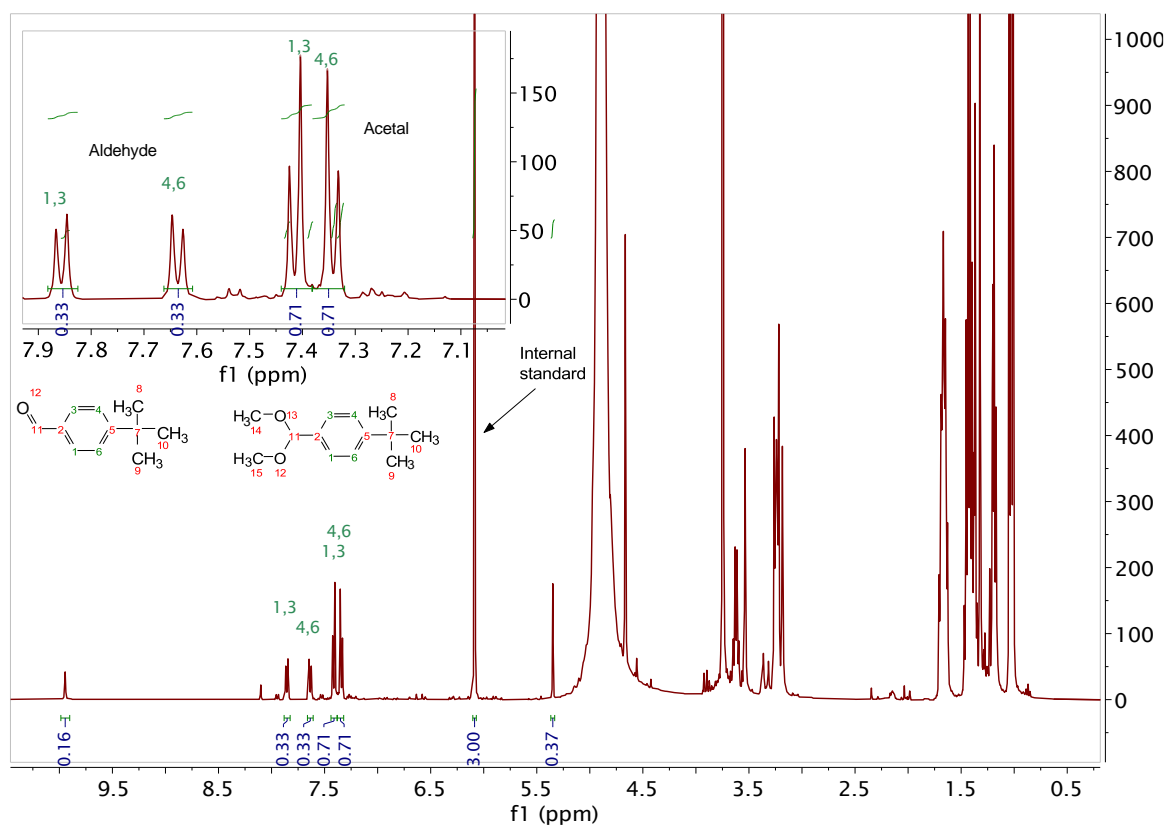


**Figure D.S21.** NMR of the final products of the methylarene oxidation reaction after 23 ModES cycles. The aromatic region is used to quantify the yield of the reaction. The aromatic peaks of the aldehyde are downfield to the aromatic peaks of the acetal. No peaks corresponding to the starting material were observed.

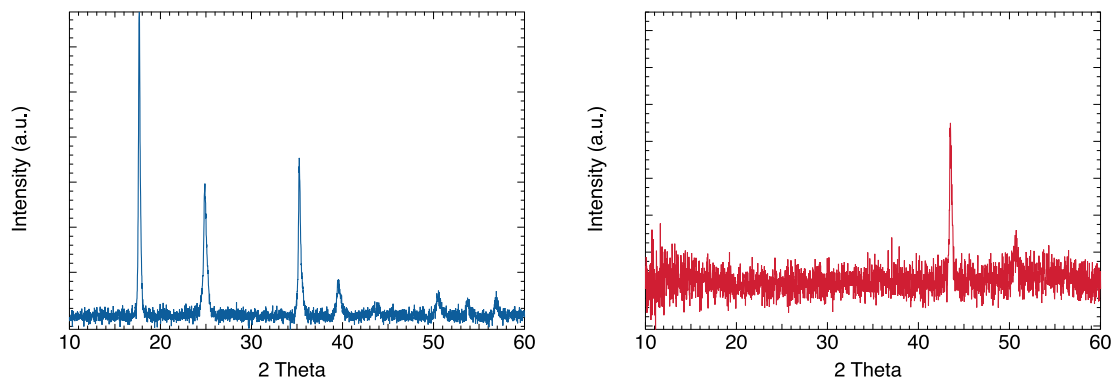


**Figure D.S22.** PXRD pattern of the NiHCF RR electrode in the fully oxidized state on SS mesh after the ModES cycling (left). PXRD pattern of bare SS mesh (right).

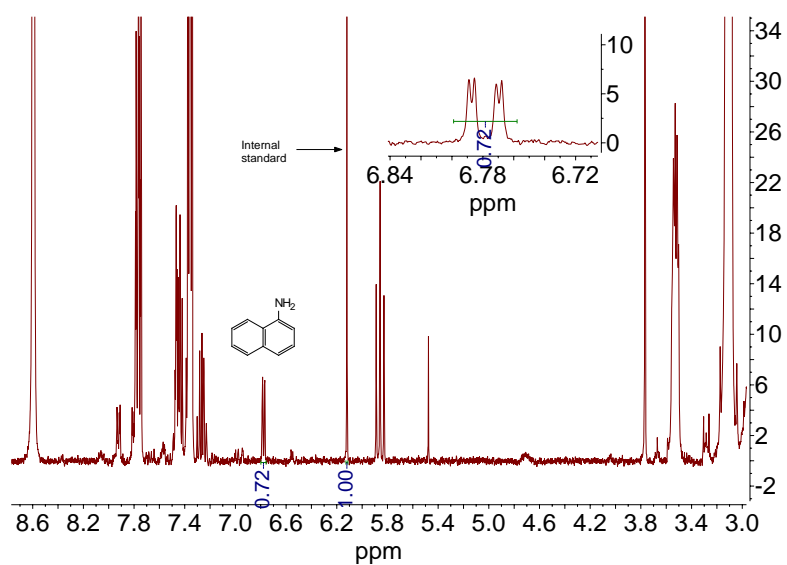


**Figure D.S23.** NMR of the 1-naphthylamine product after working up the electrochemically generated pyridinium. For the electrochemical step, a platinum counter electrode was used in a divided cell configuration. The doublet of doublets at 6.78 ppm was used to quantify the yield of the reaction.

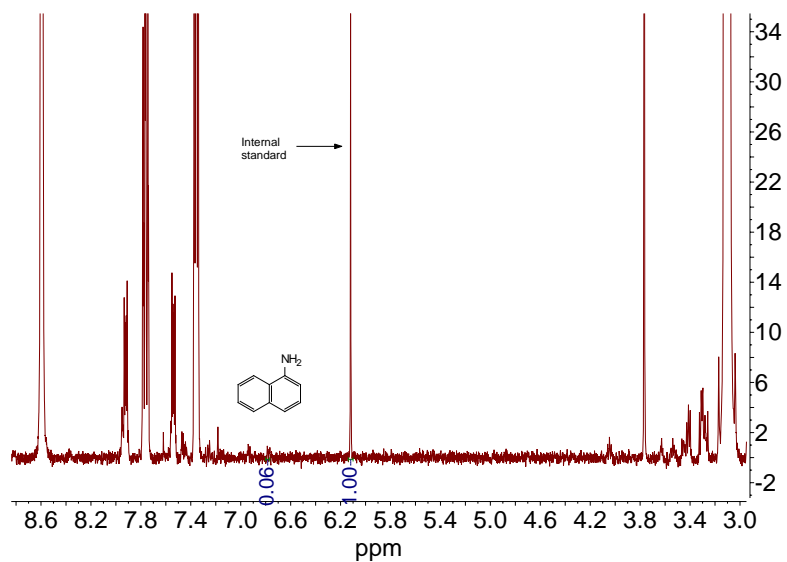


**Figure D.S24.** NMR of the 1-naphthylamine product after working up the electrochemically generated pyridinium. For the electrochemical step, a platinum counter electrode was used in an undivided cell configuration.

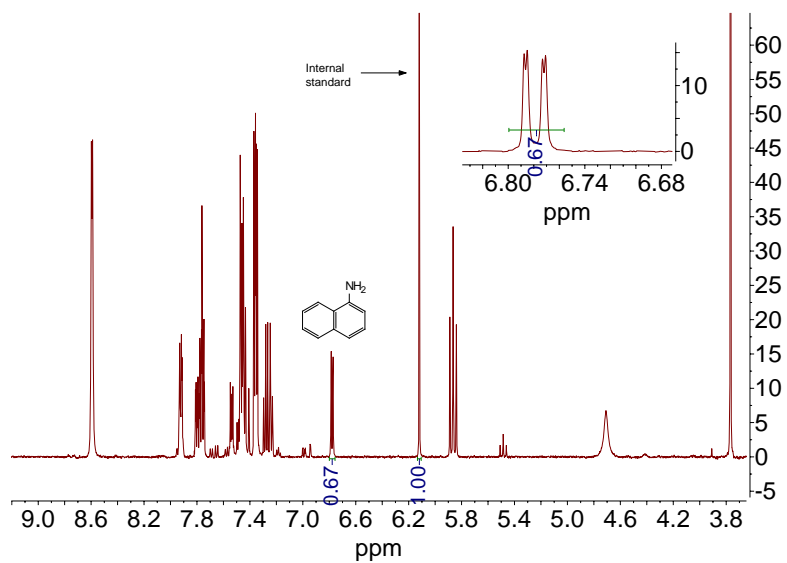
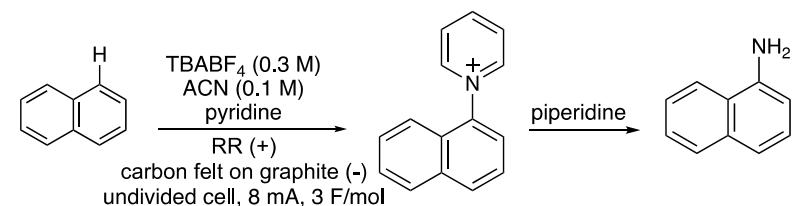


**Figure D.S25.** NMR of the 1-naphthylamine product after working up the electrochemically generated pyridinium. For the electrochemical step, an RR counter electrode was used and 20 mg of  $\text{NaClO}_4$  was added to the reaction vessel.

**Table D.S2. Summary of naphthalene amination experiments supporting the redox reservoir's ability to allow for effective reaction in an undivided cell configuration.**



Entry	Variation from above	Yield (%)
1	None	22
2	20 microL acetic acid added	30
3	40 microL acetic acid added	35
4	60 microL acetic acid added	52
5	70 microL acetic acid added	40
6	80 microL acetic acid added	41
7	20 mg NaClO <sub>4</sub> added	67 (66)
8	200 microL triflic acid added	0
9	Pt (+)	6
10	Pt (+) 200 microL triflic acid added	7
11	Pt (+) 60 microL acetic acid added	35

Yield determined by <sup>1</sup>H NMR analysis of the crude reaction mixture after work up using 1,3,5-trimethoxybenzene as an internal standard, yields shown in parentheses are isolated.

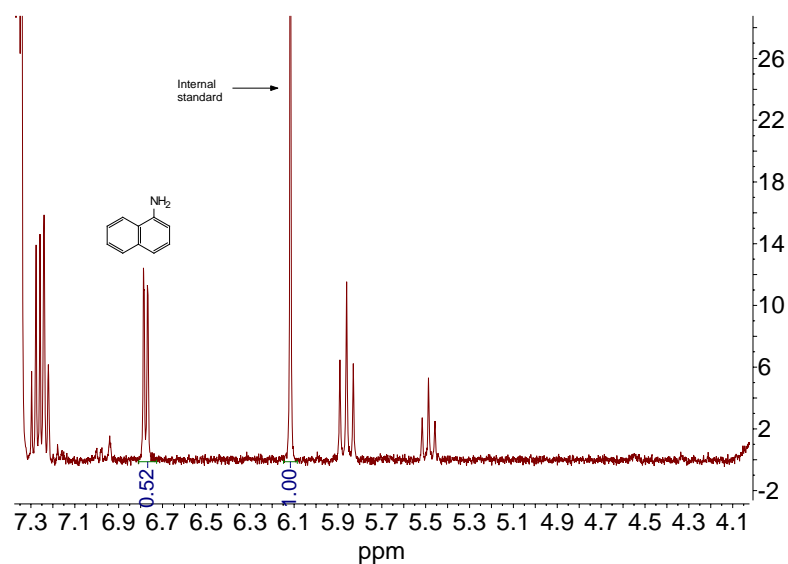


**Figure D.S26.** NMR of the 1-naphthylamine product after working up the electrochemically generated pyridinium. For the electrochemical step, an RR counter electrode was used and 60  $\mu$ L of acetic acid was added to the reaction vessel.

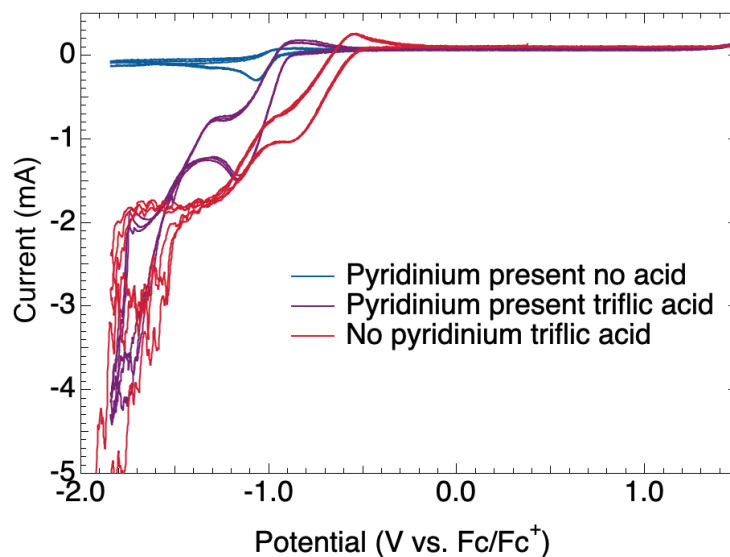


**Figure D.S27.** Cyclic voltammograms to determine the reduction potential of protons (HER onset potential) and the pyridinium produced from naphthalene amination on platinum in acetonitrile. The red trace is a CV taken before the naphthalene amination electro-synthesis is run with a platinum working electrode in the cathodic compartment of the divided cell used for electrolysis in the presence of triflic acid to determine the HER onset potential. The blue trace is a CV taken after the naphthalene amination is run in the anodic compartment (working electrode compartment) without acid to measure the reduction potential of the produced pyridinium. The purple trace is a CV taken after the naphthalene amination is run in the anodic compartment with 100  $\mu\text{L}$  of triflic acid added for comparison. 0.3 M  $\text{KPF}_6$  was used as the supporting electrolyte for all traces instead of  $\text{TBABF}_4$  and Argon gas was bubbled before scanning CV at a scan rate of 25 mV/s.

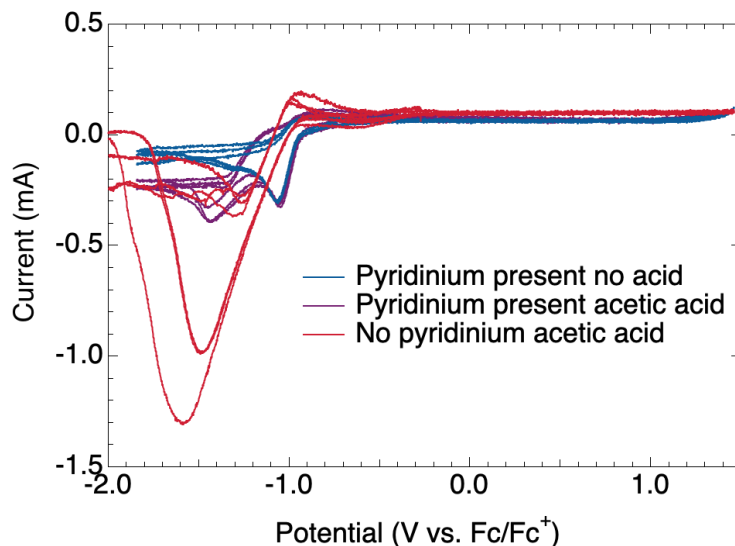


**Figure D.S28.** Cyclic voltammograms to determine the reduction potential of protons (HER onset potential) and the pyridinium produced from naphthalene amination on platinum in acetonitrile. The red trace is a CV taken before the naphthalene amination electro-synthesis is run with a platinum working electrode in an undivided cell in the presence of acetic acid to determine the HER onset potential. The blue trace is a CV taken after the naphthalene amination is run in the anodic compartment (working electrode compartment) of the divided cell used for electrolysis without acid to measure the reduction potential of the produced pyridinium. The purple trace is a CV taken after the naphthalene amination is run in the anodic compartment of the divided cell with 100  $\mu$ L of acetic acid added for comparison. 0.3 M  $\text{KPF}_6$  was used as the supporting electrolyte instead of  $\text{TBABF}_4$  for all traces and Argon gas was bubbled before scanning CV at a scan rate of 25 mV/s.

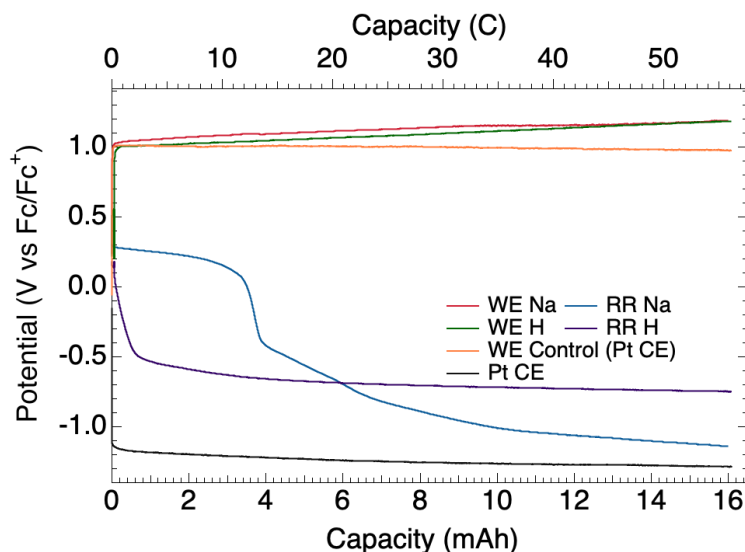


**Figure D.S29.** Potential evolution of the NiHCF RR counter electrode and carbon felt working electrode during naphthalene amination with  $\text{NaClO}_4$  (blue and red traces, respectively) and acetic acid (purple and green traces, respectively) added to the reaction vessel, with potential evolution of a platinum counter electrode in an undivided configuration with acetic acid added shown in grey (working electrode potential in orange).

## Electrodes and Reaction Setups

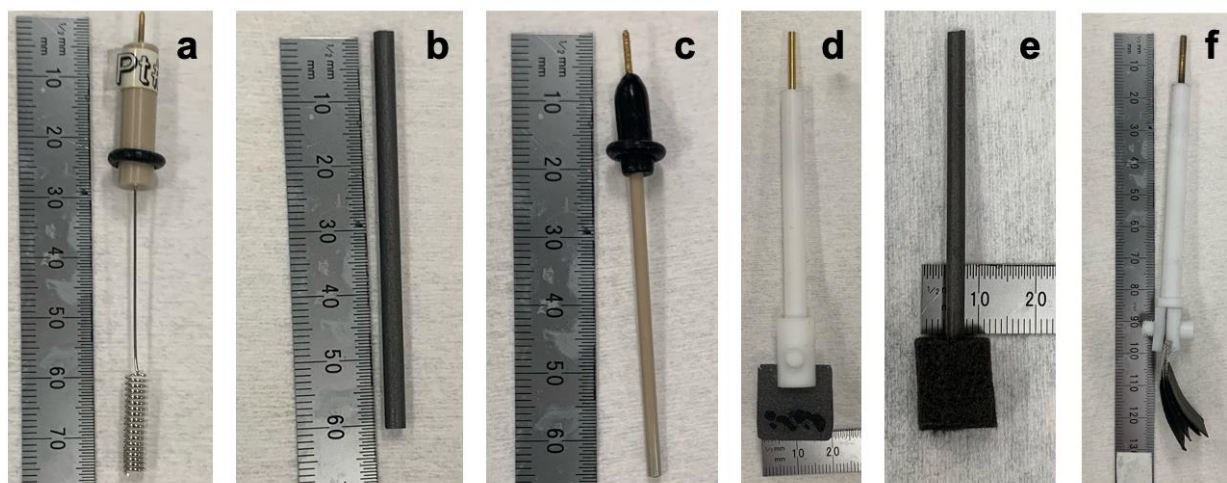


**Figure D.S30.** Photos showing the electrodes used during electrochemical experiments. (a) Pt wire electrode. (b) 3 mm wide graphite rod used as the working electrode during methylarene oxidation. (c) Leak-free reference electrode used in nonaqueous solvent during ModES. (d) Fe-CNT catalyst on carbon paper used as catalyst for  $\text{H}_2\text{O}_2$  production. (e) 1  $\text{cm}^2$  carbon felt square at the end of a graphite rod used as the working electrode during naphthalene amination. (f) Four 4  $\text{cm}^2$  NiHCF RRs clipped for use as the counter electrode during ModES.

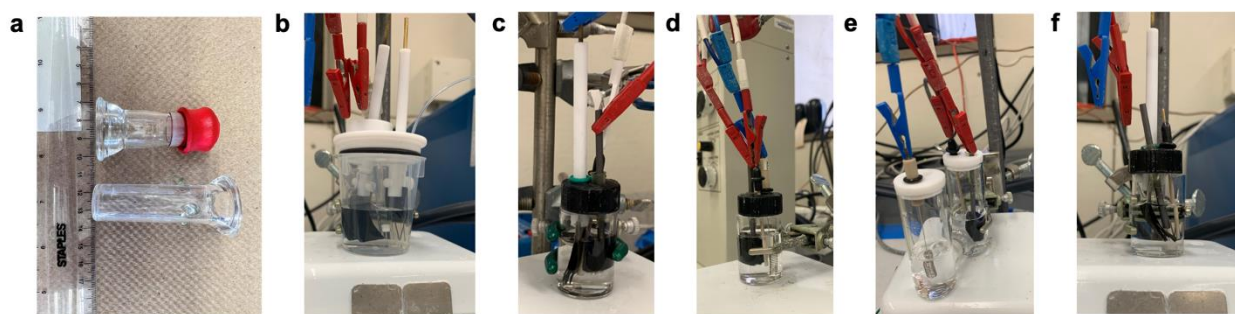


**Figure D.S31.** Photos showing the cell setups used during electrosynthesis. (a) Custom built undivided cell used for the optimization of methylarene oxidation reaction. (b) Undivided configuration setup used for  $\text{H}_2\text{O}_2$  production. The cell is a plastic beaker purchased from VWR International, Inc and the Teflon cap is custom made. (c) Undivided configuration setup for naphthalene oxidation. A 4-dram vial with the top cut off is used as the reaction vessel. A 4-dram vial lid with holes for the electrodes is used as the cap. This type of reaction vessel is used for all undivided configurations with the exception of  $\text{H}_2\text{O}_2$  production as shown in b. (d) Undivided configuration setup used for control experiments with a platinum counter electrode reported in Table D.S2. (e) Divided configuration setup for naphthalene C–H amination. A divided cell with a glass frit is used with Teflon caps. (f) Undivided configuration setup used during ModES for methylarene oxidation.

## D.VIII. References

1. Luna, P. D.; Hahn, C.; Higgins, D.; Jaffer, S. A.; Jaramillo, T. F.; Sargent, E. H. What Would It Take for Renewably Powered Electrosynthesis to Displace Petrochemical Processes? *Science* **2019**, *364*, 6438.
2. Wiebe, A.; Gieshoff, T.; Möhle, S.; Rodrigo, E.; Zirbes, M.; Waldvogel, S. R. Electrifying Organic Synthesis. *Angew. Chem. Int. Ed.* **2018**, *57*, 5594–5619.
3. Minter, S. D.; Baran, P. Electrifying Synthesis: Recent Advances in the Methods, Materials, and Techniques for Organic Electrosynthesis. *Acc. Chem. Res.* **2020**, *53*, 545–546.
4. Yuan, Y.; Lei, A. Is Electrosynthesis Always Green and Advantageous Compared to Traditional Methods? *Nat. Commun.* **2020**, *11*, 802.
5. Botte, G. G. Electrochemical Manufacturing in the Chemical Industry. *Interface Mag.* **2014**, *23*, 49–55.
6. Novaes, L. F. T.; Liu, J.; Shen, Y.; Lu, L.; Meinhardt, J. M.; Lin, S. Electrocatalysis as an Enabling Technology for Organic Synthesis. *Chem. Soc. Rev.* **2021**, *50*, 7941–8002.
7. Zhong, X.; Hoque, M. A.; Graaf, M. D.; Harper, K. C.; Wang, F.; Genders, J. D.; Stahl, S. S. Scalable Flow Electrochemical Alcohol Oxidation: Maintaining High Stereochemical Fidelity in the Synthesis of Levetiracetam. *Org. Process Res. Dev.* **2021**, *25*, 2601–2607.
8. Danly, D. E. Development and Commercialization of the Monsanto Electrochemical Adiponitrile Process. *J. Electrochem. Soc.* **1984**, *131*, 435C–442C.
9. Hilt, G. Basic Strategies and Types of Applications in Organic Electrochemistry. *ChemElectroChem* **2020**, *7*, 395–405.
10. Ibanez, J. G.; Frontana-Uribe, B. A.; Vasquez-Medrano, R. Paired Electrochemical Processes: Overview, Systematization, Selection Criteria, Design Strategies, and Projection. *J. Mex. Chem. Soc.* **2017**, *60*, 247–260.
11. Sbei, N.; Hardwick, T.; Ahmed, N. Green Chemistry: Electrochemical Organic Transformations via Paired Electrolysis. *ACS Sustainable Chem. Eng.* **2021**, *9*, 6148–6169.
12. Martínez, N. P.; Isaacs, M.; Nanda, K. K. Paired Electrolysis for Simultaneous Generation of Synthetic Fuels and Chemicals. *New J. Chem.* **2020**, *44*, 5617–5637.
13. Aust, N.; Kirste, A. *Encyclopedia of Applied Electrochemistry*; Springer, 2014; pp. 1505–1510.
14. Frontana-Uribe, B. A.; Little, R. D.; Ibanez, J. G.; Palma, A.; Vasquez-Medrano, R. Organic Electrosynthesis: A Promising Green Methodology in Organic Chemistry. *Green Chem.* **2010**, *12*, 2099–2119.
15. Sheng, H.; Janes, A. N.; Ross, R. D.; Hofstetter, H.; Lee, K.; Schmidt, J. R.; Jin, S. Linear Paired Electrochemical Valorization of Glycerol Enabled by the Electro-Fenton Process Using a Stable NiSe<sub>2</sub> Cathode. *Nat. Catal.* **2022**, *5*, 716–725.
16. Llorente, M. J.; Nguyen, B. H.; Kubiak, C. P.; Moeller, K. D. Paired Electrolysis in the Simultaneous Production of Synthetic Intermediates and Substrates. *J. Am. Chem. Soc.* **2016**, *138*, 15110–15113.
17. Hermann, P.; Heinz, H. Preparation of Phthalides. US6063256A, May 16, 2000.
18. Stecker, F.; Fischer, A.; Botzem, J.; Griesbach, U.; Pelzer, R. Electrochemical Method for Producing 3-Tert-Butylbenzaldehyde Dimethyl Acetal. US8629304B2, January 14, 2014.
19. Wu, T.; Moeller, K. D. Organic Electrochemistry: Expanding the Scope of Paired Reactions. *Angew. Chem. Int. Ed.* **2021**, *60*, 12883–12890.
20. Wang, F.; Li, W.; Wang, R.; Guo, T.; Sheng, H.; Fu, H.-C.; Stahl, S. S.; Jin, S. Modular Electrochemical Synthesis Using a Redox Reservoir Paired with Independent Half-Reactions. *Joule* **2021**, *5*, 149–165.
21. Wallace, A. G.; Symes, M. D. Decoupling Strategies in Electrochemical Water Splitting and Beyond. *Joule* **2018**, *2*, 1390–1395.

22. Dotan, H.; Landman, A.; Sheehan, S. W.; Malviya, K. D.; Shter, G. E.; Grave, D. A.; Arzi, Z.; Yehudai, N.; Halabi, M.; Gal, N.; Hadari, N.; Cohen, C.; Rothschild, A.; Grader, G. S. Decoupled Hydrogen and Oxygen Evolution by a Two-Step Electrochemical–Chemical Cycle for Efficient Overall Water Splitting. *Nat. Energy* **2019**, *4*, 786–795.
23. Chen, L.; Dong, X.; Wang, Y.; Xia, Y. Separating Hydrogen and Oxygen Evolution in Alkaline Water Electrolysis Using Nickel Hydroxide. *Nat. Commun.* **2016**, *7*, 11741.
24. Wang, F.; Sheng, H.; Li, W.; Gerken, J. B.; Jin, S.; Stahl, S. S. Stable Tetrasubstituted Quinone Redox Reservoir for Enhancing Decoupled Hydrogen and Oxygen Evolution. *ACS Energy Lett.* **2021**, *6*, 1533–1539.
25. Rausch, B.; Symes, M. D.; Chisholm, G.; Cronin, L. Decoupled Catalytic Hydrogen Evolution from a Molecular Metal Oxide Redox Mediator in Water Splitting. *Science* **2014**, *345*, 1326–1330.
26. Landman, A.; Dotan, H.; Shter, G. E.; Wullenkord, M.; Houaijia, A.; Maljus, A.; Grader, G. S.; Rothschild, A. Photoelectrochemical Water Splitting in Separate Oxygen and Hydrogen Cells. *Nat. Mater.* **2017**, *16*, 646–651.
27. Symes, M. D.; Cronin, L. Decoupling Hydrogen and Oxygen Evolution during Electrolytic Water Splitting Using an Electron-Coupled-Proton Buffer. *Nat. Chem.* **2013**, *5*, 403–409.
28. Wang, R.; Sheng, H.; Wang, F.; Li, W.; Roberts, D. S.; Jin, S. Sustainable Coproduction of Two Disinfectants via Hydroxide-Balanced Modular Electrochemical Synthesis Using a Redox Reservoir. *ACS Cent. Sci.* **2021**, *7*, 2083–2091.
29. Vantourout, J. C. From Bench to Plant: An Opportunity for Transition Metal Paired Electrocatalysis. *Org. Process Res. Dev.* **2021**, *25*, 2581–2586.
30. Perry, S. C.; Pangotra, D.; Vieira, L.; Csepei, L.-I.; Sieber, V.; Wang, L.; de León, C. P.; Walsh, F. C. Electrochemical Synthesis of Hydrogen Peroxide from Water and Oxygen. *Nat. Rev. Chem.* **2019**, *3*, 442–458.
31. Murray, A. T.; Voskian, S.; Schreier, M.; Hatton, T. A.; Surendranath, Y. Electrosynthesis of Hydrogen Peroxide by Phase-Transfer Catalysis. *Joule* **2019**, *3*, 2942–2954.
32. Yang, S.; Verdaguer-Casadevall, A.; Arnarson, L.; Silvioli, L.; Čolić, V.; Frydendal, R.; Rossmeisl, J.; Chorkendorff, I.; Stephens, I. E. L. Toward the Decentralized Electrochemical Production of H<sub>2</sub>O<sub>2</sub>: A Focus on the Catalysis. *ACS Catal.* **2018**, *8*, 4064–4081.
33. Zeng, J. S.; Manthiram, K. Redox Reservoirs: Enabling More Modular Electrochemical Synthesis. *Trends Chem.* **2021**, *3*, 157–159.
34. Wu, X.; Hong, J. J.; Shin, W.; Ma, L.; Liu, T.; Bi, X.; Yuan, Y.; Qi, Y.; Surta, T. W.; Huang, W.; Neufeind, J.; Wu, T.; Greaney, P. A.; Lu, J.; Ji, X. Diffusion-Free Grotthuss Topochemistry for High-Rate and Long-Life Proton Batteries. *Nat. Energy* **2019**, *4*, 123–130.
35. Xu, Y.; Wu, X.; Ji, X. The Renaissance of Proton Batteries. *Small Struct.* **2021**, *2*, 2000113.
36. Yi, H.; Qin, R.; Ding, S.; Wang, Y.; Li, S.; Zhao, Q.; Pan, F. Structure and Properties of Prussian Blue Analogues in Energy Storage and Conversion Applications. *Adv. Funct. Mater.* **2021**, *31*, 2006970.
37. Simonov, A.; Baerdemaeker, T. D.; Boström, H. L. B.; Gómez, M. L. R.; Gray, H. J.; Chernyshov, D.; Bosak, A.; Bürgi, H.-B.; Goodwin, A. L. Hidden Diversity of Vacancy Networks in Prussian Blue Analogues. *Nature* **2020**, *578*, 256–260.
38. Wu, X.; Sun, M.; Guo, S.; Qian, J.; Liu, Y.; Cao, Y.; Ai, X.; Yang, H. Vacancy-Free Prussian Blue Nanocrystals with High Capacity and Superior Cyclability for Aqueous Sodium-Ion Batteries. *Chemnanomat* **2015**, *1*, 188–193.
39. Lumley, M. A.; Nam, D.-H.; Choi, K.-S. Elucidating Structure–Composition–Property Relationships of Ni-Based Prussian Blue Analogues for Electrochemical Seawater Desalination. *ACS Appl. Mater. Interfaces* **2020**, *12*, 36014–36025.
40. Wu, X.; Qiu, S.; Xu, Y.; Ma, L.; Bi, X.; Yuan, Y.; Wu, T.; Shahbazian-Yassar, R.; Lu, J.; Ji, X. Hydrous Nickel–Iron Turnbull’s Blue as a High-Rate and Low-Temperature Proton Electrode. *ACS Appl. Mater. Interfaces* **2020**, *12*, 9201–9208.

41. Komayko, A. I.; Ryazantsev, S. V.; Trussov, I. A.; Arkharova, N. A.; Presnov, D. E.; Levin, E. E.; Nikitina, V. A. The Misconception of  $Mg^{2+}$  Insertion into Prussian Blue Analogue Structures from Aqueous Solution. *ChemSusChem* **2021**, *14*, 1574–1585.
42. Shi, L.; Newcomer, E.; Son, M.; Pothanamkandathil, V.; Gorski, C. A.; Galal, A.; Logan, B. E. Metal-Ion Depletion Impacts the Stability and Performance of Battery Electrode Deionization over Multiple Cycles. *Environ. Sci. Technol.* **2021**, *55*, 5412–5421.
43. Silva, J. A. B. D.; Moreira, F. G. B.; Santos, V. M. L. D.; Longo, R. L. Hydrogen Bond Networks in Water and Methanol with Varying Interaction Strengths. *Phys. Chem. Chem. Phys.* **2011**, *13*, 593–603.
44. Merk, C.; Huber, G. Process for Electrochemical Oxidation of Organic Compounds. US6398938B2, June 4, 2002.
45. Zhang, X.; Xia, Y.; Xia, C.; Wang, H. Insights into Practical-Scale Electrochemical H<sub>2</sub>O<sub>2</sub> Synthesis. *Trends Chem.* **2020**, *2*, 942–953.
46. Lu, Z.; Chen, G.; Siahrostami, S.; Chen, Z.; Liu, K.; Xie, J.; Liao, L.; Wu, T.; Lin, D.; Liu, Y.; Jaramillo, T. F.; Nørskov, J. K.; Cui, Y. High-Efficiency Oxygen Reduction to Hydrogen Peroxide Catalysed by Oxidized Carbon Materials. *Nat. Catal.* **2018**, *1*, 156–162.
47. Jiang, K.; Back, S.; Akey, A. J.; Xia, C.; Hu, Y.; Liang, W.; Schaak, D.; Stavitski, E.; Nørskov, J. K.; Siahrostami, S.; Wang, H. Highly Selective Oxygen Reduction to Hydrogen Peroxide on Transition Metal Single Atom Coordination. *Nat. Commun.* **2019**, *10*, 3997.
48. Agmon, N. The Grotthuss Mechanism. *Chem. Phys. Lett.* **1995**, *244*, 456–462.
49. Poli, I.; Eslava, S.; Cameron, P. Tetrabutylammonium Cations for Moisture-Resistant and Semitransparent Perovskite Solar Cells. *J. Mater. Chem. A* **2017**, *5*, 22325–22333.
50. Ojwang, D. O.; Grins, J.; Wardecki, D.; Valvo, M.; Renman, V.; Häggström, L.; Ericsson, T.; Gustafsson, T.; Mahmoud, A.; Hermann, R. P.; Svensson, G. Structure Characterization and Properties of K-Containing Copper Hexacyanoferrate. *Inorg. Chem.* **2016**, *55*, 5924–5934.
51. Israelachvili, J. N. *Intermolecular and Surface Forces*, 3rd Edition; Academic Press, 2011; pp. 71–90.
52. Lam, R. K.; Smith, J. W.; Saykally, R. J. Communication: Hydrogen Bonding Interactions in Water-Alcohol Mixtures from X-Ray Absorption Spectroscopy. *J. Chem. Phys.* **2016**, *144*, 191103.
53. Nordstrand, J.; Toledo-Carrillo, E.; Vafakhah, S.; Guo, L.; Yang, H. Y.; Kloo, L.; Dutta, J. Ladder Mechanisms of Ion Transport in Prussian Blue Analogues. *ACS Appl. Mater. Interfaces* **2022**, *14*, 1102–1113.
54. Sauerbrey, G. Verwendung von Schwingquarzen Zur Wägung Dünner Schichten Und Zur Mikrowägung. *Z. Phys.* **1959**, *155*, 206–222.
55. Jiang, H.; Hong, J. J.; Wu, X.; Surta, T. W.; Qi, Y.; Dong, S.; Li, Z.; Leonard, D. P.; Holoubek, J. J.; Wong, J. C.; Razink, J. J.; Zhang, X.; Ji, X. Insights on the Proton Insertion Mechanism in the Electrode of Hexagonal Tungsten Oxide Hydrate. *J. Am. Chem. Soc.* **2018**, *140*, 11556–11559.
56. Morofuji, T.; Shimizu, A.; Yoshida, J. Electrochemical C–H Amination: Synthesis of Aromatic Primary Amines via N-Arylpyridinium Ions. *J. Am. Chem. Soc.* **2013**, *135*, 5000–5003.
57. Liang, G.; Mo, F.; Ji, X.; Zhi, C. Non-Metallic Charge Carriers for Aqueous Batteries. *Nat. Rev. Mater.* **2021**, *6*, 109–123.
58. Asano, S.; Tanaka, H.-N.; Imamura, A.; Ishida, H.; Ando, H. P-Tert-Butyl Groups Improve the Utility of Aromatic Protecting Groups in Carbohydrate Synthesis. *Org. Lett.* **2019**, *21*, 4197–4200.
59. Ke, Q.; Yi, D.; Jin, Y.; Lu, F.; Zhou, B.; Zhan, F.; Yang, Y.; Gao, D.; Yan, P.; Wan, C.; Cui, P.; Golberg, D.; Yao, J.; Wang, X. Manganese Doping in Cobalt Oxide Nanorods Promotes Catalytic Dehydrogenation. *ACS Sustainable Chem. Eng.* **2020**, *8*, 5734–5741.
60. Sheng, H.; Janes, A. N.; Ross, R. D.; Kaiman, D.; Huang, J.; Song, B.; Schmidt, J. R.; Jin, S. Stable and Selective Electrosynthesis of Hydrogen Peroxide and the Electro-Fenton Process on CoSe<sub>2</sub> Polymorph Catalysts. *Energy Environ. Sci.* **2020**, *13*, 4189–4203.

61. Sheng, H.; Hermes, E. D.; Yang, X.; Ying, D.; Janes, A. N.; Li, W.; Schmidt, J. R.; Jin, S. Electrocatalytic Production of H<sub>2</sub>O<sub>2</sub> by Selective Oxygen Reduction Using Earth-Abundant Cobalt Pyrite (CoS<sub>2</sub>). *ACS Catal.* **2019**, *9*, 8433–8442.
62. Xu, H.-J.; Liang, Y.-F.; Cai, Z.-Y.; Qi, H.-X.; Yang, C.-Y.; Feng, Y.-S. CuI-Nanoparticles-Catalyzed Selective Synthesis of Phenols, Anilines, and Thiophenols from Aryl Halides in Aqueous Solution. *J. Org. Chem.* **2011**, *76*, 2296–2300.
63. Griffin, J. M.; Forse, A. C.; Tsai, W.-Y.; Taberna, P.-L.; Simon, P.; Grey, C. P. In Situ NMR and Electrochemical Quartz Crystal Microbalance Techniques Reveal the Structure of the Electrical Double Layer in Supercapacitors. *Nat. Mater.* **2015**, *14*, 812–819.